

AD 623 455

Proceedings of the
FLUID AMPLIFICATION SYMPOSIUM

October 1965

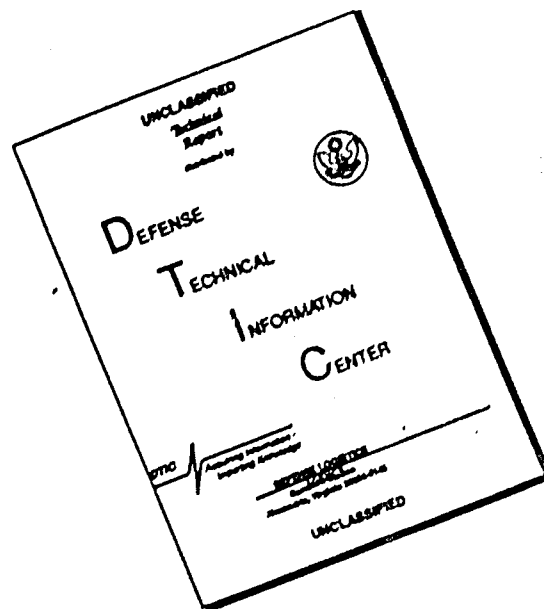
VOLUME I

CLEARINGHOUSE FOR FEDERAL SCIENTIFIC AND TECHNICAL INFORMATION			
Hardcopy	Microfiche		
\$ 7.00	\$ 1.75	3.56	20 a
ARCHIVE COPY			



U.S. ARMY MATERIEL COMMAND
HARRY DIAMOND LABORATORIES
WASHINGTON, D.C. 20438

DISCLAIMER NOTICE



THIS DOCUMENT IS BEST QUALITY AVAILABLE. THE COPY FURNISHED TO DTIC CONTAINED A SIGNIFICANT NUMBER OF PAGES WHICH DO NOT REPRODUCE LEGIBLY.

**BLANK PAGES
IN THIS
DOCUMENT
WERE NOT
FILMED**



DEPARTMENT OF THE ARMY
HARRY DIAMOND LABORATORIES
WASHINGTON, D.C. 20438

IN REPLY REFER TO
AMXDO-TS

1 September 1965

TO : Recipients of Fluid Amplification Symposium, Volume I,
October 1965

FROM : Technical Reports Group

SUBJECT: Errata in "New Comprehensive Studies on Sudden Enlargements,"
by K. P. H. Frey, N. C. Vasuki, and P. Trask, University
of Delaware (pages 119-137 of Volume I)

Fifth page, line 10 should read:

"This behavior creates three-dimensional flow, 3. A high degree of turbulence is associated with that flow type. The Coanda effect is...."

Seventh page, line 2 should read:

"...the cross section is at the minimum static pressure. Until the final analysis is conducted, the approximate assumption may be used that a velocity distribution similar to that at the inlet prevails at that cross section. This means that the change of static pressure is assumed to be due to vortex generation and turbulence. If one uses this location as...."



DEPARTMENT OF THE ARMY

HARRY DIAMOND LABORATORIES

WASHINGTON, D.C. 20438 Mr. Kirshner/cg/7556

IN REPLY REFER TO:
AMXDO-RCA

1 NOV 1965

TO : Recipients of Fluid Amplification Symposium Proceedings
Volume I, October 1965

FROM : Chief, Fluid Systems Branch, HDL

SUBJECT: Errata in "A Definition of the Mechanical Potential Necessary
to a Fluid Circuit Theory," by Joseph M. Kirshner, HDL,
(page 248)

Page 248, lines following equation (6) should read:

"...where ds_r and ds_i are the reversible and irreversible portions of the entropy change associated with heat and viscous effects, respectively; since the reversible portion of the entropy is due to the heat flux,

$$\frac{d}{dz} \int_{A_1} (T ds_r) \rho v \cdot n dA = \alpha$$

and therefore equation 5 becomes

$$\frac{d}{dz} \int_{A_1} \left[T ds_i + \frac{v^2}{2} + \int \frac{dp}{\rho} \right] \rho v \cdot n dA = 0 \quad (7) \dots "$$

Proceedings of the
FLUID AMPLIFICATION SYMPOSIUM

Sponsored by the
HARRY DIAMOND LABORATORIES

26, 27, and 28 October 1965

VOLUME I



U.S. ARMY MATERIEL COMMAND
HARRY DIAMOND LABORATORIES
WASHINGTON, D.C. 20438

CONTENTS

	<u>Page</u>
1. THEORETICAL STUDY OF A CONVERGENT NOZZLE AND FREE JET FLOW, J. C. Williams III and F. O. Smetana, North Carolina State University	5-28
2. EXPERIMENTAL STUDY OF A CONVERGENT NOZZLE AND FREE JET FLOW, Donald I. McRee, Corning Glass Works, Raleigh, North Carolina	29-59
3. PRESSURE RECOVERY CHARACTERISTICS OF COMPRESSIBLE TWO-DIMENSIONAL FREE JET FLOWS, R. E. Olson and J. F. Camarata, United Aircraft Research Labs, East Hartford, Connecticut	61-92
4. THE FLOW OF TURBULENT INCOMPRESSIBLE TWO-DIMENSIONAL JETS OVER VENTILATED CAVITIES, John R. C. Pedersen, British Aircraft Corporation (Operating) Limited, England	93-109
5. FLOW STABILITY FOR TWO-DIMENSIONAL CUSP DEVICES, Prof. K. P. H. Frey and N. C. Vasuki, University of Delaware	111-118
6. NEW COMPREHENSIVE STUDIES ON SUDDEN ENLARGEMENTS, K. P. H. Frey, University of Delaware	119-137
7. SPREADING RATES OF COMPRESSIBLE TWO-DIMENSIONAL REATTACHING JETS UPSTREAM OF REATTACHMENT, R. E. Olson, United Aircraft Research Labs, East Hartford, Connecticut	139-165
8. CALCULATION OF THE SEPARATION OF A JET ATTACHED TO A CONVEX WALL, Marcel Kadosch, France	167-179
9. ANALYSIS OF THE STEADY-FLOW PNEUMATIC RESISTANCE OF PARALLEL CAPILLARIES, Capt. Harry N. White, Harry Diamond Laboratories	181-213
10. SIMILARITY RELATIONS AND CHARACTERIZATION OF PURE FLUID ELEMENTS, H. H. Glaettli, Zurich, Switzerland	215-222
11. DYNAMIC SIMILARITY ANALYSIS OF COMPRESSIBLE VISCOUS FLUID PIPE FLOW, Fabio R. Goldschmied, Sperry Utah Company	223-243

CONTENTS (Cont'd)

	<u>Page</u>
12. A DEFINITION OF THE MECHANICAL POTENTIAL NECESSARY TO A FLUID CIRCUIT THEORY, Joseph M. Kirshner, Harry Diamond Laboratories	245-250
13. ON THE FUTURE OF DYNAMIC ANALYSIS OF FLUID SYSTEMS, Forbes T. Brown, MIT, Cambridge, Massachusetts . . .	251-265
14. AN APPROACH TO BROAD BAND FLUID AMPLIFICATION AT ACOUSTIC FREQUENCIES, H. H. Unfried, Mattel, Inc., Hawthorne, California	267-296
15. PREDICTING CLOSED LOOP STABILITY OF FLUID AMPLIFIERS FROM FREQUENCY RESPONSE MEASUREMENTS, Gary L. Roffman and Silas Katz, Harry Diamond Laboratories .	297-314
16. ON THE DYNAMICAL CHARACTERISTIC OF FLUID AMPLIFIERS AND ELEMENTS, Peter A. Orner, Giannini Controls Corporation, Malvern, Pennsylvania	315-330
17. IMPEDANCE MATCHING IN BISTABLE AND PROPORTIONAL FLUID AMPLIFIERS THROUGH THE USE OF A VORTEX VENT, W. F. Hayes and C. Kwok, Aviation Electric, Montreal, Canada	331-359
DISTRIBUTION	361-368

THEORETICAL STUDY OF A CONVERGENT NOZZLE
AND FREE JET FLOW

by

J. C. Williams, III

and

F. O. Smetana

of

North Carolina State University

Theoretical Study of a Convergent Nozzle and Free Jet Flow

Introduction

In order to improve the effectiveness of a fluid control device, it is helpful to understand the fluid dynamic phenomena which occur therein. In many cases these phenomena are extremely complicated involving as they do the interaction of the fluid with solid boundaries and imposed pressure gradients. Fortunately, however, there is an extensive legacy in fluid dynamics from which one may draw information and methods of analysis. The flow field within the power jet nozzle does not seem appreciably different from the flow in many fluid metering devices; the free jet issuing from a control nozzle does not seem to be extensively different from the free jet issuing from a wind tunnel or propulsion nozzle; etc. The primary difference between the fluid flows found in fluid control devices and the "conventional" fluid flows seems to be that of scale. Also, there is the additional difference that geometries often found in fluid control devices for reasons of manufacturing simplicity are seldom seen in larger scale devices because of poor performance.

In view of the similarity between the flow fields found in fluid control devices and those studied extensively in larger devices some qualitative statements can immediately be made regarding the design of fluid control devices. One would expect long boundary layer runs or severe adverse pressure gradients to affect performance adversely. Quantitative improvements must, however, come from analysis (or experiment) which properly accounts for geometry and scale.

The present paper is an outgrowth of a study, for the Corning Glass Works, to determine the extent to which the flow fields in a small control device could be predicted analytically, and to determine the extent of the losses in the power jet nozzle of such a device. An analysis was made of the flow field in an essentially two-dimensional (width to nozzle height ratio of 50) power jet nozzle consisting of a plenum chamber, contraction region and constant area nozzle. The analysis includes the calculation of the boundary layer growth in the throat, the discharge coefficient, the velocity profiles in the jet, the spreading of the jet and the pressure recovery in a receiver placed in the jet. The results of this analysis are compared, in a companion paper, with an experimental investigation of the flow fields in an identical power jet nozzle and jet. This comparison indicates that the analysis predicts, with reasonable accuracy, both the flow field and the losses in a small power jet nozzle.

The Power Nozzle and Free Jet

In order to make a valid comparison between the analytical and the experimental investigations it was necessary, at the outset, to decide on a configuration which was both amenable to analysis and representative of current fluid amplifier design. The configuration chosen is shown in Figure 1.* In order to simplify the analysis, a high aspect ratio (width to height) configuration was chosen so that end effects would be small and one could logically assume that the flow was essentially two-dimensional.

The power jet nozzle consists of a parallel wall plenum chamber, a quarter round contraction and a long parallel wall throat. It was necessary to have plenum chamber large enough to insure low velocity at all pressures and to damp out all entrance disturbances. Thus, the plenum chamber height was taken to be 5 times the throat height. The quarter round contraction was chosen so that the flow would remain attached to the wall at the entrance to the throat, i.e. there will be no vena contracts in the throat. The throat length was taken to be 10 times the throat height. Thus, the throat length can be systematically cut back to study the effect of throat length on the velocity distribution and on the losses in the throat (although this was not done in the experimental study). The area downstream on the throat is free of channel walls so that the analysis considers only a free jet devoid of any attachment effects.

In the analysis of the fluid flow in the power jet nozzle, the actual nozzle scale does not appear explicitly but is reflected in the flow Reynolds number. A typical Reynolds number for the present analysis was taken to be 2000 which corresponds to a throat height of 0.010 inches and a stagnation pressure of about two atmospheres in air. If the free jet is laminar, the scale is again reflected implicitly in the Reynolds number; the Reynolds numbers were taken consistent with that used in the power jet nozzle. In the turbulent jet the Reynolds number is not important since the viscous effects are small compared with the turbulent mixing phenomenon. The scale is given implicitly in a scaling factor related to the turbulent mixing. Values of this scaling factor were again taken consistent with the Reynolds number range assumed for the power jet nozzle.

Velocity Distribution, Pressure Distribution and Mass Flow in the Nozzle

(a) Velocity Distribution. For simplicity one usually assumes that the flow in a nozzle is one-dimensional, that is, the velocity is

*Figures appear on pages 25 through 28.

uniform across the channel. Two-dimensional effects and viscous effect are then lumped together in an experimentally - determined "discharge coefficient" which is a measure of the difference between the actual flow and that calculated from the measured pressures, areas, and temperature assuming one-dimensional flow. However, since the exact velocity distribution across the nozzle at its exit is very influential in determining the characteristics of the free jet, it is instructive to study the effect of the nozzle geometry on the velocity distribution throughout the nozzle.

In the plenum chamber, that is the region upstream of the contraction, the average flow velocity is limited to about 130 feet per second by the five to one contraction ratio. With a larger contraction ratio, the average plenum chamber velocity would be even lower. This value (5) is sufficiently large that the density variations across the plenum channel are less than 1%. The low velocity and the 5 to one contraction also serve to damp out most of the velocity variations present in the flow injected into the plenum, provided the plenum channel is longer than about 10 channel heights. As a result of this choice of geometry, it is reasonable to assume that the flow approaching the contraction is uniform.

The effect of the contraction on the velocity distribution across the channel is twofold: first, a boundary layer of reduced flow velocity builds up along the walls because of the retarding action of the wall friction; and second, the flow near the walls is accelerated by centrifugal forces associated with the curved walls. As a result of the second phenomenon, the flow velocity near the wall tends to be greater than at the center of the channel; the first phenomenon leads to the opposite effect. In general, the smaller the radius of the contraction, the smaller the boundary layer growth and the larger the centrifugal effect. When the contraction radius is less than about 0.25 throat heights, the flow separates from the wall. It then requires a run of several throat heights in order for the flow to reattach to the wall. If the throat is too short, reattachment will not occur and the flow velocity at the exit of the nozzle will be very non-uniform.

To facilitate the analysis, a geometry was chosen which would produce the most uniform profile possible at Reynolds numbers within the range of present interest. This entails selection of an inlet radius which leads - in so far as possible - to a cancellation of the boundary layer effect by the centrifugal effect. To determine the centrifugal effect a simplified form of the inviscid, compressible analysis of Oswatitsch and Rothstein (Reference 1) was employed. The results of the simplified analysis were found to agree with wind tunnel measurements to within 1%, the actual variation being somewhat greater than that predicted by the simple theory. In the theory of Oswatitsch and Rothstein, power series are used to represent the velocity components. In the simplified analysis only terms through second order are retained and only the flow at the throat is considered. The mass flow is con-

sidered to be the same as the one-dimensional value. One then obtains as the expression for the velocity distribution at the throat the equation

$$\frac{u}{u_{c1}} = \left(1 - \frac{h}{12R}\right) \left(1 + \frac{Y^2}{hR}\right) \quad (1)$$

where u_{c1} is the centerline velocity for one-dimensional flow

h is the channel height

R is the radius of curvature of the wall

Y is the distance measured from the centerline

In this case R was chosen as $2h$. Thus

$$\frac{u}{u_{c1}} = 0.9583 \left(1 + \frac{Y^2}{2h^2}\right) \quad (2)$$

A table of values of this equation is given below:

$\frac{u}{u_{c1}}$	$\frac{2Y}{h}$
0.9583	0
0.9595	.1
0.9631	.2
0.9691	.3
0.9775	.4
0.9883	.5
1.0014	.6
1.0170	.7
1.0350	.8
1.0553	.9
1.0782	1.0

To determine the effect on the velocity distribution caused by wall friction, the following approach was employed: Since the Mach number at the throat can never exceed unity and since the boundary layer for a $M=1$ flow is not measurably different from that for a $M=0$ flow at the same Reynolds number, the nozzle flow was assumed to be incompressible.

From the fact that the throat area in this particular case is $1/5$ the upstream area, it was assumed that the velocity just outside the boundary layer, u_δ , was given by

$$u_\delta = 5 u_\infty \sin^2 \phi$$

where ϕ is the angle of the normal to the surface measured from the upstream flow direction. The throat begins at $\phi = 90^\circ$.

According to the von Kármán momentum integral method, as modified by Waltz, for this geometry,

$$\frac{u_\infty \theta^2}{R \nu} = \frac{0.47}{(u_s/u_\infty)^6} \int_0^\phi (5 \sin^2 \phi)^5 d\phi$$

$$= 0.0395 \text{ for } \phi = 90^\circ$$

R is the radius of curvature of the contraction, θ is the momentum thickness and ν the kinematic viscosity.

Since $du_s/dx \rightarrow 0$ for the throat and beyond, it was assumed that $\delta^* = 2.554 \theta$ in this region. Now $R = 2h$; the displacement thickness δ^* is therefore

$$\delta^* = \frac{1.615 h}{\sqrt{\frac{u_s h}{\nu}}}$$

the boundary thickness, δ , can be derived from this and can be shown to be

$$\delta = \frac{5.4 h}{\sqrt{\frac{u_s h}{\nu}}}$$

Since the momentum integral method assumes a velocity profile given by

$$\frac{u}{u_s} = 2 \frac{y}{\delta} - 2 \left(\frac{y}{\delta} \right)^3 + \left(\frac{y}{\delta} \right)^4$$

where $Re = \frac{u_s h}{\nu}$ and y is measured from the wall outward, one can easily arrive at an expression for the velocity profile at $\phi = 90^\circ$ in the boundary layer of the channel under study:

$$\frac{u}{u_s} = 0.37 Re^{\frac{1}{2}} \left(\frac{1}{2} - \frac{Y}{h} \right) - 0.0127 Re^{\frac{3}{2}} \left(\frac{1}{2} - \frac{Y}{h} \right)^3$$

$$+ 0.00118 Re^2 \left(\frac{1}{2} - \frac{Y}{h} \right)^4 \quad (3)$$

Some typical values for a Reynolds number of 10^3 are

$\frac{u}{u_s}$	$\frac{2Y}{h}$
0	1.0
.543	.9
.888	.8
1.0	.7

By multiplying these results with those obtained previously for two-dimensional flow at the throat one has a good indication of the actual velocity profile at $Re = 10^3$:

$\frac{u}{u_{c1}}$	$\frac{2Y}{h}$
0	1.0
0.572	.9
0.919	.8
1.017	.7
1.0014	.6
.9883	.5
.9775	.4
.9691	.3
.9631	.2
.9583	0

As the flow moves into the constant area section, the centrifugal effect disappears and only the viscous effect is present. An analysis was carried out - again using the momentum integral method - to determine the boundary layer growth in the constant area section. From continuity considerations and the assumption of incompressible flow, the velocity outside of the boundary layer is

$$u_s = u_{s1} \frac{h - 2\delta_1^*}{h - 2\delta^*}$$

where the subscript (1) refers to conditions at the beginning of the constant area section.

Since the boundary layer grows as x increases, continuity requires that the pressure fall with increasing x . With such a pressure gradient, δ^*/θ is approximately constant. It is taken here as 2.4. The momentum integral equation can then be integrated to give

$$\frac{x}{h} \left\{ \frac{1}{Re \left[1 - 2 \frac{\delta^*}{h} \right]} \right\} 0.0235 = \left\{ \frac{\theta}{2.4h} + 0.2165 \ln \left(1 - 4.8 \frac{\theta}{h} \right) + 0.13 \left[\frac{1}{1 - 4.8 \frac{\theta}{h}} - 1 \right] \right\} \frac{\theta}{h} \quad (4)$$

$\frac{\theta}{h}|_0$ = value of $\frac{\theta}{h}$ at the beginning of constant area section. From

these results, figures 2 and 3 have been prepared. A Reynolds number of 2000 is assumed. Since $\delta = 3.33 \delta^*$ one can readily determine δ from these figures; and from δ^* , u/u_δ using the relationship given previously. It will be seen that for a throat $15h$ long and a Reynolds number of 2000, the boundary layer will completely fill the downstream end of the throat and the velocity profile is virtually parabolic.

(b) Pressure Distribution. From the distribution of velocity and a knowledge of the dissipation one can, of course, always calculate the pressure distribution. There are, however, some general observations which may be made from which one may obtain quite a reliable indication of the pressure distribution. First, for Reynolds numbers above 2000, the flow consists of a isentropic core and a boundary layer. Thus, except for perturbations caused by the boundary layer and the centrifugal effects near the contraction, the flow can be treated by isentropic one-dimensional theory. The existence of a boundary layer does not affect the pressure distribution except to the extent that the increasing displacement thickness as the flow moves downstream tends to delay the attainment of the maximum velocity (minimum pressure) until the downstream end of the nozzle. Second, two-dimensional effects - at least in the nozzle under discussion - are relatively small. At the beginning of the throat where the effect is greatest, the pressure varies from about 10% over the one-dimensional value at the centerline to about 10% under at the wall.

A good estimate of the pressure distribution can, therefore, be arrived at by first calculating the centerline Mach number at the throat exit corresponding to the overall pressure ratio. Then, from a knowledge of δ^* vs x and working upstream from the exit, calculate the pressure corresponding to the area $(h - 2\delta^*)b$ where b is the width of the throat (in this case $50h$). For example, if the overall pressure ratio is 1.896 the exit centerline Mach number should be approximately 1.0. Assuming a Reynolds number of about 2000, $\frac{\delta^*}{h}$ at $x/h = 10$ is 0.124. $1 - 2\delta^*/h$ is

0.752. At $x/h = 8$, $1 - 2\delta^*/h$ is 0.776. The ratio of areas is 1.032. The corresponding ratio of pressures is 1.225. At $x/h = 0$, the ratio of areas is 1.236 and the corresponding pressure ratio (P_x/P_{exit}) is 1.53. Compared with the upstream pressure, the pressure at the beginning of the

of the throat is 0.806 while at $x/h = 8$ it is 0.646. The authors have found that simple calculations of this type give reasonably good agreement with the measurements made on axisymmetric channels at comparable Reynolds numbers.

(c) Mass Flow. As indicated previously, one usually expresses the mass flow by the one-dimensional mass flow times a discharge coefficient. It is convenient to consider that, in the absence of significant centrifugal effects, the flow consists of a central core of uniform velocity containing all the mass of the system. The dimensions of the core are therefore $h - 2\delta^*$ and the mass flow is $\rho_s u_s (h - 2\delta^*)$. The ideal mass flow for the same pressures is $\rho_s u_s h$ so that

$$C_d = \frac{\rho_s u_s (h - 2\delta^*)}{\rho_s u_s h} = 1 - 2 \frac{\delta^*}{h} \quad (5)$$

It was also found that this expression would agree with measurement over a wider range of conditions if it is written in the form

$$C_d = \frac{1}{1 + 2 \frac{\delta^*}{h}}$$

It was shown previously that at $x/h = 10$

$$\frac{\delta^*}{h} = \frac{5.7}{\sqrt{Re}}$$

where $Re = \frac{\dot{m}}{\mu b}$

Since $C_d = \frac{1}{1 + \frac{11.4}{\sqrt{\frac{\dot{m}}{\mu b}}}}$ one can solve for \dot{m} readily

in terms of \dot{m}_i

$$\dot{m} = \dot{m}_i + 65\mu b \left[1 - \sqrt{1 + \frac{\dot{m}_i}{32.5\mu b}} \right] \quad (6)$$

where

$$\dot{m}_i = \frac{p_1 A_2}{\sqrt{T_s}} \left[\frac{2\gamma}{(\gamma-1)R} \right]^{\frac{1}{2}} \frac{\sqrt{\left(\frac{p_2}{p_1}\right)^{\frac{2}{\gamma}} \left[1 - \left(\frac{p_2}{p_1}\right)^{\frac{\gamma-1}{\gamma}}\right] \left[1 - \left(\frac{A_2}{A_1}\right)^2 \left(\frac{p_2}{p_1}\right)^{\frac{\gamma+1}{\gamma}}\right]}}{1 - \left(\frac{p_2}{p_1}\right)^{\frac{2}{\gamma}} \left(\frac{A_2}{A_1}\right)^2}$$

P_1 is the upstream pressure

P_2 is the exit pressure

$A_1 = 5bh$ (for the present nozzle)

$A_2 = bh$

γ = ratio of specific heats

R = gas constant

T_s = stagnation temperature

One would expect these relationships to be valid for Reynolds numbers above that for which the boundary layers merge and below that for which the flow becomes turbulent i.e. generally over the range from 2×10^3 to 2×10^6 .

The Free Jet

The free jet may be completely laminar, completely turbulent or transitional (transition from laminar to turbulent flow in the jet). In each of these types of flow the jet may be divided into three separate regions (see Figure 4). Region I is characterized by a more or less uniform core bounded by a mixing region. As the flow proceeds downstream, the core is dissipated by viscous (or turbulent) mixing until at the end of region I the uniform core has completely disappeared. In region III, "far" downstream, the jet is fully developed and the velocity profiles are self similar, i.e. the velocity depends upon a single similarity coordinate. Region II is a transitional region in which the velocity profiles adjust from the non self-similar profiles at the end of region I to be the self-similar profiles in region III. Experimental evidence indicates that the extent of region II is very small, hence no further consideration will be given to region II in this work.

The maximum velocity within the jet occurs at the exit of the nozzle. If this maximum velocity is less than the local sonic velocity then the jet is subsonic throughout and the static pressure is constant within the jet structure. Since there is neither pressure gradient nor

wall shear is the subsonic free jet, there is no mechanism by which the momentum content of the jet can be reduced and one is led to the important conclusion that the total momentum content within the jet is constant. The jet then only spreads the momentum by means of viscous or turbulent mixing. It is this spreading of the momentum within the jet which is of primary interest here.

Laminar Free Jet

Region I. The interest here is in determining the rate at which the jet spreads and the rate at which the uniform core is dissipated as a result of mixing. Thus for simplicity, we consider only half of the symmetrical jet as shown in Figure 4.

The analysis of the spreading of a free jet should originate with the full Navier Stokes Equations. Solutions to the full equations are, however, extremely rare. Fortunately, experience has shown that an adequate description of jet-like phenomenon can be obtained using the boundary layer equations. In the case of steady two-dimensional incompressible flow with no pressure gradients these equations are:

$$\frac{\partial u}{\partial x} + \frac{\partial v}{\partial y} = 0$$

$$\rho u \frac{\partial u}{\partial x} + \rho v \frac{\partial u}{\partial y} = \mu \frac{\partial^2 u}{\partial y^2}$$

The classical solution to these equations for the case of a free jet boundary may be found in standard texts (e.g. References 2 & 3). It will be only briefly reviewed here. In introducing the non-dimensional stream function, $f(\eta)$, defined by

$$\psi = \sqrt{U \nu x} f(\eta)$$

and the similarity variable, η , defined by $\eta = y \sqrt{\frac{U}{\nu x}}$ where U is the center line velocity in the inviscid core, the continuity equation is satisfied identically and the momentum equation becomes:

$$f''' + f f'' = 0 \quad (7)$$

Here primes denote differentiation with respect to η . Since we are considering only one side of the jet, we apply the boundary conditions at $y = \pm \infty$. These conditions are

$$y(+\infty), \quad u = U$$

$$y(-\infty), \quad u = 0$$

$$\text{or } f'(+\infty) = 2, \quad f'(-\infty) = 0$$

The above third order differential equation requires three boundary conditions for a complete solution. For the third boundary condition, we take $f(0) = 0$ which is equivalent to taking a new origin for the y axis at each x . The solution to equation (7) with the boundary conditions $f'(+\infty) = 2$, $f'(-\infty) = f(0) = 0$ has been solved by a number of investigators. We use here that solution given by Christian (Reference 4).

In the present application, we are interested in the characteristic spreading and scale of the jet. These characteristics are given by d , the width of the uniform core, δ , the width of the mixing region and L the length of the uniform core. Fortunately, even though the boundary conditions are applied at $\pm\infty$, it turns out that the solution extends only over the range $-14 \leq \eta \leq +4$. The fact that we have shifted the axis to obtain a solution (see above) leads to some difficulty but this is overcome by taking advantage of conservation of momentum within the jet. Thus

$$\int_{y_-}^{y_+} \rho u^2 dy + \int_{y_+}^{cl} \rho U^2 dy = \rho U^2 \frac{h}{2}$$

Since the fluid is incompressible this yields

$$\frac{h}{2} = d + \int_{y_-}^{y_+} \left(\frac{u}{U}\right)^2 dy$$

and using the stream function defined above

$$\frac{d}{h} = \frac{1}{2} \left\{ 1 - \sqrt{\frac{x}{h}} \frac{1}{\sqrt{U h}} \int_{-14}^{+4} f'^2 d\eta \right\}$$

Employing the solution given in Reference 4 this becomes simply

$$\frac{d}{h} = \frac{1}{2} \left\{ 1 - \frac{14.94}{\sqrt{\frac{Uh}{\nu}}} \sqrt{\frac{x}{h}} \right\} \quad (8)$$

Thus, the width of the uniform core decreases as the square root of the distance from the nozzle exit plane. The length of region I is determined by the value of x at which $d = 0$. Thus

$$\frac{L}{h} = 0.0045 \frac{Uh}{\nu} \quad (9)$$

so that the length of the inviscid core increases directly with Reynolds number.

The width of the mixing region, δ , can be obtained directly from the solution. Hence,

$$\eta_+ = +4 = \frac{y_+}{2} \sqrt{\frac{U}{\nu x}}, \quad \eta_- = -4 = \frac{y_-}{2} \sqrt{\frac{U}{\nu x}}$$

$$\frac{\delta}{h} = \frac{y_+ - y_-}{h} = \frac{36}{\sqrt{\frac{Uh}{\nu}}} \sqrt{\frac{x}{h}} \quad (10)$$

The width of the mixing region increases as the square root of the distance from the nozzle exit plane.

It is clear from the above solution that to recover a large percentage of the momentum (or total pressure) in the jet one should operate at the highest possible Reynolds number Uh/ν . The receiver should be placed as close as possible to the nozzle exit.

Region III. Unless the Reynolds number for the flow is moderately large, regions I and II in the jet will be fairly small and any receiver placed downstream in the jet will see a region III type flow. Thus, it is necessary to determine the characteristics of this type flow. The flow in this region has also been analyzed previously and the results are presented in standard texts (e.g. Reference 2). The standard treatment yields for the velocity profiles in this region

$$u = 0.4543 \left(\frac{U^2 h^2}{x \nu} \right)^{\frac{1}{3}} \left[1 - \tanh \xi \right] \quad (11)$$

$$v = 0.5503 \left(\frac{U h \nu}{x^2} \right)^{\frac{1}{3}} \quad (12)$$

$$\xi = 0.2752 \left(\frac{U h}{\nu} \right)^{\frac{2}{3}} \frac{y}{h^{\frac{1}{3}} x^{\frac{2}{3}}} \quad (13)$$

The edge of the jet is defined by the condition $u = 0$ which occurs when $\tanh \xi = 1$ or $\xi \approx 6.5$. Thus, if S is the half span of the jet one obtains from equation (13):

$$\frac{S}{h} = \frac{23.65}{(Re)^{\frac{2}{3}}} \left(\frac{x}{h} \right)^{\frac{2}{3}} \quad (14)$$

where $Re = \frac{U h}{\nu}$. Thus in region III, the jet expands as $x^{2/3}$ instead of $x^{1/2}$ as found in region I.

More important for fluid amplifier application, however, is the pressure recovery in the jet. We use the volume average total pressure defined by

$$\bar{p}_0 = \frac{2}{b l} \int_0^l p_0 b dy$$

where l is the height of the receiver (or the height over which the total pressure is averaged). Employing the above velocity profile we obtain

$$\bar{p}_0 - p_e = \frac{0.748 \rho U^2}{(l/h)} \left[\operatorname{sech}^2 \xi_u \tanh \xi_u - \frac{2}{3} \tanh^3 \xi_u \right] \quad (15)$$

where

$$\xi_u = 0.1376 Re^{\frac{2}{3}} \frac{l}{h^{\frac{1}{3}} x^{\frac{2}{3}}}$$

For the special case in which $z = h$ (receiver height equal to nozzle height), $x/h = 10$ (receiver located 10 nozzle heights from the nozzle exit) and an exit pressure of one atmosphere the ratio $(\bar{p}_o - p_e)/(p_o - p_e)$ is presented in figure (6) as a function of Reynolds number. It is seen that unless the Reynolds number is extremely small ($p_o - p_e$ very small) a very large portion of the upstream total pressure is recovered in the receiver. This is verified by equation (14) which indicates that unless the Reynolds number is very low the jet spreads very little. Thus, any reasonable size receiver placed near the nozzle will recover almost all of the momentum in the jet.

The Turbulent Jet

While the analysis of the laminar jet is extremely enlightening and important for low or moderate Reynolds numbers, the Reynolds numbers which occur in practice are generally high enough to insure turbulent flow. The analysis of the turbulent jet is, however, more complex since the phenomenon of turbulence is, as yet, not completely understood. Thus, analysis of the turbulent jet is semi-empirical.

Region I. The free jet boundary problem has been studied by several investigations. We chose to employ the analysis of Goertler as presented in Reference 2. This analysis yields the velocity distribution.

$$u = \frac{U}{2} \left\{ 1 + \operatorname{erf}(\xi) \right\} \quad (16)$$

where $\xi = \sigma y/x$ and σ is empirically determined constant which has been found to be $\sigma = 13.5$. In this case, the origin of the y axis has not been shifted. Nevertheless, some difficulty occurs in that both the upper and lower edges of the jet extend, in theory at least, to infinity. Thus, the solution given above literally applies only to half a jet boundary. If we chose the upper edge of the jet as the point where $u/U = 0.999$, then at this point $\xi = 3.09$. Referring to Figure (5), we can write

$$d + y_+ = \frac{h}{2}, \quad \xi_+ = 3.09 = \frac{\sigma y_+}{x} \quad (17)$$

or

$$\frac{d}{h} = \frac{1}{2} - 0.229 \frac{x}{h}$$

Similarly if we define the outer edge of the jet as the point where $u/U = 0.001$ we can obtain

$$\frac{\delta}{h} = 0.458 \frac{x}{h} \quad (18)$$

In this region the core of the jet decreases linearly with distance from the nozzle exit and the jet mixing region increases linearly with distance from the nozzle exit. It should be noted that the turbulent mixing tends to spread the momentum much more rapidly than the laminar mixing and that the characteristic lengths in the turbulent jet are independent of Reynolds number. The length of the core can be found directly from equation (17) to be

$$\frac{L}{h} = 2.19 \quad (19)$$

Region III

In general it is not reasonable to expect the receiver to be placed in region I since this region extends only slightly more than two nozzle heights from the nozzle exit. It is more likely that the receiver will be placed in region III of the jet. In this region the velocities are given by (References 2 & 3).

$$u = \frac{\sqrt{3}}{2} \sqrt{\frac{K\lambda}{x}} [1 - \tanh^2 \eta]$$

$$v = \frac{\sqrt{3}}{4} \sqrt{\frac{K}{\lambda x}} \{ 2\eta [1 - \tanh^2 \eta] - \tanh \eta \}$$

$$\eta = \frac{\lambda y}{x}, \quad K = U^2 h$$

where λ is an empirical constant which has been found to be $\lambda = 7.67$. The outer edge of the jet is defined by $u = 0$, which occurs at $\eta = 6.5$, thus if $\delta/2$ is the half width of the jet

$$6.5 = \frac{\lambda \delta}{2x}$$

$$\text{or } \frac{\delta}{h} = 1.692 \frac{x}{h}$$

and again the jet spreads linearly with x . More important, however, is the momentum (total pressure) recovered in a receiver placed in the jet. Using the velocity distribution given above the volume average total pressure becomes

$$\bar{p}_0 - p_e = \frac{3}{4} \rho U^2 \left\{ \tanh \eta_u - \frac{1}{3} \tanh^3 \eta_u \right\} \quad (20)$$

where $\eta_u = \frac{\lambda}{2} \frac{1}{x}$ and $\frac{1}{2}$ is again the height of the receiver. Since $\rho U^2 = 2(p_0 - p_e)$, we may write this

$$\begin{aligned} \frac{\bar{p}_0}{p_0} = & \frac{6}{4} \frac{h}{\frac{1}{2}} \left[\tanh \eta_u - \frac{1}{3} \tanh^3 \eta_u \right] \\ & + \frac{h}{\frac{1}{2}} \frac{p_e}{p_0} \left\{ 1 - \frac{6}{4} \left[\tanh \eta_u - \frac{1}{3} \tanh^3 \eta_u \right] \right\} \end{aligned} \quad (21)$$

In the turbulent case, the pressure recovery is independent of the Reynolds number and depends only on the size and location of the receiver. The ratio \bar{p}_0/p_0 is presented in figure (6) as a function of P_0/p_0 for an air jet issuing into atmospheric pressure for receiver widths of one and two nozzle widths at $x/h = 10$. For fixed pressures, if the receiver size is increased, the volume average total pressure is decreased, not because more total pressure is not recovered, but because this total pressure is averaged over a larger volume.

If pressure recovery were the only consideration, one would (1) place the receiver as close as possible to the nozzle exit and (2) operate with as small a receiver as possible.

Losses in the Free Jet Due to Shock Waves

If the ratio of the upstream plenum chamber pressure to the receiver pressure exceeds about 1.5, there is the strong possibility of local regions of supersonic flow in the free jet terminated by shock waves. As the

overall pressure ratio increases, the probability for such shock waves increases. In contrast to the subsonic jet where dissipation is minimal, the supersonic jet terminated by a shock wave is a high loss (in terms of pressure recovery) system. For example, if the jet should expand to a Mach number of 3 and then decelerates through a normal shock, two thirds of the stagnation pressure is lost. Oblique shocks, of course, result in somewhat lower losses but in general one should avoid, in so far as possible, production of any shock waves since they constitute the largest loss in the type of system studied here.

Conclusions and Implications in Fluid Amplifier Power Jet Design

An analytical study has been made of the flow fields in a simple two-dimensional power jet nozzle and in the free jet downstream of such a nozzle. A number of important conclusions, related to power jet nozzle design, may be drawn from this study.

In the power jet nozzle, it is important to design as large a contraction, from the plenum chamber to the throat, as possible. This insures low flow velocities in the plenum chamber so that disturbances are damped out before they reach the throat. The radius of curvature in the contraction should be large to minimize velocity non-uniformities due to centrifugal effects. On the other hand, the length along the surface should be minimized, as much as possible to reduce the size of the boundary layer entering the throat. Sharp corners in the contraction region must be avoided to prevent boundary layer separation.

If the centrifugal effects are not significant, the non-uniformity of the velocity profile at the exit of the throat, as well as the total pressure loss in the throat are directly related to the throat length. The longer the throat, the more non-uniform the velocity profile and the greater the loss in momentum (or total pressure). At a Reynolds number of 2000, the velocity profile is almost fully developed 15 throat heights from the throat entrance.

The actual mass flow passed through the nozzle is also reduced by the growth of the boundary layer in the nozzle. It is imperative therefore that the throat length be made as short as possible, consistent with manufacturing considerations.

In the subsonic free jet there is no large mechanism for dissipation of momentum so that the effect of viscosity or turbulent mixing is to spread the momentum. The spreading of the free jet and the velocity profiles in the jet have been calculated for both laminar and turbulent jets. The average pressure in the jet is also calculated. These calculations lead to the conclusion, which is intuitively obvious, that a receiver for the jet should be placed as close to the jet exit as possible.

The validity of these analytical predictions is borne out in the following paper which reports on an experimental investigation on a configuration identical to that analyzed here.

REFERENCES

1. Oswatitsch and Rothstein, Das Strömung in exiner Laval düse,
NACA TM 1215, 1949
2. Schlichting, H. "Boundary Layer Theory" McGraw Hill Book Company,
New York, N. Y. 1960
3. Pai, S. I. "Fluid Dynamics of Jets" D. van Nostrand Inc., New York,
N. Y. 1954
4. Christian, William J. "Improved Numerical Solution of the Blasius
Problem with Three-Point Boundary Conditions", Journal of the Aero-
space Sciences, Vol. 28, No.11 (1961), pp. 911-912

Symbols

b	-	span of the nozzle
c_d	-	discharge coefficient
d	-	half height of the uniform core in the jet
f	-	non-dimensional stream function
h	-	height of the nozzle throat
K	-	momentum per unit mass
L	-	length of the uniform core in the jet
\dot{m}	-	mass flow
p	-	static pressure
P_o	-	stagnation (total) pressure
\bar{P}_o	-	volume average stagnation pressure
R	-	gas constant
Re	-	Reynolds number
T	-	temperature
u	-	x component of velocity
u_{∞}	-	velocity in plenum
U	-	x component of velocity in the jet core
v	-	y component of velocity
x	-	geometric coordinate
y	-	geometric coordinate
Y	-	distance measured from the wall in the contraction
γ	-	ratio of specific heats
z	-	height of the receiver (or width over which total pressure is averaged)
η	-	transformed y coordinate
λ	-	empirical constant
μ	-	coefficient of viscosity
ν	-	kinematic viscosity
ξ	-	transformed y coordinate
ρ	-	density
σ	-	empirical constant
ϕ	-	angle in contraction measured from upstream direction
ψ	-	stream function

Subscripts

∞	-	upstream conditions
δ	-	at edge of boundary layer
o	-	stagnation conditions
i	-	ideal

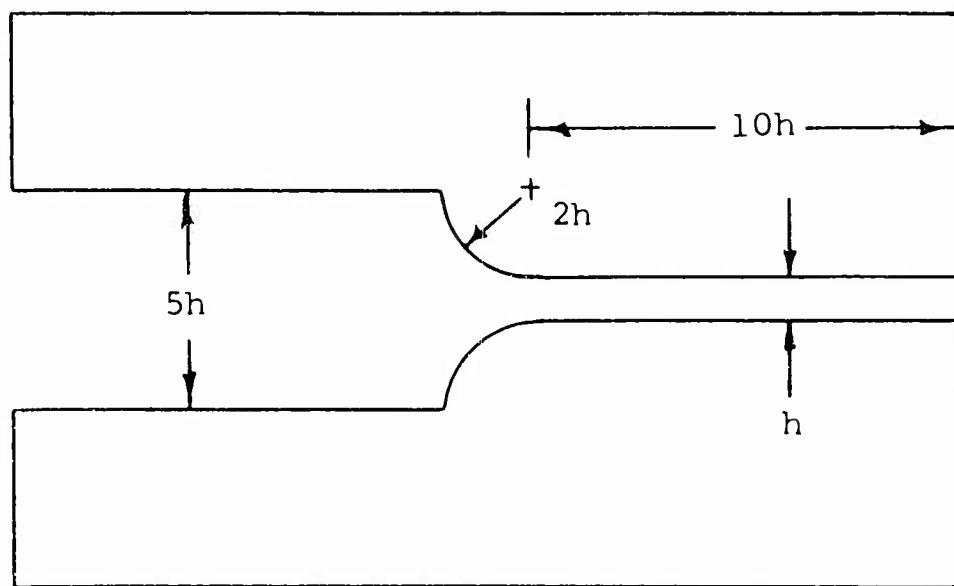


Figure 1.- POWER JET NOZZLE

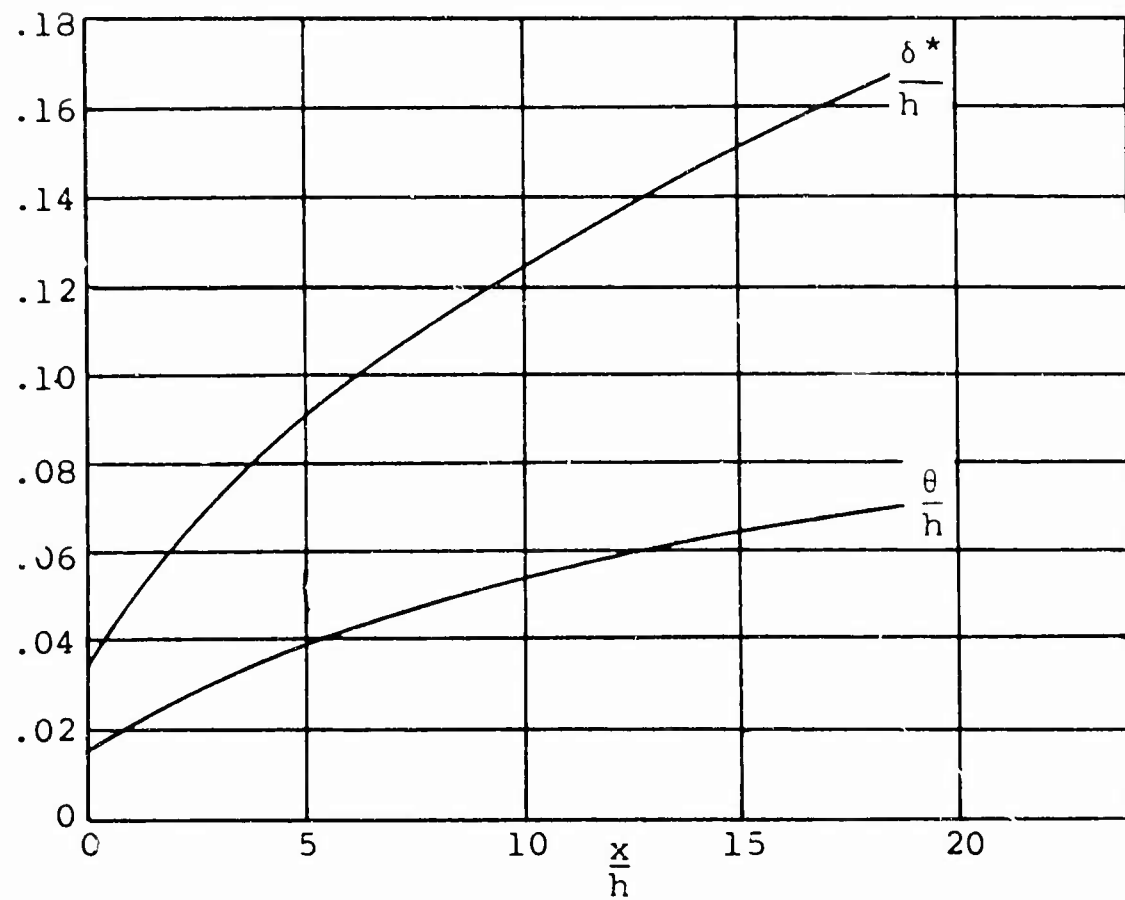


Figure 2.- DISPLACEMENT THICKNESS AND MOMENTUM THICKNESS IN THE THROAT.

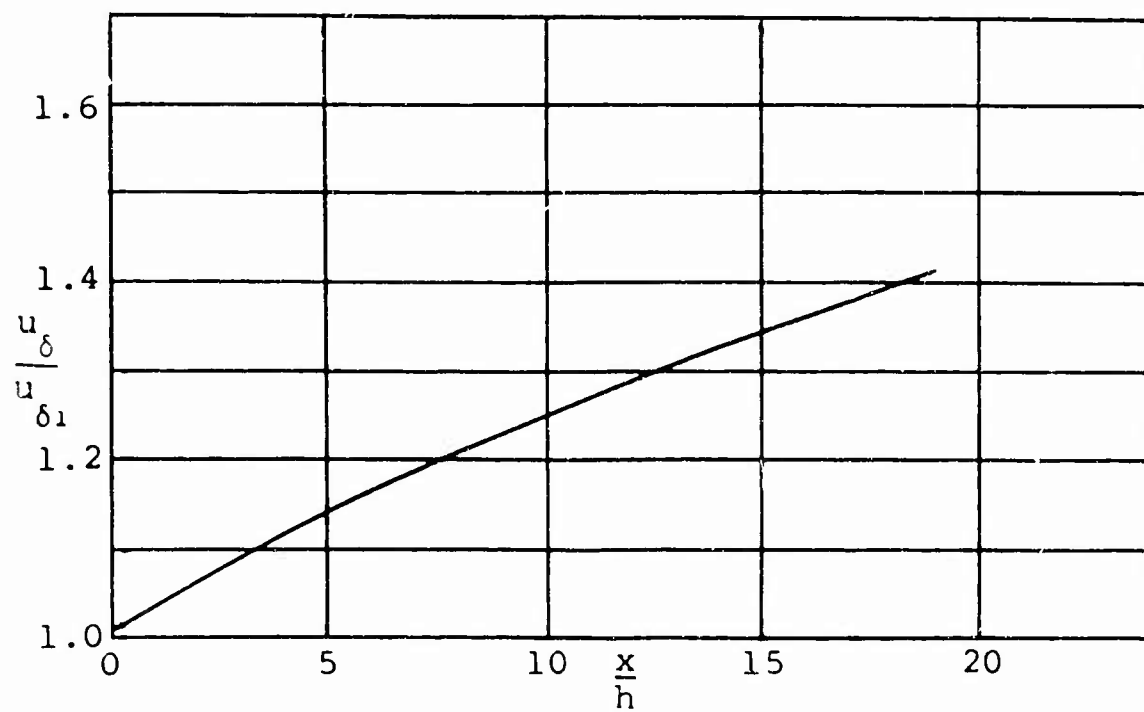


Figure 3.- CENTERLINE VELOCITY IN THE THROAT.

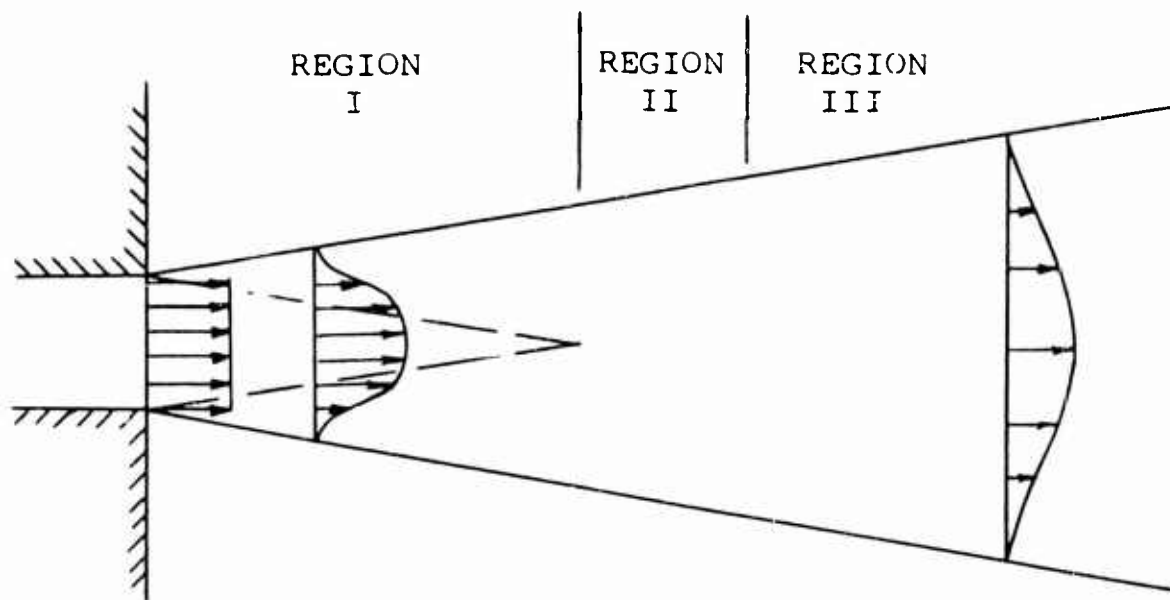


Figure 4.- THE FREE JET

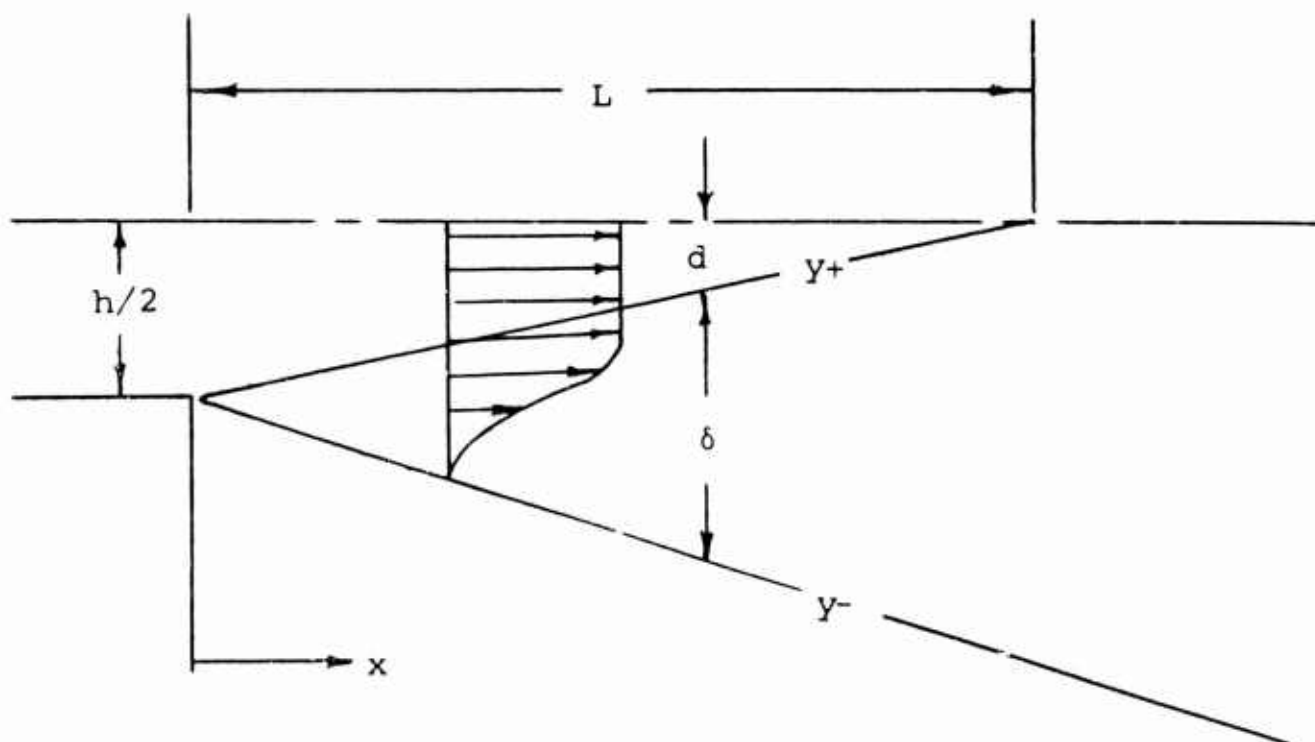


Figure 5.- THE FREE JET BOUNDARY IN REGION I

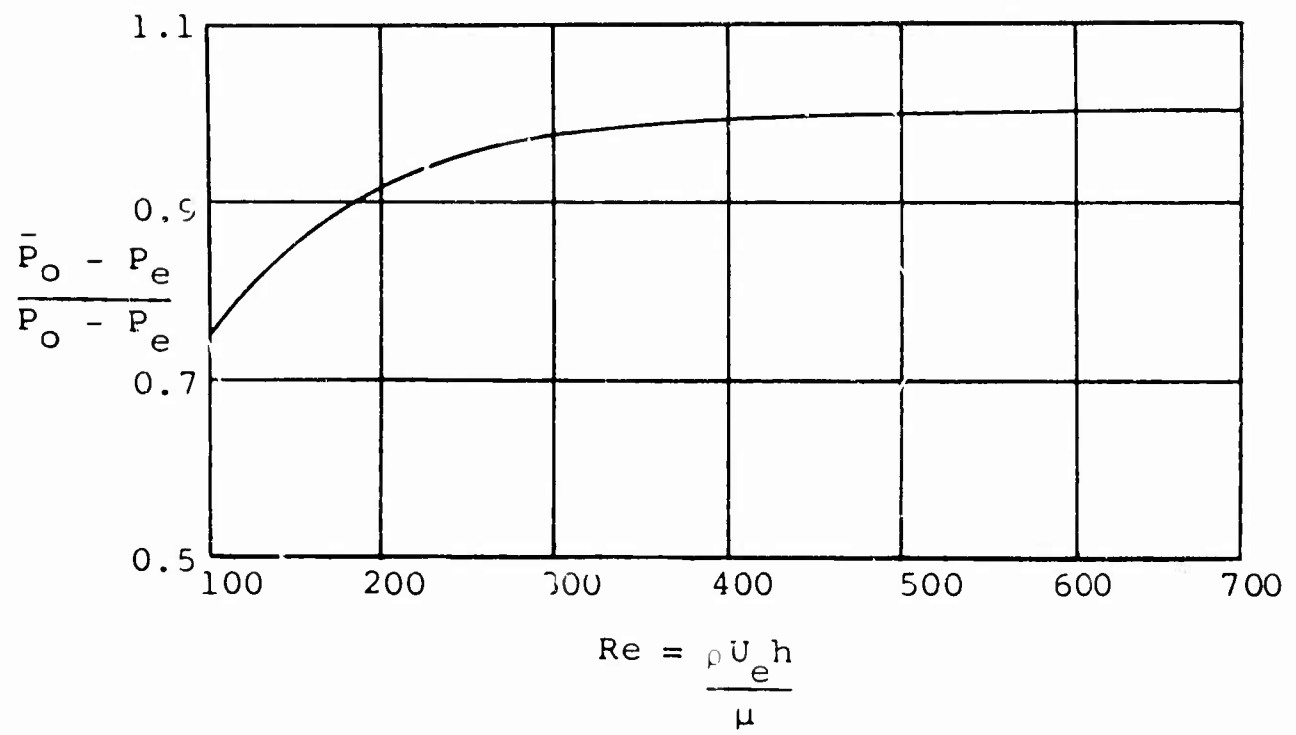


Figure 6.- PRESSURE RECOVERY IN A LAMINAR JET

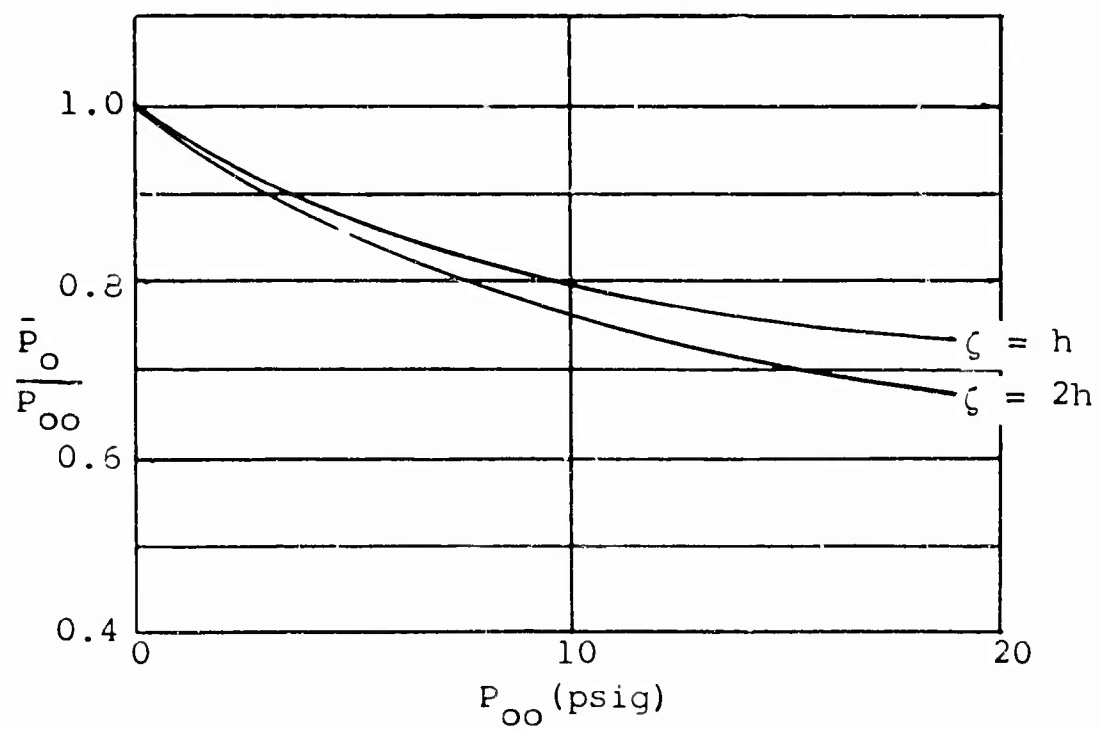


Figure 7.- PRESSURE RECOVERY IN A TURBULENT JET


EXPERIMENTAL STUDY OF A CONVERGENT NOZZLE AND FREE JET FLOW

by

Donald I. McRee

CORNING GLASS WORKS
ELECTRONIC RESEARCH LABORATORY
RALEIGH, NORTH CAROLINA

ABSTRACT



An experimental study is made of the two-dimensional convergent nozzle which was theoretically analyzed in a companion paper. Experimental results are compared with the theoretical analysis. Velocity profiles, jet core lengths, pressure loss due to mixing downstream of the nozzle exit, mass flows, and discharge coefficient are presented for jet supply pressures of approximately 16 to 31 psia. In most cases the experimental and theoretical results compared very favorably and demonstrated the usefulness of theory in predicting jet behavior.

INTRODUCTION

The operating characteristics and efficiency of a fluid amplifier are greatly dependent upon the power jet and the nature of the flow through the power jet. Very little experimental work has been done in the area of small jets (order of 0.010 inch); therefore, it is important to study small jet characteristics so as to be able to design fluid amplifiers with the highest possible efficiency and consistent operating behavior.

In the companion paper, Dr. F. O. Smetana and Dr. J. C. Williams, III have performed a theoretical analysis of a two-dimensional convergent jet. The analysis included the calculation of jet velocity profiles, core lengths, profile spreading with distance from the jet, pressure recovery 10 jet widths from the nozzle exit, mass flows for given input pressures and discharge coefficients. An experimental investigation of the jet has been performed. The supply pressure to the jet ranged from approximately 16 to 31 psia,

which corresponded to a Reynolds' number range of approximately 1500 to 6200 based on the width of the nozzle exit. Velocity surveys were taken at 1, 2, 3, 5, 10, 20, 50, 75, 100, 150, and 200 jet widths from the nozzle exit. Total pressure surveys were taken at 1, 10, and 20 jet widths from the exit. The experimental data obtained from the investigation were reduced to a form which could be compared with the theoretical analysis.

Although the physical phenomena involved in a free jet are not the same as in the bounded jet, I have, in some instances, discussed the results from the point of view that the jet being tested is the power jet or nozzle of a fluid amplifier. This method of discussing the results is used so as to view the results in terms of fluid amplifier application.

SYMBOLS

b	total profile width
C_d	discharge coefficient
h	nozzle width
\dot{M}_{actual}	theoretically calculated actual mass flow = $C_d \dot{M}_{\text{cal}}$
\dot{M}_{cal}	calculated mass flow
P_e	ambient pressure
P_{te}	nozzle exit total pressure
P_{tc}	supply total pressure
\bar{P}_t	average total pressure
P_{t10h}	integrated total pressure ten jet widths from the nozzle exit
Re	Reynolds' number based on width of nozzle, $\frac{\rho U h}{\mu}$
U	velocity
U_o	centerline velocity of any given velocity profile
U_{oo}	exit centerline velocity

SYMBOLS (continued)

x	distance from jet exit measured along a line drawn through the center of the nozzle
x'	length of core region
y	perpendicular distance from a line drawn through the center of the nozzle
δ	boundary layer thickness
δ^*	displacement thickness
η	correlating parameter, $\eta = \frac{\sigma y}{x}$
μ	absolute viscosity
ρ	mass density
σ	experimentally determined constant by Reichardt ² = 7.67

APPARATUS

Model

The jet design used in the investigation was a two-dimensional convergent nozzle. A sketch of the nozzle with dimensions is shown in figure 1(a).^{*} The model was very accurately fabricated from brass, the nozzle area being within 2 percent of design. The area of the jet chamber was 5 times the nozzle area. The aspect ratio of the model was 50. A 0.0136 inch static pressure tap was placed in the upper wall of the jet chamber 0.30 inch from the jet exit.

Instrumentation and Procedure

A schematic diagram of the test setup is shown in figure 1(b). An accurate pressure gage and regulator were used to control the supply pressure. Immediately downstream of the pressure regulator was a rotameter-type flowmeter.

^{*}Figures appear on pages 41 through 59.

The mass flow through the nozzle was obtained from the volume flow, UA , measured by the rotameter and the density, ρ , obtained from the measured static supply pressure. The static pressure in the jet chamber was measured by the static pressure tap drilled through the upper surface of the jet.

Total pressure, static pressure, and total temperature probes were used to calibrate the hot wire probes. These calibrating probes are shown in figure 1(c). The hot wire probes were used to measure the velocity profiles. The tungsten sensing wire was 0.0002 inch in diameter. Total pressure surveys were made to determine the total pressure recovery at location downstream of the jet exit. The probes were mounted in a stationary position in front of an X-Y table. The jet model was mounted on the X-Y table. Using this X-Y table, the location of the nozzle exit with respect to the probe could be measured to an accuracy better than 0.0001 inch.

RESULTS AND DISCUSSION

As indicated in the theoretical study, a free jet can be divided into three regions. Region I is a potential core region, which has a uniform core velocity bounded by a mixing region. Region II is a fully developed mixing region where the velocity profiles adjust to a similar profile region. Region III is the fully developed mixing region where the velocity profiles are similar.

The velocity profiles at different stations downstream of the nozzle exit are shown in figure 2. The velocity ratio U/U_{00} is plotted against the distance from the centerline of the jet, y . The change in shape of the velocity profiles, the decay of the centerline velocity, and the spread of the jet with increasing distance from the jet exit can easily be seen from these figures.

The decay in centerline velocity with increasing distance from the nozzle exit is shown in figure 3. Since the centerline velocities for the different supply pressures get closer together as the distance from the jet exit increases, there is a greater incremental loss in centerline velocity for higher exit velocities than for lower exit velocities. This slower decay of the lower velocity profiles could be attributed to two effects. The jets at the lower supply pressure are probably laminar jets. As a result, the mixing with the quiescent air is not as rapid; therefore, the jet does not break up as rapidly. The higher the supply pressure, the more

turbulent the mixing, the greater the shear between the air in motion and the air at rest, and consequently, the greater the loss in centerline velocity.

In the potential core region of the jet, there is a constant velocity area called the jet core. The experimentally measured length of the core region is compared with both the laminar and the turbulent theoretically calculated core lengths in figure 4. The ratio of core length to jet width is plotted against Reynolds' number. The laminar theoretical curve predicts a longer core length than was measured, since it is believed that the data points at $R = 1560$ and 2440 are laminar data points. The data points at $R = 3630$ and 4360 appear to be intermediate points (the jet not being completely laminar or turbulent but in a transition state) and those at 5350 and 6200 fall very close to the theoretical turbulent line.

The theoretically calculated growth of a laminar jet in Region I for a Reynolds' number of 2000 is shown in figure 5. Experimental points are shown for comparison. The data presented were obtained by interpolating between the experimental points taken at Reynolds' numbers of 1560 and 2440 . The theoretical shape predicted a greater spread than was obtained experimentally for distances less than 5 jet widths and less spread for distances greater than 5 jet widths. The theoretically calculated core length was approximately twice as long as the experimentally measured core length. This difference in core length could be explained by the fact that the jet is not completely free of large scale vorticity which causes the jet core to deteriorate at a faster rate than would be the case for a completely turbulent-free laminar jet.

The theoretically calculated spread of a turbulent jet in Region I (potential core region) is shown in figure 6. The experimental data for the different supply pressures are also shown. There is good agreement between the experimental width and the theoretically calculated width for turbulent jets.

The discussion of the results will now proceed to Regions II and III of the jet profile. The width of the jet profile is plotted against distance from the nozzle exit in figure 7 at $U/U_0 = .5$. The width at $U/U_0 = .5$ is the width of profile where there exists a velocity equal to or greater than one-half the centerline velocity. The jet width at $U/U_0 = .5$ is almost constant for the first five jet widths downstream and then varies approximately linearly as the distance increases. For Regions II and III, the equation $b/h = 0.215 (x/h)$ is a good approximation of the experimental data and would predict accurately the width of the jet at $U/U_0 = .5$.

When applying information from a jet study to fluid amplifiers, it is important to look closely at the jet characteristics at 10 jet widths from the nozzle exit. This is due to the fact that the splitter of the output ports is usually located at or near this location. The width of the jet for $U/U_{00} = .1$ for distances from the nozzle is shown in figure 8. $U/U_{00} = .1$ was chosen as the limit for the profile width because of the scatter in the measured velocity at velocities lower than $U = 0.1U_{00}$.

This scatter at lower velocities was due to room air currents, slight changes in room temperature, and the high sensitivity of the hot wire. The width of the jet at 10h is approximately 3 jet widths wide for the supply pressure of 15.88 psia and approximately 4 jet widths wide for higher supply pressures. From this information, a receiver of 4 jet widths or 0.040 inch would be required to receive all the flow with velocity $U/U_{00} > .1$. Again it is realized that the free jet phenomenon is not the same as that found in a fluid amplifier, but comparisons are of value.

Region III of the jet is a fully developed mixing region where velocity profiles are similar. The theoretical profile shape for this region was calculated using the method presented in chapter XXIII of Boundary Layer Theory by Hermann Schlichting¹ and presented in the companion paper. The equation obtained for the velocity was

$$U = \frac{U_0}{\sigma\sqrt{x}} \left[2\eta (1 - \tanh^2 \eta) - \tanh \eta \right]$$

where $\eta = \sigma y/x$ where σ is an experimentally determined constant found by H. Reichardt² to be 7.67.

The comparison of the theoretically calculated non-dimensional profiles and the experimental non-dimensional profiles for Region III are shown in figures 9(a), 9(b), and 9(c). In these figures, the ratio of velocity at a given point of the profile to the centerline velocity is plotted against η . In general, there is good agreement between the theoretical curves and the experimentally measured value. The experimental data agree more closely for the profiles at higher supply pressures (higher velocities or Reynolds' numbers) than for the lower supply pressures. The theoretical curve indicates a faster decay of velocity to zero with distance from the jet centerline than was measured experimentally. However, an accurate prediction of velocity profile shape in Region III for

Reynolds' numbers of approximately 2400 to 6200 can be made using the theoretical equation.

An important objective of the investigation was to determine the pressure drop through the nozzle. The pressure loss is presented in figure 10(a). The total supply pressure to the jet chamber is plotted against total jet exit pressure. The 100 percent recovery pressure curve is presented for comparison. The maximum pressure loss through the nozzle was 0.75 pound. Therefore, at a total supply pressure of approximately 15.4 psi above ambient, there is only a 5 percent loss in pressure. The loss of total pressure due to the nozzle ranged from approximately 4 percent at 1 psig supply to 5 percent at 15 psig supply. Although the theoretically analyzed and experimentally tested nozzle is not an efficiently designed jet, the losses through the nozzle are small. The pressure loss can be seen more clearly from figure 10(b). The total supply pressure is plotted against the difference in the total supply pressure and the total exit pressure ($\Delta P = P_{tc} - P_{te}$).

The total pressure loss of a jet is an important parameter when one is interested in the pressure available at a downstream location. The total pressures recovered at various jet widths from the nozzle exit are shown in figure 11. Total pressure surveys were taken at 0, 1, 10, and 20 jet widths from the exit. The curves connecting the data points, especially at distances close to the exit, are probably not the true total pressures. The data points, however, are actual measured values and the curves themselves are probably accurate between 5 jet widths and 20 jet widths from the nozzle. The two different curves, solid and broken, represent the integrated pressures over a 0.010 inch width ($x/h = 1$) and a 0.020 inch width ($x/h = 2$), respectively.

For fluid amplifier application, the receiver inlet is usually located at approximately $x/h = 10$. The pressure recovered at $x/h = 10$ is plotted against total supply pressure in figure 12(a). Also shown in the figure is the 100 percent pressure recovery curve and the theoretically calculated pressure recovery curve for a turbulent jet. The turbulent theoretical curve was calculated from the equation

$$\bar{P}_{t,10h} - P_e = 0.543(P_{tc} - P_e)$$

which was theoretically determined in the companion paper.

The theoretical curve predicted a straight line recovery value. However, the experimental data showed a curved line

which crossed the theoretical line at two different values. The first two data points were higher than the theoretical curve. This is believed to be due to the fact that the jet was not fully turbulent and the losses from mixing were not as great as predicted by turbulent theory. The theoretical curve predicted the experimental data within an accuracy of ± 5 percent in the worst case and in most cases better than ± 5 percent. The ratio of total pressure recovery in psia to total supply pressure in psia is plotted in figure 12(b) against supply pressure in psia. The agreement between the theoretical curves and the data is within 3 percent for supply pressure less than 27 psia and is within approximately 5 percent for supply pressures between 27 and 31 psia. Again it can be vividly seen that the theory predicted the pressure recovery to an accuracy of ± 5 percent for both the 0.010" and 0.020" width of profile.

Since in most cases the fluid amplifier device will be operated with atmospheric pressure surrounding it, it is more meaningful to calculate the ratio of recovery pressure to nozzle width from the jet exit to supply total pressure in terms of gage pressure, that is

$$\frac{P_{t,10h} - P_e}{P_{tc} - P_e}$$

These values are shown in figure 13 and give a more accurate picture of the percent of input pressure recovered with atmospheric pressure as a reference point. The recovery pressure for a 0.010 inch width of profile is highest at supply pressures less than 3 psig and reaches a minimum of approximately 47 percent at supply pressures between 6 and 8 psig. As the supply pressure increases above 8 psig, the percent recovery increases until, at a supply pressure of 16.28 psig, the recovery pressure is 60 percent.

The conclusion that can be drawn from this, as far as application to fluid amplifiers, is that for operating pressures greater than 3 psig, the maximum recovered pressure at the receiver inlet will be of the order of 50 to 60 percent of the supply pressure for a 0.010 inch width. If a 0.020 inch width of jet profile is received at x/h of 10, the pressure recovery at the receiver inlet of 40 to 50 percent will be obtained for supply pressures greater than 3 psig.

The discussion has, of course, been concerned with the geometrical design of figure 1. It is hoped that by choosing

a more efficient jet design, the pressure loss through the jet and to 10 jet widths downstream will be decreased. Since the greatest loss in pressure is due to the mixing with the quiescent air rather than through the nozzle itself, the problem should be considered from the standpoint of obtaining reduced loss in the mixing region.

The last parameter to be considered is the mass flow through the nozzle and the discharge coefficient of the nozzle at various Reynolds' numbers. Figure 14(a) presents the measured mass flow as a function of supply pressure. Also shown is the experimentally calculated mass flow. The equation used to calculate the theoretical mass flow was the inviscid one-dimensional equation given in the companion paper. Using the equation for discharge coefficient

$$C_d = \frac{1}{1 + \frac{2\delta^*}{h}}$$

where $\frac{2\delta^*}{h}$ is the ratio of decrease in nozzle width to total jet width due to viscous effects, a discharge coefficient of .897 was calculated. Using this discharge coefficient and the mass flow calculated from the inviscid one-dimensional flow equation, a theoretical actual mass flow, \dot{M}_{actual} was obtained from the equation

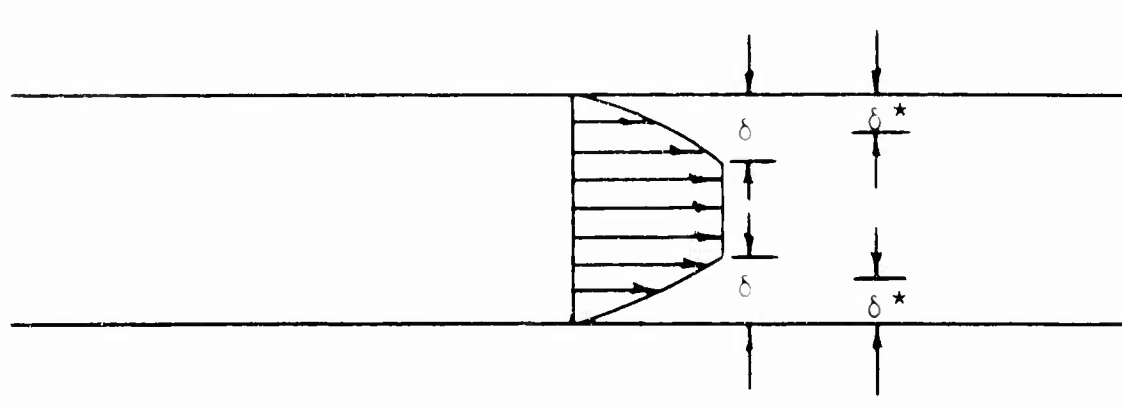
$$\dot{M}_{actual} = C_d \dot{M}_{cal}$$

This value is shown in figure 14(a). The difference between the experimentally measured mass flow and the true calculated mass flow, using a discharge coefficient of .897, is only 2.5 percent. Therefore, there is excellent agreement between the theoretically calculated \dot{M}_{actual} and the measured \dot{M}_{meas} for a supply pressure of 27.85 psia.

The discharge coefficient C_d is presented in figure 14(b) for different Reynolds' numbers based on nozzle width ($Re = \frac{\rho U h}{\mu}$).

The variation in discharge coefficient for Reynolds' numbers ranging from approximately 1500 to 6200 is from .77 to .89. With discharge coefficients greater than .7, the flow in the nozzle is probably of the inviscid core type, which means the boundary layer does not extend across the entire nozzle.

The diagram below shows the probable shape of the profile in the nozzle.



The velocity profile just downstream of the nozzle exit verifies this shape since there is a constant velocity in the central portion of the measured velocity profile.

CONCLUDING REMARKS

An experimental investigation has been made of a two-dimensional convergent jet. The experimental results were compared to a theoretical analysis performed by Dr. F. O. Smetana and Dr. J. C. Williams, III of the Mechanical Engineering Department, North Carolina State of the University of North Carolina at Raleigh in a companion paper. The following results were obtained:

1. The higher exit velocity profiles lost a greater amount of velocity with increasing distance from the jet exit than did the profiles with the lower exit velocities.
2. The laminar theory predicted a greater core length than was measured. The turbulent theory accurately predicted the core length for the fully turbulent jet.
3. The theoretical calculation of the width of a jet in Region I for a Reynolds' number of 2000 (using laminar theory) overestimated the jet width for $x/h < 4$ and underestimated the width for $x/h > 4$. Although the turbulent theory predicts the same jet width in Region I for different supply pressures, experimental data show a variation in jet width for different supply pressures. The theoretical curve did represent a jet width which agreed with the average width for all the supply pressures.

4. For Regions II and III the width of the jet at $U/U_0 = .5$ could accurately be determined from the relation $b/h = 0.215(x/h)$.
5. In Region III where the velocity profiles are similar, the theoretical profile accurately predicted the shape of the velocity profile for Reynolds' numbers of 2400 to 6200. The only variation from the theory was in the outer portions of the profile where the decay of velocity to zero was not as rapid as theoretically determined.
6. The pressure drop through the nozzle due to separation and shear along the nozzle surfaces was approximately 5 percent for all supply pressures.
7. The pressure recovered ten jet widths downstream from the nozzle exit was 50 to 60 percent (depending on the supply pressure) for a 0.010 inch width (one jet width) of profile and 40 to 50 percent for 0.020 inch width of profile based on gage pressures. The theory predicted the pressure recovery for both a 0.010 in $\frac{1}{2}$ and a 0.020 inch width of profile at ten jet widths from the nozzle within ± 5 percent of the measured value. Since most of the pressure drop is downstream of the nozzle rather than through the nozzle itself, an efficient design should be approached from the standpoint of reducing mixing losses rather than reducing losses in the nozzle.
8. The inviscid one-dimensional equation was used to calculate the mass flow. For a supply pressure of 27.85 psia and for a theoretically determined discharge coefficient of .897, the calculated mass flow differed from the measured mass flow by only 2.5 percent.
9. The measured discharge coefficients varied from 0.77 to 0.89 for a Reynolds' number range of approximately 1500 to 6200.

DIM:ds

REFERENCES

1. Schlichting, Hermann, BOUNDARY LAYER THEORY, McGraw-Hill Book Company, 1960, Chapter XXIII.
2. Reichardt, H., Gesetzmäßigkeiten der freien Turbulenz VDI-Forschungsheft, 414, 1942, second edition 1951.

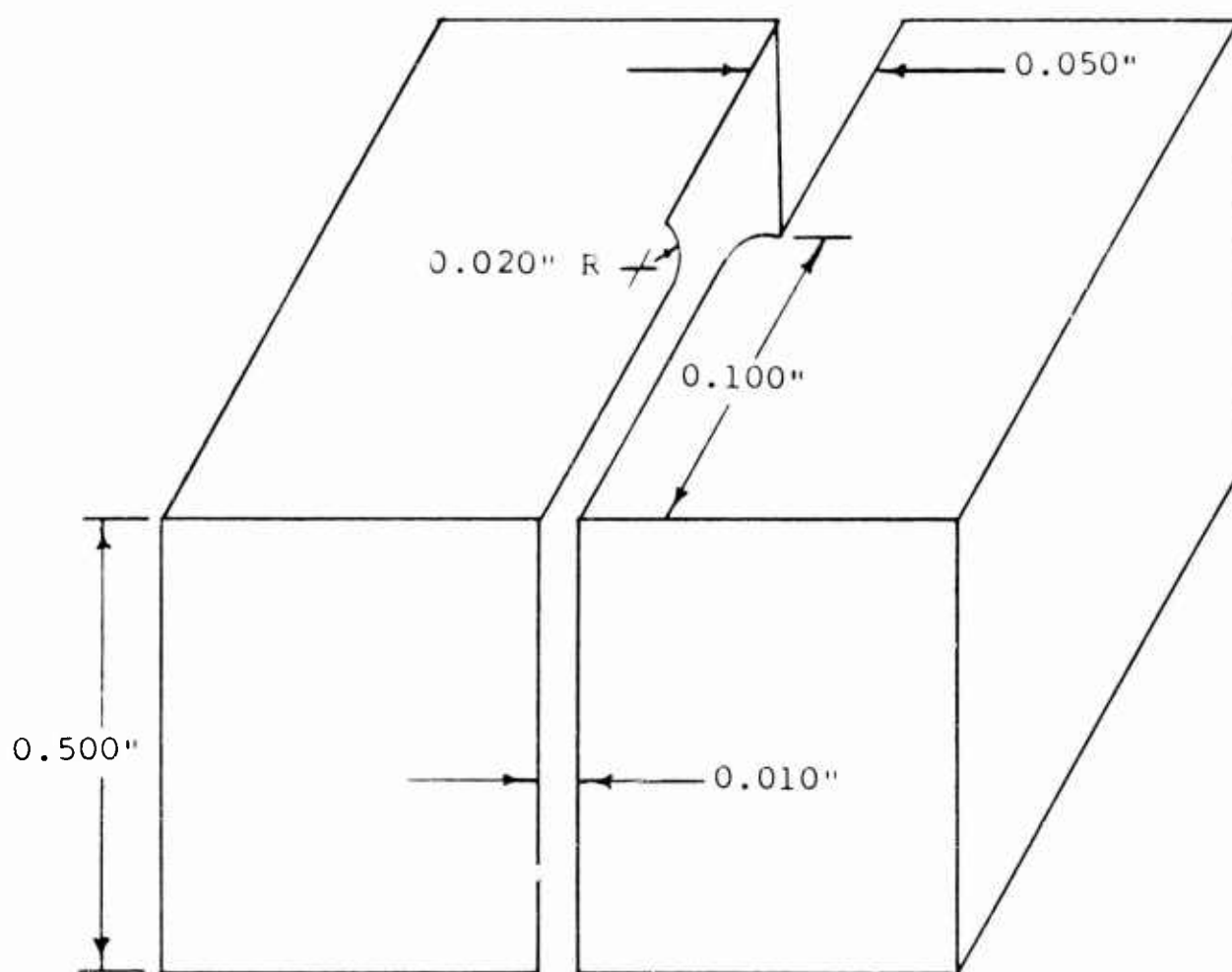


Figure 1 (a).- SCHEMATIC DIAGRAM OF EXPERIMENTAL JET

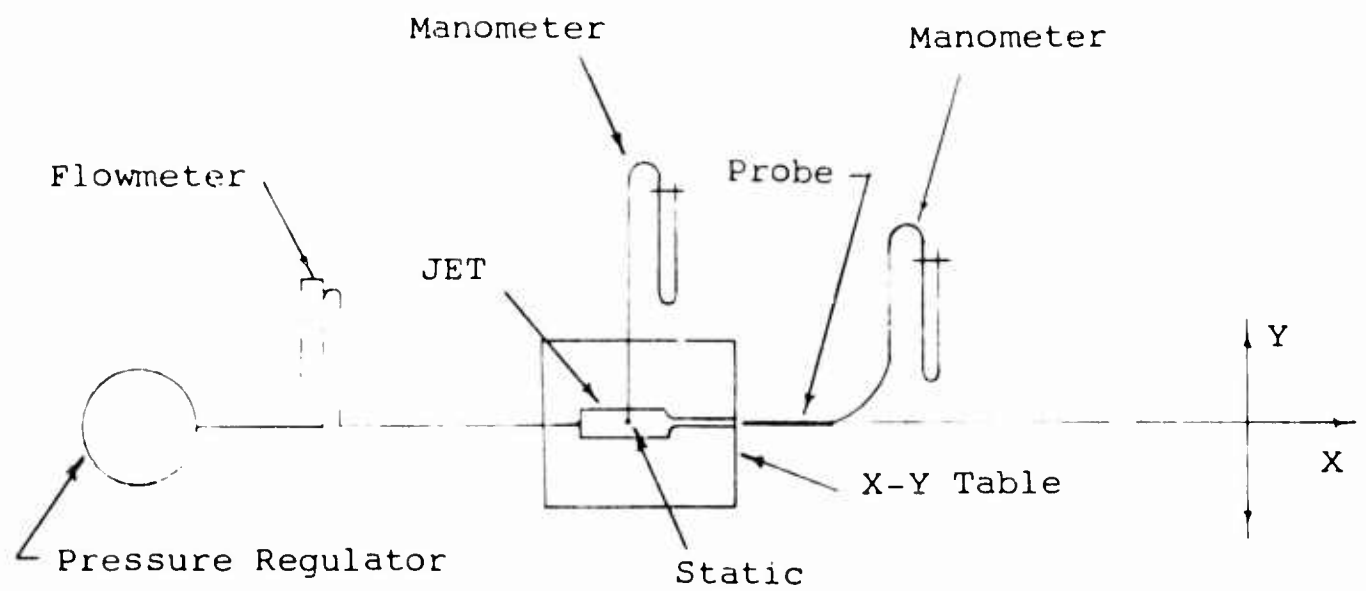


Figure 1 (b).- EXPERIMENTAL TEST SETUP

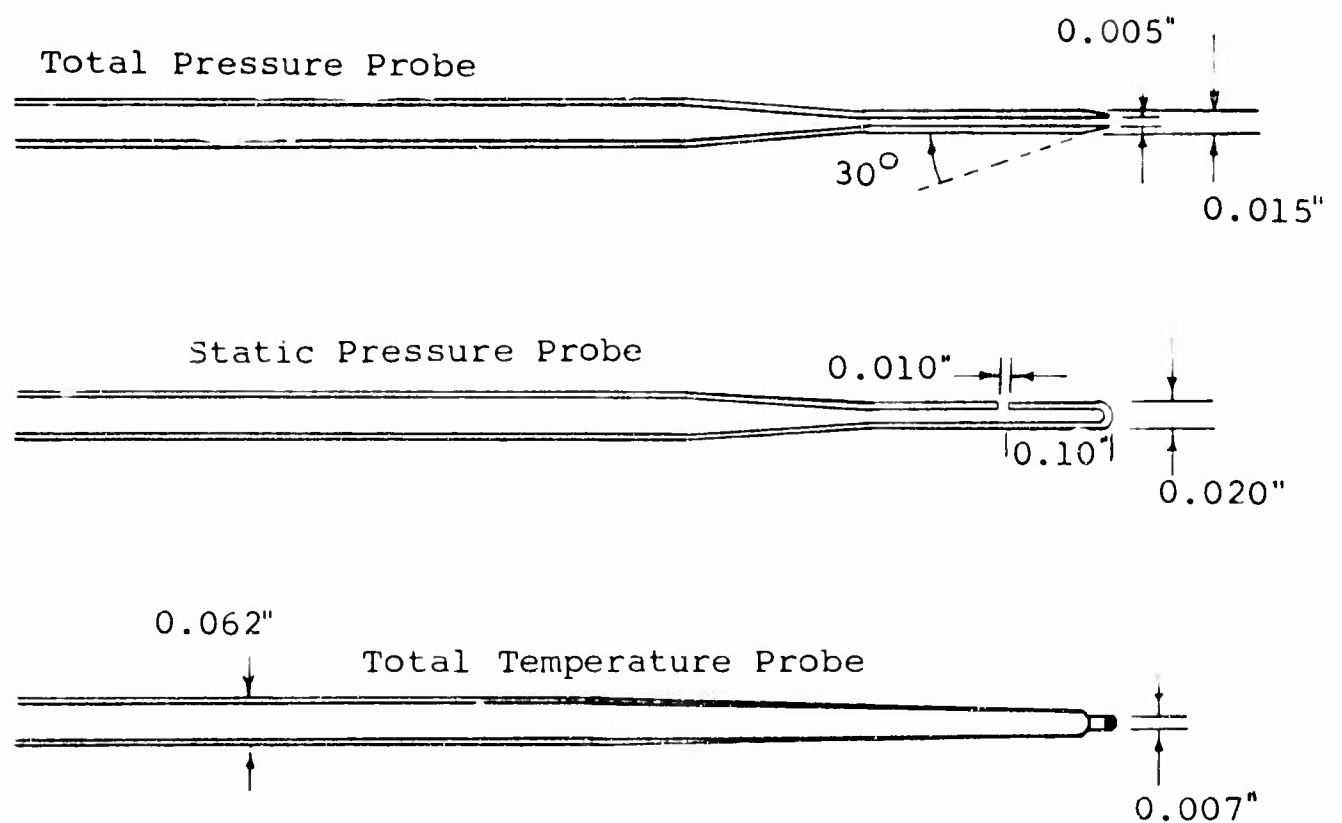
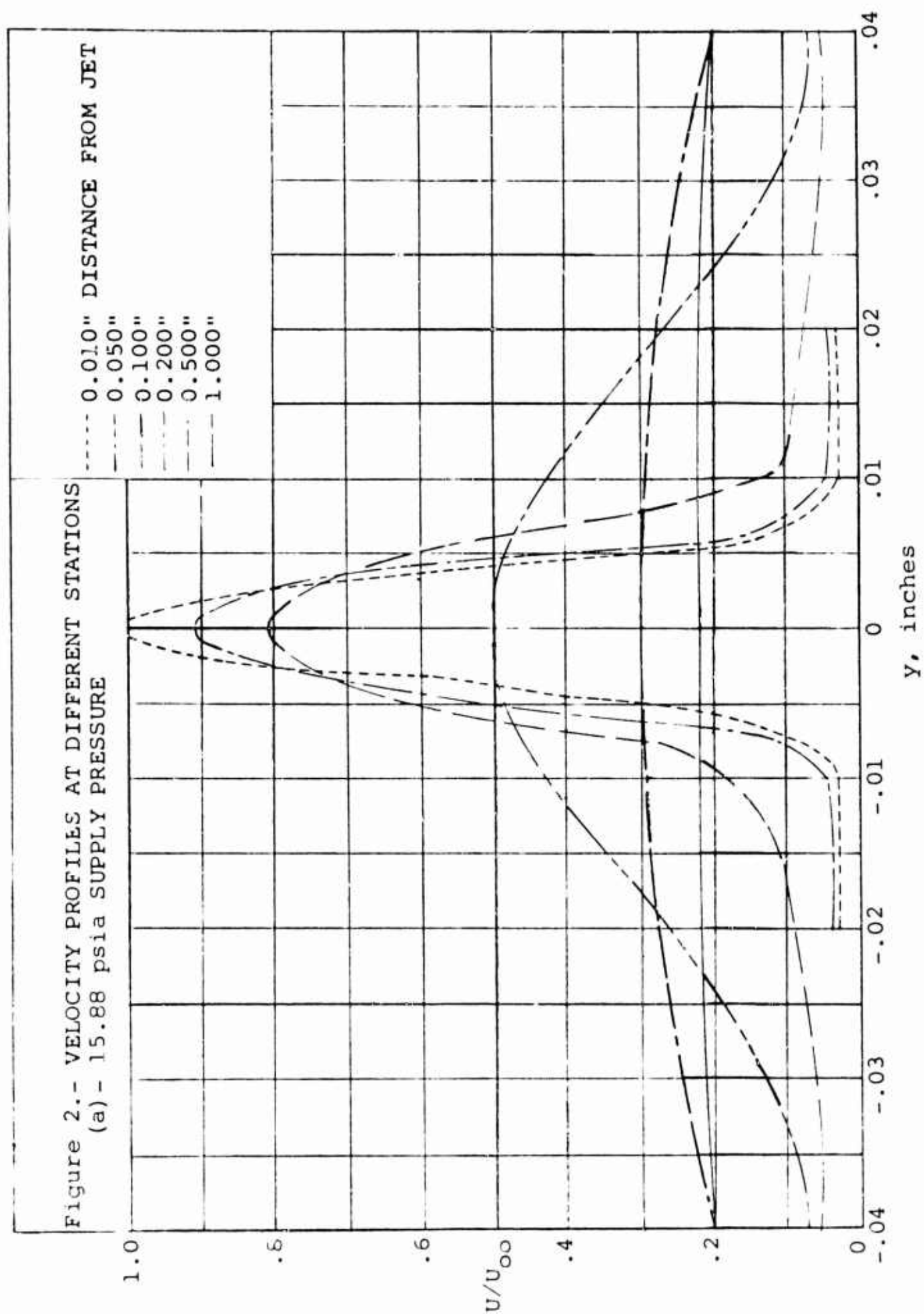
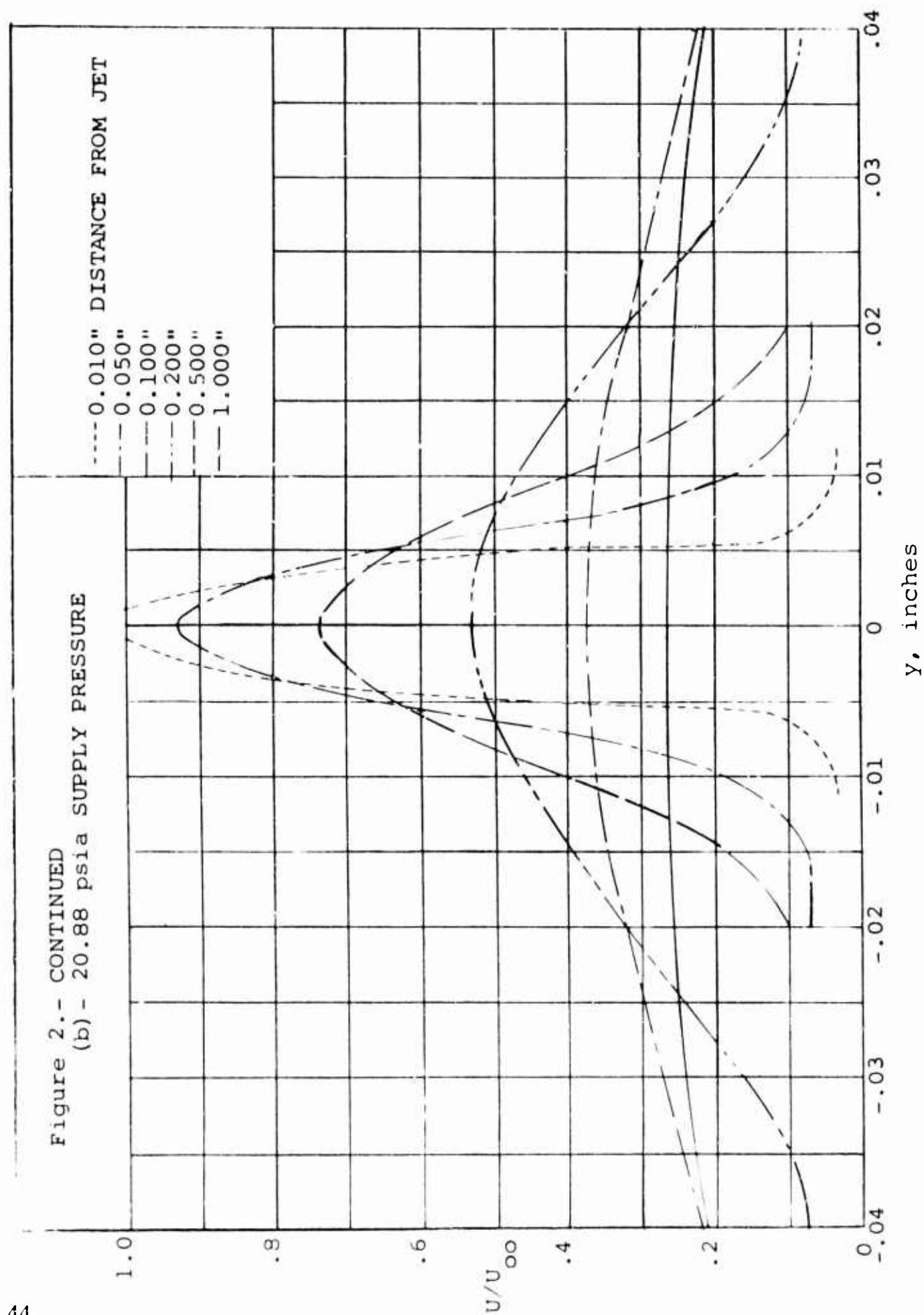


Figure 1 (c).- PROBES USED IN THE EXPERIMENTAL INVESTIGATION





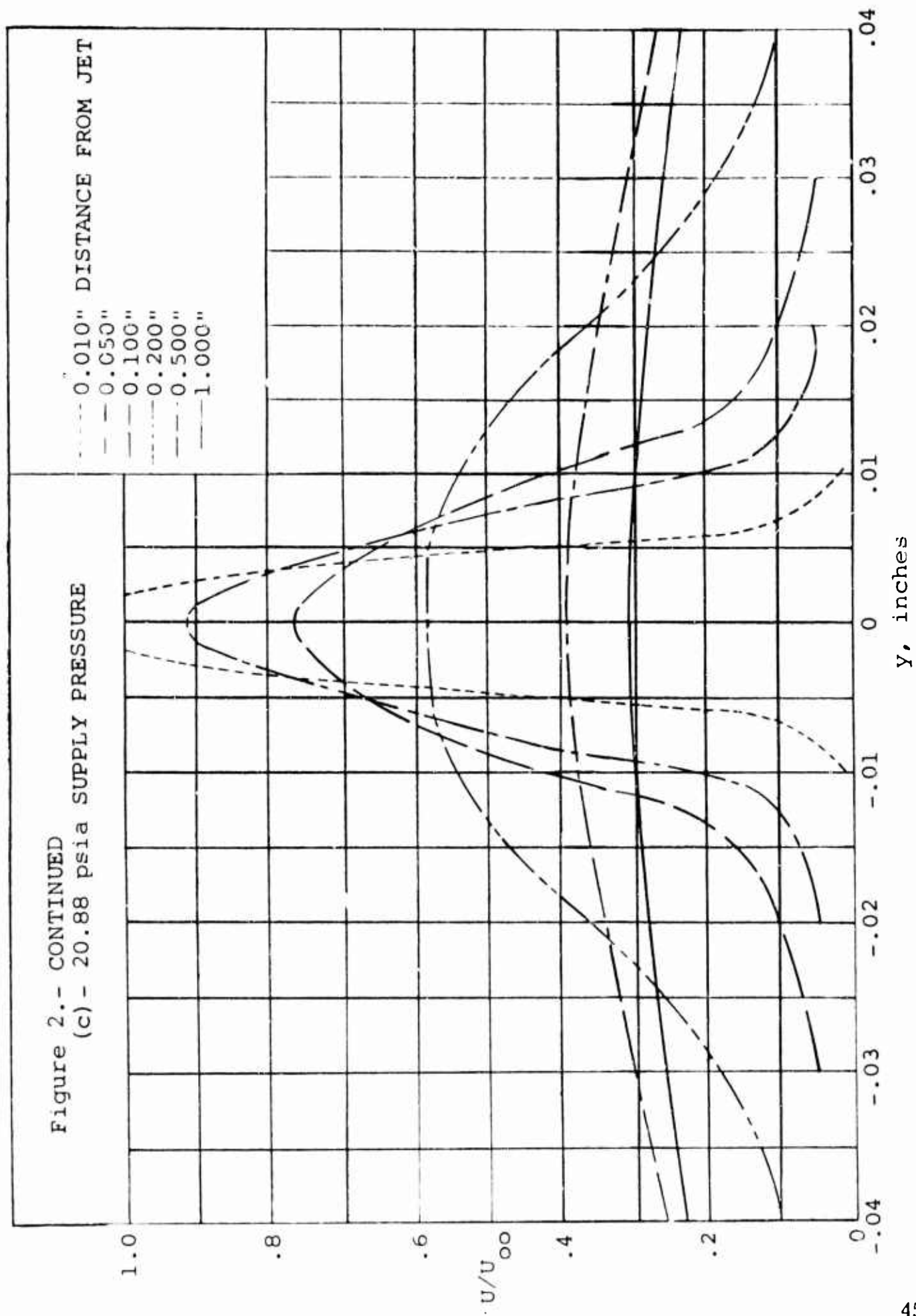
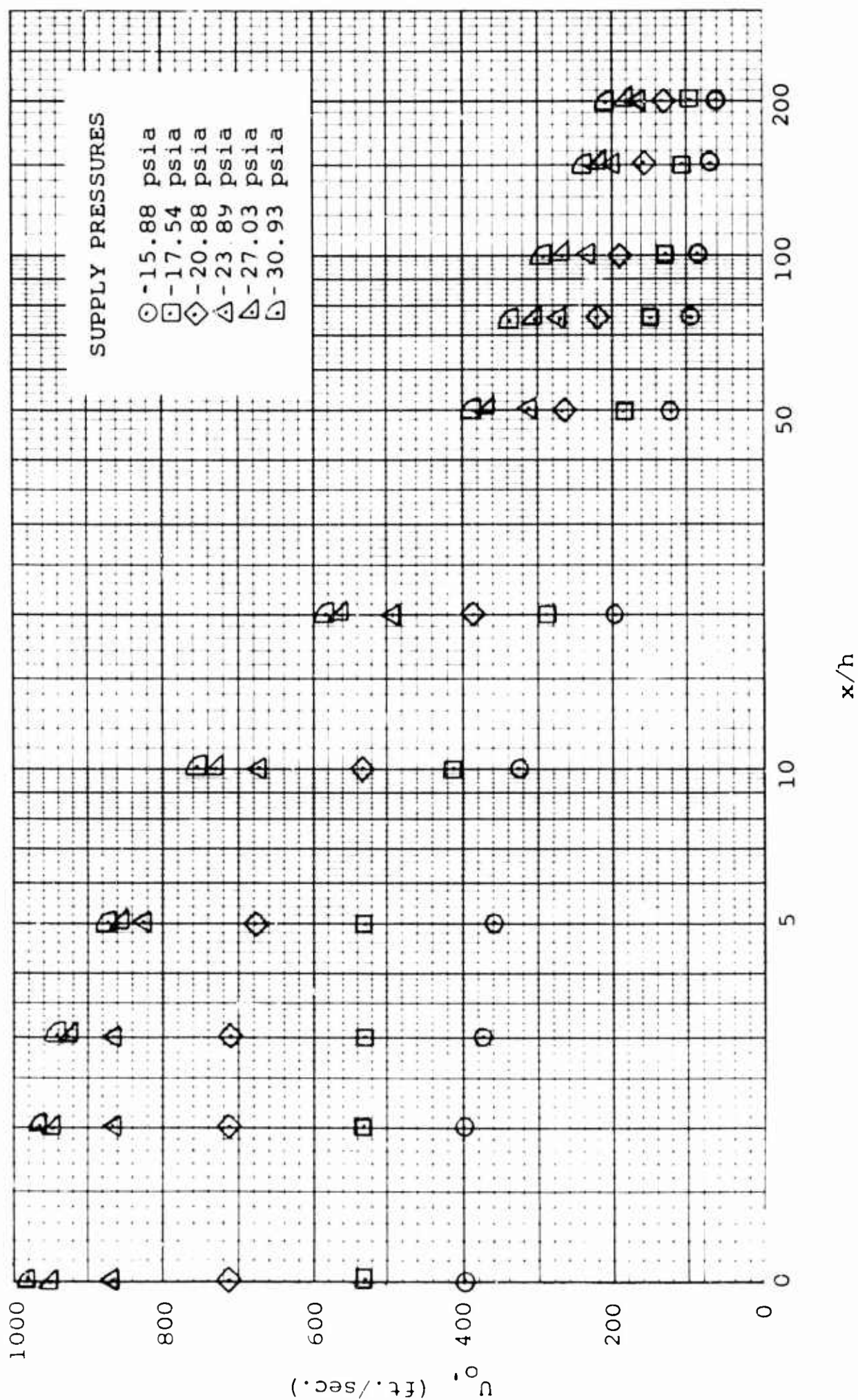


Figure 3.- DECREASE IN CENTERLINE VELOCITY WITH INCREASING
DISTANCE FROM THE NOZZLE EXIT.



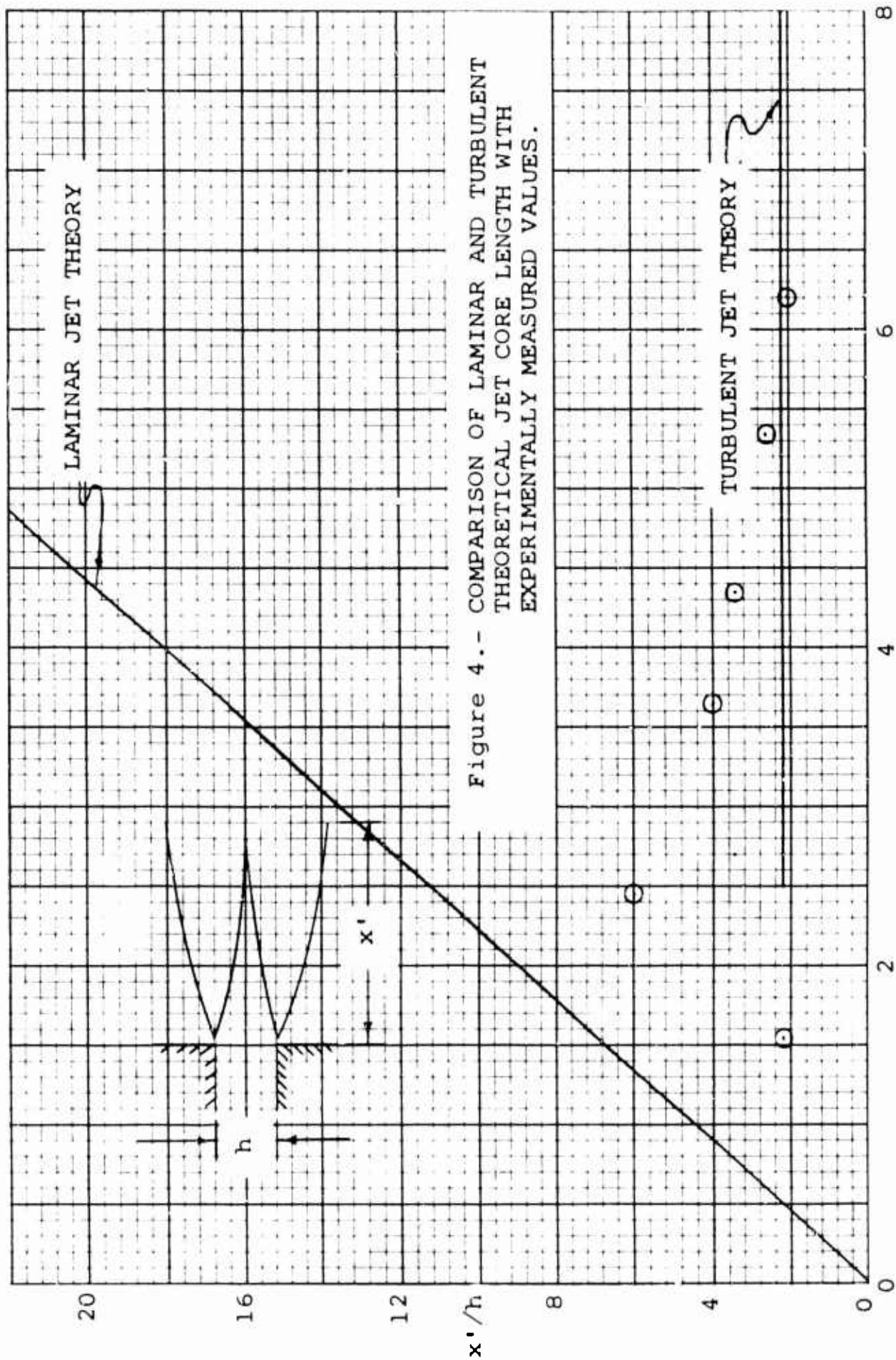
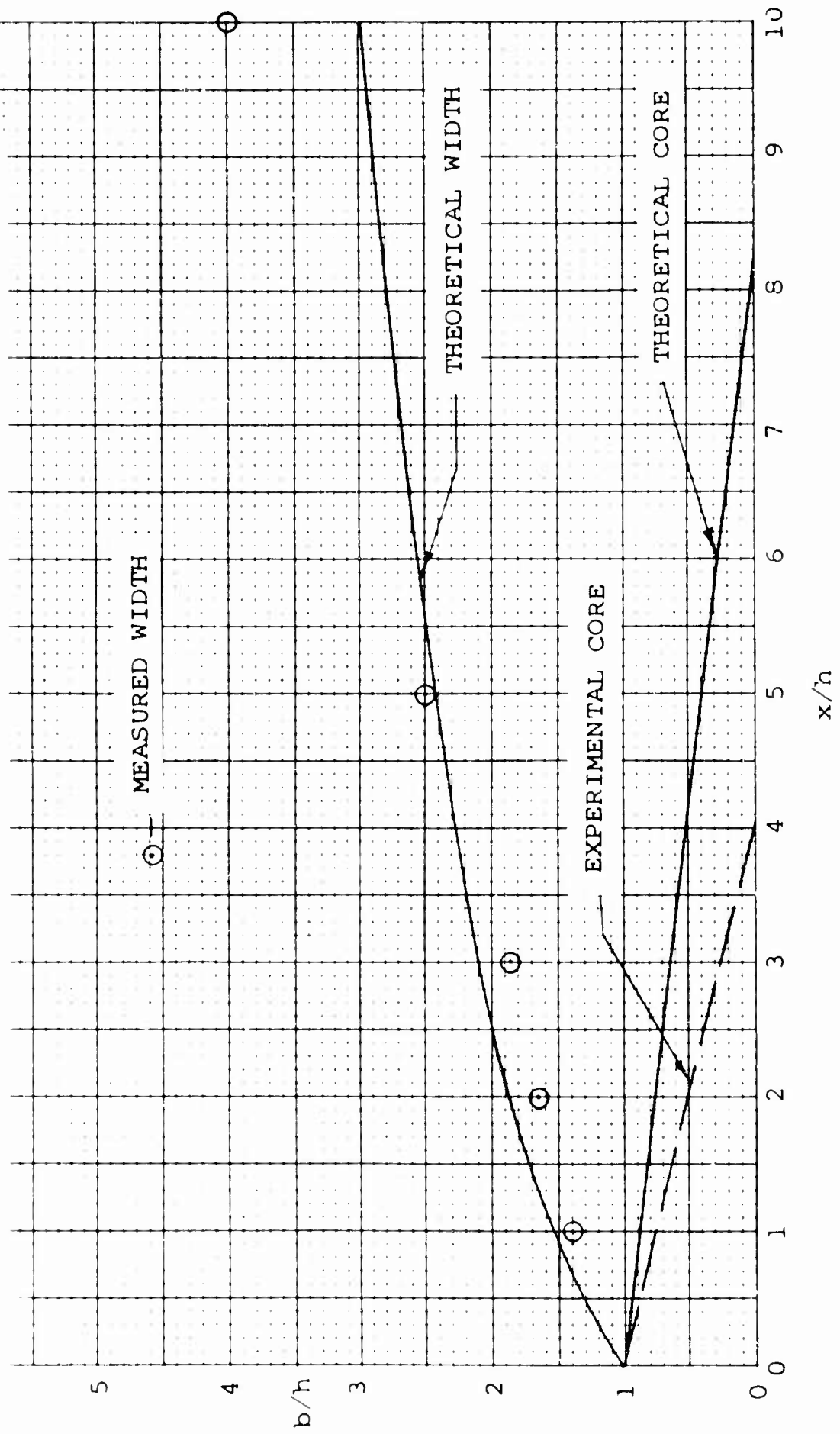


Figure 5. - COMPARISON OF THEORETICALLY CALCULATED JET PROFILE SHAPE
TO EXPERIMENTALLY MEASURED SHAPE FOR A $Re = 2000$.



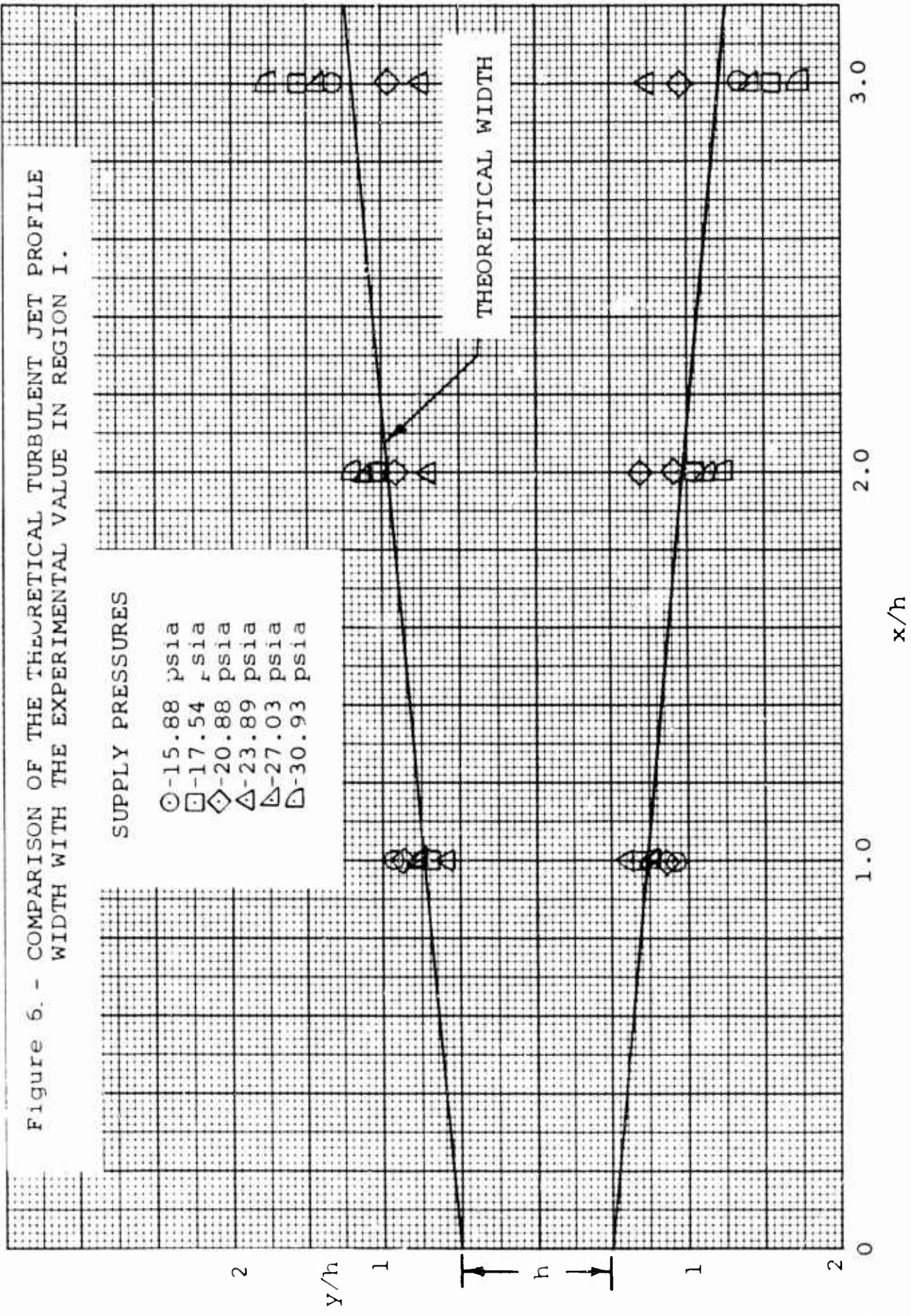
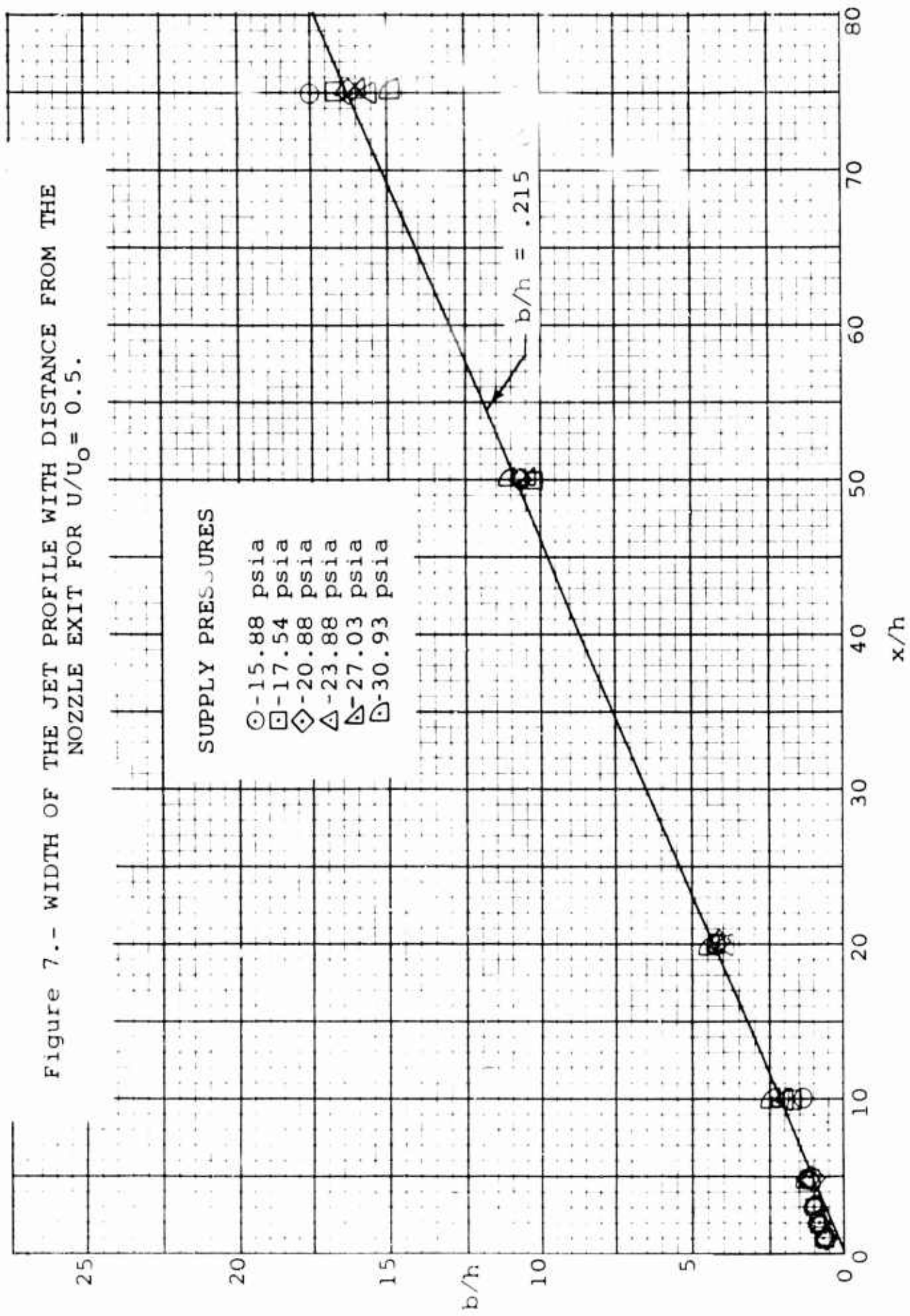


Figure 7.- WIDTH OF THE JET PROFILE WITH DISTANCE FROM THE
NOZZLE EXIT FOR $U/U_0 = 0.5$.



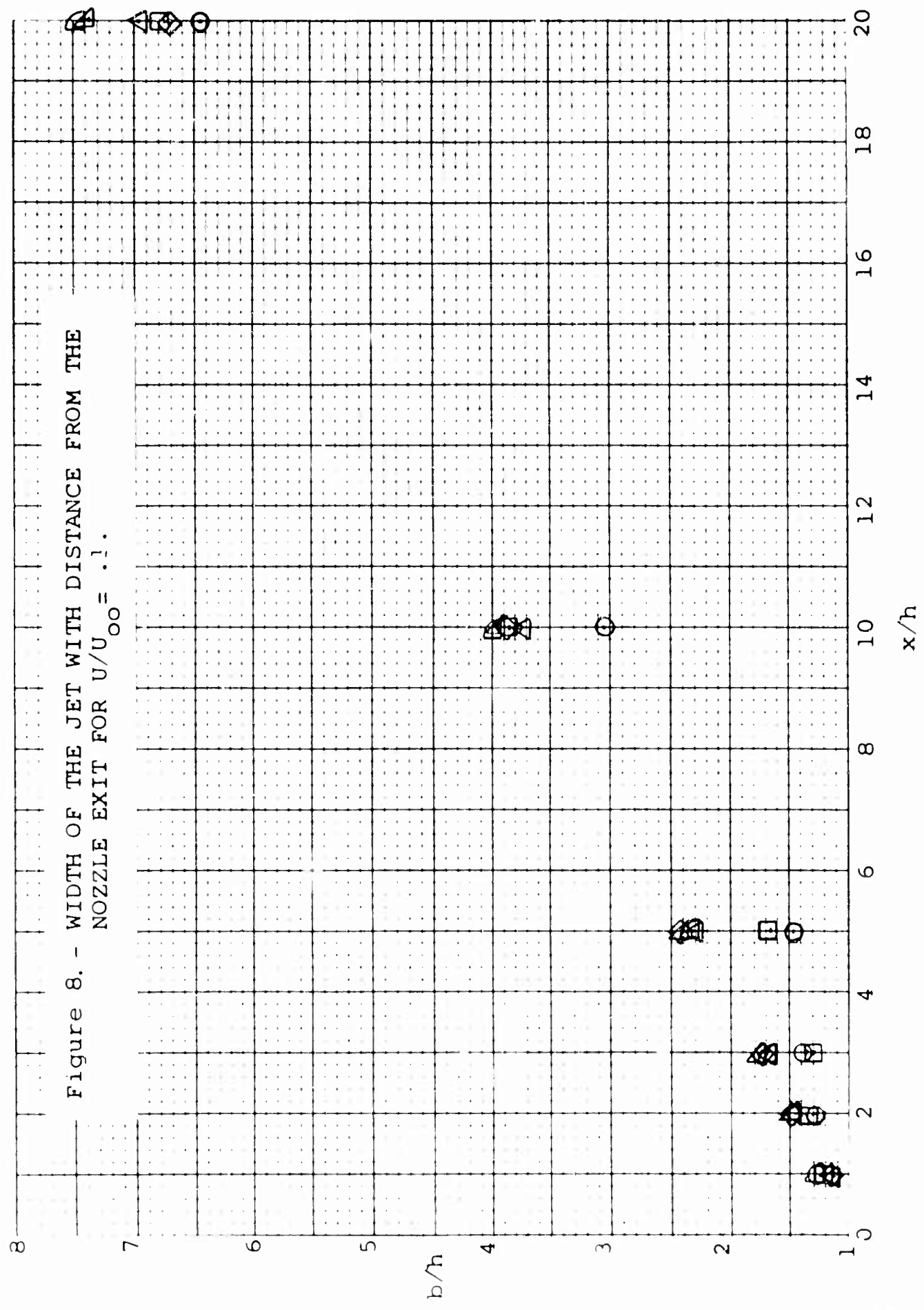


Figure 9. - COMPARISON OF THEORETICALLY PREDICTED VELOCITY PROFILE WITH THE MEASURED PROFILE IN THE SIMILAR PROFILE REGION OF THE JET (REGION 3).

(a) - SUPPLY PRESSURE OF 17.54 psia (Re = 2440).

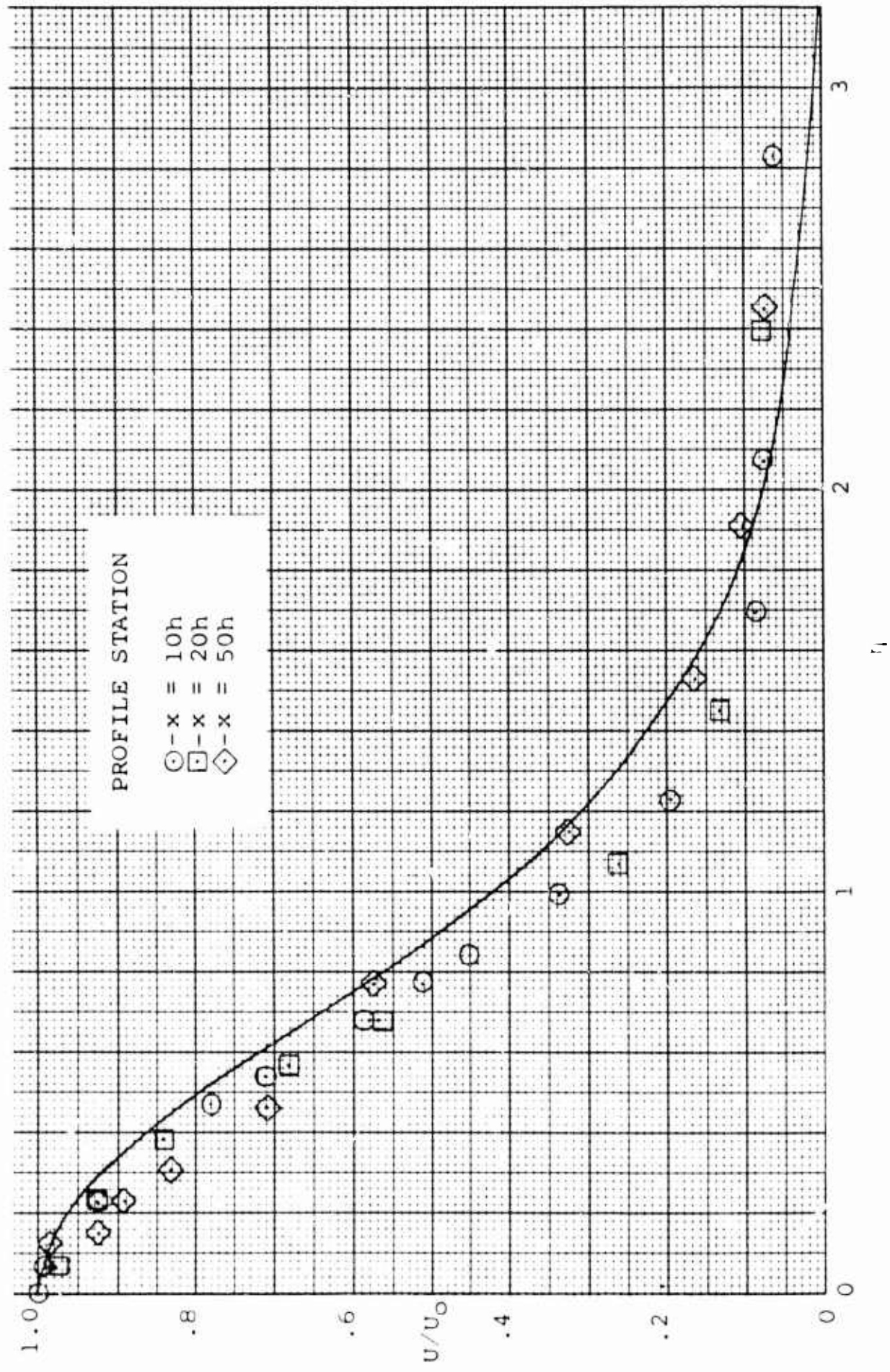
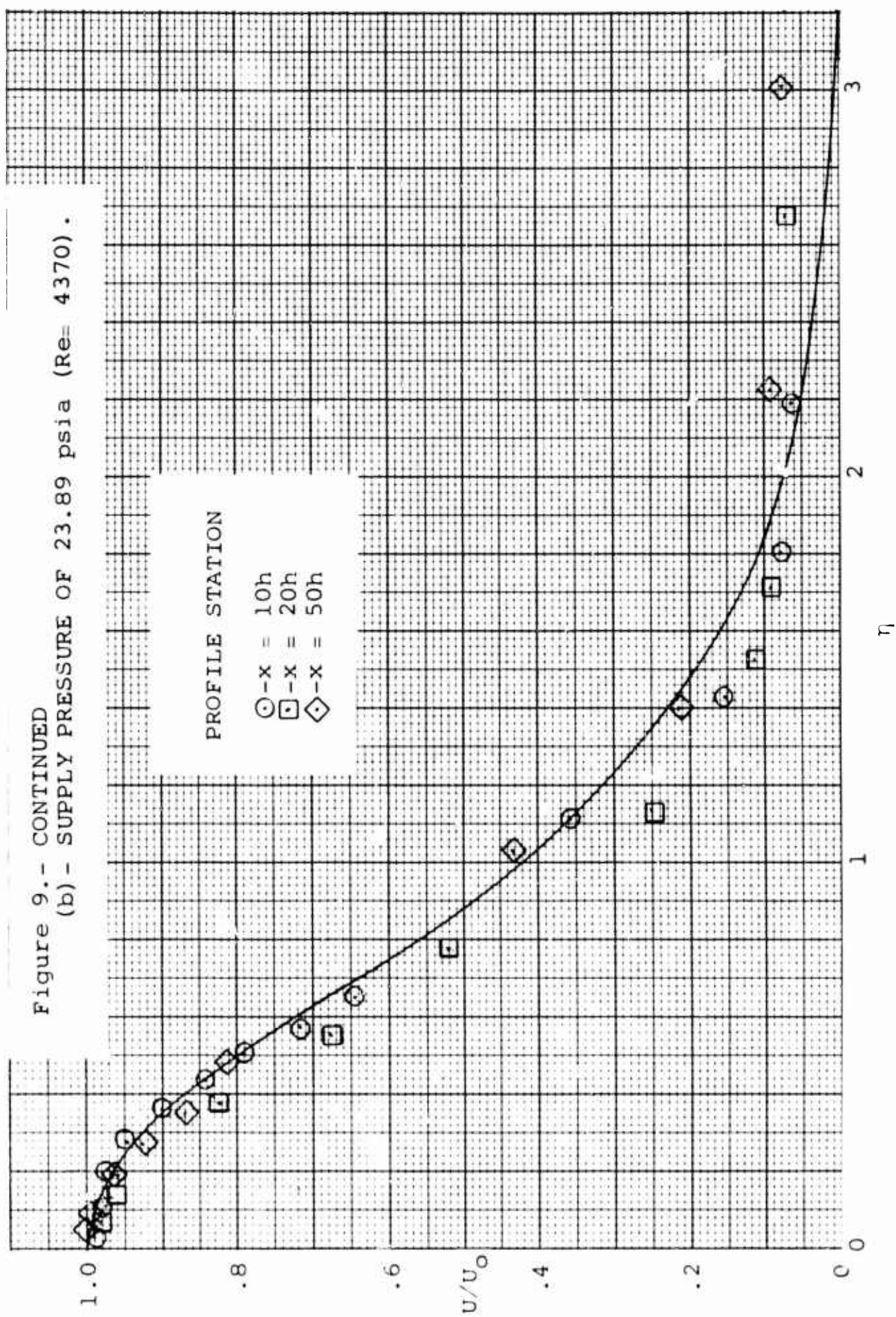


Figure 9.- CONTINUED
 (b) - SUPPLY PRESSURE OF 23.89 psia (Re= 4370) .



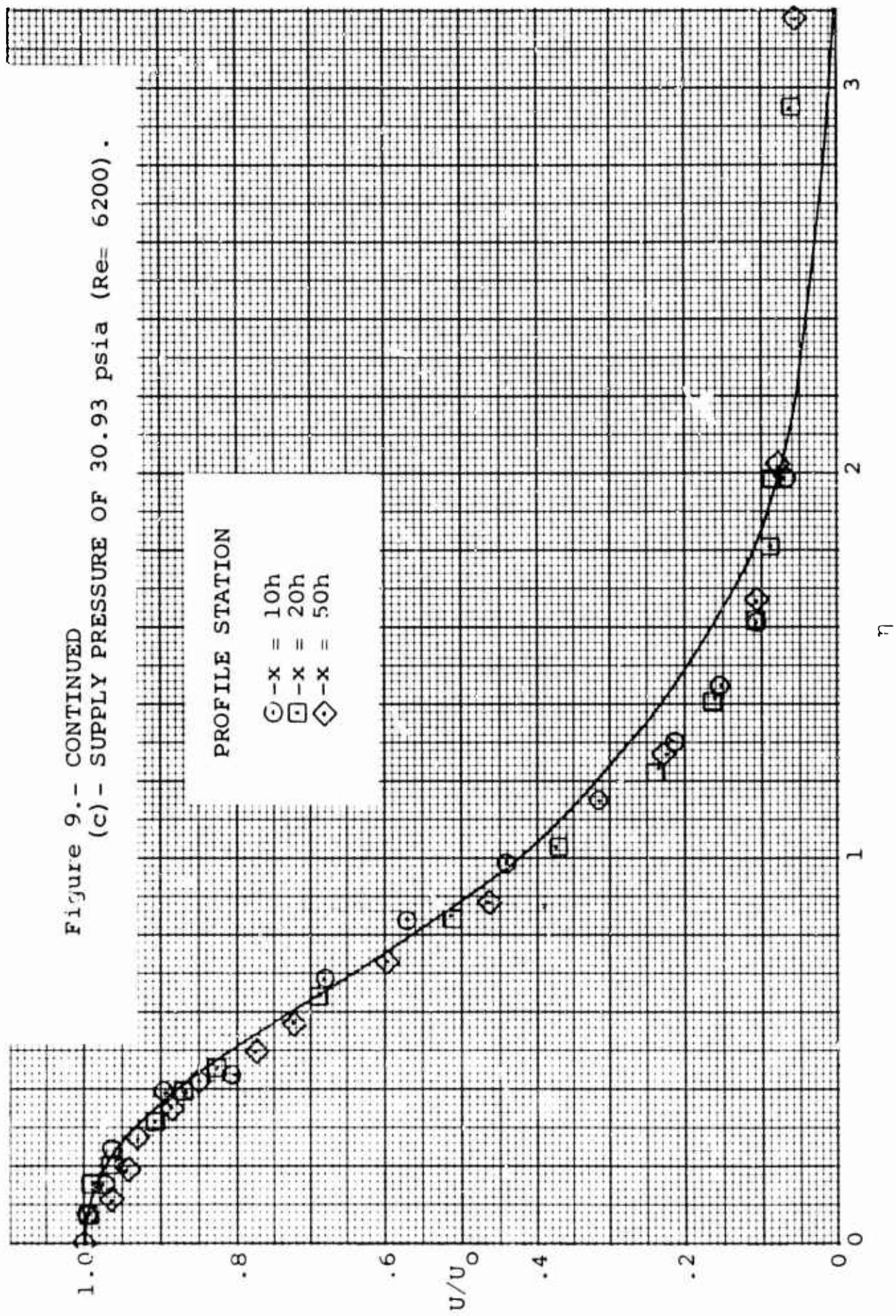


Figure 10 (a) .- TOTAL PRESSURE RECOVERED AT THE NOZZLE EXIT.

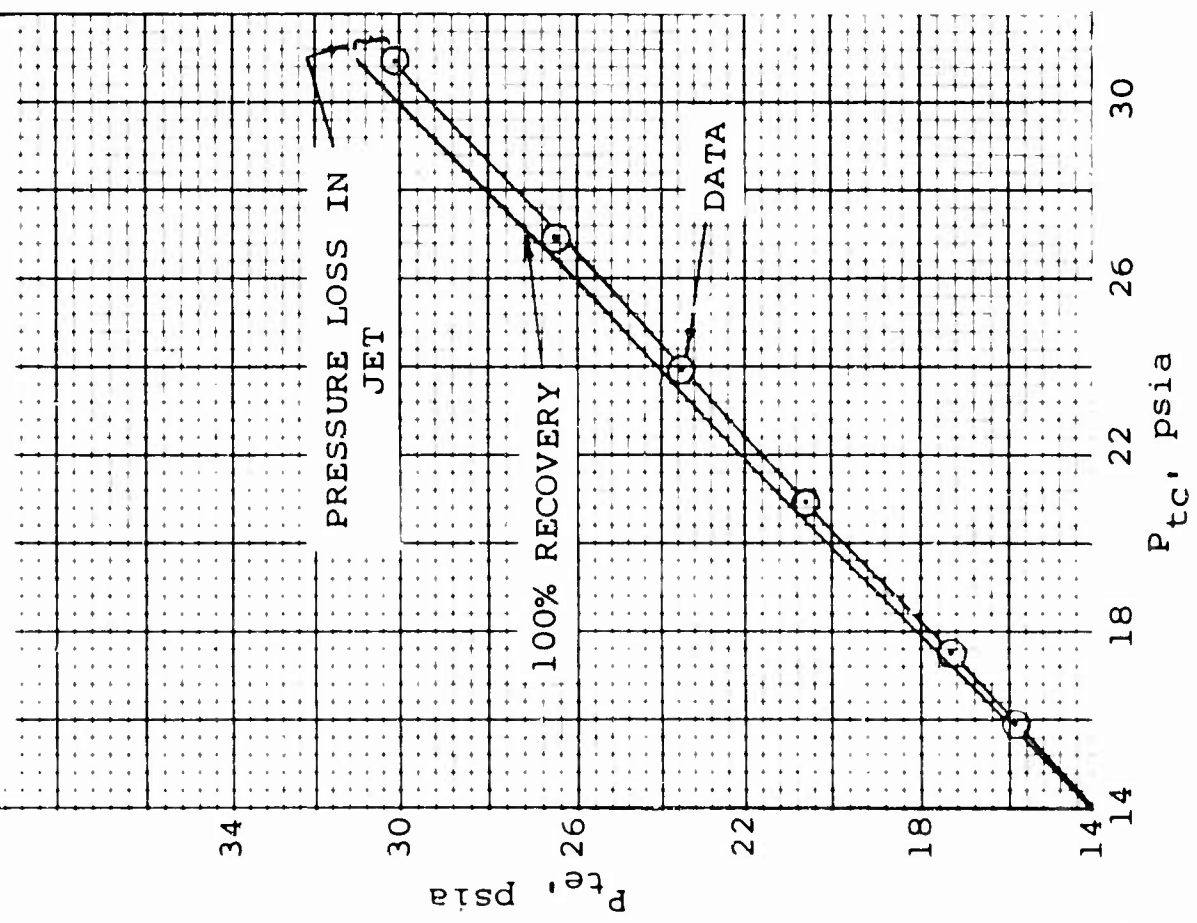
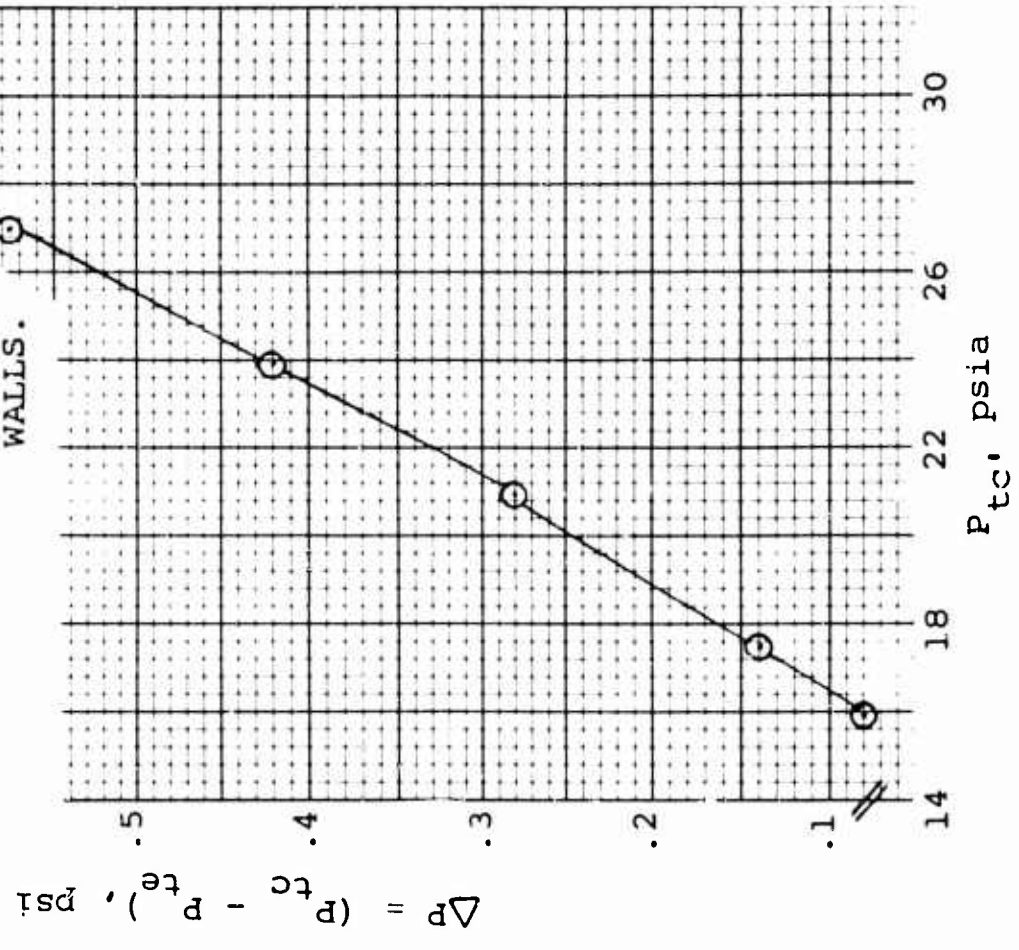
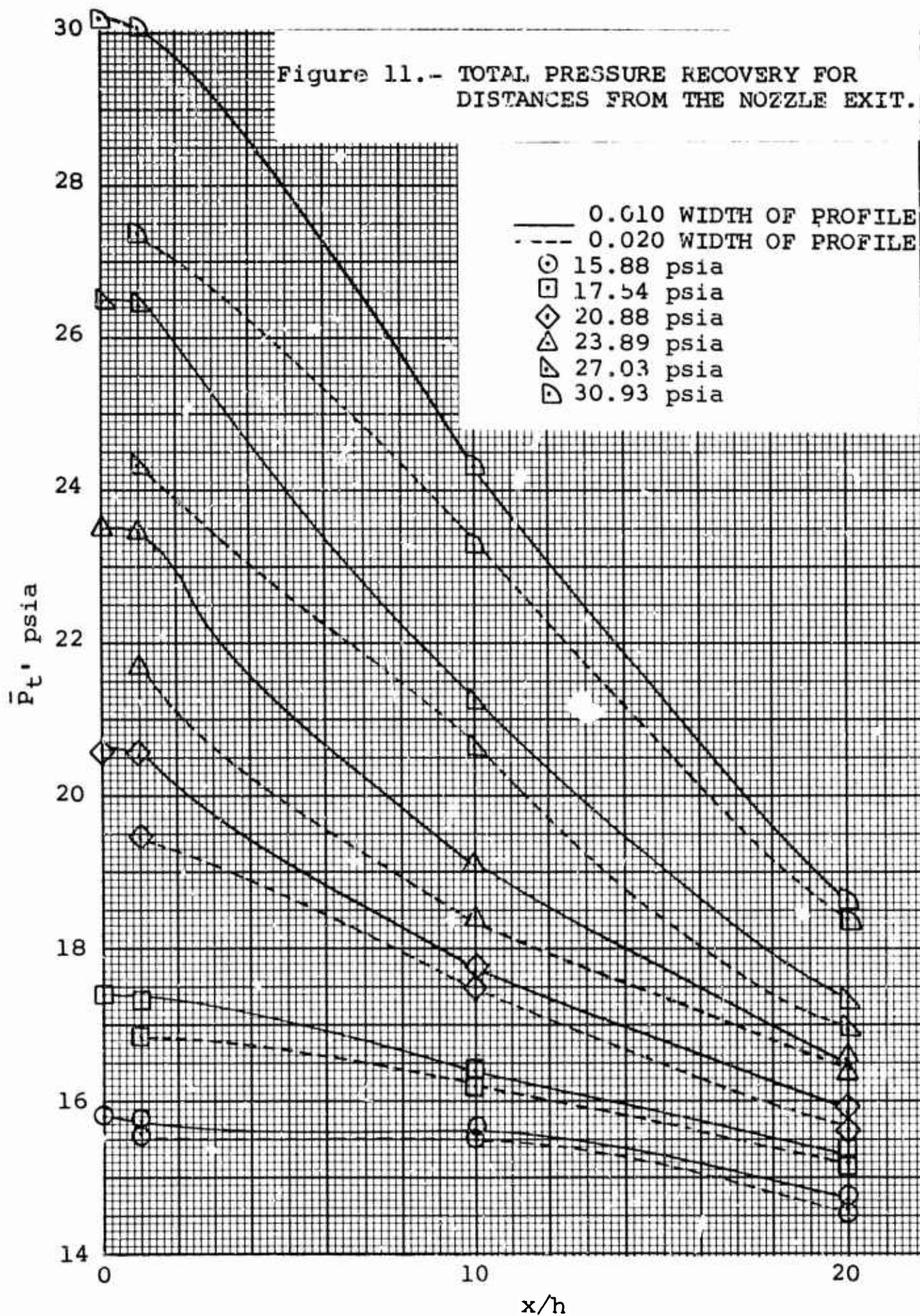
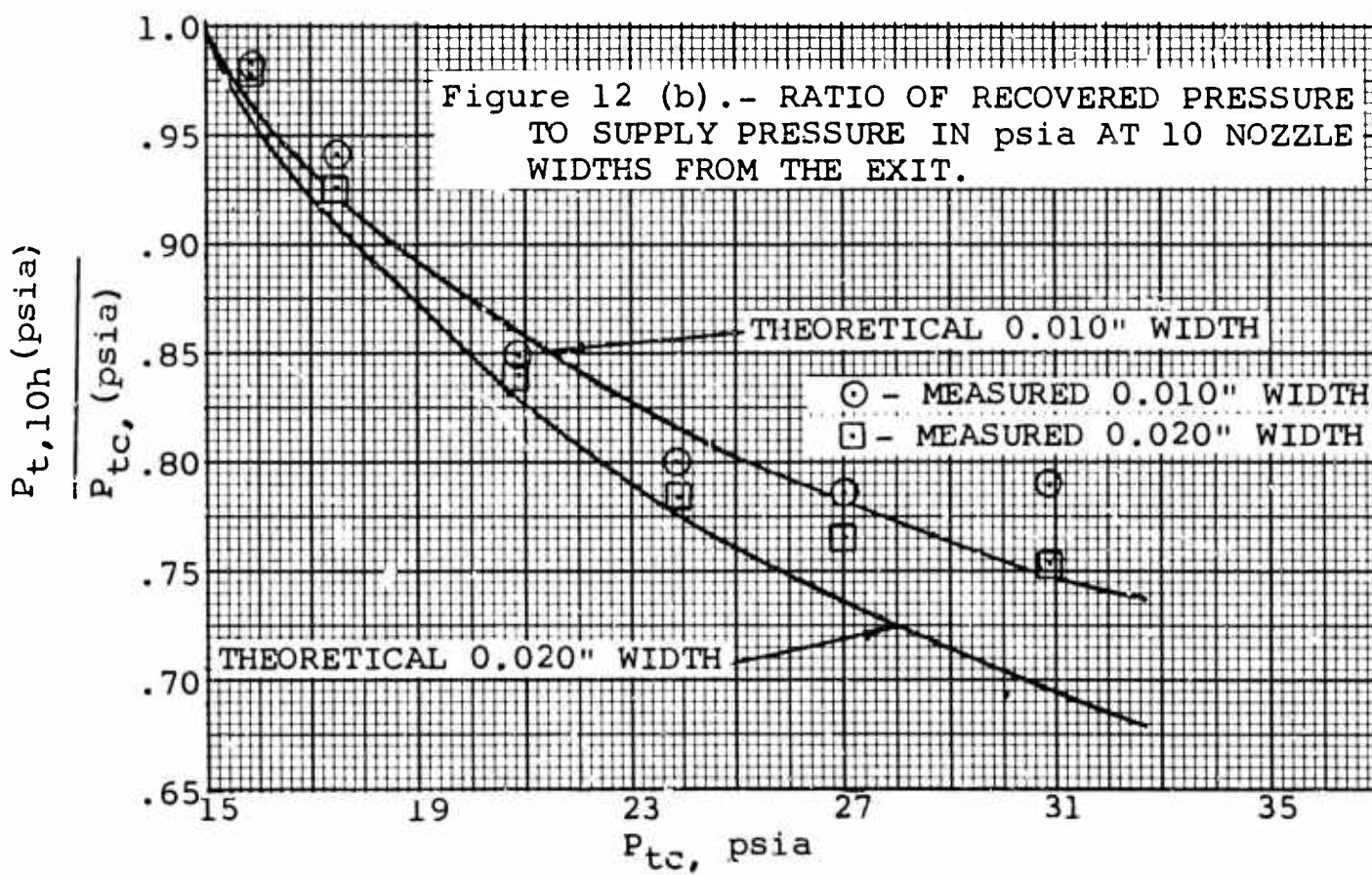
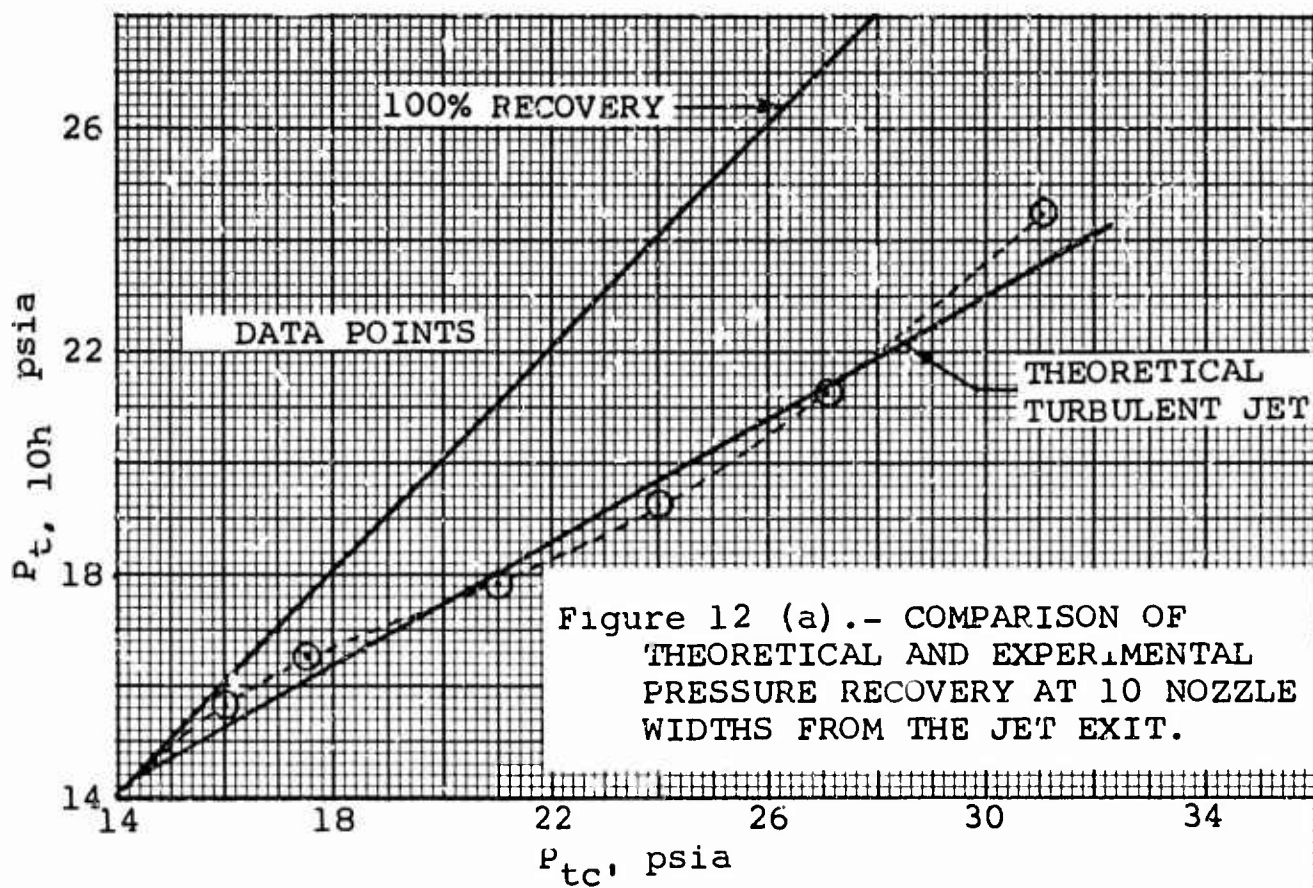
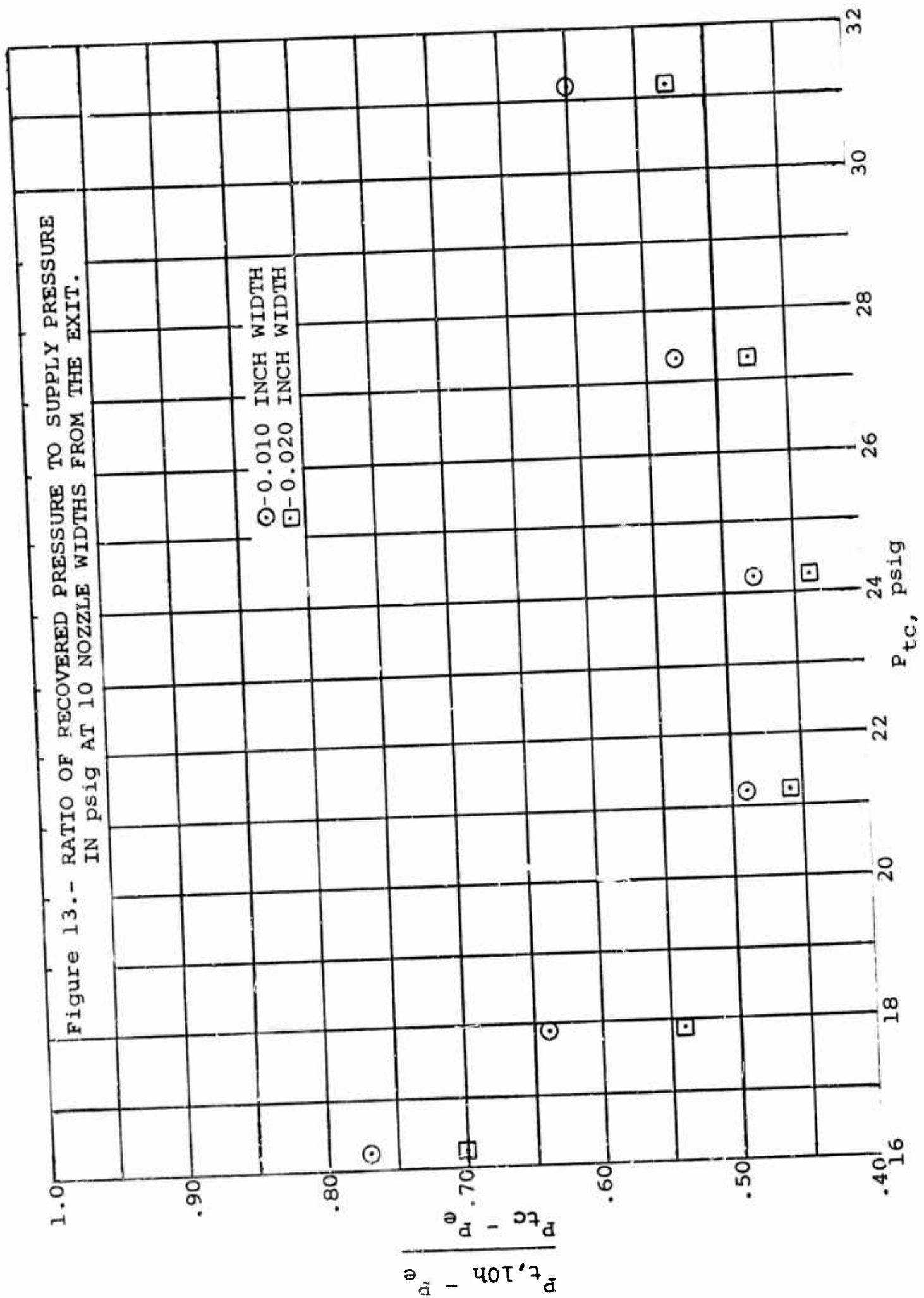


Figure 10(b) .- TOTAL PRESSURE LOSS THROUGH THE NOZZLE DUE TO SEPARATED REGIONS AND SHEAR ALONG THE NOZZLE WALLS.









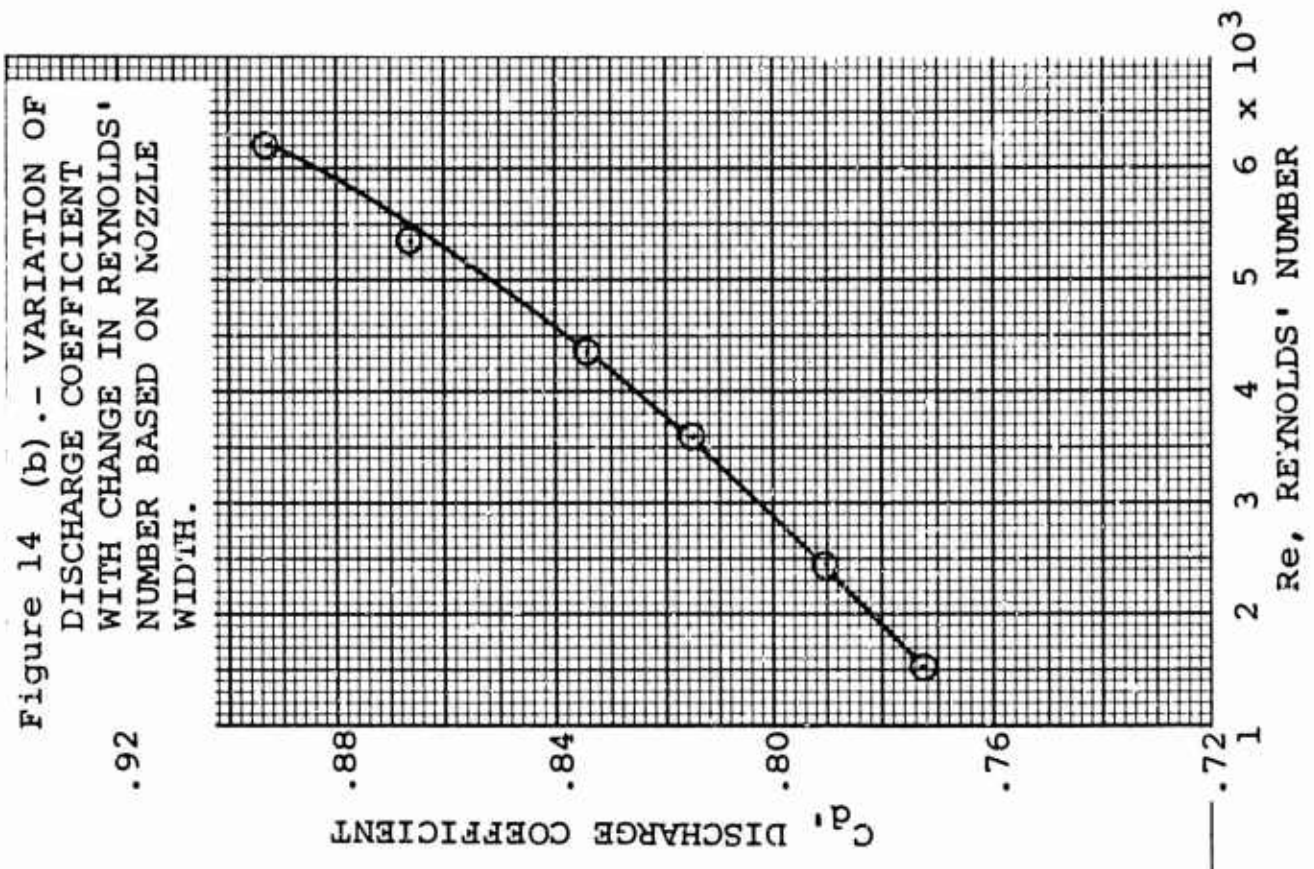
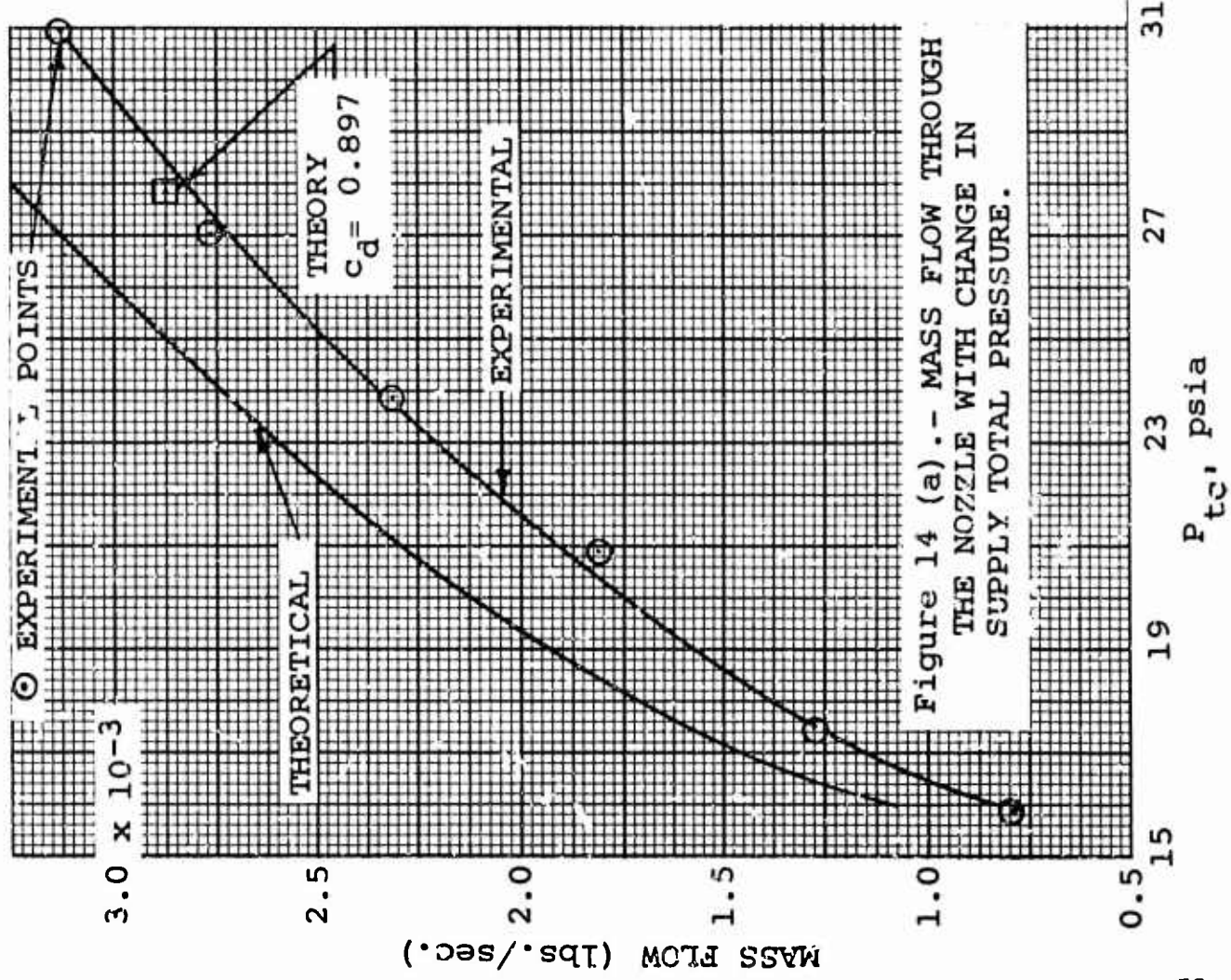


Figure 14 (b). - VARIATION OF DISCHARGE COEFFICIENT WITH CHANGE IN REYNOLDS NUMBER BASED ON NOZZLE WIDTH.

Figure 14 (a). - MASS FLOW THROUGH THE NOZZLE WITH CHANGE IN SUPPLY TOTAL PRESSURE.

Pressure Recovery Characteristics of Compressible
Two-Dimensional Free Jet Flows

b₂

R. E. Olson

and

J. F. Camarata
United Aircraft Research Laboratories
East Hartford, Connecticut

ABSTRACT

Results of an experimental investigation of the pressure recovery characteristics of subsonic, compressible, two-dimensional, free jet flows are presented for a range of diffuser geometries. The weight flow characteristics of the diffusers are presented together with velocity profiles upstream of the diffusers and at various stations within the diffusers for a range of diffuser back pressures.

An analytical procedure is developed for predicting diffuser performance for a range of jet Mach numbers, diffuser capture heights and diffuser back pressures. Results obtained from this analytical procedure are presented and compared with the experimental results. Good agreement is shown between the analytical and experimental results for the range of variables investigated.

These studies were conducted as part of a general investigation of jet flows in fluid amplifiers for Harry Diamond Laboratories under Contract DA-49-186-AMC-66(X).

INTRODUCTION

The development of design criteria for fluid-state devices, particularly momentum-exchange proportional amplifiers, requires knowledge of the pressure recovery characteristics of diffusers capturing nonuniform streams having velocity profiles characteristic of those for a free jet. Such diffuser pressure recovery characteristics are generally required for a range of diffuser output resistances including the limiting case of blocked load.

Although previous investigations of diffusers for wind tunnels and propulsion systems (e.g., Refs. 1, 2 and 3) have provided information regarding the pressure recovery characteristics of diffusers capturing uniform streams, or streams composed mainly of boundary layers, the results obtained apply only qualitatively to diffusers capturing jet flows. The studies which have been conducted regarding the pressure recovery characteristics of jet flows, such as those presented in Ref. 4, have generally been limited to incompressible jets.

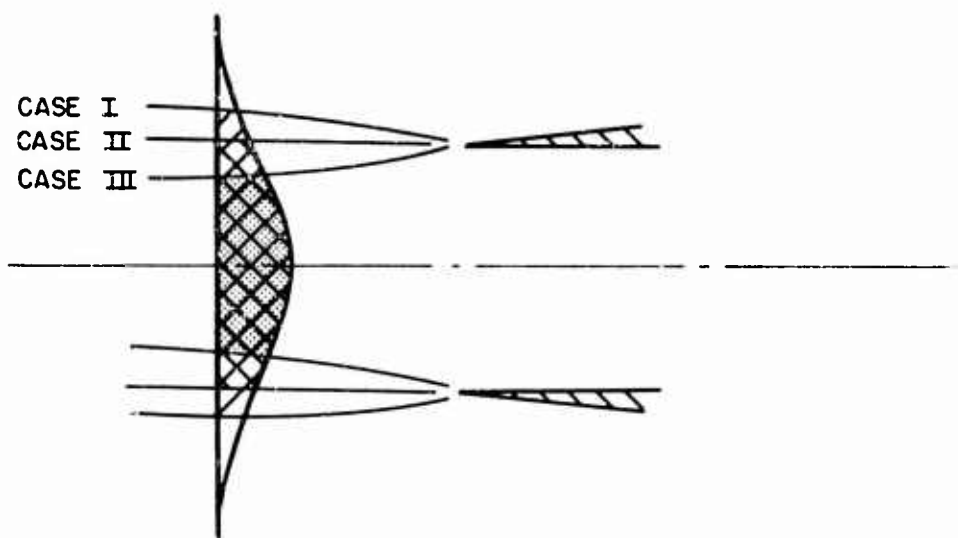
Consequently, studies were conducted to determine the pressure recovery characteristics of diffusers capturing compressible jet flows for a range of jet Mach numbers. This paper presents the significant results of the studies for subsonic jet Mach numbers.

DESCRIPTION OF DIFFUSER FLOW REGIMES

In general, three flow regimes (hereafter termed Case I, II and III) may be encountered as the diffuser is operated over a range of back pressures. These regimes are illustrated in the upper portion of Fig. 1. For Case I, the diffuser captures flow from outside the undisturbed streamline (i.e., the streamline which was at the location of the diffuser lip position without the diffuser installed); for Case II, the diffuser captures all the flow bounded by the undisturbed streamline; for Case III the flow is spilled around the lip of the diffuser. For subsonic jet Mach numbers the Case II regime is encountered only for a single back pressure and is commonly referred to as the design condition. Hence, Cases I and III may be considered as "off-design" operating conditions. Progression from Case I to Case III corresponds to an increase in the diffuser back pressure. In the Case III flow regime, the stagnation streamline is shown to be located at the diffuser lip. In actuality for high diffuser back loading the stagnation streamline is located within the diffuser. Such a condition results in a reverse flow being established along the outer walls of the diffuser at the diffuser inlet.

SHADED PORTION OF VELOCITY PROFILE
CONTAINS MASS FLOW ENTERING DIFFUSER

FINITE OUTPUT RESISTANCE



INFINITE OUTPUT RESISTANCE (BLOCKED LOAD)

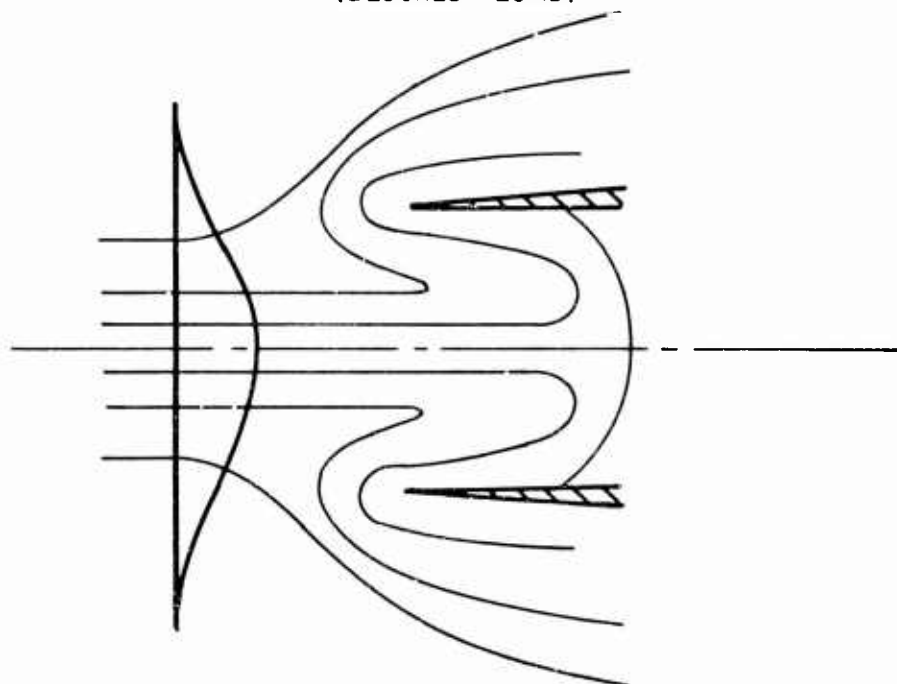


FIGURE 1 DIFFUSER FLOW REGIMES

The limiting case of diffuser "blocked-load" operation is illustrated in the lower portion of Fig. 1. For this case, a portion of the jet flow enters the diffuser, proceeds toward the diffuser exit and is subsequently reversed in direction, flows along the diffuser walls, and exhausts at the diffuser inlet.

DIFFUSER PRESSURE RECOVERY ANALYSIS FOR DESIGN OPERATION

Consider the diffuser shown in Fig. 2 capturing a nonuniform stream having a velocity profile shape characteristic of that for a free jet and operating at design. The diffuser is shown to consist of a constant area entrance section and a subsonic diffuser. For diffusers capturing subsonic jets the purpose of the entrance section is to provide a length for adjustment of the poor inlet profiles, if required, prior to diffusion.

The weight flow entering the diffuser referenced to the weight flow in a uniform stream having a velocity equal to the jet centerline velocity and a momentum equivalent to the jet momentum can be expressed as

$$\frac{\dot{w}}{\dot{w}_0} = \int_{-h/2w}^{+h/2w} \frac{\rho u}{\rho_0 u_0} d(y/w) \quad (1)$$

where w is the width of the equivalent uniform jet.

For constant total temperature and static pressure at the diffuser inlet, the density ratio in Eq. (1), for a perfect gas, becomes

$$\frac{\rho}{\rho_0} = \left\{ 1 + \frac{\gamma-1}{2} M_c \left[1 - \left(\frac{u}{u_c} \right)^2 \right] \right\}^{-1} \quad (2)$$

Substituting Eq. (2) into Eq. (1) yields

$$\frac{\dot{w}}{\dot{w}_0} = \int_{-h/2w}^{+h/2w} \frac{\left(\frac{u}{u_c} \right)}{1 + \frac{\gamma-1}{2} M_c^2 \left[1 - \left(\frac{u}{u_c} \right)^2 \right]} d(y/w) \quad (3)$$

Similarly, the stream thrust in the portion of the jet entering the diffuser referenced to the stream thrust in the equivalent uniform jet can be expressed as

$$\frac{F}{F_0} = \int_{-h/2w}^{+h/2w} \frac{1}{1 + \gamma M_c^2} \left\{ 1 + \frac{\gamma \left(\frac{u}{u_c} \right)^2 M_c^2}{1 + \frac{\gamma-1}{2} M_c^2 \left[1 - \left(\frac{u}{u_c} \right)^2 \right]} \right\} d(y/w) \quad (4)$$

Employing Eqs. (3) and (4), the average total pressure at the diffuser inlet (station 2) can be determined as follows. Letting

$$\Phi(M) = K \frac{F}{\dot{w} \sqrt{T_T}} \quad (5)$$

where $\dot{w} = P A g \sqrt{\frac{\gamma}{R}} M \left(1 + \frac{\gamma-1}{2} M^2 \right) / \sqrt{T_T}$, $K = g \sqrt{\frac{\gamma}{2(\gamma+1)R}}$ and

$\Phi(M)$ is a Mach number function tabulated in Ref. 5, $\Phi(\bar{M}_2)$ for constant total temperature can be written as

$$\Phi(\bar{M}_2) = \Phi(M_c) \frac{\left(\frac{F}{F_0} \right)}{\left(\frac{\dot{w}}{\dot{w}_0} \right)} \quad (6)$$

where \bar{M}_2 is the stream thrust average Mach number at the diffuser inlet. From continuity for constant total temperature

$$\frac{\bar{P}_{T_2}}{\bar{P}_{T_c}} = \frac{\bar{m}(M_c) w}{\bar{m}(\bar{M}_2) h} \left(\frac{\dot{w}}{\dot{w}_0} \right) \quad (7)$$

where

$$\bar{m}(M) = g \sqrt{\frac{\gamma}{R}} M \left[1 + \frac{\gamma-1}{2} M^2 \right]^{-\frac{\gamma}{2(\gamma-1)}}$$

From Eqs. (3) and (7) the average total pressure at the diffuser inlet referenced to the jet centerline pressure becomes

$$\frac{\bar{P}_{T_2}}{\bar{P}_{T_c}} = \frac{\bar{m}(M_c)}{\bar{m}(\bar{M}_2)} \left(\frac{y^*}{h} \right) \int_{-h/2y^*}^{h/2y^*} \frac{\frac{u}{u_c}}{1 + \frac{\gamma-1}{2} M_c^2 \left[1 - \left(\frac{u}{u_c} \right)^2 \right]} d(y/y^*) \quad (8)$$

where y^* is the distance from the jet centerline to the location in the jet where the velocity is one half the centerline velocity.

From a mass and momentum balance between stations 2 and 3 (outlined in the appendix*), the average total pressure ratio between stations 2 and 3 can be expressed as

$$\frac{\bar{P}_{T_3}}{\bar{P}_{T_2}} = \frac{\bar{m}(\bar{M}_2)}{\bar{m}(\bar{M}_3)} \quad (9)$$

The average Mach number at station 3, \bar{M}_3 , in Eq. (9) can be evaluated from the stream thrust ratio at that station. From Eq. (32) in the appendix, the stream thrust ratio becomes

$$\Phi_3 = \frac{K \left\{ 1 + \gamma \bar{M}_2^2 \left[1 - \frac{\bar{C}_f}{2} \left(\frac{A_w}{A_2} \right) \right] \right\}}{\dot{m}(\bar{M}_2)} \quad (10)$$

where

$$K = g \sqrt{\frac{\gamma}{2(\gamma+1)R}} \quad (11)$$

$$\dot{m}(\bar{M}) = g \sqrt{\frac{\gamma}{R}} M \left[1 + \frac{\gamma-1}{2} M^2 \right]^{1/2} \quad (12)$$

$$\bar{C}_f = \frac{F_{\text{WALL FRICTION}}}{\bar{Q}_2 A_w} \quad (13)$$

*Appendix on pp. 90-92.

and A_w is the wetted area of the constant area passage. Knowing Φ_3 from Eq. (10), \bar{M}_3 can be obtained from the tables of Ref. 5.

From the definition of subsonic diffuser efficiency the pressure ratio between stations 3 and 4 can be expressed as

$$\frac{\bar{P}_{T_4}}{\bar{P}_{T_3}} = \frac{\bar{P}_3}{\bar{P}_{T_3}} + \eta_D \left(1 - \frac{\bar{P}_3}{\bar{P}_{T_3}} \right) \quad (14)$$

where η_D is the subsonic diffuser efficiency and $\bar{P}_3 / \bar{P}_{T_3}$ can be determined as a function of \bar{M}_3 from the Ref. 5 tables.

Computed values of overall diffuser pressure recovery obtained from Eqs. (8), (9) and (14) are presented in Fig. 3 for a range of jet Mach numbers and diffuser inlet heights relative to the nondimensionalizing jet width, y^* . For these computations, the skin friction coefficient for the constant area passage was assumed to be 0.0015. This skin friction coefficient, which is somewhat below a typical flat plate value, was chosen to reflect the lower skin friction associated with profile adjustment in the constant area entrance section. Since the pressure loss due to skin friction in the constant area passage is normally small, errors in skin friction coefficient will not seriously affect the calculated diffuser pressure recovery. The wetted area for the constant area passage was computed assuming the profile adjustment length was two diffuser inlet heights. The subsonic diffuser efficiency was taken to be 0.80.

DIFFUSER PRESSURE RECOVERY ANALYSIS FOR "BLOCKED-LOAD" OPERATION

Consider the diffuser shown in Fig. 4 for which a portion of the jet flow enters, proceeds toward the diffuser exit and is subsequently reversed in direction, flows along the diffuser walls and exhausts at the diffuser inlet.

Assuming that (1) the width of the streamtube in the undisturbed flow containing the mass flow which enters the diffuser is one-half the diffuser capture width, (2) the velocity profile of the reversed flow at station 2 is identical to that of the jet flow entering the diffuser, and (3) wall friction is negligible, the momentum equation for the

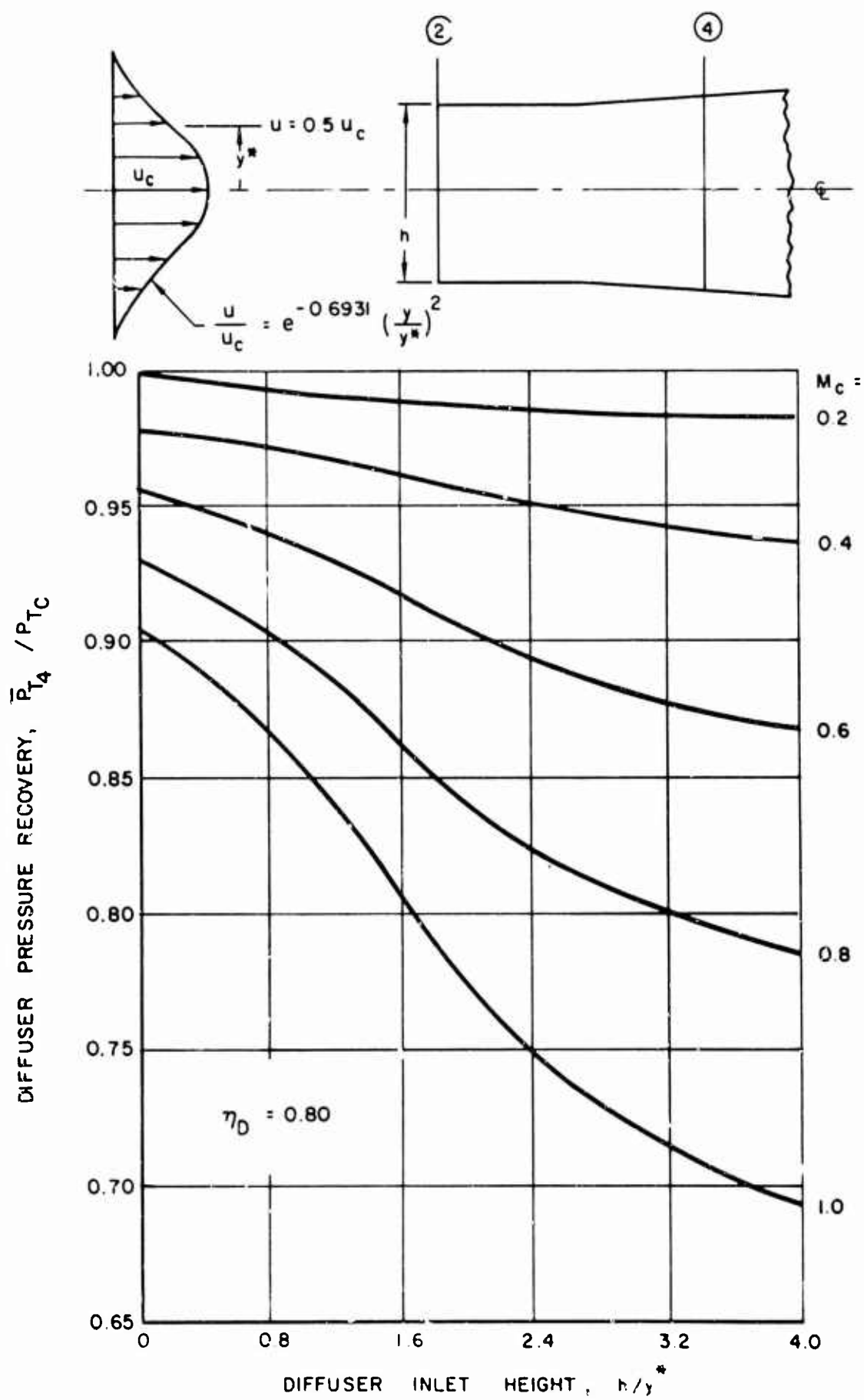


FIGURE 3 VARIATION OF DESIGN PRESSURE RECOVERY WITH DIFFUSER INLET HEIGHT

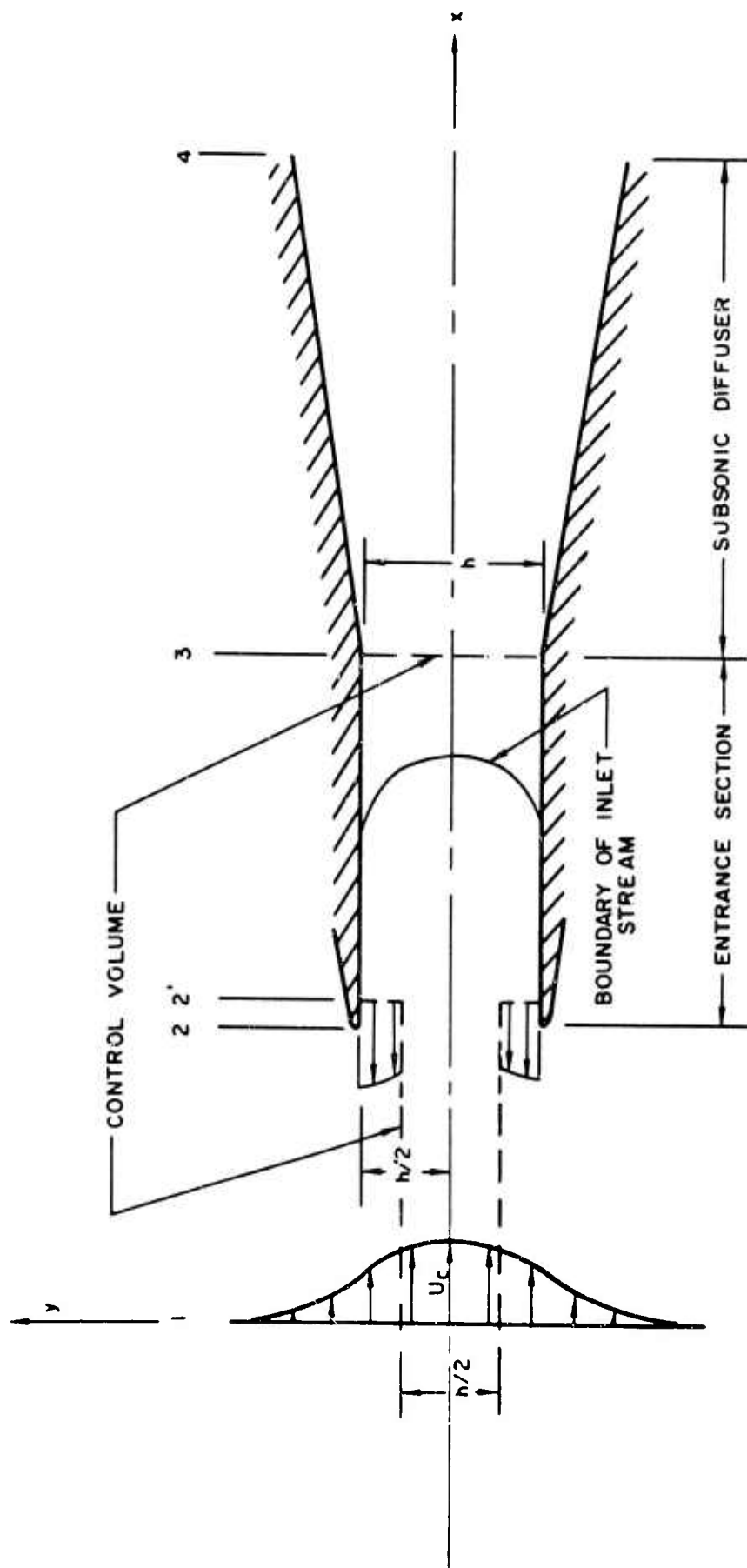


FIGURE 4 FLOW MODEL FOR "BLOCKED-LOAD" ANALYSIS

control volume shown in dashed lines in Fig. 4 becomes

$$\int_s [P \bar{n} + \rho \bar{u} (\bar{u} \cdot \bar{n})] ds = 0 \quad (15)$$

where s is the surface area per unit width of the control volume and \bar{n} is the unit vector normal to the surface s . For the control volume being considered Eq. (15) reduces to

$$(\bar{P}_3 - P_1)h = \left(\int_{s_1} \rho u^2 ds + \int_{s_2} \rho u^2 ds \right) \bar{i} \quad (16)$$

or

$$\frac{\bar{P}_3}{P_1} = 1 + \frac{2}{P_1 h} \int_0^{h/4} \rho u^2 dy \quad (17)$$

If the approaching stream is uniform and incompressible and has a velocity equal to the jet centerline velocity, Eq. (17) reduces to

$$\bar{P}_3 = P_1 + \frac{\rho u_c^2}{2} \quad (18)$$

Similarly Eq. (17) must reduce, for a compressible uniform flow, to

$$\bar{P}_3 = P_1 \left[1 + \left(\frac{\gamma-1}{\gamma P_1} \right) \frac{\rho u_c^2}{2} \right]^{\frac{\gamma}{\gamma-1}} \quad (19)$$

Therefore Eq. (17) for a nonuniform stream can be written as

$$\frac{\bar{P}_3}{P_1} = \left[1 + \frac{2(\gamma-1)}{\gamma P_1 h} \int_0^{h/4} \rho u^2 dy \right]^{\frac{\gamma}{\gamma-1}} \quad (20)$$

Nondimensionalizing with respect to the jet centerline velocity and the jet width, v^* , as in Eq. (8), Eq. (20) becomes

$$\frac{\bar{P}_3}{P_1} = \left[1 + 2(\gamma-1)M_c^2 \left(\frac{y^*}{h}\right) \int_0^{h/4y^*} \frac{\left(\frac{u}{u_c}\right)^2}{1 + \frac{\gamma-1}{2} M_c^2 \left[1 - \left(\frac{u}{u_c}\right)^2\right]} d(y/y^*) \right]^{\frac{\gamma}{\gamma-1}} \quad (21)$$

and finally

$$\frac{\bar{P}_3}{P_1} = \left(\frac{P_1}{P_{Tc}}\right) \left(\frac{\bar{P}_3}{P_1}\right) \quad (22)$$

where for isentropic flow

$$\frac{P_1}{P_{Tc}} = \left[1 + \frac{\gamma-1}{2} M_c^2\right]^{-\frac{\gamma}{\gamma-1}} \quad (23)$$

Computed values of "blocked-load" pressure recovery obtained from Eq. (22) are presented in Fig. 5 for a range of jet Mach numbers and diffuser inlet heights relative to the nondimensionalizing jet width, y^* .

EXPERIMENTAL STUDIES

Test Equipment and Procedure

A schematic diagram and photograph illustrating the test rig configuration employed for the experimental studies are presented in Figs. 6 and 7, respectively. The diffuser model shown in Fig. 6 was supported by struts fastened to the top and bottom walls of the test rig. These struts were adjustable to vary both the capture height of the diffuser and the location of the diffuser relative to the nozzle exit. Removable diffuser entrance sections were provided which attached at the subsonic diffuser inlet station. Aft of this attachment position the diffuser assembly was the same for all tests. The nozzle blocks and the forward portion of the diffuser were enclosed by side plates sufficient to provide a two-dimensional flow passage. The area between the side plates was open to the atmosphere to allow entrainment along the free jet boundaries and eliminate resonant cavities which would contribute to jet instabilities. Fairings were provided at the base of the nozzle blocks to minimize jet edge oscillations at the diffuser entrance. The aft

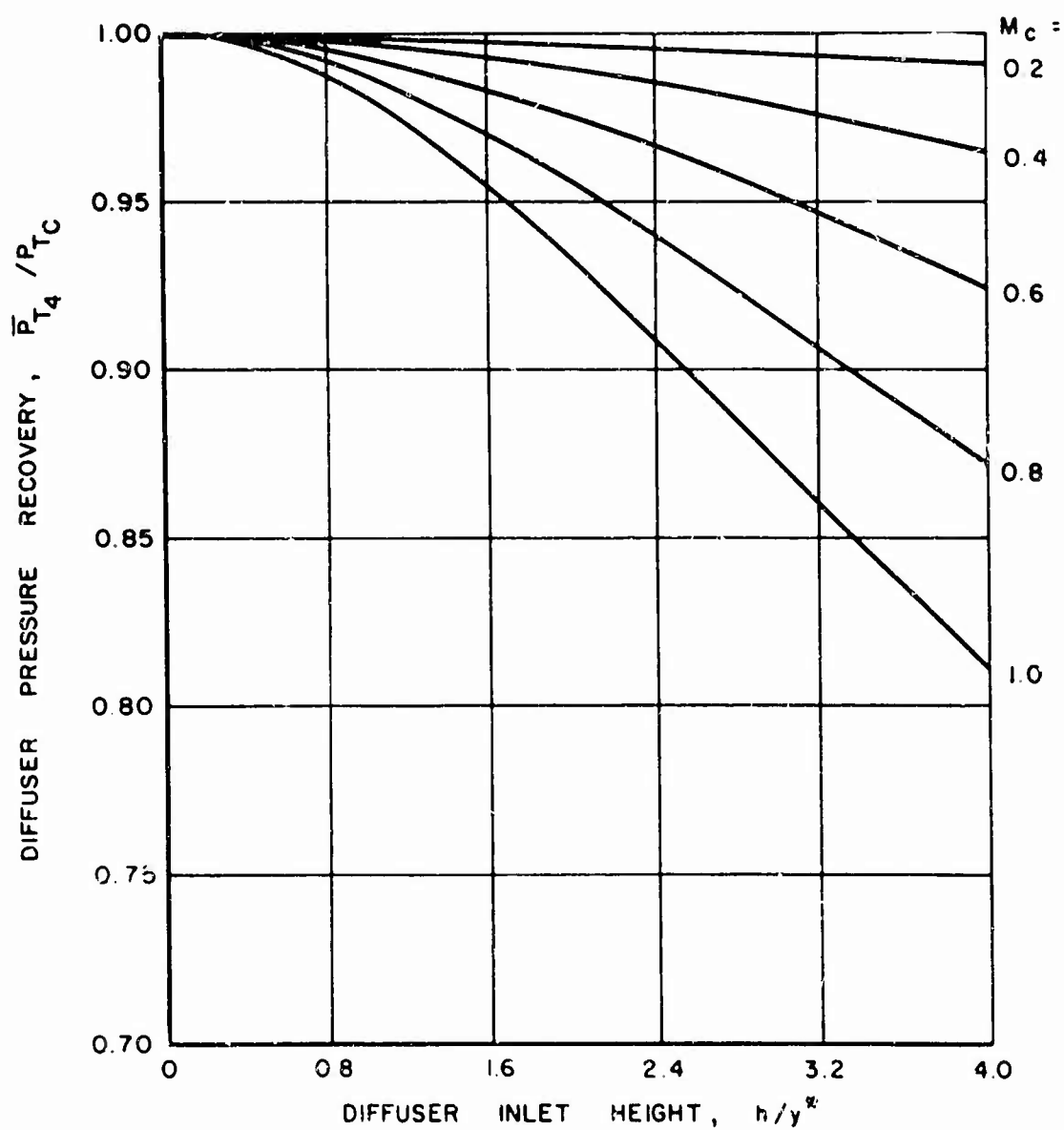
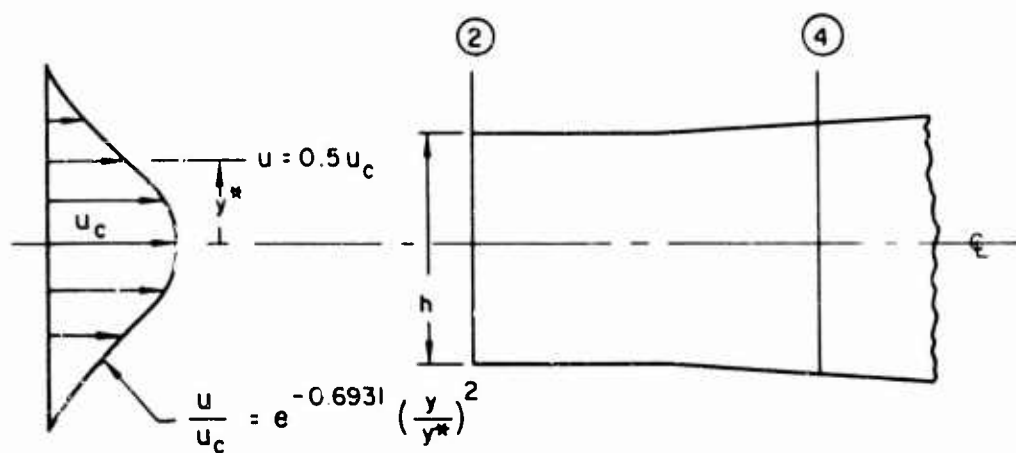


FIGURE 5 VARIATION OF "BLOCKED-LOAD" PRESSURE RECOVERY WITH DIFFUSER INLET HEIGHT

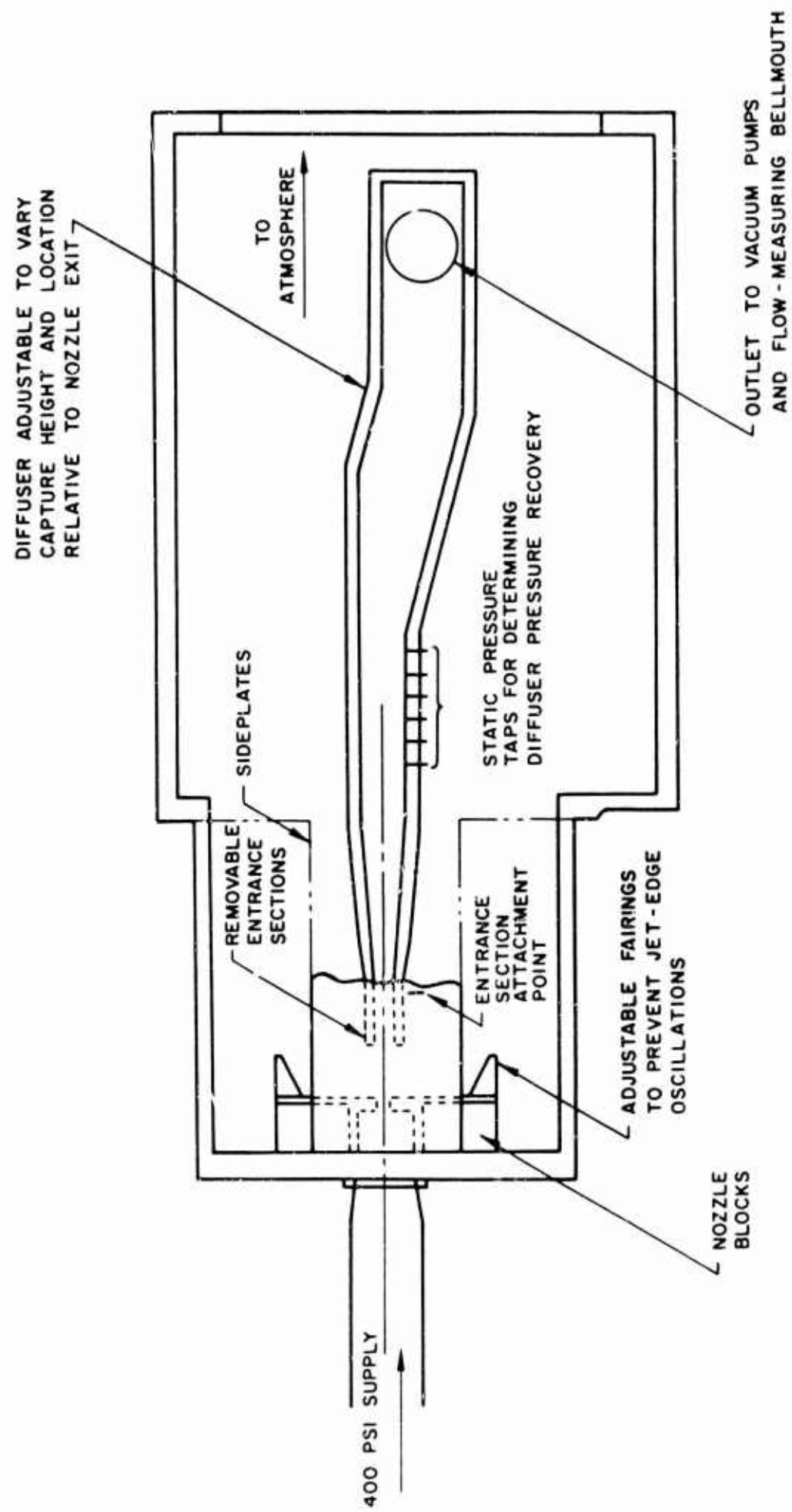


FIGURE 6 SCHEMATIC DIAGRAM OF TEST RIG

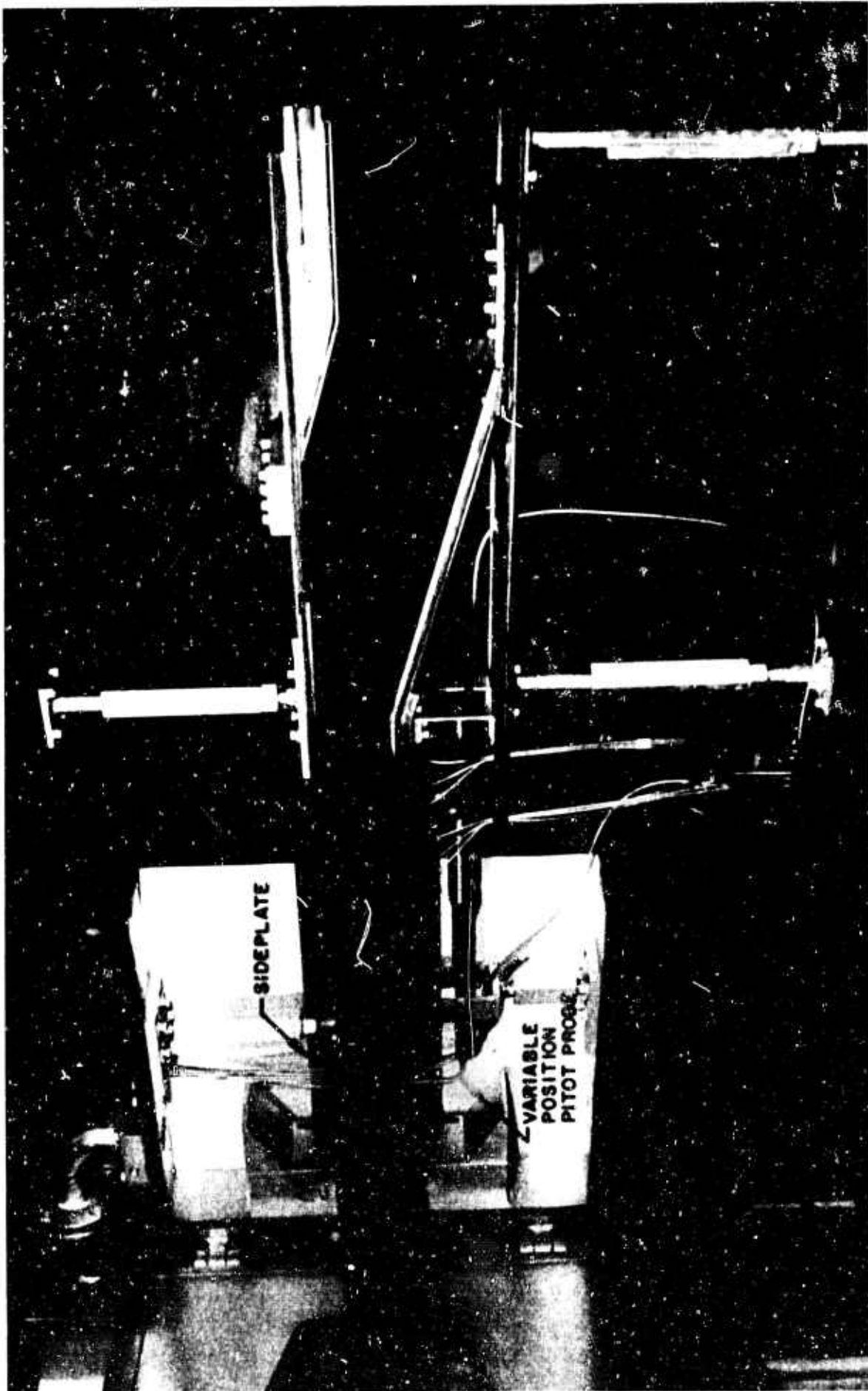


FIGURE 7 PHOTOGRAPH OF TEST RIG

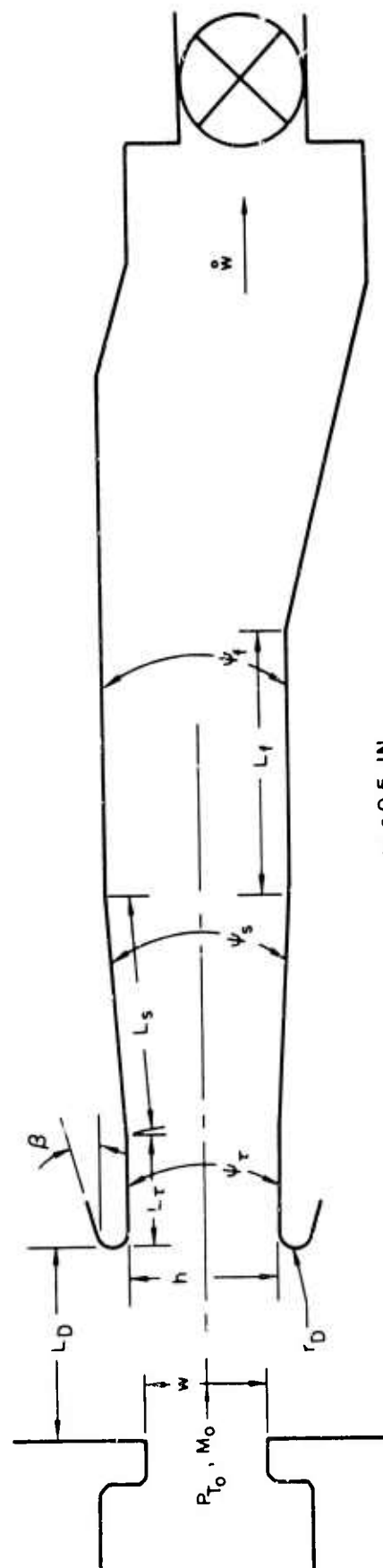
portion of the diffuser assembly was enclosed by the hinged side walls of the test rig over its entire height. The ends of this portion of the test rig, however, were open to atmosphere.

For all tests, static pressure taps were provided along the length of the entrance sections midway between the side plates to measure wall static pressure distribution and in the constant area passage downstream of the subsonic diffuser to measure the diffuser pressure recovery. The pitot pressure probe shown in Fig. 7 was employed to obtain profiles at both the upstream and downstream ends of the entrance section and stations upstream of the diffuser. All pressures were read on an electronic readout system having a resolution of 0.001 in.

A detailed description of the diffuser models employed for the studies is presented in Fig. 8. The diffuser models consisted of a constant area entrance section ($\psi_r = 0$) followed by a diffuser having a divergence angle of 11.0 deg ($\psi_s = 11.0$ deg). The purpose of the entrance section was to allow the nonuniform profile at the diffuser inlet to adjust to a more stable profile before diffusing. It was believed that by providing this profile adjustment length the tendency to separate in the subsonic diffuser is reduced and the subsonic diffuser efficiency is thereby increased.

Tests on these diffuser models were performed by throttling the exit of the diffuser passage while the jet total pressure and the pressure on the free boundary of the jet were held constant. Pressure on the free boundary of the jet was atmospheric, and the jet total pressure for a given Mach number was therefore a function of the barometric pressure. Tests were initiated with the diffuser throttle valve in the full-open position and continued until the throttle was closed or until the jet became unstable. For each throttle position, measurements of the diffuser weight flow and diffuser exhaust static pressure were obtained. From these measurements the continuity-average total pressure at the diffuser exit was calculated.

For selected throttle settings, pitot pressure profiles were obtained upstream of the diffuser inlet and at both the upstream and downstream ends of the constant area entrance section. Velocity profiles were obtained from the measured pitot pressures and assumed static pressure profiles throughout the jet for constant total temperature. For the stations upstream of the diffuser the static pressure was taken to be constant and equal to the pressure on the free boundary of the jet. For stations within the diffuser, the static pressure was taken to be constant across the diffuser and equal to the wall static pressure at that station.



$$\begin{aligned}
 \psi_\tau &= 0 & \psi_s &= 11.0 \text{ DEG} & \psi_f &= 0 \\
 L_s/w &= 17.1 & L_f/w &= 22.5
 \end{aligned}$$

MODEL NO.	L_D/w	h/w	L_r/w	r_D/w	β -DEG
1	7.3	2.0	7.44	0.25	0
2	7.3	2.0	4.48	0.25	0
3	7.3	2.0	1.80	0.25	0

FIGURE 8 SKETCH OF MODELS

Measurements of the pitot pressure profiles inside the diffuser could not be obtained at distances less than approximately 0.060 in. from the bottom diffuser wall because of probe interference. Consequently, the velocity profiles for this portion of the stream were estimated by assuming profile similarity about the diffuser centerline and using the velocity profile determined at the upper wall.

Discussion of Experimental Results

Considerable trouble was experienced with jet instabilities caused by jet-edge oscillations which excited resonant frequencies of the test rig. These instabilities were eliminated by providing only partial side plates in the forward portion of the test rig as shown in Fig. 6 with the remaining area open to atmosphere, and also by providing fairings at the base of the nozzle blocks. By proper positioning of these fairings, also shown in Fig. 6, the jet oscillations could be essentially eliminated. Typical velocity profiles obtained at the diffuser entrance with and without jet-edge oscillations are presented in Fig. 9 for the same diffuser back pressure and initial jet Mach number. The velocity profile with jet-edge oscillations was obtained with the fairings at the base of the nozzle blocks removed. The comparison presented in Fig. 9 shows the maximum velocity and hence the maximum total pressure is decreased by the presence of oscillations but that the profile shape is somewhat improved. The improved profile shape with jet oscillation is believed to be a result of increased mixing which is promoted by the oscillation in the vicinity of the diffuser entrance. All the subsequent results presented were obtained with the fairings positioned to minimize jet-edge oscillations.

Velocity profiles obtained upstream of the diffuser inlet and immediately downstream of the inlet for an initial jet Mach number 0.66 are presented in Fig. 10 for the three flow regimes encountered. At upstream stations of 0.9 and 0.4 diffuser inlet heights, the velocity profiles are shown to be relatively unaffected by diffuser back pressure. These results suggest that diffuser "over-ingestion" or "spillage" is a relatively local effect for the range of conditions shown. Within the diffuser, however, as would be expected, the velocities decrease as the back pressure is increased. Corresponding velocity profiles at the end of the constant area profile adjustment lengths are presented in Fig. 11. For each flow regime the velocity profiles presented in Fig. 11 for the three profile adjustment lengths were obtained at the same value of diffuser inlet static pressure relative to the jet total pressure. It is shown in this figure that symmetrical well-developed velocity profiles are not obtained for the two shorter profile adjustment lengths tested

$$M_0 = 0.66$$

● WITH JET-EDGE OSCILLATIONS

○ WITHOUT JET-EDGE OSCILLATIONS

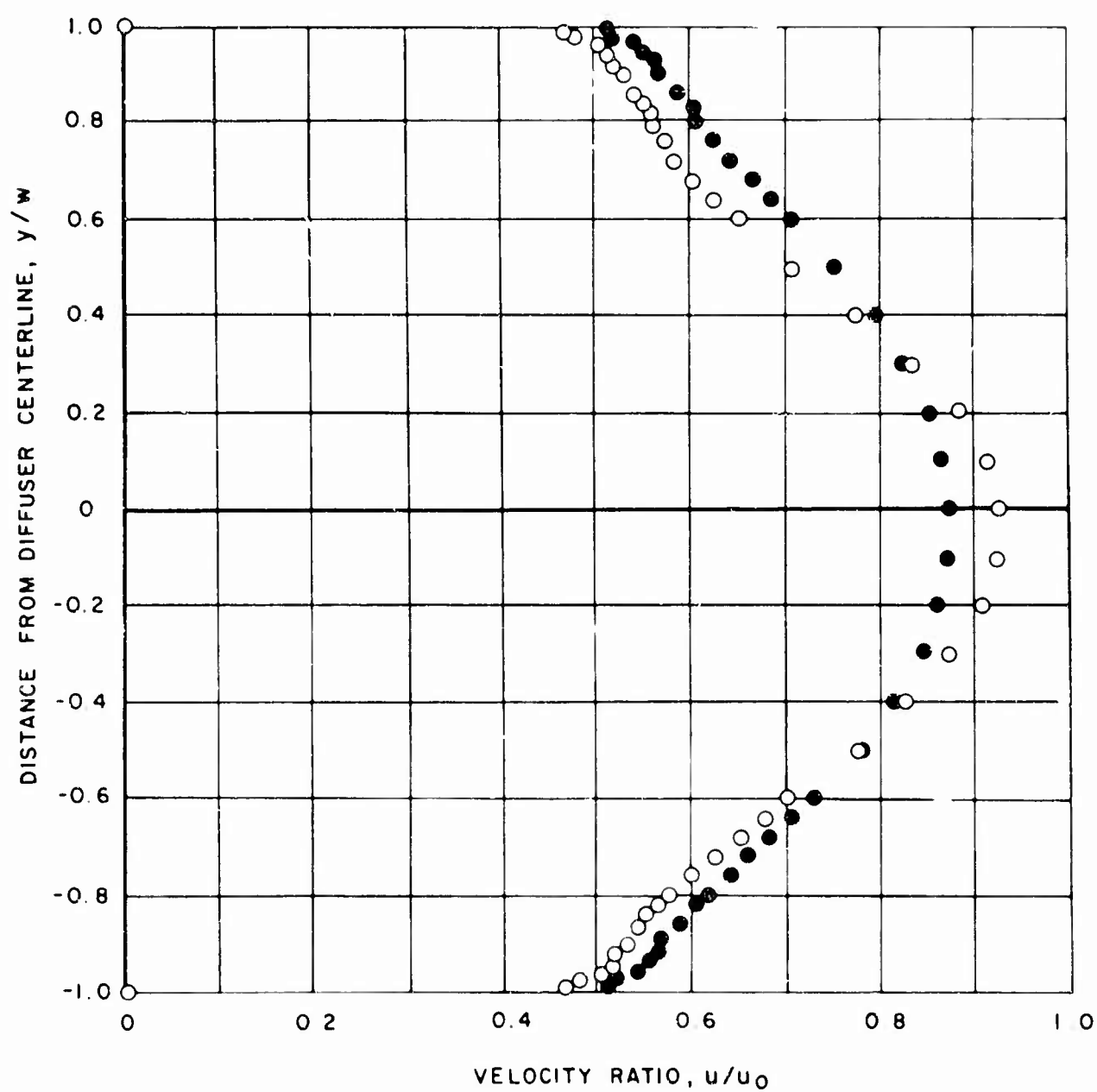


FIGURE 9 TYPICAL VELOCITY PROFILES AT DIFFUSER INLET

$M_0 = 0.66$
 $h/w = 2.0$

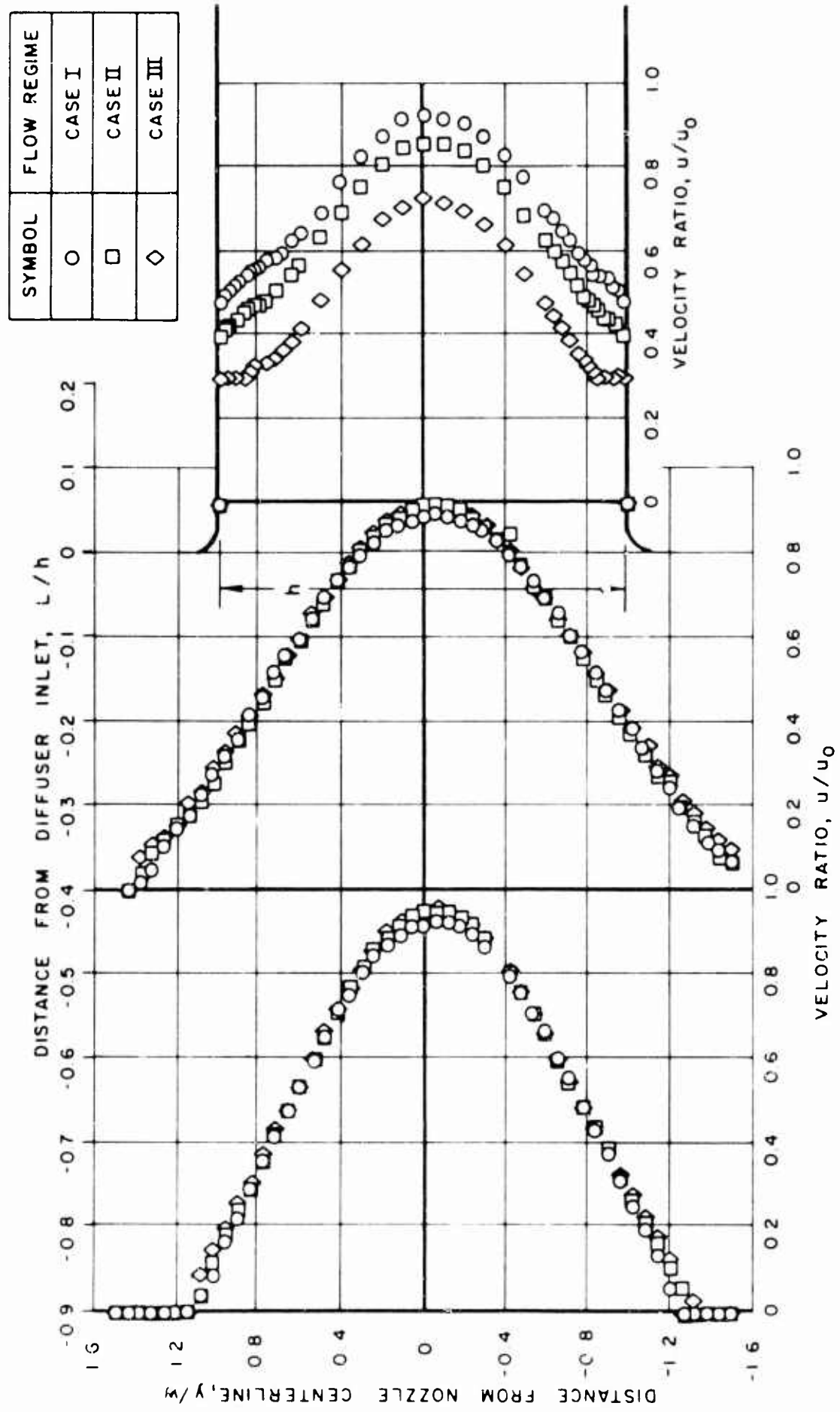


FIGURE 10 VELOCITY PROFILES AT INLET OF DIFFUSER

$$M_0 = 0.66$$

$$h/w = 2.0$$

SYMBOL	FLOW REGIME
○	CASE I
□	CASE II
◇	CASE III

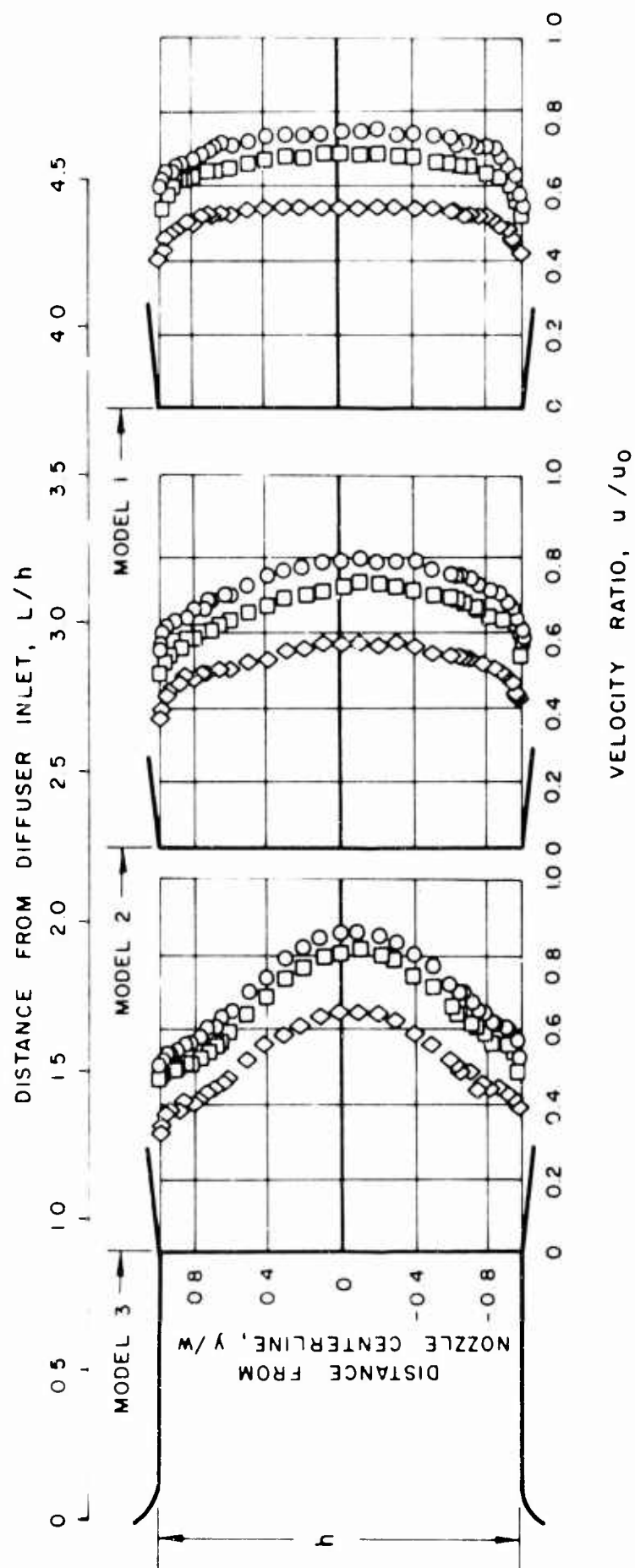


FIGURE 11 VELOCITY PROFILES AT END OF PROFILE ADJUSTMENT LENGTH

although such a profile is approached for the model having the longest entrance section length. Static pressure distributions along the wall of the profile adjustment section for the three lengths tested are presented in Fig. 12. The static pressure distributions for the three profile adjustment lengths are shown to be comparable in the region of overlap for the Case II and III flow regimes. For the Case I flow regime, however, these static pressure distributions are slightly different. For all flow regimes the static pressure rise is only slightly greater for the profile adjustment length of 3.7 diffuser heights than for the length of 2.2 diffuser heights, whereas the static pressure rise for the shorter length is considerably less. These results suggest that the major portion of the profile adjustment occurs within 2.0 diffuser heights. This result is also evident by comparing the velocity profiles in Fig. 11.

COMPARISON OF ANALYTICAL AND EXPERIMENTAL RESULTS

Diffuser pressure recovery characteristics are presented in Fig. 13. In this figure the diffuser exit total pressure, \bar{P}_{T_d} , relative to the ambient static pressure, P_0 , divided by the initial jet total pressure, P_{T_0} , also relative to ambient pressure, is plotted as a function of the weight flow captured by the diffuser, \dot{w} , divided by the initial jet weight flow, \dot{w}_0 . The three flow regimes are designated in order that this figure might be related to the previous figures. The conditions at which the velocity profiles presented previously were obtained are also indicated on the figure. The results presented show that extremely small differences in diffuser performance exist for the various profile adjustment lengths investigated, suggesting that the loss in diffuser efficiency attributable to poor inlet profiles is small for low-angle subsonic diffusers. The design diffuser pressure recovery and the "blocked-load" pressure recovery obtained from Figs. 3 and 5, respectively, for the inlet conditions existing for the test, are indicated. Good agreement is shown between the analytical and experimental results for the design condition. The "blocked-load" pressure recovery also appears to be in good agreement with the extrapolated experimental results.

The theoretical variation of pressure recovery with diffuser weight flow shown in dashed lines in Fig. 13 was obtained by fairing a parabola through the analytical results at design and "blocked-load" utilizing a specified slope at design. The slope at design was obtained by assuming that the variation in diffuser pressure recovery with diffuser weight flow, near design, could be simulated by changes in diffuser capture height. Such an approximate approach appears to yield reasonable agree-

$$M_0 = 0.66$$

$$h/w = 2.0$$

SYMBOL	MODEL	L_T/h
○	1	3.72
□	2	2.24
◇	3	0.90

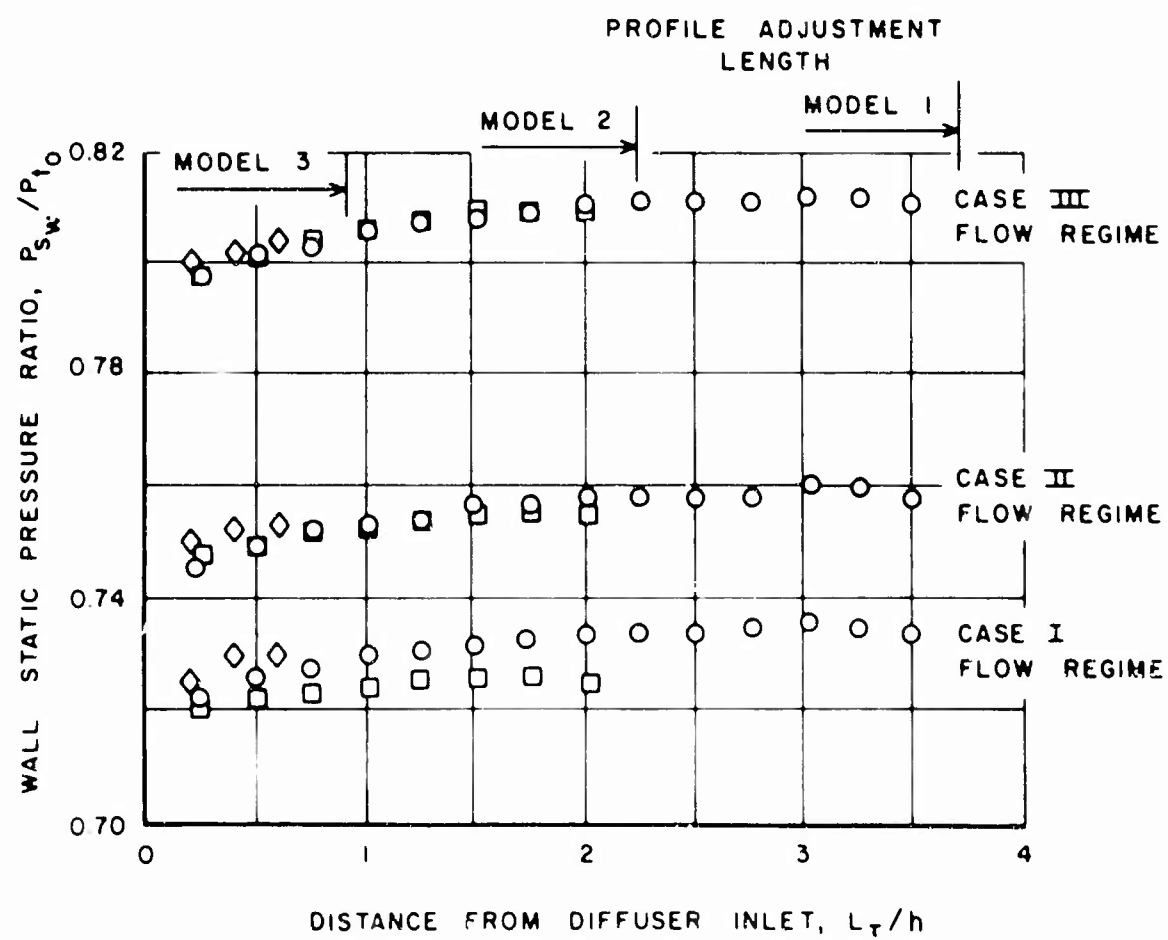


FIGURE 12 STATIC PRESSURE DISTRIBUTIONS ALONG PROFILE ADJUSTMENT LENGTH

$$M_0 = 0.66$$

$$h/w = 2.0$$

SYMBOL	MODEL	L_r/h
○	1	3.72
□	2	2.24
◇	3	0.90

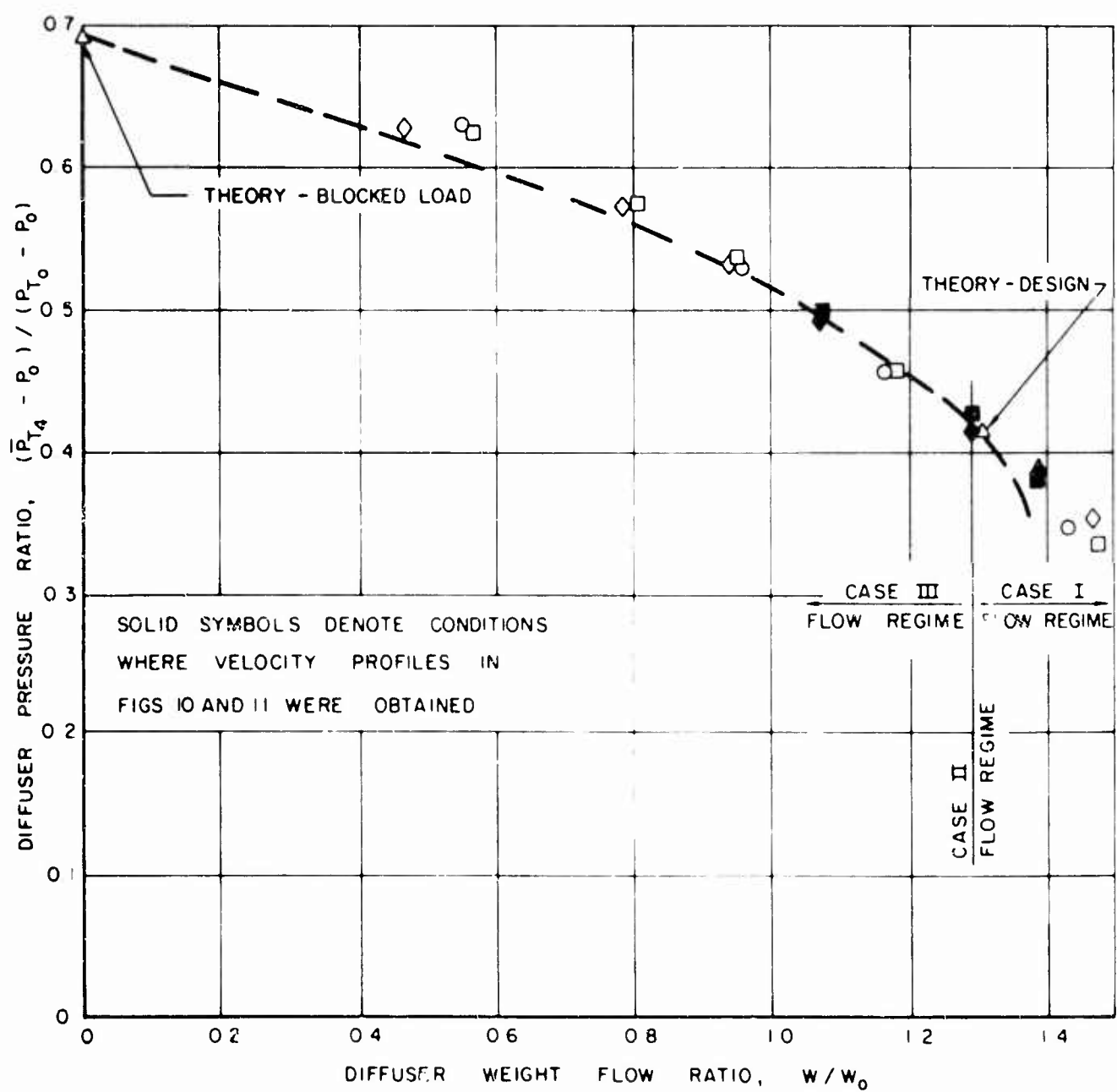


FIGURE 13 WEIGHT FLOW AND PRESSURE RECOVERY CHARACTERISTICS

ment with the experimental results for the Case III flow regime with somewhat poorer agreement shown for the Case I flow regime. A more rigorous analysis for obtaining "off-design" diffuser pressure recovery characteristics requires detailed knowledge of the characteristics of the flow immediately upstream of the diffuser.

LIST OF REFERENCES

1. McLafferty, C. H., E. L. Krasnoff, E. D. Ranard, W. G. Rose and R. D. Vergara: Investigation of Turbojet Inlet Design Parameters. UAC Research Laboratories Report R-0790-13, December, 1955.
2. Kepler, C. E.: Investigation of the Performance of a Variable-Geometry Diffuser for the AEDC Propulsion Wind Tunnel. UAC Research Laboratories Report R-0667-26, August 15, 1955.
3. Cnossen, J. W., and R. L. O'Brien: Investigation of the Diffusion Characteristics of Supersonic Streams Composed Mainly of Boundary Layers. ASD Technical Documentary Report, ASD TDR 62-528 (to be published).
4. Research and Development of Fluid Amplifiers for Turbopropulsion System Control. Massachusetts Institute of Technology Report DSR 9159-2, June 30, 1964.
5. Kennedy, E. C., D. W. Sonheim, and A. M. Barnes: New Mach Number Tables for Internal Ramjet Flow Analysis. OAL Memorandum Report CF 1798, April, 1952.

LIST OF SYMBOLS

A	Passage cross section area
A_w	Wetted area of diffuser constant area passage
\bar{C}_f	Average skin friction coefficient in constant area passage
F	Stream thrust
g	Acceleration due to gravity, $\frac{ft}{sec^2}$
h	Diffuser entrance height
K	Constant in expression for stream thrust ratio, Eq. (5)
L	Length of diffuser section
L_D	Distance between jet nozzle and diffuser inlet lip measured parallel to jet centerline
\bar{m}	Mass flow function defined in Eq. (26)
\dot{m}	Mass flow function defined in Eq. (27)
M	Mach number
\bar{n}	Unit vector normal to control surface in Fig. 4
P	Static pressure
P_T	Total pressure
q	Dynamic pressure
r_D	Diffuser inlet lip radius of curvature
R	Gas constant, ft-lbf/Slug-°R
s	Surface area of control volume in Fig. 4
T_T	Total temperature
u	Velocity

LIST OF SYMBOLS
(Cont.)

\vec{U}	Velocity vector
U	Ratio of local centerline velocity to initial jet velocity
w	Width of equivalent uniform jet
\dot{w}	Weight flow
x	Distance along jet centerline
y	Distance perpendicular to jet centerline
y^*	Value of y at which $u/u_c = 0.5$
β	External diffuser lip angle
γ	Ratio of Specific heats
ψ	Included angle of diffuser section
η_D	Subsonic diffuser efficiency defined in Eq. (34)
ρ	Density
Φ	Stream thrust ratio

Subscripts

0	Denotes conditions in the equivalent uniform jet
1	Denotes conditions upstream of the diffuser inlet lip
2	Denotes conditions at the diffuser inlet lip
3	Denotes conditions at the end of the constant area passage
4	Denotes conditions at the diffuser exit
c	Denotes power jet centerline
f	Denotes final subsonic diffuser section

LIST OF SYMBOLS
(Cont.)

- s Denotes initial subsonic diffuser section
- r Denotes entrance section of diffuser
- ∞ Denotes conditions at infinity

Superscripts

- Average conditions

APPENDIX

Development of Procedure for Computing Diffuser Pressure Recovery for Design Operation

Consider the diffuser shown in Fig. 2 capturing a nonuniform stream having a velocity profile characteristic of that for a free jet.

From a mass balance between stations 2 and 3, assuming that $T_{T_2} = T_{T_3}$, it follows that

$$\bar{P}_{T_3} \bar{m}(\bar{M}_3) A_3 = \bar{P}_{T_2} \bar{m}_2(\bar{M}_2) A_2 \quad (24)$$

and

$$\bar{P}_3 \dot{m}(\bar{M}_3) A_3 = \bar{P}_2 \dot{m}_2(\bar{M}_2) A_2 \quad (25)$$

where

$$\bar{m}(M) = g \sqrt{\frac{\gamma}{R}} M \left[1 + \frac{\gamma-1}{2} M^2 \right]^{-\frac{\gamma}{2(\gamma-1)}} \quad (26)$$

and

$$\dot{m}(M) = g \sqrt{\frac{\gamma}{R}} M \left[1 + \frac{\gamma-1}{2} M^2 \right]^{1/2} \quad (27)$$

From a momentum balance between stations 2 and 3,

$$\bar{P}_3 A_3 (1 + \gamma \bar{M}_3^2) = \bar{P}_2 A_2 (1 + \gamma \bar{M}_2^2) - F_{\text{WALL FRICTION}} \quad (28)$$

Let

$$F_{\text{WALL FRICTION}} = \bar{Q}_2 \bar{C}_f A = \frac{\gamma \bar{P}_2 \bar{m}_2^2}{2} \bar{C}_f A_w \quad (29)$$

where

$$A_w = \text{wetted area of wall} \quad (30)$$

Substituting Eqs. (29) and (30) into Eq. (28) yields

$$\bar{P}_3 A_3 (1 + \gamma \bar{M}_3^2) = \bar{P}_2 A_2 \left\{ 1 + \gamma \bar{M}_2^2 \left[1 - \frac{\bar{C}_f}{2} \frac{A_w}{A_2} \right] \right\} \quad (31)$$

Dividing Eq. (31) by Eq. (27) yields upon substitution into Eq. (5)

$$\Phi_3 = K \frac{\left\{ 1 + \gamma \bar{M}_2^2 \left[1 - \frac{C_f}{2} \frac{A_w}{A_2} \right] \right\}}{\bar{m}(\bar{M}_2)} \quad (32)$$

which can be employed together with the tables of Ref. 5 to obtain \bar{M}_3 . Rearranging Eq. (24), the average total pressure ratio between stations 2 and 3 can be expressed as

$$\frac{\bar{P}_{T_3}}{\bar{P}_{T_2}} = \frac{\bar{m}(\bar{M}_2) A_2}{\bar{m}(\bar{M}_3) A_3} \quad (33)$$

From the definition of subsonic diffuser efficiency, namely,

$$\eta_D = \frac{\bar{P}_4 - \bar{P}_3}{(\bar{P}_{T_3} - \bar{P}_3) - (\bar{P}_{T_4} - \bar{P}_4)} \quad (34)$$

or rearranging,

$$\eta_D = \frac{\frac{\bar{P}_4}{\bar{P}_3} - \frac{\bar{P}_3}{\bar{P}_{T_4}}}{\left(1 - \frac{\bar{P}_3}{\bar{P}_{T_3}}\right) \cdot \frac{\bar{P}_{T_4}}{\bar{P}_{T_3}} - \left(1 - \frac{\bar{P}_4}{\bar{P}_{T_4}}\right)} \quad (35)$$

it can be seen that if \bar{M}_4 is small, $\bar{P}_4 \approx \bar{P}_{T_4}$ and

$$\eta_0 = \frac{\frac{\bar{P}_{T_4}}{\bar{P}_{T_3}} - \frac{\bar{P}_3}{\bar{P}_{T_3}}}{1 - \frac{\bar{P}_3}{\bar{P}_{T_3}}} \quad (36)$$

Therefore, the total pressure ratio between stations 3 and 4 becomes

$$\frac{\bar{P}_{T_4}}{\bar{P}_{T_3}} = \frac{\bar{P}_3}{\bar{P}_{T_3}} + \eta_0 \left(1 - \frac{\bar{P}_3}{\bar{P}_{T_3}} \right) \quad (37)$$

where \bar{P}_3/\bar{P}_{T_3} may be determined from \bar{M}_3 .

THE FLOW OF TURBULENT INCOMPRESSIBLE
TWO-DIMENSIONAL
JETS OVER VENTILATED CAVITIES

JOHN R.C. PEDERSEN*
BRITISH AIRCRAFT CORPORATION,
UNITED KINGDOM

ABSTRACT

A flow model is presented which leads to a simple analysis for the shape of a curved two dimensional jet reattaching to an offset inclined wall, when the cavity beneath the jet is ventilated. Experimental results which support the analysis are also presented, good agreement is shown for ventilation flow rates up to some fifteen per cent of the main jet flow. For larger relative ventilation the momentum of the ventilating flow becomes significant but due allowance can be made for this.

The results are significant in forming one step towards ability to calculate the performance of fluid logic devices.

* The Author acknowledges with gratitude the help of Mr. Colin Brown who undertook all the experimental work involved.

1. INTRODUCTION

Before it is possible to proceed with the numerical design of turbulent reattachment elements it is necessary to know the effect of geometry on the flow and pressure required to cause switching. This problem can be divided into two parts. The first is to determine the effect of wall geometry and "control" or "secondary" flow on the characteristics of the jet, and the second part is to determine the jet characteristics, in particular the geometry relative to the splitter geometry, required for the jet to have neutral position stability (that is, to be on the point of switching). This paper describes some work done towards a solution to the first part of the problem.

I have made two simple generalizations to a flow model, which is reported by Sawyer, (ref.1), who acknowledges its origin to be a thesis by Dodds (ref.2). These modifications are, firstly to introduce the effect of ventilation into the cavity and secondly to generalise the geometry sufficiently for fluid logic element work.

By ventilation, above, I mean the addition or removal of fluid to or from a cavity without altering the flow momentum. By cavity I mean the space bounded on the one side by the jet between separation and reattachment, and on the other sides by the solid walls.

The model flow considers only two dimensional jets and does not take into account any effect of end plates. However a free empirical constant (the spreading parameter σ) is available whose value is controlled in part by the effect of end walls and aspect ratio of the flow.

Our extension of the model, and experimental tests, are only concerned with incompressible flow. However, Olson in a series of papers (ref.3) has shown good agreement for a similar model by making the spreading parameter sensitive to Mach. number of the jet. Olson has not, to date, published enough test data using ventilation to establish unequivocally the extension to compressible flow with ventilation but there seems little reason why such an extension should not be valid. Except in the case of power amplifiers it is probable that supersonic jets will not be used in reattachment devices because of difficulty in manufacturing accurate convergent - divergent nozzles in appropriate sizes, and because a large part of the applications field covers power supplies at low pressures, and therefore, we feel that an incompressible model has extensive applications.

The model considered includes "ventilation" but specifically excludes the momentum of the control flow. This is not embarrassing because in the case of the usual arrangement the control flow would be appreciably smaller than the main flow, and the Control Port larger than the main jet slot. These factors both reduce control flow momentum relative to main flow momentum. Moreover, if necessary the control jet momentum can be added to the main jet to produce a new main Jet Momentum and direction, the vector sum of the original main jet and the control jet momenta. The analysis presented can then be applied to this new flow.

Thus, although we are concerned here only with the ventilation effect, the model can accommodate control jet momentum in the cases where this is important.

In view of comments made by Keto (ref.4.) in which he establishes that it is possible for the jet to be switched on momentum alone, we have calculated the relative effectiveness of momentum and ventilation for a fairly typical case. We assumed a setback to jet height ratio of 10: where setback is the dimension h in fig.1., the distance from slot centre line to reattachment point projected in a plane normal to the initial jet direction in the no control flow state. Then for a control flow of 1/10 main jet flow, (a flow gain of 10), and control port width equal to main slot width, the effect of momentum alone is to produce downstream movement of reattachment of $\frac{\Delta l}{l_{\text{momentum}}} = 0.011$

The effect of the ventilation alone is to produce downstream shift of reattachment of $\frac{\Delta l}{l_{\text{ventilation}}} = 0.03$.

This relative magnitude is not strongly dependant on wall angle so the result is fairly typical. It seems that Keto's comments are probably only applicable to quite small flow gains.

Since Sawyers 1960 paper, used as the basis for our extension, Sawyer has published (ref.5.) an improved version. In this he gives more detailed attention to the effect of the original boundary layers on the jet walls, as well as to the pressure distribution near reattachment. He also has changed the analysis to be based on entrainment rather than spreading and has introduced an analysis for the effect of curvature on entrainment rate.

Sawyer's new analysis is more complicated and we considered that the original was adequate in view of the modifications which we had to make. Similar modifications can be made to the new theory at a later date if it is

found to be necessary to extend the theory to cover extreme cases for which an arbitrary choice of σ , such as we have made, would be unrealistic.

Some results have been calculated from the theory and compared with experimental data obtained on a water table rig. The agreement is excellent within the range of parameters likely to be of interest in the design of fluid logic devices.

2. THE MODEL FLOW

To reproduce all Sawyers arguments verbatim would be tedious and is unnecessary since his paper is easily accessible. I therefore will briefly outline the analysis, explaining the necessary modifications and presenting the complete equations. This note is self contained in that the line of argument is started at the beginning and is continuous, although not detailed.

2.1 We retain Sawyer's nomenclature and analysis introducing two new parameters. These are β , the angle between the wall at reattachment, and the initial jet direction, see fig. 1. and B the relative ventilation flow.

$$B = \frac{2 \text{ m ventilation}}{\text{m main jet}} \quad \text{The factor of 2 arises naturally in the analysis.}$$

Sawyer's analysis can be outlined as follows:-

The jet velocity profile is:

$$\frac{u}{U_{\max}} = \text{sech}^2 \eta$$

where $\eta = \sigma \frac{y}{x}$ and $X - Y$ are co-ordinates along and perpendicular to the curved jet. $X = 0$ is an effective origin, not the slot position.

σ is larger than the plan jet value of 7.67 for various reasons

1. The effect of jet curvature increases σ on the cavity side.
2. The effect of end plates causing extra dissipation of turbulence, and increasing σ (ref.6).
3. The effect of a standing vortex in the cavity increases σ by causing a streamwise flow just outside the jet on the cavity side.
4. Compressibility (where appropriate).

We consider σ to be a free empirical constant and in the case of our calculations we have taken $\sigma = 18.25$. This somewhat arbitrary choice is made to simplify later arithmetic. Sawyer finds $14 < \sigma < 20$ for his unventilated experiments.

Returning to the main argument.

The jet momentum per unit span is given by

$$J = \frac{4}{3} \rho U_{\max}^2 \frac{x}{\sigma},$$

Volume flow per unit span by

$$Q = 2U_{\max} \frac{X}{\sigma}$$

hence

$$Q = \sqrt{\frac{3JX}{\sigma \rho}} \text{ and } U_{\max} = \sqrt{\frac{3}{4} \frac{\sigma J}{\rho X}} \quad (1)$$

The jet arc radius is R so that the pressure difference across the jet is

$$\Delta p = \frac{J}{R} \quad (2)$$

X_1 is the station at reattachment and is assumed to be the point at which the locus of $\frac{U}{U_{\max}} = 0.1$ would strike the wall in the absence of local reattachment effects.

If δ_1 is the jet thickness at reattachment

$$\begin{aligned} \frac{\delta_1}{2X_1} &= \frac{1}{\sigma} \tanh^{-1} \sqrt{0.9} \\ &= \frac{1.825}{\sigma} = K \text{ say} \end{aligned} \quad (3)$$

hence putting $\sigma = 18.25$ makes $K = \frac{1}{10}$.

$$\text{Geometrically } X_1 - X_0 = R \theta \quad (4)$$

Where X_0 is slot position

$$h = R(1 - \cos \theta) + \frac{1}{2} \delta_1 \cos \theta \quad (5)$$

for simplicity put $l = R \sin \theta$ (6)

At this point we modify Sawyer's argument and introduce the ventilation flow m_v .

The mass flow between the jet centre line and the reattaching streamline at reattachment is equal to

$$\frac{1}{2} \sqrt{Jt\rho} + m_v$$

Sawyer's expression for the reattaching streamline then becomes

$$\frac{1}{2} \sqrt{Jt\rho} + m_v = T_1 \sqrt{\frac{3}{4} \rho \frac{JX_1}{\sigma}}$$

where $T_1 = \tanh \eta_{R_1}$ corresponds to the value of η on the reattaching streamline at reattachment.

$$\text{hence } \frac{\frac{1}{2} \sqrt{Jt\rho} (1 + 2m_v)}{\sqrt{Jt\rho}} = T_1 \sqrt{\frac{3}{4} \rho \frac{JX_1}{\sigma}}$$

But $\sqrt{Jt\rho}$ is the mass flow leaving the slot $= m_J$

$$\text{Putting } \frac{2m_v}{m_J} = B \text{ we obtain } \frac{(1+B)^2}{T_1^2} = \frac{3X_1}{\sigma t} \quad (7)$$

This replaces Sawyer's equation 7, $\frac{1}{T_1^2} = \frac{3X_1}{\sigma t}$, and is simply a more general form.

$$\text{But also } X_0 = \frac{\sigma t}{3} \quad (8)$$

$$\text{hence, generally, } \frac{X_0}{X_1} = \left(\frac{T_1}{1+B} \right)^2 \quad (9)$$

Combining all these equations

$$\frac{h}{t} = \frac{\sigma}{3} \left(\frac{1+B}{T_1} \right)^2 \frac{1}{\theta} \left(1 - \left(\frac{T_1}{1+B} \right)^2 \right) \left(1 - \cos \theta + \frac{K\theta \cos \theta}{1 - \left(\frac{T_1}{1+B} \right)^2} \right) \quad (10)$$

$$\frac{1}{h} = \frac{\sin \theta}{1 - \cos \theta + \frac{K\theta \cos \theta}{1 - \left(\frac{T_1}{1+B} \right)^2}} \quad (11)$$

$$\frac{h\Delta p}{J} = 1 - \cos \theta + \frac{K\theta \cos \theta}{1 - \left(\frac{T_1}{1+B}\right)^2} \quad (12)$$

It is now simply necessary to relate T_1 to θ to complete the solution.

Sawyer concludes, after some discussion of an alternative form, that the most accurate description of the reattachment momentum division, neglecting pressure effects, would be

$$\cos \theta = \frac{3}{2} T_1 - \frac{1}{2} T_1^3 \quad (\text{Sawyer's equ. 14})$$

But this is for the case where the wall is parallel to the original jet direction. We introduce an additional inclination so that

$$\cos (\theta - \beta) = \frac{3}{2} T_1 - \frac{1}{2} T_1^3 \quad (13)$$

is the appropriate general form.

We then solve equs. 10, 11 and 13 by selecting a range of values of T_1 , solving for θ , substituting these T_1 and θ into equs 10 and 11 and plotting (13) the results.

3. THE EXPERIMENTS

Our rig is a free surface water table fed from a constant head supply. The water depth is slightly more than 1 inch. For these tests we used a $\frac{1}{4}$ inch wide slot run at a velocity of 0.86 ft/sec. as measured by Rotameter and water depth at the slot. The slot Reynolds number was approximately 1.5×10^3 . This is considerably higher than the larger Critical Reynolds number found by Glaettli et al ref. 6 for the aspect ratio which was 4.8.

A few check tests over a range of flow rates showed that the results were practically independent of Reynolds number.

The ventilation flow was passed into the cavity across the largest width available for each test, and through a gauze screen. See fig. 2.

This was done to remove as much momentum from the ventilation flow as possible. Because of the rig construction this process was successful at larger $\frac{h}{l}$ and smaller β .

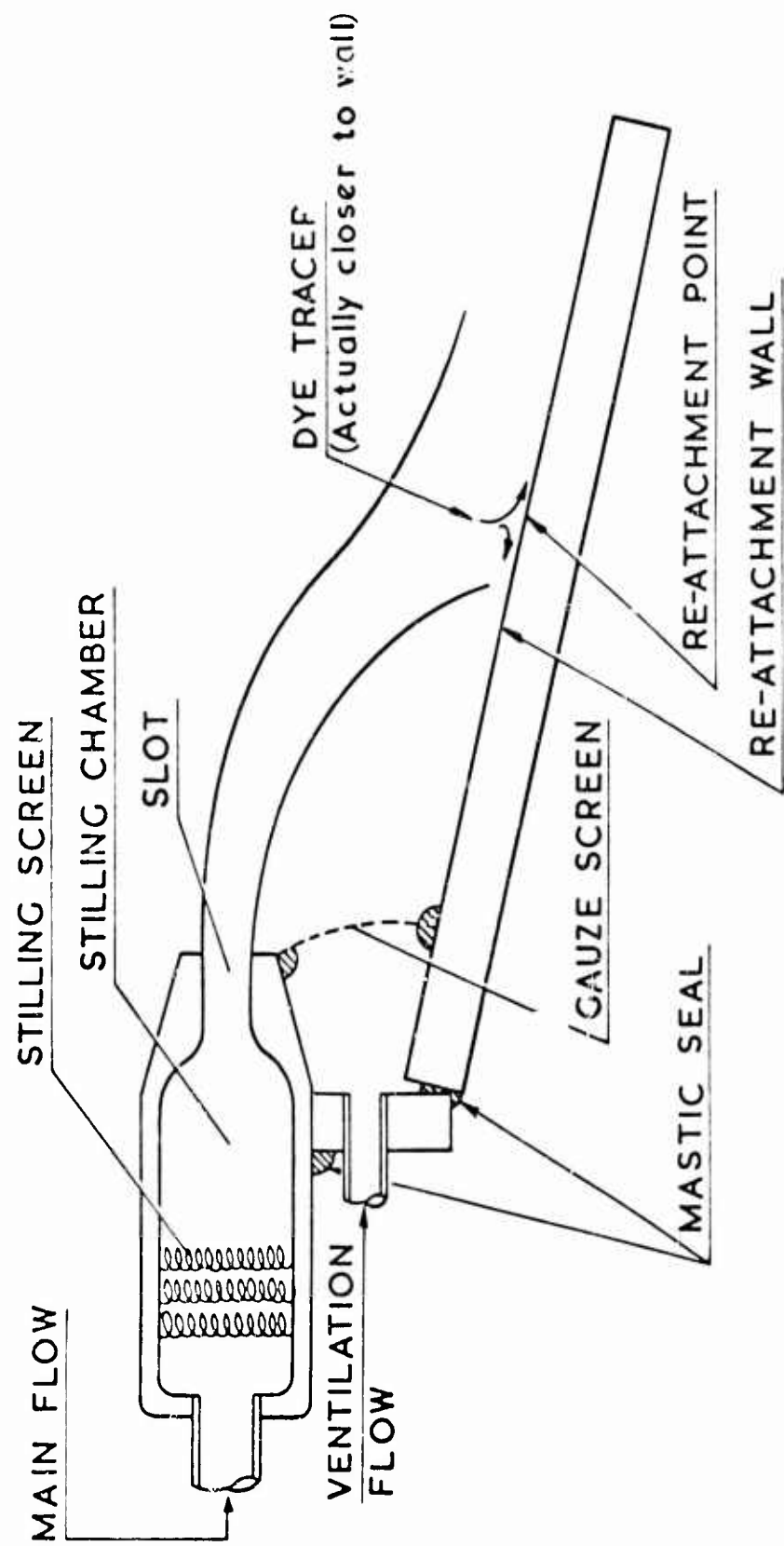


FIG.2 SKETCH OF TABLE RIG LAYOUT

The instrumentation used consisted simply of Rotameter flowmeters for the main and ventilation flows. Reattachment location was indicated by means of a hypodermic probe carrying dye. When positioned very close to the reattachment wall, direction of dye drift was a sensitive indicator of the stagnation point position. The probe was mounted on a traversing carriage and an illuminated graticule was available immediately below the tank plate glass floor. The Engineer operating the rig considered that he could locate reattachment, and position the walls to within less than 1/10 ins. This is about 3% of the shortest distances involved. The limitation is largely the effect of the water meniscus.

Rig components were simple metal blocks with well finished bases. These sealed to the glass floor under their own weight. Vertical joints were sealed with modelling clay.

Since the rig geometry was changed some fifteen times during the investigation it is possible that some data points have leakage. One point in particular $B = 0, \tan \beta = 3/10, \frac{h}{t} = 26.1$ fig.3 has measured $\frac{h}{t}$ large compared with its neighbour points and with theory. This discrepancy can be "explained" by assuming a leak of magnitude $B = 0.1$. Unfortunately, because of work load on the rig., it has been impossible to repeat any runs.

Tests were done with B up to 1.3 but these are only compared with calculated values up to $B = 0.65$ since for larger B an increasing difference was found between experiment and theory. A large part of this is undoubtedly due to momentum effects but since we were not equipped to measure velocities no attempt has been made to calculate the momentum effect. In any case, real devices would have different geometry (and momentum effects) and a range of B only up to about 0.2 (flow gain of 10).

4. COMPARISON OF THEORY WITH EXPERIMENT

Experimental results are plotted for $B < 0.65$ in figs.3, 4, and 5 for comparison with the theory. Fig.3 shows a collection of results from other workers for $B = \beta = 0$.

The convention has been adopted that our experimental points are linked to corresponding points on the theoretical curves since otherwise the number of figures would become prohibitive.

It is seen that the agreement is generally good, but deteriorates at small

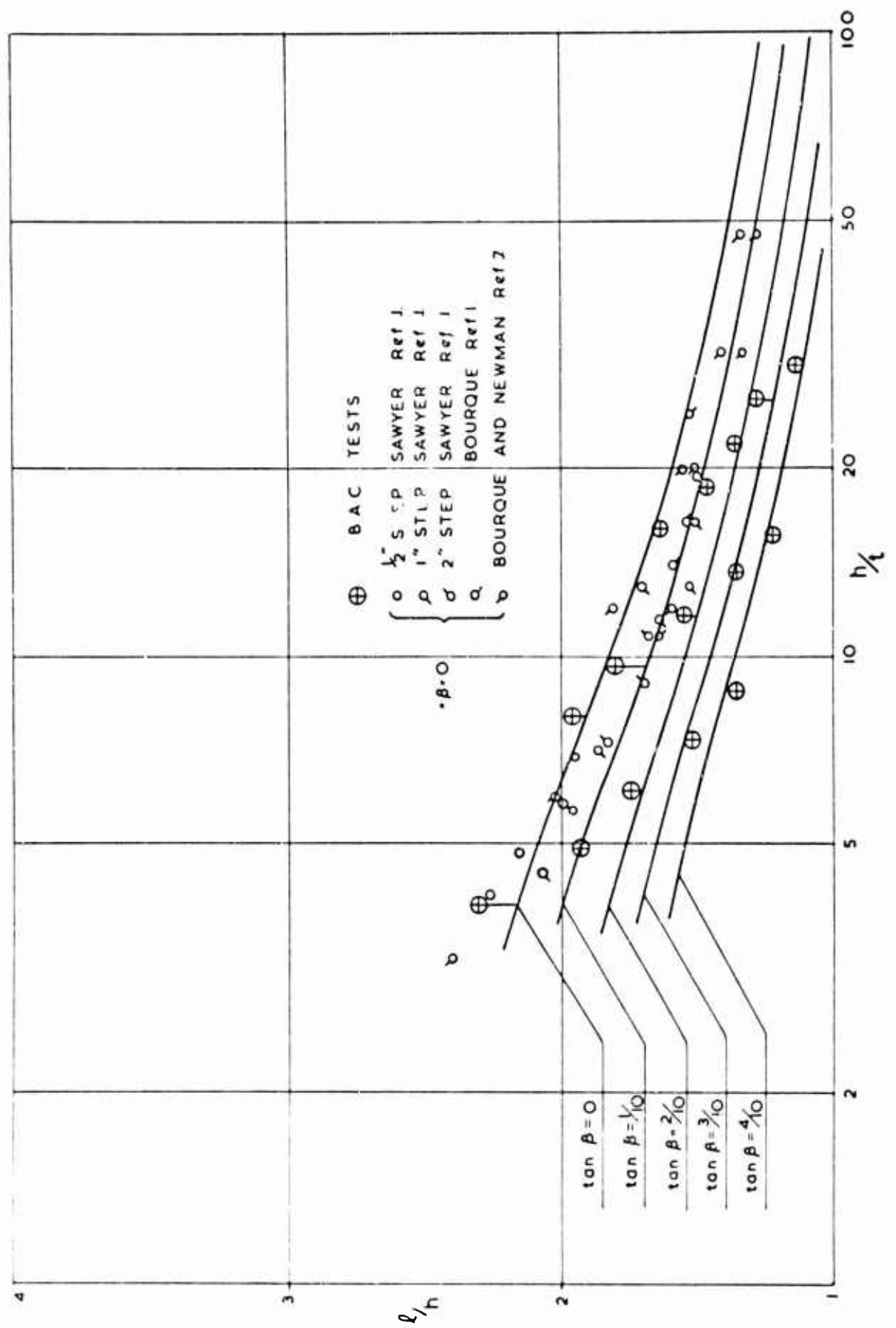


FIG.3. RESULTS FOR $B = 0$

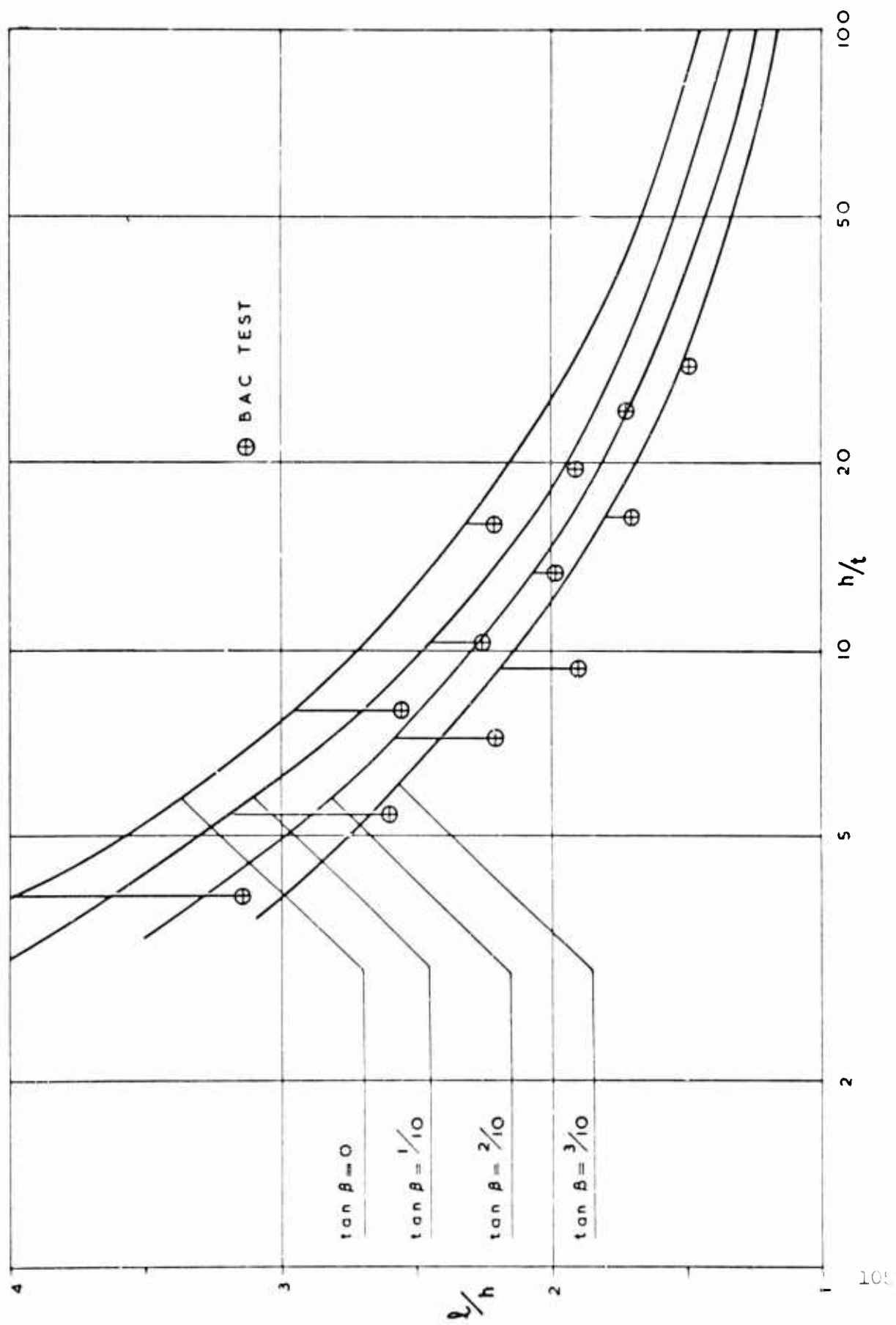


FIG.5 RESULTS FOR $\beta = 0.653$

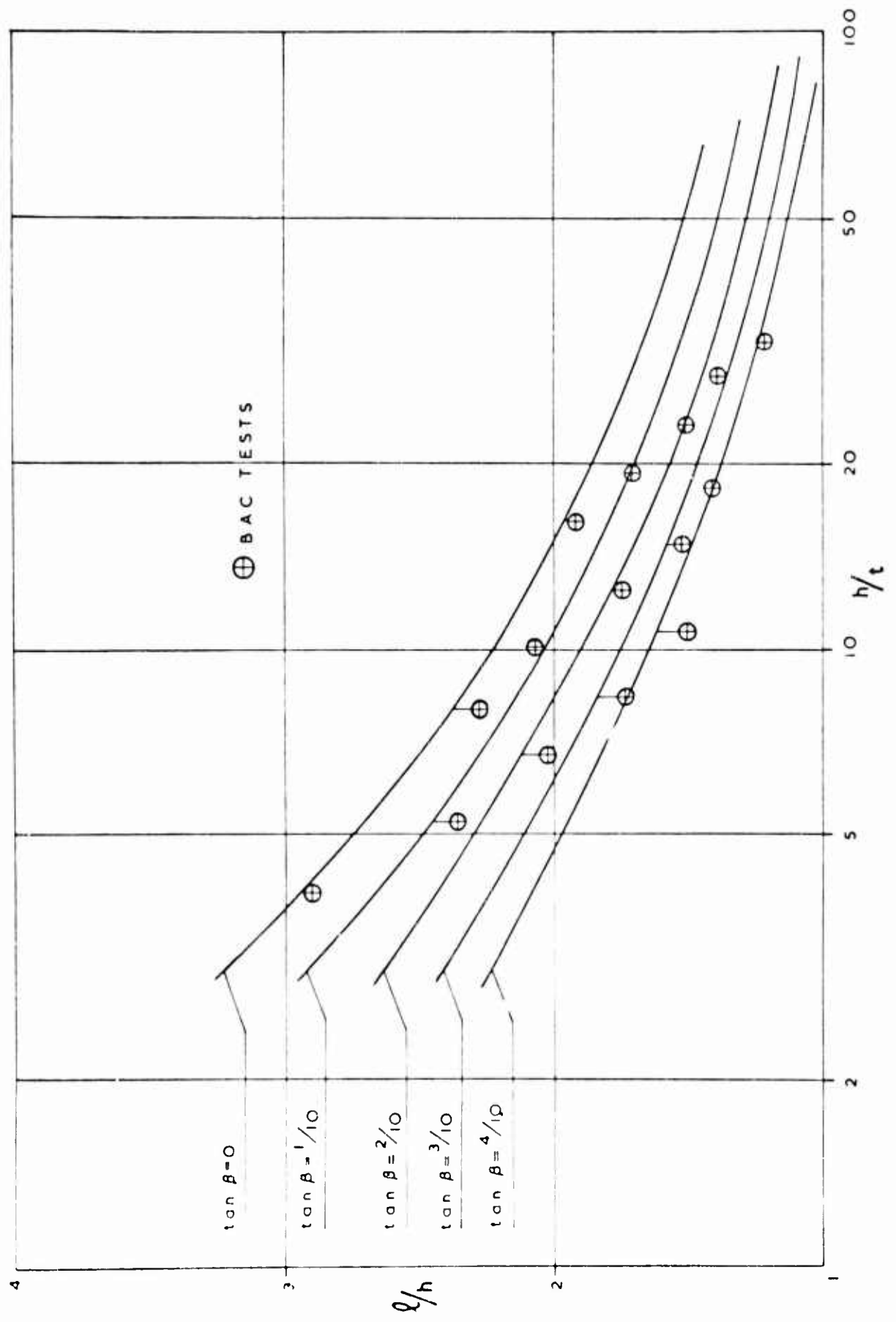


FIG.4 RESULTS FOR $B = 0.3265$

$\frac{h}{t}$ and large B . However we believe that the useful range is adequate to cover most fluid logic applications.

5. CONCLUSIONS

A simple theoretical model has been shown to give good agreement with experimental results over a wide range of parameters.

Extensions of the theoretical model for larger control flow rates is easy, by introducing the effect of an initial momentum deflection of the jet. Extension for greater accuracy at more extreme geometrical configurations has already been provided for the unventilated case and this work can be adapted for ventilated cavities using modifications precisely analogous to these here applied to the more simple model.

POSTSCRIPT

Transient Behaviour

If it is true that the shape of the jet is governed by ventilation processes, change of ventilation rate will cause movement of the jet at lateral velocities comparable with the entrainment velocities. These can be determined as follows:

$$\text{The volume flow in a half jet} = \frac{Q}{2} = \frac{1}{2} \sqrt{\frac{3JX}{\sigma\rho}} \quad \text{P.1.}$$

per unit span

$$\frac{d(Q/2)}{dX} = \frac{1}{4} \sqrt{\frac{3J}{\sigma\rho X}} \quad \text{P.2.}$$

but this is equal to the inflow velocity at X: V_x

$$\sqrt{J} = U_J \sqrt{\rho t} \quad \text{P.3.}$$

where U_J is the slot velocity

$$\text{then } \frac{V_x}{U_J} = \sqrt{\frac{3}{16}} \sqrt{\frac{t}{\sigma X}} \quad \text{P.4.}$$

now if $\frac{t}{X}$ is, typically about $\frac{1}{20}$ for $\frac{X}{h} \approx 2$, $\frac{h}{t} \approx 10$.

$$\text{we have } \frac{V_x}{U_J} \approx \sqrt{\frac{3}{16}} \cdot \frac{1}{18} \cdot \frac{1}{20} \approx \frac{1}{44}$$

Then the switching time, for complete instantaneous shift of control flow from one side to the other is $\frac{Y}{V_x}$

where Y is the distance the jet must move laterally, this is typically $\approx h$, since the jet width is approximately h at the splitter,

$$\text{Time} = \frac{h}{V_x} = \frac{44h}{U_J} \approx \frac{22X}{U_J}$$

It seems to us that this derivation of switching times is fundamentally acceptable being based on only one independently available empirical constant, σ , and realistic mechanisms. The alternative of an "empirical" Strouhal number using the X dimension, rather than the width, seems less direct.

NOTATION

B	ventilation relative mass flow, equ.7
h	length of perpendicular from reattachment point to slot axis plane
J	Jet momentum/unit span
K	a constant: equ 3.
l	distance projected onto slot axis plane from slot to reattachment
m_J	slot mass flow
m_v	ventilation mass flow
P	static pressure
Δp	pressure difference across the jet
Q	volume flow in jet/unit span
R	Radius of curvature of jet
t	slot thickness
T	$\tanh \eta_R$
T_1	value of T at X_1
U_{max}	max jet velocity of X
U_J	slot exit velocity
V	jet inflow velocity
X, Y	co-ordinates fixed in curved jet
X_1	X at reattachment
β	angle between wall and slot axis plane at reattachment
δ_1	jet thickness at X_1
ρ	density of fluid - assumed uniform
σ	jet spreading parameter
θ	angle between jet centre line and slot axis plane at reattachment
η	Y/X non dimensional jet profile co-ordinate
η_R	value of η on reattaching streamline.

REFERENCES

1. Sawyer R.A. 1960 Journal of fluid mechanics. Vol.9 P.543.
The flow due to a two dimensional jet issuing parallel to a flat plate.
2. Dodds J.L.1960 PhD Thesis Cambridge University.
3. Olsen R.E. & Miller D.P.1963 Harry Diamond Laboratories
Aerodynamic studies of free and attached jets. DDC catalogue no. AD 427325
4. Keto HDL Fluid amplification Symposium 1964 Proceeding Vol. III
The transient behaviour of Bistable Fluid Elements.
5. Sawyer R.A.1963 Journal of fluid mechanics Vol. 17 P.481.
6. Glaetli HH et al 1964 HDL Fluid amplification Symposium Proceedings
Vol.I Remarks of the limitations of Pure fluid elements.
7. Bourque C & Newman B.G. Aeronautical Quarterly Aug.1960
Reattachment of a two dimensional incompressible jet to an adjacent flat plate.

FLOW STABILITY FOR TWO DIMENSIONAL CUSP DEVICES.*

K.P.H. FREY** AND N.C. VASUKI***

In a previous paper the authors had used sequence photography to present the flow starting from rest to steady state of flow for various kinds of sudden enlargements (1).**** A cusp diffuser was included in these studies to clarify the behavior of cusp diffuser models from that of other sudden enlargements as predicted by the potential vortex motion theory (2), (3). The tests were conducted in a new facility, the versatile flume, (4), in order to get the first comparable results under conditions where unnecessary interactions at decisive locations of cusp diffusers could be avoided. The primary interest in these studies was to gain more information on transitions of varying stability of flows.

According to literature, the unique cusp diffuser theory was not yet ready for commercial use (5). The cusp boundaries were calculated to retain a permanent vortex such that the relative velocity between the vortex and the main jet stream is zero. The previously offered experimental verification (2), (3) admitted to interactions at decisive locations. They belonged to the flow system of concern.

Our recent tests (1) failed to yield predicted results. In response, a refined theory was introduced incorporating stability criteria. The new boundaries derived (6) are no longer diffusers. Again, new tests were conducted to verify the reviewed theory and analyze the physical facts for basic judgment.

The two devices tested are shown in Figures 1-6 and 7-10. The boundaries of the new devices have a common asymptote upstream of the cusp zone. Previously, the downstream boundary would have been tangential at 0, Figures 1 and 7. The physical concept underlying the revised theory is that an appropriate choice of the stagnation point will trap the initially produced vortex permanently; however, this concept requires verification. The flow reattachment is at the stagnation point, 6.

The figures present top views. All boundaries are rectangular to the test section bottom. The opposite boundary (not shown) is 17 inches away from the cusp edge and is parallel to the asymptote of the

*The project was sponsored by the Department of Civil Engineering.

**Professor, Engineering Mechanics, Department of Civil Engineering, Fluid Mechanics Laboratory, University of Delaware.

***Sanitary Engineer, Water Pollution Commission, Dover, Delaware.

****Numbers in parenthesis refer to similar numbers in the bibliography.

upstream and downstream boundaries of the cusp devices. In Figures 1-6 the cusp zone is approximately 6 inches in diameter. In Figures 4-7 the cusp depth (parallel to the water surface, indicated by a dotted line at 0 in Figure 7) is 6 inches. The water is 16.5 inches deep. The main stream steady state velocity is 2.25 in./sec. in Figures 1-5 and 7-8. It is 5.56 in./sec. in Figures 6 and 10.

The clock is photographed with the visualized flow for better coordination of the individual flow occurrences. The clock hands turn counterclockwise. A battery driven sequence camera is used to take pictures approximately every two seconds.

Lycopodium powder is sifted on the water surface. The individual particles are 20 to 32 microns in diameter. They are water repelling and light yellow in color. Subsurface tests are not recorded because they did not disclose additional significant findings

Discussion of the Photographs

Figures 1-5 show 5 phases of the flow development starting from rest in one model type at the low velocity range. The time elapsed is 6 minutes and 10 seconds during observations. In Figure 1 where the exposure time is approximately 3 seconds, the center of the initially produced starting vortex travels along 1-1. During this period of growth of the vortex, the stagnation point, 6, where flow divides into two opposite directions (arrows), moves considerably at the beginning only. It then remains stationary in all figures. Small fluctuations of the stagnation point, 6, are immaterial. The center of the vortex, 1, in Figures 1-4, moves eccentrically in the cusp zone for approximately 4 minutes. In Figure 4, the cusp vortex shows a wide and broad zone of greatly reduced velocity from 7 to 8. On the opposite side near the stagnation point, 6, there is a stretched section at the end of which a nucleus of a vortex is forming, 3. This tendency was previously encountered, Figures 2, 3. Produced in conjunction with the main flow and the eccentric motion of the vortex, 1, the phenomenon vanished for the same reason, Figure 3a.

Figures 4 and 5 demonstrate that the vortex arrangement 1-3 switches to that of 2-3 within approximately 2 minutes. The transition from 1 to 2 comprises a change of the velocity distribution from potential vortex type to that of enforced vortex. At the same time the rotary motion of 3 is greatly increased. The connecting line 2-3 marks a zone where tangential velocities prevail rather than the rotary motion of the starting vortex, 1, along the connecting line 1-3, Figure 3. The fluid boundary, 9, is of special interest. There is a substantial velocity gradient normal to the fluid boundary. The boundary layer generated in the preceding nozzle section and swept downstream of the cusp edge is now sandwiched between the main flow and the vortex

flow. Viscosity effects are gradually felt at this boundary also.

Figure 6, at higher velocities, shows that the phenomena along 2-3, Figure 5, develop into a fluid boundary 4-5 consisting of a row of small vortices having vertical axes. Their effect on the flow is equivalent to that of the configuration 2-3.

The flow characteristics of Figures 7-9 are equivalent to those shown in Figures 1-5. Also characteristics of Figure 10 resemble basically those of Figure 6. A special comment may be made on Figure 9. The figure shows that the transition from the initial starting vortex to the enforced vortex motion can be quite violent. The large disturbance, 10, shows that a starting vortex escaped and collapsed under the impact of the main flow. In Figure 9, the black zone indicates three dimensional flow. This violent action has affected the fluid boundary, 9, between main stream and vortex flow also. The layer of discontinuity becomes wavy easily. In approximately one minute the eddied jet boundary and the steady state of flow are established, Figure 10. The line, 4-5, which separates two regions of opposite flow directions exists again as shown.

The cusp device shown in Figures 7-10 was put into the test section of the wind tunnel also and tested in velocities up to approximately 130 ft./sec. The agreement with the flow shown in Figure 10 was excellent. The stagnation point, 6, was at the same location, the sharp separation line of the flow direction along 4, 5 as well as the eddied fluid boundary, 9, were located again.

The applicability of the potential vortex motion theory still did not overcome inherent difficulties, even though great changes in boundaries were made, and the stagnation point, 6, soon became stable. There were speculations that the theory was not successful because the axis of the initial vortex had a finite length (test bottom, free surface - air). Open end cusp devices were used to overcome this objection. For these tests, the axis of the cusp zone was turned 90 degree (horizontal) and normal to the main flow and the cusp length normal to flow was increased by 100%. Large end plates, 30 inches long, were placed on each end of the cusp zone. They were gradually displaced in parallel. Finally they were removed. The distance from model edge to flume boundary at each side was, then, 15 inches on each side. The open end cusp resulted in a complex flow. The analysis was possible by starting the flow from rest. The open ends generate a special starting vortex each, which penetrate deep into the cusp zone from either side. A permanent disturbance remains. Turning the model around a vertical axis to apply sweptback positions for the cusp edge creates a special flow configuration. This is beyond the scope of interest here.

Conclusions

The potential vortex motion theory applied to models of two dimensions can be verified during an initial period only, too short in time to be disclosed in air flow tests of appreciable velocities. What is missing in theory is the transition to that other vortex system which is known from the concepts of layers of discontinuity. The latter concept is that which describes the phenomena relatively best for steady state of flow. This concept admits that the solid boundary upstream of the inlet releases a boundary layer which is entrained in the starting vortex. The instability of such surfaces or layers of discontinuity is known. Eddy formation and reverse flow are produced.

The potential vortex motion theory and the concept of layers of discontinuity actually are not contradictory. They are merely valid for different phases of the whole problem. The transition phase shown is missing in the two concepts.

The stationary stagnation point is encountered in various phases of the cusp flow and, therefore, that position is not conclusive regarding the specific status of flow within the cusp. Because of the significance of transition phases of flow, it is hoped that further experimental and theoretical studies will be pursued.

Bibliography

- (1) K. Frey, N.C. Vasuki, "Tests on Flow Development in Diffusers", pp. 40-47, Symposium on Fully Separated Flows, ASME Fluids Engineering Division Conference, May 1964.
- (2) G.V. Lachman, Ed. "Boundary Layer and Flow Control", Section "Flow Control", pg. 293, Pergamon Press, 1961.
- (3) F.O. Ringleb, "Two-Dimensional Flow with Standing Vortices in Ducts and Diffusers", ASME Paper 60-HYD-15, 1960.
- (4) Facility see "Description of Facilities" Fluid Mechanics Laboratory, Department of Civil Engineering, University of Delaware, April 1965.
- (5) R.C. Dean, Jr., pp. 11-33, "Separation and Stall", Section II of Handbook of Fluid Dynamics; Editor in Chief V.L. Streeter, McGraw-Hill, 1961.
- (6) F.O. Ringleb, "Discussion of Problems Associated with Standing Vortices and Their Applications", pp. 33-39, Figures 3, 5, Symposium on Fully Separated Flows, ASME Fluids Engineering Division Conference, May 1964.



Fig. 1



Fig. 2

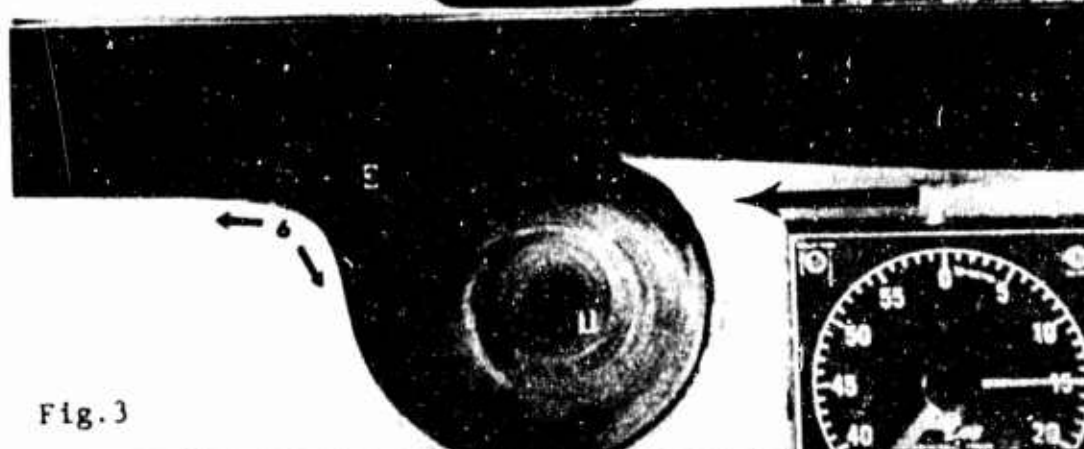
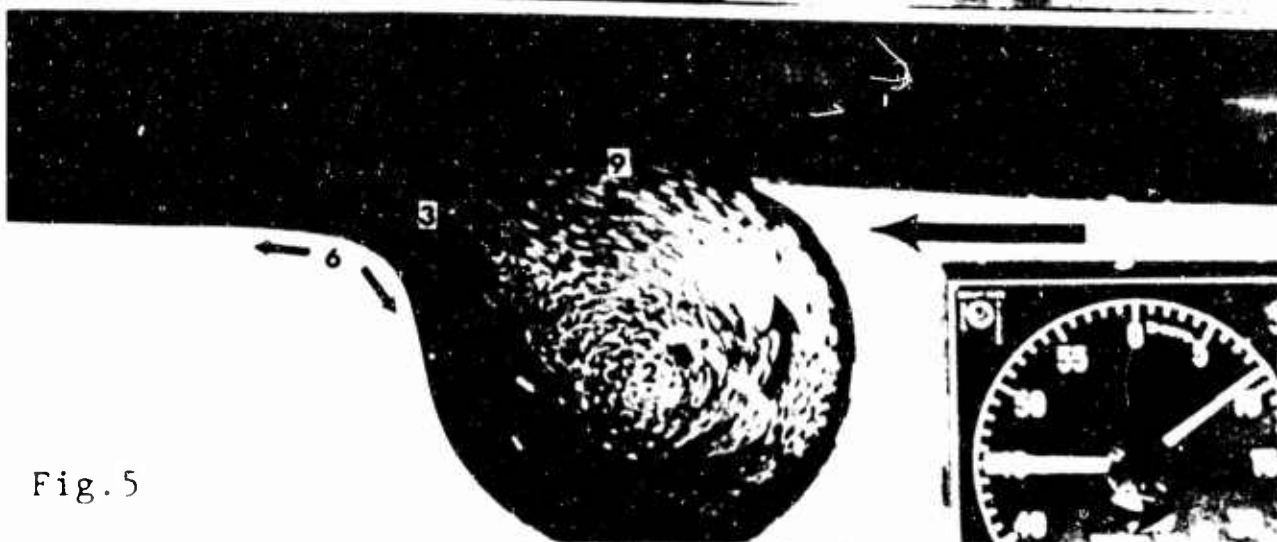
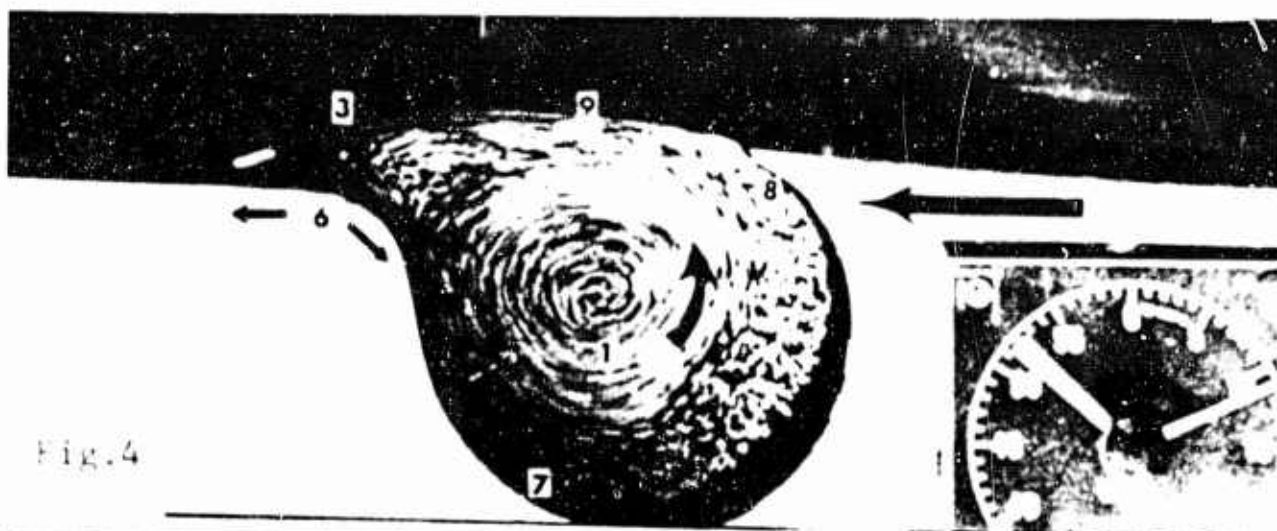


Fig. 3



Fig. 3a

Figs. 1-3, 3a Groove Like Cusp Design Showing the Initial Period of a Starting Vortex, Eccentric Motion.



Figs.4-5. Continuation Showing Transition From One Vortex System to Another One.



Fig.6. Continuation of Observation; Increased Velocity; A Row of Small Vortices is Formed Allowing Tangential Velocities Only. The Row is Oblique Resembling Guiding Baffle.

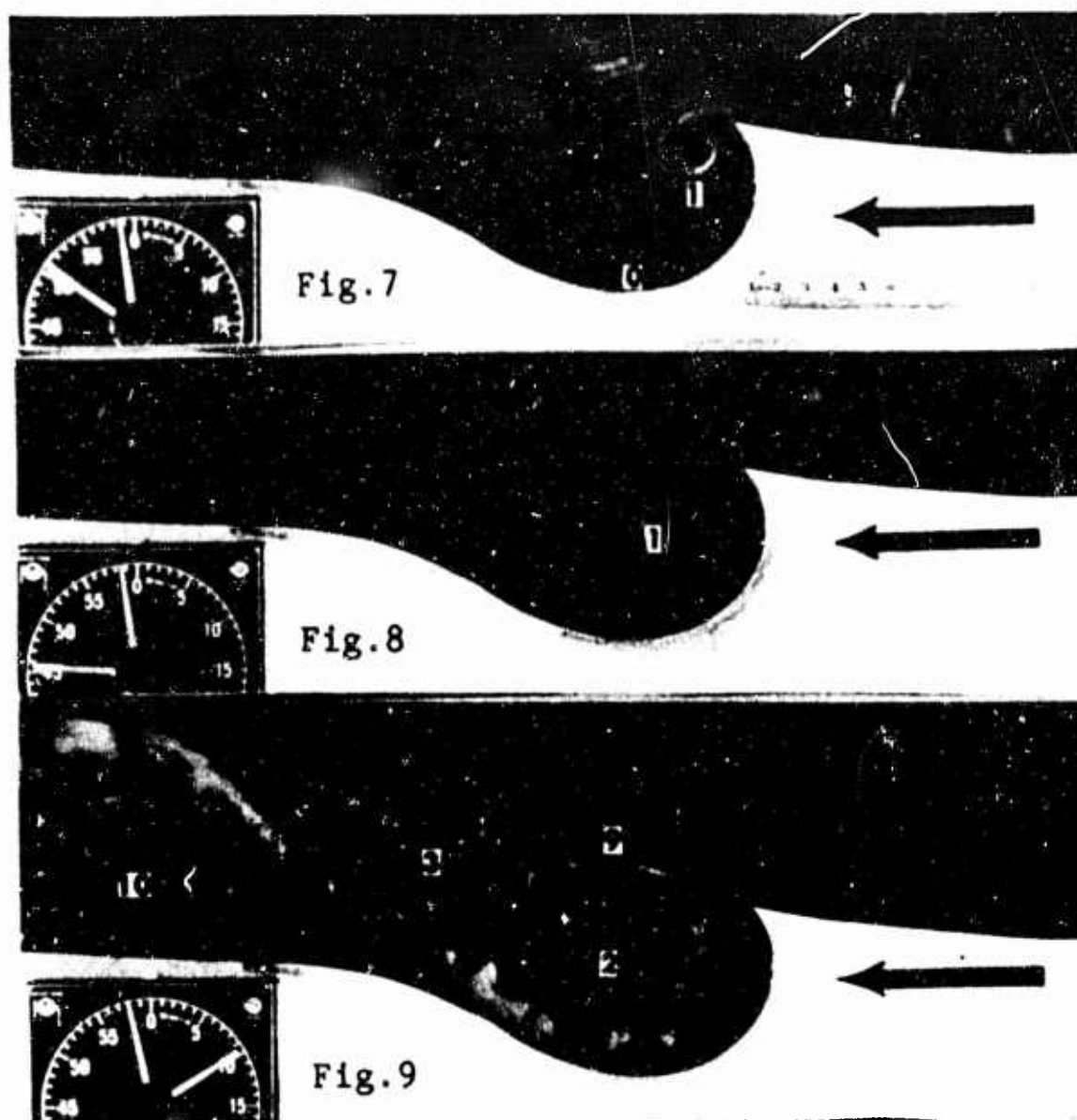


Fig.7-9. More Opened Cusp Device; Formation and Decay of Starting Vortex.



Fig.10 Continuation at Increased Velocity; Steady State of Flow Resembles Concept of Flow Through Enlargements.

New Comprehensive Studies on Sudden Enlargements¹

K.P.H. Frey², N.C. Vasuki³, and P. Trask⁴

Introduction

Recent studies on sudden enlargements (1)⁵ have confirmed by classifying types of flow that large ratios of length over width are significant in flow redistribution and performance. The study of starting vortices clarified physical aspects(2). The applicability of the potential vortex motion theory to flow control by cusp diffusers was reconsidered (3)-(6). Finally, it was experimentally shown that the various concepts used for sudden enlargements are not contradictory. They merely present different phases of the flow with a transition between the two phases. This was clearly demonstrated in the study of some special cusp devices (7).

The significance of transition flow phenomena from one kind of stability to another one, suggested more studies of the previous and related kind. In addition, the interest in making use of the theory of potential vortex motion, and of comparing results with those of the impulse momentum theorem, (8), led to this paper on "New Comprehensive Studies on Sudden Enlargements".

Models

Four models were chosen, Figs. 1-3.⁶ Figure 1 shows a plexiglass cusp diffuser model of circular cross section. Two tubes were added at the downstream side to have a ratio of length over inlet width of 20. The ratio of expansion is 4.7. The model is interchangeable from the test section of the versatile flume to that of the newly redesigned wind tunnel (9). This is an open loop type low-turbulence wind tunnel, nozzle contraction ratio nominal 10.8, test section 1.5 ft. wide, 1.5 ft. high, 12 ft. long, maximum velocity 130 to 140 ft./sec. The contour of the cusp boundary shown in Fig. 1, was also used as a templet for a two-dimensional model, expansion ratio 1:1.9, for studies in water, Figs. 4-8, and in air, Figs. 11-14. The airflow studies were made in the old closed loop type high turbulence wind tunnel. The test cross section was the same, however, the length was only 4 ft. long instead of 12 ft. long now.

In the case of the two-dimensional model, cylinders were also

¹) Laboratory project of the Civil Engineering Department; sponsored by the University of Delaware Research Foundation; also part of Contract of the U.S. Army's Harry Diamond Laboratory, Fluid System Branch.

²) Professor of Engineering Mechanics, Civil Engineering Department, University of Delaware.

³) Sanitary Engineer, Water Pollution Commission, Dover, Delaware.

⁴) Senior student, Mechanical Engineering Department, University of Delaware.

⁵) Numbers in parenthesis refer to similar numbers listed in the Bibliography.

⁶) Figures 1 through 20 appear on pages 128-137.

placed into the cusp zones, Figs. 12 and 14. In the case of the three-dimensional model, an annular plate could be inserted into the cusp zone as shown by the dotted lines with a star in Fig. 1.

Figure 2 presents a nozzle, inlet 18 by 18 inches, exit 10.25 by 10.42 inches, contraction ratio 1:3. The nozzle was placed into the new wind tunnel's test section. Using the wind tunnel boundaries as model boundaries of the extended part, the expansion ratio is 1:3. The maximum value of length over inlet width was chosen.

Figure 3 presents half of the model of a symmetrical nozzle in two dimensions. The jet streams from wall to wall through a cross section of 18 by 6 inches into a sudden enlargement of the ratio of 1:3, measured in the new wind tunnel. Again, the maximum value of length over inlet width was chosen.

Test Concepts

It was of interest to verify whether the various concepts apply to different phases of flow development in two or three-dimensional cusp diffusers and other abrupt enlargements. This includes a check on the effect of flow and performance with and without cusp zones (cylinder, or plate placed into the cusp zone). There should be no appreciable effect for steady state of flow in the present line of physical understanding, while the flow control theory based on the potential vortex theory expects a decisive difference in results.

Consequently, the steady state of flow of the two-dimensional version of Fig.1 model and the results of the two-dimensional model of Fig.3 should basically agree with each other. Primarily, this refers to the occurrence of the Coanda effect. In these tests, water to air velocity ratios ranged from 1:50 to 1:500. Without high speed photography for air it is impossible to compare starting conditions in air and water (11).

On the other hand, the tests of the three-dimensional version of Fig.1⁶ and those of Fig.2 should basically agree with each other. Primarily, this refers to the absence of the Coanda effect and to the assumption that the potential vortex motion theory cannot be satisfied in viscous fluid flow. The jet should expand having a straight center line.

The three dimensional models are supposed to produce starting vortices around the whole jet boundary. After decaying they generate a jet fully surrounded by detached flow. In this zone, any potential change of static pressure must quickly equalize. This should control the directions of the jets of the three-dimensional models, Figs. 1 and 2, to stream straight while expanding.

There should be still an appreciable difference in the results

⁶) The model was made of Plexiglass by Mr. Richard Bullock, a graduate student of the Mechanical Engineering Department; the drawing was made by Siavash Zand-Yazdani, a graduate student of the Civil Engineering Department, who also participated in the preliminary studies in the newly reconstructed wind tunnel including tuft observations, Pitot tube and hot wire measurements.

because of the varied inlet contours. The circular cross section creates an infinitely long (closed) vortex line. This is a relatively stable vortex formation. The square model must also create an infinitely long vortex formation, however, having straight branches and corners. Hence, this infinite vortex line may be regarded as a configuration of pairs of vortices of finite lengths. Each pair consists of parallel, counterrotating vortices. The four vortices intersect each other at 90 degrees and mutually interact. The interaction is particularly strong at each intersection. This configuration appears to be less stable, supporting a quick redistribution of flow.

The vortices of two-dimensional models are of finite lengths. In the range of the occurrence of the von Karman vortex trail, mutual interactions produce stable zig-zag positions of the vortices. Experimentation verified that the range of stable zig-zag arrangements is substantially broader than theoretically predicted (19). The transition to instability is inherent due to viscosity. However, the mechanics may differ(2). On the other hand, the wall to wall jet of two-dimensional sudden enlargements cuts off the self-controlled equalization of static pressures of three-dimensional models. The straight jet direction becomes unstable. The jet approaches the other stable flow development, the diverted jet, reattaching on one side first, later on the opposite side.

Test Methods

Flow visualization in water flow of 2 to 12 inches/sec. is used in two and three dimensions. Only surface patterns are recorded, Figs. 4-8. In air flow, tuft observations were made up to the maximum velocity, Figs. 11-14 and 19-20.

Static head and also dynamic head measurements were done with Pitot static tubes of various sizes in the wind tunnel at various locations of interest, Figs. 11-14 and 15-16.

In addition, the degree of turbulence was evaluated, (Figs. 17-18) using hot wire techniques^{7,8}. In parallel to these measurements, an oscilloscope⁹ was connected with the electronic constant temperature anemometer⁷ for the visual presentation of voltage oscillations created by the turbulent flow. Such oscillations were photographed¹⁰, Figs. 9-10.

⁷) Disa Constant Temperature Anemometer, Type 55A01, probes (single wire) Type 55A22.

⁸) Disa Constant Temperature Anemometer, Instruction Manual pg. 11, equation 6.

⁹) Cathode-Ray Oscillograph, Type 304A, A.B. DuMont Laboratory.

¹⁰) Oscillograph-Recording Camera, Type 200, A.B. DuMont Laboratory, Polaroid Film Type 47, 5000 ASA.

Test Results

LIST OF FIGURES ON TEST RESULTS

FIGURES	DESCRIPTION
4-8	Formation and Decay of Starting Vortices in Cusp Diffuser; expansion ratio 1:1.9, free surface flow patterns, two-dimensional model.
9-10	Oscillations at 120 ft./sec. Air-Flow Through Cusp Diffusers of Circular Cross Section. See locations in Fig.1; annular plate installed.
11-14	Continuation of Figs. 4-8 in Airflow (old wind tunnel).
11-12	Cusp Diffuser Without and With Cylinder Placed in the Cusp Zone. Tufts show the jet boundaries; Pitot-static tube placed just outside the jet boundary.
13-14	Same Arrangement as in Figs. 11-12, however, Pitot-static tube just inside the jet boundary, 1/2" displaced.
15	Static Head Recovery, Three-Dimensional Models, Figs. 1 and 2; Reattachment Zones; Classification of Static Head Zones.
16	Static Head Recovery, Two-Dimensional Model, Fig. 3; Coanda Effect; Reattachment Zones.
17	Formation and Decay of Turbulence (Shown in Percent), Circular Cross Sections, Fig.1; Reattachment region; Classification of Zones.
18	Formation and Decay of Turbulence (Shown in Percent), Two-Dimensional Nozzle, Fig.2, Reattachment Regions, Classification of Zones.
19,20	Tuft observation in First Extension Tube, Circular Cusp Diffuser Fig. 1; Representing near maximum velocity tests.

Discussion of Results

Figures 4-8 show (in capsule presentation) that for free surface flow of water at low velocity, a recent finding on two-dimensional cusp devices (1) applies to flow through cusp diffusers (3)-(6) also. The common steady state of flow consideration based on the phenomenon of layers of discontinuity and their instability is correct. However, it cannot be traced to the beginning. The starting phase can be predicted by the potential motion theory. But, it cannot be extended to the description of the steady state of flow. The two concepts are not in contradiction because experimentation shows that they are connected with each other by a transition phenomenon. The potential vortex type arrangement is transformed into an enforced vortex system.

Figures 4-6 demonstrate that downstream of the inlet edge (dotted line 0-0 in Fig.4), the boundary layer of the inlet nozzle is sustained, but soon becomes unstable, 1. Eddies are formed. The stagnation points are sliding approximately symmetrically, 6. They present the instantaneous reattachment. The transition of vortex formations may take a while at low water velocities and depend on test conditions. However, the transition will be encountered as the acceleration vanishes. The

Figs. 4-8 present this transition from one kind of vortex system to another one. The stagnation point, 6, becomes stationary and may be referred to as a region. This behavior of the reattachment flow cannot be regarded as a general criterion for the prevailing type of vortex. The transition phase is noticeable along the jet boundary and by the behavior of the reverse flow. The latter separates from the boundary, 2, and forms a counter rotational flow at the bottom of the cusp zone while streaming toward the jet fluid boundary where fluid entrained into vortices needs to be replaced. At increased velocity, this behavior is associated with that flow type. The Coanda effect is encountered. It is characterized by the diverted jet stream forming a short detached zone, 4, and a large detached zone, 5, at the opposite side. The potential flow type does not exist at steady state of flow. The high degree of turbulence expected by the tests discussed is verified in Fig. 10 as compared to Fig. 9. The oscillations of voltages are photographed and are the basis of the calculation of the degree of turbulence⁸⁻¹¹.

The degree of turbulence at the inlet cross section is 0.67 percent. The diagrams are taken at locations shown in Fig. 1 for circular cross section, with plate (* and dotted line). The reference cross section is downstream of the inlet cross section a distance equal to 7 percent of the inlet width. Fig. 9 refers to the center; Fig. 10 to the jet boundary. The same scale is used in the oscilloscope for the two figures. By moving the probe gradually from the center toward the outer boundary, the tests have shown that the transition to the heavy oscillation is sudden. It reflects the periodical generation of vortices downstream of the inlet. The oscillation remains strong in the detached zone. This kind of observation was done continuously. However, the recording was discontinued in view of the scope of this study.

Figures 11-14 show the setup and results of tests with the model of Figs. 4-8 adjusted to measurements in the old closed loop wind tunnel. The effect on the flow of the installation of cylinders in the cusp zone is of concern, particularly near the inlet section. A ratio of length over inlet width of eight is then feasible, because the flow continues to stream straight through a 10 ft. long diffuser. Observations by tufts attached at the upper and lower nozzle boundary show the jet stream boundaries. The velocity is more than 100 ft./sec. and constant in all figures as indicated at "A". The manometer "A" measures the boundary pressure at the center of the inlet cross section, 7, versus atmosphere. The short exposure time, 1/500 sec., shows the individual tuft instantaneously and the various figures show that the jet boundary varies little. Basically, the Coanda effect is confirmed. With and without cylinders inserted, the flow diverts, during these tests, in upward direction at the same slope. No appreciable change of slope was encountered by a large reduction of the velocity.

Other measurements are shown for the Pitot-static tube, 8, which is displaced 1/2 inch in vertical direction between Figs. 11, 12 and

Figs. 13, 14. The jet boundary is just between these two positions of the Pitot-tube. This follows from the measurements at "C". At "B", the static pressure difference (7 to 9) is shown, between inlet plane and static holes of the tube, 8. There is no significant difference in any case. Hence, there is no appreciable increase of static head due to the cusp shape. At "C", the dynamic head is shown; 10 refers to the total head and 7 to the static head. The dynamic head is practically zero in Figs. 11, 12; and large, but equal in Figs. 13 and 14. The comparison of Figs. 11 and 12 clearly shows the existence of a detached zone as indicated at "C". If there were a potential vortex, a high velocity should have been measured, equal to that of the main stream.

The tests for models, Figs. 1-3, done in the low turbulence wind tunnel at a test section 12 ft. long, and shown in Figs. 15-20, demonstrate the following.

Figures 15 and 16 present the measured static head recovery for the three models downstream from the inlet section. The dimensionless ratio of length over width shown varies for individual models, especially because of different inlet widths. The difference between the static head at a local position, $(h_{st})_{local}$, and that at the center of the inlet cross section, $(h_{st})_{inlet}$, is divided by the dynamic head at the inlet $(h_{dyn})_{inlet}$, in order to have a meaningful dimensionless term in the comparison with the application of the impulse momentum theorem. The difference between zero and the maximum value should be compared with the result when using the impulse momentum equation. If the theoretical assumptions were satisfied immediately downstream of the inlet and at the location of the maximum value of the head recovery there would be a full agreement; if not, at least the basic interrelation must be verified.

Figure 15 shows the static head recovery for the two models of three-dimensions. The lower curve is for the model in Fig. 1 expansion ratio 1:3. The upper curve for that of Fig. 2, expansion ratio 1:4.7. Therefore, for the same oncoming velocity the impulse momentum theorem would yield a 30 percent higher head increase for the upper curve model, Fig. 2, than for the lower curve model, Fig. 1. The recovery was an additional 33 percent higher. This shows that the claimed superiority of the cusp diffuser cannot be verified. On the other hand, the cusp diffuser produces considerable negative heads downstream of the inlet before the recovery of head begins¹¹. The only location along

¹¹) Classification of Head Zones, Fig. 1; head reduction, A; head recovery to inlet status, B; total head recovery, C; recovery above inlet status, D; Constant head, E; slight decrease, F; 92 percent total recovery, G; 86 percent of recovery above inlet status, H.

the detached zone where the static pressure is the same throughout the cross section is at the inlet. If one uses this location as physical basis for the application of the impulse momentum because the inlet assumptions are best satisfied, the total head change agrees fairly with that of the measurement. On this modified basis, the cusp diffuser functions equivalently to that of Fig. 2. One may conclude that the assumptions for the cross sections at maximum head seem to satisfy. However, this must be verified.

It is interesting to note that variations, such as greatly differing velocities and elimination of the cusp zone by a plate, show only effects which are limited to certain regions of the head recovery curve. The most characteristic points, such as the position of the reattachment point and the maximum static head are not appreciably affected.

The expected interactions of inlet vortex formation for models of a square cross section, Fig. 2, revealed in flume studies (not shown) a quick redistribution of turbulent flow. Tift observations basically confirmed the results in the wind tunnel. The detached zone is shown in Fig. 15. At each mid-side boundary the flow sharply deflects outwardly at the inlet edge with a strong component toward each corner. At the corners, the reattachment takes place at a larger distance from the inlet, but still closer to the inlet than for the cusp diffuser.

Figure 16 shows the static head recovery for the two-dimensional model, Fig. 3. The expansion ratio of 1:3 is the same as for the three-dimensional model, Fig. 2. (Its head recovery is shown in Fig. 15, upper curve). According to the impulse momentum equation, the head recovery between origin and maximum should be the same for the two cases. It is not. However, again using the location near the inlet which satisfied the assumptions most, the total recovery in each case from minimum to maximum would yield the satisfactory agreement. The measurements along the center line are used as basis of comparison. Again, one would have to check whether the assumptions satisfy downstream at maximum head recovery.

In Fig. 16, the Coanda effect is indicated by the two widely separated reattachment zones, the different static pressures at some distance away at both sides from the center line, and the very gradual increase of the static head. This increase substantially continues beyond the second reattachment range, A_1 . The maximum value is almost asymptotically reached at the end of the test section at a length over inlet width ratio of 20 to 21.

The Figures 17 and 18 show, in addition, two examples of the formation and decay of turbulence in sudden enlargements; Fig. 17 refers to the circular cusp diffuser, Fig. 1, with and without plate; and Fig. 18 to the two-dimensional model, Fig. 3. The lines of constant degree of turbulence $7-10$ are shown throughout the entire sudden enlargements. At the inlet center, the degree of turbulence is only 0.67 percent.

Supplementing the turbulence characteristic, Fig. 17 shows the position of the reattachment zone and the classification of zones in conjunction with the static head recovery shown in Fig. 15.

Figure 18 shows a similar presentation demonstrating the relevant phenomena for the Coanda effect.

Figures 15 to 18 reveal difficulties in defining the second reference cross section for sudden enlargements in applying the impulse momentum concept. The degree of turbulence still decreases when the maximum head recovery is gradually attained, and the slope of duct resistance is only gradually encountered. Flume tests basically reveal the same difficulties on a qualitative basis and in a different manner. Naked eye observation, still and sequence photographs, and movies from a point at rest or traveling with the mean velocity of the flow, may appreciably correlate and supplement other data. Oscillograms (Figs. 9,10) and hot film measurements in water can be important. They may be supplemented by tuft observations in air, such as shown in Figs. 11-14 and 19,20. The curves of the degree of turbulence are of interest regarding the capabilities of turbulence to promote the transition of laminar to turbulent boundary layer flow along solid objects inserted into the flow at a lower Reynolds number.

Conclusions

1. The successful analysis of transition phenomena which correlate the application of the potential vortex motion theory and the concept of surfaces or layers of discontinuity, has been substantially generalized and verified. Two and three-dimensional models were studied in water and air. The predominant characteristics of flow and performance were similar for the respective models.
2. The predominant characteristics are obtained as results of comprehensive studies. They comprise flow visualization in flume and wind tunnel, static head curves, and fields of the degree of turbulence in various sorts of sudden enlargements, including cusp diffusers. The correlation of these data is informative.
3. The comprehensive method shows that, due to assumptions, the impulse and momentum theorem, based on inviscid fluid flow cannot always be exactly applied to viscous fluid flow through sudden enlargements. However, the qualitative agreement must prevail and is fundamentally important. The erroneous conception of the application of the potential vortex motion theory to flow control by cusp diffusers is also verified when analyzed by the impulse-momentum theorem.
4. The continuation of work would enhance the physical understanding and analysis of the mechanics of flow. This, in turn, would be of help in flow control, design, and development.

BIBLIOGRAPHY

1. Kline, S.J., D.E. Abbott, and F.W. Fox: Optimum Design of Straight-walled Diffusers, Trans. ASME, J. Basic Eng., D81 (3):321, September 1959; and pp. 11-26 Handbook of Fluid Dynamics, Editor-in-Chief V.L. Streeter; Section and Stall by R.C. Dean, Jr., Chapter 11; 1st ed. McGraw-Hill Book Co., N.Y., N.Y.
2. Frey, K., N.C. Vasuki: Tests on Flow Development in Diffusers, pp. 40-47, Symposium on Fully Separated Flows, ASME Fluids Engineering Division Conference, May 1964.
3. Lachmann, G.V., Editor: Boundary Layer and Flow Control; Section: Flow Control by F.O. Ringleb, pp. 265-294, Pergamon Press, 1961.
4. Ringleb, F.O.: Two Dimensional Flow with Standing Vortices in Ducts and Diffusers, ASME Paper 60-HYD-15, 1960.
5. Ringleb, F.O.: Discussion of Problems Associated with Standing Vortices and Their Applications, pp. 33-39, *ibid* 1.
6. Helmbold, Th.: Stabilization Devices for Generating and Guiding Potential Whirls, USA Patent 3,144,202; 1964.
7. Frey, K., N.C. Vasuki: Flow Stability for Two Dimensional Cusp Devices, submitted as paper to the U.S. Army's Harry Diamond Laboratory, Washington, D.C., 1965.
8. Schlütt, Mitteilungen des Hydraulischen Institutes der Technischen Hochschule München, 1 (1926), 42. Abstract: Seite 681, 4233 Widerstand in erweiterten, verengten und gekrümmten Rohren; Schiller, 423 Strömung durch Rohre: Landolt-Börnstein, Zahlenwerte und Funktionen, 6. Auflage, IV. Band, Technik, I. Teil, J. Springer Verlag Berlin-Goettingen-Heidelberg, 1955.
9. Fluid Mechanics Laboratory, Department of Civil Engineering, University of Delaware, Newark, Del.: Description of Facilities, Frey, K., Seidel, B., April 1965.
10. Wille, R.: Über Strömungserscheinungen im Uebergangsgebiet von geordneter zu ungeordneter Bewegung, Jahrbuch der Schiffbautechnischen Gesellschaft, Band 46, 1952, Seiten 176-179.
11. Wille, R., Seiten 180-185, *ibid* 10.

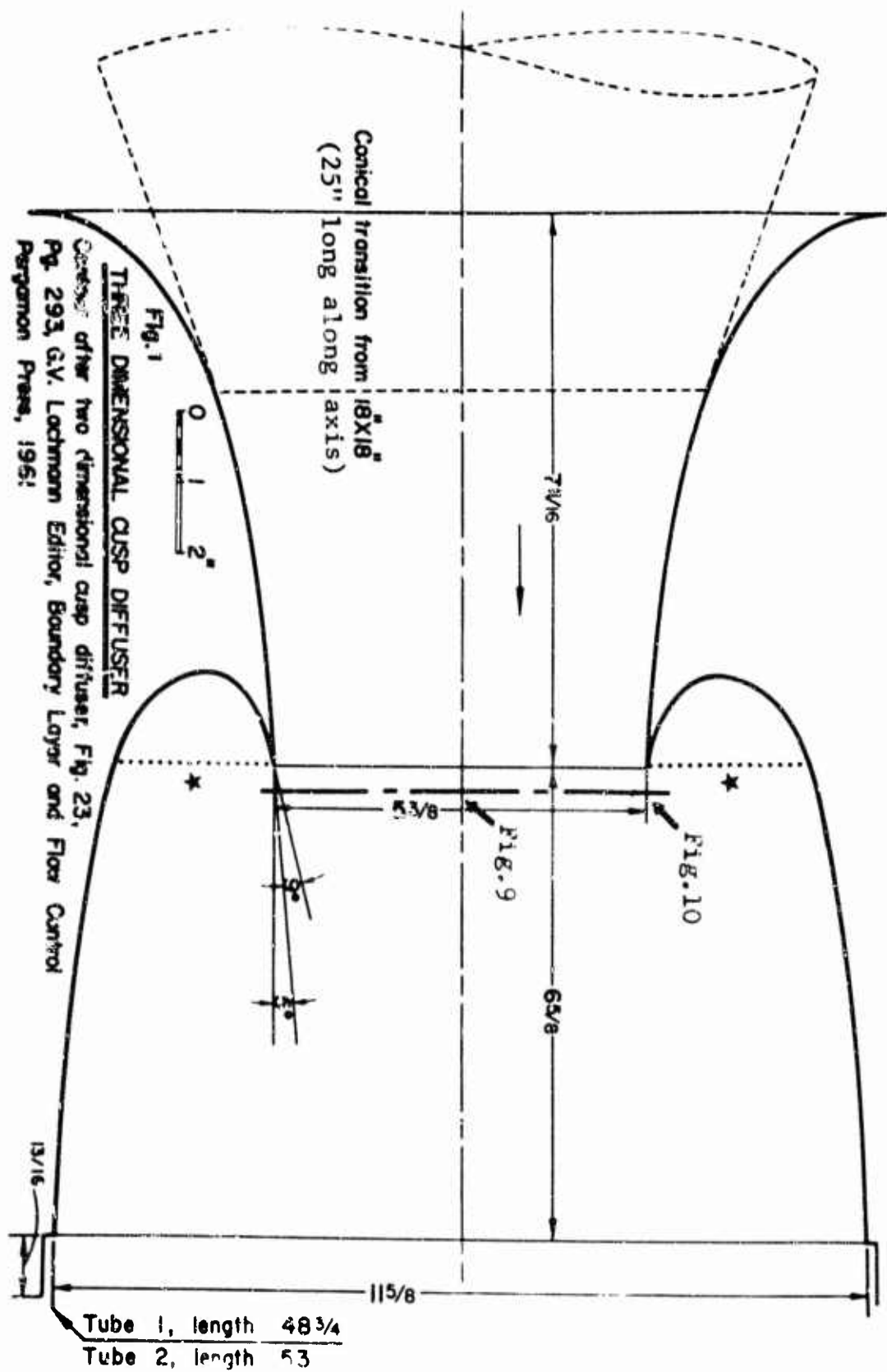




Fig.2.View of Nozzle of Square Cross Section.The Discharge, 10.25 by 10.4(inches) is Inlet of Sudden Enlargement,Ratio of Expansion is approximately 1:3.



Fig.3. View of Lower Nozzle Boundary for Sudden Enlargement, Ratio of Expansion 1:3. If Similar Upper Boundary is Placed Symmetrically, the Nozzle Discharge is 18 in. by 6 in. from Wall to Wall. Longitudinal Lengths of Figs. 2 and 3 are equal.



Fig. 4



Fig. 5



Fig. 6



Fig. 7



Fig. 8

Figs. 4-8. Formation and Decay of Starting Vortices in Cusp Diffuser, Shape of Boundaries as in Fig. 1, Rectangular Cross Section, Length over Inlet Width Ratio 15:1; Water 7 in. deep, Velocities 7"/sec in Figs. 4-7, 12"/sec. in Fig. 8 for Steady State of Flow.



Fig. 9

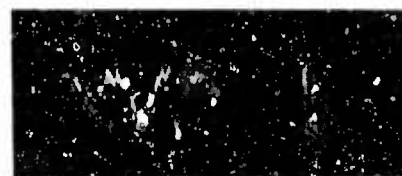


Fig. 10

Figs. 9-10. Oscillations at 120 ft./sec. in Cusp Diffuser of Circular Cross Sections (Fig. 1, plate * installed) in Plane Parallel to Inlet at a Distance of 0.07 times Inlet Diameter. Photographed in Center, Fig. 9; at Jet Boundary, Fig. 10.

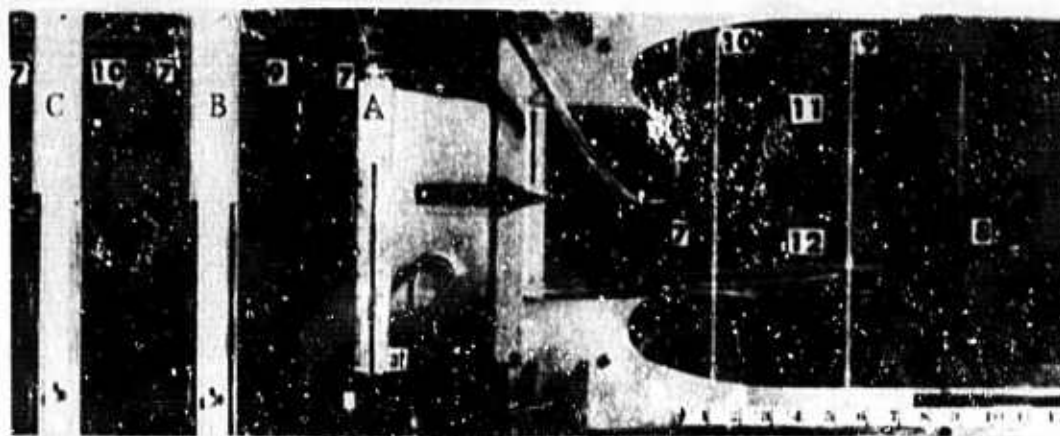


Fig. 11



Fig. 12



Fig. 13

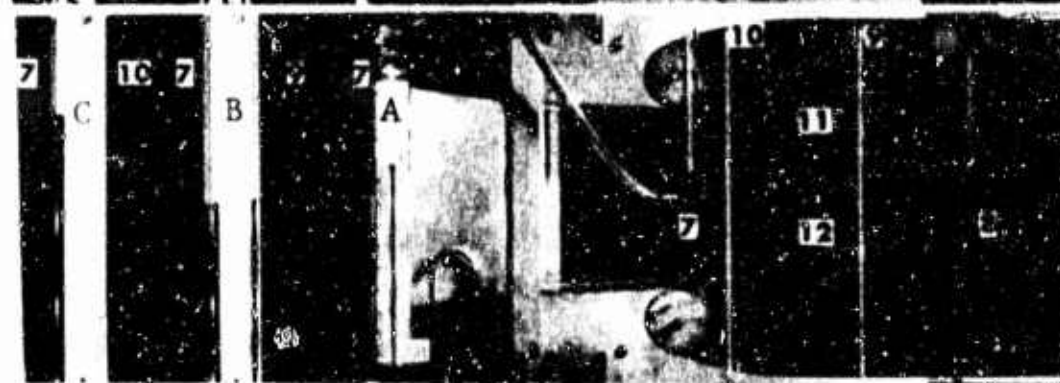


Fig. 14

Figs. 11-14. Airflow for Models of Figs. 4-8. Effect on Flow of Cusp and Cylinder Boundaries Shown by Tuft, Pitot-Static Tube, and Boundary Pressure at Discharge Plane; 1/2" Displacement of Tube Near Jet Boundary for Figs. 11, 13 & 12, 14.

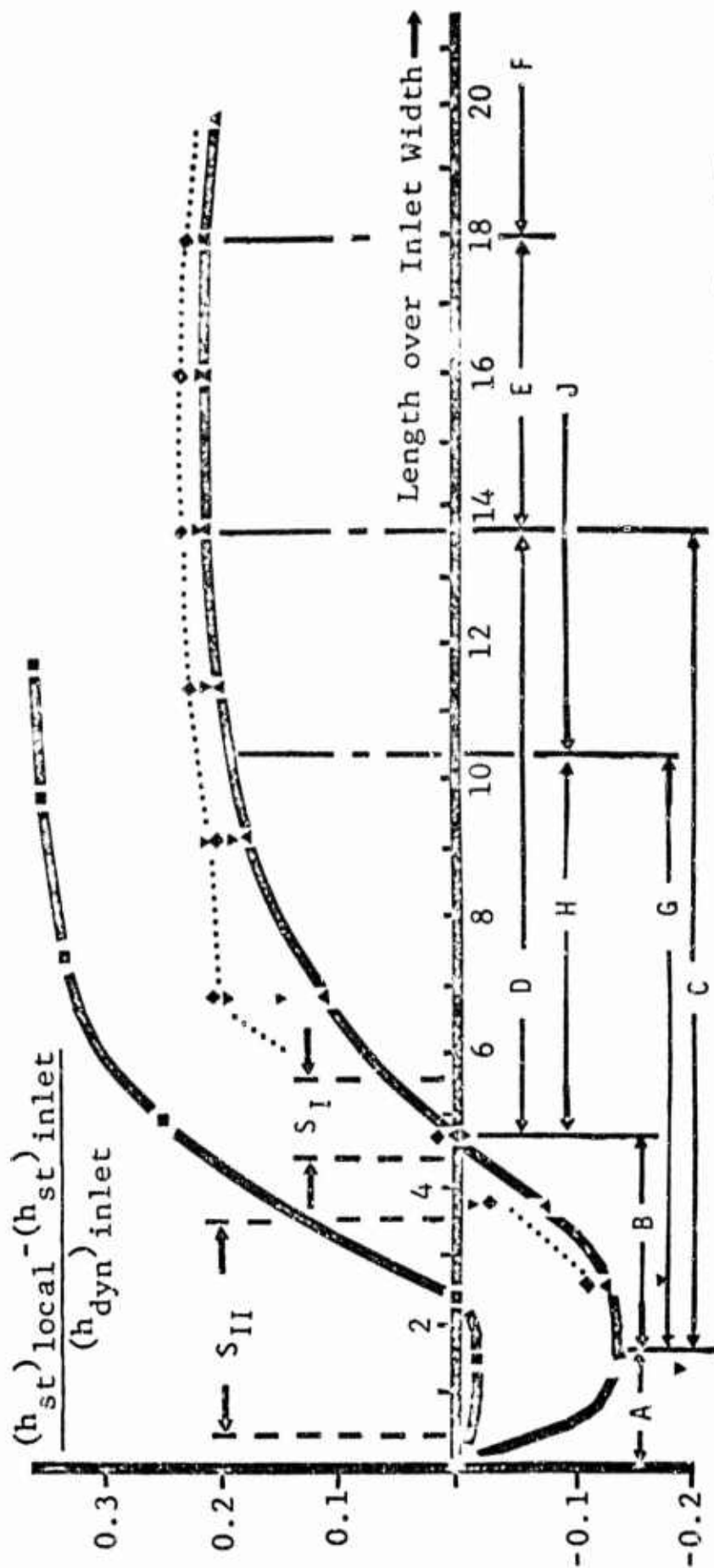


Fig.15 STATIC HEAD RECOVERY, THREE-DIMENSIONAL MODEL, Figs.1 and 2.

Circular Cusp Diffuser, Fig.1, expansion ratio 1:4.67; lower solid curve, dotted curve. Original Cusp Boundary; solid curve: inlet velocity 118 ft./sec. Δ ; 60 ft./sec. ∇ . Cusp Zone with Plate (dotted curve):inlet velocity 118 ft./sec. \blacklozenge .

Square Cross Sections, Fig. 2, exp. ratio 1:3, upper sol. curve; inlet vel. 118 ft./sec. \blacksquare

Reattachment (Stagnation) Regions: Circular Cusp S_I , 360° ; Square Model

S_{II} : lower limit at mid-point of each boundary, upper limit at each corner. Classification of Head Zones: See Text.

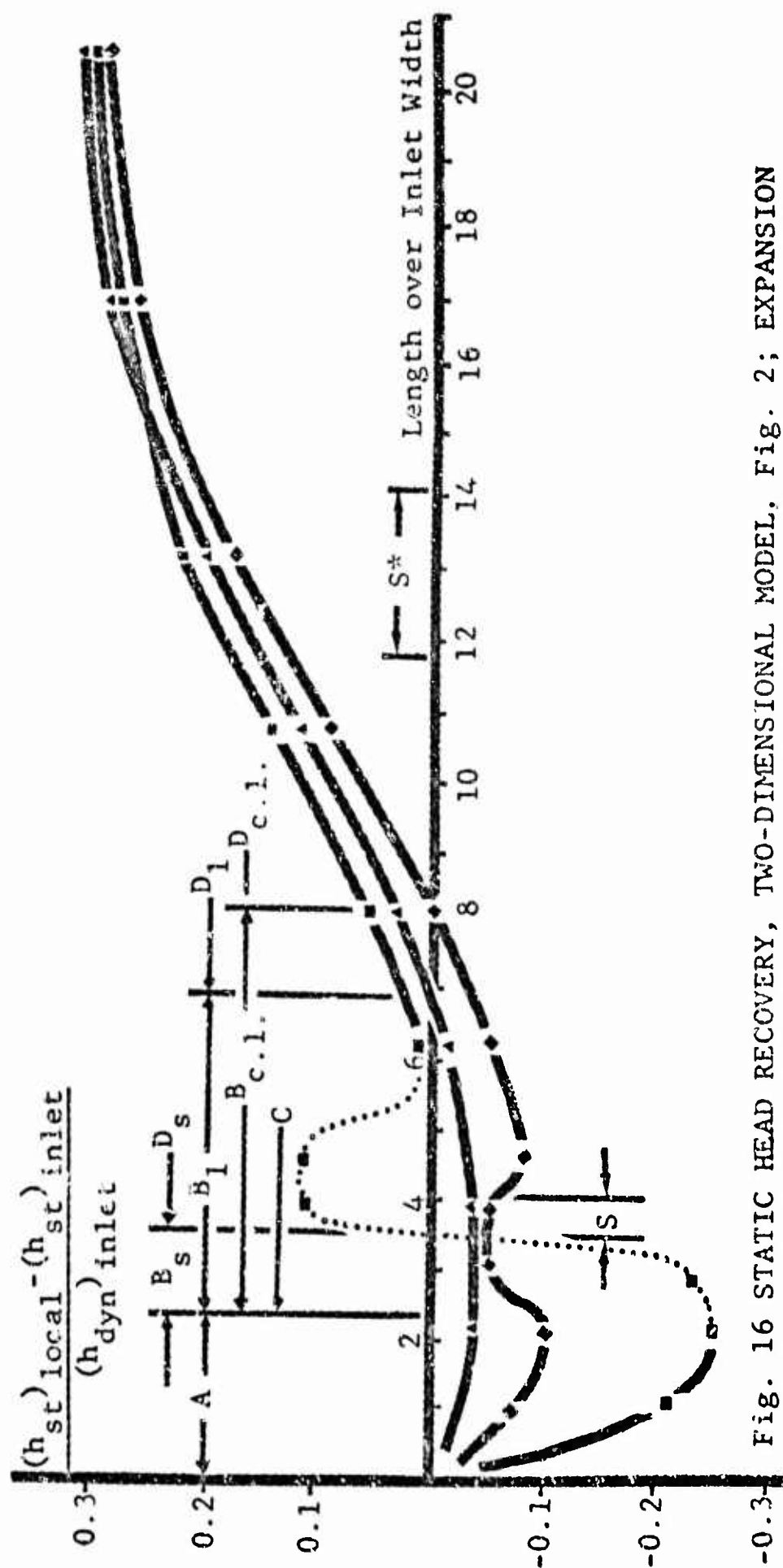


Fig. 16 STATIC HEAD RECOVERY, TWO-DIMENSIONAL MODEL. Fig. 2; EXPANSION RATIO 1:3; COANDA EFFECT; one short and one long reattachment (stagnation) zone S and S* respectively. STATIC HEAD MEASUREMENTS in vertical longitudinal plane at approximately 118 ft./sec. (normal and small diameter Pitot-static tubes); along center line \diamond ; same along parallels at 6 inch distances at either side from center line: on side of short detached zone \blacksquare ; on side of long detached zone \blacktriangle . HEAD RECOVERY: continues beyond S*. CLASSIFICATION OF HEAD REGIONS: depressions, A; increase to inlet head level, B; maximum increase, C: increase above inlet, D.

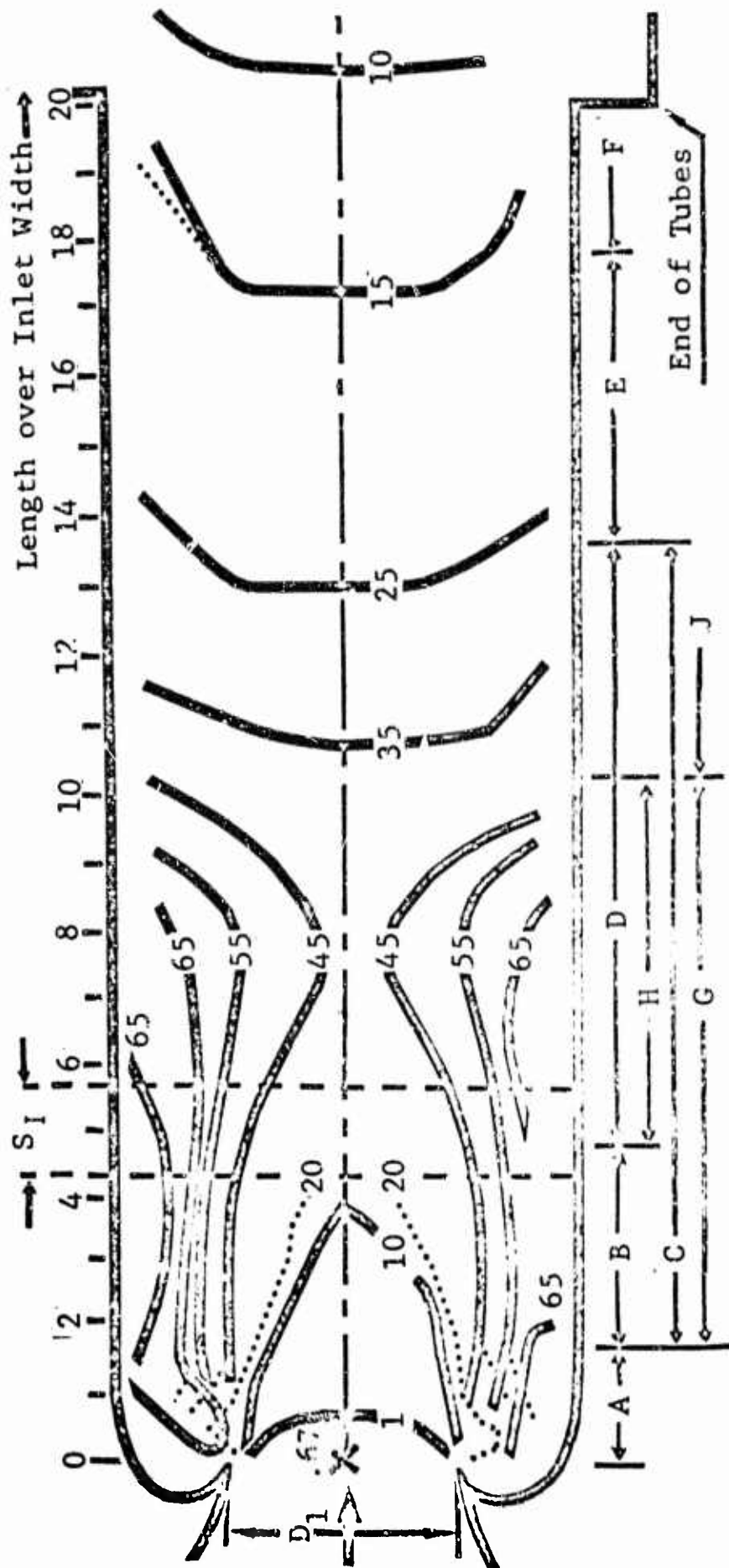


Fig. 17 FORMATION & DECAY OF TURBULENCE SHOWING DEGREE OF TURBULENCE IN %;
CIRCULAR CUSP DIFFUSER, Fig. 1; solid lines for original boundary; same lines
continued into dashed lines: cusp diffuser with plate (Fig. 1); at inlet
118 ft./sec.; $D_1 = 5 \frac{3}{8}$ ". REATTACHMENT (STAGNATION) ZONE, S_I , throughout 360° .
CLASSIFICATION OF HEAD ZONES: same as in Fig. 15, showing interrelation of
head change and change of turbulence characteristic.

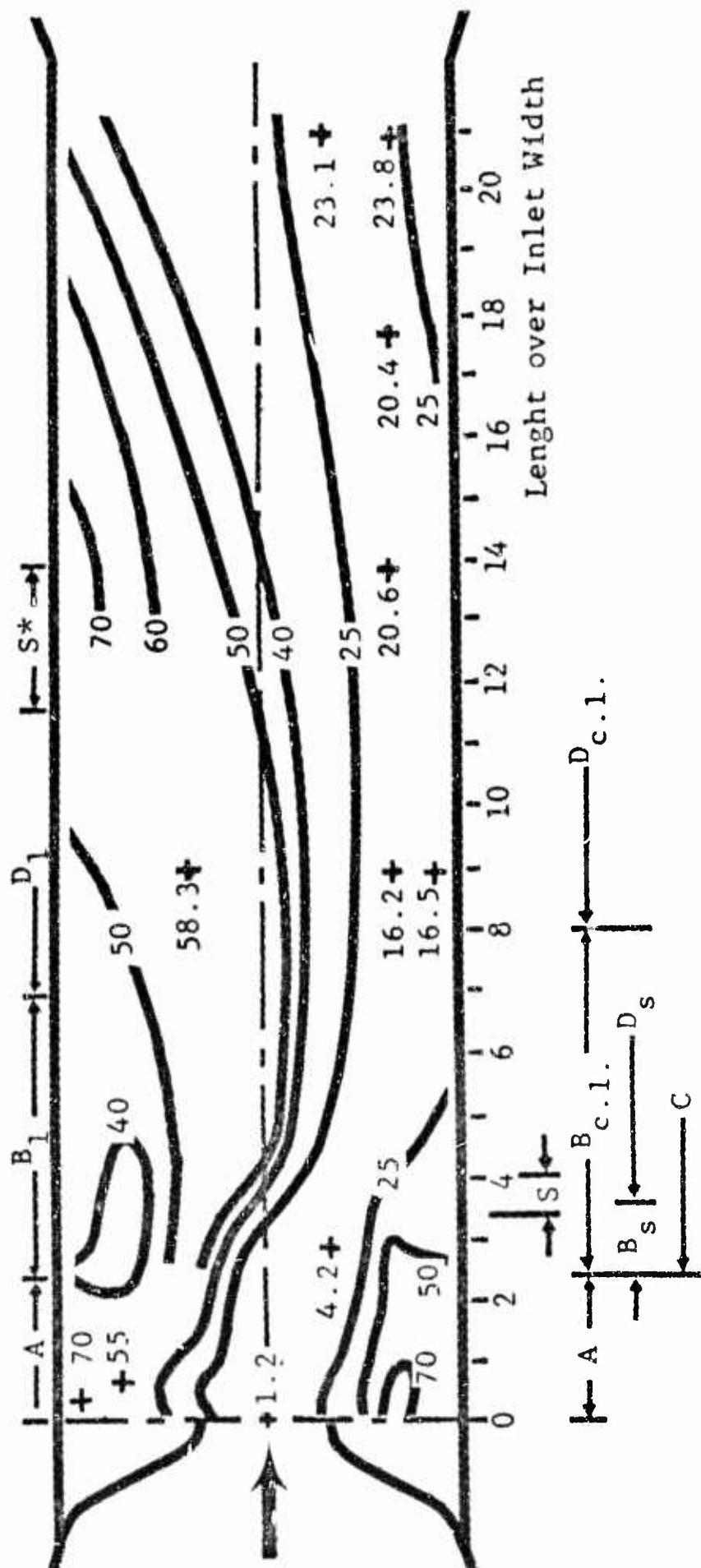


Fig. 18 FORMATION & DECAY OF TURBULENCE SHOWING DEGREE OF TURBULENCE IN %; TWO-DIMENSIONAL MODEL, Fig. 3. EXPANSION RATIO 1:3; COANDA EFFECT: one short detached zone, reattachment zone, S; one long detached zone, S* (lower limit less clearly distinguished for S*). CLASSIFICATION OF HEAD ZONES: see Fig. 16. Depression A; increase to inlet head level B_s, B₁, B_{cl} (side of short detached zone, subscript_s; of long detached zone, subscript_l; along center line, subscript_{cl}; increase above inlet D_s, D_l, D_{cl}). Note: Shape of nozzle distorted for convenience of turbulence presentation.

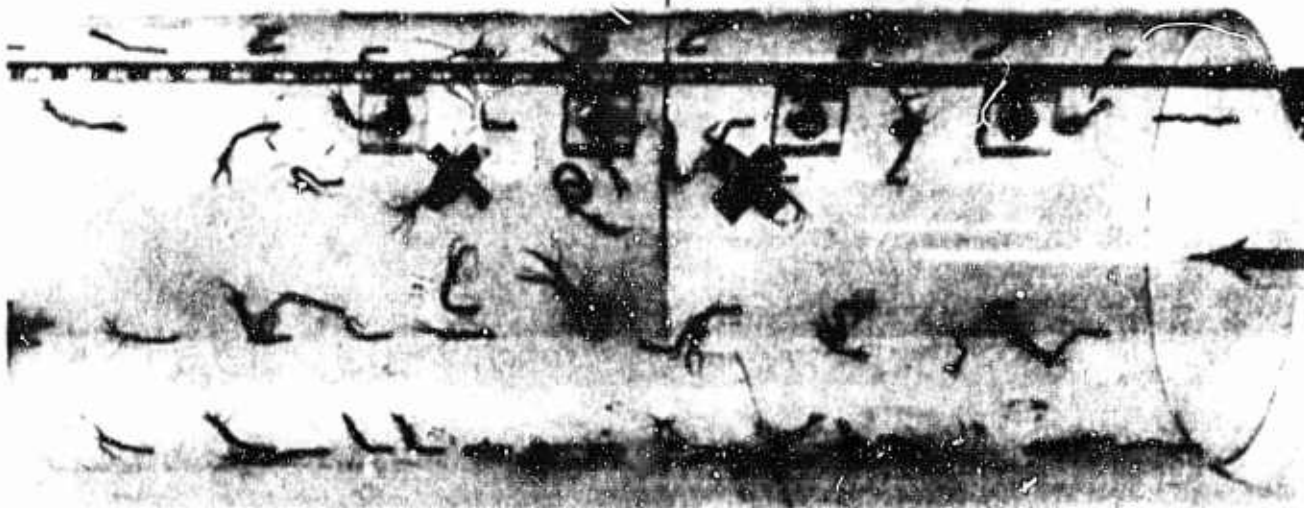


Fig.19

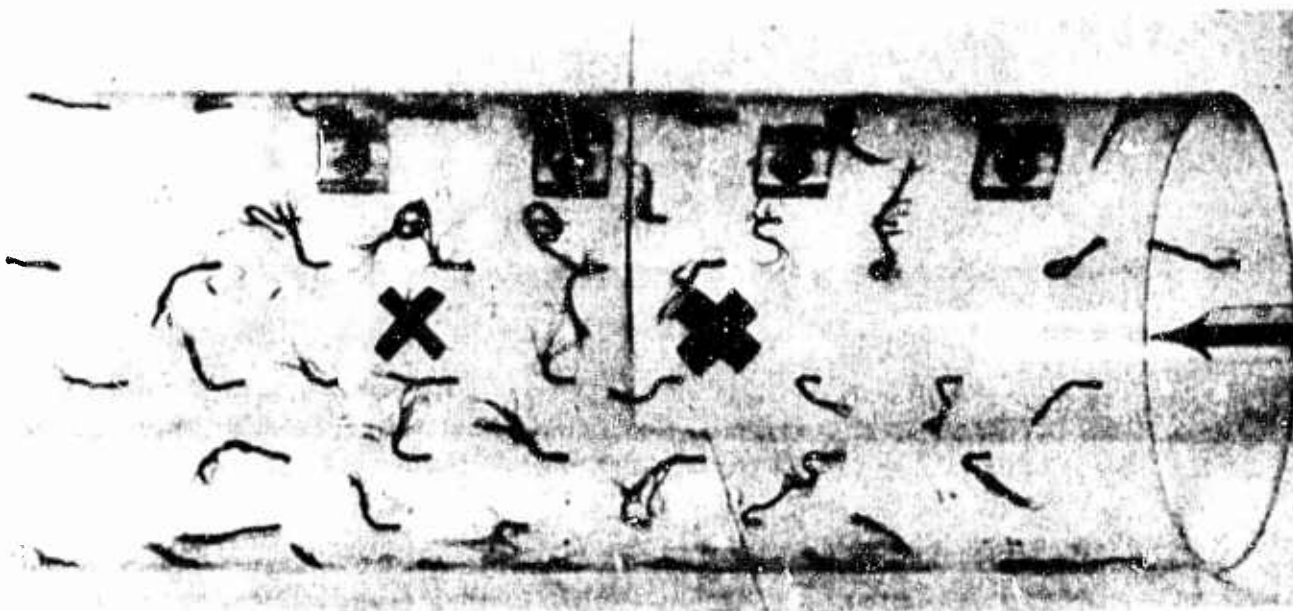


Fig.20

Figs. 19 and 20. TUFT OBSERVATION IN FIRST EXTENSION TUBE, TRANSPARENT, CIRCULAR CUSP DIFFUSER, FIG.1. Tuft attached at one end by tape at the inner tube boundary throughout 360 degrees shows heavy turbulence in the reattachment zone between crosses; also upstream in the detached zone; and a short distance downstream. Static electricity attached the free end of the tuft on the boundary. Photographs were taken after the tube was removed. The ruler is attached to the front section of the tube.

Spreading Rates of Compressible Two-Dimensional

Reattaching Jets Upstream of Reattachment

by

R. E. Olson

United Aircraft Research Laboratories

East Hartford, Connecticut

ABSTRACT

The results of experimental studies to determine the spreading rates of two-dimensional reattaching jets upstream of reattachment are presented for a range of jet Mach numbers between 0.66 and 2.0 and a range of geometries both with and without flow into the separation bubble. The jet spreading rates are presented in terms of the shear stress constant in Prandtl's expression for the eddy viscosity. The values of shear stress constant were determined from velocity profile measurements perpendicular to the jet centerline at various axial stations upstream of reattachment.

The results presented indicate that the variation in the spreading rate of the jet boundary enclosing the separation bubble can be correlated with the jet Mach number and the percentage distance to reattachment for a range of geometries and flow rates into the separation bubble. The spreading rates for the outer boundary of the jet were found to correlate with Mach number and the jet radius of curvature.

These studies were undertaken as part of a general investigation of the characteristics of reattaching jets conducted for the Harry Diamond Laboratories under Contract DA-49-186-AMC-144(D).

INTRODUCTION

The development of analytical techniques for predicting the characteristics of turbulent jet reattachment in wall-attachment type fluid-state devices requires knowledge of the jet spreading rates upstream of reattachment. The jet spreading rate is generally expressed in terms of an aggregate empirical coefficient which must be determined experimentally. Such an empirical approach is required since the lack of fundamental understanding of turbulent mixing precludes a purely analytical determination of the jet spreading characteristics.

Although experimental studies, such as those of Refs. 1, 2 and 3, have provided information regarding the spreading characteristics of free-jet flows, the studies reported in Ref. 4 indicate that the spreading rates obtained from free-jet studies are not applicable to reattaching-jet flows. The studies which have been conducted for reattaching-jet flows, such as those of Ref. 5, are generally limited to incompressible jets. Such studies are also limited in that consideration has not been given to the effect of flow introduced into the separation bubble externally on the jet spreading rates; an understanding of which is required to evaluate the effect of control flow in a wall-attachment device.

Consequently, studies were conducted to determine the spreading rates of compressible reattaching jet flows upstream of reattachment for a range of jet Mach numbers both with and without flow introduced into the separation bubble. This paper presents the significant results of these studies and provides information required in the further development of analytical techniques for predicting the characteristics of jet reattachment in fluid-state wall-attachment type devices.

CHARACTERISTICS OF JET BOUNDARY MIXING UPSTREAM OF REATTACHMENT

A generalized flow model illustrating the nature of turbulent mixing along the boundaries of a reattaching jet upstream of reattachment is presented in Fig. 1.* In the separation region upstream of reattachment, the turbulent mixing which occurs between the jet and the stalled flow in the separation bubble results in the formation of a shear layer along the inner boundary of the jet. A similar shear layer is developed along the outer boundary as a result of mixing between the jet and quiescent surroundings. These shear layers spread inwardly into the

*Figures appear on pages 154 through 165.

inviscid core of the jet and at some downstream station converge to form a fully developed turbulent jet. Within the conservation of total momentum, there is a continuous momentum exchange in the jet boundary mixing process between layers of fluid moving at different velocities, with the fluid adjacent to the jet boundary gaining momentum at the expense of fluid originally in the jet. The turbulent mixing intensities which determine the jet boundary spreading rates are generally different on the inner and outer boundaries of the jet as a result of the jet curvature and the increased proximity of the inner boundary of the jet to the wall.

Although the jet boundary mixing zones are shown to have zero thickness at the nozzle exit, in actuality these shear layers have a finite thickness at the origin with the velocity profile being that of the initial nozzle boundary layer. Kirk (Ref. 6) suggested that at some distance x downstream of the nozzle exit the turbulent shear layer behaves in much the same manner as an equivalent layer developing from zero thickness over a greater distance $x + x'$. By assuming that over the distance x' the equivalent mixing layer attains a momentum thickness equal to the momentum thickness, θ , of the real boundary layer and employing Gortler's first approximation that the momentum thickness of an asymptotic turbulent shear layer equals 1/30th of the distance from the origin, Kirk reasoned that the distance to the virtual origin, x' , could be expressed as

$$x' = 30 \theta \quad (1)$$

Nash (Ref. 7) concludes from a more rigorous treatment of this transition region that Kirk's approximation is valid for downstream distance greater than approximately 8 boundary layer thicknesses. For thin boundary layers relative to the nozzle exit the shift in origin of the mixing layer is not significant and can be neglected.

Providing that the flow introduced externally into the separation bubble is a small fraction of the jet flow, the mixing along the inner and outer boundaries of the jet in the initial expansion length occurs at essentially constant pressure, and the velocity profiles are characteristic of the profiles in an asymptotic free shear layer. As the flow introduced into the separation bubble increases, however, significant static pressure gradients are developed within the separation bubble and velocity profile similarity within the shear layer on the inner jet boundary no longer exists for all streamwise stations in the initial expansion length. During recompression a transition occurs on the inner

jet boundary between the free shear layer developed in the initial expansion length and the redeveloping boundary layer downstream of reattachment. In this recompression length, velocity profile similarity cannot be expected either with or without flow being introduced into the separation bubble.

TEST EQUIPMENT AND PROCEDURE

A schematic diagram and photograph of the test rig employed for the studies are presented in Figs. 2 and 3, respectively. The test rig was two-dimensional throughout its length and was provided with hinged side plates 3 in. apart. A portion of these side plates was glass to enable schlieren observation.

Removable nozzle blocks were provided to obtain both subsonic and supersonic jet Mach numbers. Subsonic jet Mach numbers were obtained with a smooth-approach convergent nozzle. Convergent-divergent nozzles designed for uniform flow at the exit were employed to obtain supersonic jet Mach numbers. The exit height, w , for all nozzles was equal to 0.5 in., thereby providing an aspect ratio (distance between side plates divided by the nozzle height) equal to 6.0. A single boundary wall was provided downstream of the nozzle blocks for jet reattachment. This boundary wall was adjustable to vary both the wall displacement distance (setback) and the wall angle. Sealing of the nozzle blocks and the boundary wall at the side plates was accomplished with flat rubber gaskets.

Airflow was supplied to the rig from a 400-psia compressor and was throttled to provide a nozzle upstream plenum pressure of approximately 22 psia for all tests. With this upstream plenum pressure, the Reynolds number based on the nozzle exit height was approximately 2.5×10^5 and varied somewhat with the jet Mach number. Control flow was bled upstream of the nozzle plenum chamber through a throttling valve and introduced through a slot in the boundary wall at the nozzle exit station. A standard ASME bellmouth was provided for measuring the control flow. The boundary layer thickness on the nozzle walls at the exit was less than 0.010 in. resulting in a maximum boundary layer momentum thickness of less than 0.001 in.

Pitot and static pressure measurements within the jet were obtained employing the variable position pitot probe and the sliding-wire static probe shown in Fig. 3. The pitot probe was a flattened-head probe having a 0.004-in. opening and a wall thickness of 0.002 in. The probe

was motorized in the direction perpendicular to the boundary walls and in the streamwise direction but was positioned manually in the direction perpendicular to the side plates. The position of the probe in the motorized direction was obtained from an electronic read-out system. The sliding-wire static probe, employed for obtaining static pressure measurements along the jet centerline (defined as the locus of points of maximum jet velocity) was specially designed to eliminate the probe body interference effects associated with conventional probes and to reduce the effects of flow angularity. The probe was comprised of a 0.058-in. OD slotted hypotube which was bent to the contour of the jet centerline. A second 0.035-in. OD movable hypotube, with a static pressure orifice was contained within the first. The slot in the first hypotube was oriented so that the static pressure orifice faced the side plate. The inner sliding hypotube extended upstream into the nozzle plenum chamber and downstream beyond the end of the boundary wall through the bottom wall of the test rig. This probe was positioned manually and the pressure read on a mercury manometer.

In determining the velocity profiles within the jet, both the pitot and static pressures must be known. Pitot pressures were obtained from traverses perpendicular to the jet centerline employing the variable position pitot probe. Static pressure distributions within the jet were obtained in the following manner. From the approximate equation of motion in the direction perpendicular to the jet, it can be shown that the static pressure gradient is zero at the wall or outer extremity of the jet where the streamwise velocity is zero. By differentiating this equation it can further be shown that the curvature of the static pressure profile is zero at the location of maximum stream velocity where the velocity gradient is equal to zero. These static pressure gradients and the measured static pressures on the outer extremities of the jet and on the jet centerline were employed to establish the static pressure profiles. On the outer boundary of the jet, the static pressure was assumed equal to the measured pitot pressures. On the inner boundary of the jet, the measured wall static pressure was used. Typical static pressure profiles together with the measured pitot pressure profiles are presented in Fig. 4.

Velocity distributions were computed from the pitot and static pressure distributions using one-dimensional compressible flow relations assuming constant total temperature throughout the jet. The velocity distributions obtained were employed to determine the jet boundary spreading rates.

In order that the spreading rates determined in this manner might be generalized and compared with previous results obtained for a free

jet, efforts were made to obtain the velocity profiles perpendicular to the jet boundary. Since the jet boundary is curved for a reattaching jet, it becomes difficult to define the local jet boundary direction accurately and thus to determine accurately the correct direction of traverse. A study was conducted, therefore, to assess the inaccuracies in the measured spreading rates associated with traversing the jet boundary mixing zone at angles other than perpendicular to the boundary.

A schematic diagram of the shear layer along the jet boundary is presented in Fig. 5. The inviscid boundary shown in Fig. 5 represents the position of the jet boundary for no mixing between the jet and external surroundings. The inner boundary of the mixing zone represents the edge of the shear layer where the velocity is equal to the velocity in the inviscid core of the jet. The streamwise lines at an angle β to the inviscid boundary and at a distance ξ from the edge of the shear layer represent the locus of points of constant velocity in the shear layer. The velocity profile shown as a solid curve indicates the profile that would be obtained from a traverse of the mixing zone perpendicular to the inviscid boundary, whereas the profile indicated by the dashed curve represents the profile obtained from a traverse at an angle ϕ measured from the perpendicular to the inviscid boundary. Development of a procedure based on Fig. 5 for evaluating the inaccuracies associated with employing skewed velocity profiles in the determination of the jet boundary spreading rates is presented in the appendix.

The error in jet boundary shear stress constant as a function of skew angle, ϕ , obtained from Eq. (18) in the appendix, is presented in Figs. 6 and 7 for Mach numbers of 0.66 and 1.5 for various values of shear stress constant. It can be seen from the results presented in these figures that for both Mach numbers the error in shear stress constant is less than two percent for positive skew angles less than 7 deg and for negative skew angles less than 14 deg. These results suggest that shear stress constants obtained from traverses at small skew angles are not significantly in error. In view of the relative insensitivity of the experimental shear stress constants to skew angle, the velocity profiles obtained were utilized directly to obtain the jet boundary spreading rates without correction for skew angle.

JET BOUNDARY SPREADING RATES

The jet boundary spreading rates were determined in terms of the shear stress constant, κ , in Prandtl's expression for the turbulent eddy viscosity, namely,

$$\epsilon = \kappa \xi^* \frac{u_0}{2} \quad (2)$$

where ξ^* is the width of the mixing region (defined as the distance from the edge of the mixing zone to the location in the shear layer where the velocity is one half of the velocity on the edge of the mixing zone) and u_0 is the velocity on the edge of the mixing zone.

From Ref. 8, the shear stress constant can be expressed as

$$\kappa = 2C_2 f_4(1) \frac{d\xi^*}{dx} \quad (3)$$

where x is the distance along the jet centerline and C_2 and $f_4(1)$ are Mach number functions defined in the appendix. Since the mixing region width, ξ^* , in Eq. (3) cannot be determined from the velocity profiles by direct measurement, due to the inability to define the edge of the shear layer, other methods must be employed. Two methods are available for determining ξ^* from the measured velocity profiles. For a Gaussian velocity profile of the form

$$\frac{u}{u_0} = e^{-0.6931 (\xi/\xi^*)^2} \quad (4)$$

which represents a good correlation of the measured velocity profiles, the mixing region width can be expressed as

$$\xi^* = \frac{0.6931}{\left[-\frac{d(u/u_0)}{d\xi} \right]_{u/u_0 = 0.5}} \quad (5)$$

From Eq. (5), ξ^* can be determined knowing the slope of the experimental velocity profile at the location where $u/u_0 = 0.5$. However,

evaluating such a slope is often difficult and quite arbitrary. An alternate method, suggested in Ref. 9, consists of plotting the velocity profile on a graph ruled such that the Gaussian velocity profile appears as a straight line. The value of ξ'' is then simply the scale factor which when multiplied times the coordinate ξ , perpendicular to the mixing zone, matches the slope of the measured profile to that of the Gaussian profile as expressed in Eq. (4). This technique allows more of the points of the measured velocity profile to be utilized. The mixing region width was therefore determined using this alternate technique. A typical velocity profile in the jet boundary mixing zone, plotted on Gaussian coordinates, is presented in Fig. 8.

Upon determining the mixing region width for various stations along the jet boundary, the derivative $d\xi''/dx$ in Eq. (3) was evaluated from plots of ξ'' vs. x and the shear stress constant computed.

Spreading rates of the jet boundary enclosing the separation bubble, obtained from the measured velocity profiles, are presented in Figs. 9 through 11 for jet Mach numbers of 0.66, 1.5, and 2.0 and for control flows equal to 0, 5 and 15 percent of the jet flow. These spreading rates are presented in terms of an effective shear stress constant which would correctly predict the mixing region width at a given axial distance along the jet centerline if the mixing rate were constant between the nozzle exit and the given axial station. The shear stress constants presented are for streamwise locations where the velocity profile was a well-developed Gaussian profile. Shear stress constants were omitted for the upstream stations where the velocity profiles were distorted by the control flow. Expressing the shear stress constant in this manner is consistent with its utilization in analytical techniques for predicting the location of jet reattachment.

It is evident from Figs. 9 through 11 that for all Mach numbers the effective shear stress constant along the inner boundary of a reattaching jet correlates quite well with the percentage distance to reattachment for control flow ratios of 0 and 0.05. For a control flow ratio of 0.15, somewhat poorer correlation is shown, particularly at the higher jet Mach numbers. The mixing intensities for all Mach numbers are similar to mixing intensities for free jet boundary mixing at streamwise stations less than approximately 20 percent of the distance to reattachment, but decrease below the free jet value for locations closer to reattachment. The decrease in shear stress constant with increasing distance toward reattachment is indicative of suppression of mixing due to increasing proximity of the wall.

Effective shear stress constants for the outer boundary of the jet are presented in Fig. 12 for the streamwise station immediately upstream of recompression. From the limited results presented, it appears that the shear stress constant correlates with the non-dimensional jet curvature (defined as the reciprocal of the local radius of curvature of the jet centerline multiplied by the jet nozzle width). The mixing intensities are shown to be considerably higher than for a free jet boundary with no curvature.

In reattaching jet theories, although it has been recognized that the spreading rates are different on the inner and outer jet boundaries, it has generally been assumed that the spreading rate is constant along each boundary. The results of this study indicate that the spreading rate along the inner jet boundary can vary significantly as a function of the percentage distance to reattachment and consequently such a variation should be recognized in the formulation of a reattaching jet flow model.

REFERENCES

1. Albertson, M. L., Y. B. Dai, R. A. Jensen, and H. Rose: Diffusion of Submerged Jets. American Society of Civil Engineers Proceedings, Vol. 74, No. 10, December, 1948.
2. Warren, W. R.: An Analytical and Experimental Study of Compressible Free Jets. Aeronautical Engineering Laboratory Report No. 381, Princeton University, Princeton, New Jersey, 1957.
3. Olson, R. E., and D. P. Miller: Aerodynamic Studies of Free and Attached Jets. Report No. 6, Fluid Amplification Series, Harry Diamond Laboratories, Washington, D. C., June 16, 1963.
4. Mueller, Thomas J., and Robert E. Olson: Spreading Rates of Compressible Two-Dimensional Reattaching Jets. Proceedings of the Second Fluid Amplification Symposium, Vol. 1, May, 1964.
5. Sawyer, R. A.: Two-Dimensional Reattaching Jet Flows Including the Effects of Curvature on Entrainment. Journal of Fluid Mechanics, Vol. 17, December, 1963.
6. Kirk, F. N.: An Approximate Theory of Base Pressure in Two-Dimensional Flow at Supersonic Speeds. R. A. E. Tech. Note Aero. 2377, 1954. (Published 1959)
7. Nash, J. F.: An Analysis of Two-Dimensional Turbulent Base Flow Including the Effect of the Approaching Boundary Layer. NPL Aero. Report 1036, 1963.
8. Olson, R. E., T. J. Mueller, and S. J. Shamroth: Studies of Jet Flows in Fluid Amplifiers. United Aircraft Corporation Research Laboratories Report C910079-13, June, 1964.
9. Zumwalt, G. W., and H. H. Tang: Transient Base Pressure Study of an Axisymmetric Supersonic Missile Flying Head-on Through a Blast Wave. Research Report SBW-6, School of Mechanical Engineering, Oklahoma State University, February, 1964.

LIST OF SYMBOLS

C_2	Constant defined in appendix (Eq. (7))
$f_1(l)$	Mach number function defined in Eq. (8)
$f_2(l)$	Mach number function defined in Eq. (9)
$f_3(l)$	Mach number function defined in Eq. (10)
$f_4(l)$	Mach number function defined in Eq. (11)
M	Mach number
P	Static pressure
P_p	Pitot pressure
P_t	Total pressure
S	Setback distance between boundary wall and inner wall of nozzle at nozzle exit (see Fig. 2)
u	Velocity parallel to jet centerline
w	Total height of nozzle at exit (see Fig. 2)
w_c	Control jet width (see Fig. 2)
\dot{w}_c	Control jet weight flow
\dot{w}_0	Initial jet weight flow
x	Distance along jet centerline measured from nozzle exit
x'	Distance between virtual origin of mixing and nozzle exit measured parallel to nozzle centerline
x_R	Distance to reattachment measured along jet centerline from nozzle exit
y	Distance perpendicular to jet centerline measured from jet centerline

LIST OF SYMBOLS
(Cont.)

β	Angle between lines of constant velocity in jet boundary shear layer and inviscid boundary (see Fig. 5)
ϵ	Turbulent exchange coefficient (see Eq. (2))
η	Coordinate at angle ϕ to inviscid boundary (see Fig. 5)
θ	Boundary wall angle measured from nozzle centerline (see Fig. 2) and boundary layer momentum thickness
κ	Shear stress constant (see Eq. (2))
κ'	Shear stress constant for skewed velocity profile (see Eq. (16'))
ξ	Distance perpendicular to inviscid boundary measured from inner boundary of mixing zone (see Fig. 5)
ϕ	Traverse skew angle measured from perpendicular to inviscid boundary (see Fig. 5)

Subscripts

e	Denotes effective value
o	Denotes conditions at nozzle exit

Superscripts

*	Denotes conditions where the velocity in the shear layer is one half of the velocity on the edge of the mixing zone
---	---

APPENDIX

Development of Procedure for Computing Effect of Traverse Skew Angle on Jet Boundary Spreading Rates

Referring to Fig. 5, the angle between the inner boundary of the mixing zone and the inviscid boundary can be expressed, from Ref. 8, as

$$\beta_0 = \tan^{-1} \frac{\kappa}{2C_2} \quad (6)$$

where

$$C_2 = \frac{0.5 [f_2(1) + f_4(1)] - f_1(1)}{2 f_3(1) f_4(1)} \quad (7)$$

and

$$f_1(1) = \int_0^1 \frac{\left(\frac{u}{u_0}\right)^2}{1 + \frac{\gamma-1}{2} M_0^2 \left[1 - \left(\frac{u}{u_0}\right)^2\right]} d\left(\frac{\xi}{\xi^*}\right) \quad (8)$$

$$f_2(1) = \int_0^1 \frac{\left(\frac{u}{u_0}\right)}{1 + \frac{\gamma-1}{2} M_0^2 \left[1 - \left(\frac{u}{u_0}\right)^2\right]} d\left(\frac{\xi}{\xi^*}\right) \quad (9)$$

$$f_3(1) = \frac{0.6931}{2} \left[\frac{1}{1 + \frac{\gamma-1}{2} M_0^2 (1 - 0.25)} \right] \quad (10)$$

$$f_4(1) = \int_0^\infty \frac{\left(\frac{u}{u_0}\right)^2}{1 + \frac{\gamma-1}{2} M_0^2 \left[1 - \left(\frac{u}{u_0}\right)^2\right]} d\left(\frac{\xi}{\xi^*}\right) \quad (11)$$

Also, from Ref. 8, the distance from the edge of the mixing zone to the location in the shear layer where the velocity is one half of its value on the edge of the mixing zone can be expressed as

$$\xi^* = \frac{\kappa x}{2C_2 f_4(1)} \quad (12)$$

From geometry and Eqs. (6) and (12) it can be shown that any line having a constant value of ξ/ξ^* is at an angle to the inviscid boundary of

$$\beta = \text{TAN}^{-1} \frac{\kappa}{2C_2} \left[1 - \frac{\xi/\xi^*}{f_4(1)} \right] \quad (13)$$

where β is positive when measured in a direction toward the inviscid core.

Considering a velocity profile obtained at an angle ϕ relative to the perpendicular to the inviscid boundary as shown in Fig. 5,

$$\eta^* - \eta = (\xi^* - \xi) \frac{\text{SIN}(90^\circ \pm \beta)}{\text{SIN } \gamma}$$

where

$$\gamma = 90^\circ - (\phi \pm \beta) \quad (14)$$

In Eq. (14) the positive sign is employed for positive values of β (measured clockwise) and the negative sign for negative values of β (measured counterclockwise).

Also, from geometry

$$\eta^* = \xi \frac{\text{SIN}(90^\circ \pm \beta_0)}{\text{SIN } \gamma_0} \quad (15)$$

Expressing η^* in the same manner as ξ^* in Eq. (12)

$$\eta^* = \frac{\kappa' x}{2C_2 f_2(\phi)} \quad (16)$$

where κ' is the shear stress constant consistent with the skewed velocity profile. From Eqs. (12) and (16),

$$\frac{\eta^*}{\xi^*} = \frac{\kappa'}{\kappa} \quad (17)$$

or

$$\frac{\eta^*}{\xi^*} - 1 = \frac{\Delta\kappa}{\kappa} \quad (18)$$

which expresses the percentage error in shear stress constant as a function of the skew angle ϕ .

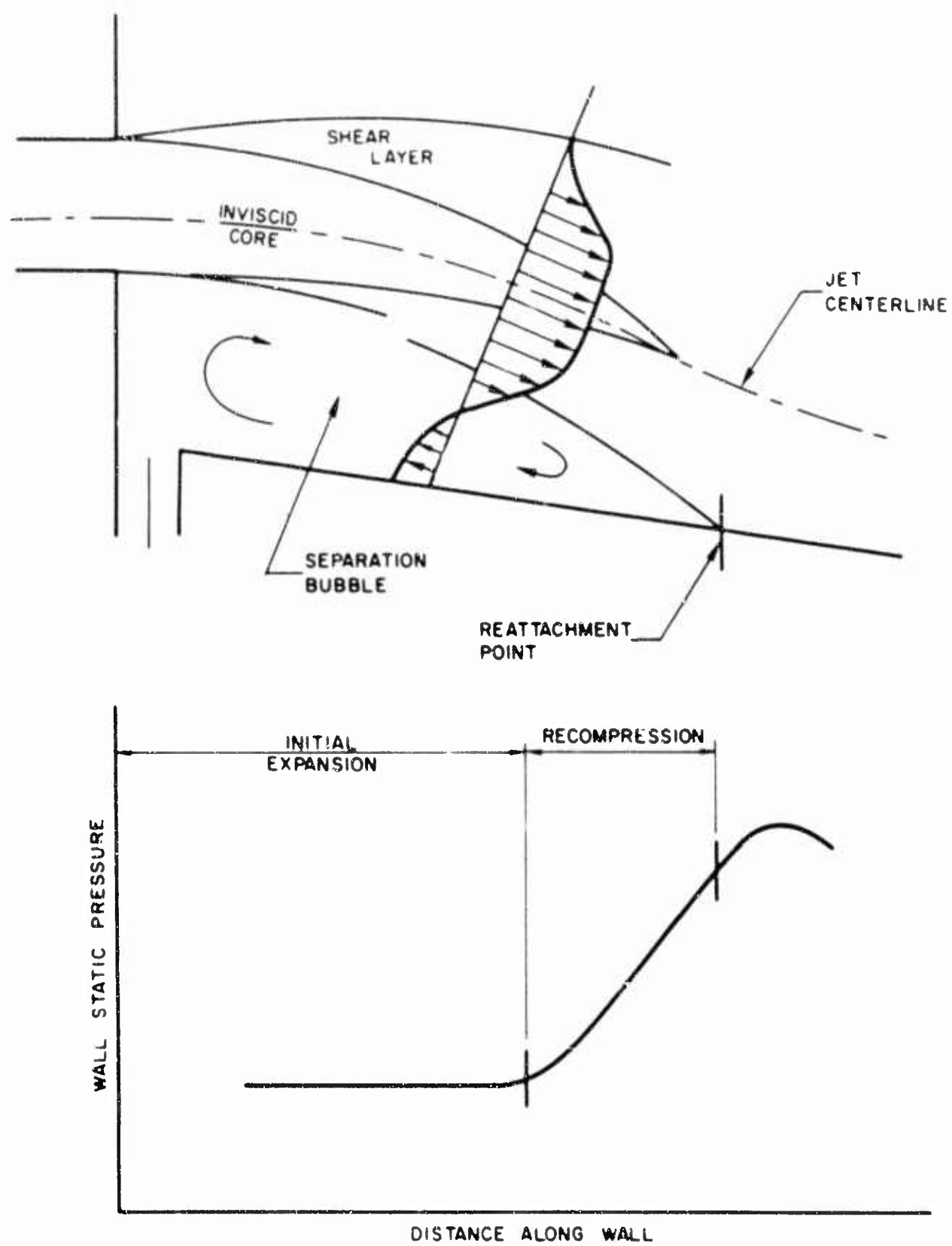


FIGURE 1 FLOW MODEL FOR REATTACHING JET

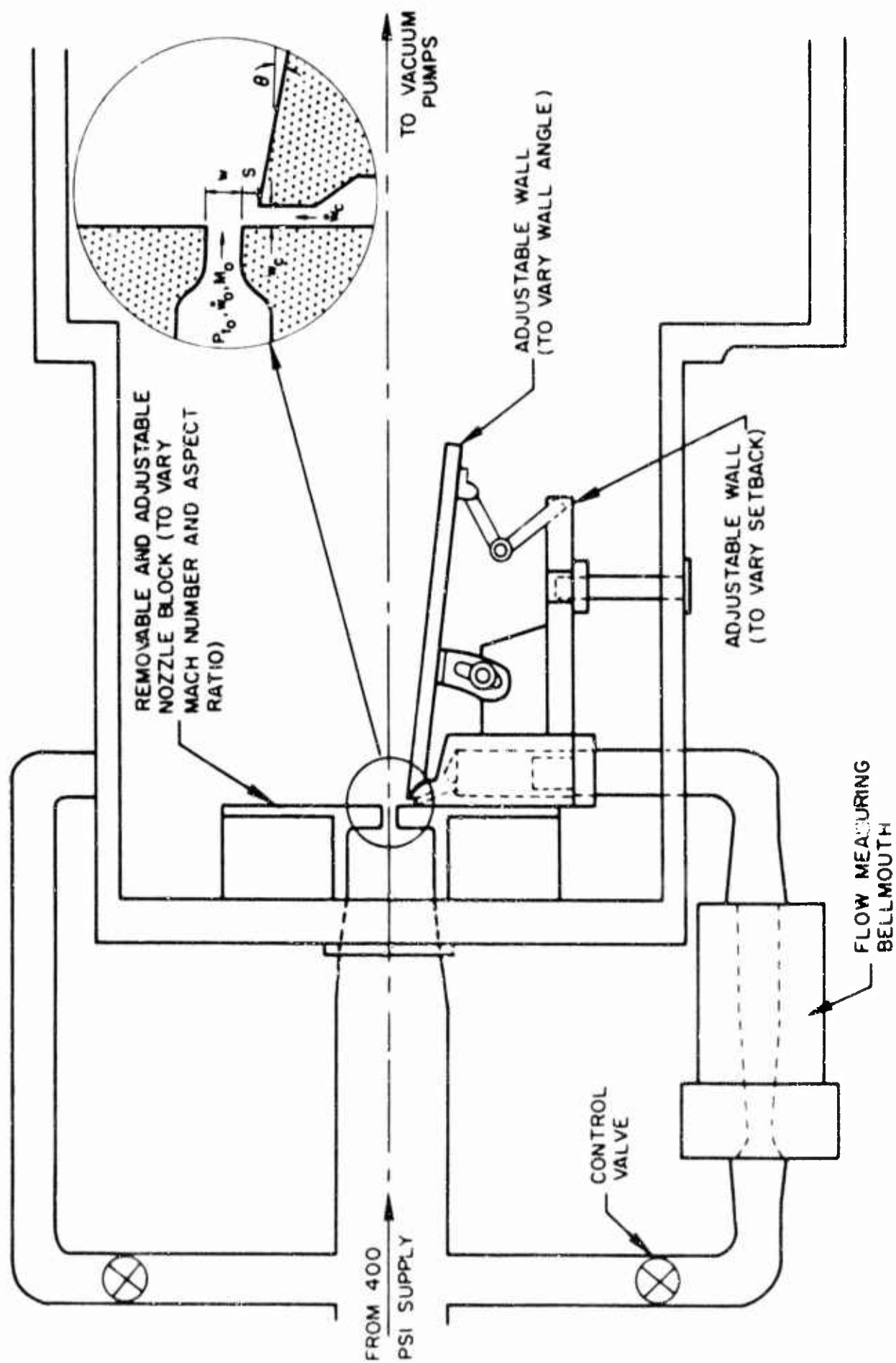


FIGURE 2 SCHEMATIC DIAGRAM OF TEST RIG

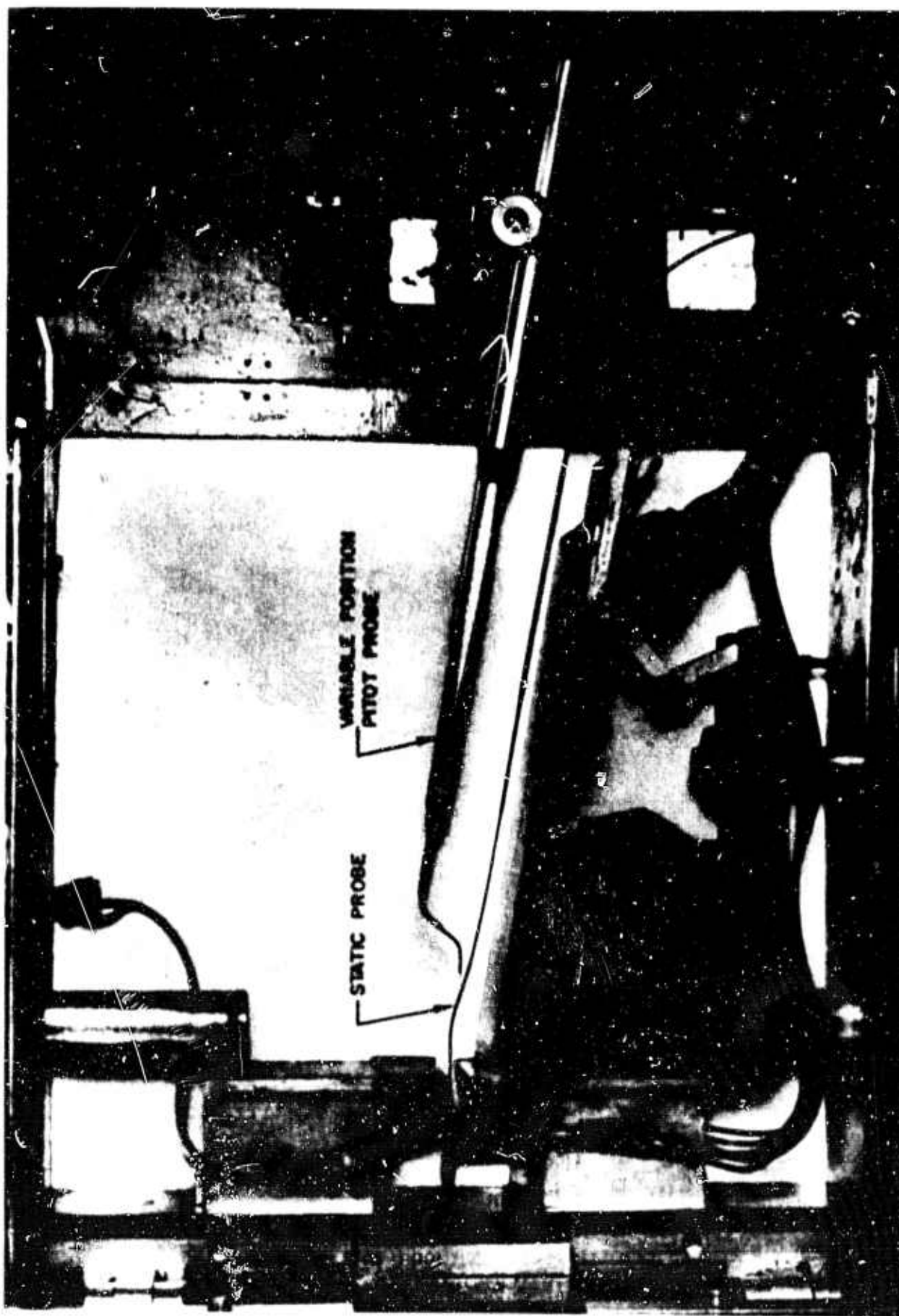


FIGURE 3 PHOTOGRAPH OF TEST RIG

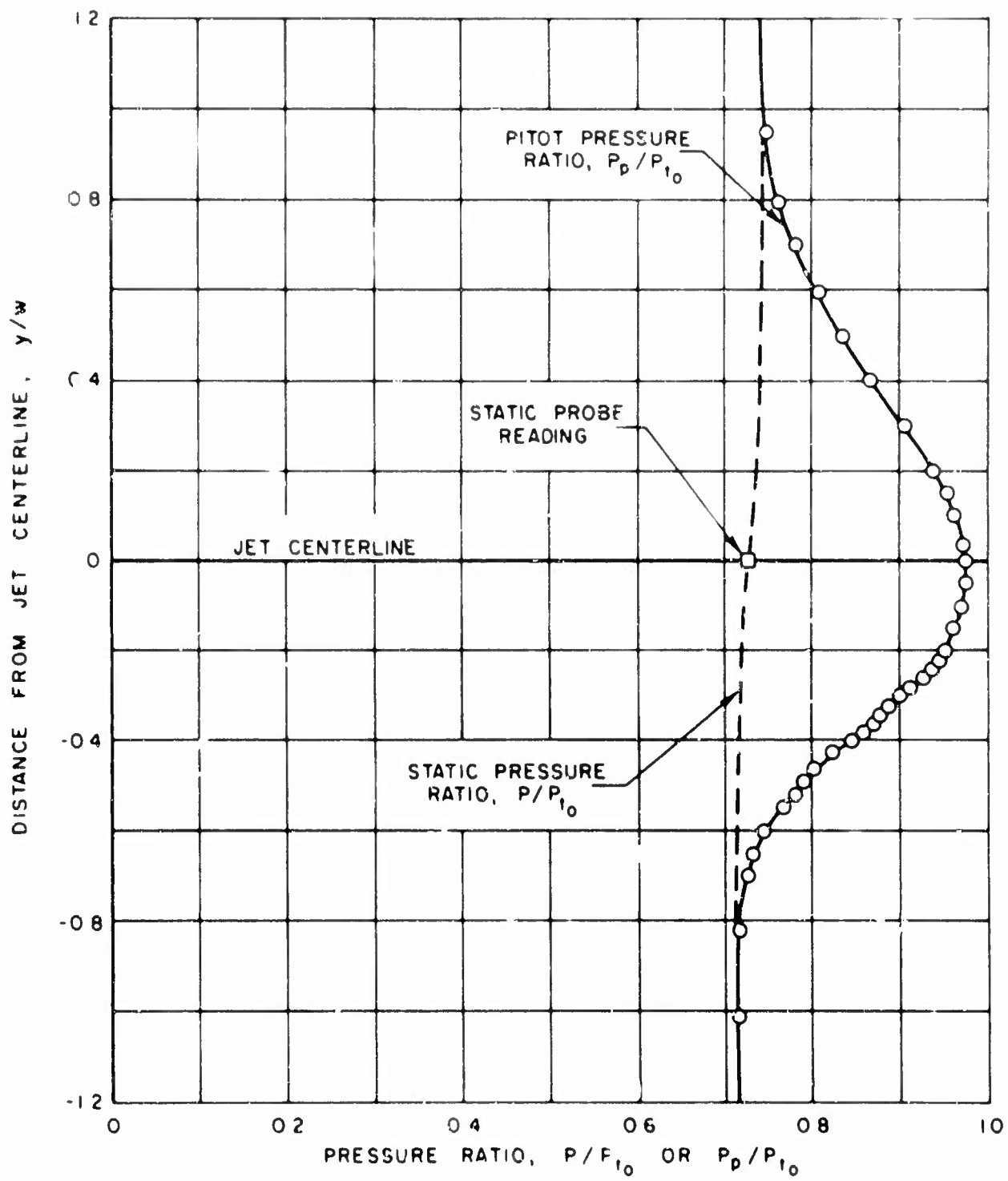


FIGURE 4 TYPICAL PITOT AND STATIC PRESSURE PROFILES UPSTREAM OF REATTACHMENT

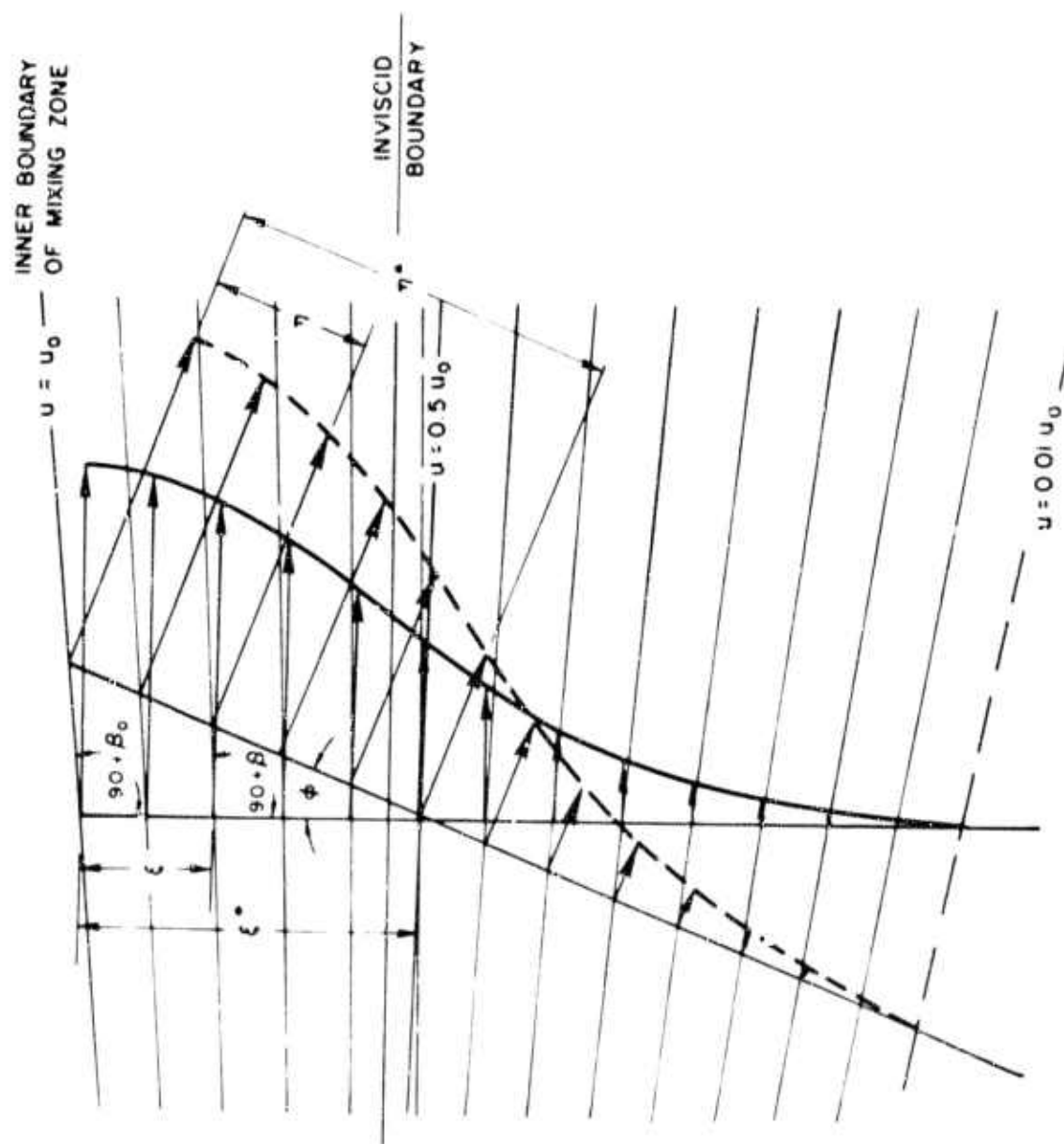


FIGURE 5 SCHEMATIC DIAGRAM OF SKEW VELOCITY PROFILE

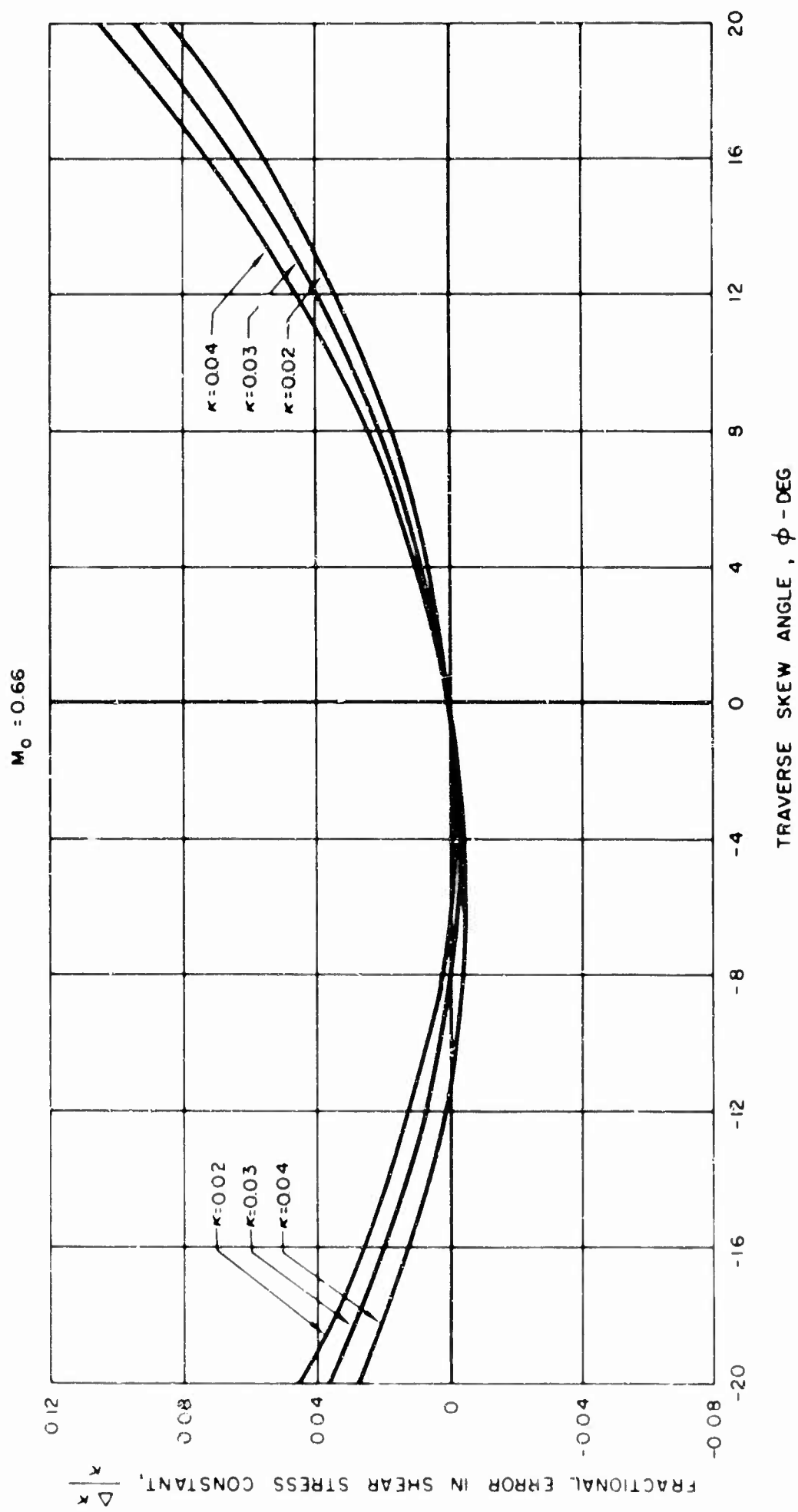


FIGURE 6 EFFECT OF TRAVERSE SKEW ANGLE ON SHEAR STRESS CONSTANT

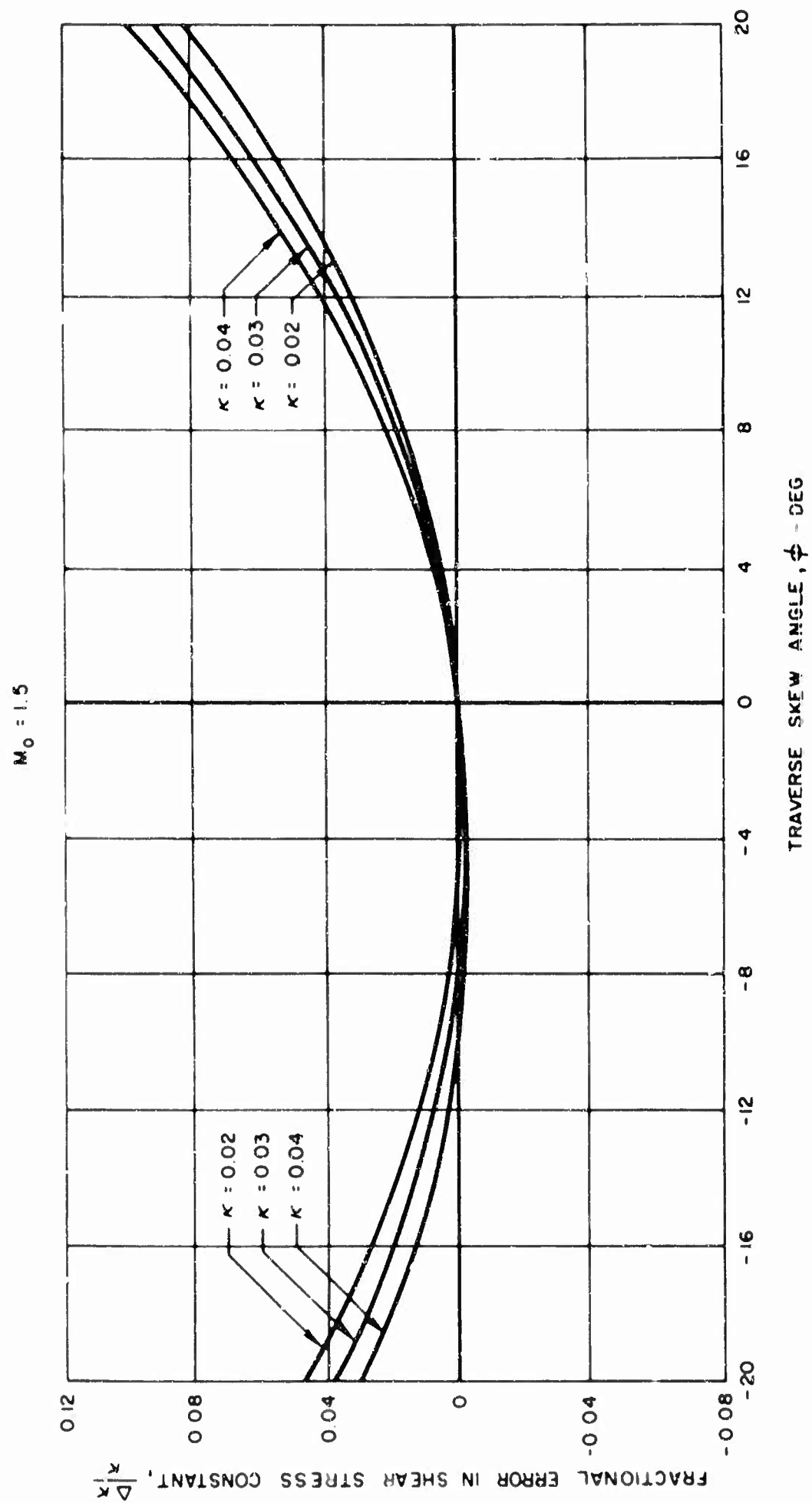


FIGURE 7 EFFECT OF TRAVERSE SKEW ANGLE ON SHEAR STRESS CONSTANT

$M_0 = 0.66$
 $w = 0.5 \text{ IN}$ $\frac{w_c}{w_0} = 0$
 $S/w = 1.0$ $\theta = 6^\circ$

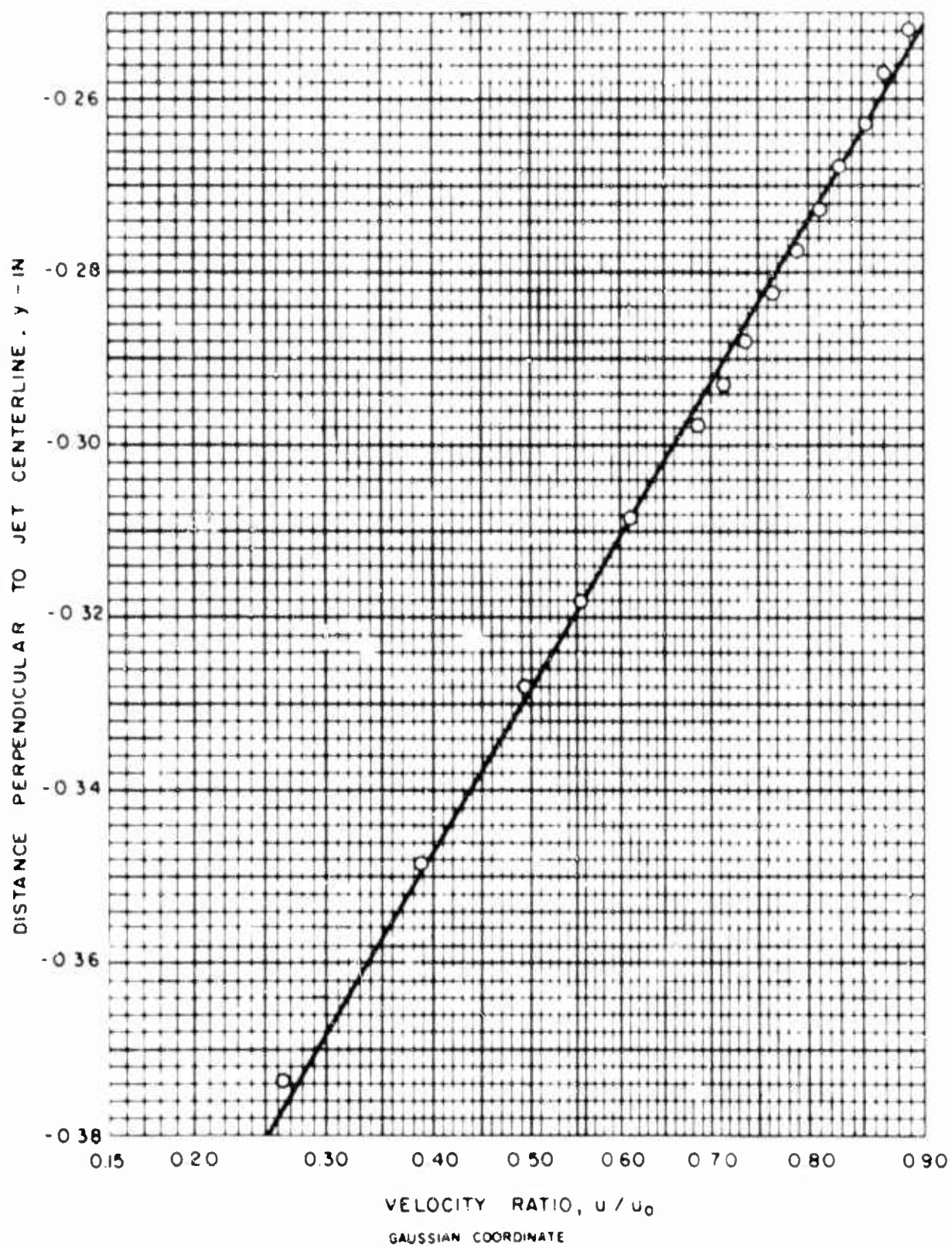


FIGURE 8 TYPICAL VELOCITY PROFILE UPSTREAM OF REATTACHMENT

$M_0 = 0.66$
 $w = 0.5 \text{ IN.}$
 $w_c / w = 0.5$

SYMBOL	S/w	θ - DEG
\diamond	1.0	6°
\square	1.0	10°
\triangle	1.0	13.5°
\circ	0.5	10°

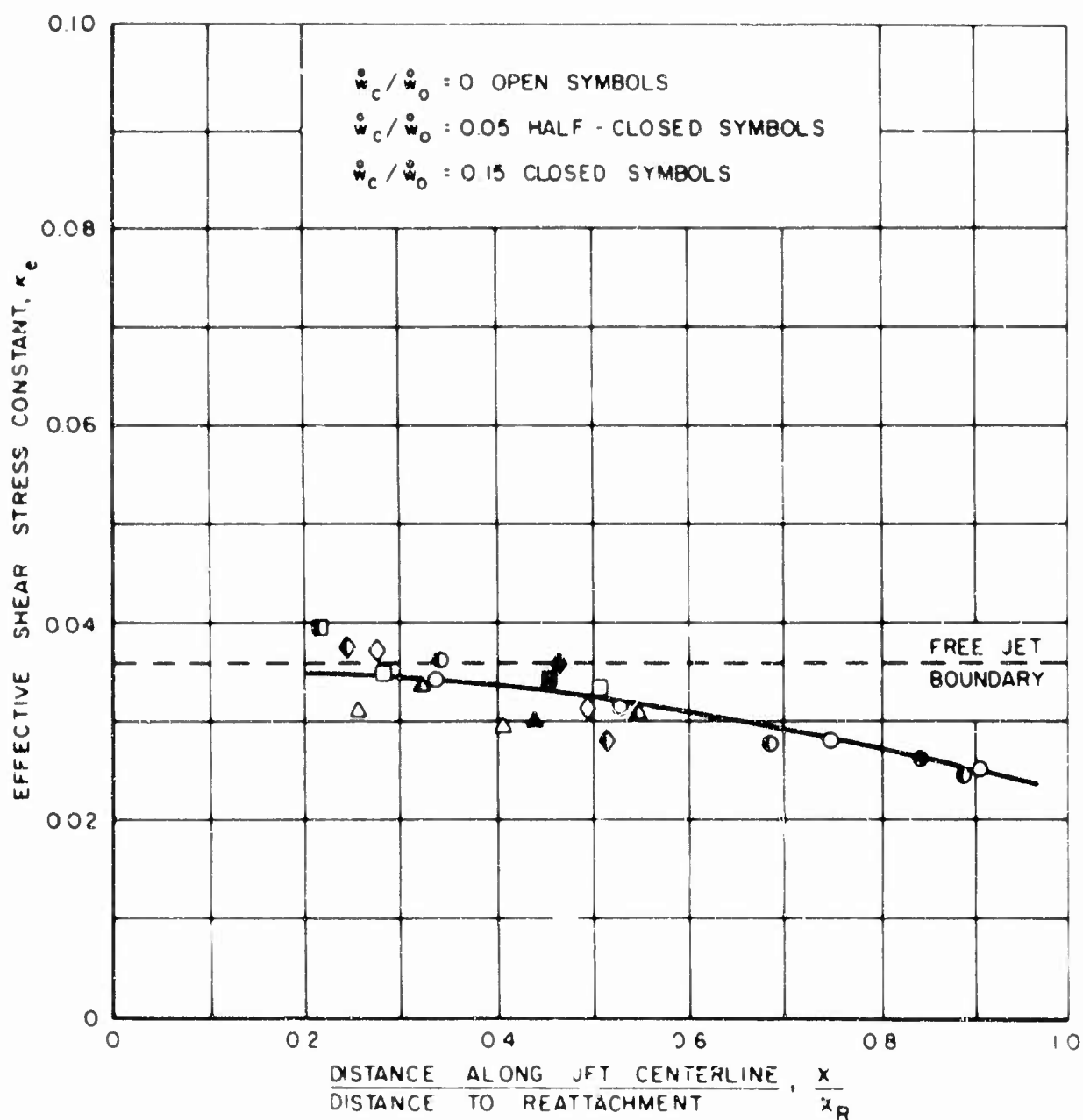


FIGURE 9 VARIATION OF SHEAR STRESS CONSTANT WITH DISTANCE FROM REATTACHMENT FOR INNER BOUNDARY OF REATTACHING JET

$M_0 = 1.5$
 $w = 0.5 \text{ IN}$
 $w_c/w = 0.5$

SYMBOL	S/w	θ - DEG
\diamond	10	6°
\square	10	10°
\triangle	10	13.5°
\circ	0.5	10°

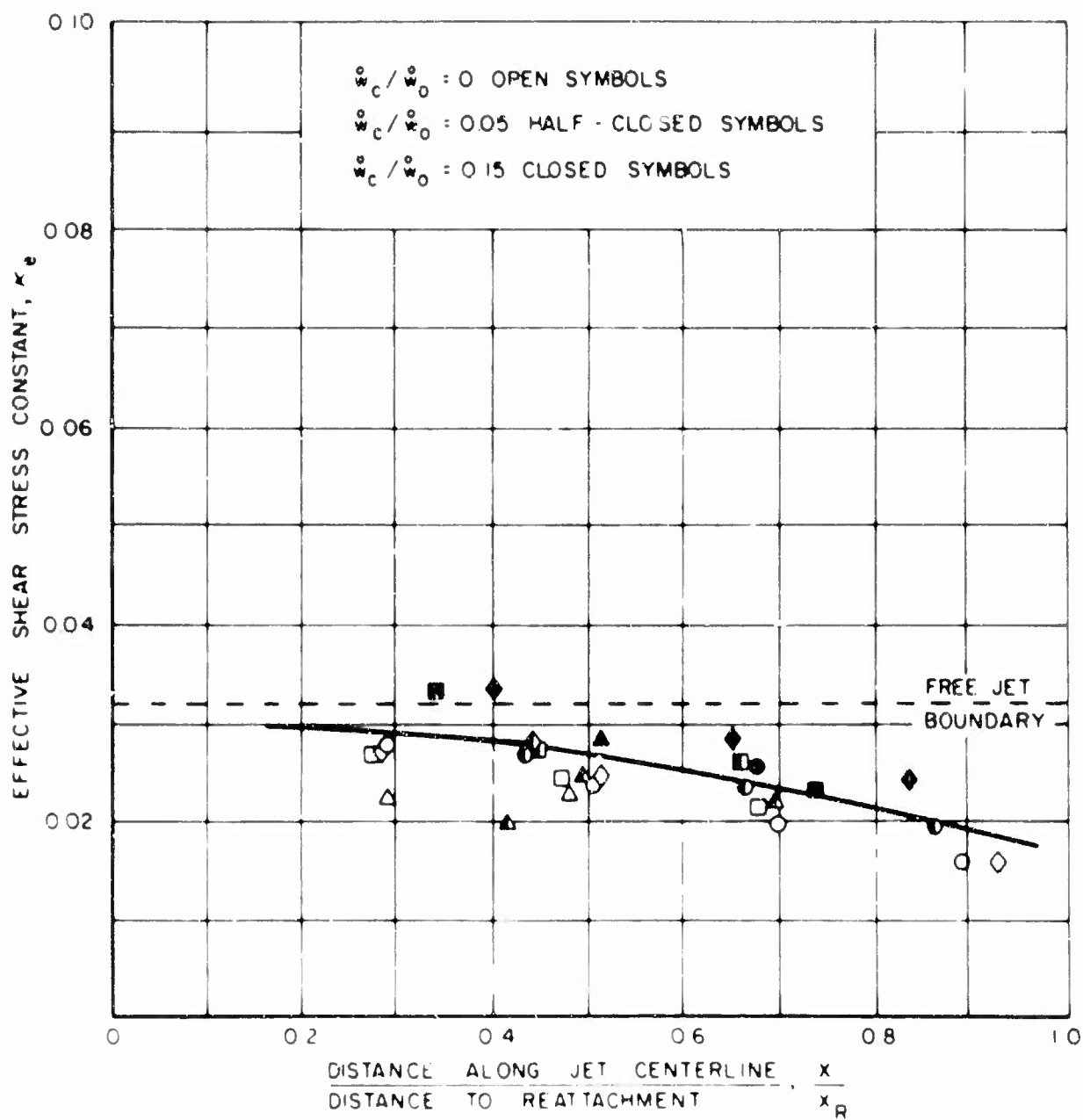


FIGURE 10 VARIATION OF SHEAR STRESS CONSTANT WITH DISTANCE FROM REATTACHMENT FOR INNER BOUNDARY OF REATTACHING JET

$M_0 = 2.0$
 $w = 0.5 \text{ IN}$
 $w_c / w = 0.5$

SYMBOL	S / w	θ - DEG
\diamond	10	6°
\square	10	10°
\triangle	10	13.5°
\circ	0.5	10°

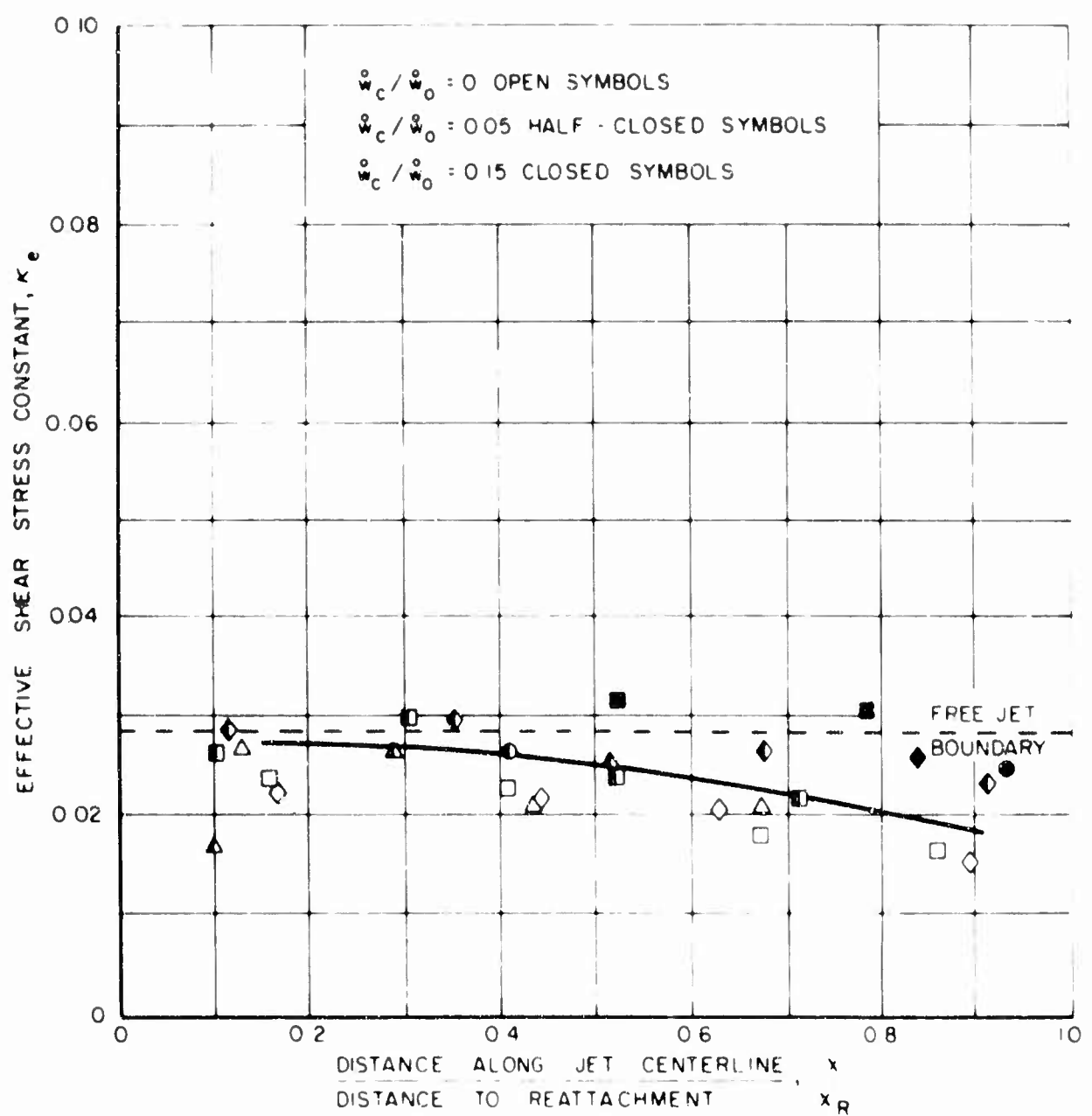


FIGURE 11 VARIATION OF SHEAR STRESS CONSTANT WITH DISTANCE FROM REATTACHMENT FOR INNER BOUNDARY OF REATTACHING JET

$w = 0.5 \text{ IN}$ $w_c/w = 0.5$
 $\theta = 10^\circ$ $S/w = 0.5$
 $x/x_R = 0.65$

SYMBOL	M_0
○	0.66
△	1.5
□	2.0

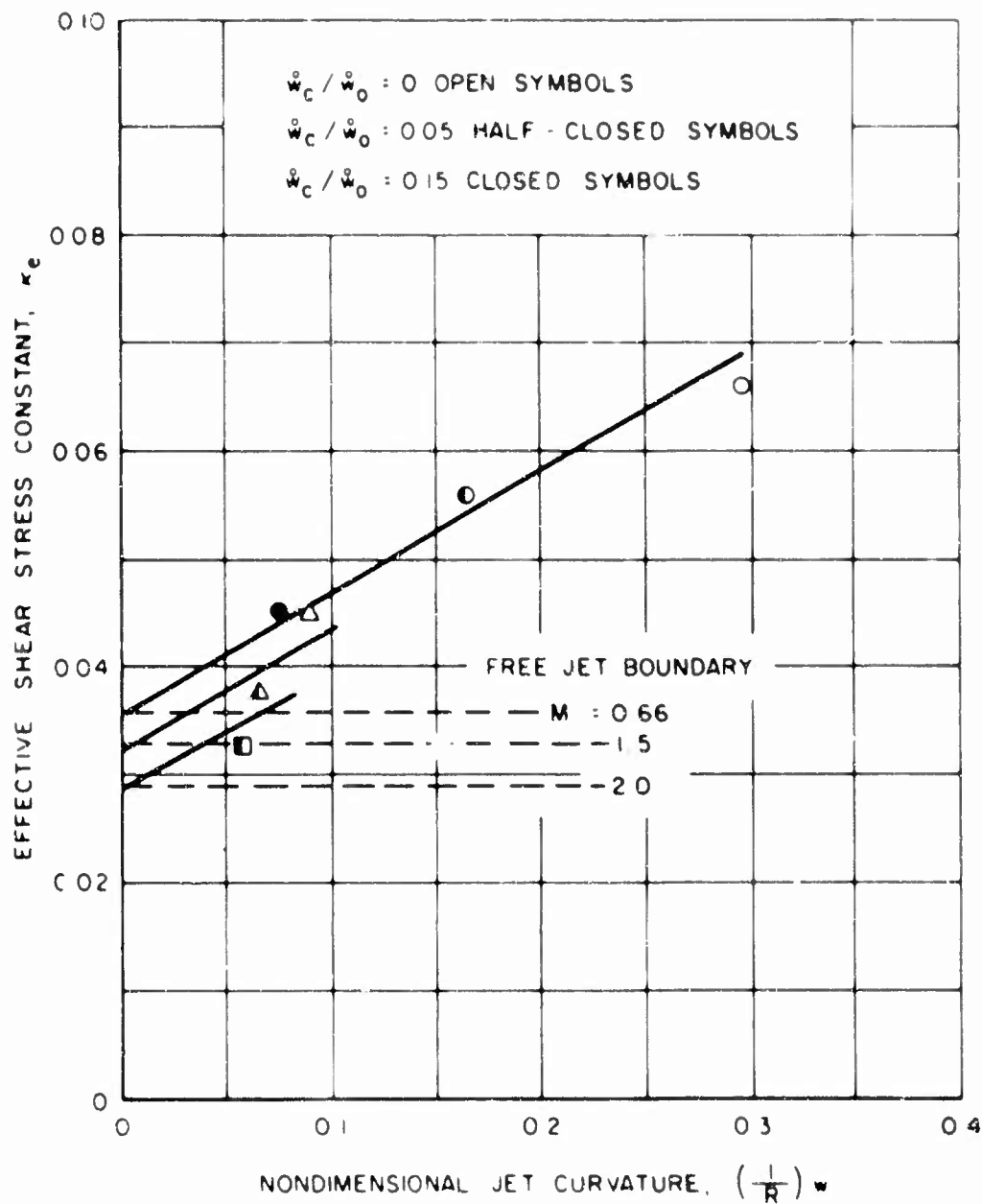


FIGURE 12 VARIATION OF SHEAR STRESS CONSTANT WITH JET RADIUS OF CURVATURE FOR OUTER BOUNDARY OF REATTACHING JET

CALCULATION OF THE SEPARATION OF A
JET ATTACHED TO A CONVEX WALL

by

Marcel KADOSCH

Société BERTIN & Cie, PLAISIR (S.&O.) FRANCE

ABSTRACT

The separation of a jet of width w along a wall of constant radius of curvature r is calculated using the formulae of turbulent boundary layers with positive pressure gradient. An illustrative example shows that separation occurs at a distance $w (r/r_0)^{5/5}$ increasing with r when r is greater than a critical radius r_0 which depends slightly upon Reynolds number.

INTRODUCTION

In a previous paper ⁽¹⁾ presented at the 2nd Symposium, we recalled our former investigations ⁽²⁾ about attachment and separation of a jet discharged along a convex curved wall with constant curvature (fig. 1). * There is no magic in the constant curvature, but a convenient means of measuring attachment and deflection by angles ; the variation of curvature is one more parameter, probably important, whose influence should preferably be investigated apart. In our experiments, the Reynolds number was about 10^6 , and we found that if the ratio r/w is small enough (< 2), the jet separates at a small angle which does not vary much ($EF_1 \sim 20^\circ$) ; if the ratio r/w is large enough (> 3), the angle of attachment increases with r , rather quickly. The figure (5) shows some measured pressure distributions, and the figure (6) shows the lateral thrust coefficient K_y and mean pressure coefficient K_p , obtained from the measures. We suggested a hint for a theoretical approach in order to explain these results through the calculation of the potential flow pressure distribution.

Now, at the first European Mechanics Colloquium (Euromech I) which was held at Berlin on April 5-6, 1965, the subject was : "Boundary Layers and jets along highly curved walls, Coanda Effect", and it was pointed out that no other

extensive experiments could be reported with a radius of curvature smaller than $4w$, which is in our opinion beyond the critical range $2w < r < 3w$; moreover the main emphasis was generally made upon the behaviour of the jet at a distance of the nozzle where the turbulent mixing velocity profile is fully developed.

We hope to learn here that more experimental results are available in the critical range, and that the influence of Reynolds number has been investigated. We claim that important things happen when $r < 4w$, at a distance of the nozzle where a potential core still exists. This paper is devoted to a calculation of separation under these conditions and gives the theoretical prediction of the above results and of a small influence of the Reynolds number.

Some applications to fluid amplifiers are recalled :

1. The calculation indicates that the whole phenomenon depends upon the local description of the separated region, which can be altered by various known means ⁽³⁾.
2. A variation of r/w in the critical range might be controlled without moving parts, producing a progressive deflection through the blockage effect of a secondary injection on the wall opposite to curved wall, which reduces w , as is shown in the photographs 6 and 7, reference (1). However it should not be concluded that the ratio r/w must be chosen in the critical range for any application. The best value of this ratio certainly depends upon the downstream geometry and the load, which control the separation characteristics.
3. As a new application, we developed a pressure-limited respirator (fig. 7), a bi-stable device ⁽⁴⁾ for which the required operational characteristics were obtained with rather high values of r/w .

DISCUSSION OF ASSUMPTIONS

In order to calculate the flow represented by the fig (1), it is convenient to introduce first the following set of assumptions :

- a) existence of a potential core $D E F C C B A$, where the flow is assumed two-dimensional incompressible inviscid.
- b) the boundary layer $D' E' F'$ along the "inner" wall separates at FF' under the influence of the positive pressure gradient along the wall.
- c) the static pressure in the stalled region after FF' is equal to ambient pressure.

d) the turbulent mixing zone $F' BB''$ reaches the inner boundary at a point B' downstream of F'' .

e) the transverse equation of the dissipative region $B' BB''$ reduces to :

$$\frac{\partial p}{\partial n} = \rho v_{\theta}^2 / R$$

f) the transverse kinetic energy is negligible with respect to the longitudinal one in the dissipative region $BB' B''$: $v_r^2 \ll v_{\theta}^2$

The hypothesis (c) holds if we neglect the underpressure in F and the back flow PQ induced by the separated jet : this is quite an assumption.

The hypothesis (d) holds if separation occurs at a distance smaller than $BB' \sim 3$ to $5 w$ according to the curvature. If assumptions (e) and (f) hold, then the existence of the external mixing region can be ignored, and the potential core can be calculated assuming limiting streamlines at constant ambient pressure along BC and FC (Helmholtz-Kirchhoff theory).

But it is necessary to fix the theoretical separation point F "a priori" so that there exists a one-parameter family of possible potential flows ; moreover the pressure gradient is found to increase indefinitely in the vicinity of F . Therefore the calculation of the boundary layer under the assumption (b) always indicates separation at some point S upstream of F ; the distance SF only is found, not the position of S , nor of F . At this point, we must introduce a new set of assumptions in order to achieve the calculation.

g) On ng to the range of Reynolds numbers, the boundary layer is assumed turbulent.

h) The transition is assumed to occur at point E for convenience, and the thickness of laminary sublayer is neglected. Point E is near the minimum pressure point.

i) For the calculation of S , when F is given, the A. Buri's approximate method using the analogy with Pohlhausen's laminar boundary layer theory, is chosen for simplicity.

j) As an additional separation criterium for the location of S , it is assumed that at the distance $SS' = \delta^*$ from the wall (displacement thickness), the static pressure is equal to the ambient pressure.

It is well known ⁽⁵⁾ that all methods for the calculation of turbulent boundary layers against a positive pressure gradient are semi-empirical in nature ; the characteristic boundary layer dimension is the momentum thickness θ , and the criterium of separation is given as specifying the value of a

velocity profile shape factor. Experimental basis is provided by Nikuradse's measurements in divergent channels with various angles, and more recently by Rotta's measurements of velocity profiles from which a relationship is deduced between the shape factors $H = \frac{\delta^*}{\theta}$ and $\bar{H} = \frac{\delta^{**}}{\theta}$ (δ^{**} energy thickness).

Among the available analytical methods, a first choice is made of Buri's which is based upon Nikuradse's measurements, and of the much more sophisticated Truckenbrodt's method, for the other methods involve the integration of a differential equation, which is not practical for our purpose. Truckenbrodt's method is quite satisfactory, but gives complicated numerical calculations which do not allow the phenomenological explanation we look for. On the other hand, Buri's method is simple enough, but does not agree very well with shape factor's measurement, so that quantitative prediction is not expected to be quite correct. All methods are in good agreement with momentum thickness measurements.

Whatever the method, the given quantities include the potential velocity distribution along the wall, therefore the theoretical point F is supposed to be known, from which a separation point S is calculated. It is impossible to assume that F is at the trailing edge of the actual inner wall, for this assumption would be in strong disagreement with the measured pressure distribution, fig. 6. Now it can be demonstrated in various ways ⁽⁵⁾ that a boundary layer causes the irrotational flow outside it to be that about not the solid surface itself, but a surface displaced into the fluid through a distance δ^* . To take into account the influence of the boundary layer on the flow outside it, we introduce the assumption (j) according to which the irrotational velocity is calculated first along the actual wall at F where $v_F = v_0$ and at S where $v_S = v_F - SF \frac{\partial v}{\partial n}$.

Then the radius r is given a variation δ^* , whence at the new boundary of equivalent irrotational flow :

$$v_{S'} = v_S + \delta^* \frac{\partial v}{\partial n} < v_S \quad v_{F'} = v_F + \delta^* \frac{\partial v}{\partial n} < v_0$$

Therefore the potential flow around the "Rankine body : $r' = r + \delta^*$ " cannot be taken with a streamline beginning at F', but at some point upstream. If :

$$v_{S'} = v_0 - SF \frac{\partial v}{\partial s} + \delta^* \frac{\partial v}{\partial n} = v_0, \text{ or } SF \frac{\partial v}{\partial s} = \delta^* \frac{\partial v}{\partial n} \quad (1)$$

then the equivalent irrotational flow streamline may start from S', so that the corresponding point F and pressure distribution are just the ones to be taken into account. Whether this description of separation is correct or not will at first depend upon agreement with experience.

ILLUSTRATING EXAMPLE

We simplify the fig (1) to the two-dimensional channel flow fig (2) for which we calculate first a family of potential flows depending upon F , then a Buri's turbulent boundary layer model giving at the wall a separation point S .

1. Potential Flow.

The consideration of the complex potential f or reduced complex potential $Z = X + iY = \pi f / 2 v_\infty w$ shows (fig 3) that the flow depends upon the circulation parameter : $\chi_0 = \frac{q}{v_\infty} \frac{F}{2 v_\infty w}$ or alternatively upon the reference angle :

$$\gamma = \varphi_F / r v_\infty$$

Conformal mapping on the ζ - plane fig (4) :

$$e^{2\zeta} = \frac{e^{2Z} + e^{-2\chi_0}}{e^{2\chi_0} - e^{2Z}} \quad \zeta = \xi + i\eta \quad 0 < \eta < \frac{\pi}{2}$$

and use of L.C. Woods' formulae (7) gives the following value for the logarithm of complex velocity $v_0 = ia$:

$$\log \frac{v_0}{v} + i(a - a_F) = - \frac{2w}{\pi^2 r} \int_E^F \frac{v_0}{v(\xi')} \log \frac{1 + e^{\xi' - \zeta}}{1 - e^{\xi' - \zeta}} \frac{d\xi'}{d\xi'} d\xi'$$

where X' , ξ' refer to the integration path EF . The velocity $v(\xi')$ is the solution of the integral equation :

$$\log \frac{v_0}{v(\xi)} = - \frac{2w}{\pi^2 r} \int_{\xi_E}^{+\infty} \frac{v_0}{v(\xi')} \log \left| \frac{1 + e^{\xi' - \xi}}{1 - e^{\xi' - \xi}} \right| \frac{d\xi'}{d\xi'} d\xi'$$

which can be solved by successive approximations. We consider the first approximation obtained by integration with $v(\xi') = v_0$ in the right-hand side, and we are interested in the derivative :

$$\frac{d[\log v - ia]}{dZ} = \frac{2w}{\pi^2 r} \frac{d\zeta}{dZ} \int_E^F \frac{d\xi'}{d\xi'} \frac{d\xi'}{\sinh(\xi' - \zeta)} + i\pi \frac{2w}{\pi^2 r}$$

By direct calculation :

$$\begin{aligned} \frac{\pi^2 r}{2w} \frac{d(\log v - ia)}{dZ} &= \log \frac{1 + e^{\zeta - \xi_E}}{1 - e^{\zeta - \xi_E}} - \frac{\cosh \zeta}{\cosh 2\chi_0} \log \frac{e^{\xi_E} + e^{-2\chi_0}}{e^{\xi_E} - e^{-2\chi_0}} \\ &= 2 \frac{\sinh(\zeta + 2\chi_0)}{\cosh 2\chi_0} \cotang^{-1} e^{\zeta} \end{aligned} \quad 171$$

$$\xi_E = -X_0 - 1/2 \log \sinh 2 X_0$$

The table I gives the asymptotical values of velocity gradient near F, when X_0 varies.

TABLE I

(1)	(2)	(3)	(4)
Functions of Z	X_0 small	X_0 large $\neq X$	X_0 large $\neq X$
$\frac{dv}{v dX} \text{ (S)}$	$-\frac{4w}{\pi^2 r} \sqrt{\frac{2X_0}{Y_0 - X}}$	$-\frac{w}{\pi r} \sqrt{\frac{2}{(X_0 - X)}}$	$-\frac{2w}{\pi r} e^{X-X_0}$
$\frac{dv}{v dY} \text{ (S')}$ ($Y = (X_0 - X) \tan \beta$)	$-\frac{4w}{\pi^2 r} \sqrt{\frac{X_0 \sin \beta (1 - \cos \beta)}{Y}}$	$-\frac{w}{\pi r} \sqrt{\frac{\sin \beta (1 - \cos \beta)}{Y}}$	

Comparison of columns (2) and (4) shows that at a finite upstream distance from F, the longitudinal gradient is much smaller for X_0 large, so that separation may occur for a large value of γ (the so-called "Coanda effect"), if γ is allowed to increase, which remains to be proved.

2. Boundary layer calculations.

The separation criterium (1) must be interpreted as follows :

$$SF = -\frac{2w}{\pi} (X_0 - X_B) \quad SS' = \delta'' = \frac{2w}{\pi} Y = SF \tan \beta$$

$$(X_0 - X_B) \frac{\partial v}{\partial X} = Y \frac{\partial v}{\partial Y}$$

Table I shows that whatever the value of X_0 , large or small, this results in an equation giving the value of β for which v is stationary :

$$\sin^2 \beta (1 - \cos \beta) = 2 \cos \beta \quad \beta = 72^\circ \quad (2)$$

$$SF = 0.528 \delta^* = 0.421 \theta$$

The momentum thickness θ is given by the equation (5) :

$$\theta \left(\frac{v \theta}{\nu} \right)^{0.25} = \frac{0.016}{v^4} \int_0^s v^4 ds \quad (3)$$

We have ignored the laminar layer and taken the s-origin rather arbitrarily at E, the beginning of curved wall. The mean value of v^4 will be calculated below in two extreme cases.

The analogy with laminar boundary layer states that the velocity profile is characterised by the shape factor :

$$\Gamma = \frac{\theta}{v} \frac{dv}{ds} \left(\frac{v \theta}{\nu} \right)^{0.25} \quad (4)$$

Separation occurs when $\Gamma_s = -0.06$ approximately.

1st Case : X_0 large.

As the longitudinal gradient is very small over most of the wall length, the velocity curve is flattened approaching the constant value :

$v = v_0 \exp(w/r)$ save in the vicinity of F. Therefore (3), (4), and table I give :

$$\theta \left(\frac{v \theta}{\nu} \right)^{0.25} = 0.016 s \quad \Gamma = 0.016 \frac{X dv}{v dX}$$

$$X_0 - X_s = 0.035 \quad \gamma^2 = 0.421 \frac{\pi \theta}{2w}$$

Elimination of θ gives finally :

$$X_0 = \frac{\pi}{2} \frac{r}{w} \gamma = 1.15 \left(\frac{r}{w} \right)^{5/3} \left(\frac{v_0 w}{\nu} \right)^{-1/6} \quad (5)$$

According to this formula, both the circulation X_0 or attachment length $(r \gamma)$, and the attachment angle or deflection γ_0 are increasing functions of (r/w) , with a small influence of Reynolds number.

2nd Case : X_0 small.

In the vicinity of F, it is found that :

$$\log (v/v_0) \sim \frac{8\gamma}{\pi} \sqrt{\frac{X_0 - X}{2X_0}}$$

and this is also the asymptotic value of the velocity over EF when X_0 is very small. With this value we obtain :

$$\Gamma \sim -0.001\gamma \sqrt{\frac{2X_0}{X_0 - X}} \quad X_0 - X_8 = 0.0576 X_0 \gamma^2$$

$$\theta = 0.137 \pi \gamma^3$$

Elimination of θ : leads to : $\gamma = 0.57 (v_0 \pi r / \nu)^{-0.1}$

$$X_0 = \frac{\pi}{2} \frac{r}{w} \gamma = 0.9 \left(\frac{r}{w}\right)^{10/11} \left(\frac{v_0 w}{\nu}\right)^{-1/11} \quad (6)$$

According to this formula, γ is almost a constant, depending very slightly upon the Reynolds number $(v_0 \pi r / \nu)$. The circulation increases nearly as r .

Discussion.

Comparison of (5) and (6) suggests that when r increases, γ being first a constant, the circulation increases slowly, then much more rapidly when a critical reduced circulation X_0 of order unity is reached. Therefore attachment and deflexion are consecutive to the achievement of an aerodynamical load on the curved wall corresponding to a reduced circulation > 1 .

The relation between γ and (r/w) depends only upon the local conditions in the vicinity of F. We found exactly the same formula with a free jet along a curved wall corresponding to a very different potential flow. Of course the considered wall geometry has a strong influence on the value of X_0 which must be taken into account.

Consideration of the function $\log v(X)$ itself (see appendix) shows that $X_0 = 1$ and even $X_0 = 0.5$. are by no means small (nor large) values for which

the above asymptotical formulae apply. If nevertheless we put $X_0 = 1$ in (5) or (6) with a Reynolds number 10^6 , we find the "critical values"

$$(6) \quad r_0 = 4.4 w \quad \gamma = 0.145 = 8^\circ$$

$$(5) \quad r_0 = 7.6 w \quad \gamma = 0.175 = 10^\circ$$

Laminar boundary layer.

We have no experimental results in the laminar range : the schematic description of the flow fig. (1) is probably inadequate in this range, in application to fluid amplifiers ; unless the entrance length AB is very short, it is unlikely that there exists a potential flow region ; anyhow, the Pohlhausen's method corresponding to Buri's, is not applicable in the vicinity of F. Fairly accurate predictions of separation are reported with the Curle-Skan relation :

$$\left(\frac{sdC_p}{ds} \right)^2 C_p = 1.04 \times 10^{-2} \quad C_p = 1 - \frac{v^2}{v_{\max}^2}$$

But as in the turbulent case, we need another criterium for the choice of the actual pressure distribution. Criterium (1) is convenient only if we know δ^* in terms of the distribution. Using the Walts's integral of momentum equation⁽⁵⁾ and the Pohlhausen's value of $\delta^* = 3.5 \theta$ would be just as objectionable as direct use of Pohlhausen's method, which, incidentally, leads to :

$$X_0 = 0.133 \left(\frac{r}{w} \right)^{4/3} \left(\frac{v_0 w}{\nu} \right)^{-1/3} \quad X_0 \text{ large} \quad (5')$$

$$X_0 = 0.5 \left(\frac{r}{w} \right)^{0.8} \left(\frac{v_0 w}{\nu} \right)^{-0.2} \quad X_0 \text{ small} \quad (6')$$

These relations show qualitatively that the influence of Reynolds number is much stronger than in the turbulent case, and that the laminar boundary layer separates with a much smaller pressure gradient, which is well known in aerodynamics. Quantitatively they predict attachment and deflection only for very small Reynolds numbers and curvatures (w/r).

CONCLUSION

The separation of a jet from a curved wall is predicted both qualitatively and quantitatively using the formulae of turbulent boundary layers with positive pressure gradient, if an additional criterium (1) is made for the choice of the pressure distribution among a one-parameter family of potential flows : the parameter indicates the circulation around the wall and allows easy physical interpretation.

It seems difficult to apply the same method to the laminar case.

APPENDIX

The integration of the equation given for an approximate value of $\log v$ may be performed if we introduce the Euler dilogarithm function :

$$L_2(x) = \sum x^n/n^2$$

We find, for $\xi = \xi$ real :

$$\begin{aligned} \frac{\pi^2 r}{4w} \log \frac{v}{v_0} &= \tanh^{-1} e^{-\xi} E \tanh^{-1} e^{-\xi} - \tanh^{-1} e^{-\xi} E^{-2X_0} \tanh^{-1} e^{-\xi} E^{-2X_0} \\ &+ (\bar{x} - X_0) \tanh e^{\xi} E^{-\xi} + F(e^{\xi} E^{-\xi}, e^{\xi} E^{-2X_0}) - F(e^{\xi} E^{-\xi}, 10^{\xi} E) \end{aligned}$$

$$4F(x, y) = L_2\left(\frac{1+x}{1-y}\right) + L_2\left(\frac{1+x}{1+y}\right) - L_2\left(\frac{1-x}{1-y}\right) - L_2\left(\frac{1-x}{1+y}\right)$$

$$\text{If } X_0 \text{ is small : } \frac{\pi^2 r}{4w} \log \frac{v}{v_0} \sim 4 X_0 e^{\xi} E^{-\xi}$$

$$\text{If } X_0 \text{ is large : } \log \frac{v}{v_0} \sim \frac{w}{r}$$

There is a singularity at E , but it must be smoothed out in the successive approximations of the function $\log v$.

REFERENCES

1. KADOSCH, M. : "Attachment of a jet to a Curved wall" Proceedings of the 2nd Fluid Amplification Symposium, Vol IV, May 1964.
2. KADOSCH, M. : "Mécanisme de la Déviation des Jets Propulsifs" D. Thesis, Paris, 5. January 1957. Publications Scientifiques et Techniques du Ministère de l'Air N° BST.124.
3. CURTISS, H.A., FEIL, O.G. and LIQUORNIK, D.J. : "Separated Flow in Curved Channels with Secondary Injection". Proceedings of the 2nd Fluid Amplification Symposium, Vol IV, May 1964.
4. PAVLIN, C. : "Mechanical Characteristics of a pure fluid respirator with curved walls". Fluid Logic and Amplification Conference, September 1965, Cranfield.
5. SCHLICHTING, H. : "Boundary Layer Theory, chap. XXII.
6. Lighthill, M.J. : "On displacement thickness" Journal of Fluid Mechanics. Vol 4, 1958, 383-392.
7. WOODS, L.C. : "Compressible Subsonic Flow in two-dimensional Channels with mixed boundary conditions". The Quarterly Journal of Mechanics and Applied Mathematics, Sept. 1954, VII, 263.

NOTATIONS

K_p	$= v^2/v_c^2$ average -1	α	velocity angle
K_y	momentum ratio, transverse/axial	β	$Y = (X_0 - \bar{X}) \tan \beta$ at F
r	radius of wall	γ	$= \varphi_F / r v_0 = \frac{2W}{\pi r} X_0$
o, n	Curvilinear coordinates	δ^*	displacement thickness
v	velocity	ζ	$= \xi + i\eta$ conformal transform
ve^{-ia}	complex velocity	θ	momentum thickness
v_0	exit velocity	ν	kinematic viscosity
w	nozzle width	f	$= \varphi + i\psi$ potential
X_0	circulation parameter at F	Γ	shape factor (4)
X_0	circulation at separation		
Z	$= X + iY$ reduced potential		

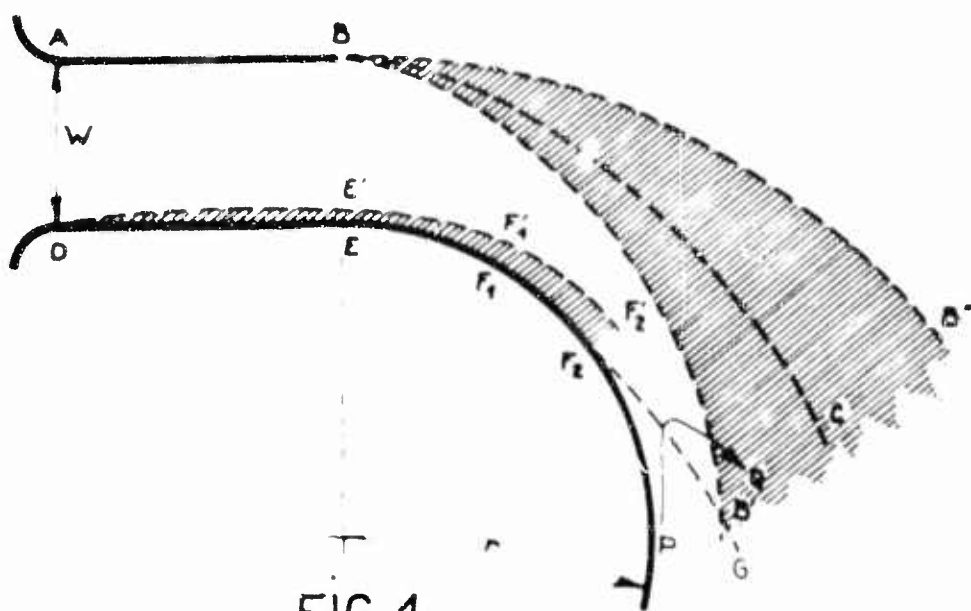


FIG. 1

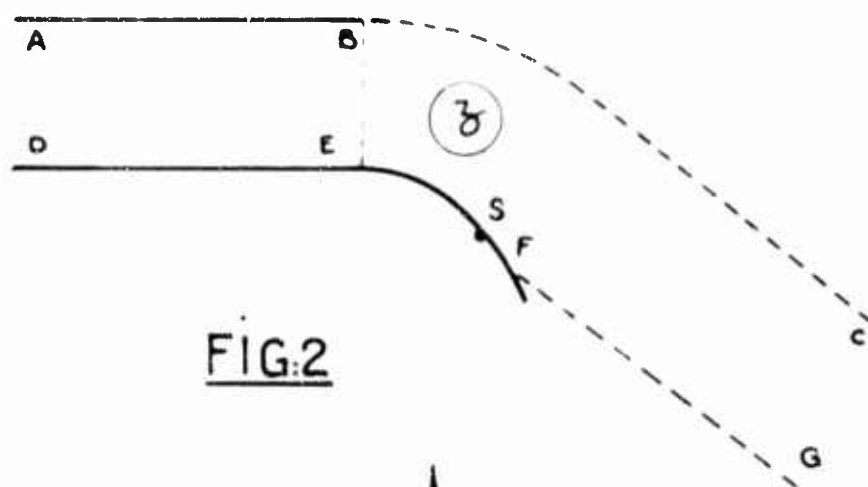


FIG. 2

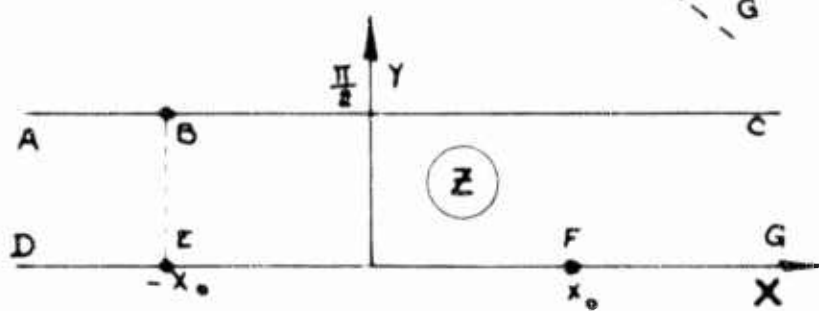


FIG. 3

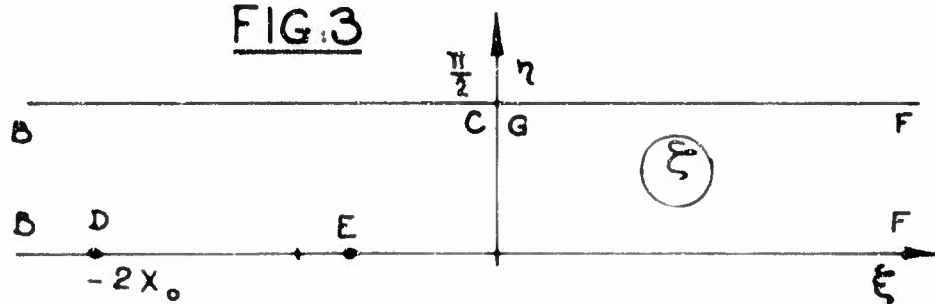


FIG. 4

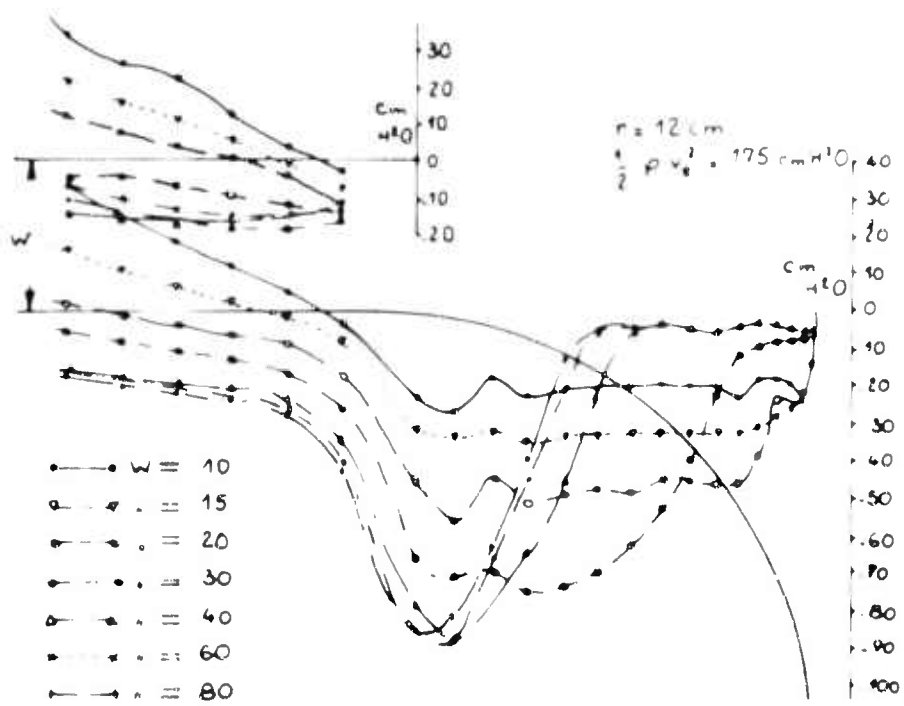


FIG. 5

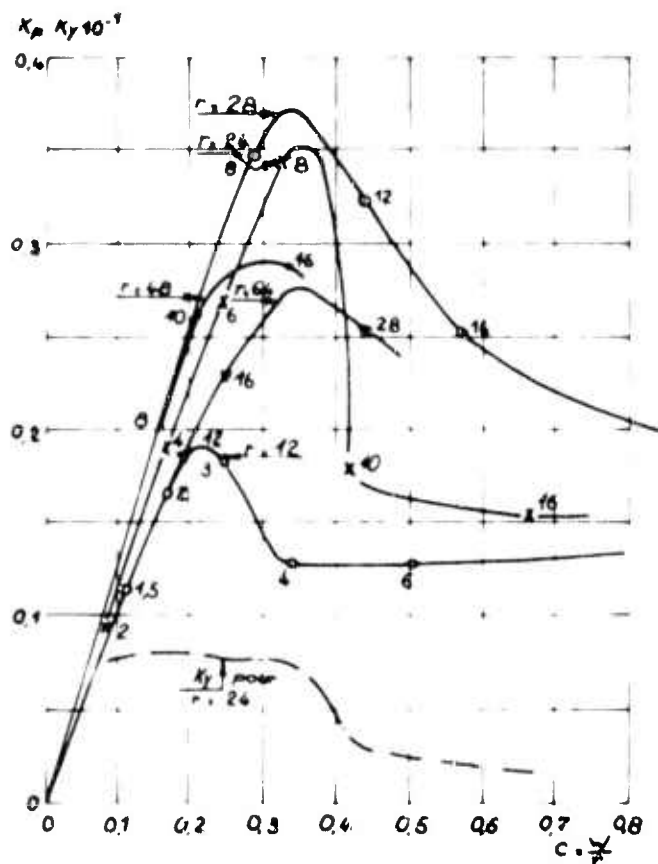


FIG. 6



FIG. 7

- $r = 12 \text{ cm}$
- × $r = 24 \text{ cm}$
- ⊙ $r = 28 \text{ cm}$
- $r = 48 \text{ cm}$
- ▼ $r = 64 \text{ cm}$

HARRY DIAMOND LABORATORIES
WASHINGTON, D. C. 20438

ANALYSIS OF THE STEADY-FLOW PNEUMATIC
RESISTANCE OF PARALLEL CAPILLARIES

by

CAPT. HARRY N. WHITE

ARMY MATERIEL COMMAND

DEPARTMENT OF THE ARMY

ABSTRACT

In this paper an expression is found for the overall pressure drop as a function of volume flow, under conditions of equilibrium, through a pneumatic resistor consisting of capillaries in parallel.

The resistance, defined as the overall pressure drop divided by the volume flow, is shown to be a function of the flow, and therefore nonlinear. This nonlinearity is due to an accumulated viscous loss in the entrance of the capillaries and the dissipation of kinetic energy at the outlets of the capillaries.

The analysis is in good agreement with experimental data. It provides a basis for designing resistors of desired values and for reducing the nonlinearity of the resistance.

LIST OF SYMBOLS

Q	volume flow (ft ³ /sec) (cm ³ /sec)
V	mean velocity (ft/sec) $V = Q/A$ (m/sec)
U	core velocity
\vec{v}	velocity of a fluid particle $\vec{v} = u \hat{a}_x + v \hat{a}_r + w \hat{a}_\theta$
\hat{a}	unit vectors
x	axial coordinate
r	radial coordinate
θ	angular coordinate
L	resistor length (ft) (cm)
L*	entrance length
x*	stretched axial coordinate
X	dimensionless length $X = vx/VR^2$
ϵ	stretching factor $x = \int_0^{x*} \epsilon dx*$
R	radius of capillary
R ₁	radius of support tubing
D	diameter of capillary $D = 2R$
A	area of right cross section of capillary
σ	arbitrary area
da	element of area
\hat{n}	unit normal to da
ω	dimensionless velocity $\omega = u/V$
η	dimensionless radial distance $\eta = r/R$
u_{fd}	fully-developed velocity profile
u_{max}	maximum velocity
μ	viscosity (lbf-sec/ft ²) (Ns/m ²)
ν	kinematic viscosity $\nu = \frac{\mu}{\rho}$ (ft ² /sec) (m ² /s)
ρ	density (lbf-sec ² /ft ⁴) (kg/m ³)
δ	boundary layer thickness
y	radial coordinate measured from $r = R$ toward $r = 0$ $r = R - y$
p	static pressure (lbf/in ²) (N/m ²)

Δ	incremental change
R_p	pneumatic resistance (lbf-sec/ft ⁵) (Ns/m ⁵)
τ_w	shear stress at wall (lbf/ft ²) (N/m ²)
Re_x	length Reynolds number $Re_x = Vx/\nu$
Re_D	diameter Reynolds number $Re_D = VD/\nu$
γ_m	eigenvalues, roots of $J_2(\gamma) = 0$
g_m	eigenfunctions
c_m	constants $c_m = 2V/\gamma_m$
C	number defined $C = \nu \pi N L / Q$
$F(C)$	function defined $F(C) = \sum_{m=1}^{\infty} \frac{1}{\gamma_m^2} e^{-\gamma_m^2 C}$
\mathcal{E}	function defined $\mathcal{E} = 4 F(C) - 12 F(2C)$
B	number defined $C = \ln B$
e	base (2.71828 . . .)
ξ	constant
α	ratio of kinetic energy contained in arbitrary velocity profile to kinetic energy contained in uniform profile

1. INTRODUCTION

Consider air flowing in a tube. Any constriction placed in the tube will result in an additional static pressure drop, Δp , above that characteristic of the tube. (See Figure 1.) The constriction is a pneumatic resistor. Assuming that the flow remains incompressible permits a relationship between volume flow and static pressure drop (1).

$$\Delta p = f(Q) \quad (1)$$

Then pneumatic resistance is defined by (2).

$$R_p = \frac{\Delta p}{Q} \quad (2)$$

Pneumatic resistance is often thought of as analogous to electrical resistance. A significant difference exists, however, in that electrical resistance is entirely dissipative whereas pneumatic resistance is only partly dissipative. Pneumatic resistance is a combination of viscous dissipation and increases in the total kinetic energy of the fluid particles making up a flow cross-section. Pressure drops owing to this latter effect may be partly recovered by proper shaping of the resistor. The consequences of this fact will be discussed later.

Whereas the primary design feature of an electrical resistor is the material property called resistivity, the pneumatic resistor is characterized by its shape. Because there is no general solution of the fluid equations for arbitrary shapes, any analysis must be preceded by the choice of a particular shape. There is hope, however, that having chosen a particular shape, the resulting analysis will direct the search for a better shape.

In this investigation the design criteria will be limited to linearity and selectivity. Selectivity is the ability to select arbitrary values of resistance. Future investigations should consider time and frequency response as criteria.

Because fully-developed tube flow begins at 80 to 200 diameters downstream from the tube entrance and results in a linear resistance, a capillary tube was chosen as the initial shape [1]. Experiments showed, however, that for capillary lengths sufficient for linearity the value of the resistance is too large for use with many practical

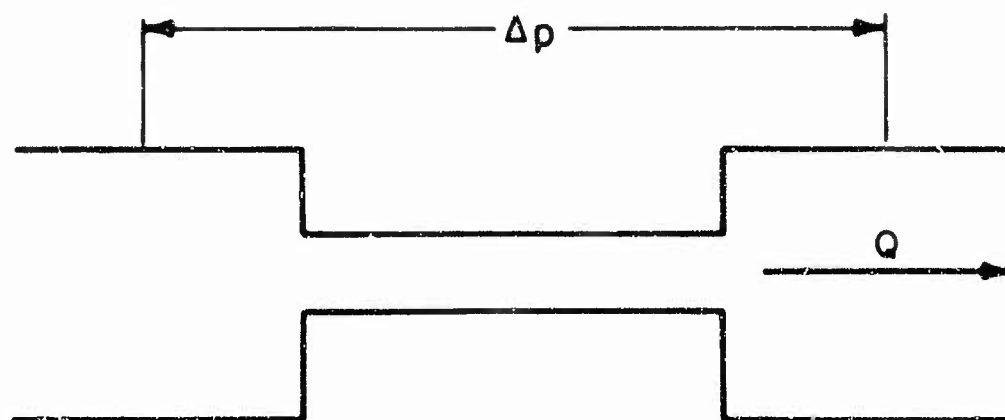


Figure 1. Pneumatic Resistor Consisting of Constriction and Entrance and Outlet Configuration

size pneumatic amplifiers. The next step was to reduce the resistance by placing a number of capillaries in parallel. The result was promising enough to undertake a search for an analytical expression for the resistance of such a collection of capillaries. An analytical expression for the resistance would provide guidance in the selection of the best length, diameter, and number of capillaries for a particular need and provide assistance in system design.

2. THEORY

2.1. General Comments on Flow

The volume flow, Q , of a collection of fluid particles through a surface, σ , is defined by (3).

$$Q = \int_{\sigma} \vec{v} \cdot \hat{n} \, da \quad (3)$$

Furthermore, if it is assumed that the surface is oriented normal to the longitudinal axis in cylindrical coordinates, (3) reduces to (4).

$$Q = VA = 2\pi \int_0^R ur \, dr \quad (4)$$

In general the volume flow is a function of time and the axial position. Integrating the continuity equation (5)

$$\frac{1}{\rho} \frac{\partial \rho}{\partial t} + \frac{\partial u}{\partial x} + \frac{1}{r} \frac{\partial}{\partial r} (vr) = 0 \quad (5)$$

over a cross-section gives (6).

$$\frac{\partial Q}{\partial x} = -2\pi \int_0^R \frac{1}{\rho} \frac{\partial \rho}{\partial t} r \, dr \quad (6)$$

where: $v(x,0) = v(x,R) = 0$

Thus for fixed boundaries and axially symmetric flow, Q can depend on the axial position only if the density is a function of time. For this case fluid would be stored within a volume of the tube. This storing is characteristic of capacitance rather than resistance. Thus for a pure resistor the volume flow is at most a function of time due to fluctuations in the axial velocity.

2.2. Laminar Entrance Flow in a Tube

2.2.1 Nature of the Problem

To many investigators the study of fluids is primarily a study of mathematics, substantiated by experiment. Except for the few cases where the Navier-Stokes equations have an exact solution, the mathematics is a search for the best approximate solution rather than for a new theory. A comprehensive example of the difficulties of such an investigation is the study of steady, axially symmetric, incompressible flow in the entrance of a straight tube of circular cross-section.

The axial component of the Navier-Stokes equation for boundary layer flow is given by (7) where the term

$$v \frac{\partial^2 u}{\partial x^2}$$

is assumed negligible in accordance with the usual boundary layer theory [2].

$$u \frac{\partial u}{\partial x} + v \frac{\partial u}{\partial r} = - \frac{1}{\rho} \frac{dp}{dx} + \nu \left[\frac{\partial^2 u}{\partial r^2} + \frac{1}{r} \frac{\partial u}{\partial r} \right] \quad (7)$$

For fully-developed flow the inertia forces in (7) vanish giving (8).

$$\frac{\partial^2 u}{\partial r^2} + \frac{1}{r} \frac{\partial u}{\partial r} = \frac{1}{\mu} \frac{dp}{dx} \quad (8)$$

with boundary conditions:

$$u(x, R) = 0, \quad \left. \frac{\partial u}{\partial r} \right|_{r=0} = 0$$

The solution (9) of (8), expressing the equilibrium between viscous and pressure forces, is the classical, Hagen-Poiseuille, parabolic velocity profile [2].

$$\begin{aligned}
 u_{fd} &= - \frac{R^2}{4\mu} \frac{dp}{dx} \left(1 - \frac{r^2}{R^2} \right) \\
 &= u_{\max} \left(1 - \frac{r^2}{R^2} \right) \\
 &= 2V \left(1 - \frac{r^2}{R^2} \right)
 \end{aligned}
 \tag{9}$$

The situation is quite different in the entrance length. The entrance length is defined as that distance over which the transition from the entrance profile to the parabolic profile occurs. During this transition the inertia terms do not vanish and the Navier-Stokes equations have not yielded to an exact solution.

There are in general two approaches to finding an approximate solution in the entrance length. The first is to assume an approximate form for the changing velocity profile and then determine the nature of the transition from continuity and momentum considerations. The second approach is to choose a linearized form of the Navier-Stokes equations that best describes the flow. The latter method is more easily adapted to finding an analytical expression for resistance; but the former method gives much insight into the physical nature of the flow.

2.2.2 Approximate Velocity Profile

The choice of an approximate velocity profile is based on the assumption of a model for the problem as illustrated in Figure 2. Note that a uniform profile is assumed at the entrance.

Due to a viscous drag on the fluid at the wall, a boundary layer of thickness δ is assumed to grow from zero at the entrance until it completely fills the tube for fully-developed flow. The problem is particularly complicated because the growth of the boundary layer causes an acceleration of the frictionless core resulting in a negative pressure gradient in the flow direction that in turn affects the boundary layer growth. The main conclusion that can be made from the model is that the ratio of the local velocity to the core velocity probably depends upon the ratios

$\frac{y}{\delta}$ and $\frac{\delta}{R}$ [3], [4], [5]. Assuming a fourth-order polynomial in

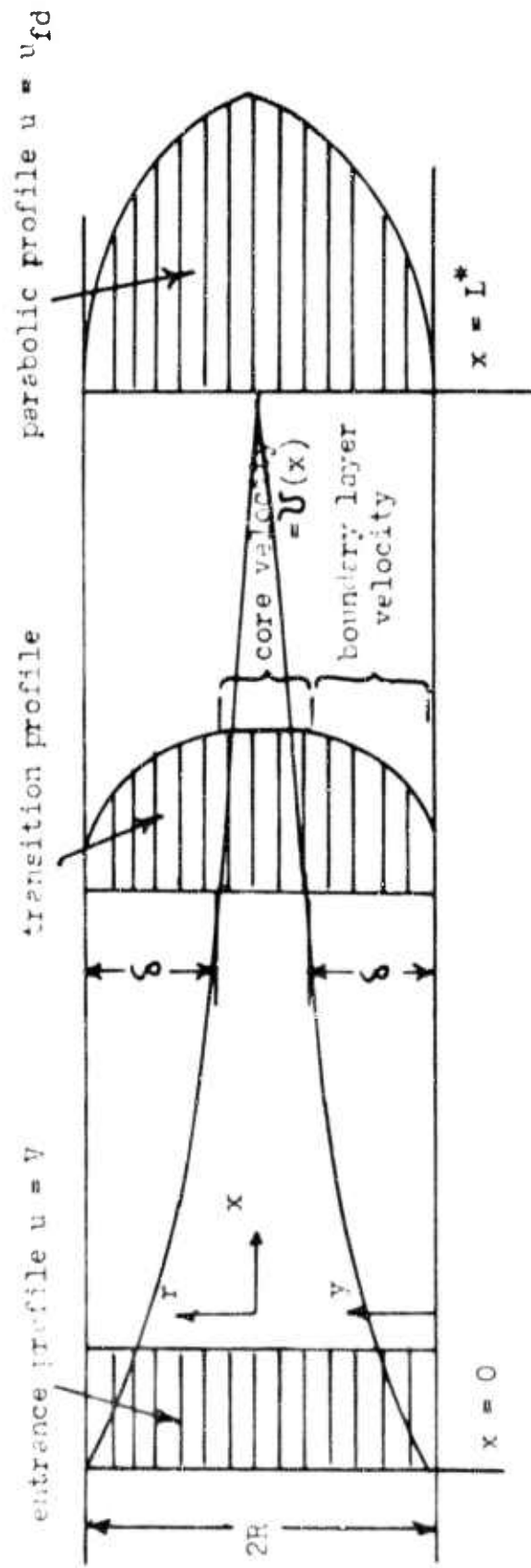


Figure 2. Velocity Profile Development in a Circular Tube.

these ratios and applying pressure and velocity boundary conditions, one can justify the following profile:

$$\frac{u}{U} = \left[\frac{3}{2} \left(\frac{y}{\delta} \right) - \frac{1}{2} \left(\frac{y}{\delta} \right)^3 \right] \left[1 - \frac{\delta}{R} \right] + \left[2 \left(\frac{y}{\delta} \right) - \left(\frac{y}{\delta} \right)^2 \right] \left[\frac{\delta}{R} \right] \quad (10)$$

Details of the above formulation and the following calculations may be found in [3]. As $\frac{\delta}{R}$ goes to zero the profile becomes the familiar cubic profile within the boundary layer on a flat plate. This is the situation where the boundary layer is thin relative to the radius, near the immediate entrance. On the other hand as $\frac{\delta}{R}$ tends toward unity, the profile takes the fully-developed parabolic shape. Other profile assumptions exist that give similar results. The profile (10) is chosen as an example only.

Having obtained the approximate velocity profile (10), we may determine the dependence of the core velocity, U , upon δ from a form of the continuity equation (11) derived from (4) where:

$$\begin{aligned} r = R - y \quad \text{and} \quad u = u(x, y) \quad \text{from } y = 0 \quad \text{to } y = \delta \\ u = U(x) \quad \text{from } y = \delta \quad \text{to } y = R \end{aligned}$$

$$V\pi R^2 = 2\pi \left[\int_0^\delta u (R-y) dy + \frac{U}{2} (R - \delta)^2 \right] \quad (11)$$

Substitution of (11) into (10) leaves the only unknown as the dependence of the boundary layer thickness on the distance down the tube. Once this is found the problem is solved.

An integral form of the momentum equation as it applies to this problem can be derived from a control volume in the entrance flow. The resultant of shear and pressure forces are equated to the net outgoing flux of momentum (12). Then the pressure is set to the

$$\frac{-dp}{dx} \pi R^2 - \tau_w 2\pi R = \frac{d}{dx} \int_{\text{control volume}} \rho u^2 dA \quad (12)$$

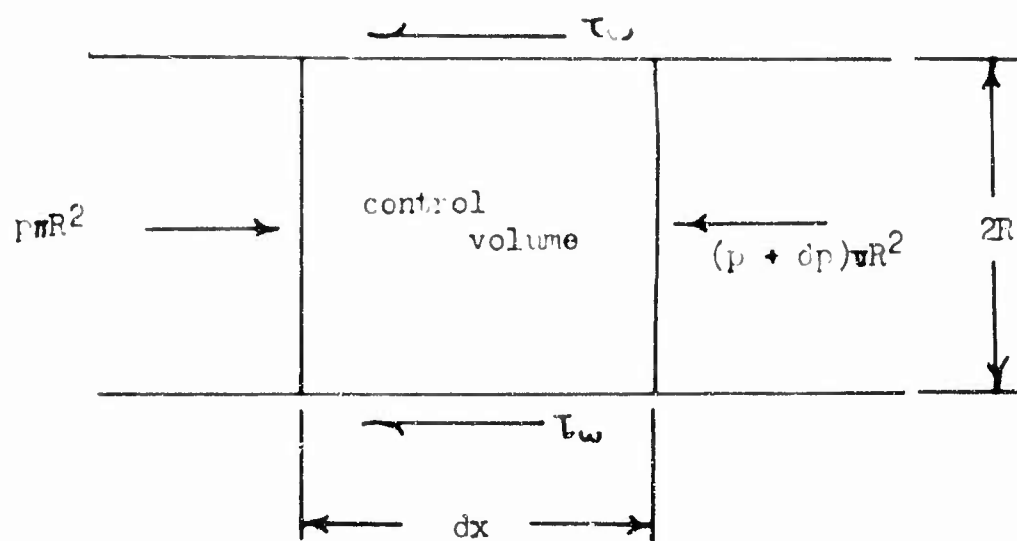


Figure 3. Control Volume in a Circular Tube.

core pressure and evaluated using the Bernoulli equation. (Some authors feel it is better to calculate the pressure gradient by an energy integral over the whole flow including the inviscid portion [5]). The shear at the wall, τ_w , is given by (13). The result is (14).

$$\tau_w = \mu \left. \frac{\partial u}{\partial y} \right|_{y=0} \quad (13)$$

$$U \frac{dU}{dx} - \frac{2\nu}{R} \left. \frac{\partial u}{\partial y} \right|_{y=0} = \frac{2}{R^2} \frac{d}{dx} \left[\int_0^\delta \left(\frac{u}{U} \right)^2 (R-y) dy + \left(1 - 2\left(\frac{\delta}{R}\right) + \left(\frac{\delta}{R}\right)^2 \right) \frac{U^2}{2} \right] \quad (14)$$

Simultaneous solution of (11), (12), and (14) is complicated but numerically integrable problem for

$$\frac{Re_x}{(Re_D)^2}$$

as a function of $\frac{\delta}{R}$. Some of the results are tabulated in Table 1. Since transition is assumed to be completed at $\frac{\delta}{R}$ equal unity, Table 1 shows the transition length, L^* , to be given by (15).

$$\begin{aligned} L^* &= \frac{0.03002}{\pi} \frac{VD^2}{\nu} \\ &= \frac{0.12008}{\pi} \frac{Q}{\nu} \end{aligned} \quad (15)$$

For air at 20 degrees C flowing with a mean velocity of 20 feet per second through a .0139-inch radius capillary, the flow becomes fully-developed after a distance of .242 inches or 8.7 diameters. For the same velocity flow through a .12-inch radius tube the flow does not develop until a distance of 1.5 feet or 75 diameters.

By using the results as in Table 1 with equations (10) and (11) one may determine the velocity at any location in the entrance length.

δR	$\frac{Re_x}{(Re_D)^2}$
0.050	0.0000318
0.100	0.000135
0.200	0.000638
0.300	0.00164
0.400	0.00328
0.500	0.00566
0.600	0.00887
0.700	0.01299
0.800	0.01794
0.900	0.02364
1.000	0.03002

Table 1. Summary of the Solution of Equations (11), (12) and (10).

The most significant disadvantage of this velocity solution is that it appears in numerical form. A more useful solution for the problem at hand would be in analytical form.

2.2.3 Linearizing the Momentum Equations

The lack of a general solution to (7) is due to the non-linearity of the inertia terms, $u \frac{\partial u}{\partial x} + \frac{\partial u}{\partial t}$. By replacing the inertia terms with $V \frac{\partial u}{\partial x}$, where V corresponds to a constant velocity of convection equal to the mean velocity, the linearized equation (16) is obtained [6].

$$V \frac{\partial u}{\partial x} = - \frac{1}{\rho} \frac{dp}{dx} + \nu \left[\frac{\partial^2 u}{\partial r^2} + \frac{1}{r} \frac{\partial u}{\partial r} \right] \quad (16)$$

After multiplying (16) by r and integrating over the cross-section one obtains (17)

$$V \frac{\partial u}{\partial x} + \frac{2\nu}{R} \frac{\partial u}{\partial r} \bigg|_{r=R} = \nu \left[\frac{\partial^2 u}{\partial r^2} + \frac{1}{r} \frac{\partial u}{\partial r} \right] \quad (17)$$

with boundary condition:

$$u \bigg|_{r=R} = 0$$

Assuming that the velocity solution of (17) can be written in the form (18) where U_{fd} is known as (9), the developing part of (18) can be substituted into (17) giving (19).

$$u(\eta, x) = U_{fd} + \sum_{m=1}^{\infty} c_m g_m(\eta) e^{-\gamma_m^2 X} \quad (18)$$

where $\eta = \frac{r}{R}$ and $X = \frac{x}{V\tau^2}$

$$\frac{d}{d\eta} \left(\eta \frac{dg_m}{d\eta} \right) + \gamma_m^2 \eta g_m = 2\eta \frac{dg_m}{d\eta} \bigg|_{\eta=1} \quad (19)$$

with boundary condition $g_m \big|_{\eta=1} = 0$

The solution of (19) can be verified as (20) where γ_m are the roots of $J_2(\gamma) = 0$.

$$g_m(\eta) = \frac{2}{\gamma_m} \left\{ \frac{J_0(\gamma_m \eta)}{J_0(\gamma_m)} - 1 \right\} \quad (20)$$

The requirement that $u(\eta, 0) = V$ and the orthogonal properties of the eigenfunctions of (19), specifically:

$$\int_A g_m dA = \int_A g_m g_n dA = 0 \quad m \neq n$$

determine

$$c_m = 2V/\gamma_m$$

Finally, the complete solution of (17) is (21).

$$\frac{u}{V}(r, x) = 2 \left(1 - \frac{r^2}{R^2} \right) - 4 \sum_{m=1}^{\infty} \frac{1}{\gamma_m^2} \left[1 - \frac{J_0\left(\frac{\gamma_m r}{R}\right)}{J_0(\gamma_m)} \right] e^{-\frac{\gamma_m^2 vx}{VR^2}} \quad (21)$$

More recently, an improved solution was obtained by weighting the mean velocity in the inertia term of (16) by a function, $\epsilon(x)$, defined by (22) [7].

$$dx = \epsilon dx^* \quad (22)$$

Then by equating the pressure gradient obtained from integrating the momentum equation (7) over the cross-section to that obtained from first multiplying (7) by $u(r, x)$ (mechanical energy equation), one finds an expression for $\epsilon(x)$.

$$\epsilon = \frac{\int_0^1 (2\omega - 1.5\omega^2) \left(\frac{\partial \omega}{\partial x^*} \right) \eta d\eta}{\left. \frac{\partial \omega}{\partial \eta} \right|_{\eta=1} + \int_0^1 \left(\frac{\partial \omega}{\partial \eta} \right)^2 \eta d\eta} \quad (23)$$

where

$$\omega = \frac{u}{V}, \text{ and } X^* = \frac{x^*/R}{VR/\nu}.$$

The velocity solution of this modified, linearized equation is the same as (21) except with x replaced by the stretched coordinate x^* . Both solutions agree reasonably well with experimental data and the results of part 2.2.2.

2.3 Pressure Drop Versus Volume Flow for a Tube

Of the several expressions for the velocity profile transition the only one given by (21) appears to strike the best balance between being accurate and being analytic. Now the pressure drop must be related to the velocity profile. For this (12) will be used. Substituting for τ_w , from (13) dividing by $\frac{\pi R^2 \rho V^2}{2}$, and integrating over the length gives (24).

$$\frac{p_o - p_x}{\rho V^2/2} = - \frac{4\nu}{RV} \int_0^x \left. \frac{\partial(\frac{u}{V})}{\partial r} \right|_{r=R} dx + \frac{2}{\pi R^2} \int_A \left(\frac{u}{V}\right)^2 dA - 2 \quad (24)$$

From (21) it is apparent that the velocity is the sum of the fully developed velocity, U_{fd} , and the developing velocity, $U - U_{fd}$. Using this fact and rearranging (24) gives (25).

$$\frac{\Delta p}{\rho V^2/2} = - \frac{4\nu}{RV} \int_0^x \left. \frac{\partial}{\partial r} \left(\frac{U_{fd}}{V} \right) \right|_{r=R} dx + \frac{2}{\pi R^2} \int_A \left(\frac{u}{V}\right)^2 dA - 2 - \frac{4\nu}{RV} \int_0^x \left. \frac{\partial}{\partial r} \left(\frac{U - U_{fd}}{V} \right) \right|_{r=R} dx \quad (25)$$

From (25) the pressure drop is seen to consist of four terms. The first term is the drop due to the viscous dissipation in the fully-developed flow. Substituting (9) into (25) and using (4) gives (26), which is recognized as

$$\Delta p = \left(\frac{8\mu x}{\pi R^4} \right) Q \quad (26)$$

the linear relationship characteristic of fully-developed flow.

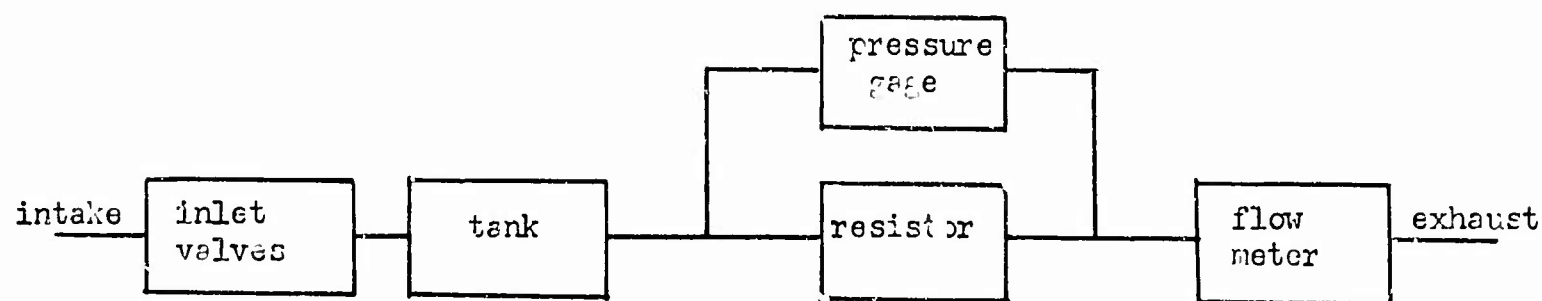


Figure 4. Schematic of Test Apparatus.

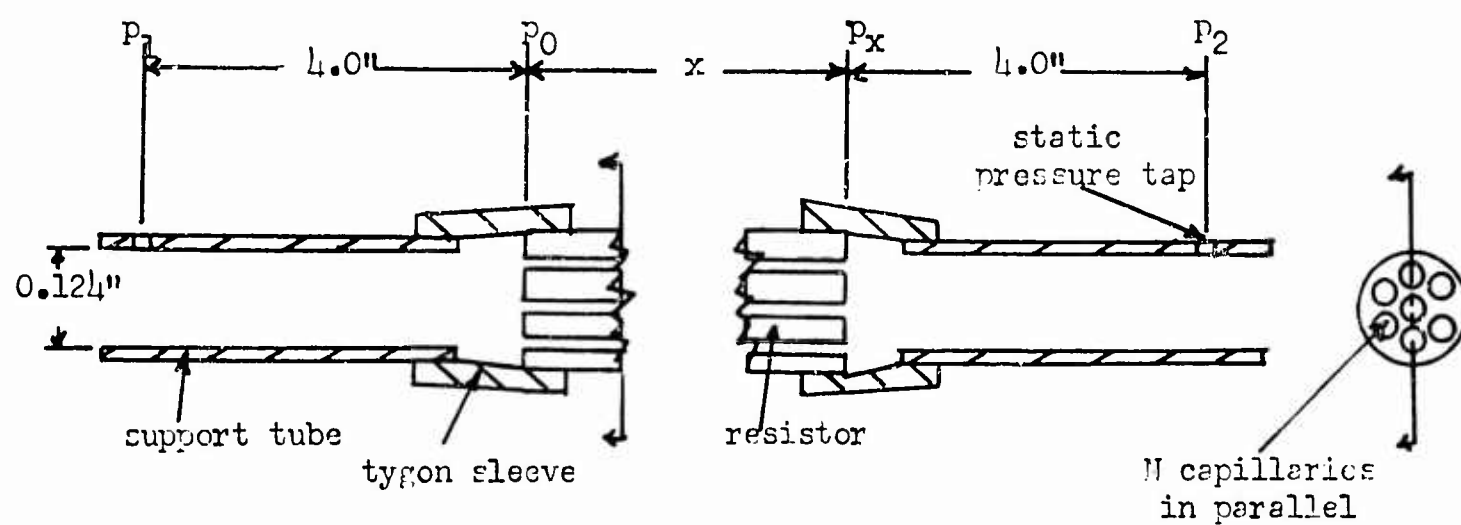


Figure 5. Test Resistor with Supports.

The second and third terms of (25) represent a pressure drop due to the increase in the kinetic energy contained in a cross-section as the flow develops. The fourth term represents an accumulated viscous loss that exists in the entrance section only.

Since the ratio, $\frac{u}{V}$, is known, the second term may be evaluated as (27).

$$\begin{aligned} \frac{2}{R^2} \int_A \left(\frac{u}{V}\right)^2 dA &= 2 \int_0^1 \left(\frac{u}{V}\right)^2 \eta d\eta = 2 \int_0^1 [2(1-\eta^2)]^2 \eta d\eta \\ &+ 2 \int_0^1 4(1-\eta^2) \sum_{m=1}^{\infty} \frac{2}{\gamma_m} g_m e^{-\gamma_m^2 X} \eta d\eta + 2 \int_0^1 \left[\sum_{m=1}^{\infty} \frac{2}{\gamma_m} g_m e^{-\gamma_m^2 X} \right]^2 \eta d\eta \\ &= \frac{8}{3} - \sum_{m=1}^{\infty} \frac{8}{\gamma_m^2} (2) e^{-\gamma_m^2 X} + \sum_{m=1}^{\infty} \frac{8}{\gamma_m^2} e^{-2\gamma_m^2 X} \end{aligned} \quad (27)$$

Similarly, after substitution the fourth term becomes (28)

$$\begin{aligned} \frac{4\gamma}{RV} \int_0^X \frac{\partial}{\partial r} \left(\frac{U-Ufd}{V} \right) \Big|_{r=R} dx &= \sum_{m=1}^{\infty} - \frac{8}{R^2 V \gamma_m} \int_0^X \frac{\partial g_m}{\partial \eta} \Big|_{\eta=1} e^{-\gamma_m^2 X} dx \\ &= - \sum_{m=1}^{\infty} \frac{8}{\gamma_m^2} e^{-\gamma_m^2 X} + \sum_{m=1}^{\infty} \frac{8}{\gamma_m^2} \\ &= - \sum_{m=1}^{\infty} \frac{8}{\gamma_m^2} e^{-\gamma_m^2 X} + \frac{2}{3} \end{aligned} \quad (28)$$

Substituting (26), (27), and (28) into (25) gives after re-arrangement:

$$\frac{\Delta P}{4V^2/2} = \frac{16vx}{VR^2} + \frac{4}{3} + \sum_{m=1}^{\infty} \frac{8}{\gamma_m^2} (e^{-\gamma_m^2 x} - 3) e^{-\gamma_m^2 x} \quad (29)$$

Substituting for X and writing in terms of the volume flow

$$p_0 - p_x = \left(\frac{8\mu x}{\pi R^4}\right)Q + \left(\frac{2\rho}{\pi^2 R^4}\right)\left[\frac{1}{3} + 2 \sum_{m=1}^{\infty} \frac{1}{\gamma_m^2} \left(e^{-\frac{\gamma_m^2 vx}{Q}} - 3\right)e^{-\frac{\gamma_m^2 vx}{Q}}\right]Q^2 \quad (30)$$

Equation (30) represents the pressure drop within a circular tube of constant radius from a uniformly distributed flow at p_0 to some axial location x .

2.4 The Test Resistors

2.4.1 Adapting Theory to Test Conditions

The test resistors consisted of groups of capillaries in parallel. The static pressure versus volume flow characteristics of these resistors was measured in an apparatus illustrated in Figure 4 and Figure 5.

The static pressure $p_1 - p_2$ was measured with a Barton gage that was calibrated to ± 0.02 psi on a dead weight tester. The volume flow was measured with rotometers that were calibrated with a volume meter to within $\pm 0.05 \times 10^{-3}$ ft³/sec.

The pressure $p_1 - p_2$ was measured because it represents the pressure drop as the resistor would be used in some fluid circuit.

Since (30) represents $p_0 - p_x$ for one capillary, several adjustments must be made before it can be used to predict $p_1 - p_2$.

The volume flow through the network of N capillaries must be divided by N to give the flow through one capillary.

Some of the static pressure p_1 is converted into kinetic energy as the flow approaches $x = 0$ because of the area reduction at the entrance of the resistor. This static pressure drop, $p_1 - p_0$,

can be calculated, if dissipation is neglected, by integrating the Bernoulli equation over the cross-sections at p_1 and p_0 . If the mean velocity, Q/A , is substituted for the actual velocity distribution in the integration, an error results. This error may be accounted for by a function, α , varying from 1 to 2, that takes into consideration the profile differences between the two locations [8]. The resulting equation is (31).

$$p_1 - p_0 = \frac{\rho Q^2}{2\pi^2} \left[\frac{1}{(NR^2)^2} - \frac{\alpha}{R_1^4} \right] \quad (31)$$

For the range of values in this problem, $R_1^4 \gg R^4$, the second term of (31) is negligible. Thus (31) reduces to (32).

$$p_1 - p_0 = \frac{\rho Q^2}{2(\pi NR^2)^2} \quad (32)$$

The most significant effect of the whole problem occurs at the outlets of the capillaries. The static pressure drop up to that cross-section, $p_1 - p_x$, is a combination of viscous dissipation and increases in the total kinetic energy of the fluid particles making up the cross-section. Because of the very sharp expansion at the end of the capillaries, practically all of the kinetic energy is dissipated. Thus the static pressure drops due to increases in kinetic energy become static pressure losses, $p_x - p_2 \approx 0$.

Two effects have been neglected. The pressure drop $p_1 - p_2$ with the resistor removed is less than the probable experimental error for all flows. And, stagnation losses at the entrance to the resistor are of the order of the kinematic viscosity; therefore, very small.

Since the theory presented thus far is valid for only laminar flow, the diameter Reynolds number as defined by (33) must not be exceeded.

$$R_{eD} = \frac{2Q_{\max}}{\pi R_0 N} \leq 2300 \quad (33)$$

Thus the pressure-flow relationship (30) for a capillary resistor with its entrance and exit configurations as described and for flows limited as above is given by (34).

$$p_1 - p_2 = \left(\frac{8\mu L}{\pi N R^4} \right) Q + \left(\frac{\rho}{\pi^2 N^2 R^4} \right) \left[\frac{7}{6} + \sum_{m=1}^{\infty} \frac{4}{\gamma_m^2} \left(e^{-\frac{\gamma_m^2 v \pi N L}{Q}} - 3 \right) e^{-\frac{\gamma_m^2 v \pi N L}{Q}} \right] Q^2 \quad (34)$$

$$\mu = 3.75 \times 10^{-7} \frac{\text{lb-f-sec}}{\text{ft}^2}$$

$$v = 1.60 \times 10^{-4} \frac{\text{ft}^2}{\text{sec}}$$

$$\rho = 2.34 \times 10^{-3} \frac{\text{lb-f-sec}^2}{\text{ft}^4}$$

3. EXPERIMENTAL RESULTS

A total of ten different resistors were tested. For five of the tests the number of capillaries, N , was varied and for the other five tests the lengths, V , were varied. The flow was varied from $0.1 \times 10^{-3} \text{ ft}^3/\text{sec}$ up to the critical value, Q_{max} , at which the transition to turbulent flow takes place. In no case, however, did the flow exceed $4.0 \times 10^{-3} \text{ ft}^3/\text{sec}$. For each value of flow the static pressure, $p_1 - p_2$, was measured for the tests summarized in Table 2.

The minimum value of the term, $\frac{v \pi N L}{Q}$, appearing in the exponential series of (34) for the various experimental resistors was 0.39. In the Appendix it is shown that this minimum value permits neglecting the series terms without significant error. Thus (34) becomes (35).

$$\Delta p = \left(\frac{8\mu L}{\pi N R^4} \right) Q + \left(\frac{7\rho}{6\pi^2 N^2 R^4} \right) Q^2 \quad (35)$$

The experimental data was plotted against (35) in Figures 6 and 7. Finally, the pneumatic resistance is given by (36).

$$R_p = \frac{8\mu L}{\pi N R^4} + \frac{7\rho}{6\pi^2 N^2 R^4} Q \quad (36)$$

test number	length x (inches)	capillaries N	diameter 2R (inches)	maximum laminar flow Q _{max} (ft ³ /sec x 10 ³)
1	3.0	1	.0120	.29
2	3.0	3	.0120	.87
3	3.0	4	.0120	1.16
4	3.0	8	.0120	2.31
5	3.0	24	.0120	6.94
6	1.0	25	.0139	8.36
7	1.5	25	.0139	8.36
8	2.0	25	.0139	8.36
9	3.0	25	.0139	8.36
10	4.0	25	.0139	8.36

Table 2. Summary of Tests.

4. CONCLUSIONS

Figures 6 and 7 show a good agreement of the theory (35) with experiment for the tested resistors. However, the nonlinearity seems to decrease somewhat with higher values of resistance contrary to (36). Equation (36) is very accurate for pressures less than 1.5 psi, wherein much of the work with pneumatic amplifiers is conducted.

The nonlinear term of (36) is due to three sources. That is

$\frac{2\rho}{6\pi^2 N^2 R^4}$ of the term arises from kinetic energy increases in the capillaries, $\frac{2\rho}{6\pi^2 N^2 R^4}$ is due to an accumulated viscous loss in the entrance section, and $\frac{3\rho}{6\pi^2 N^2 R^4}$ comes from a kinetic energy increase at the entrance of the capillaries due to the area reduction. The pressure drops due to conversion of static pressure to kinetic energy become losses because of the abrupt outlet condition.

In addition the negative term $\sum_{m=1}^{\infty}$ vanishes because the factor

$C = \nu \pi N L / Q$ is large.

It would seem that by proper shaping of the outlet and proper choice of C , that the nonlinearity of the resistor may be reduced. This work and the study of the non-steady problem are a source of future investigation.

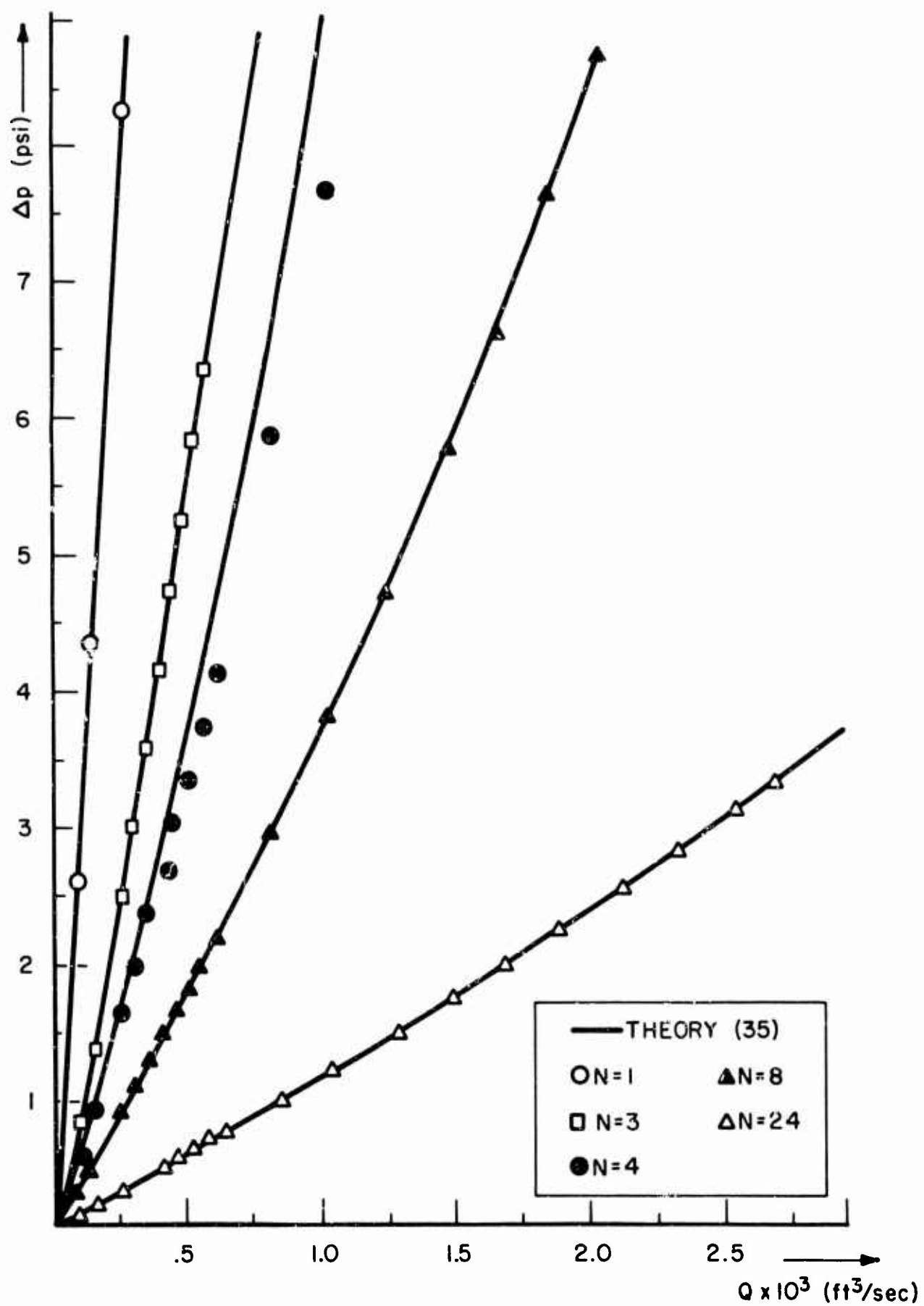


Figure 6. Pressure Versus Flow Varying N

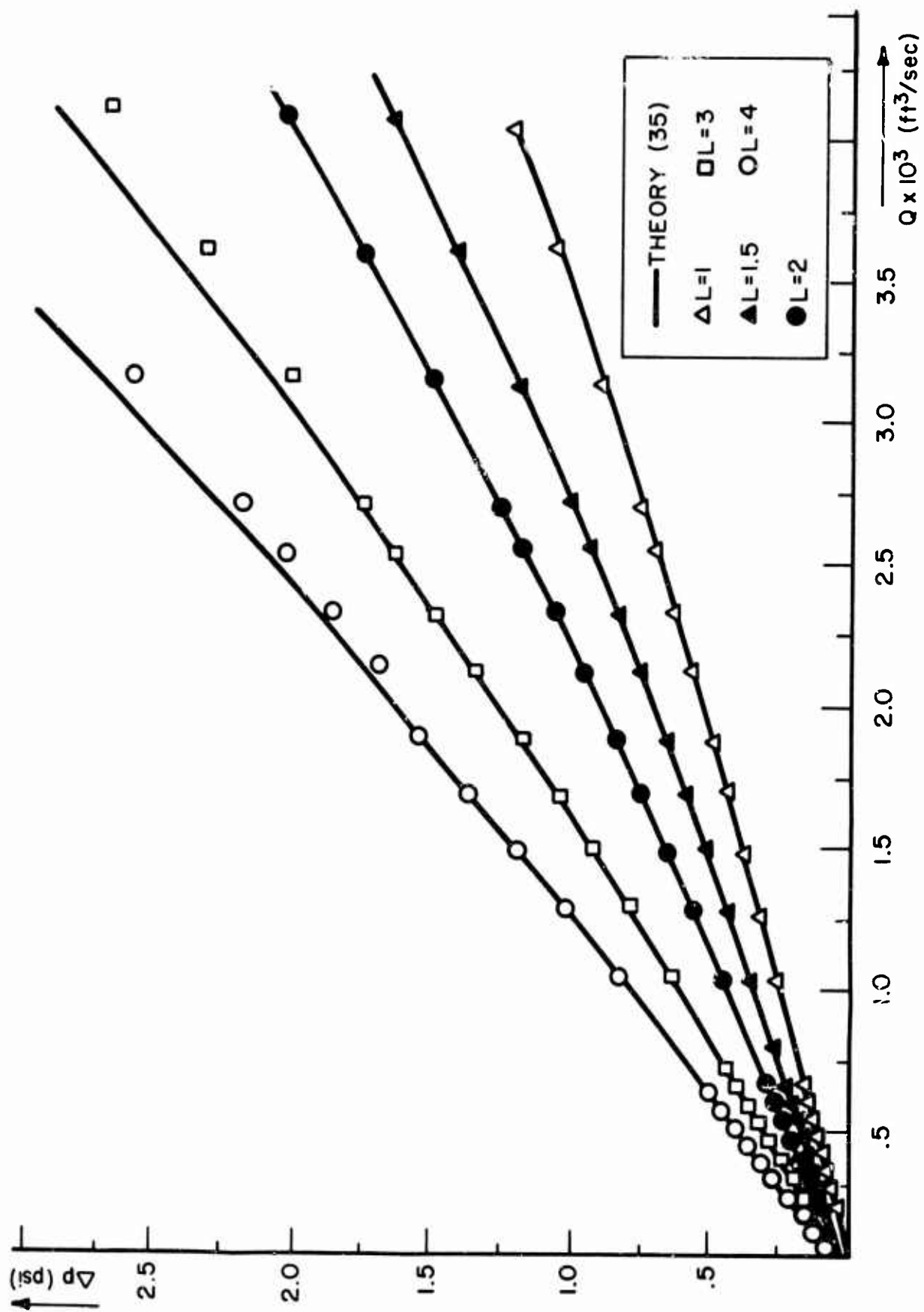


Figure 7. Pressure versus Flow Varying L .

A P P E N D I X

CONVERGENCE OF SERIES TERM OF EQUATION (34)

\sum , Of particular importance is the convergence of the series terms, given by (37).

$$\sum = 4F(2C) - 12F(C) \quad (37)$$

where

$$F(C) = \sum_{m=1}^{\infty} \frac{1}{\gamma_m^2} e^{-\gamma_m^2 C}$$

and

$$C = \frac{v \pi N L}{Q}$$

The eigenvalues, γ_m , begin as shown in Table 3 and eventually approach a separation of π .

In the limit where C goes to zero, $\sum = -2/3$, where $F(C)$ and $F(2C)$ are given by (38).

$$F(C) = F(2C) = \sum_{m=1}^{\infty} \frac{1}{\gamma_m^2} = \frac{1}{12} \quad (38)$$

As C increases from zero to infinity, the series, \sum , will increase from $-2/3$, which may not be ignored with respect to $7/6$ in (34), to zero. We wish to know what error will be introduced by ignoring \sum for $C < \infty$.

If $C = \ln B$ where B must be ≥ 1 , equation (39) is obtained.

$$F(B) = \sum_{m=1}^{\infty} \frac{e^{-\gamma_m^2 \ln B}}{\gamma_m^2} = \sum_{m=1}^{\infty} \frac{e^{\ln(B^{-\gamma_m^2})}}{\gamma_m^2} = \sum_{m=1}^{\infty} \frac{B^{-\gamma_m^2}}{\gamma_m^2} \quad (39)$$

m	γ_m	γ_m^2
1	5.14	26.42
2	8.42	70.90
3	11.62	135.0
4	14.80	219.0
5	17.96	322.6
6	21.12	446.1
7	24.27	589.0

Table 3. The First Values of γ_m .

From fundamental calculus we have (40)

$$\int_a^b f(\gamma) d\gamma = \lim_{\Delta\gamma \rightarrow 0} \sum_{i=(a,b)} f_1^*(\gamma) \Delta_1\gamma \quad (40)$$

where $f_1^*(\gamma)$ = mean value of $f_1(\gamma)$ in the interval $\Delta_1\gamma$

If instead, $\Delta\gamma \rightarrow \pi$, (40) becomes (41)

$$\sum_{m=1} f(\gamma_m) < \frac{1}{\pi} \int_{\gamma_1 - \pi/2}^{\gamma_\infty} f(\gamma) d\gamma \quad (41)$$

Substituting $f(\gamma_m) = \frac{B^{-\gamma_m^2}}{\gamma_m^2}$ into (41) gives (42).

$$F(B) < \frac{1}{\pi} \int_{\gamma_1 = 5.14 - \pi/2}^{\gamma_\infty = \infty} \frac{B^{-\gamma^2}}{\gamma^2} d\gamma \quad (42)$$

Since $B > 1$, the functions $\frac{B^{-\gamma^2}}{\gamma^2}$, $B^{-\gamma^2}$, and $\frac{1}{\gamma^2}$ are monotone

nonincreasing and less than unity in the interval $\gamma(3.57, \infty)$. Moreover, for $B > 1.22$ we must have (43), as illustrated in Figure 8.

$$\frac{B^{-\gamma^2}}{\gamma^2} < B^{-\gamma^2} < \frac{1}{\gamma^2} \quad (43)$$

For the case where $B = e$, using (43) gives (44).

$$F(e) < \frac{1}{\pi} \int_{\gamma=3.57}^{\infty} e^{-\gamma^2} d\gamma$$

$$F(e) \approx 0$$

Thus for $C \geq 1$ ($B \geq e$) we have $\sum \approx 0$.
Also from (43) we have (45).

$$F(B) < \frac{1}{\pi} \int_{3.57}^{\infty} \frac{1}{\gamma^2} d\gamma = \frac{1}{\pi(3.57)} \quad (45)$$

But this is too conservative. If we examine for what values of a constant, ξ , equation (46) is valid,

$$F(B) < \frac{\xi}{\pi} \int_{3.57}^{\infty} \frac{1}{\gamma^2} d\gamma \quad \begin{matrix} \gamma(3.57, \infty) \\ B(1.22, \infty) \end{matrix} \quad (46)$$

we see

$$\xi \geq \max B^{-\gamma^2} = 1.22^{-(3.57)^2}.$$

This gives (47).

$$F(B) < \frac{(1.22)^{-(3.57)^2}}{\pi(3.57)} = .0071 \quad (47)$$

Thus for $C > .20$ ($B > 1.22$) we have $.057 > \sum > 0$. The results of (38), (44), and (47) are tabulated in Table 4.

Finally, if $C > 0.2$, the error introduced by neglecting \sum is less than 6.4% of the contribution of the Q^2 term to the total pressure.

A few representative values of \sum were calculated on a computer using the first twenty eigenvalues for values for C between zero and one. Some of the data is given in Table 5.

B	C	$ \Sigma $
$\geq e$	≥ 1.0	~ 0.0
> 1.22	> 0.2	< 0.0852
1.00	0.0	$2/3$

Table 4. Summary of Convergence Results.

C	$4F(2C)$	$12F(C)$	$ \Sigma $
.0001	.30	.924	.624
.0003	.28	.876	.596
.001	.24	.799	.559
.003	.18	.664	.484
.01	.105	.463	.358
.03	.029	.216	.187
.1	.0008	.0325	.0317
.3	.0	.0	.0

Table 5. Values of Σ for $0 < C < 1$.

REFERENCES

- [1] Schlichting, H., Boundary Layer Theory, McGraw-Hill Book Co., Inc. 1960, pp. 171.
- [2] Hunt, J. N., Incompressible Fluid Dynamics, Wiley and Sons, Inc. New York, N.Y., 1964, pp 26-27.
- [3] Siegel, R., and Shapiro, A. H., "The Effect of Heating on Boundary Layer Transition for Liquid Flow in a Tube," Report submitted under Contract N5ori-07871, June 1953, pp 36-52.
- [4] Shapiro, A. H., Siegel, R., and Kline, S. J., "Friction Factor in the Laminar Entry of a Round Tube," Proceedings of the Second U.S. National Congress of Applied Mechanics, ASME, 1954, pp 733-741.
- [5] Cambell, W.D., and Slattery, J. C., "Flow in the Entrance of a Tube," Journal of Basic Engineering, Vol. 85, Series D, No. 1, March 1963, pp 41-46.
- [6] Slezkin, N. A., Dynamics of Viscous Incompressible Fluids (in Russian) (Gostekhizdat, Moscow, 1955).
- [7] Sparrow, E. M., Lin, S. H., and Lundgren, T. S., "Flow Development in the Hydrodynamic Entrance Region of Tubes and Ducts," The Physics of Fluids, Vol. 7, No. 3, March 1964, pp 338-347.
- [8] Russell, G. E., Hydraulics, Henry Holt and Co., Inc., 1942, pp 79-81.

SIMILARITY RELATIONS AND CHARACTERIZATION OF PURE FLUID ELEMENTS

by

H. H. Glaettli

International Business Machines Corporation
Zurich Research Laboratory, Rüschlikon-ZH
Switzerland

Many attempts have been made to provide short descriptions of pure fluid components, for instance in the form of data sheets. In spite of the fact that many valuable data are given on such occasions, two serious disadvantages of past approaches become more pronounced as time goes on: On the one hand, the given data do not represent the full value of the results obtained through the development of the element in question, and on the other hand, there is no base for comparison of various elements one with another. There are mainly two reasons: Neglect of similarity relations (which alone would maintain the generality of experience gained and would provide a base for comparisons over a wide range), and insufficient data. Many examples in Ref. 1 and many proposals concerning "new" elements are good illustrations for all this: Response times or operating pressures are mentioned without giving any further information such as size, fluid, Reynolds number, aspect ratio, amplifier data and modulation factor.

It is the purpose of this paper to demonstrate a simple elementary manner to arrive at a few dimensionless constants, which, together with the representative size and the fluid properties (viscosity, density) give an effective description of fluid elements. The first steps in this direction were taken in Ref. 2. - In addition to several details worked out since then, some new results are given as to the choice of aspect ratio. Last but not least, some remarks will be made as to the limits of similarity relations.

The first step consists in defining the Reynolds number R . This is done by introducing the average flow velocity through the nozzle, derived from flow rate measurements, into the definition of the Reynolds number:

$$R = \frac{\rho \cdot \dot{Q}}{k_2 \cdot l \cdot \eta} \quad (1)$$

ρ is the density and η the viscosity of the fluid used. \dot{Q} is the measured volumetric flow rate. For simplicity reasons, the whole layout is assumed to be essentially two-dimensional: l is the nozzle width and k_2 the aspect ratio. In some cases, it may be convenient to measure the mass flow rate $\rho \cdot \dot{Q}$ directly.

The operating pressure p of an element is closely related to the pressure drop through the nozzle and can be described by

$$p = k_1 \cdot \frac{R^2 \cdot \eta^2}{2 \rho l^2} \quad (2)$$

k_1 is the first constant to be determined experimentally. It takes into account any losses and a possible pressure recovery and does not differ too much, therefore, from one. k_1 is also the first constant entering the data sheet.

The operating power P of a pure fluid element is given by

$$P = k_1 \cdot k_2 \frac{R^3 \cdot \eta^3}{2 \rho l} \quad (3)$$

As mentioned above, k_2 is not a constant to be determined experimentally. It must, however, be emphasized at this point that R has been defined on a two-dimensional base. Any critical value R_{crit} , therefore, must depend on k_2 . Some information on how R_{crit} depends on k_2 is given in Ref. 3. The experimental results shown there indicate an appreciable influence of the flow character on the dependence of R_{crit} on k_2 . It is, therefore, suggested that any indication of R_{crit} be followed by the corresponding k_2 -value at which R_{crit} was determined.

It has also been shown in Ref. 3 that a k_2 -value of 2 to $\sqrt{5}$ leads to a minimum power consumption. For practical reasons (mainly manufacturing difficulties), an aspect ratio $k_2 = 1$ was used by the author in most cases. Meanwhile, additional experiments have been carried out, which speak in favor of this relatively low aspect ratio, and which will be described briefly in the appendix.

One of the main difficulties arises when the response times of various elements are to be compared. Following Ref. 2, the response time τ of a pure fluid amplifier can be described by

$$\tau = k_3 \cdot k_4 \cdot \frac{\rho \cdot l^2}{R \cdot \eta} \quad (4)$$

It would certainly be quite simple if the product $k_3 \cdot k_4$ could be determined experimentally. The response time, however, depends on the gain of the amplifier. There are many ways to derive such a relationship. One such possibility starts with considerations of the (hypothetic) free jet amplifier. Idealized assumptions allow the product $k_3 \cdot k_4$ to be expressed in terms of amplifier data. τ becomes:

$$\tau = \frac{\rho \cdot l^2}{R \cdot \eta} \cdot \mu_{\dot{Q}} \cdot \sqrt{\mu_p} \cdot \frac{1}{2} \left[1 + \left(\frac{\mu_{\dot{Q}} + 1}{\mu_{\dot{Q}}} \right)^2 \right] \quad (5)$$

$\mu_{\dot{Q}}$ is the flow rate, μ the pressure gain. Formula (5) simplifies for sufficiently high values of $\mu_{\dot{Q}}$ to

$$\tau = \frac{\rho \cdot l^2}{R \cdot \eta} \cdot \mu_{\dot{Q}} \cdot \sqrt{\mu_p} \quad (6)$$

The response time of practical embodiments will be longer. The fact that τ is described by a product of factors forming two groups (the first group representing operating conditions, the second giving important amplifier data) and similarity relations that hold for quite a range of Reynolds numbers, suggests the following additions to (5) and (6):

First of all, a further factor f_m should take into account the mixing of the power jet with the surrounding fluid, which may lead to higher values of $\mu_{\dot{Q}}$, but which always reduces the pressure gain considerably. This not only lowers the gain of the amplifier but also increases the response time due to the reduction in average jet velocity.

The second modification consists in adding another factor f_{NL} , which adjusts τ for the nonlinearity of the element. The product of both factors may easily be determined experimentally and may be considered as a figure of merit. This figure of merit then enters the data sheet and may be used to compare various amplifiers.

Such comparisons are possible independent of whether momentum or boundary layer control is used. It must, however, be borne in mind that (5) and (6) are based on similarity relations. These similarity relations may find an end when cavitation or

compressibility effects become appreciable.

Typical examples showing how amplification of monostable elements decreases with increasing Mach number, whereas the gain of bistable elements increases under the same change of conditions, have been published in references 4 and 5.

The range over which similarity relations hold closely enough to be of practical value, has to be stated explicitly by giving a maximum and possibly also a minimum Mach number in the case of compressible fluids. - There are some difficulties in connection with incompressible fluids: cavitation depends considerably on impurities. Last but not least, it takes a certain time to set up cavitation because of limited thermal conductivity. Both effects together cause the upper limit for the operating pressure, where significant cavitation effects start to vary with size, which according to Ref. 2 would not be true under ideal circumstances.

So far only isolated amplifiers have been considered. It is, however, true that not only a single amplifier can be built in different sizes, but also a whole circuit: There also exists at least a minimum, but under certain circumstances also a maximum Reynolds number, which defines the range of successful operation; the Mach number range will also be limited. - In the case of a parallel adder, the carry propagation time per stage may be considered instead of the response time, and in the case of a binary counter, the resolving time for counting or frequency dividing plays a corresponding role.

In the case of circuits other than just amplifier circuits, the situation becomes somewhat simpler: only the minimum carry propagation time per stage or the minimum resolving time is of interest. These minima occur at the minimum gain which compensates for the losses, i. e., at an overall gain 1. In such a case it would be sufficient to mention the value of the product $k_3 \cdot k_4$ in its generalized meaning for a whole circuit.

A typical example of data concerning a binary counter circuit is given in the following. The geometry is shown in Fig. 1

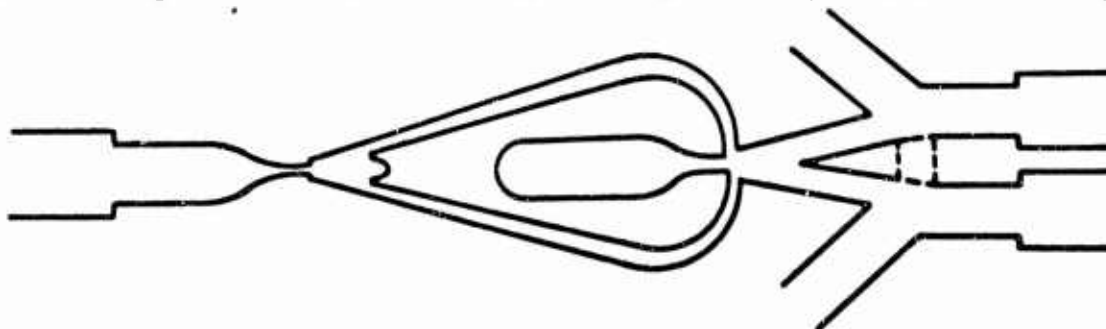


Fig. 1 Geometry of Binary Counter

The circuit was proposed by R. W. Warren (Ref. 6). The minimum Reynolds number at which the active element has to be operated for proper functioning of a multistage adder at an aspect ratio $k_2 = 1$ was found to be 1900. k_1 equals 1.05. The product $k_3 \cdot k_4$ was determined to be 465.

The Mach number range has not yet been determined completely: The design shown in Fig. 1 requires a minimum Mach number of .35. The maximum Mach number lies between .4 and .8. It is not yet certain whether it depends on the Reynolds number (especially in the case of Reynolds numbers between 2000 and about 5000) or whether this wide range is due to manufacturing tolerances, which would not express themselves through the minimum Reynolds number.

By omitting the bypass between the two output channels the circuit works at any Mach number below .35. The minimum Reynolds number decreases to 1800, whereas k_1 and $k_3 \cdot k_4$ remain unchanged, which speaks in favor of the proposed description with a few dimensionless constants.

There now remains the step from dimensionless numbers to specified data such as response time in msec, power in watts, pressure in atm, etc. for a certain fluid and a certain size. - This is easily done with the aid of a nomogram similar to those proposed in Ref. 2. A logarithmic scale is used both on the abscissa and the ordinate, which show the nozzle width and the operating power, respectively. Curves for constant Reynolds number, constant operating pressure and constant response time are shown. According to expressions (2), (3) and (4), all these curves are represented by straight lines. Their tangents are as follows: -1, +2 and +5. The author fixed k_1 and $k_2 = 1$, whereas it is more convenient to assume $k_3 \cdot k_4 = 100$.² The following ranges were chosen for air: .01 mm $\leq d \leq 10$ mm and 10^{-5} Watts $\leq P \leq 10$ kW

Such a chart allows determination of operating pressure, power consumption and response as a function of the representative size at a glance; it is, however, not suited for reproduction in black and white or in small size. This is the reason why no example is shown in the proceedings. It is intended to publish examples in a future publication by the author.

Any correction for k_i -values ($i = 1, 2, \dots, 4$) differing from the above assumptions can easily be done by multiplication with factors that are usually very near to 1, or at least between 1 and about 5 in the case of $k_3 \cdot k_4$.

Thus it has been shown that the characterization of pure fluid elements by dimensionless numbers offers the possibility of direct comparisons because it maintains the generality of the available information, and at the same time there is no drawback due to the fact that a simple chart provides fast specific answers to specific questions.

APPENDIX

There is a significant advantage in making a layout of a whole circuit in such a way that as many elements as possible, through which a signal (for instance, a carry signal) should pass at the highest possible speed, are contained in one plane. This often requires the power to be fed into that plane through perpendicular ducts. This easily introduces disturbances which should be smoothed out sufficiently in the inlet section before they reach the nozzle contraction.

A design study was started in order to find out what the minimum length of the inlet should be to provide adequate damping. Nozzles with a fixed contraction ratio of 5:1, various aspect ratios and a variable inlet length were built. Pressure was applied through a vertical tube, the inner diameter of which was equal to the width of the inlet section.

This arrangement was used in connection with a bistable element, the critical Reynolds number required to maintain the jet in the attached position were taken as criteria.

Figure 2 shows a typical observation. It is quite clear that a sufficiently long inlet section is advantageous in lowering R_{min} , which is more important in most cases than R_{crit} . This not only results in a power saving in bistable elements, but also improves the signal-to-noise ratio in monostable elements. In all cases, however, sufficient damping in an inlet section of suitable length improves the definition of the response time by eliminating jitter. Last but not least, there is a beneficial influence on the symmetry of all devices.

Measurements presently in progress with higher aspect ratios indicated that a much longer inlet or other measures would be required to provide a smooth flow in the nozzle: Whereas a total length of the nozzle arrangement of about 30 nozzle widths is sufficient at $k_2 = 1$, the relative inlet length has to be more than doubled for an aspect ratio $k_2 = 2$. This finally tends to affect the packaging density. It is, therefore, concluded that this is another indication towards aspect ratios around 1 to 1.5.

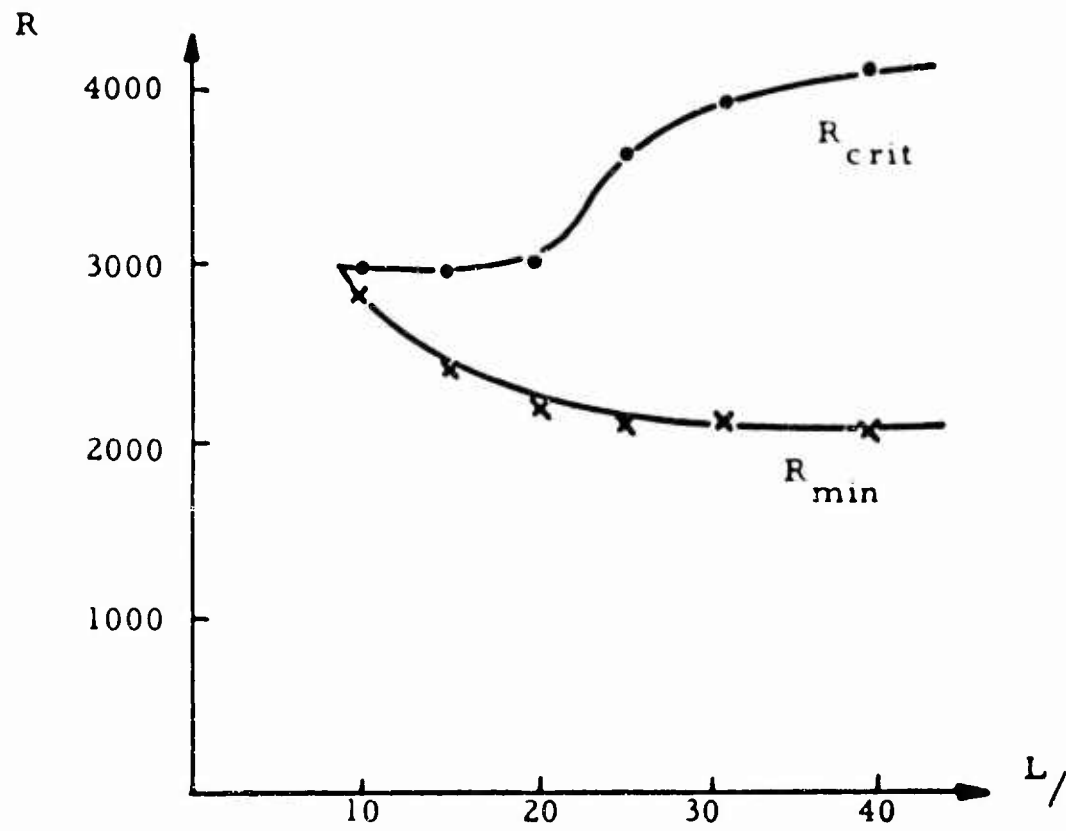


Fig. 2 Influence of the Length of the Inlet Section on the Hysteresis of a Bistable Element

REFERENCES

- 1 - Control Engineering, September 1964
(Special issue on fluid amplification)
- 2 H. H. Glaettli "Digital Fluid Logic Elements"
Chapter in the book "Advances in
Computers"
(Academic Press, New York, 1963),
p. 169-243.
- 3 H. H. Glaettli Remarks on the Limitations of Pure
H. R. Mueller Fluid Elements. Proceedings of the
R. H. Zingg Second Fluid Amplification Symposium
at the Harry Diamond Laboratory.
Washington D. C., May 1964
- 4 H. H. Glaettli "Problems in Connection with Mini-
aturization of Fluid Mechanic Compo-
nents"
Paper to be given at the IFAC/IFIP-
Symposium, München, Oct. 21-23, 1965.
- 5 H. H. Glaettli Basic Properties of Fluid Mechanic
Components Proceedings of the Fluid
Logic and Amplification Conference,
Cranfield, September 1965.
- 6 R. W. Warren U. S. Patent No. 3 016 698

DYNAMIC SIMILARITY ANALYSIS OF COMPRESSIBLE VISCOUS
FLUID PIPE FLOW*

FABIO R. GOLDSCHMIED**
RESEARCH AERODYNAMICIST
SPERRY UTAH COMPANY
DIVISION SPERRY RAND CORP.
SALT LAKE CITY, UTAH

1. Introduction

A rapid growth has been seen in the past few years in the new technology of fluidic amplifiers and fluidic servo controls.

Fluidic technology is based on some of the most sophisticated fluid dynamic phenomena encountered by the aerodynamicist, not to mention the control engineer, i.e., the problem of transient flow in a complex fluid network. As the response of the fluid amplifier is made faster and the circuit frequencies increase, these problems will become more and more acute.

The basic equations of motion of a viscous time-dependent flow, the Navier-Stokes eqs., are strongly non-linear and intractable analytically, even in the two-dimensional incompressible case.

In Ref. 1, Section 1.1, computational techniques are developed for the numerical solution of the equations for a limited flow field. Large computers will be needed to extend the flow field to the dimensions required by practical problems.

Furthermore, the Navier-Stokes equations are applicable strictly only to the laminar flow case, i.e., to such flows where the Reynolds Number remains below some limiting value (depending on the flow geometry).

Above this value, turbulent flow prevails, for which there is no exact mathematical description, because the number of unknowns exceeds the number of available equations; additional empirical relationships have been formulated by many research workers to fit a variety of flow configurations, with varying success.

In view of the difficulties (even the impossibility, in case of turbulent flow) of adequate analytical treatment and since numerical solutions are not yet obtainable for flow fields of practical size, the aerodynamicist has relied heavily on experimental data and empirical investigations; this will also hold true, to an even higher degree, for the workers in the new fluidic technology.

The purpose of this paper is to discuss the necessity of employing dimensional analysis when relying on the empirical approach in fluid problems and in particular to present the Stokes-Reynolds Similarity Laws for dynamic flow circuits.

*This work has been carried out under NASA contract NAS 8-11236.

**Now at University of Utah.

2. Dimensional Analysis.

2.1 General.

All phenomena in mechanics are determined by a series of variables, such as energy, velocity and mass, which take definite numerical values in given cases. Problems in dynamics or statics reduce to the determination of certain functions and characteristic parameters; the relevant laws of nature and geometrical relations are represented as functional equations, usually differential equations. In purely theoretical investigations, we use these equations to establish the general qualitative properties of the motion and to calculate the unknown physical variables by means of mathematical analysis. However, it is not always possible to solve a mechanics problem solely by the process of analysis and calculation. Sometimes the mathematical difficulties are too great, as in the case of laminar flow, and sometimes the problem cannot be formulated mathematically because the phenomenon to be investigated is much too complex to be described by a satisfactory theoretical model, as in the case of turbulent flow. In these cases, we have to rely mainly on experimental methods of investigation, to establish the essential physical features of the problem.

In general, we begin investigations of a natural phenomenon by finding out which physical properties are important and seeking relationships between such properties which govern the phenomenon.

Many phenomena cannot be investigated directly for practical reasons and therefore to determine the laws governing them we must perform experiments on similar phenomena which are easier and more convenient to handle. To set up the most suitable experiments, we must make a general qualitative analysis and bring out the essentials of the phenomenon in question; it is very important (and time-saving) to select the dimensionless parameters correctly. They should be as few as possible, while still reflecting all the fundamental effects.

The preliminary analysis of the phenomenon and the choice of a system of definite dimensionless parameters is made possible by the technique of dimensional analysis and similarity theory. These techniques have been developed to a high degree and have been presented by many authors, Langhaar², Sedov³, etc.

In order to bring out the essential techniques and parameters in the most concise manner, a simple pipe flow will be investigated, comprising both a mean flow and an oscillatory component of small amplitude.

2.2 Dynamic and Steady-State Fluid Motion in a Pipe.

Let us consider a round pipe of diameter D and length L with a sinusoidal oscillatory flow of small amplitude and frequency ω over a mean flow Q_0 ; let the fluid be a viscous compressible gas.

All the parameters which seem pertinent to the problem will be listed below.

2.2.1 List of Physical Factors.

Gas Characteristics:

- | | |
|-----------------------------|--|
| 1. Mass density, mean | ρ_o [lb sec ² /ft ⁴] |
| 2. Absolute viscosity, mean | μ_o [lb sec/ft ²] |
| 3. Ratio of specific heats | k [0] |
| 4. Gas constant | R_g [ft/°R] |

Heat Transfer Conditions:

- | | |
|------------------------|---------|
| 5. Polytropic exponent | n [0] |
|------------------------|---------|

Geometric Conditions:

- | | |
|------------------|----------|
| 6. Pipe diameter | D [ft] |
| 7. Pipe length | L [ft] |

Flow Conditions:

- | | |
|----------------------------------|------------------------------|
| 8. Volumetric flow, mean | Q_o [ft ³ /sec] |
| 9. Pressure, mean (absolute) | P_o [lb/ft ²] |
| 10. Temperature, mean (absolute) | T_o [°R] |

Dynamic Conditions:

- | | |
|---------------------------|--------------------|
| 11. Oscillatory frequency | ω [rad/sec] |
|---------------------------|--------------------|

[The lb notation refers to pounds force.]

There are eleven parameters listed above; it is quite clear that the number of combinations and permutations of parameters will be extremely large, so that it is quite unproductive to undertake experimental work for a sufficient variation of each parameter to cover a meaningful range.

As this problem is a basically simple one in the fluid technology field, matters will be worse when complex fluid circuits will have to be studied experimentally and understood. Fluids employed will range from air at std. conditions to gaseous hydrogen at -250°F to hot combustion gases at 2000°F, in a pressure range from .1 psia to 1000 psia.

In this very confusing situation, in the absence of an adequate theoretical treatment, the aerodynamicist looks for his first basic tool, the Laws of Dynamic Similarity. The laws of similarity will allow building up an experimental solution of the problem with data from experiments under different sets of conditions.

The laws of similarity will allow the extrapolation of data under one set of conditions to another and different set of conditions, and will prescribe the correct conditions for a model experiment to be valid for a prototype.

The laws of similarity will also serve to classify quantitatively dynamic fluid regimes for generalized application to complex fluid circuits.

2.2.2 List of Dimensionless Parameters.

The following three dimensionless parameters have been found to be of basic importance for our problem:

1. Reynolds Number $R_e = \frac{U D \rho_0}{\mu_0}$

2. Acoustic Reynolds Number $R_{e_n} = \frac{C D \rho_0}{\mu_0}$

3. Stokes Number $S = \frac{\omega D^2 \rho_0}{\mu_0}$

where velocity of sound $C = \sqrt{k R_g T_g}$ or $\sqrt{n R_g T_g}$ (depending on heat transfer)

reference flow velocity $U = \frac{Q_0}{\frac{\pi}{4} D^2}$ (mean pipe velocity)

Other dimensionless parameters, which can all be derived from the first three, have been found useful in particular ways:

4. Strouhal Number $St = \frac{S}{R_e} = \frac{\omega D}{U}$

5. Longitudinal Acoustic Strouhal Number $St_{LA} = \frac{S}{R_{e_A}} \cdot \frac{L}{D} = \frac{\omega L}{C}$

6. Transverse Acoustic Strouhal Number $St_{TA} = \frac{S}{R_{e_A}} = \frac{\omega D}{C}$

Finally, if the mean pipe flow velocity is sufficiently high, fluid compressibility effect must be accounted for by the Mach number.

$$7. \text{ Mach Number } M_a = \frac{U}{C}$$

Fortunately in fluid control technology, pipe velocities are generally low.

Seven dimensionless parameters are listed above; this number is still too high for indiscriminate application to practical experimental work. Previous aerodynamic experience, both theoretical and experimental, will serve to demonstrate the particular usefulness of each parameter to the experimenter.

If the Mach Number is neglected, there are only three basic parameters, the classical Reynolds and Stokes Numbers and another version of the Reynolds Number comprising the acoustical velocity in the pipe (instead of the flow velocity).

A discussion will be given below for each parameter, with supporting experimental evidence and physical interpretation as required.

2.3 The Reynolds Number.

The Reynolds Number may be derived from dimensional analysis

$$R_e = \frac{U D}{\nu} \left[\frac{\text{ft}}{\text{sec}} \frac{\text{ft}}{\text{ft}^2} \right] = [0]$$

Furthermore, it acquires fundamental significance from the fact that it can be derived from the steady-state Navier-Stokes eqs. of viscous fluid motion.

The steady-state Navier-Stokes eqs. are written in cylindrical coordinates r and x , with axial flow symmetry for pipe flow, below:

$$\rho \left(v \frac{\partial v}{\partial r} + u \frac{\partial v}{\partial x} \right) = - \frac{\partial p}{\partial r} + \mu \left(\frac{\partial^2 v}{\partial r^2} + \frac{1}{r} \frac{\partial v}{\partial r} - \frac{v}{r^2} + \frac{\partial^2 v}{\partial x^2} \right)$$

$$\rho \left(v \frac{\partial u}{\partial r} + u \frac{\partial u}{\partial x} \right) = - \frac{\partial p}{\partial x} + \mu \left(\frac{\partial^2 u}{\partial r^2} + \frac{1}{r} \frac{\partial u}{\partial r} + \frac{\partial^2 u}{\partial x^2} \right)$$

where v is the velocity in the r direction

u is the velocity in the x direction

If now U , D and P are taken as references of velocity, length and pressure:

$$v^* = \frac{v}{U} \quad \text{and} \quad u^* = \frac{u}{U}$$

$$r^* = \frac{r}{D} \quad \text{and} \quad x^* = \frac{x}{D}$$

$$p^* = \frac{p}{P}$$

Then it is obtained for the steady-state Navier-Stokes eqs. after dividing each term by $\rho \frac{U^2}{D}$:

$$v^* \frac{\partial v^*}{\partial r^*} + u \frac{\partial v^*}{\partial x^*} = - \left[\frac{P}{\rho U^2} \right] \frac{\partial p^*}{\partial r^*} + \left[\frac{\mu}{\rho U D} \right] \left(\frac{\partial^2 v^*}{\partial r^{*2}} + \frac{1}{r^*} \frac{\partial v^*}{\partial r^*} - \frac{v}{r^{*2}} + \frac{\partial^2 v^*}{\partial x^{*2}} \right)$$

$$v^* \frac{\partial u^*}{\partial r^*} + u^* \frac{\partial u^*}{\partial x^*} = - \left[\frac{P}{\rho U^2} \right] \frac{\partial p^*}{\partial x^*} + \left[\frac{\mu}{\rho U D} \right] \left(\frac{\partial^2 u^*}{\partial r^{*2}} + \frac{1}{r^*} \frac{\partial u^*}{\partial r^*} + \frac{\partial^2 u^*}{\partial x^{*2}} \right)$$

The pipe flows can become similar only if the solutions expressed in terms of the coefficients $\left[\frac{P}{\rho U^2} \right]$ and $\left[\frac{\mu}{\rho U D} \right]$ are identical.

The first coefficient $\left[\frac{P}{\rho U^2} \right]$ is automatically satisfied in incompressible flow, leaving the coefficient $\left[\frac{\mu}{\rho U D} \right]$ as the criterion of similarity. This coefficient is the inverse of the Reynolds Number.

For the pipe problem, the Reynolds Number has been found indispensable for the correlation of steady-state pressure-loss data, regardless of pipe size, fluid velocity (flow rate) and fluid density and viscosity.

A pressure-loss coefficient may be defined as follows:

$$\frac{\Delta P}{\frac{1}{2} \rho U^2} = \lambda \frac{L}{D}$$

Figures 2.3-1 and 2.3-2 show the plot of λ against Re .

A "laminar" fluid regime may be defined up to $R_e = 2000$ and a "turbulent fluid regime may be defined from $R_e = 3300$. In the "transitional" area $2000 < R_e < 3300$ there is no clear correlation between λ and R_e .

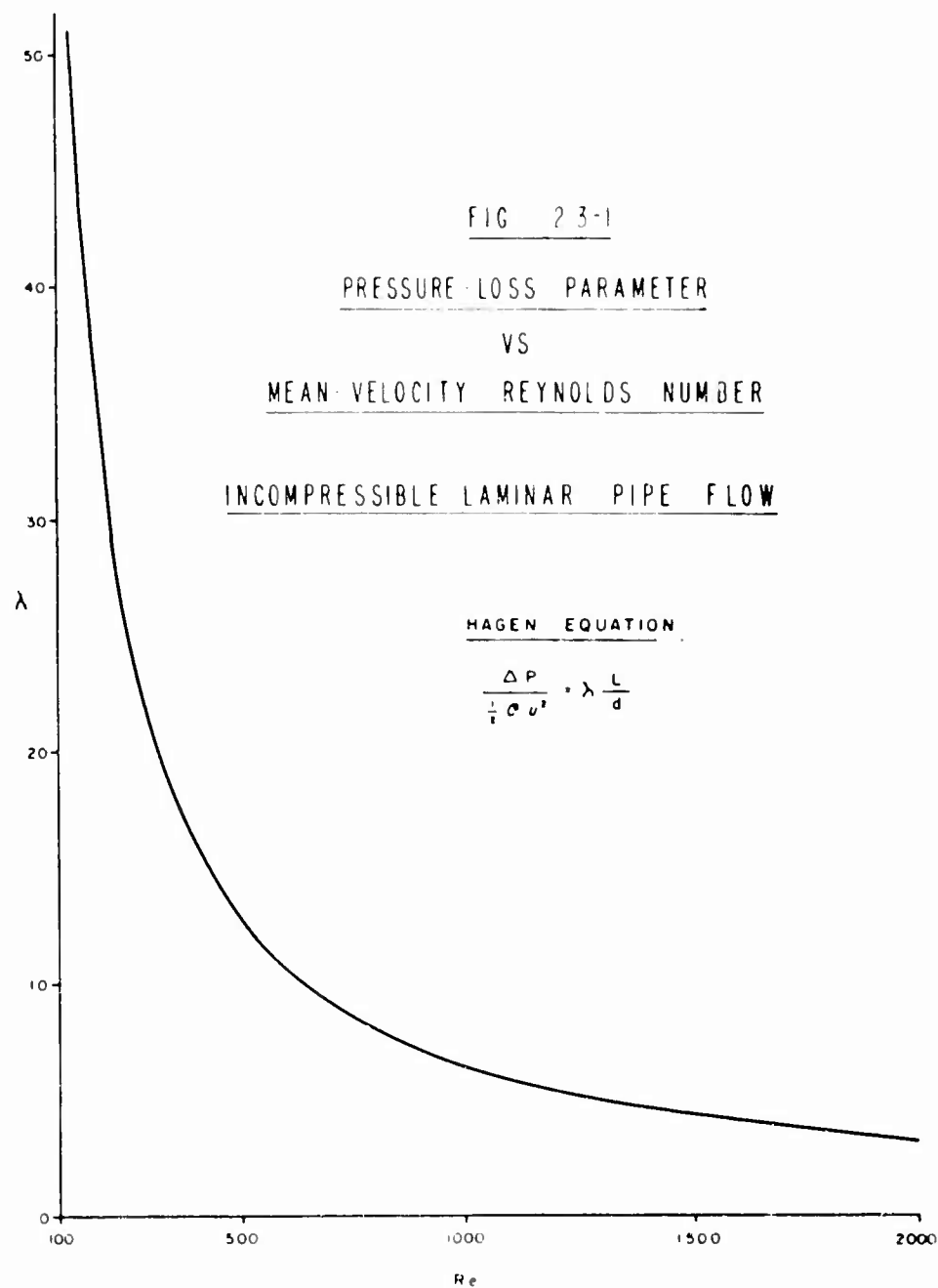
Analytically, for the laminar case the Hagen-Poiseuille law holds:

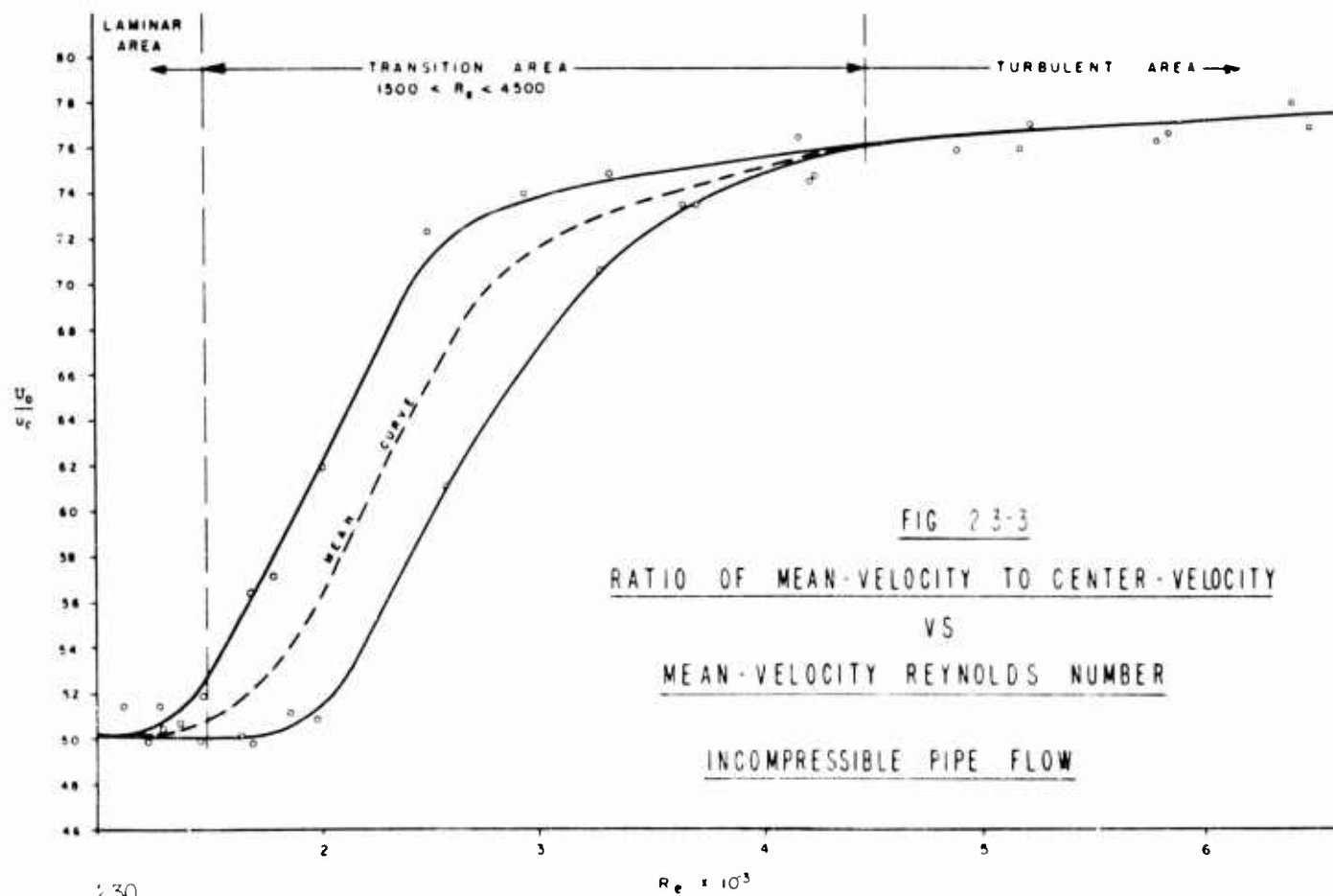
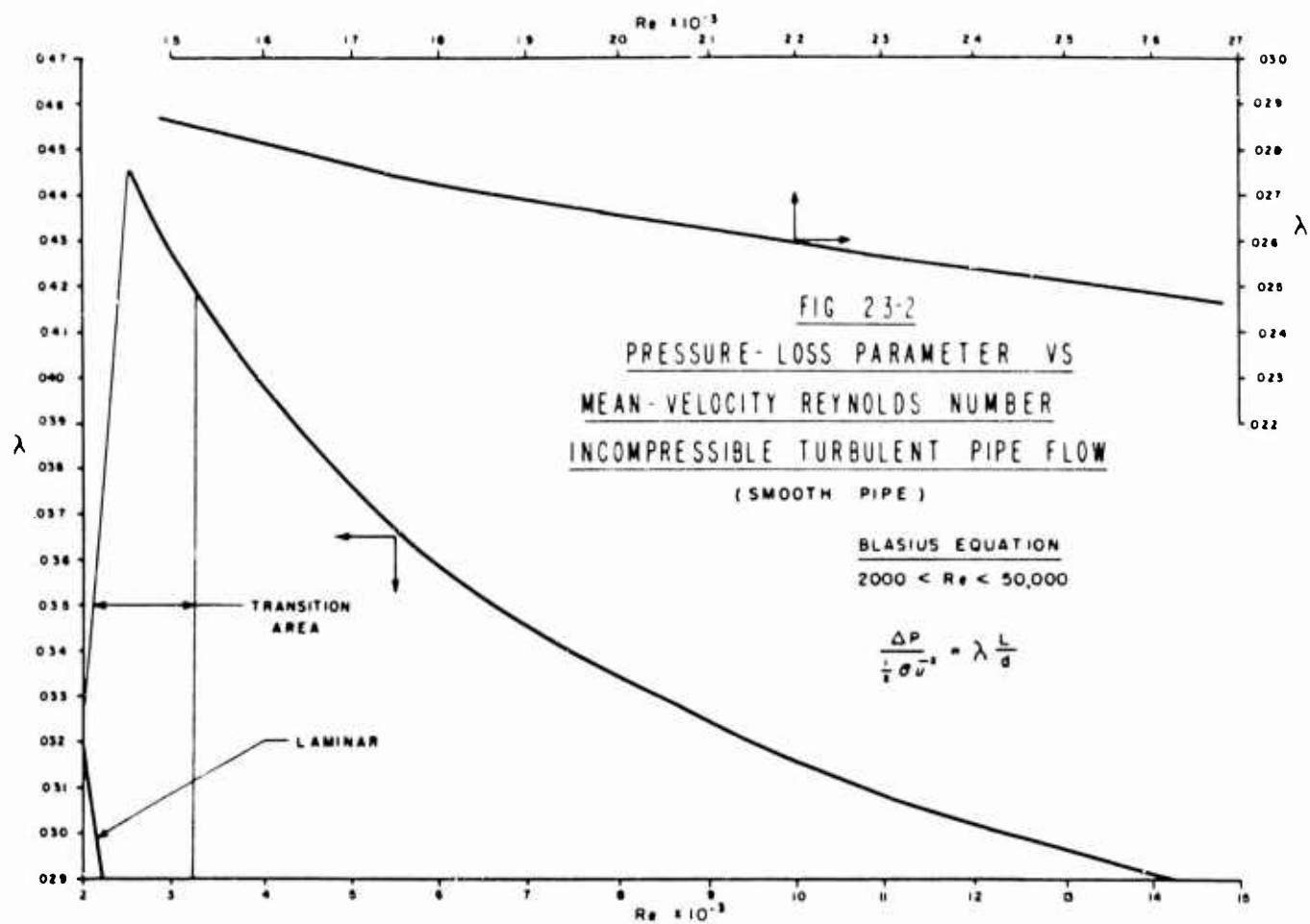
$$\lambda = \frac{64}{R_e}$$

and for the turbulent case the Blasius law holds up to $R_e = 50,000$:

$$\lambda = \frac{0.316}{R_e^{1/4}}$$

For both cases, λ is a function of R_e alone.





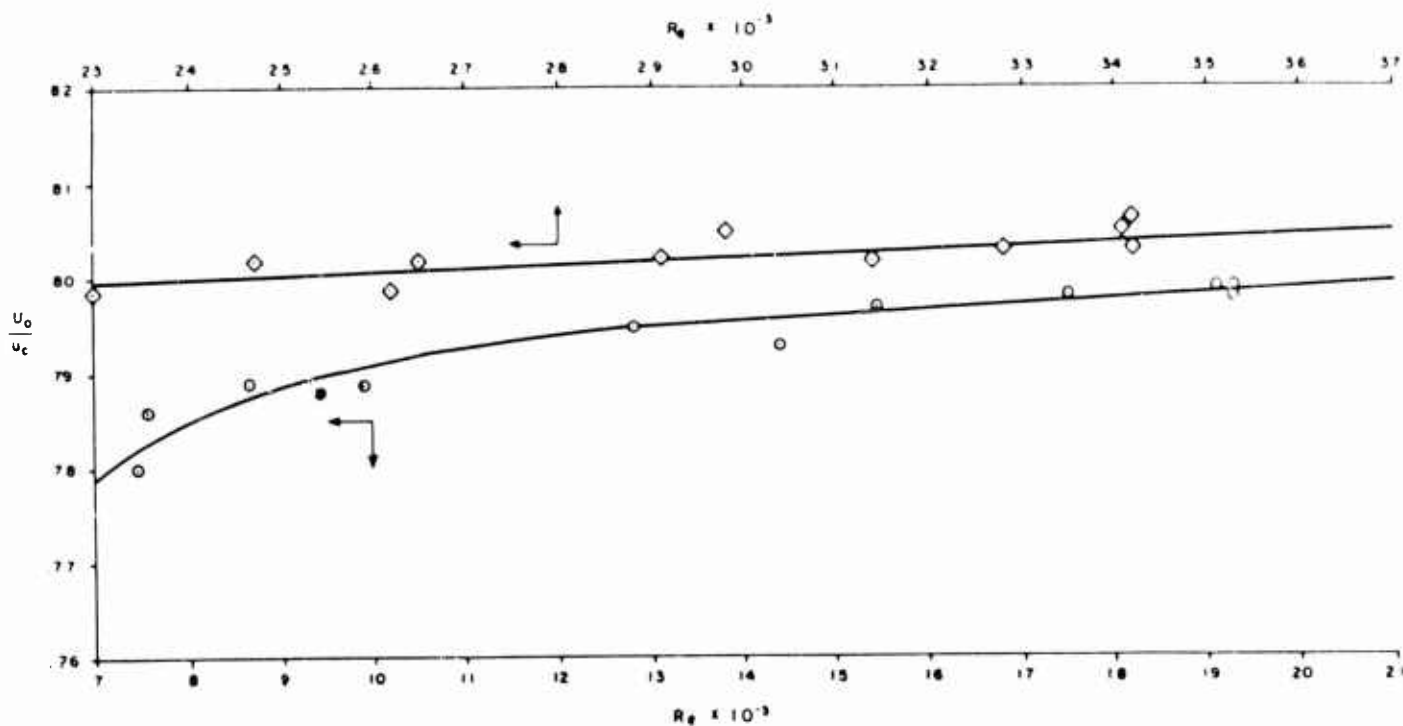


FIG 2.3-4

RATIO OF MEAN-VELOCITY TO CENTER-VELOCITY VS MEAN-VELOCITY REYNOLDS NUMBER
INCOMPRESSIBLE TURBULENT PIPE FLOW

Of interest in fluid technology instrumentation is the ratio of mean pipe velocity to center velocity, because in many cases a center measurement in a pipe must be made to yield total flow rate.

Again this ratio is only a function of Re , as shown in Figures 2.3-3 and 2.3-4. There is to be noted that in the laminar regime this ratio is constant and equal to 0.5, and that the transitional area is wider, from $Re = 1500$ to $Re = 4500$.

2.4 The Acoustical Reynolds Number

The Acoustical Reynolds Number may be derived from dimensional analysis:

$$Re_A = \frac{CD}{\nu} \left[\frac{\text{ft}}{\text{sec}} \frac{\text{ft sec}}{\text{ft}^2} \right] = [0]$$

It deviates from the classical Reynolds Number only by the use of the acoustical velocity C instead of the flow velocity U . Physically it can be interpreted as the ratio of acoustic inertia to viscous damping or as the limiting value of Re .

It generally appears in dynamic fluid analysis only as a modifier of the Stokes Number, in the form $\frac{S}{Re_A}$ and $\frac{S}{Re_A^2}$.

2.5 The Stokes Number.

The Stokes Number may be derived from dimensional analysis:

$$S = \frac{\omega D^2}{\nu} \left[\frac{t t^2 \text{ sec}}{\text{sec ft}^2} \right] = [0]$$

Furthermore, it acquires fundamental significance from the fact that it can be derived from the time-dependent vorticity transport equations.

These equations are transformations of the Navier-Stokes eqs. in terms of the vorticity vector. Physically the vorticity is the angular velocity of a fluid element. In cartesian coordinates x and y , with velocity components u and v :

$$\omega = \frac{1}{2} \left(\frac{\partial v}{\partial x} - \frac{\partial u}{\partial y} \right)$$

The two-dimensional time-dependent Navier-Stokes eqs. are reduced to:

$$\frac{\partial \omega}{\partial t} + u \frac{\partial \omega}{\partial x} + v \frac{\partial \omega}{\partial y} = \frac{\mu}{\rho} \left(\frac{\partial^2 \omega}{\partial x^2} + \frac{\partial^2 \omega}{\partial y^2} \right)$$

If the vorticity ω , the time t , the coordinates x and y and the velocities u and v are reduced to dimensionless ω^* , t^* , x^* , y^* , u^* and v^* by the introduction of reference quantities of frequency Ω , time T , length D and velocity V , then the vorticity equation will be governed by two dimensionless coefficients:

$$\frac{D}{\Omega T} \quad \text{and} \quad \frac{\nu}{D^2 \Omega}$$

The first coefficient is satisfied automatically while the second coefficient is the inverse of the Stokes Number.

Stokes' work antedates Reynolds' by more than thirty years, but for some reason the Stokes Number never achieved the popularity of the Reynolds Number. This is perhaps due to the fact that most fluid work has been directed toward steady-state phenomena.

For our pipe problem, the Stokes Number allows a physical interpretation as a dynamic damping index; it serves to classify dynamic fluid processes into arbitrary high-damping, intermediate-damping and low-damping regimes.

Experimentally, the Stokes Number will tell the investigator which frequency parameter to use to obtain a workable correlation for the amplitude attenuation ratio and the phase angle.

In conclusion, the Stokes Number is as basic to dynamic flows as the Reynolds Number is to steady-state flows.

2.6 The Strouhal Number.

The Strouhal Number may be derived from dimensional analysis:

$$St = \frac{\omega b}{U} \left[\frac{\text{ft sec}}{\text{sec ft}} \right] = [0]$$

It is not a primary parameter because it can be derived as the ratio ω/Re .

It does not contain viscosity and therefore it must be used either for theoretical "inviscid" flows or for conditions where the viscosity is negligible (as when the frequency is quite high). Also it has been found useful to correlate the frequency of self-oscillating fluid phenomena with the characteristics of the parent steady-state flow; here it would be plotted against Re .

An example of "inviscid" flow application is given in Figure 2.6-1, from the theoretical work of H. G. Elrod⁴, for pulsating flows in conical nozzles. The Strouhal Number is plotted against amplitude attenuation factor and phase angle for several subsonic Mach Numbers.

Obviously here the Stokes Number would not be applicable because of the absence of fluid viscosity from the analysis.

Two examples of self-oscillating fluid phenomena arising from steady-state flows are given in Figure 2.6-2 (the Karman Vortex Street) and in Figure 2.6-3 (typical edge-tone). In both figures the Strouhal Number is plotted against the Reynolds Number.

A third example of self-oscillating fluid phenomenon arising from steady-state flows is given in Figure 2.6-4 (acoustic gap radiation). Here the Strouhal Number is plotted against Mach Number, for a given range of Reynolds Number (laminar boundary-layer flow over the plate), because the Mach effect predominates.

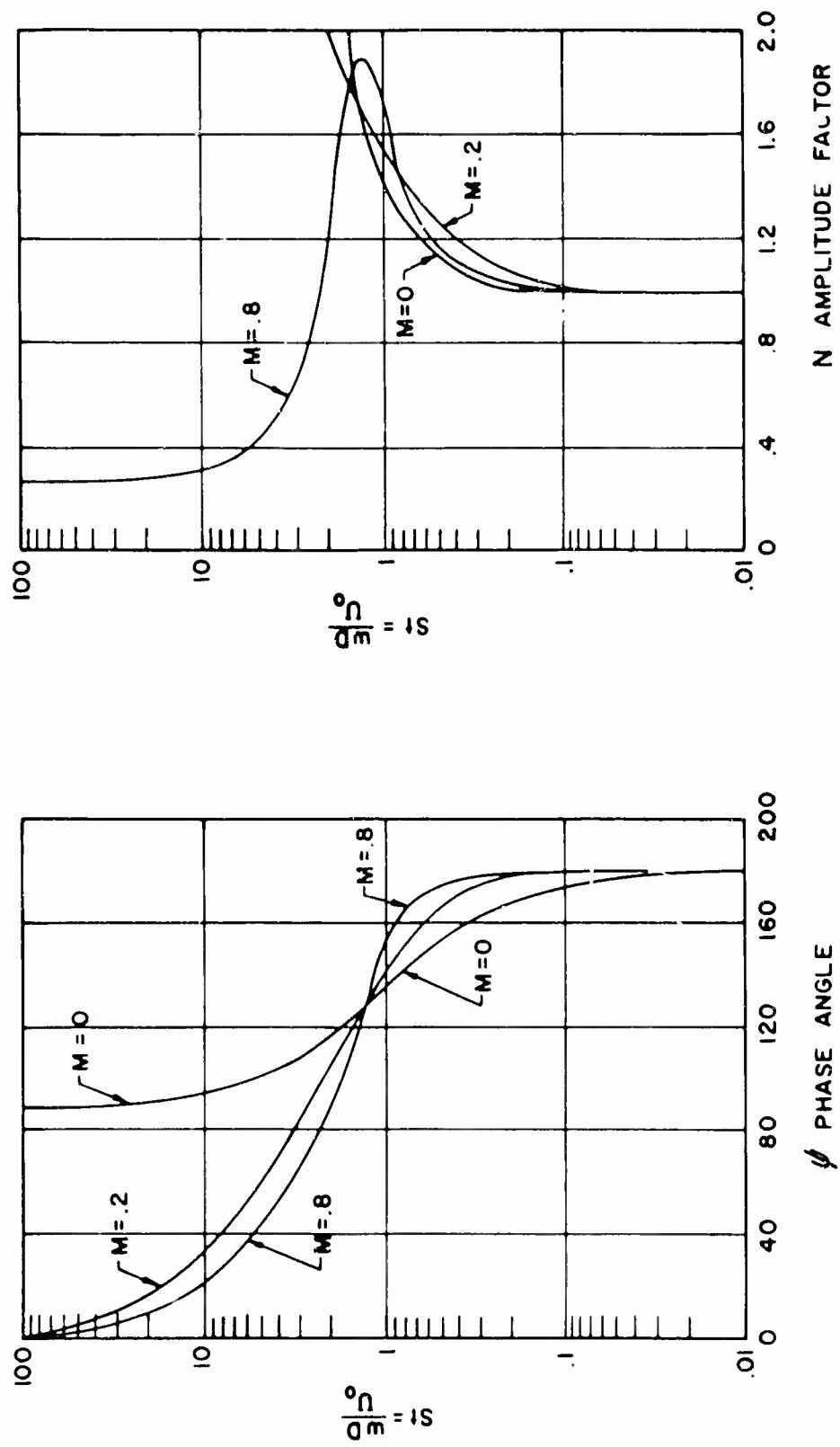
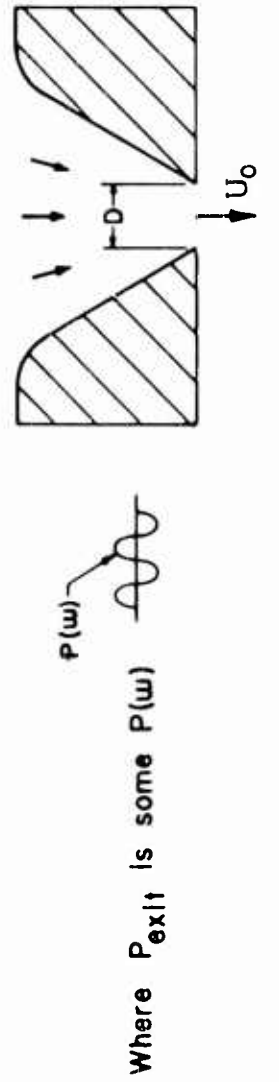


Fig. 2.6-1 Conical nozzle with sinusoidally fluctuating exit pressure



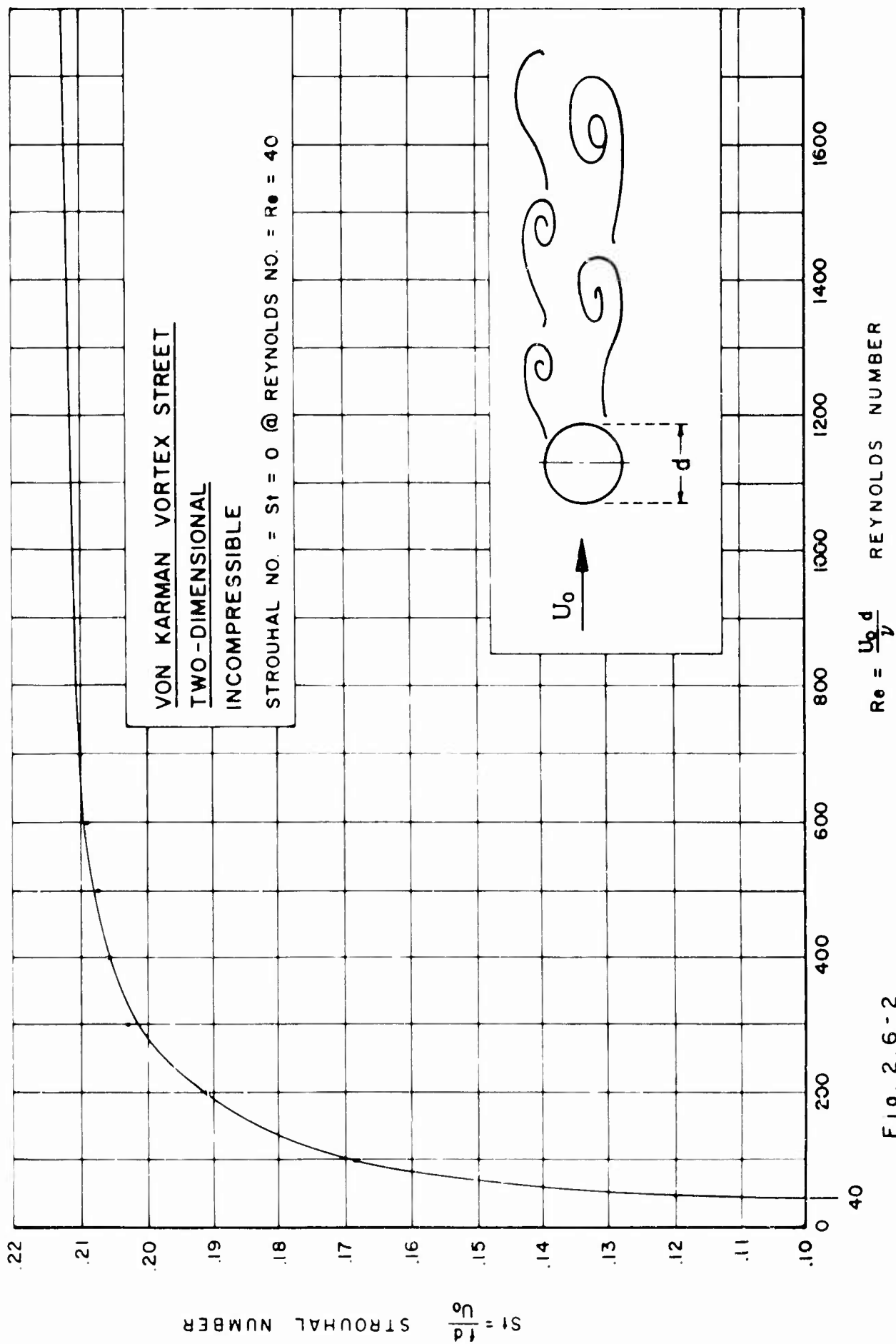


Fig. 2.6-2

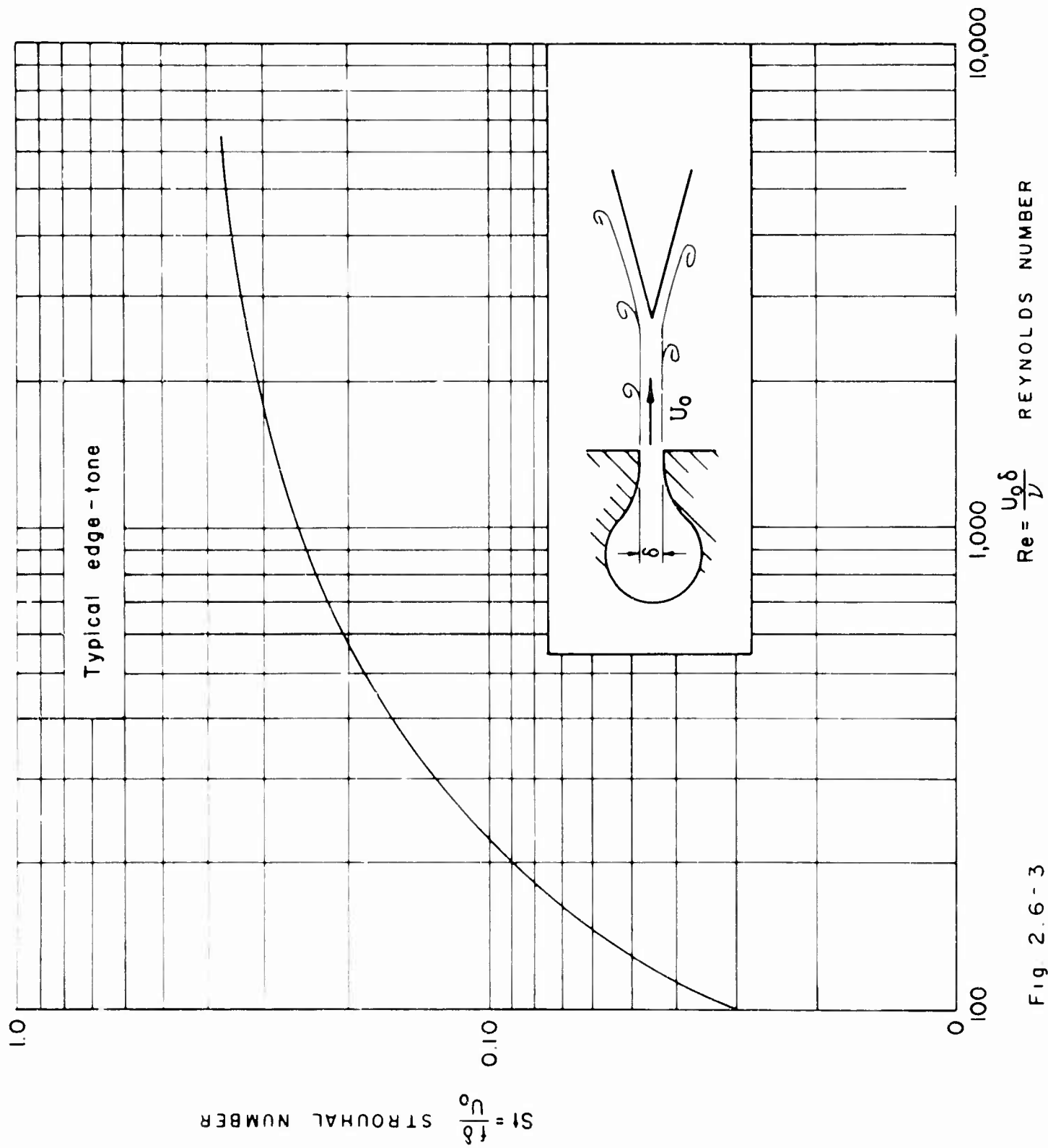


Fig. 2.6-3

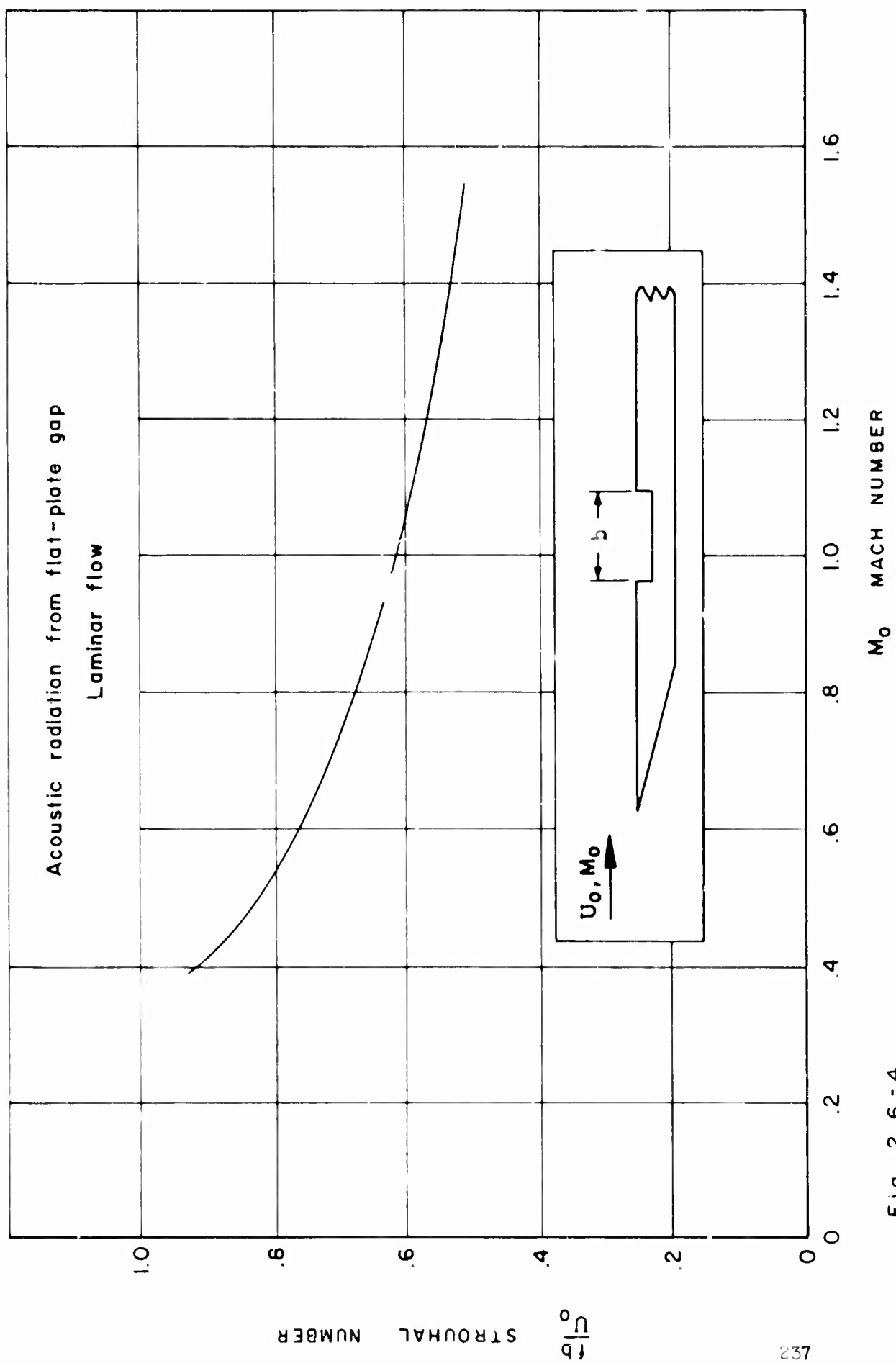


Fig. 2.6-4

2.7 The Longitudinal Acoustic Strouhal Number.

The longitudinal acoustic Strouhal Number is a special form of the Strouhal Number, where the pipe length L is used, rather than the diameter D , and the velocity of sound C is used, rather than the flow velocity U .

$$St_{LA} = \frac{\omega L}{C}$$

It can be derived from the Stokes Number, the Acoustic Reynolds Number, and the pipe aspect ratio.

$$St_{LA} = \frac{S}{Re_A} \cdot \frac{L}{D}$$

It is used as the frequency parameter in the low-damping regime, where the acoustic effects become predominant.

2.8 The Transverse Acoustic Strouhal Number.

The Transverse Acoustic Strouhal Number is a special form of the Strouhal Number, where the velocity of sound C is used, rather than the flow velocity U .

$$St_{TA} = \frac{\omega D}{C}$$

It can be derived from the Stokes Number and the Acoustic Reynolds Number:

$$St_{TA} = \frac{S}{Re_A}$$

It is used as a limiting criterion for the application of simple longitudinal-wave acoustic theory in a pipe because it predicts the onset of transverse acoustic waves.

The lowest transverse acoustical mode in a pipe is the first asymmetrical mode, which occurs at:

$$St_{TA} = 3.68$$

as shown by Wright and Miller⁵.

2.9 The Mach Number.

The Mach Number is the ratio of flow velocity U to the velocity of sound C . Above a Mach Number value of 0.2 to 0.3, the flow pattern will begin to change because of the fluid compressibility. In general pipe flow velocities are kept low ($M < 0.2$) to reduce pressure losses.

In the active amplifiers, however, analysis of the jet may require the application of Mach Number because velocities may be high, even supersonic.

3. Laws of Stokes - Reynolds Similarity.

For two pipe flows of equal $\frac{L}{D}$ ratio to be equivalent in both steady and dynamic states, the three basic dimensionless parameters #1, #2 and #3 must be equal. This, of course, applies if the flow velocity is low enough that Mach Number effects can be neglected. Otherwise four parameters must be kept equal.

Using subscript 1 for the one flow and subscript 2 for the other flow, it can be written:

$$Re = \frac{U_1 D_1 \rho_1}{\mu_1} = \frac{U_2 D_2 \rho_2}{\mu_2} \quad (1)$$

$$Re_A = \frac{C_1 U_1 \rho_1}{\mu_1} = \frac{C_2 U_2 \rho_2}{\mu_2} \quad (2)$$

$$S = \frac{\omega_1 D_1^2 \rho_1}{\mu_1} = \frac{\omega_2 D_2^2 \rho_2}{\mu_2} \quad (3)$$

From eq. (1):

$$\frac{\mu_2}{\mu_1} = \frac{U_2}{U_1} \frac{D_2}{D_1} \frac{\rho_2}{\rho_1} \quad (4)$$

From eq. (2):

$$\frac{\mu_2}{\mu_1} = \frac{C_2}{C_1} \frac{U_2}{U_1} \frac{\rho_2}{\rho_1} \quad (5)$$

From eq. (3):

$$\frac{\mu_2}{\mu_1} = \frac{\omega_2}{\omega_1} \frac{D_2^2}{D_1^2} \frac{\rho_2}{\rho_1} \quad (6)$$

Since all three eqs. must be valid by definition:

$$\frac{U_2}{U_1} \frac{D_2}{D_1} \frac{\rho_2}{\rho_1} = \frac{C_2}{C_1} \frac{D_2}{D_1} \frac{\rho_2}{\rho_1} = \frac{\omega_2}{\omega_1} \frac{D_2^2}{D_1^2} \frac{\rho_2}{\rho_1} \quad (7)$$

$$\begin{array}{lcl}
 \text{Therefore:} & \frac{U_2}{U_1} = \frac{C_2}{C_1} = \frac{\omega_2}{\omega_1} = \frac{D_2}{D_1} & (8) \\
 \text{and} & \frac{U_2}{U_1} = \frac{C_2}{C_1} = \frac{\omega_2}{\omega_1} = \frac{D_2}{D_1} & \\
 & \frac{C_2}{C_1} = \frac{U_2}{U_1} = \frac{\omega_2}{\omega_1} = \frac{D_2}{D_1} & \\
 & \frac{\omega_2}{\omega_1} = \frac{C_2}{C_1} = \frac{D_1}{D_2} = \frac{U_2}{U_1} = \frac{D_1}{D_2} & \\
 & \frac{D_2}{D_1} = \frac{U_2}{U_1} = \frac{\omega_1}{\omega_2} = \frac{C_2}{C_1} = \frac{\omega_1}{\omega_2} &
 \end{array}
 \left. \vphantom{\begin{array}{l} \\ \\ \\ \\ \end{array}} \right\} \begin{array}{l} \text{Stokes-Reynolds} \\ \text{Similarity Laws} \\ \text{for} \\ \text{Constant Fluid} \\ \text{Viscosity} \end{array} \quad (9)$$

Again from eq. (1):

$$\frac{U_2}{D_1} = \frac{U_1 C_1 \mu_2}{\mu_1 U_2 C_2} = \frac{U_1}{U_2} \frac{C_1}{C_2} \frac{\mu_2}{\mu_1} \quad (10)$$

and from eq. (2):

$$\frac{U_2}{D_1} = \frac{C_1 C_1 \mu_2}{\mu_1 C_2 C_2} = \frac{C_1}{C_2} \frac{C_1}{C_2} \frac{\mu_2}{\mu_1} \quad (11)$$

and from eq. (3):

$$\frac{U_2^2}{D_1^2} = \frac{\omega_1 C_1 \mu_2}{\mu_1 \omega_2 C_2} = \frac{\omega_1}{\omega_2} \frac{C_1}{C_2} \frac{\mu_2}{\mu_1} \quad (12)$$

Since all three must be valid by definition:

$$\frac{U_1}{U_2} \frac{C_1}{C_2} \frac{\mu_2}{\mu_1} = \frac{C_1}{C_2} \frac{C_1}{C_2} \frac{\mu_2}{\mu_1} = \left(\frac{\omega_1}{\omega_2} \right)^{\frac{1}{2}} \left(\frac{C_1}{C_2} \right)^{\frac{1}{2}} \left(\frac{\mu_2}{\mu_1} \right)^{\frac{1}{2}} \quad (13)$$

Therefore:

$$\frac{U_1}{U_2} \left(\frac{C_1}{C_2} \right)^{\frac{1}{2}} \left(\frac{\mu_2}{\mu_1} \right)^{\frac{1}{2}} = \frac{C_1}{C_2} \left(\frac{C_1}{C_2} \right)^{\frac{1}{2}} \left(\frac{\mu_2}{\mu_1} \right)^{\frac{1}{2}} = \left(\frac{\omega_1}{\omega_2} \right)^{\frac{1}{2}} \quad (14)$$

Thus:

$$\left. \begin{aligned}
 \frac{U_2}{U_1} = \frac{C_2}{C_1} &= \left(\frac{\omega_2}{\omega_1} \right)^{\frac{1}{2}} \left(\frac{\rho_1}{\rho_2} \right)^{\frac{1}{2}} \left(\frac{\mu_2}{\mu_1} \right)^{\frac{1}{4}} \\
 \frac{C_2}{C_1} = \frac{U_2}{U_1} &= \left(\frac{\omega_2}{\omega_1} \right)^{\frac{1}{2}} \left(\frac{\rho_1}{\rho_2} \right)^{\frac{1}{2}} \left(\frac{\mu_2}{\mu_1} \right)^{\frac{1}{4}} \\
 \frac{\omega_2}{\omega_1} = \left(\frac{U_2}{U_1} \right)^2 \frac{\rho_2}{\rho_1} \frac{\mu_1}{\mu_2} &= \left(\frac{C_2}{C_1} \right)^2 \frac{\rho_2}{\rho_1} \frac{\mu_1}{\mu_2} \\
 \frac{\mu_2}{\mu_1} = \left(\frac{U_2}{U_1} \right)^2 \frac{\omega_1}{\omega_2} \frac{\rho_2}{\rho_1} &= \left(\frac{C_2}{C_1} \right)^2 \frac{\omega_1}{\omega_2} \frac{\rho_2}{\rho_1} \\
 \frac{\rho_2}{\rho_1} = \left(\frac{U_1}{U_2} \right)^2 \frac{\omega_2}{\omega_1} \frac{\mu_2}{\mu_1} &= \left(\frac{C_1}{C_2} \right)^2 \frac{\omega_2}{\omega_1} \frac{\mu_2}{\mu_1}
 \end{aligned} \right\} \begin{array}{l} \text{Stokes-Reynolds} \\ \text{Similarity Laws} \\ \text{for} \\ \text{Constant} \\ \text{Pipe Diameter} \end{array} \quad (15)$$

Interpreting the results of eq. (9), it is seen that scaling procedures are prescribed for the velocity U , the velocity of sound C , the frequency ω and the pipe diameter D if the fluid viscosity μ is kept constant. The mass density ρ does not appear in the similarity laws for constant fluid viscosity and therefore it does not need to be considered.

The absolute temperature T enters into the problem through the velocity of sound $C = \sqrt{R_g T}$. The thermodynamic fluid properties k and R_g enter only through the velocity of sound, as shown above.

Interpreting the results of equation (15), it is seen that scaling procedures are prescribed for the velocity U , the velocity of sound C , the frequency ω , the fluid viscosity μ and the fluid mass density ρ if the pipe diameter D is kept constant.

The absolute temperature T enters into the problem through the velocity of sound $C = \sqrt{R_g T}$, through the temperature-dependent fluid viscosity μ and through the fluid mass density ρ .

The thermodynamic fluid properties k and R_g enter the problem through the velocity of sound, as shown above, and through the fluid mass density ρ .

The absolute pressure does not enter the problem except for a minor influence on μ .

It remains to demonstrate explicitly that both the steady-state characteristics (pressure-loss coefficient and transverse velocity distribution) and the dynamic characteristics (amplitude attenuation ratio and phase angle) are maintained between a model pipe flow (subscript 1) and a prototype pipe flow (subscript 2) if the Reynolds Number, the Acoustic Reynolds Number and the Stokes Number are kept constant.

It is well known and it has been summarized in section 2.3 that all steady-state characteristics are dependent only on the Reynolds Number (in the absence of Mach Number effects). In Reference 1, Chapter 2 it has been shown theoretically, after Ibrall⁶, that the amplitude attenuation ratio and the phase angle are functions (for a given geometry) of a parameter χ_{To} or Z and of the Stokes Number. The choice of χ_{To} or Z depends on the range of the Stokes Number.

$$\text{Now } \chi_{To} = \omega \frac{\mu_o}{n\rho_o} \left(\frac{L}{D}\right)^2$$

$$\text{However } \mu_o = \rho_o \nu_o$$

$$\text{and } \frac{n\rho_o}{\rho_o} = nR_g T_g = C^2 \quad (\text{polytropic velocity of sound})$$

$$\text{Thus } \chi_{To} = \omega \frac{\nu_o}{C^2} \left(\frac{L}{D}\right)^2$$

$$\text{and } \chi_{To} = \frac{S}{Re_A^2} \left(\frac{L}{D}\right)^2$$

It is seen that, since the $\frac{L}{D}$ ratio is constant by definition of geometric pipe similarity, then the parameter χ_{To} depends only the Stokes Number and the Acoustic Reynolds Number.

If these two numbers are constant, then χ_{To} will be constant.

$$\text{Furthermore } Z = \frac{\omega L}{C} = St_{LA} \quad (\text{the Longitudinal Acoustic Strouhal Number})$$

$$\text{and } Z = \frac{\omega L D^2 \nu}{C D^2 \nu} = \left(\frac{\omega D^2}{\nu}\right) \left(\frac{\nu}{CD}\right) \left(\frac{L}{D}\right)$$

$$\text{thus } Z = \frac{S}{Re_A} \left(\frac{L}{D}\right)$$

Again the parameter Z depends only on the Stokes Number and on the Acoustic Reynolds Number, the ratio $\frac{L}{D}$ being constant by definition of geometric pipe similarity.

Therefore, if the theory of Reference 1 is even qualitatively correct, all the flow characteristics, both steady-state and dynamic, are maintained if the three basic dimensionless parameters, Reynolds Number, Acoustic Reynolds Number and Stokes Number, are constant.

4. Conclusions.

It has been shown that the steady-state and dynamic flow of a viscous compressible fluid in a pipe depends only on three dimensionless fluid parameters, i.e. the Reynolds Number, the Acoustical Reynolds Number and the Stokes Number, plus the geometric pipe aspect ratio.

Similarity (scaling) laws have been derived for the case of constant fluid viscosity and for the case of constant pipe diameter. These will permit the extrapolation of experimental data, amplitude ratio and phase angle, to other sets of conditions.

5. List of References.

1. F. R. Goldschmied et al. "Analytical Investigation of Fluid Amplifier Dynamic Characteristics." Volume I
NASA CR - 244 1965.
2. H. L. Langhaar "Dimensional Analysis and Theory of Models"
Wiley, 1951.
3. L. I. Sedov "Similarity and Dimensional Methods in Mechanics"
Academic Press, 1959.
4. H. G. Elrod "The theory of Pulsating Flow in Conical Nozzles"
ASME Paper 62-WA-221, 1962.
5. D. V. Wright and D. F. Miller "Dynamics of Refrigeration Systems -
1. Introduction to Gas Vibrations."
Westinghouse Electric Corp. Sept. 3, 1957
Research Report 8-0527-R2.
6. A. S. Iberall "Attenuation of Oscillatory Pressures in Instrument
Lines."
NBS Research Paper RP 2115, July 1950.

HARRY DIAMOND LABORATORIES
Washington, D.C. 20438

A DEFINITION OF
THE MECHANICAL POTENTIAL NECESSARY TO A FLUID CIRCUIT THEORY

by

Joseph M. Kirshner

ARMY MATERIEL COMMAND

DEPARTMENT OF THE ARMY

ABSTRACT

This paper attempts to define the mechanical potential (the analog of the voltage) for a fluid circuit. From the energy equation, it is shown that for an ideal gas a logical possibility is

$$e = \frac{v^2}{2} + \int \frac{dp}{\rho}$$

where v = velocity,

p = pressure,

ρ = density, and the average is taken over the cross-sectional area.

INTRODUCTION

Since its recognition as a new technology, the field of interaction devices has advanced to the point where complexes containing over a hundred units have been successfully operated. To build up these systems, the techniques of the systems engineers and particularly of the electronic engineers are being adapted to fluid devices.

Unfortunately it is only for low fluctuation velocities that we can quantitatively apply many of these techniques. They are useful only as qualitative guideposts when finite amplitude waves are to be considered.

At this stage of development it is already obvious that a fluid circuit theory as elegant as electronic circuit theory is impossible. The "fluetic" engineer is always going to have to rely to a much larger extent on cut-and-try techniques than does the electronic engineer.

The phenomena which make fluid circuit theory much more difficult than electronic circuit theory are:

1. The fundamental equations are nonlinear.
2. Momentum must be taken into account.
3. Heat flow into and out of the circuit must be considered.
4. The amount of turbulence must be taken into account.
5. Last but not least, the voltage analog if it exists at all is not a thermodynamic property.

The Current Analog

Since the flow into a junction must equal the flow out in any kind of circuit theory, it is apparent that the current analog must obey the continuity equation, and therefore the current analog must be mass flow.

The Voltage Analog

The voltage analog is not nearly so obvious. If mass flow is the current analog, then the dimensions of the voltage analog should be

energy per unit mass. This rules out pressure, which is the obvious first choice, as the voltage analog. There is another reason for ruling out the pressure. The correct analogs when properly applied must obey the fluid equations. For example, current times voltage in an electronic circuit gives the same energy flow per unit time through the circuit as is obtained by use of Maxwell's equations.

To help define the voltage analog, it therefore seems reasonable to consider the energy equation for flow. For simplicity we assume circular symmetry, although the results hold for any duct.

The integral form of the energy equation is

$$\begin{aligned} \int_V \frac{\partial}{\partial t} \rho \left(u + \frac{v^2}{2} \right) dV + \int_A \rho \left(u + \frac{v^2}{2} + \frac{p}{\rho} \right) \mathbf{v} \cdot \mathbf{n} dA \\ + \int_A \mathbf{q} \cdot \mathbf{n} dA = \int_V \rho \mathbf{f} \cdot \mathbf{v} dV + \int_V \Phi dV \end{aligned} \quad (1)$$

where (as in figure 1):

V = volume of a section of duct
 A = boundary surface of the volume
 u = internal energy per unit mass
 \mathbf{v} = vector velocity
 ρ = density
 \mathbf{q} = heat flux through the walls
 \mathbf{f} = body force per unit volume per unit mass
 \mathbf{n} = unit vector perpendicular to the surface
 Φ = the viscous loss. For circular symmetry,

$$\Phi = 2\mu \left[\left(\frac{\partial v_r}{\partial r} \right)^2 + \left(\frac{v_r}{r} \right)^2 + \left(\frac{\partial v_z}{\partial z} \right)^2 \right] + \mu \left(\frac{\partial v_r}{\partial z} + \frac{\partial v_z}{\partial r} \right)^2 \quad (2)$$

where v_r and v_z = velocity components along r and z
 r = radial distance from axis of symmetry of the duct
 z = axial distance along the duct

For convenience, we restrict ourselves to ideal gases and drop the body force term. Then we can write for the duct element

$$\begin{aligned} \frac{d}{dz} \int_{A_1} \left(u + \frac{v^2}{2} + \frac{p}{\rho} \right) \rho \mathbf{v} \cdot \mathbf{n} dA + \frac{d}{dz} \int_V \frac{\partial}{\partial t} \rho \left(u + \frac{v^2}{2} \right) dV \\ + \alpha - \frac{d}{dz} \int_V \Phi dV = 0 \end{aligned} \quad (3)$$

where α is the rate of inward heat flow through the walls per unit length, and A_1 is the cross-sectional area of the duct at the axial position, z .

Now the integral containing ϕ is a measure of conversion of work into internal energy and there must exist a u' such that

$$\frac{d}{dz} \int_{A_1} u' \rho v \cdot n dA = \frac{d}{dz} \int_V \phi dV \quad (4)$$

Assuming no storage of energy (steady state), we have

$$\frac{d}{dz} \int_{A_1} \left(u + u' + \frac{v^2}{2} + \frac{p}{\rho} \right) \rho v \cdot n dA = \alpha \quad (5)$$

But

$$\left(u + u' + \frac{p}{\rho} \right) = T \int ds_r + T \int ds_i + \int \frac{dp}{\rho} \quad (6)$$

where ds_r and ds_i are the reversible and irreversible portions of the entropy change associated with heat and viscous effects, respectively; and therefore equation 5 becomes

$$\frac{d}{dz} \int_{A_1} \left[T \int ds_r + T \int ds_i + \frac{v^2}{2} + \int \frac{dp}{\rho} \right] \rho v \cdot n dA = 0 \quad (7)$$

Since we are interested in the change in mechanical power, we rewrite the equation to define mechanical power as follows.

$$\begin{aligned} \frac{dP_m}{dz} &= \frac{d}{dz} \int_{A_1} \left[\frac{v^2}{2} + \frac{dp}{\rho} \right] \rho v \cdot n dA \\ &= - \frac{d}{dz} \int_{A_1} \left[T \int ds_i \right] \rho v \cdot n dA \end{aligned} \quad (8)^*$$

where dP_m is the change in mechanical power and where the average is taken over the cross-sectional area. It is necessary to average since otherwise the pertinent terms cannot be removed from the integral.

*See NOTE, p 249

$$\frac{dP_m}{dz} = \frac{d}{dz} \left\{ \left[\frac{v^2}{2} + \int \frac{dp}{\rho} \right] \int_{A_1} \rho v \cdot n dA \right\} \quad (9a)$$

$$= \dot{m} \frac{d}{dz} \left[\frac{v^2}{2} + \int \frac{dp}{\rho} \right] \quad (9b)$$

From (9b) the change in potential, de , is given as

$$de = d \left[\frac{v^2}{2} + \int \frac{dp}{\rho} \right]$$

or the mechanical potential e is

$$e = \frac{v^2}{2} + \int \frac{dp}{\rho} \quad (10)$$

This points out the unfortunate fact that the mechanical potential as defined above is dependent on the state path and cannot be uniquely defined unless the thermodynamic process is given.

This potential energy is not necessarily the energy available at a branch since in making a turn into a branch, velocity gradients appear that convert mechanical energy into heat. It follows that there is a nonlinear impedance associated with a branch point. This impedance depends on the branching angle as well as on other geometric factors and on the fluid parameters. To some extent it may be possible by use of the momentum equations and friction factors to obtain a semiempirical theory for the impedance at a branch as a function of the relevant quantities.

In summary, the fluoric engineer must recognize the fact that the analysis of his circuits will always require graphical and computer techniques to a much larger extent than does the analysis of the electronic engineer's circuits.

NOTE: We can justify averaging this way if we make the reasonable assumption that the energy per unit mass, J , defined as

$$J \equiv T \int ds_i + \frac{v^2}{2} + \int \frac{dp}{\rho}$$

is a constant. In that case equation (7) becomes

$$\frac{d}{dz} (j\dot{m}) = 0$$

and

$$\dot{m} \frac{d}{dz} \left[\frac{v^2}{2} + \int \frac{dp}{\rho} \right] = - \dot{m} \frac{d}{dz} [T \int ds_i]$$

We then define mechanical power as

$$\frac{dP_m}{dz} = \dot{m} \frac{d}{dz} \left[\frac{v^2}{2} + \int \frac{dp}{\rho} \right] = \dot{m} \frac{d}{dz} \left[\frac{v^2}{2} + \int \frac{dp}{\rho} \right]$$

(It should be noted that J is the total energy per unit mass excluding any energy due to heat flow into or out of the duct. One would not expect the energy per unit mass to be constant or even independent of radius if the effect of heat flow were included.)

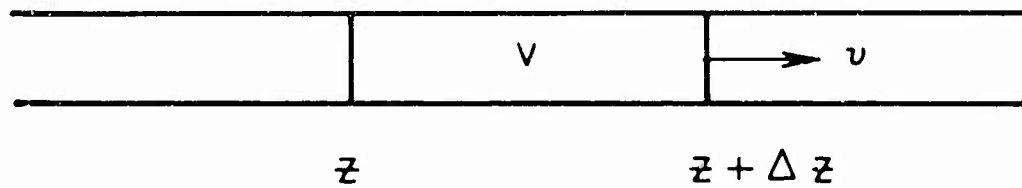


FIGURE 1

ON THE FUTURE OF DYNAMIC
ANALYSIS OF FLUID SYSTEMS

by

Forbes T. Brown

Assistant Professor
Department of Mechanical Engineering
Massachusetts Institute of Technology
Cambridge, Massachusetts

Abstract

Analyses of fluid amplifier systems at frequencies for which the basic amplification regions themselves exhibit significant dynamic effects have scarcely been done. The possibility of effective future analysis is discussed. Prime-element conceptual models of the components and systems are concluded to be the best approach, from the viewpoints of information content, intuitive feel, and ease of computation. Lumped, mixed lumped-distributed, and pure distributed models are compared, with emphasis on the last. Particular dynamic effects in jet amplifiers are discussed.

CRITERIA FOR ANALYSIS

Fluid amplifiers and systems thereof have been developed largely empirically. Moreover, nearly all of the analyses which have been performed consider only static behavior. Is dynamic analysis of these components and systems going to become viable and useful? If so, what role will it play? What form will it take?

Answers to these questions are attempted herein. Some of the material is in the realm of opinion and speculation and some in relatively explicit suggestions.

Several analytical studies have been published regarding the attachment of jets to flat plates or knife edges. But no direct quantitative use of the analyses seems to have been made. Why? Because the assumptions used to achieve a tractable solution usually are so restrictive that the results do not apply to any real device. Neglected factors include secondary flow (three-dimensional flow), the presence of flow splitters, cusps, opposite walls, and finite-length walls, and the detailed structure of the jet itself. If these restrictions are not made, the results are so complicated that we all recoil in horror and note, quite truthfully, that their use is not matched economically to our resources.

The above analyses are based largely on so-called first principles. The results are an equation or set of equations. Another approach is phenomenological; the characteristics of an element are measured, experimentally, and the results expressed analytically for later combination with other expressions to give, ultimately, semi-analytic predictions of system performance. But this approach has also usually failed because the phenomenological representation is so often incomplete. A very simple example is the incorrect prediction for the pressure gain of a cascade of fluid jet amplifiers as the product of the individual component pressure gains.

Has analysis actually been so barren? No, not really. In fact, we owe our most useful concept of similitude (including the use of the Reynold's, Mach, Prandtl, and Strouhal numbers) to analysis. Analytical idealizations have given us the perspective of potential possibility and inherent limitation which help us judge actual performance. And, most important, analysis has given us a physical insight into complex behavior (including the jet attachment phenomenon). Without this knowledge, or feeling, empirical development would be infinitely more haphazard than it really is.

The author has concluded that optimum analysis of complicated engineering structures should

- (i) include all the significant information necessary to meet the goal, and nothing else.
- (ii) provide physical insight as well as (or even more than) numerical answers.

These criteria may sound obvious, whereas in fact they can lead to profound results and decisions. Most analyses have in fact violated them. Some attempts were doomed from the start because Criteria (ii) was precluded in the problem statement (e.g., the highly quantitative wall-attachment studies). Others include insufficient information (e.g., the pressure-gain prediction) or excessive information (such as a broad-frequency-band model for a narrow-band problem). If the criteria cannot be reasonably well met, as often they cannot, recourse to experiment usually is advisable.

The question now is, what approaches to dynamic analysis are available, how do they compare with regard to the above criteria, and indeed are useful solutions potentially achievable. Certainly, if both criteria can be reasonably well satisfied, a most significant improvement in the rate of development of the fluid amplifier field would occur.

TYPES OF SOLUTION REPRESENTATIONS

Problems with undetermined parameters are assumed here, for if all parameters are prescribed beforehand, we lose immediately too much of the physical insight (Criteria (ii)) upon which we insist.

Three general types of solution representations (models) can be identified with undetermined-parameter problems:

1. Mathematical (e.g., an equation or transfer function or set thereof).
2. Functional (block or signal flow) diagram.
3. Reticulation (sub-division) into network of interconnected prime elements.

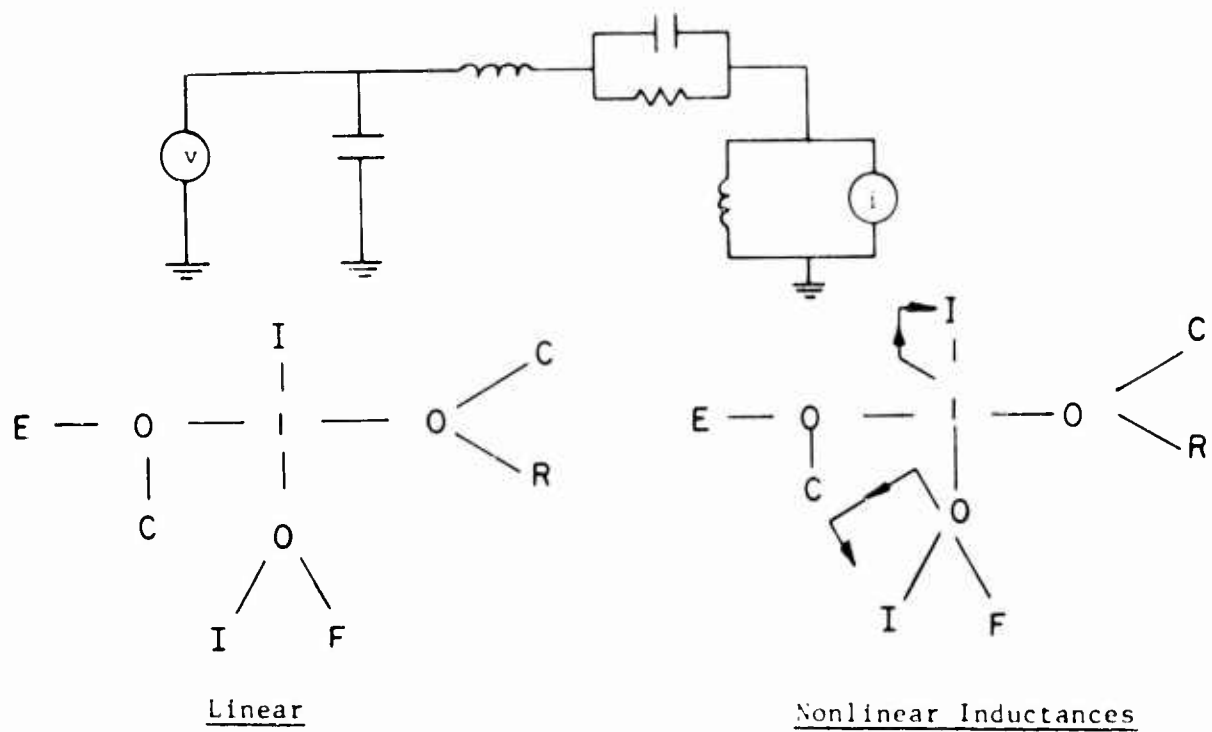
Presumably items 1 and 2 are familiar to the reader. Item 3 has its most familiar example in the equivalent (electrical) circuit diagram. Here the resistors and capacitors, etc., may or may not represent physically salient objects, but in any case they do represent physically real resistance and capacitance, etc., or their analogs.

The ubiquity of circuit diagrams attests to their values of insight and communication. Even non-electrical constructs are thus modeled by analogy, even when the available standard building blocks are not particularly appropriate. Consequently, the author feels that modeling in terms of ideal prime elements is optimum for fluid systems as well as other systems. But the elements need not be the standard lumped electrical analogs, as shown below.

One can readily go from a prime-element model to a signal-flow diagram or mathematical function, should this become appropriate for actual computation with a particular problem. The reverse process, however, is generally extremely obscure. Signal-flow diagrams have their origin and forté in dealing with a special degenerate class of problems in which signals or efforts (e.g., voltages) are unaffected by the associated flows (e.g., currents). When this condition does not apply to the majority of the ports of a system, such as in fluid amplifier systems, the prime-element model is superior. Degeneracies then can be handled explicitly, as they are in electrical circuit diagrams in the form of voltage and current sources.

LUMPED MODELS

Electrical circuit diagrams usually are composed of lumped linear elements. In Fig. 1 we see a very simple system expressed also in terms of the bond graph devised by Prof. Henry M. Paynter¹ at M.I.T. The symbols R for resistance, L for inertance (inductance), and C for compliance (capacitance) normally imply the ordinary linear relationships between the effort and flow variables, without distinguishing whether the actual



(a) Simple electric system and bond graph equivalents

(b) Other lumped elements:

transformer:	$\frac{e_1}{f_1}$	TF	$\frac{e_2}{f_2}$	m is dimensionless	}	$e_1 = m e_2$
transducer:	$\frac{e_1}{f_1}$	TD	$\frac{e_2}{f_2}$	m is dimensional		$f_1 = \frac{1}{m} f_2$
gyrator:	$\frac{e_1}{f_1}$	GY	$\frac{e_2}{f_2}$			$e_1 = m f_2$
threeport:	—	TRI	—			$f_1 = \frac{1}{m} e_2$
				necessary for amplifiers, modulators		

Fig. 1 Lumped Elements

system is electrical, mechanical, fluid, or mixed. The connections are indicated with bars or bonds, and the junctions by 0 if the associated flows sum to zero (a flow junction, as at an electrical junction) and by 1 if the efforts sum to zero (an effort junction, as with series combinations of elements). The symbols E and F represent effort and flow sources, respectively.

Bond graphs are introduced here simply to allow other elements, which have no direct electrical circuit symbol, to be used. Examples include the ideal lossless transformer, — TF —, transducer, — TD — gyrator, — GY —, and the element which composes the heart of amplifiers and modulators, the three-port, (— TR1 —). Moreover, every element has a modulus (more than one in the case of the three-port) associated with it (e.g., the value of a resistance, or the transformation factor of a transformer), and nonlinear systems are distinguished from linear systems simply because some of the moduli are not constant, but are functions of the state of the system. This can be indicated, as also shown in Fig. 1, by directed lines (indicated with arrows) with which particular functional relationships are associated.

The bond graph form discussed here is not unique;* the point is that any proper reticulation into a limited class of prime elements conveys clearly to the practiced observer the assumptions which have been made and allows automatic programming of either an analog or digital computer to solve for particular responses. If the system is comprised of lumped elements only, as above, the computation is direct. But fluid amplifiers also contain wave-like transmission lines, which are distributed rather than lumped.

MIXED LUMPED - DISTRIBUTED MODELS

Bilateral delay lines, which can represent fluid lines, can also be considered a prime element of a bond diagram and are indicated by — TM — (for "transmitter"). The efforts and flows e_1 and f_1 at one end of any

*Professor Paynter has also devised bond graphs based on a minimum set of element types, only three in number, plus activation.

symmetric element are related to the efforts and flows e_2 and f_2 at the other end by

$$\begin{bmatrix} e_1 \\ f_1 \end{bmatrix} = \begin{bmatrix} \cosh \Gamma & Z_c \sinh \Gamma \\ \frac{1}{Z_c} \sinh \Gamma & \cosh \Gamma \end{bmatrix} \begin{bmatrix} e_2 \\ f_2 \end{bmatrix} \quad (1)$$

For uniform lines Γ is known as the propagation operator and Z_c as the characteristic impedance. Both are operators or functions of frequency. We will consider only the pure delay line, however, for which

$$\Gamma = T \frac{d}{dt} \quad \text{or} \quad j \omega T$$

where T is the delay time, ω is frequency, d/dt is the time derivative operator, and Z_c is a real constant resistance.

In this special case of pure delays, the use of wave scattering variables is most helpful. If the oppositely propagating waves are represented by u and v ,

$$u_{1,2} = \frac{1}{\sqrt{Z_c}} e_{1,2} + \sqrt{Z_c} f_{1,2} \quad (2)$$

$$v_{1,2} = \frac{1}{\sqrt{Z_c}} e_{1,2} - \sqrt{Z_c} f_{1,2}$$

which when combined with Eq. (1) shows that

$$\begin{bmatrix} u_2 \\ v_2 \end{bmatrix} = \begin{bmatrix} e^{-T \frac{d}{dt}} & 0 \\ 0 & e^{-T \frac{d}{dt}} \end{bmatrix} \begin{bmatrix} u_1 \\ v_1 \end{bmatrix} \quad (3)$$

This result, expressed graphically² in Fig. 2, is directly useful for analog or digital computer representation of the delay line. The terms $e^{-Td/dt}$ simply represent the pure delays of the oppositely travelling waves. Since these delays are not readily achieved on analog machines, digital computation is usually called for.

Digital solution of mixed lumped and pure-delay systems, represented by differential-delay equations, has been discussed by Koepke.³ It is inefficient and unnecessary to compute the state of the system for nearly

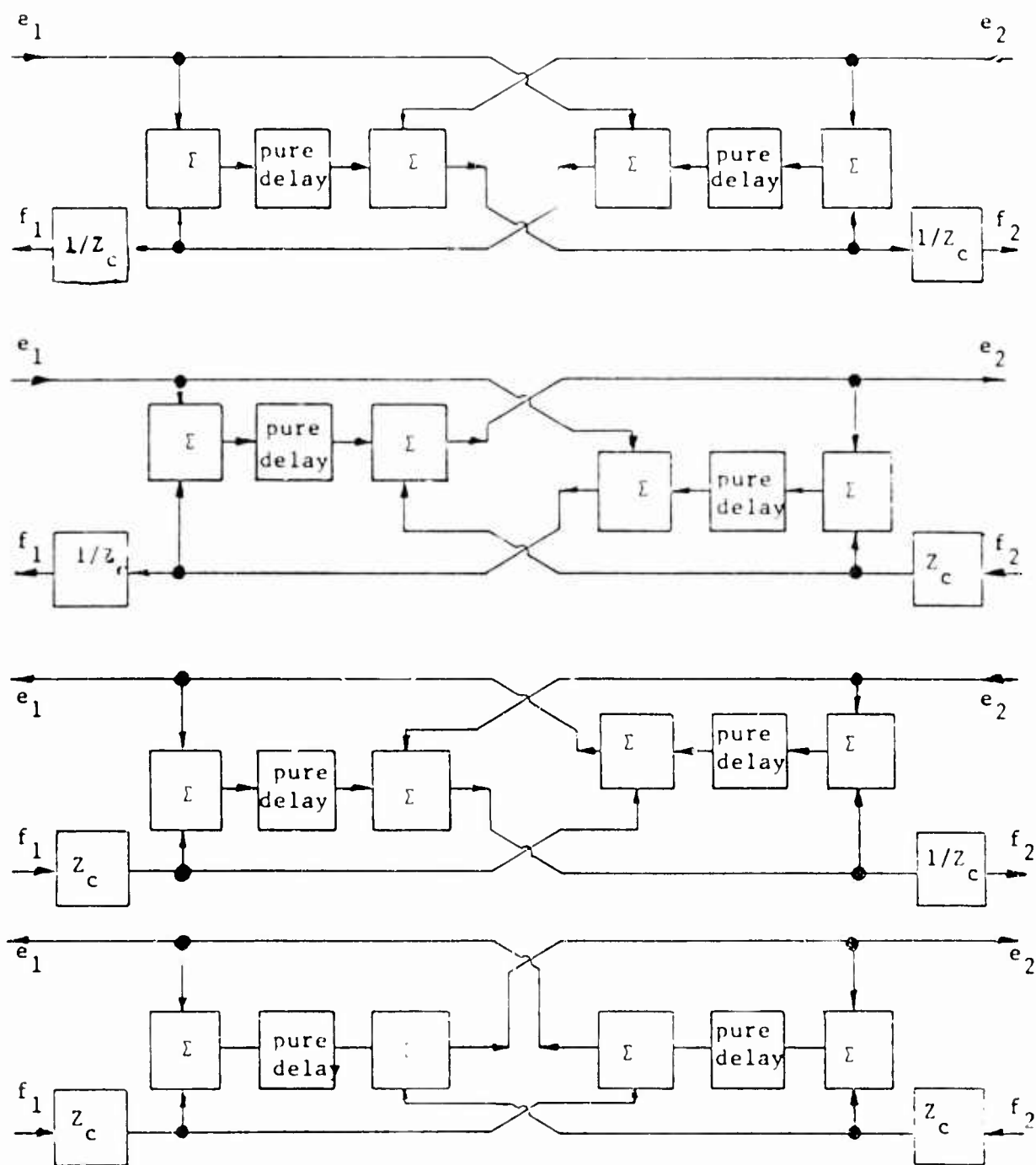


Fig. 2 Computational Diagrams of Bilateral Pure Delay
(after Paynter and Ezekial)

infinitesimal time intervals, compared with the various time constants and delays. Rather, long intervals should be chosen. But this requires the state of the system for a large number of consecutive solution clock times to be stored in order to compute the next state solution. This complicates nearly any problem way beyond the realm of hand computation and requires significant computer storage and time. Nevertheless, it is a powerful technique. And the computation of the state of each part of a complex system is usually far better than use of a single functional transfer function which is extremely complicated and only gives the solution at a single point in the system.

REDUCTION TO LUMPED SYSTEM

If the delay lines can be adequately replaced by a few lumped compliances and inertances, the model becomes entirely lumped and solutions are much easier to compute. For a limited frequency band, a single pi or tee network of these lumped elements, shown in Fig. 3, is quite adequate. A double or triple pi or tee ladder can be used to achieve good modeling over wider frequency bands (which need not, incidentally, be centered at zero frequency).

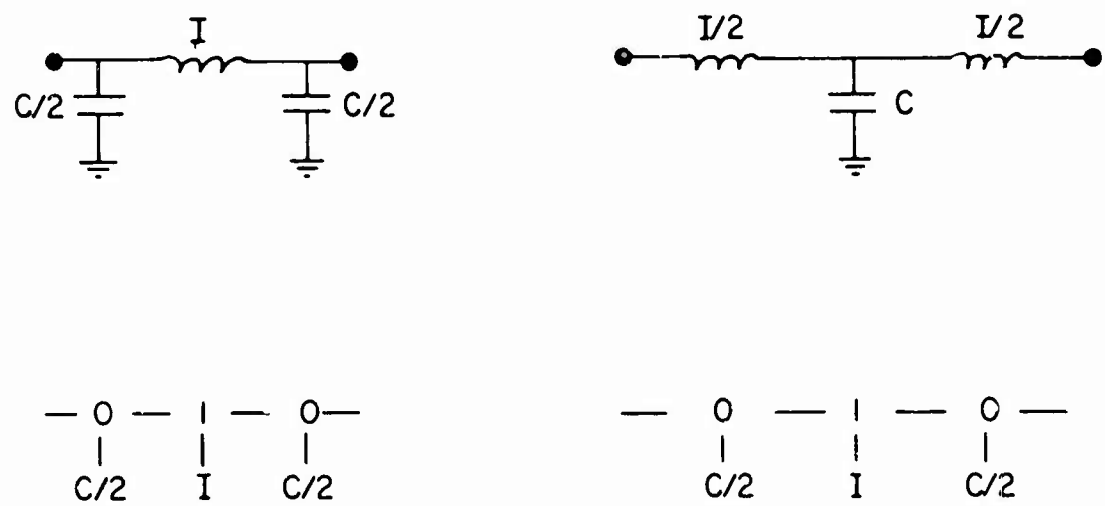


Fig. 3 Single Ideal Pi and Tee Models of Delay Line

Criterion (i) of optimum analysis insists upon not complicating the model and/or the solution computation with extraneous information. Consequently, if the frequency band of interest is so limited that a simple ladder structure suffices, it probably should be used. But an alternative approach is sometimes superior.

REDUCTION TO PURE-DELAY SYSTEM

Just as it is possible to model any system with only lumped dynamic elements, it is also possible to model any system with only distributed dynamic elements. Further, if all nonlinearities and nonsymmetries are static, the only dynamic elements needed are the pure bilateral delays.* Varying the time delays and characteristic impedances serves the same function as varying the compliances and inertances (not respectively) or lumped models. Losses are represented in the static elements, which are the generally resistive, nonlinear, and active junctions.

A particularly simple example is shown in Fig. 4. The fundamental simplifications are two-fold. First, the various delay times are all simple multiples of a common delay time. If the ratios of the various delay times were irrational, the solution process would become greatly more complicated; for one thing, an order-of-magnitude more state information would have to be stored. However, any desired degree of accuracy can be achieved by approximating all these ratios with ratios of integers. Then an overall synchronism of waves results, and it becomes very simple to compute the state of the system at time intervals equal to the common-denominator time delay or any multiple thereof.

The second simplification, which is not necessary, is to assume linear (but generally active) junctions. In this case the state at time kT is related to the state at time $(k-1)T$ by the simple invariant matrix relationship given in Fig. 4. If it is desired to compute the state vector less frequently, to save computation time, the square matrix can be raised to the integer power corresponding to the number of base delay-times in the desired computing interval. No error whatsoever is introduced by this procedure.

* Non-symmetric delays can also be used to represent non-symmetric dynamic properties. Hence, nearly any system can be effectively modeled.

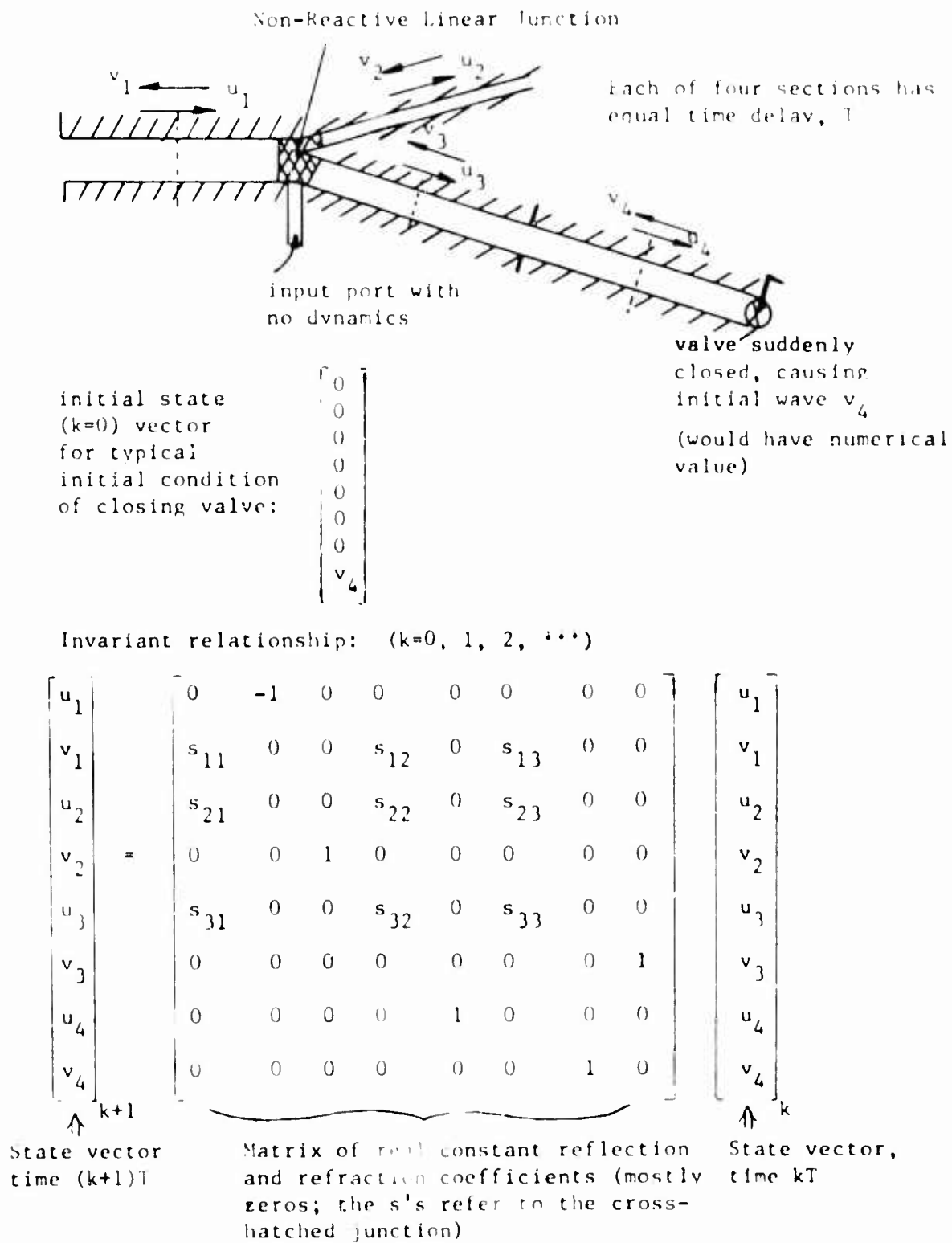


Fig. 4 Simple Example of Pure-Delay Model

Bistable fluid jet amplifiers are not linear, of course, and the matrix relationship does not apply. However, a digital computer can handle the appropriate nonlinear relation with little extra effort; the basic advantage of clock-synchronism remains, although it is no longer possible to calculate the state of the system only at infrequent intervals, rather than at the common-denominator-delay interval. And note, again, that the junctions can be active, that is, have power inputs not represented by the delay lines.

The pure-delay system model is the simplest computationally, allowing even hand calculation if the system is linear. Although it probably conveys somewhat less feel to the engineer than the mixed lumped-delay model, it might well prove to be the generally most useful dynamic model for describing fluid jet amplifiers.

PRESENT KNOWLEDGE OF THE DYNAMICS OF FLUID AMPLIFIERS

The closest published approach known to the author, toward a description of the dynamics of a fluid jet amplifier in terms of a prime-element reticulation, is by Belsterling and Tsui.⁴ A beam-deflection proportional amplifier is represented by impedance elements and ideal amplifiers. Dynamic modeling is limited to incremental differential operation; the rather simple model includes resistances, compliances, and an ideal amplifier with a pure time delay. Unfortunately, experimental data apparently corroborated reasonably well with the dynamic model at non-static conditions only when volumes were added to the output legs; no other comparison is offered. These volumes would strongly tend to mask the dynamics of the fluid amplifier itself. Reportedly these pioneering results have been subsequently improved, but the work is not yet published.

The author expects very shortly to have "black box" data for similar amplifiers⁵ which can be very helpful in constructing a prime-element reticulation. Such phenomenological testing must be used in conjunction with first-principle reasoning, however.

D. Letham and H. Fox⁶ have modeled a proportional amplifier of the impact-modulator type. The lumped elements include one dynamic element, a capacitor analog. Again, however, experimental results were inconclusive.

W. Boothe⁷ has used the transfer-function approach to represent a beam-deflector proportional amplifier. Although no prime-element model is directly given, the equivalent model would have fluid inertance in the control and output legs, plus a unilateral pure delay in the jet. Data are inconclusive.

The above approaches tend to model only the simpler passive fluid line and volume appendages of the jet amplifiers, plus a nearly negligible transport delay. This more obviously is misleading for bistable amplifiers, which are more complex dynamically as well as statically than proportional amplifiers. Working partly with the author, R. Gurski has made a rather extensive study⁸ of the simple single-control knife-edge pneumatic bistable amplifier shown in Figure 5.

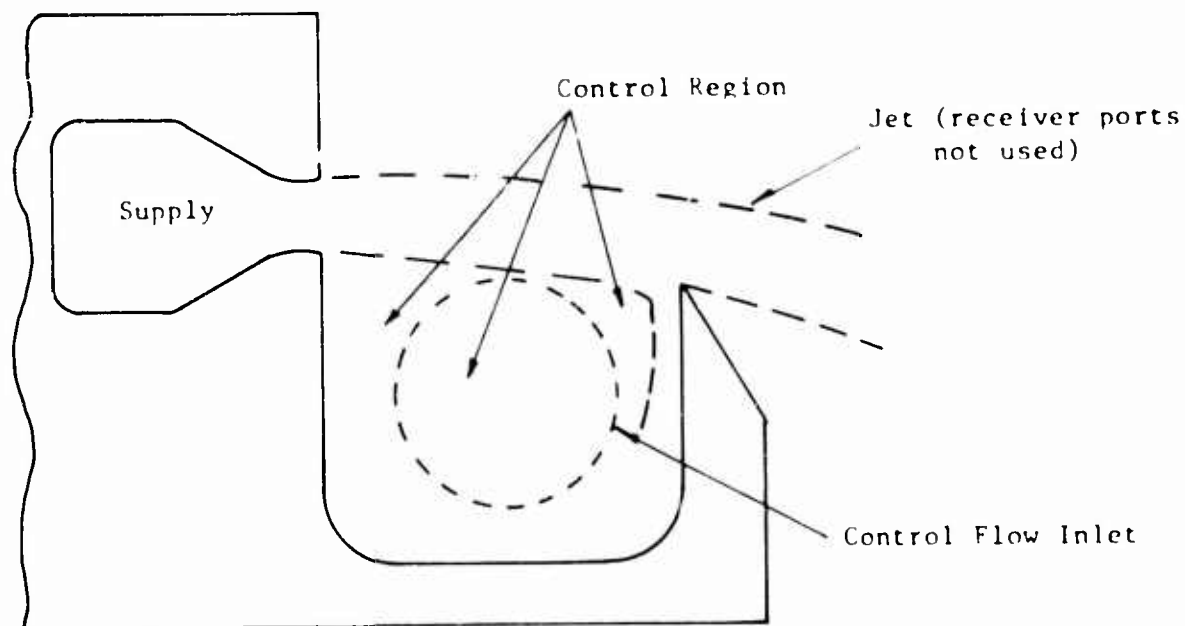


Fig. 5 Knife-Edge Amplifier Of Gurski (Schematic)

The first half deals with the static behavior, most particularly the complex flow in the vicinity of the knife edge. The second half deals with the dynamics.

The vortex in the control region constituted the only significant dynamic factor in the frequency range of normal operational interest. If control inputs were varied too rapidly, both theory and experiment showed that the jet would be harder to deflect. The work indicates that delays in the frequency response of bistable fluid jet amplifiers are primarily associated with vortical flows.

At higher frequencies the linear inertia of the jet and surrounding fluid coupled with the jet transport and the pumping effect resulting from the displacement of the jet become important. It is demonstrated both experimentally and analytically that instabilities can occur because of these phenomena. The frequency of these oscillations is so high that in practice they are undoubtedly usually dismissed as "noise." The compressibility effect in the control region was found to be insignificant except at very high frequencies indeed.

Criterion (1) would suggest that not all of the above phenomena would need to be included in a minimal model which would only have to apply to a limited frequency range.

CONCLUSIONS

Extremely useful prime-element dynamic models of linear and nonlinear fluid amplifiers and logic elements should be achievable by concerted efforts, using a marriage of first-principle theoretical and phenomenological experimental techniques. Many complex phenomena in the immediate vicinity of the jet can be included. Lumped, pure delay, and mixed models offer different compromises between the physical feeling they impart and the ease with which they can be realized computationally. All, however, are superior to mathematical or signal-flow-diagram representations.

The first use of these models would be to aid the synthesis of practical systems from given elements.

The second use would be to focus attention to those detailed phenomena which limit dynamic performance, and consequently hopefully to significantly improve the components themselves as well as their matching.

REFERENCES

1. H. M. Paynter, "Analysis and Design of Engineering Systems," M.I.T. Press, 1963.
2. H. M. Paynter and F. Ezekiel, "Computer Representations of Engineering Systems Involving Fluid Transients", Trans. ASME, v. 79, No. 8, November 1957, pp. 1840-1850.
3. R. W. Koepke, "On the Control of Linear Systems with Pure Time-Delay", 1964 Joint Automatic Control Conference, pp. 397-403 of preprints.
4. C. A. Belsterling and K. C. Tsui, "Application Techniques for Proportional Pure Fluid Amplifiers", Proc. of Fluid Amplification Symposium, Harry Diamond Laboratories, Washington, D.C., v. 1, p. 163-189.
5. F. T. Brown, S. D. Graber, R. E. Wallhagen, "Investigation of Stability Predictions of Fluid Jet Amplifier Systems", NASA Report NASA CR 54244, October 30, 1964, plus later as yet unnumbered reports.
6. F. Goldschmied, H. Fox, D. L. Letham, "Analytical Investigation of Fluid Amplifier Dynamic Characteristics", NASA Report N65-19772, v. 11, 30 December 1964
7. W. A. Boothe, "A Lumped Parameter Technique For Predicting Analog Fluid Amplifier Dynamics", 1964 Joint Automatic Control Conference, pp. 534-540 of preprints.
8. R. J. Curski, "Static and Dynamic Modeling of a Pressure-Controlled Subsonic Fluid Jet Modulator", Sc.D. Thesis, Engineering Projects Lab, M.I.T., Cambridge, Massachusetts, May 1965.

AN APPROACH TO BROAD BAND FLUID
AMPLIFICATION AT ACOUSTIC FREQUENCIES

Happy Hugh Unfried
Mattel, Inc.
Hawthorne, California

ABSTRACT

The philosophy of operating conjugate fluid jets in the highly nonlinear flow region for acoustic amplification is outlined. Operation is necessarily restricted to laminar flows which are inherently sound sensitive and which are allowed to develop into vortex flow patterns; hence the amplifier is best suited for low level input signals. A sound sensitive jet is by itself somewhat selective frequency-wise with an operational bandwidth on the order of an octave, whereas the nature of the conjugate jet system allows bandwidths of many octaves; and perhaps its most novel feature is amplification over the important acoustic speech range of from 200 cps to 8,000 cps. The power gain per stage is generally smaller than the gains reported for other types of fluid amplifiers which typically operate at lower frequencies.

PHILOSOPHY OF OPERATION

Under appropriate operating conditions laminar jets are sensitive to sound; that is, sound may disturb the normal flow pattern or streamlines and it is this feature which we utilize in pure fluid amplification of acoustic signals. When a jet is in a "sensitive" state it has a limited bandwidth and a maximum sensitivity at some frequency which depends on the geometry of the jet and various associated flow parameters. The useful bandwidth of a sensitive jet is generally on the order of an octave. Obviously, amplification over an octave centered in the voice spectrum would not be very satisfactory. For instance, telephone lines use about $3\frac{1}{2}$ octaves to cover the frequency band from 300 cps to 3,600 cps and to preserve fidelity or voice character more octaves are desired.

Our approach is to operate the fluid jet system at frequencies above the audio band. If the jets are sensitive, say at 20 kcps, then an octave from 15 kcps to 30 kcps is covered which allows a 15-kcps bandwidth. Of course, this is reminiscent of features successfully practiced in radio communication, although we do not employ any electronic elements. The device employs conjugate jets which are both sensitive at some frequency which may be called the carrier frequency. The first jet, is referred to as a modulator, is modulated by an acoustic signal which is at a lower power level than the ideally recoverable modulation signal from the transmitted carrier; and the output of the demodulator is a reproduction of the original modulation signal at a power level above that which is ideally recoverable with full wave rectification of the input carrier signal. The net power gain of the conjugate system depends also on the transmission line, waveguide, etc. between the modulator and demodulator. It has not been anticipated to restrict operation to the case where the conjugate jets are in close proximity

nor to applications where the power gain is the essential feature; nor is it expected that amplitude linearity will be well preserved; because of the nonlinearities one can expect such characteristics as amplitude compression which may have significant usefulness in speech applications as well as in control circuits.

It seems that the most novel feature of the device is its inherent broadband frequency capabilities, although the sole accomplishment of pure fluid amplification over the greater part of the audio spectrum and at normal voice levels is in itself novel.

THE AMPLIFIER SYSTEM

Because development work is in a relatively infant stage, we will present our approach to acoustic amplification in a rather broad sense without specific reference to any particular application. Figure 2.1 illustrates the generalized system.*

Modulation Device

The jet modulator produces an acoustic signal of essentially constant amplitude and frequency in the absence of an input acoustic signal. In the presence of an input signal, the modulator output is modulated in amplitude, or frequency, or perhaps both, depending on the type of device. In general, our devices are considered as amplitude modulators although a small amount of frequency modulation always exists. Usual operation is of the double sideband plus carrier type although in practice the sidebands are not necessarily of equal amplitude. Operation in the single sideband plus carrier mode does not seem likely although an approach to this behavior is possible with consequent improvements in theoretical bandwidth. For such operation, the demodulator characteristics should be of the square-law detector type and, as is later indicated, this is possible in practice.

Transmission Line

The transmission line can take on various meanings and forms, but in general, its purpose is merely a means of conducting the modulated carrier, which is an acoustic signal, from the modulator to the demodulator. No dc flow from modulator to demodulator is necessary and in fact it is detrimental because the demodulator will not accept dc flow. The transmission line could be a short or a long waveguide or it could be some means of obtaining a sound beam with radiator and receiver elements such as horns or reflectors.

Demodulator

The jet demodulator plays the roll equivalent to that of a transistor detector in radio communication where the transistor is operated in a

*Figures appear on pages 281 through 296.

condition of cutoff or saturation so that the input signal is amplified as well as rectified. For amplitude modulation detection, the jet demodulator may be operated without any acoustic resonant elements, although resonant elements may be incorporated to increase sensitivity, but of course, at the expense of frequency bandwidth. For frequency modulation detection, an acoustic resonant element is incorporated so that slope detection is possible before rectification is performed. In the event that both frequency modulation and amplitude modulation are to be detected in one stage, operation is on the low frequency side of resonance so that the detected outputs are partially additive. As indicated with the transistor analog, the jet demodulator has the advantage that it functions as an amplifier (suitably called a hydrodynamic traveling-wave amplifier) as well as a detector. The modulator output power can easily be made an order of magnitude larger than that which can be accepted by a single demodulator; therefore, for cases where modulator and demodulator are closely coupled, a multiplicity of demodulators connected in parallel becomes useful.

Low Pass Filter

This element is not essential to the operation of the device as an amplifier but its inclusion is at times advantageous. In the event that the carrier from the output of the demodulator is at an audible level, an acoustic low pass filter may be used to increase the signal-to-noise ratio. When the demodulator is operated at low gain, the output contains a component at the carrier frequency which has an amplitude comparable to the modulating signal, but at high gain settings, the carrier contribution becomes negligible and there is no need for a filter.

It will be noted that the inclusion of feedback in the circuit has been omitted. This is primarily because the application of feedback has received very little of our attention and applicable results are not available. We have thus far operated the conjugate jet system with carrier frequencies ranging from 6 kcps to 22 kcps, but this range is not necessarily indicative of the possible range of operation. For certain control circuits perhaps carrier frequencies as low as a kilocycle may be useful whereas the upper limit for carrier operation will probably be dependent on the smallest possible or practical jet dimension, which may correspond to perhaps 50 kcps.

MODULATION

Types of Modulation

A modulator is essentially an oscillator with the output signal varying functionally with an input signal referred to as the modulating signal. The output of the oscillator in the absence of a modulating signal is called the carrier. In general, the output of the modulator is of the form:

$$p(t) = P(t) \cos \theta(t) \quad 3.1$$

When the modulating signal controls $P(t)$, we have amplitude modulation; and when it controls $\theta(t)$ we have angle modulation which is a generalization of phase and frequency modulation. In fluid modulators both forms of modulation are possible although the prominent form of modulation in the systems herein reported is amplitude modulation.

For amplitude modulation we take:

$$P(t) = P_0 (1 \pm m \frac{\cos w_m t}{\sin w_m t}) \quad 3.2$$

$$\text{and} \quad \theta(t) = w_c t + \theta \quad 3.3$$

with m = modulation coefficient
 w_m = angular frequency of modulation
 w_c = angular frequency of carrier

The phase angle θ can be arbitrarily set equal to zero by appropriate selection of time $t=0$. By using trigonometric identities with eqs. 3.2 and 3.3 substituted in eq. 3.1, we obtain the general form of amplitude modulation for single tone modulation.

$$p_c(t) = P_0 \left\{ \cos w_c t + \frac{\pm m}{2} \left[\begin{array}{l} \cos (w_c - w_m)t + \cos (w_c + w_m)t \\ \sin (w_c - w_m)t - \sin (w_c + w_m)t \end{array} \right] \right\} \quad 3.4$$

Figures 3.1a and 3.1b illustrate the spectrum of the modulating signal and modulated signal, respectively. In this example two-tone modulation is shown to illustrate the inversion of the lower sideband. Note that the modulated signal spectrum does not contain the modulation spectrum which we frequently refer to as the audio signal. It is interesting to note that only the upper and lower sidebands contain the essential modulating signal information, and that transmission of only a single sideband is essential if reinsertion of the carrier is performed at the demodulator. Figure 3.2 illustrates the familiar AM signal with approximately 50% modulation.

With the notation defined in figure 3.2 the modulation coefficient m may be written as:

$$m = \frac{A_2 - A_1}{A_2 + A_1}$$

In the event we have the instantaneous frequency w as

$$w = w_c t \pm \Delta w \begin{matrix} \cos w_m t \\ \sin w_m t \end{matrix} \quad 3.5$$

and $P(t) = P_o \quad 3.6$

the resulting modulated output becomes

$$P_c(t) = P_o \left\{ \cos w_c t \begin{matrix} + \frac{\Omega}{2} \left[\cos(w_c - w_m) t - \cos(w_c + w_m) t \right] \\ + \frac{\Omega}{2} \left[\sin(w_c - w_m) t + \sin(w_c + w_m) t \right] \end{matrix} \right\} \quad 3.7$$

with Ω = frequency modulation coefficient

$$\Omega = \frac{\Delta w}{w_m} \quad \text{where we have assumed } \Omega \ll \frac{\pi}{2} \quad 3.8$$

which is the representation of single-tone frequency modulation. Figure 3.3 illustrates the familiar FM signal and defines the symbols used in evaluating the modulation coefficient:

$$\Omega = \frac{\tau_{max} - \tau_{min}}{\tau_{max} + \tau_{min}} \quad 3.9$$

Figure 3.4 shows the disposition of the FM sidebands. Equation 3.7 is similar to the AM representation(eq. 3.4) in that the signal also has upper and lower sidebands. On the other hand, the upper and lower sidebands combine to form a component which is in phase quadrature with the unmodulated carrier, whereas for AM the sidebands form a component in phase with the unmodulated carrier. This phase shift must be taken into account when superimposing AM and FM signals which may be useful in certain applications.

Although we have considered only systems with a single carrier frequency, it is possible to modulate a noise carrier. On the other hand, bandwidth constraints and the ability to obtain relatively high efficiencies with single frequency resonant type modulators leaves the scheme of noise modulation at a disadvantage for practical fluid systems.

Fluid Oscillators

The fluid modulators discussed in this paper are oscillators whose output is controlled by an input modulating signal. The two basic types of fluid oscillators are the relaxation oscillator and the feedback oscillator (12). We are interested in the latter which are well known. The edgetone generator is well known for its applications in musical instruments as well as being the most common type of whistle that children encounter. The "bird call"(1) generator, recently labeled the "hole tone"(2), is found in many tea kettles. Both of these tone generators, or oscillators, are basically fluid amplifiers with positive feedback. Lord Rayleigh(3) was the first to show an understanding of the important roll played by sound sensitive jets, their ability to amplify small disturbances, and the inclusion of acoustic feedback to form a fluid oscillator; and A. Powell(4) has greatly furthered the scientific understanding of these topics as is exemplified by his work on the edgetone.

The edgetone and bird call generators have much in common although the edgetone is a device with a plane jet primarily sensitive to transverse pressure gradients with respect to the jet axis and flow disturbances growing into an asymmetrical vortex pattern, while the bird call employs a circular jet which is generally sensitive to an axial pressure gradient and with flow disturbances developing in a symmetrical vortex flow. Figures 3.5 and 3.6 show the region of flow instability to small disturbances for free plane and circular jets, respectively. Figure 3.5 comes from a large amount of edgetone data taken by this author while at the Aerosonics Laboratory under the direction of Professor Powell. This data were published in references (4) and (5). The assumed region of maximum sensitivity is shown by the solid line, with increasing instability occurring for increasing values of Reynolds and Strouhal numbers. For a fluid device employing a plane jet, its operating region should fall within the designated region of operation if it is intended for the device to be unstable to small disturbances. On the other hand, if instability is a problem, the relationship between the spectrum of the noise disturbance and the Reynolds number should be adjusted above or well below the region of operation shown in figure 3.5. Note that the assumed line of maximum sensitivity does not lie in the middle of the region of instability. This is because the spacial gain of the free jet falls off very fast in the upper region of instability as compared to the slowly varying spacial gain for lower frequencies. The physical reasoning is that the jet becomes stable as the disturbance wavelength (in the flow) reaches the order of magnitude of the jet dimension, the induced velocity effect becomes incoherent, and the process of vortex coalescence, which is fundamentally the mechanism for the spacial gain, is reduced. For small R-S numbers the spacial gain is reduced by the increasing action of viscosity

and for large R but small S the spacial gain falls off primarily because the disturbance wavelength is sufficiently long that the disturbance is convected away from the region of interest before any gross amplification can take place.

Figure 3.6 illustrates the region of operation for circular laminar jets. Data taken from the work of A.B.C. Anderson (6) were initially reduced and plotted on the R-S plan. Then this author performed studies on a 1-mm diameter smoke-laden air jet in a small anechoic chamber. The jet issued from a 10-cm long tube and was excited by the sound from a loudspeaker. With the velocity set and sound amplitude held relatively constant the frequency would be adjusted until maximum flaring of the jet existed. The locus of these points appears in figure 3.6. The data given as figure 6 in the recent paper by Chanaud(2) and Powell has also been added to figure 3.6.

The inclusion of a resonator to the edgetone improves the acoustic radiation from dipole to monopole source characteristics, enhances the feedback thereby stabilizing the frequency and increasing acoustic output. Figure 3.7 is a sketch of a simple resonator-coupled edgetone-type oscillator. Under some circumstances the operation can be further improved by including a horn as an additional impedance coupler to the radiation load.

The bird call or circular jet oscillator is shown in figures 3.8 and 3.9. Both the longitudinal and the radial mode resonators increase the axial pressure gradient across the nozzle or first orifice and hence augments the flow pulsations responsible for the generation of symmetrical ring vortices. When using the longitudinal resonator, the fluid supply enters at an acoustic quarter wavelength from the rigid end (a low acoustic impedance location) thus minimizing influence of the input port on acoustic resonator operation. For the radial mode resonator the normal mode equation given by Morse (7) has been used. The frequency calculated using this equation generally yields values on the order of 5% higher than found in the laboratory models. Note that our resonators have a small hole at the center of the resonator which is a high impedance region for the radial modes and hence a critical location for a hole.

$$f = \frac{C \alpha_{r,n}}{D} \text{ (cps)}$$

c = speed of sound
 $\alpha_{r,n}$ = characteristic value = 1.219 for first radial mode
D = diameter of cylinder

Fluid Modulators

Since the oscillators described are essentially regenerative amplifiers operating in a saturated state, a reasonable way to modulate the carrier would be to modulate the feedback. For all three oscillators illustrated it is possible to modulate the carrier merely by introducing the modulating signal in the vicinity of the jet orifice. In practice this is found to be a relatively ineffective approach since the acoustic modulating signal must be on the order of magnitude of the feedback pressure to accomplish large percentage modulation.

Another approach, and an extremely effective one, is to disturb the jet initially with the modulating signal. Then let this disturbance grow as it is convected downstream toward the oscillator stage and allow the induced vorticity from the modulating disturbance to partially augment or cancel the redistribution of the jets vorticity by the oscillator feedback signal. This approach has the added advantage that the modulating signal is effectively hydrodynamically amplified before it reaches the oscillator section. We refer to this type of modulator as a single-jet two-stage modulator. Figure 3.10 illustrates the two-stage modulator for the radial mode coupled resonator oscillator. Similarly, the same approach works for the longitudinal resonator coupled circular jet oscillator and the resonator coupled edgetone oscillator.

Now let us look at some typical modulator characteristics. Figures 3.11a and 3.11b show the unmodulated carrier; and the modulated carrier compared to the electrically demodulated modulated carrier for a typical two-stage modulator operating at 12.5 kcps. The modulating signal is at 1 kcps. The carrier and modulated carrier are signals from a B & K 4134 condenser microphone, which was placed several feet away, but along the axis of the circular jet modulator. (All measurements taken in an anechoic chamber.) The modulating signal is from a probed B & K type 4134 microphone located in the modulating stage cavity.

Figure 3.12 illustrates a 17.6-kcps modulator response. The solid curve is the modulating signal pressure in the modulating stage cavity, whereas the dashed curve is an electrical demodulation of the modulated carrier. The amplitudes are only relative and the curves have been adjusted to coincide at the low frequency end. The curves show a low frequency cutoff at about 400 cps, which is the characteristic of the Altec 804A horn driver. The modulator response is quite good down another octave. The solid curve has been corrected for the probe microphone response, which is well behaved up to 5 kcps. At higher frequencies the correction factor can be doubted. The probe microphone was calibrated using the B & K probe microphone kit.

Figure 3.14 indicates operation in the R-S plane. Note how the operating point for the carrier was selected well above the region of maximum sensitivity. Furthermore, the oscillator, although operating at 17.6 kcps, is near a condition of instability (but not too near since we want a quiet carrier) where it could jump to a lower "stage" at 14 kcps and operate as a more stable oscillator for its operating Reynolds number. It has been found, as would be expected, that the best modulating sensitivity as well as amplitude linearity are obtained when the modulator is in a "weak condition" of oscillation which is found just before or after a frequency jump from one jet stage to another.

The ratio of radiated modulator power to input acoustic power can range from 1 to 50, with a typical well behaved modulator operating around a ratio of 30:1 for 50 % single-tone modulation. This means that a power gain of 9.6 from the modulator stage is possible. Additional gain from the demodulator is also possible as is described later. As the sensitivity and power gain of the modulator are increased, the operating conditions become more critical. For the most sensitive modulators tested, the tolerable supply pressure variations could not exceed 7%, whereas variations on the order of 20% were tolerable for modulators having power gains as low as 4.

DEMODULATION

Brief Theory of Jet Demodulation

The jet demodulator is basically a sound sensitive jet with certain aspects of the developed vortex flow separated. First, the fluid jet is adjusted so that the Reynolds number and Strouhal number are such that the stream is unstable to acoustic disturbances at the carrier frequency. Second, the induced stream disturbance is allowed to develop into its natural vortex flow pattern using the inherent hydrodynamic traveling-wave amplification characteristics of the jet. Thirdly, the developed vortex flow is suitably clipped thereby producing the desired results of sound amplification and demodulation. The jet demodulator can be either a plane jet or a circular jet. A circular jet having the same characteristic dimension as a plane jet has greater sensitivity to sound, and operates at slightly higher frequencies for the same average velocity. The plane jet has the advantage that its total power output can greatly exceed that of the circular jet. To overcome this disadvantage, circular jets can be operated in parallel.

Let us now describe the presumed mechanism for jet demodulation. Operation of a circular jet device is given below and the general approach also holds for the plane jet demodulator, with, of course, suitable changes in the separation plate design and location. In figure 4.1 we illustrate the outline of the free jet when it is disturbed by a periodic signal such

as the carrier frequency. Note that the jet is circular and that the disturbances are symmetrical with respect to the axis of the jet and furthermore that the developed flow saturates in vortex rings. Now let us consider the flow as seen by an observer located at some location $x = h$ downstream from the nozzle. Here we assume that the flow is not saturated at h (that is, the vortices have not reached their maximum size). Figures 4.2a and 4.3a illustrate the applied disturbance at $x = 0$ without modulation and with single-tone modulation. Figures 4.2b and 4.3b illustrate the flow as seen by an observer at $x = h$ when the jet is subjected to the respective disturbances. Savic (8) illustrates that for a plane jet undergoing asymmetrical disturbances that the locus of points describing the center of vortex filaments coincides with the line (or surface) defining the region of maximum vorticity for the undisturbed jet. If we assume that a similar condition exists for the circular jet, then a cone describes the locus of circular vortex filaments, and the center of the vortices as they are convected past the location $x = h$ lie on a circle with a diameter D which is independent of the size of the vortex. Note that this condition, if valid in the highly nonlinear vortex flow development, puts a certain limiting size on the vortex. If we use the velocity profile given by Schlichting (9), insert the momentum flow rate for a parabolic stream ($\dot{M} = \frac{\pi d^3}{3} \rho U_0^2$), apply an end correction which satisfies volume flow rates ($\dot{V} = R_d \frac{d}{\sqrt{2}}$), and differentiate twice over, we obtain the surprisingly simple expression given as eq. 4.1 which relates the locus of vorticity to the Reynolds number, at the orifice, and the dimensionless distance downstream.

$$\frac{D}{d} = 1 + \frac{32}{R_d} \frac{h}{d} \quad 4.1$$

Figure 4.4 is an illustration of the use of this equation.

Now the developed vortex flow of the free jet, to a second-order approximation, generates no sound. But, if the flow confined within the circle defined by the locus of vorticity could be separated from the flow outside the circle, the mass flow rate would be time dependent (thus sound generation) and is illustrated in figures 4.2c and 4.3c. Of major importance is figure 4.3c, where it is immediately obvious that the frequency spectrum of the mass flow rate within the circle contains a large component at the modulation frequency. It also contains the carrier frequency and its sidebands as well as harmonics thereof. Since the carrier frequency is assumed to be well above the modulation frequency, the harmonic distortion of the carrier is of no consequence. Interestingly enough, there is little harmonic distortion of the modulation signal if vortex saturation is not reached. Of course if the applied disturbance is sufficiently large, or if the applied signal is over-modulated, then harmonic distortion can become significant. Amplitude linearity is in general not preserved due to the highly nonlinear spacial gain characteristics of the free jet. Under various

operating conditions it is possible to obtain augmentation or compression of the signal. This point is discussed later.

To accomplish demodulation we use a flow divider as shown in figure 4.4. When the upstream side of the flow divider is isolated from the downstream side, with the exception of the hole, the mass flow fluctuations through the orifice produce sound with the spectrum previously described. The sound source is effectively dipole in nature but with the infinite baffle it appears as a monopole from either side. Hence, the demodulated sound signal exists on either side of the flow divider although the two effective sources are 180 degrees out of phase. This phase inverted output signal is useful in feedback circuits.

Up to now we have described the demodulation phenomenon with the idea that the free jet flow is not influenced by the presence of the flow divider, which in fact is not true. If the surface of the flow divider was contoured to that of the jet streamlines, then its presence would not alter the flow. On the other hand, the streamlines are a function of the disturbance amplitude so that in general this criterion cannot be met. Fortunately, we have found that a sharp contoured flow divider, as illustrated, works astonishingly well. The previous presumed description of jet demodulation also holds for a circular jet having an asymmetrical vortex flow as well as for a plane jet, although in such cases the action is analogous to full-wave rectification.

The illustrations of the jet with well developed vortex flow have been rather idealistic. Flow patterns(10) of this sort probably will not be observed in the laboratory except in a fluid with extremely low kinematic viscosity. In reality the vortices corresponding to each wave of the carrier diffuse rather rapidly, but the overall modulation, which is an order of magnitude larger in wavelength, seems to withstand the diffusion of the individual vortices. As a result, the amplified carrier signal is at a much lower level than expected and in general at a level well below the reproduced modulating wave. Fortunately this is an advantage, thus requiring less filtering or attenuation of the carrier frequency in the event that it is troublesome.

Jet Demodulator Characteristics

Consider the carrier wave driving the jet demodulator to be of the form given in eq. 3.2. Full wave rectification of this signal results in.

$$p_r(t) = \frac{2P_o}{\pi} + \frac{2P_o m}{\pi} \cos \omega_m t \quad 4.2$$

plus higher order harmonics of carrier, and sum and difference frequencies.

The desired signal is $\frac{2P_o m}{\pi} \cos \omega_m t$

Figure 4.5 illustrates typical response of a jet demodulator to a 15-kcps

carrier 50% modulated at 1 kcps. The unmodulated carrier level was 85 db SPL. Hence, with ideal full-wave rectification the acoustic output would reach approximately 75 db. The knee in the curve is typical of the transition in the flow where the amplitude response for larger Reynolds numbers is highly nonlinear. The input and output pressure measurements were taken in tubes having the same diameter. It is obvious that considerable pressure gain is possible (greater than 40 db) in addition to effective rectification. This particular example illustrates the maximum practical gain. Larger gains result in self-sustained oscillation. To prevent the early onset of such oscillation due to acoustic feedback, this demodulator has an antifeedback plate which tends to keep the sound generated at the flow divider or separation plate from disturbing the jet at the orifice where it is most sensitive. Such a contrivance allows about 10 db more gain without oscillation. By adjustment of separation plate orifice diameter and Reynolds number it is possible to develop a variety of output vs. input characteristics. If operated above the knee in the curve, a square law detector is very closely approximated. Hence, for double sideband modulation there will be harmonic distortion which increases with the percentage modulation. On the otherhand, if single sideband plus carrier operation were employed, the output would be virtually free of harmonic distortion.

Superimposed on the same graph is another curve which represents a jet demodulator response to a 10-kcps carrier 50% modulated at 2 kcps. Here the carrier level is 70 db SPL; the pressure gain was not intended to be very large although it approaches 40 db. This example includes an antifeedback plate along with acoustic absorbing material to help suppress oscillation. There is no sign of impending oscillation and the amplitude response is one which shows a great deal of signal compression. This is shown in figure 4.6. For some applications a response of this sort would be detrimental, but for signals of varying strength such as speech, amplitude compression can contribute a great deal in improving intelligibility. Note that amplitude compression is not directly related to frequency distortion.

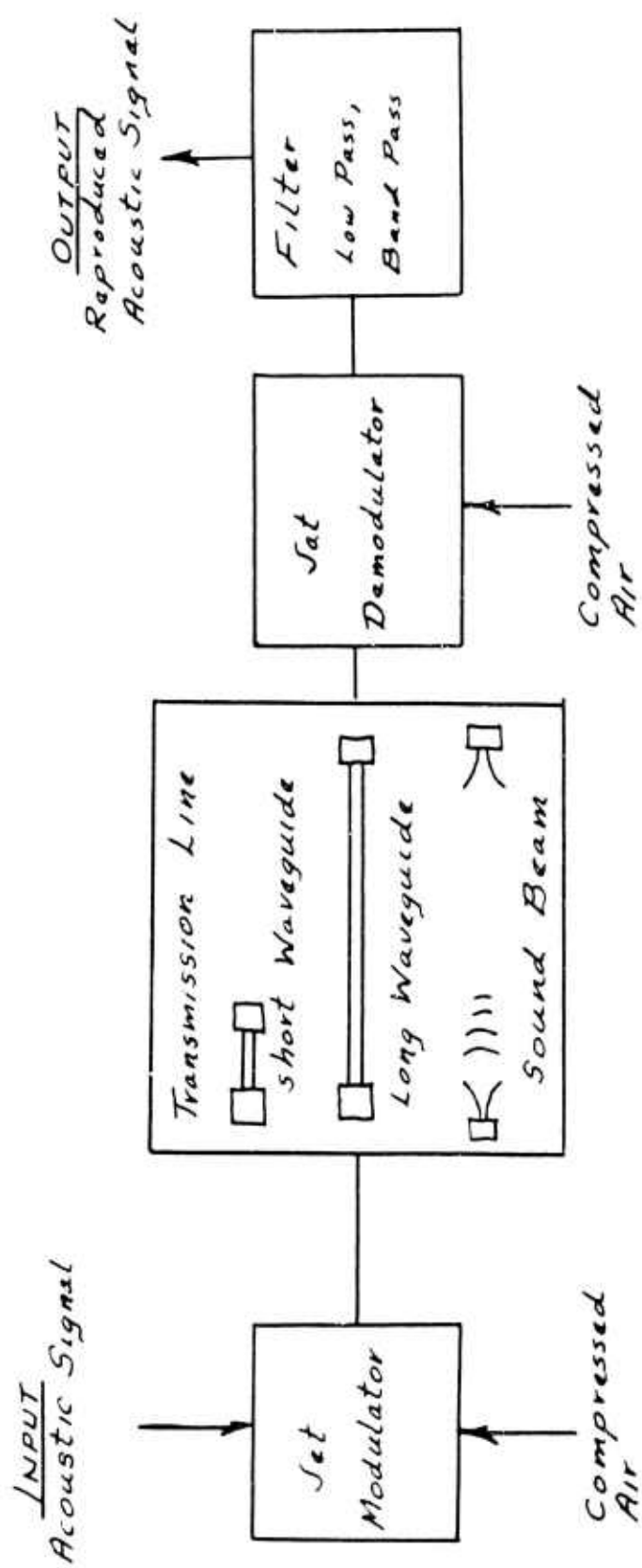
Figure 4.7 illustrates the demodulated frequency response for a 17.6-kcps carrier which also has 50% modulation. The peak at 3 kcps is associated with the input waveguides as well as are many other peaks. Beyond 4 kcps the accuracy of the curve is on the order of ± 3 db. The frequency response, in general, seems to depend more on the acoustic coupling and terminations than on any peculiar response due to the jet itself; therefore, with sufficient care and experimentation one might expect to obtain a much improved response with a probable decrease in gain resulting from the inclusion of acoustic resistances and well terminated waveguides.

SUMMARY

An approach to acoustic amplification using laminar sound sensitive jets has been outlined. The approach is somewhat analogous to rudimentary AM transmission and reception as practiced in radio communication. An attempt has been made to explain jet modulation and jet demodulation on a physical basis and some of the more interesting characteristics of the experimental system, such as modulator linearity and response, demodulator signal compression and response, and gain per jet stage, were discussed. Speech reproduction is generally considered good if not 100% intelligible. The device in its present form is not meant to be a power amplifier although potential for low level input acoustic power amplification exists. It seems best suited for communications or control circuitry involving signal or information transmission and reception. Applications in control circuitry including the incorporation of the Acoustically Activated Fluid Dynamic Switch(11), which is a frequency selective device that can be activated by the demodulator output, with the combination of the jet modulator and jet demodulator are expected where coding or information transmission through a noisy environment is required.

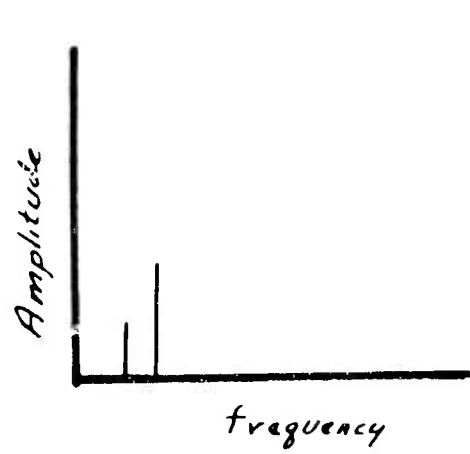
References

- 1 Lord Rayleigh, "Theory of Sound", (Dover Pub., Inc., New York, 1945) vol. 2.
- 2 R. Chanaud & A. Powell, J. Acoust. Soc. Am., vol. 37, p 902, (May 1965)
- 3 Lord Rayleigh, "Scientific Papers", vol. 1, p 474; vol.4, p 44; vol. 5, p 166.
- 4 A. Powell, J. Acoust. Soc. Am., vol. 32, p 395 (1961).
- 5 A. Powell & H. Unfried, Univ. Calif. at Los Angeles Dept. Engr. Rept. 64-49, (1964).
- 6 A.B.C. Anderson, J. Acoust. Soc. Am., vol. 25, p 628, (1953).
- 7 P.M. Morse, "Vibration and Sound", (McGraw-Hill Book Co., Inc., 1948) p 398.
- 8 P. Savic, Phil. Mag., Ser. 7, vol. 32, p 245, (1945).
- 9 H. Schlichting, "Boundary Layer Theory", (Pergamon Press, New York 1955), p 161.
- 10 E.N.DaC. Andrade, Proc. Roy. Inst., vol. 29, p 320, (1936).
- 11 H. Unfried, "Experiment & Theory on Acoustically Controlled Fluid Dynamic Switches", paper submitted for Third Fluid Amplification Symposium, HDL, Washington D.C.
- 12 A. Powell, Acoustica, vol. 3, p 233, (1953).



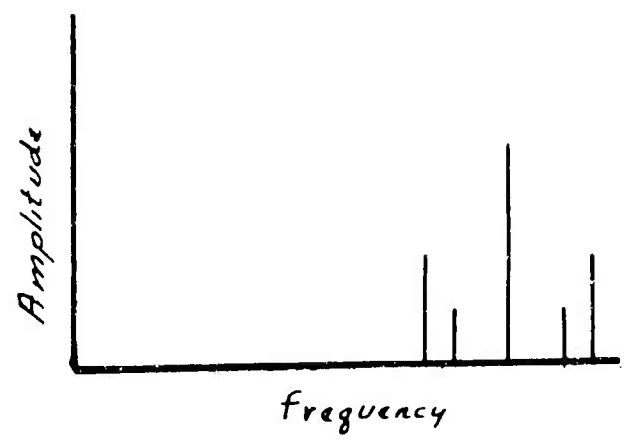
Block Diagram of Acoustic Amplifier System

Fig 2.1



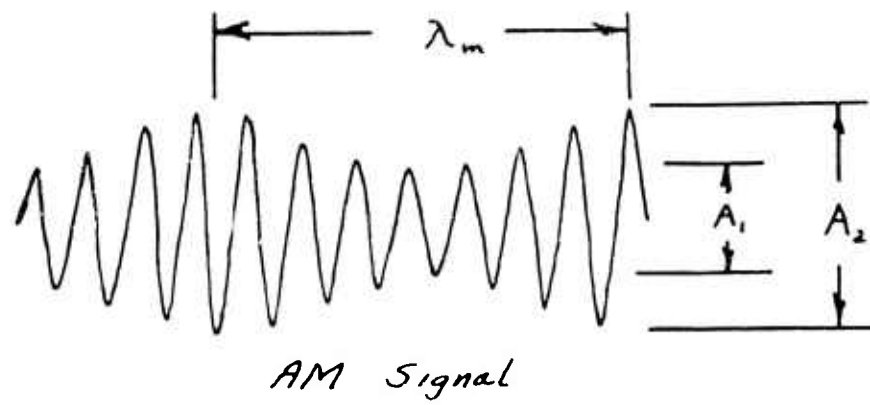
AM modulating signal spectrum

Fig 3.1 a



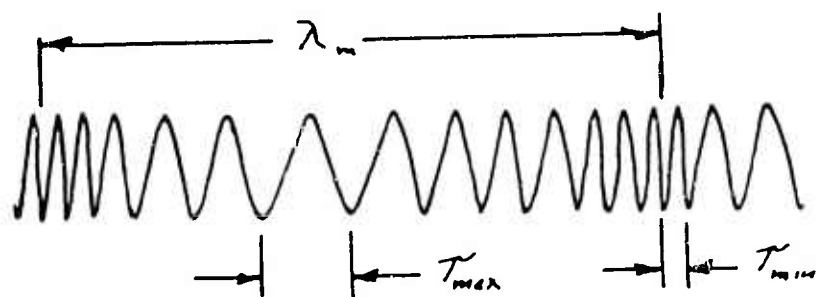
AM modulated signal spectrum

Fig 3.1 b



AM Signal

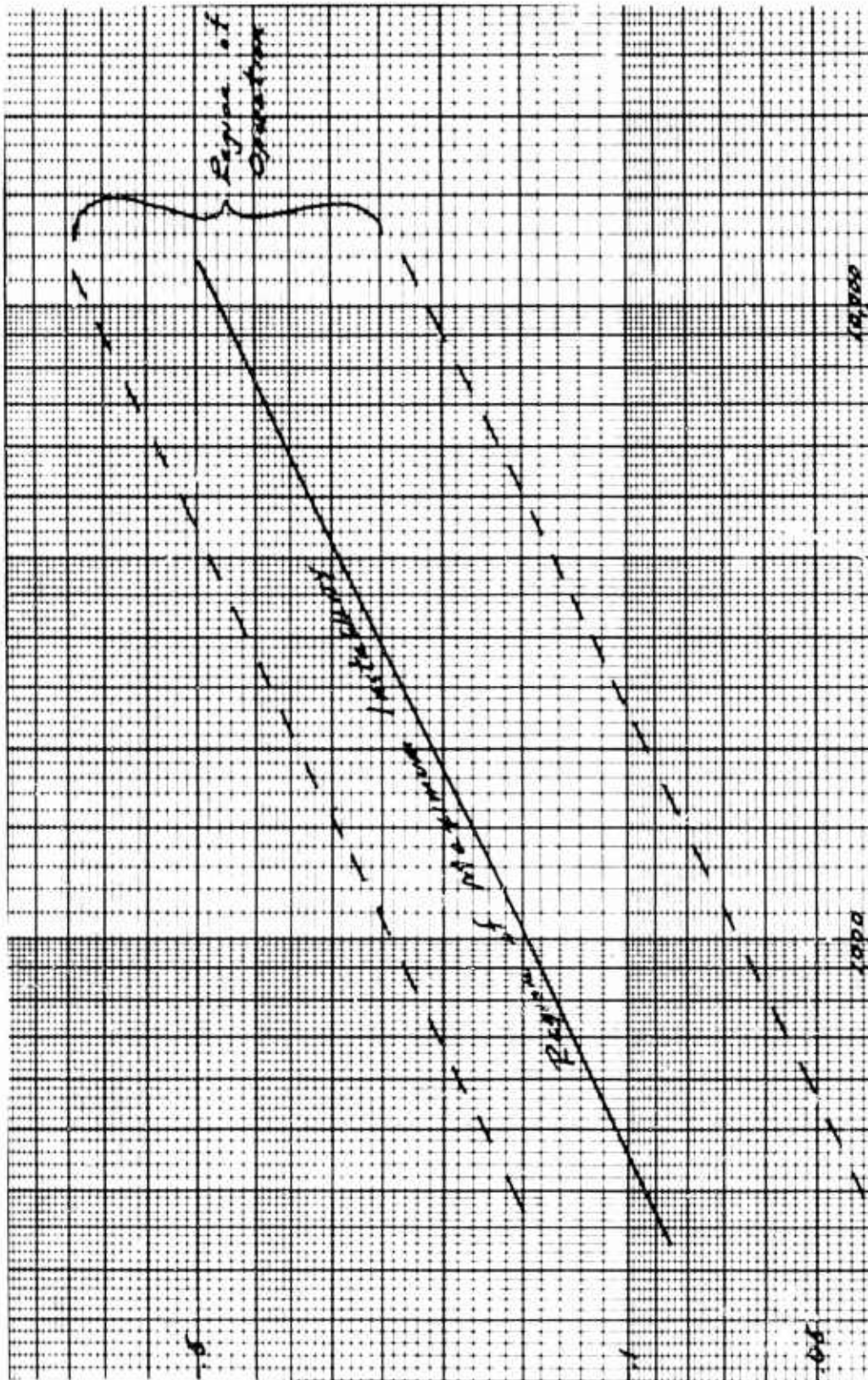
Fig 3.2



FM Signal

Fig 3.3

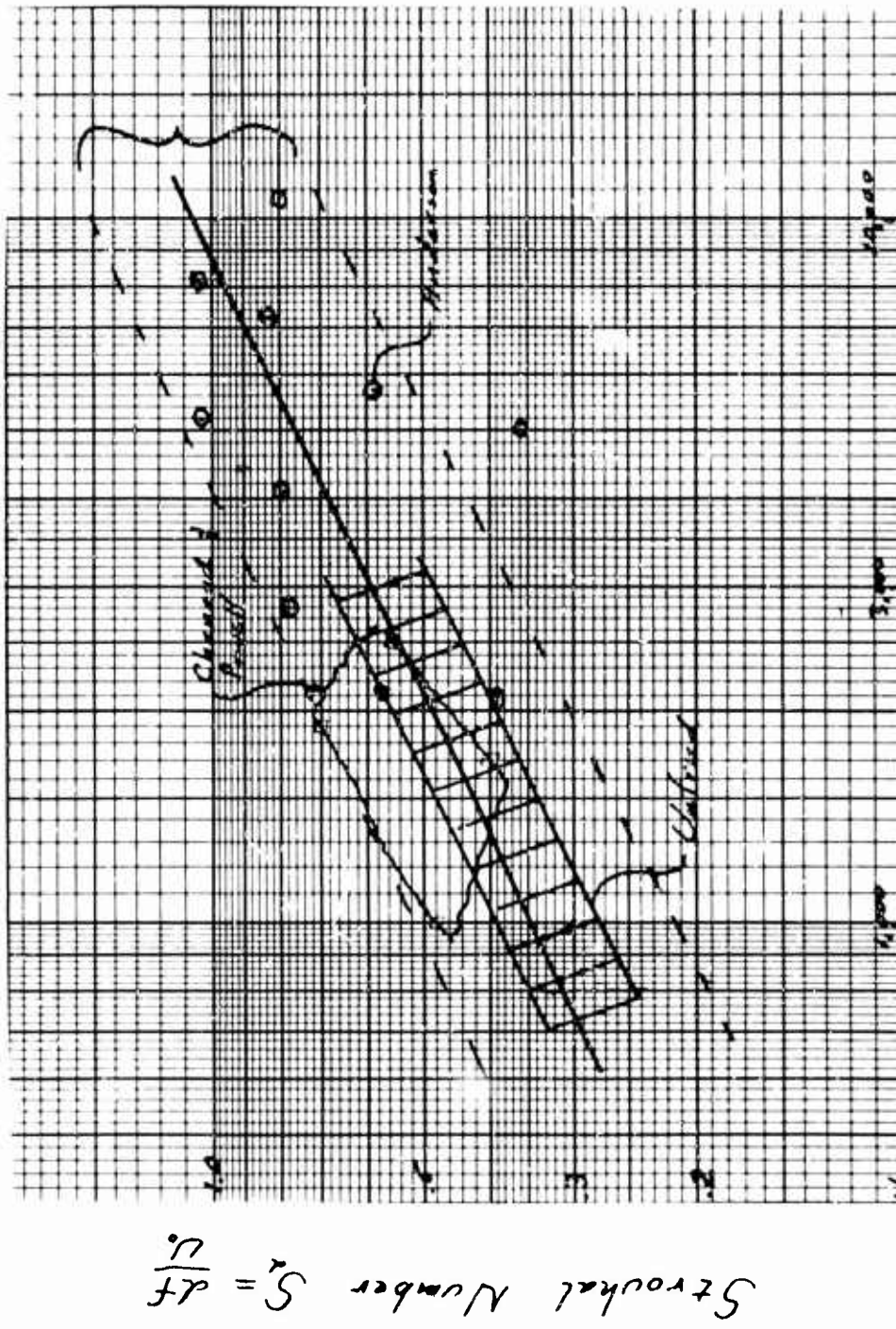
Strouhal Number
 $S_t = \frac{f}{U}$



Reynolds Number $Re = \frac{\rho U_0}{\mu}$

Region of Instability for Plane Jets

Fig 3.5



Region of Instability for Circular Flows

Fig 3.6

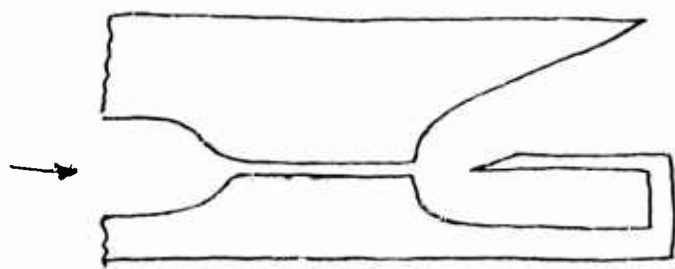


Fig 3.7

Horn & Resonator Coupled Edgetone Oscillator

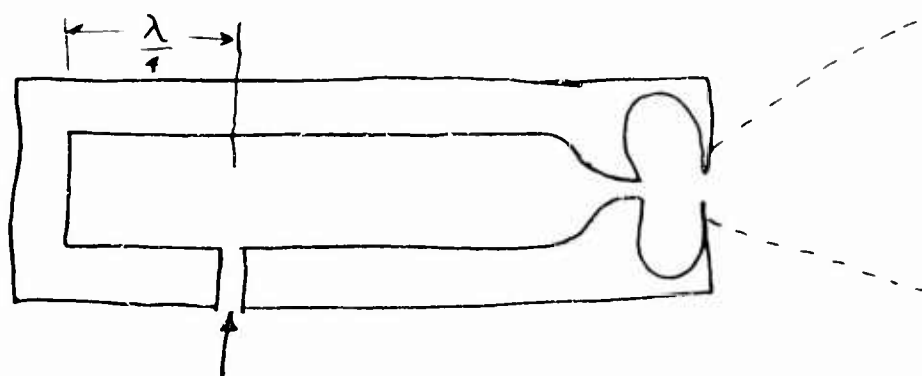


Fig 3.8

Longitudinal Resonator Coupled
Circular Slot Oscillator

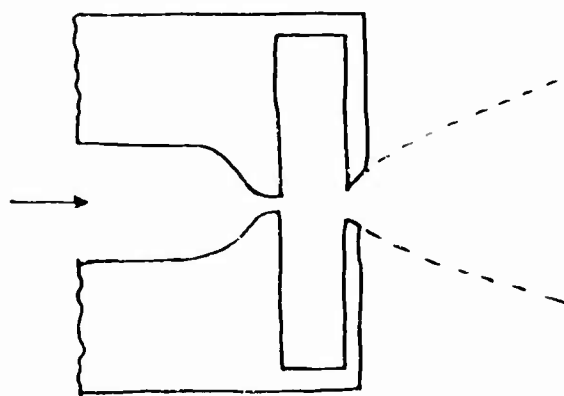
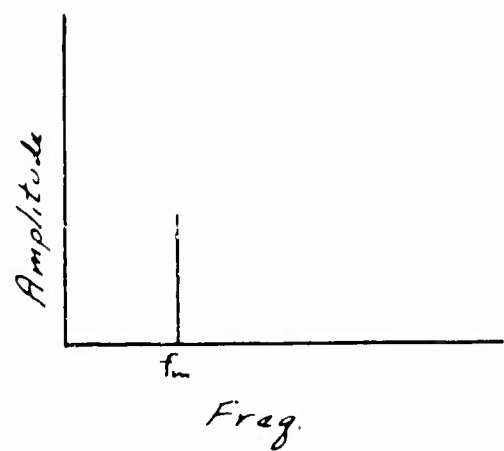


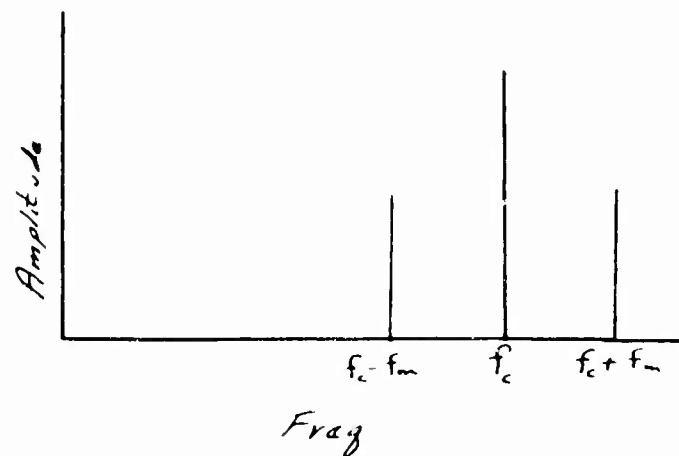
Fig 3.9

Radial Mode Resonator Coupled
Circular Slot Oscillator



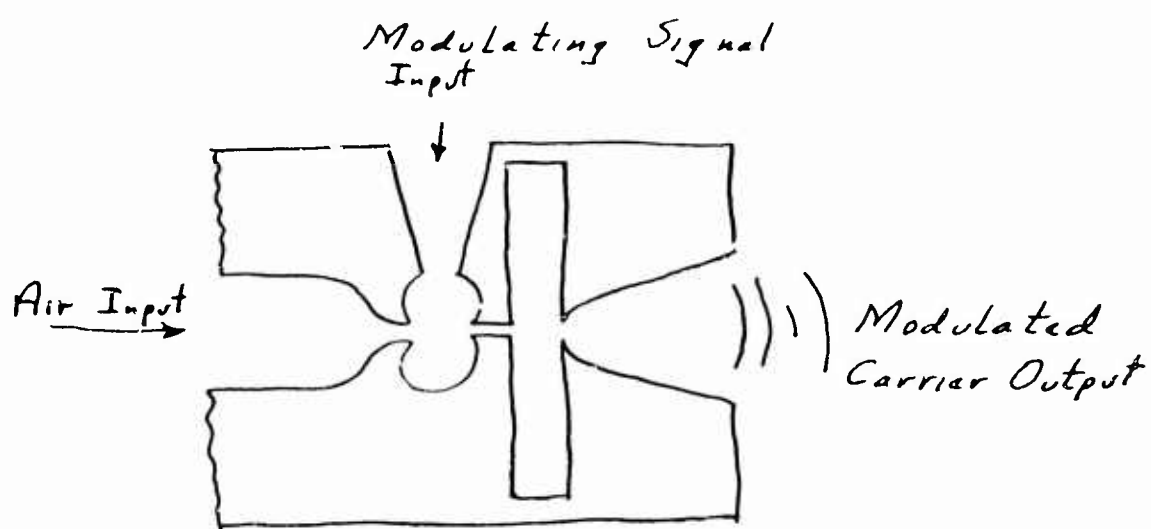
Modulating Spectrum

Fig 3.4 a



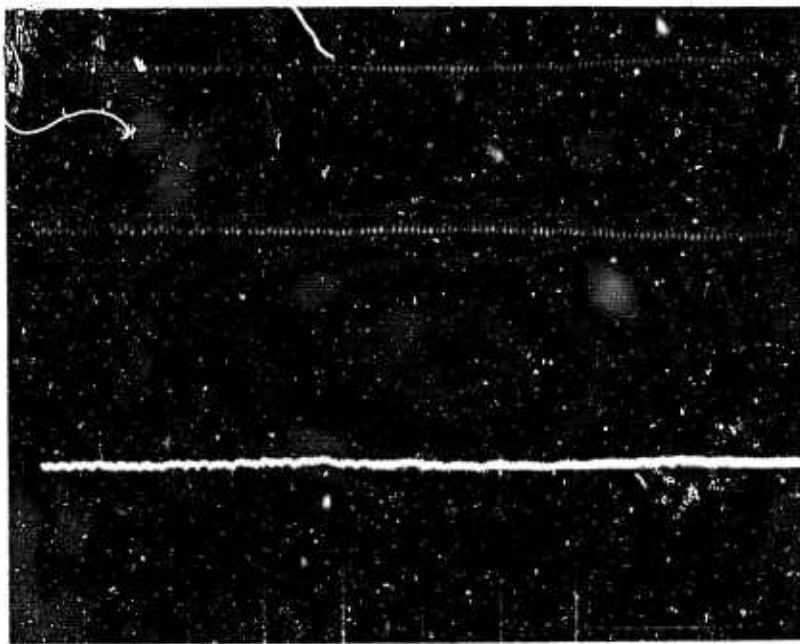
FM modulated signal spectrum

Fig 3.4 b



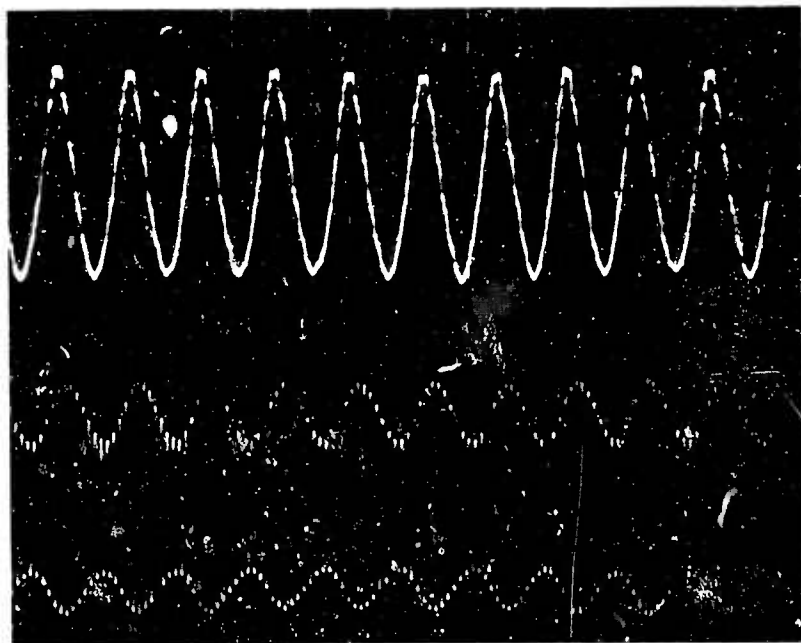
Two Stage Radial Mode Circular
Set Modulator

Fig 3.10



Carrier
 $f_c = 12.5 \text{ Kcps}$

Fig 3.11a

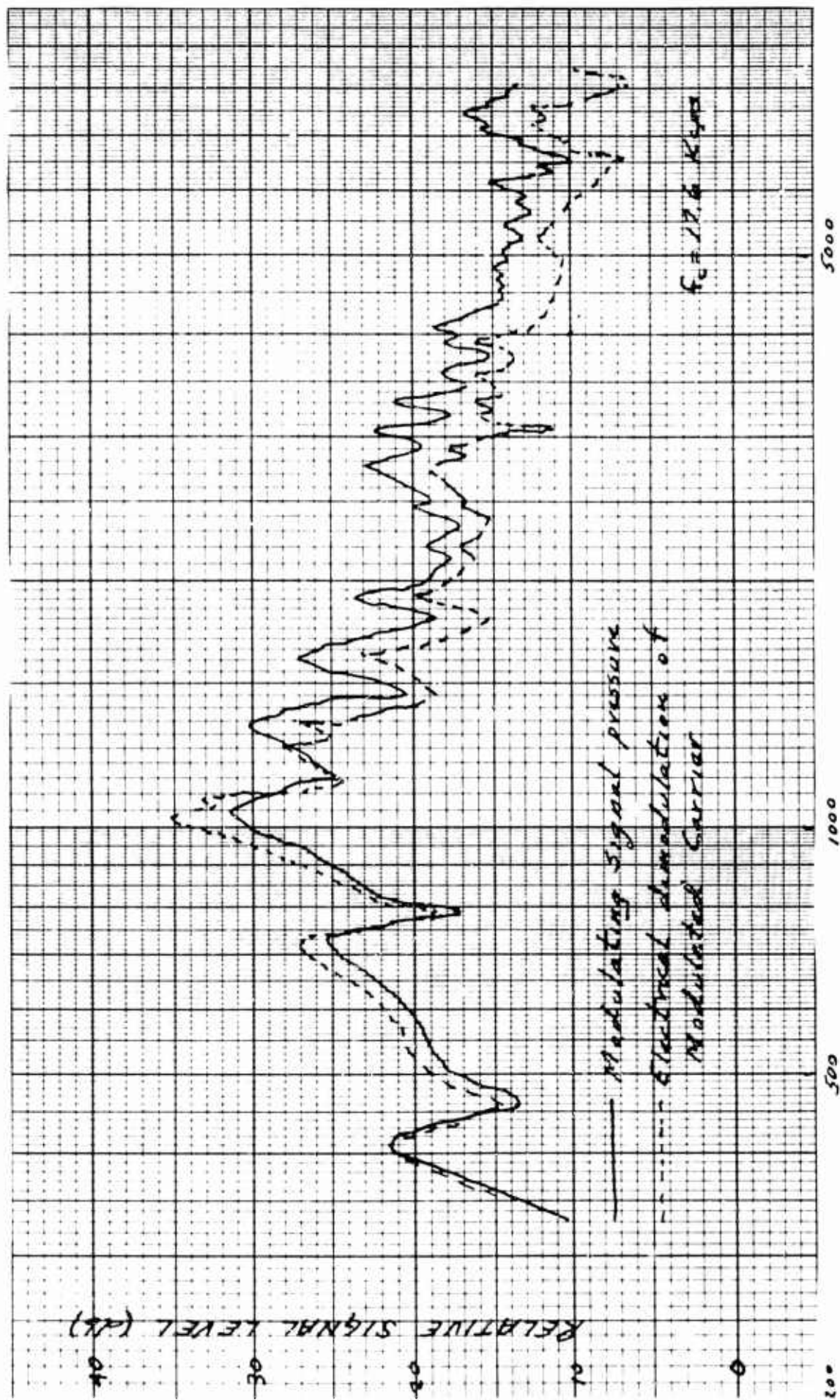


Electrically
 Demodulated
 Carrier

Modulated
 Carrier

$f_m = 1 \text{ Kcps}$
 $f_c = 12.5 \text{ Kcps}$
 $m \approx .5$

Fig 3.11b



Set Modulator Response

FIG 3.12

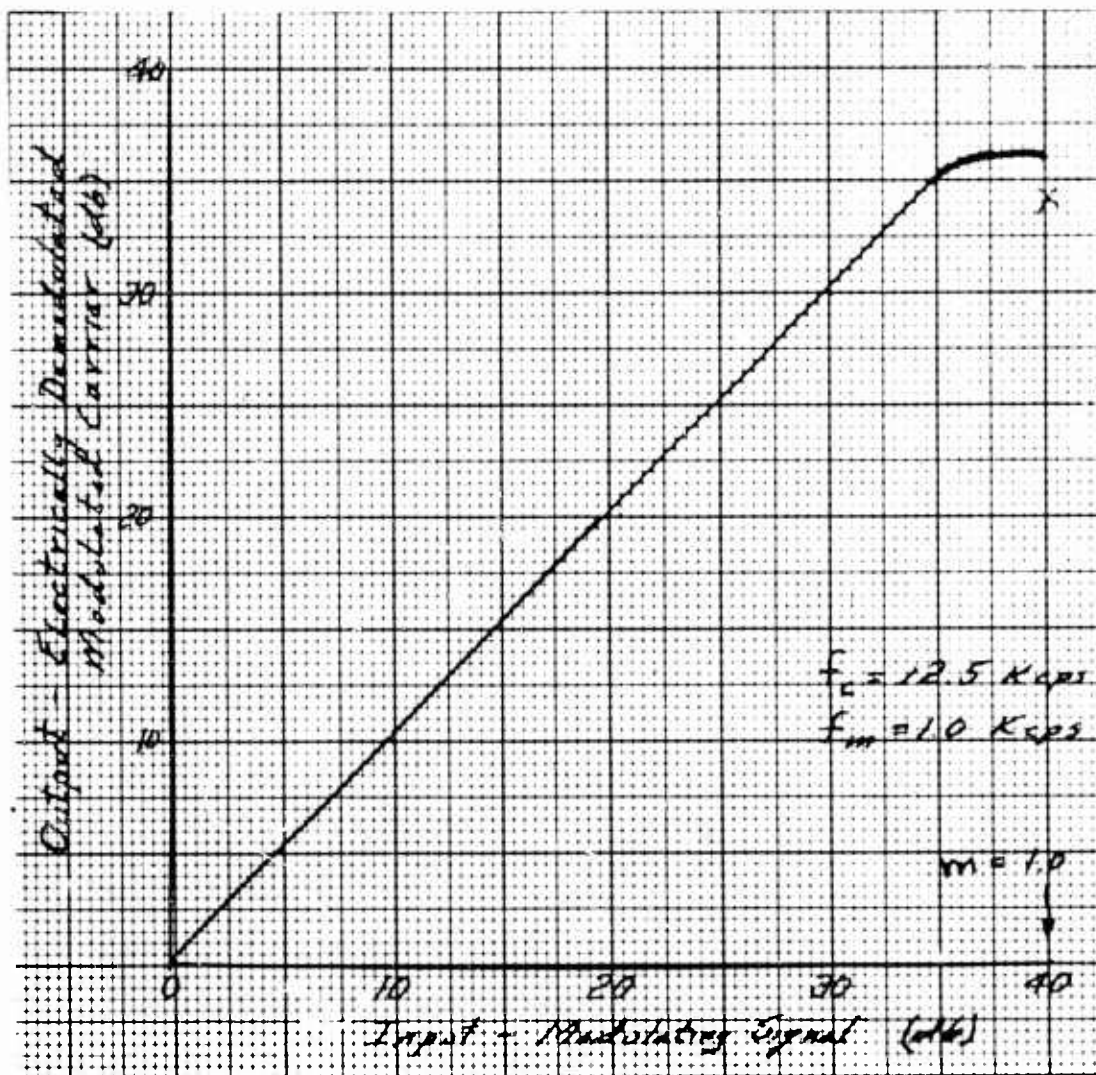


FIG 3.13

Modulator Amplitude Linearity

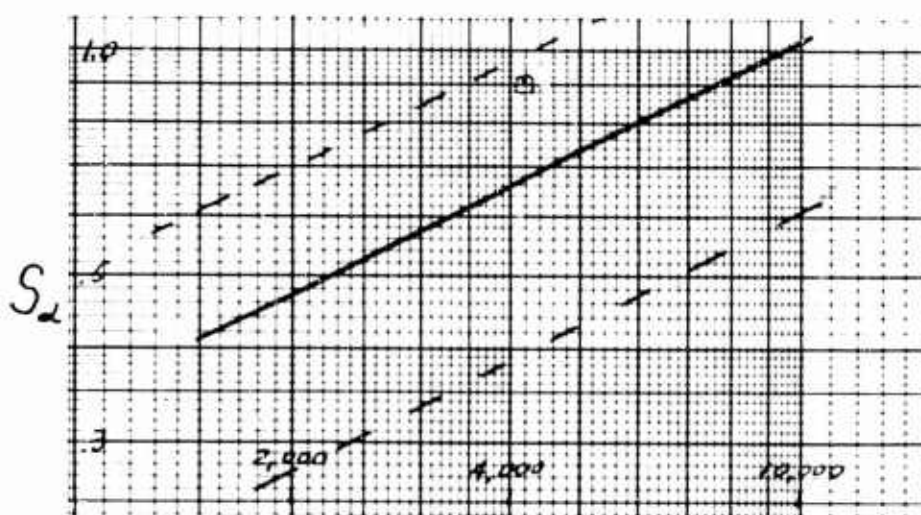
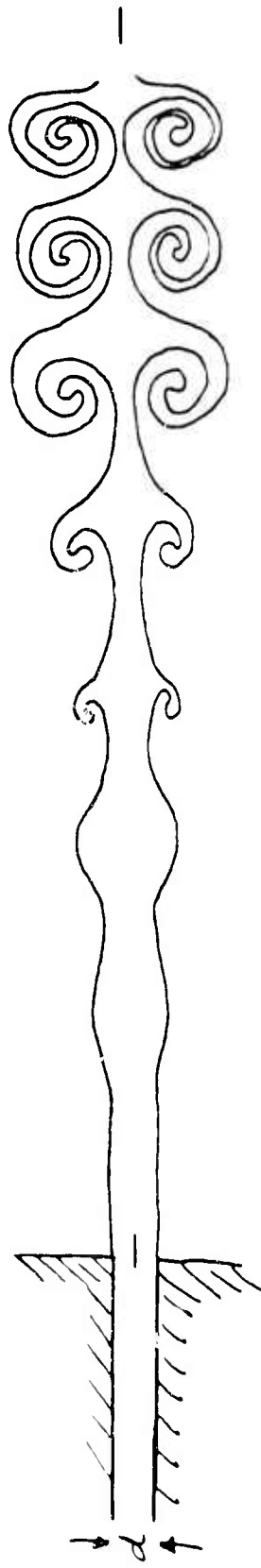


FIG 3.14

R_d
 Modulator Operating Point



*Idealized Ring Vortex Flow of
Sound Sensitive Circular Jet*

Fig 4.1

ACOUSTIC CARRIER ONLY

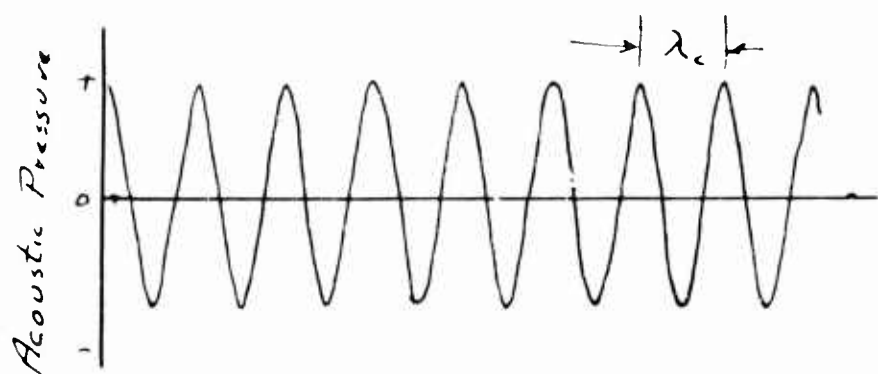


Fig 4.2a

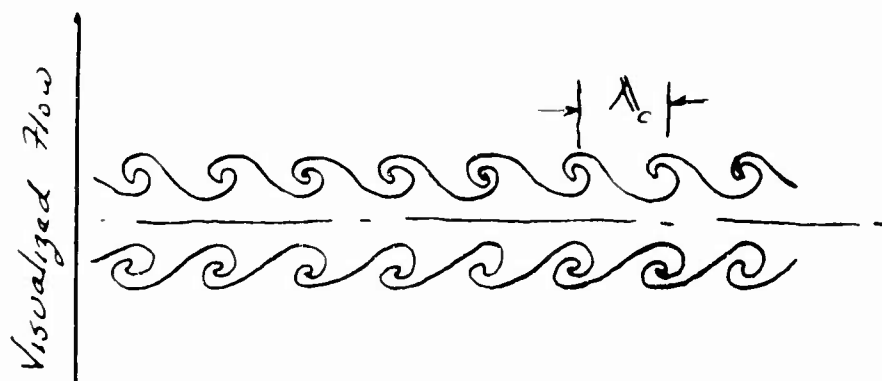


Fig 4.2b

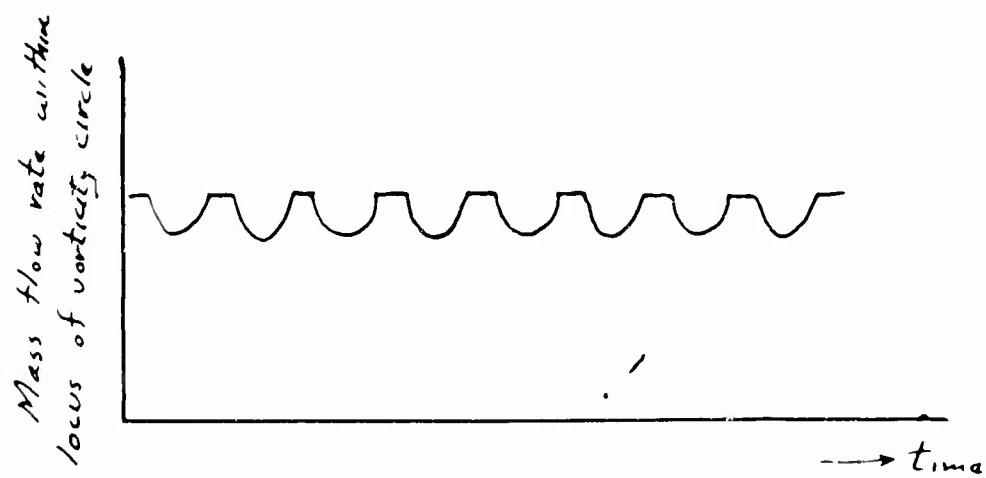
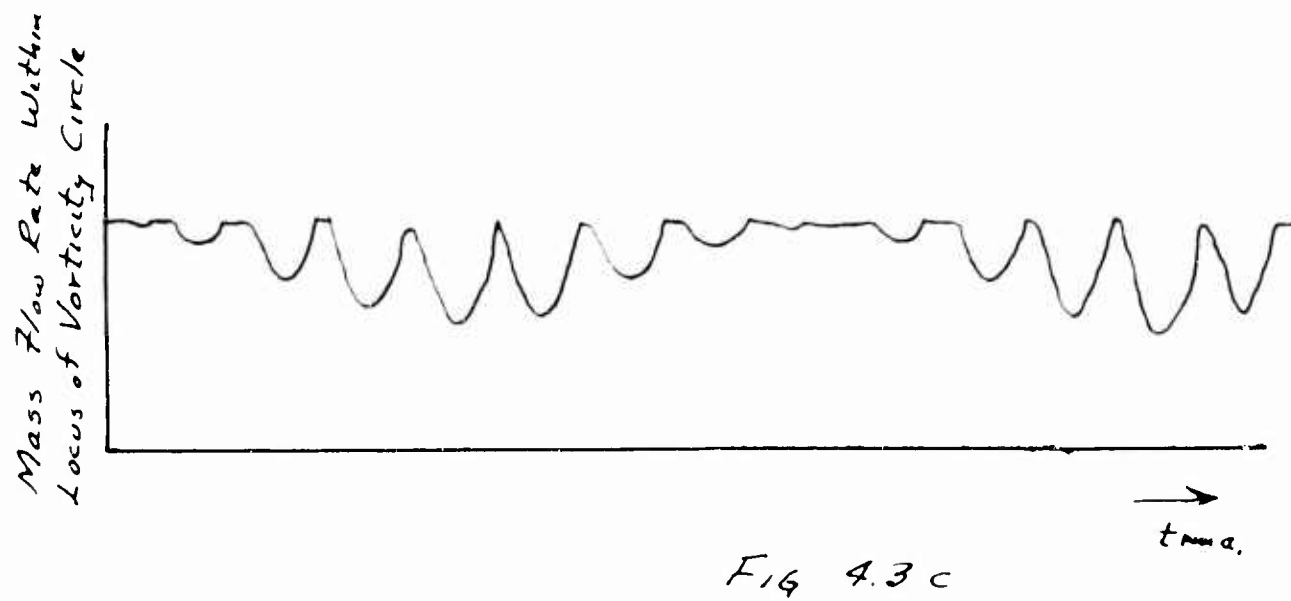
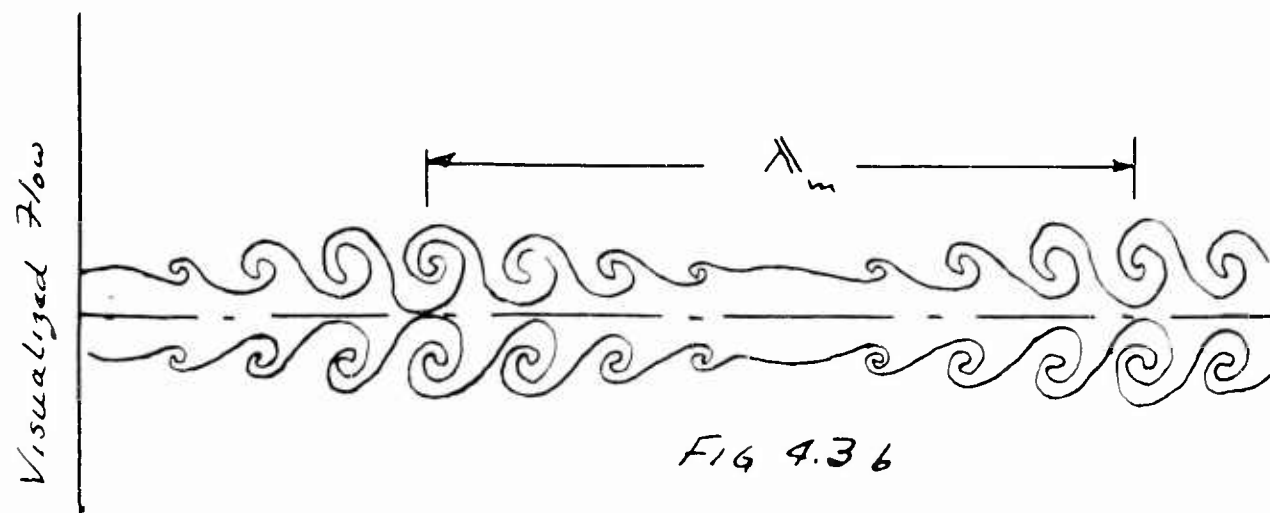
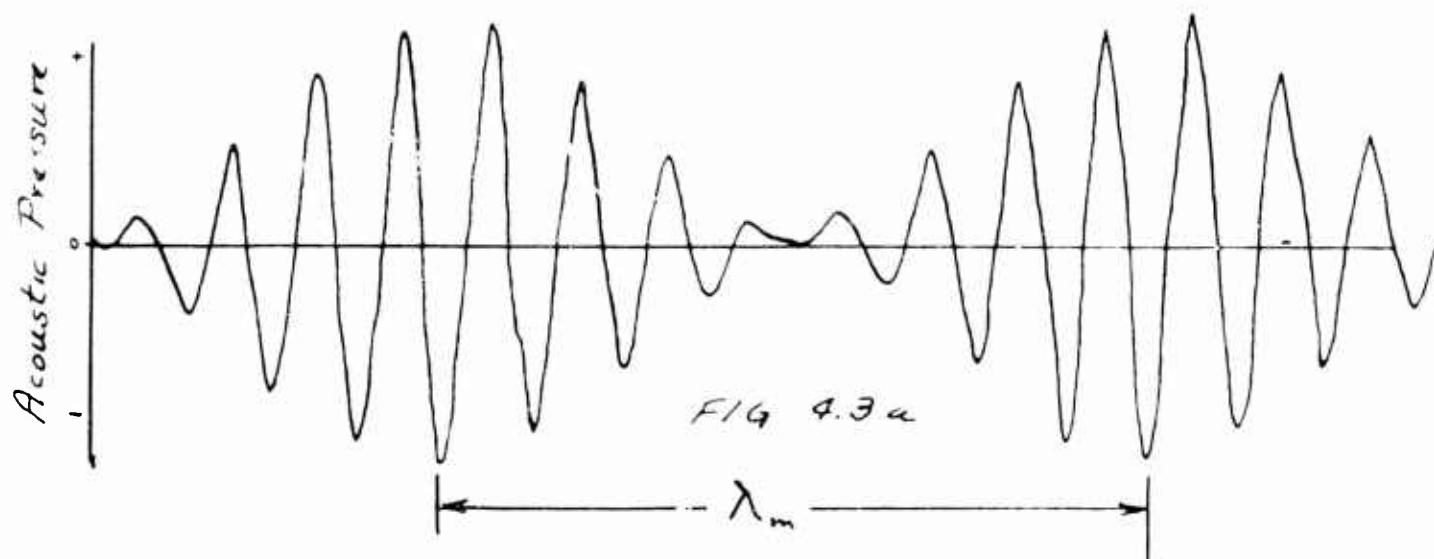
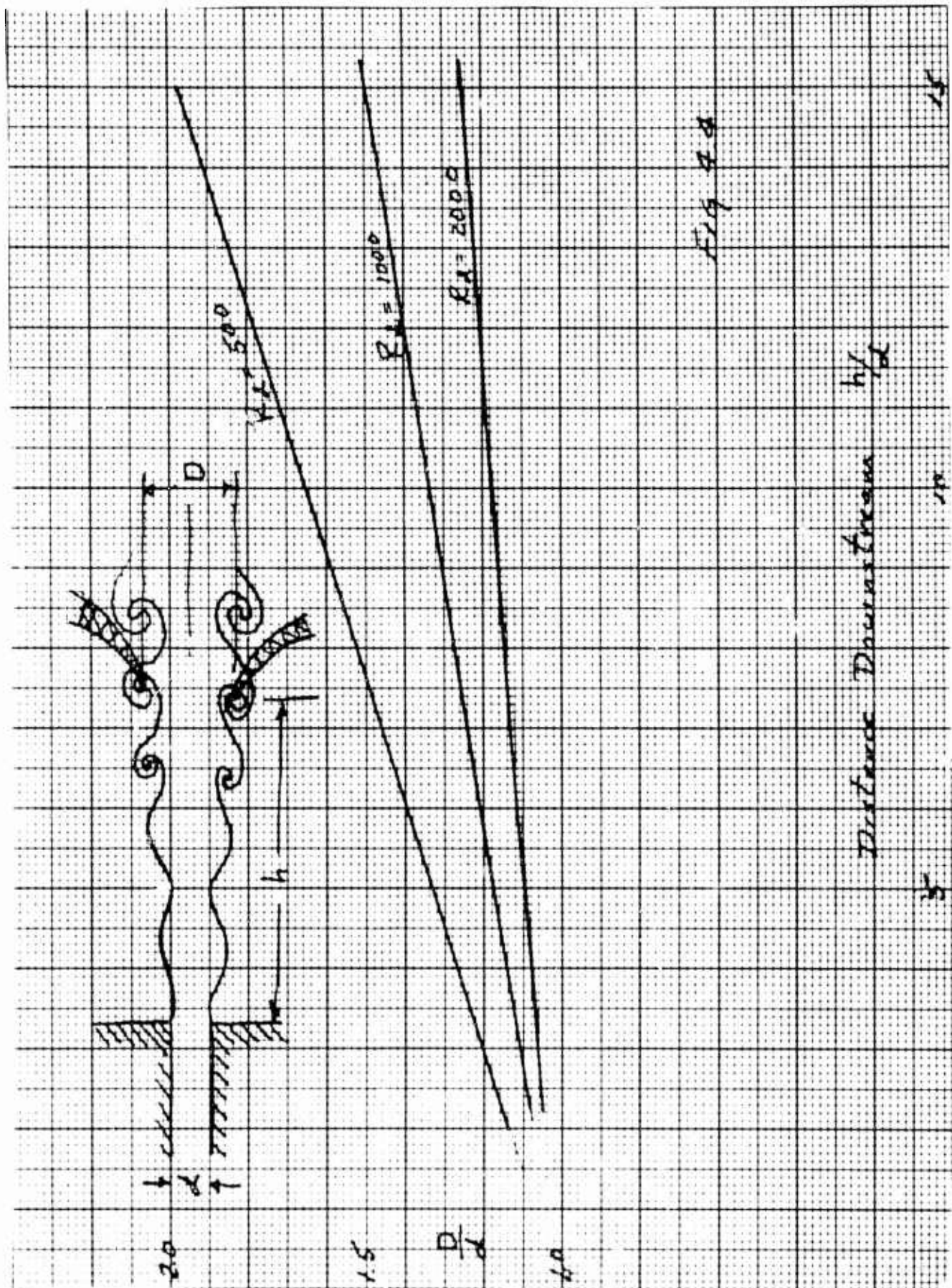


Fig 4.2c

ACOUSTIC AMPLITUDE MODULATED WAVE





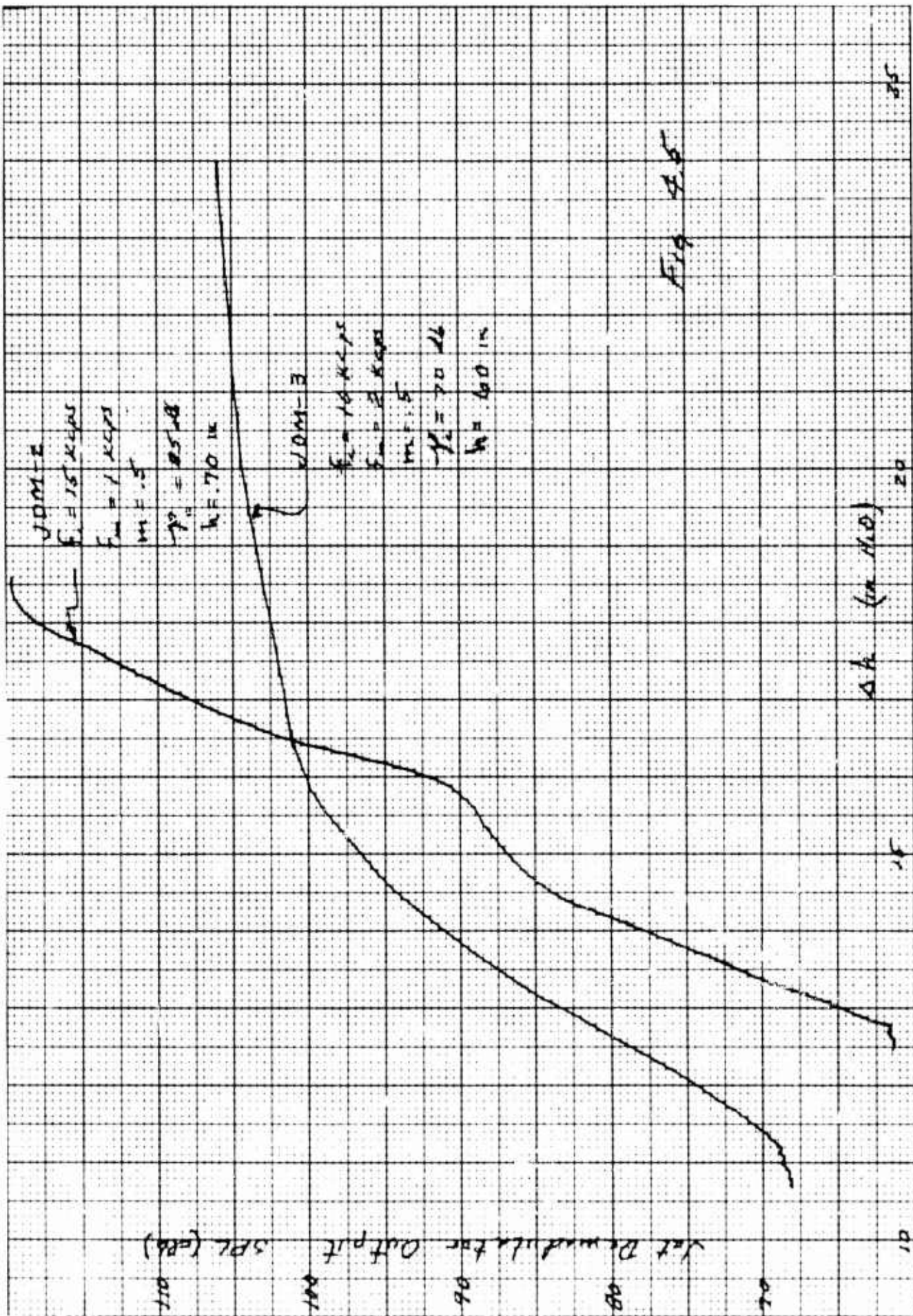
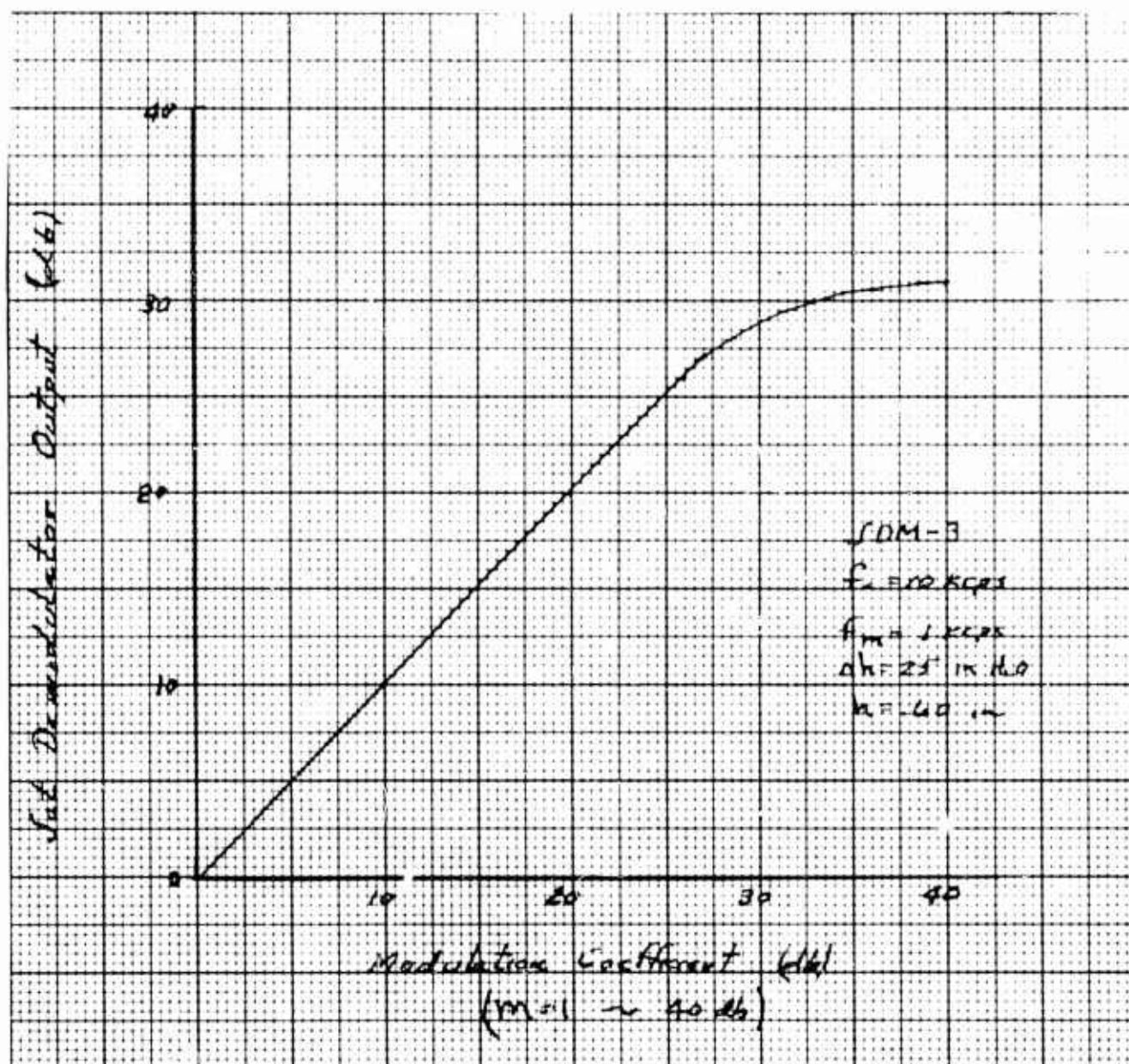
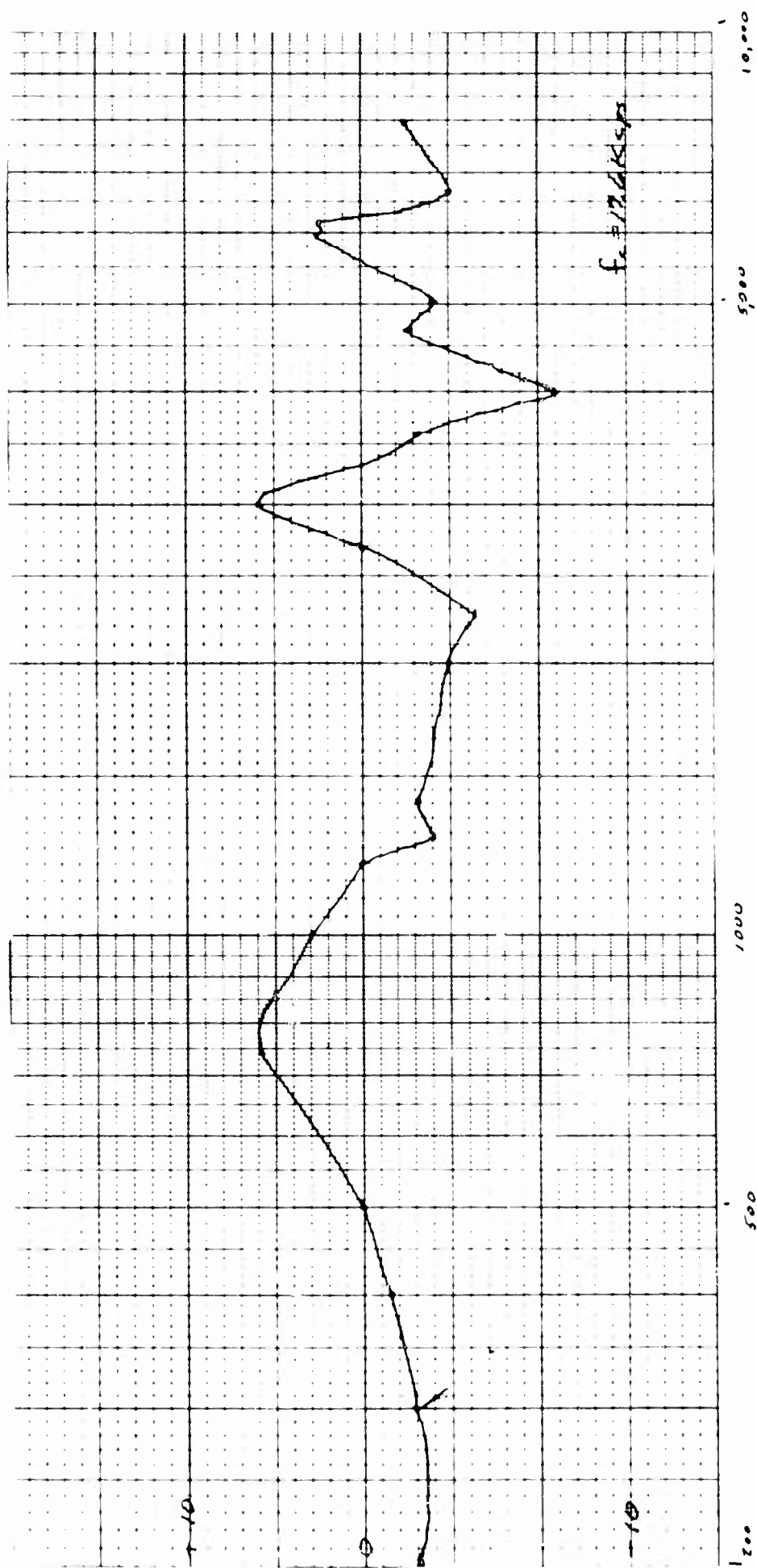


Fig 4.5



Typical Compression Characteristic

Fig 4.6



Set Demodulator Frequency Response

Fig 4.7

HARRY DIAMOND LABORATORIES
WASHINGTON, D. C. 20438

PREDICTING CLOSED LOOP STABILITY OF FLUID
AMPLIFIERS FROM FREQUENCY RESPONSE MEASUREMENTS

by

GARY L. ROFFMAN
and
SILAS KATZ

ARMY MATERIEL COMMAND

DEPARTMENT OF THE ARMY

ABSTRACT

Open loop frequency response measurements were made on a loaded fluid amplifier. The measurements showed frequency response resonance peaks up to 8000 cps. Using the Nyquist criteria, the stability of the closed loop system is predicted. The oscillation frequency of unstable systems is also discussed.

1. INTRODUCTION

The static characteristics of proportional fluid amplifiers have received considerable attention. However, before fluid amplifiers can be used in control systems, a knowledge of their dynamic characteristics is necessary. At present, only a few studies have been made of the dynamic characteristics of jet deflection fluid amplifiers. Belsterling and Tsui (ref 1) have developed an equivalent electrical circuit representation for the jet deflection fluid amplifier. From this circuit, the response of the amplifier has been predicted, and these predictions have been confirmed by experiments at frequencies up to 300 cps. Boothe (ref 2) has introduced a similar method using lumped parameter circuit theory and has some experimental verification up to 1000 cps.

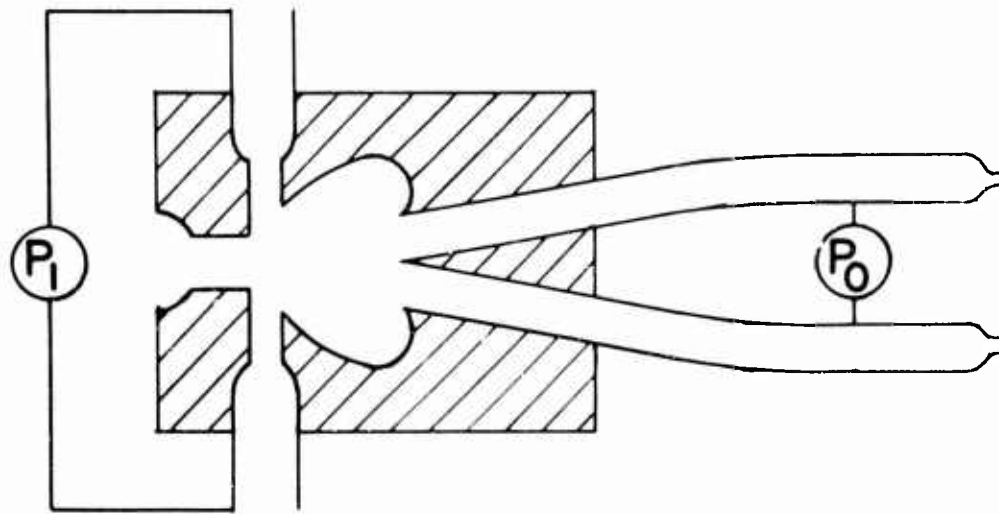
On the basis of present theories and measurements, the stability of closed loop fluid amplifier control systems has not always been predictable. When these theories fail at high frequencies, it is primarily because the jet deflection amplifier cannot be adequately described by lumped parameter theory.

The purpose of this investigation is to present the experimental open loop frequency response of a jet deflection fluid amplifier over a wide range of frequencies and to show how these characteristics can be applied to predict the closed loop stability of the amplifier with feedback. In those cases where the closed loop system is unstable, a sustained oscillation results. Standard compensation circuits can then be used to stabilize the system. However, if an oscillator is desired, the open loop frequency response can also be used to predict the frequency of oscillation.

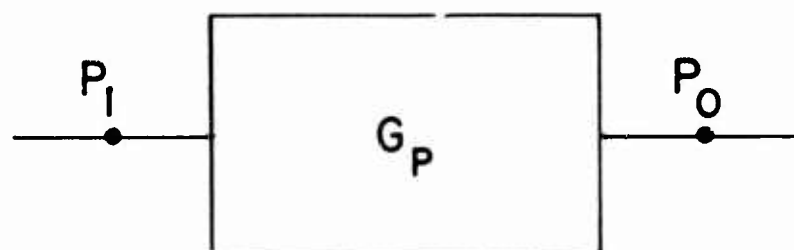
2. STABILITY CRITERIA

A vast body of information on the stability of linear feedback systems exists in the fields of control systems and electronics. The criteria for stability are well established and these criteria are applicable to fluid amplifiers.

Consider a proportional fluid amplifier and its load impedance as a linear "black box" whose dynamic characteristics are desired (fig.1). Although the load impedance may be treated separately, it is more convenient to combine it with the amplifier. The amplifier used has bleeds; therefore, it can be represented by a simple transfer function rather than a matrix. The effect of the bleeds is to decouple the input from the output. The response of a black box to a sine wave input, $G_p(j\omega)$, may then be expressed as



(a) PHYSICAL REPRESENTATION



(b) 'BLACK BOX' REPRESENTATION

PROPORTIONAL AMPLIFIER WITH LOAD IMPEDANCE .

FIGURE 1

$$G_p(j\omega) = \frac{p_o(j\omega)}{p_i(j\omega)} \quad (1)$$

where

$p_o(j\omega)$ = output pressure magnitude at the frequency ω
(pressure difference between left and right outputs)

$p_i(j\omega)$ = input pressure magnitude at the frequency ω
(pressure difference between left and right inputs)

$$j = \sqrt{-1}$$

and

ω = angular frequency, rad/sec

Because the jet deflection proportional fluid amplifier is a differential amplifier, either positive or negative gain may be obtained from one stage. That is, the output for d-c input signals may be in phase or 180 deg out of phase with the input. When this amplifier is used with feedback, the feedback can be positive (in phase) or negative (out of phase) even at very low frequencies. In the present case the feedback is always connected in a negative sense. A fluid amplifier is shown with negative feedback in figure 2. The closed loop transfer function $T(j\omega)$ is

$$T(j\omega) = \frac{G_p(j\omega)}{1 + H(j\omega) G_p(j\omega)} \quad (2)$$

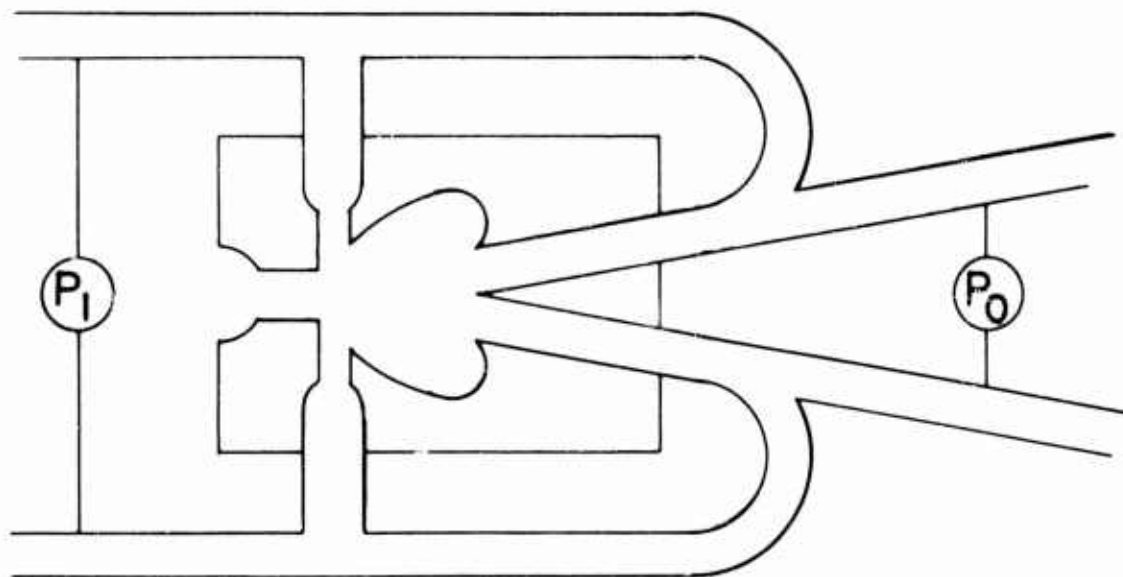
where

$H(j\omega)$ = transfer function of the feedback loop

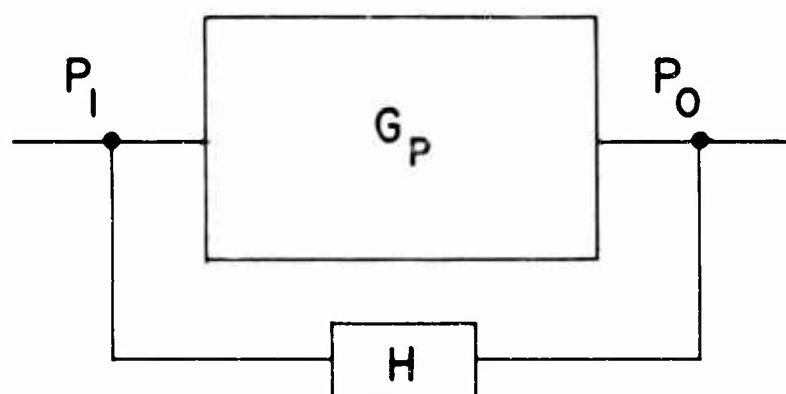
and

$H(j\omega) G_p(j\omega)$ = open loop transfer function

A Bode plot of the open loop transfer function, $H(j\omega) G_p(j\omega)$, is often used to present frequency response characteristics of components. In this plot the log of the magnitude, $\log H(j\omega) G_p(j\omega)$, and the phase of $H(j\omega) G_p(j\omega)$ are given in terms of $\log \omega$. When the equation of the transfer function is not known, which is often the case, a Bode plot can be found experimentally. On this plot the magnitude appears in decibels [$20 \log H(j\omega) G_p(j\omega)$] and the phase angle in degrees. In these units a gain of unity is equivalent to 0 db. A typical frequency response plot is shown in figure 3.

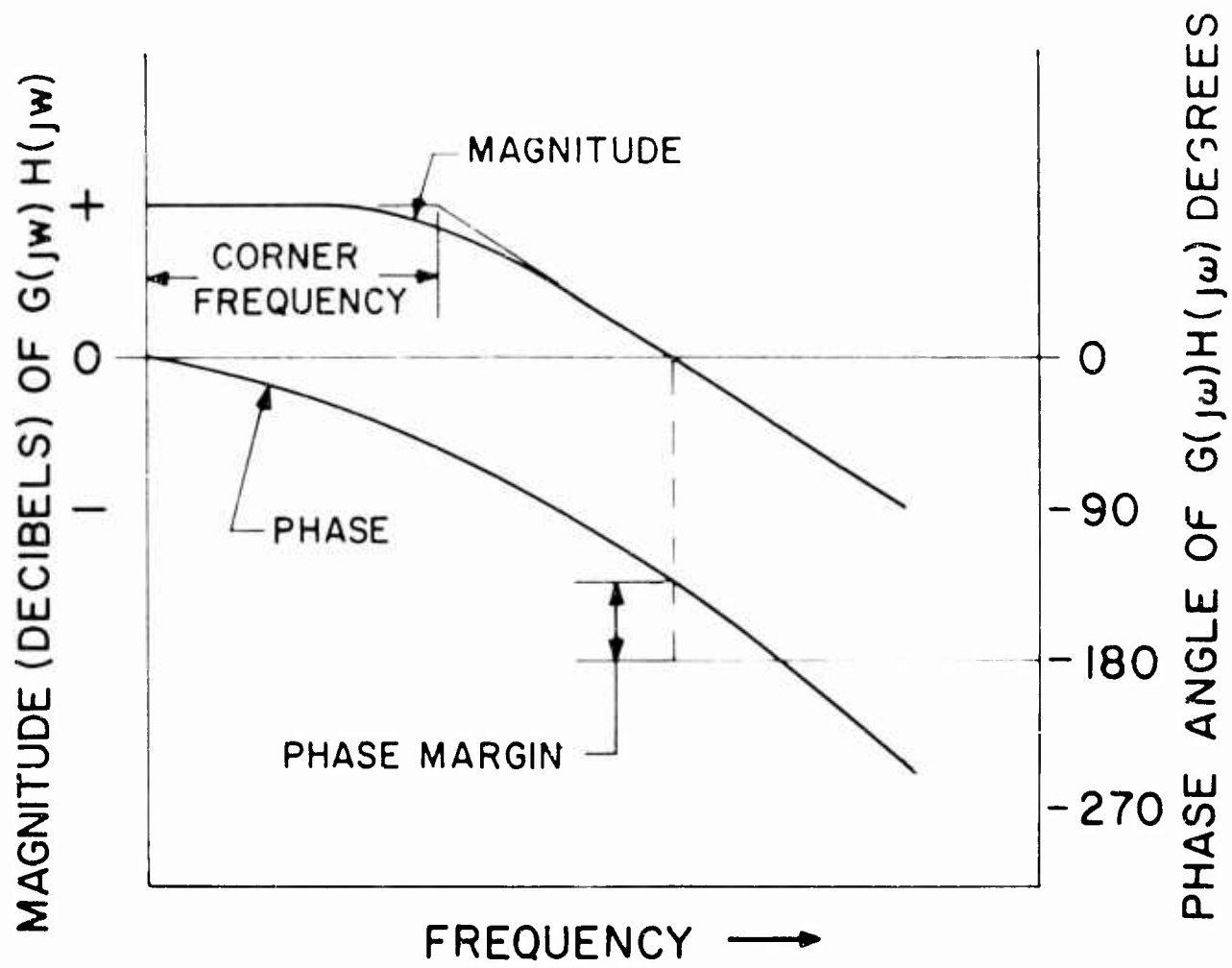


(a) PHYSICAL REPRESENTATION



(b) BLOCK DIAGRAM

PROPORTIONAL AMPLIFIER WITH FEEDBACK
FIGURE 2



TYPICAL FREQUENCY RESPONSE CURVE

FIGURE 3

To predict stability from the Bode plot, it is convenient to consider the Nyquist criteria. Nyquist has shown (ref 3) that a necessary condition for a closed loop system to be unstable is that

$$H(j\omega) G_p(j\omega) \geq 1 \quad (3)$$

$$H(j\omega) G_p(j\omega) = -180^\circ (2n + 1)$$

where

$$n = 0, 1, 2, 3, \dots$$

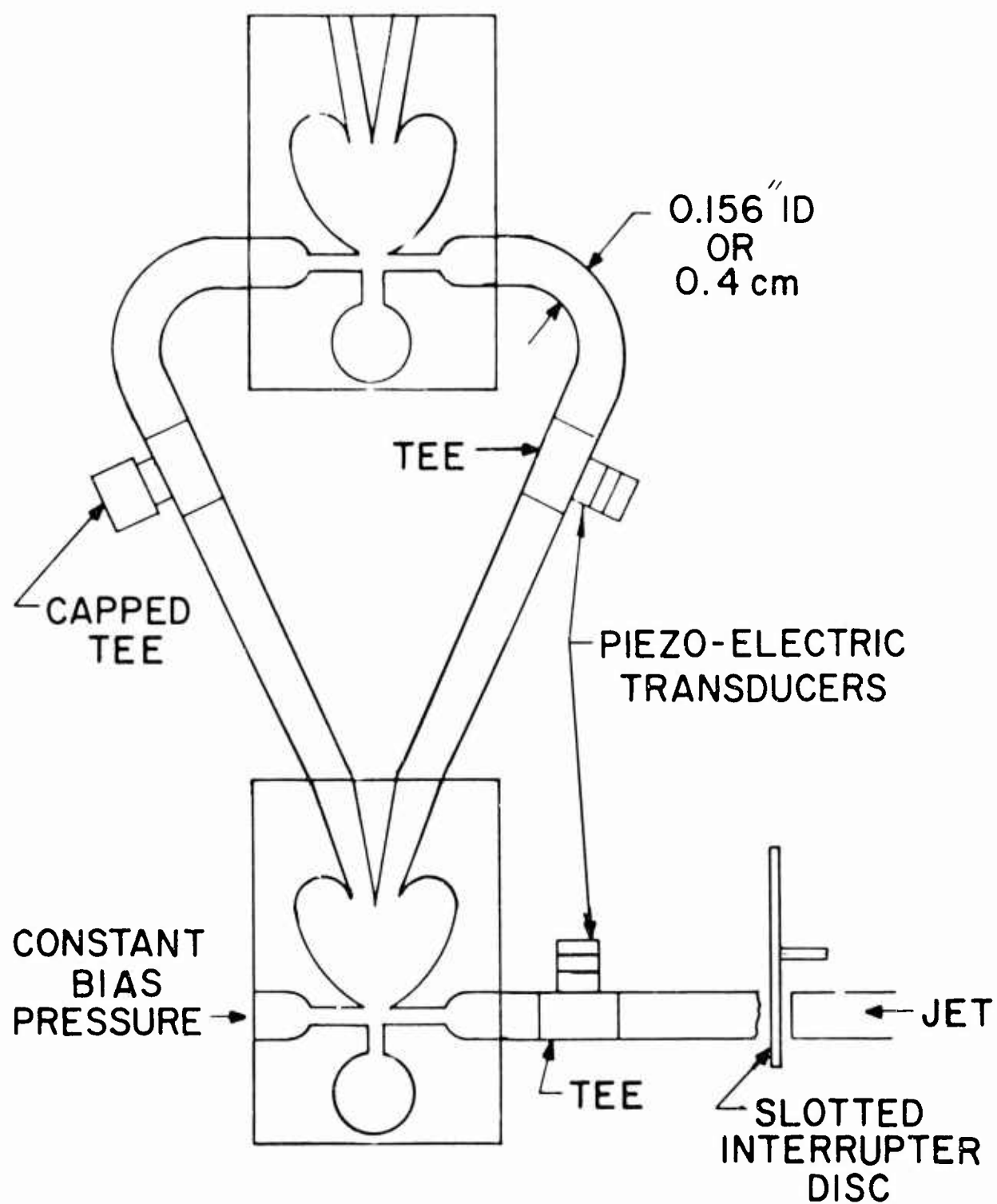
Using these criteria, the closed loop stability of many systems can be determined directly from the Bode plot. That is, if the magnitude is greater than 0 db at a frequency where the phase is $-180^\circ (2n + 1)$, the closed loop system will be unstable. These criteria are usually both necessary and sufficient for most fluid systems because in these systems the phase decreases monotonically with increasing frequency.

A physical interpretation of the Nyquist criteria is that when the phase changes by 180 deg (or 540 deg, 900 deg,) negative feedback becomes positive feedback. The output signals are thus returned to the input in phase with the input signals. If, in addition, this happens when the gain is greater than 0 db, a regenerative escalation takes place, tending to drive the output toward infinity. However, as the output increases, nonlinearities reduce the gain until a magnitude is reached at which the gain is unity, after which the system will oscillate at a constant frequency and magnitude.

3. EXPERIMENTAL TEST SETUP

The experimental setup used to measure the frequency response of the amplifier and load combination is shown schematically in figure 4.

The variable-frequency sinusoidal signal is generated by using either of two specially slotted rotating disks to interrupt a jet of air. One disk had 24 slots and the other had 300 slots. The interrupter disk method was adopted because high frequency signals (up to 8000 cps) were desired. Using the disk with 300 slots, these frequencies could be obtained at relatively low rotational speeds (1800 rpm).



FREQUENCY RESPONSE EXPERIMENTAL SET-UP

FIGURE 4

The signal passing through the disk was a distorted sinusoid. Attenuation of the undesired frequencies present in this distorted wave was accomplished with variable tanks and orifices, as well as by adjusting the length of the input line.

The signal was then applied to one control of a jet deflection type proportional fluid amplifier while the other control was maintained at constant pressure. This pressure or bias level was set at the same value as the pressure recovered at the output legs under static conditions, when the load was another identical amplifier. This particular bias pressure was selected to insure that the open loop frequency response would not be altered under closed loop conditions except, of course, if the combination became unstable. The bias level was approximately 30 percent of the power jet pressure. In these tests the power jet pressure was 41 kN/m^2 (6 psi).

The amplifier tested had a power jet 0.025 cm (0.010 in.) wide and 0.063 cm (0.025 in.) deep. The control output apertures were 0.038 cm (0.15 in.) by 0.063 cm (0.025 in.) and the overall size of the amplifiers was 2.5 cm (1 in.) by 5 cm (2 in.). Each output was connected to the controls of an identical amplifier through a 0.4-cm (0.156-in.) I.D. tubing. In these tests three different lengths of connecting line were used (10 cm, 30 cm, and 45 cm).

Piezoelectric transducers were used to measure the input and output signals. The transducers themselves had no inclosed volume. They were, however, mounted in the perpendicular branch of a small tee-fitting so that a small additional volume was added. The input-measuring transducer was positioned close to the input of the amplifier under test. The output-measuring transducer was positioned at the end of the connecting line, close to the input of the load amplifier. Since only the pressure ratio is important, these transducers were not calibrated absolutely. Rather they were tested against each other. They were found to be linear in the range of pressure used and for the same input gave readings almost equal in magnitude. Often, during a test, the transducer positions were reversed to determine if any changes had taken place. At these times, no appreciable differences were noted. The output of the transducers was displayed on an oscilloscope, and the data were taken directly from this.

To obtain the magnitude of the open loop frequency response, the reading of the transducer in the output leg had to be doubled, because with the experimental setup used the input transducer read the whole input signal amplitude while the output transducer, in one leg of the differential amplifier, read only half the output signal.

4. FREQUENCY RESPONSE TEST RESULTS

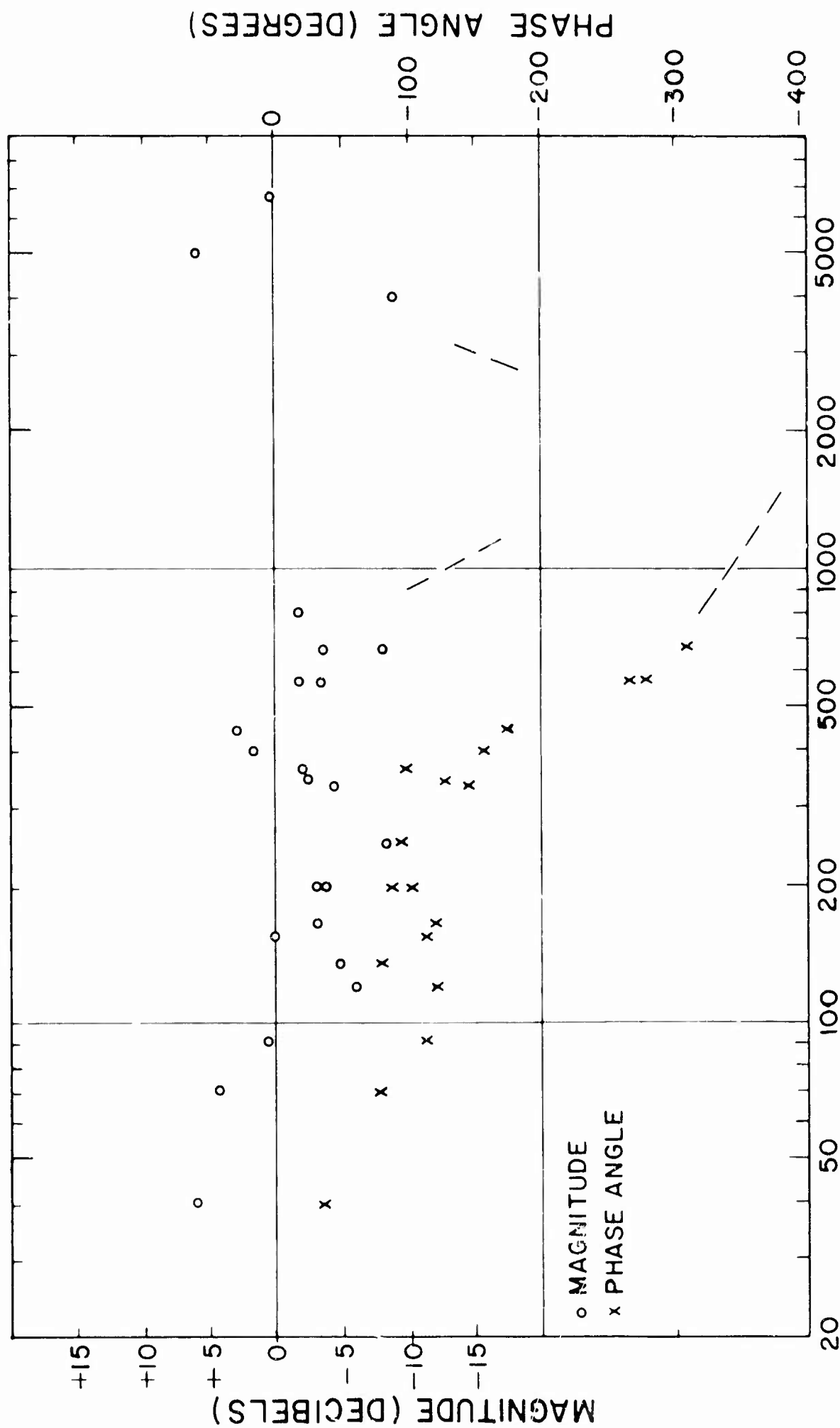
The amplifier was tested with 10-, 30-, and 45-cm lengths of tubing. The results plotted in figures 5, 6, and 7 do not permit a smooth curve to be drawn through the data. Repeat tests often produced widely different results. This occurred primarily because of the signal generator used. Usually the wave generated showed considerable distortion, which made it difficult to obtain accurate measurements. However, while no great accuracy can be claimed for a single test, the overall frequency response pattern is clear; large gains appear at discrete frequencies after the gain initially drops below 0 db. These peaks cannot be explained by lumped parameter theory, but are due to the presence of the cavities (ref 4) and to the length of connecting line. Reflections are returned from the sides of these cavities to produce an internal feedback effect.

Three distinct frequency ranges showed considerable peaks for the tests performed. For example, on figure 5, peaks occurred at 480, 820 and 5000 cps. In addition, weak peaks were noticed at about 1250 and 2500 cps. The dashed lines on the figure indicate that the output signal was too small to measure between 1000 and 3000 cps.

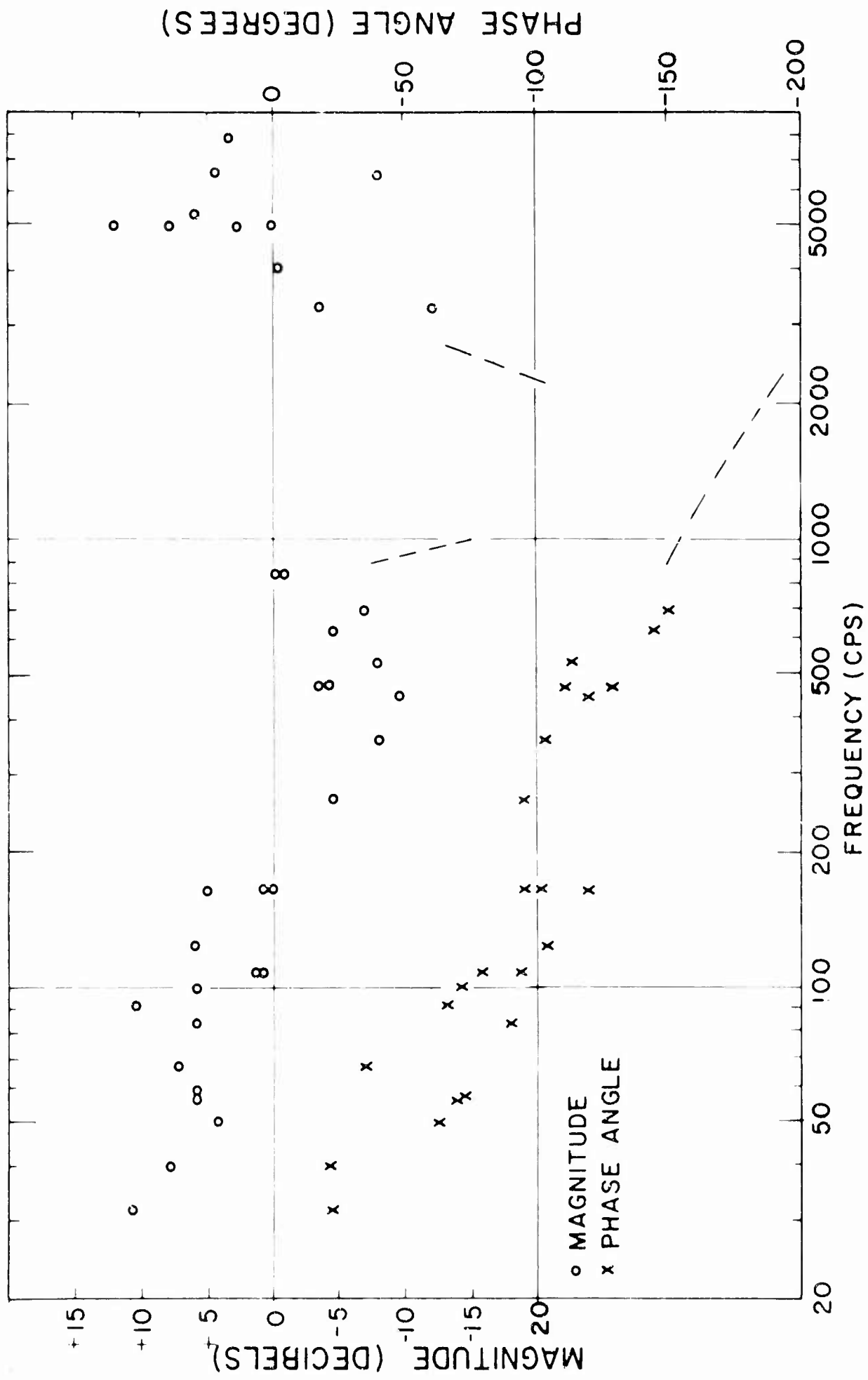
The magnitude of the peak depended on the response of the connecting line at the outputs. The 10-cm line produced low gain peaks in the lower range and a high gain peak around 5000 cps. The 30-cm line produced considerable peaks in both the high and low ranges. The 45-cm line showed high peaks in the low range and low gain peaks in the high range.

Figure 8 shows the oscilloscope traces of the amplifier responding to a 5000-cps input signal generated by an identical amplifier used as an oscillator. These wave forms are more nearly sinusoidal than the signals produced by the slotted discs, but, it was possible to produce oscillations only at a few frequencies (sect. 5). Here the amplitude increased as the length of the connecting line decreased.

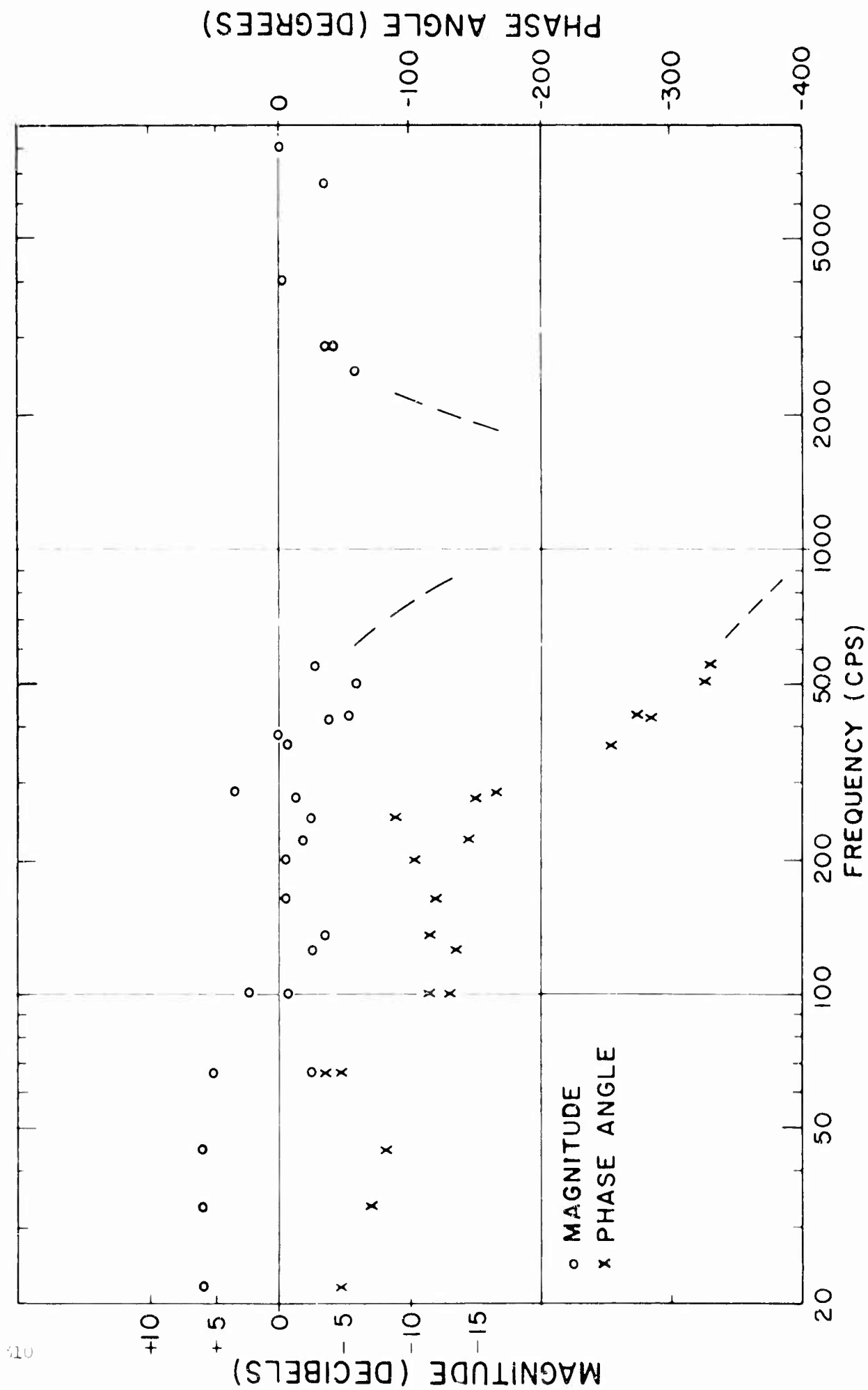
As indicated in equation (3), the phase angle must also be considered. The phase angle is a function of the transport delay as well as the properties of the lines. At the high frequencies the phase angles are very large ($>360^\circ$). Since there were regions of response too low to measure, it was not possible to follow the phase step by step. Thus the absolute phase shift is lost at the high frequencies. However, in the vicinity of a peak the phase changes rapidly and becomes an odd multiple of -180 deg even within the narrow frequency range of the peak, thereby satisfying the criteria for instability.



FREQUENCY RESPONSE OF AMPLIFIER AND 30 cm LINE
FIGURE 6

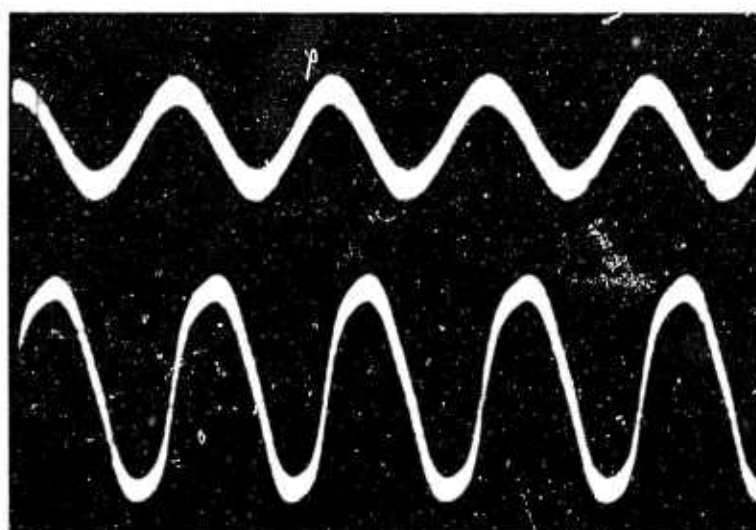


FREQUENCY RESPONSE OF AMPLIFIER AND 10cm LINE
FIGURE 5



FREQUENCY RESPONSE OF AMPLIFIER AND 45 cm LINE

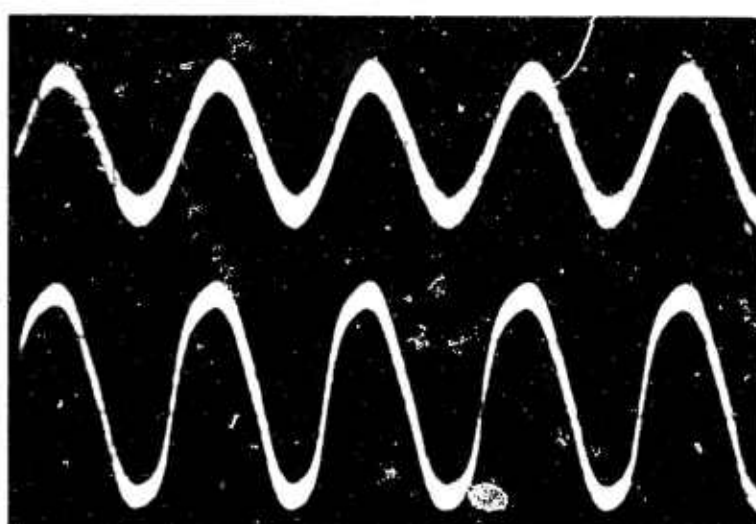
FIGURE 7



Output

45 cm line
sweep = 0.1 ms/div.

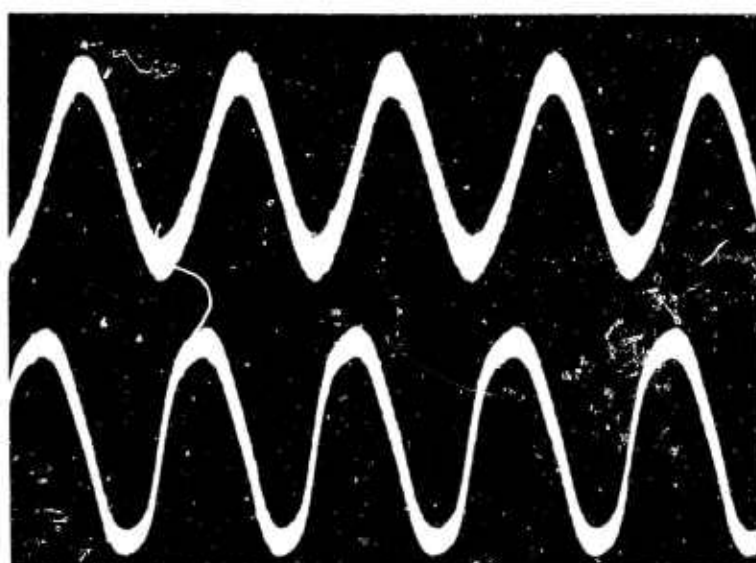
Input



Output

30 cm line
sweep = 0.1 ms/div.

Input



Output

10 cm line
sweep = 0.1 ms/div.

Input

935-65

Figure 8. Response to 5-KC signal from fluid oscillator.

5. CLOSED LOOP STABILITY

In these tests the outputs of the amplifier were connected directly to the inputs through the same lengths of line with which the amplifier was tested open loop (10, 30 and 45 cm).

From figure 5, the open loop data for the 10-cm line show that the gain is above 0 db below 200 cps and between 5 and 8 kc. To determine the stability (equation 3) the phase angle at these frequencies must be examined. At the low frequencies, the phase angle is never greater than -120 deg; at the high frequency peak, the phase is greater than -180 deg and probably goes through an odd multiple of -180 deg when the gain is above 0 db. The open loop data predict that the system will be unstable and will oscillate at a frequency between 5 and 8 kc. When the loop was closed, a sustained oscillation at 7100 cps occurred. The phase may pass through several odd multiples of -180 deg between 5000 and 8000 cps when the gain is greater than 0 db. It was found that by pinching and releasing the line the system would oscillate at 6 kc. This suggests that more than one peak exists in the range between 5 and 8 kc.

The open loop data for the 30-cm line (fig. 6) show gains greater than 0 db below 150 cps, between 400-550 cps and about 5 kc. Examination of the phase shows that below 150 cps it was less than -180 deg. The phase angle in the 500-cps range was about -180 deg. The phase was greater than -180 deg in the 5-kc range and as before changed rapidly near the peak. The open loop data therefore predict an oscillation at both 500 cps and 5 kc. Closing the loop resulted in an oscillation at 425 cps, but a slight disturbance of the feedback lines changed the frequency to 4750 cps. By disturbing the line again, the oscillation returned to 425 cps.

The open loop data given in figure 7 for the 45-cm line show that it has gains greater than 0 db below 100 cps and between 300 and 350 cps. The high frequency peak at 5 kc was lowered by the line. In this case only the 300-cps range has the gain and phase for instability and the oscillation is expected only in this range for the closed loop system. When the loop was closed, an oscillation of 300 cps was produced. No amount of disturbance to the line shifted the frequency.

The open loop frequency tests were performed only at a power-jet pressure of 41 kN/m². The power-jet pressure was varied when the loop was closed, and the effect on the oscillation was noted. For the low frequency oscillation, the frequency was constant and the magnitude varied directly with the power-jet pressure for pressures from

14 to 97 kN/m². This shows that the phase of the open loop system does not vary much with power-jet pressure in the range tested. A gain of unity is required for constant amplitude oscillation and, due to the nonlinearity of the amplifier, this was achieved with larger amplitude signals at the higher power-jet pressures.

The high frequency oscillation (5 kc) changed abruptly in both frequency and magnitude as the power-jet pressure was changed. The frequency change was small; the magnitude change was great. Once a new mode occurred it remained if the pressure was reduced, but the previous mode could be made to return by disturbing the tubing. This effect was noted before, where disturbing the lines caused a change in the frequency of oscillation. The changing of the power-jet pressure made oscillation at one frequency more likely than oscillation at another frequency where the phase differs by 360 deg.

6. SUMMARY AND CONCLUSIONS

Open loop frequency response measurements were made on a proportional amplifier and load combination. The load was another identical amplifier connected to the test amplifier by different lengths of tubing. The measurements showed gain peaks at regular intervals up to 8000 cps. The magnitude of the peaks depends on the length of the connecting line, whereas the frequency at which the peaks occur depends on the internal cavities of the amplifier.

From the open loop measurements, the stability of the closed loop system was predicted using the Nyquist criteria. These predictions were confirmed by closed loop experiments. When the system was unstable it was also possible to predict the frequency of its oscillation. In some cases two or more oscillating frequencies are possible.

Compensating circuits can be used to stabilize the system or to shift the frequency of the oscillation. However, it is always important to know the characteristics over a wide frequency range because of resonance effects.

REFERENCES

1. Belsterling, C. A. and Tsui, K. T., "Analytical Technique for Applying Fluid State Amplifiers," Control Engineering, August 1965.
2. Boothe, W. A., "A Lumped Parameter Technique for Predicting Analog Fluid Amplifier Dynamics," ISA Transactions, Vol. 4, No. 1, Jan 1965.
3. Nyquist, H., "Regeneration Theory," Bell Telephone Technical Journal, Jan 1932.
4. Gottron, Richard N., "Noise Reduction by Jet-Edge and Resonator Coupling," Proceedings of the Fluid Amplification Symposium, Vol. 1, HDL, May 1964.

ACKNOWLEDGEMENT

The authors wish to express their appreciation to E. G. Hastie for his assistance with the experiments.

ASTROMECHANICS RESEARCH DIVISION
Giannini Controls Corporation
Malvern, Pennsylvania

ON THE DYNAMICAL CHARACTERISTICS
OF
FLUID AMPLIFIERS AND ELEMENTS

by

Peter A. Orner

A Paper Prepared For
The Third Fluid Amplification Symposium
Harry Diamond Laboratories, Washington D.C.
October 1965

ON THE DYNAMICAL CHARACTERISTICS
OF
FLUID AMPLIFIERS AND ELEMENTS

by

Peter A. Orner

Giannini Controls Corporation
Astromechanics Research Division
Malvern, Pennsylvania

ABSTRACT

The problem of intrinsic instability in fluid jet amplifiers is examined. Both linear and nonlinear oscillations are discussed. Various pertinent aspects of the acoustic feedback loop theory for sustained oscillations in a jet-edge system are conceptually applied to the stability of beam amplifiers. Some experimental data showing self-induced high frequency oscillations in a vented proportional beam amplifier are presented.

The basically nonlinear acoustic-flow interaction is suggested as the possible cause of many low frequency blocked load instabilities. Experimental evidence of a load-resonance-sensitive blocked load instability is presented for a proportional device utilizing boundary layer separation. Semianalytical stability prediction techniques for amplifiers and circuits are discussed.

INTRODUCTION

In the past four years, a great deal of effort has been directed toward the development of proprietary pure fluid amplifiers and specific pneumatic sensors and circuits employing these devices. As with any promising new technology, and especially one which is largely empirical, there have been many attempts at cut-and-try solutions to a wide variety of application problems. Some of these investigations have been fruitful, yielding both usable hardware and a basic understanding (phenomenological and/or analytical) of the principles and techniques employed therein. However, many of these studies have resulted in highly tailored, one-of-a-kind laboratory hardware, sometimes meeting the original performance specifications, and sometimes not; but generally suffering from the lack of a sound phenomenological understanding.

The engineering situation is quite complex, since continuous fluid

amplifier designs at present make use of a wide variety of operating phenomena, c.f. jet momentum interaction, pressure controlled jet deflection, knife edge jet deflection, edge tone modulation, laminar-turbulent jet transition control, axi-symmetric jet impact, boundary layer controlled jet deflection, curved elbow flow acceleration control, and vortex control. Of these fluid flow phenomena, only the two-dimensional high aspect ratio and the axi-symmetric momentum-interaction devices appear amenable to meaningful static analysis. This is not to say that analytical models cannot be constructed for the other devices, but rather that, to the author's knowledge, the success of any such attempts has been limited to very small operating ranges under assumed idealized operating conditions. As a result, two major engineering problems arise. First, it is quite difficult to "scale" a given device, or determine its limits of application with only a meager analytical description. This is a fluid mechanical problem and its solution involves careful analytic approaches to each type of device, coupled with intelligent testing under selected similitude considerations.

The second, and possibly more significant, problem is the inter-connection of several devices in a useful circuit configuration. The usual technique employed is a combination of quasi-static graphical impedance matching and substantial amounts of circuit "tuning". It is implicitly assumed that the individual devices are stable, i.e., that the actual static circuit behavior will be approximated by the aggregate behavior of its components as described by static loading curves, etc. This assumption appears to hold for simple circuits with weak feedback paths and relatively "quiet" devices (high signal-to-noise ratio). It can even be employed in an intuitive manner to produce the linearized dynamic response (transfer function) of certain fluid amplifier circuits subject to time varying inputs. When this is done, the amplifier itself must be treated quasi-statically, using the static loading curves, jet transport lags, etc., in conjunction with experimentally or analytically determined sinusoidal response characteristics of the passive circuit components (amplifier inlet and outlet ports, connecting lines, restrictors, volumes, etc.).

If the amplifier is intrinsically stable, has a high signal-to-noise ratio, and has negligible terminal interaction, one would expect to be able to predict the small signal dynamic behavior satisfactorily. Unfortunately, such common phenomena as blocked load instability, high frequency noise transmission, low frequency drift, etc. are not explainable by this quasi-static approach. However, these phenomena are vitally important to anyone attempting to construct control circuits even with simple momentum-interaction amplifiers. The problem is even more acute with many proprietary devices, such as vortex and boundary layer separation controlled amplifiers.

Intrinsic instabilities and dynamic nonlinearities can obviously

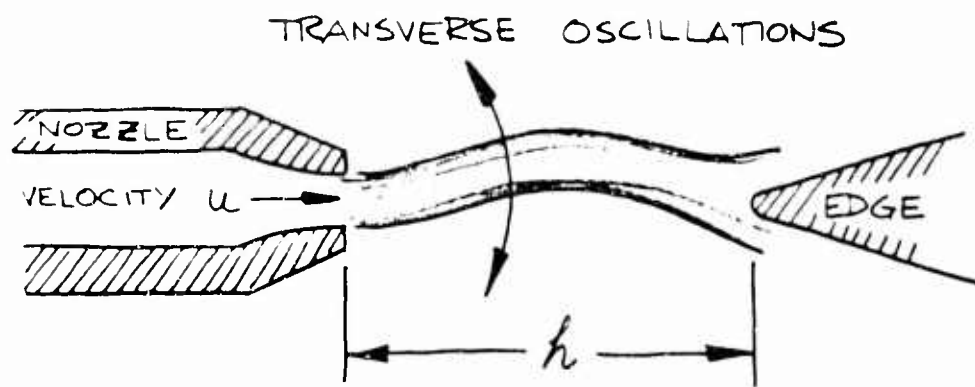
affect the circuit response to an imposed signal, producing large discrepancies between the quasi-static transfer function model and reality. Whenever elemental instabilities or nonlinearities are present, circuit design for static stability, minimum noise, etc. takes precedence over any other design criteria. It would therefore be desirable to have semianalytical nonlinear dynamic models of the important fluid state devices. The intent of this paper is to realistically appraise the problems involved, to evaluate proposed methods of formulating dynamic models, and to show preliminary experimental evidence of important fluid element nonlinearities and instabilities.

OBSERVED INSTABILITIES AND NONLINEARITIES

Edge Tones

Fluid jet amplifiers often exhibit high frequency oscillatory instabilities. Over the range of frequencies usually encountered, passive elements such as flow restrictors, amplifier receivers, and connecting lines are predominantly influenced by acoustic wave phenomena. Further, any meaningful dynamical description of the active elements must take into consideration transverse and longitudinal wave effects and edge vortex formation in the power jet. It may be reasoned that an acoustic mode must exist in either the power jet or the region immediately surrounding it to produce output-load-sensitive oscillations, especially in "open vented" devices. This intuitively provides the only feasible mechanism for transmitting the load-induced flow disturbances back "upstream" to the power jet origin.

Considerable attention has been directed to the production of both symmetric and asymmetric transverse jet oscillations by means of an obstacle placed several jet widths downstream from the jet origin as in Figure 1 (e.g. the edgetone, hole tone, ringtone, etc. 1,2,3,4). Sound sensitive jets and flames were observed over a hundred years ago (see Rayleigh, Theory of Sound, Vol. 2, Chapter 21), with a considerable accumulation of experimental evidence indicating that the jet flow fields could be strongly affected by a contiguous acoustic field. However, the concept that an acoustic field could be generated by a jet impinging on a stationary downstream obstacle and that this acoustic field could disturb the jet (i.e. cause vortex formation and/or lateral displacement) as the jet issues from the nozzle was not experimentally verified until recently by Powell⁵. Although the notion of such an "acoustic feedback loop" had been introduced much earlier by Rayleigh and others, its actual physical existence was, and in some cases still is, a very controversial topic. Nyborg⁶ and others have proposed a variety of acoustic and hydrodynamic feedback mechanisms, such as the generation of an alternating pressure gradient across the entire jet length.



FREQ. OF OSCILLATION $\cong .466 j \frac{u}{h}$
 $j = 1, 2.3, 3.8, 5.4$
 (AFTER G.B. BROWN)

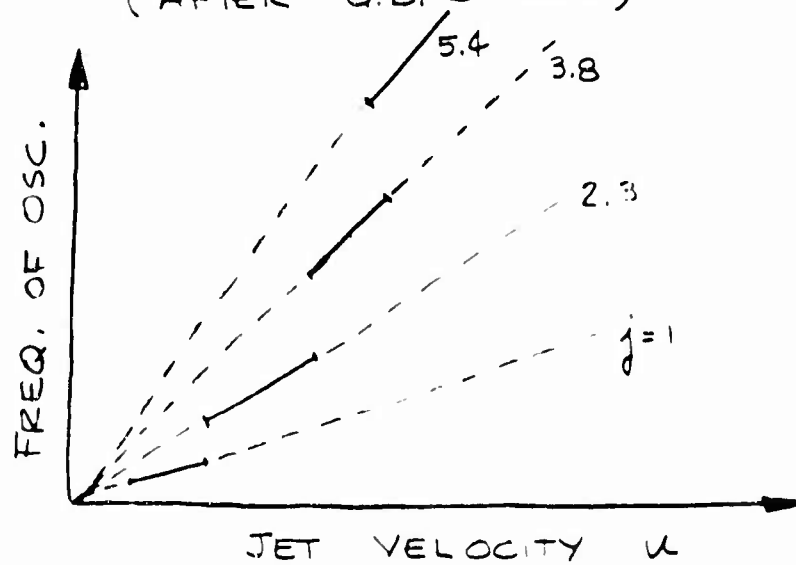


FIGURE 1 JET-EDGE SYSTEM

Whether the feedback is viewed as purely acoustic (perhaps audible) as with high speed edgetones¹; hydrodynamic-acoustic as in the case of low speed edgetones^{5,7}; or purely hydrodynamic^{3,4,8}; the concept of a nonlinear feedback loop is now rather firmly entrenched in the theory of oscillations of a free jet impinging on a downstream obstacle.

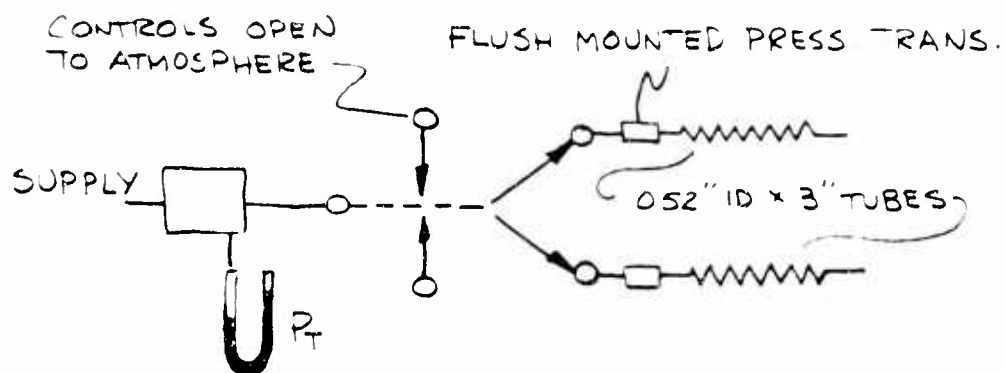
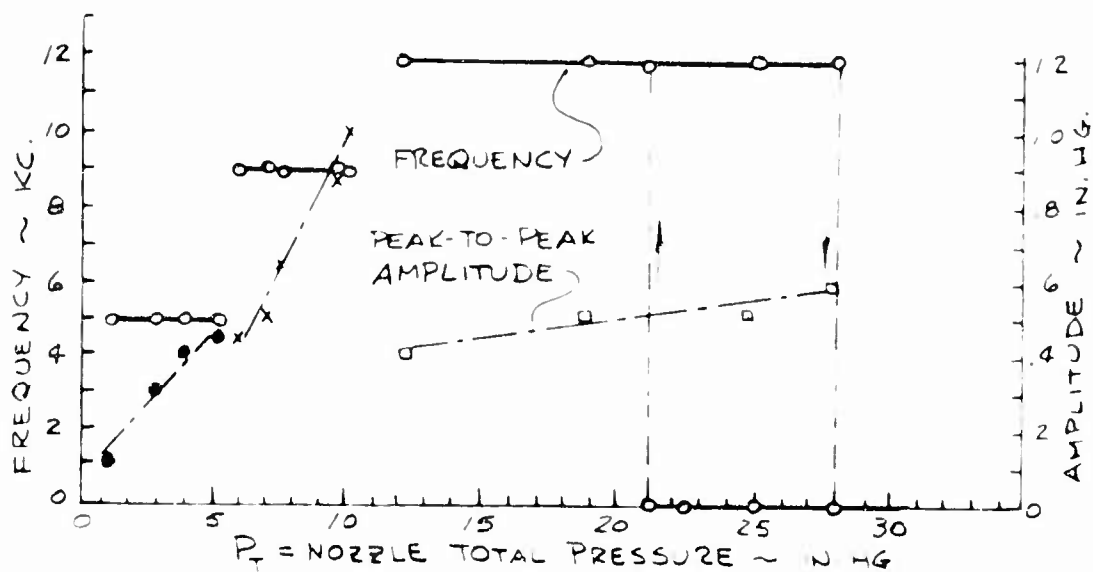
It is apparent, therefore, that an attack on the high frequency instability problem using the mathematical tools of either classical or modern feedback systems theory is in order. Powell has used a simplified version of this approach in predicting the modes of a free jet-edge system⁷. The latter's method is semiempirical, utilizing operating point linearization to achieve a simple criterion for sustained oscillations. An extended application of this linearized acoustic feedback method to the elimination of audible noise in beam amplifiers has not, to this author's knowledge, been attempted. Pursuing such an investigation with a plurality of feedback loops could very well lead to a valuable insight into the so-called signal-to-noise ratio problem. It is entirely possible that much of what is casually dismissed as "high frequency noise" is in reality the high frequency instability of a complex system with a large number of modes.

Edgetone - Resonator Systems

In a two-dimensional proportional fluid jet amplifier, the edgetone type of instability would most likely occur for relatively low load impedances, causing the receiver(s) to act essentially as a group of closely spaced "edges" or splitters. Not surprisingly, many early amplifier designs behaved instead as edgetone oscillators. This design problem has been partially eliminated (not solved) by tedious cut-and-try changes in the interaction region and venting designs. Also, the trend to smaller nozzle sizes has, in most cases, elevated the frequencies outside the audible range.

Experimental frequency-velocity data on a typical momentum-interaction beam amplifier are presented in Figure 2. In this case, the total pressure of the supply jet is given as the velocity variable. It is rather surprising that once a mode has been established, the frequency remains constant over a wide range of jet velocities.

It was observed that amplifier oscillation could be induced by manipulating a flat plate in the vicinity of the vent holes. If a plate covering one of the vent holes was lifted away to a distance on the order of an inch, the audible noise level would become painful to the unprotected ear. Also, no matter what the control pressure differential was (within a very wide range), the output pressures (measured on manometers) would become equal, reaching a value very much in excess of the normal null value.



TEST SET-UP

AMPLIFIER SPECS: .030" WIDE x .060" DEEP SUPPLY,
CONTROL, AND RECEIVER CHANNELS
.240" RECEIVER SETBACK
3/12" DIA. COVER VENT HOLES

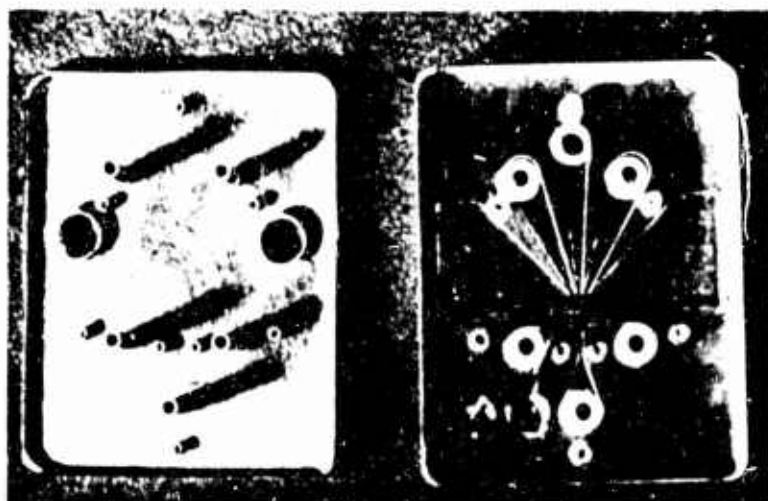


FIGURE 2 BEAM AMPLIFIER INSTABILITY MODES

It was further found that there were several critical spacings, each of which corresponded to a sharp audible sound intensity maximum. The largest of these spacings was several inches at the higher jet velocities. By setting the supply pressure at values which corresponded to frequency jumps (e.g. 5.5 to 6.0, or 10.4 to 12.0 in. Hg.), it was found that either of the modes could be established, depending on the plate location.

This experiment was only of a preliminary nature, but it supported the validity of the acoustic feedback theory, as applied to fluid amplifiers. The strong coupling of the D.C. value of the output pressures with the amplitude of oscillation emphasizes the essential role of nonlinearities in these cases. It is believed due to the "acoustic pumping" action described in the next section.

Nyborg⁹ has experimentally investigated the coupled modes of a two-dimensional jet-edge system and an "organ pipe" resonator positioned normal to the jet axis, as shown in Figure 3. His results show the expected modal coalescence with strong sound intensity maxima near the coalescent points. The coalescent points in this case were, of course, those at which the velocity-dependent edgetone frequency was equal to one of the harmonics of the resonator. Gottron¹⁰ experimentally investigated a jet-edge system coupled to a pair of resonators diametrically opposed and normal to the jet axis. While the results in the latter paper indicated relative changes in the sound intensity as the jet velocity was increased, no data was presented for the jet-edge system alone, and thus it is difficult to see whether the edgetone intensity was actually reduced or increased. Gottron's frequency spectra are interesting, in that they depict quite dramatically the wide band frequency mix one often encounters in fluid amplifier work, and which one equally often dismisses as "noise".

Nyborg shows the presence of subharmonics in the free jet-edge-resonator system, while some of Gottron's data for the confined jet strongly suggests the same. The subharmonic behavior is of special interest, since it would form a necessary part of any theory which attempted to explain the familiar low frequency blocked load amplifier instabilities by the existence of an acoustic loop. This is discussed in the next section.

Low Frequency Oscillations

That subharmonic behavior should appear in fluid jet devices is not surprising, due to the fundamental nonlinearities in the equations of fluid motion. Specifically, the convective terms in the velocity (e.g. $u \partial u / \partial x$) couple the modes from zero frequency (D.C.) up through the higher Fourier harmonics. The modal interaction is bilateral (although not reciprocal), in that energy can be trans-

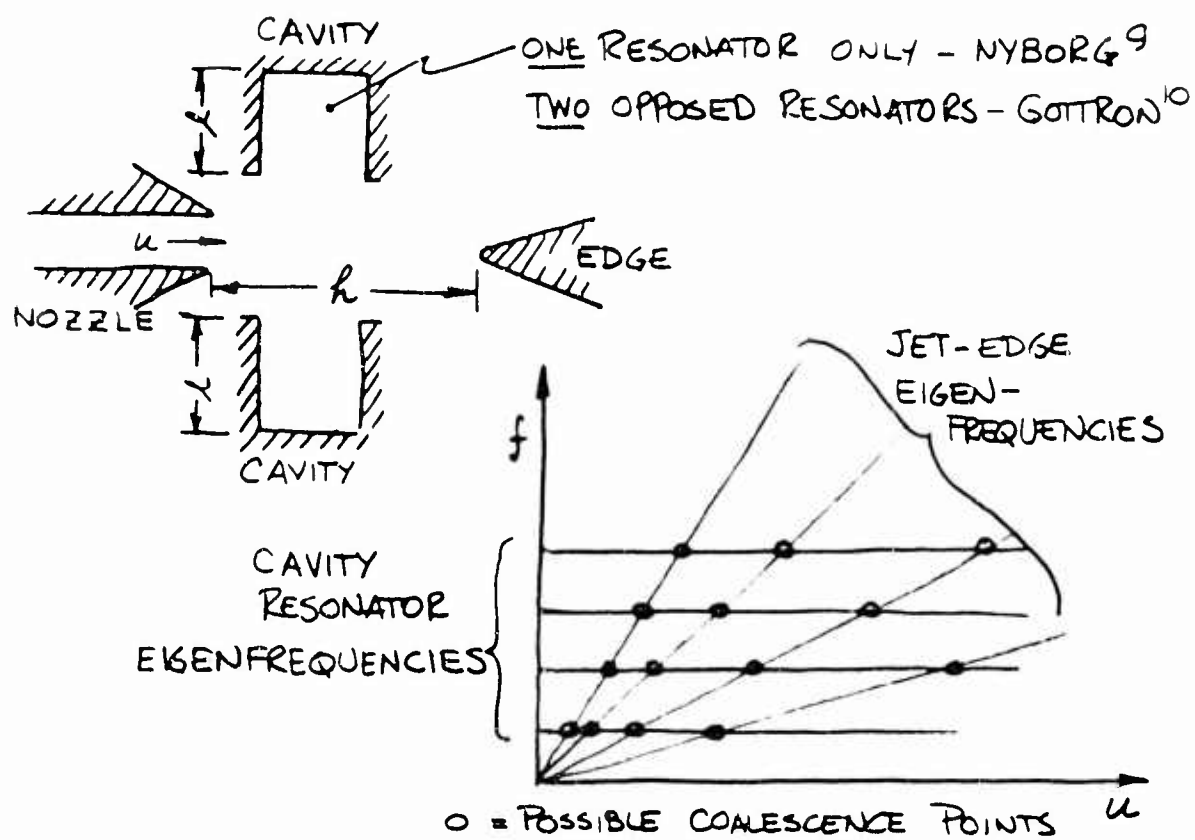


FIGURE 3 JET-EDGE - RESONATOR SYSTEM

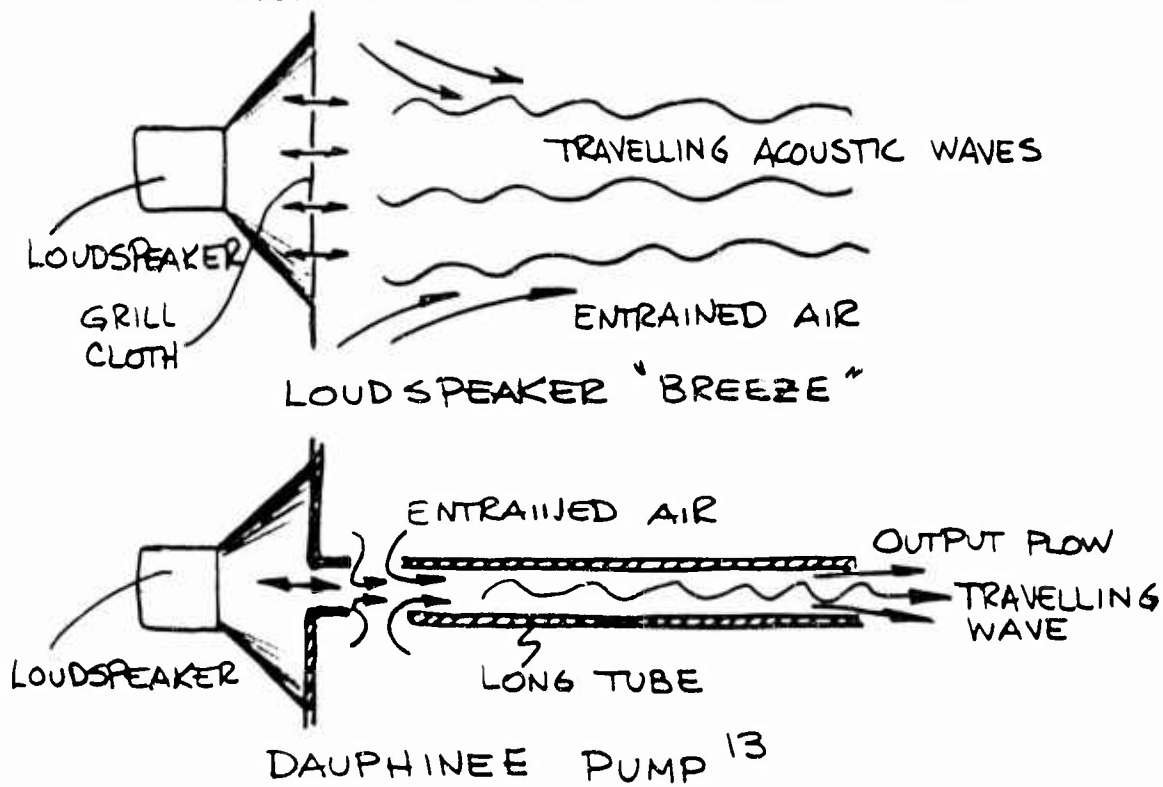


FIGURE 4 ACOUSTIC PUMPING

ferred from high frequency modes to lower frequency modes (including D.C.); as well as from a fundamental mode to the high harmonics. Physical examples of the high frequency-to-D.C. coupling ("acoustic pumping") are the motion of dust particles in a Kundt's tube, acoustic streaming from the mouth of a Helmholtz resonator (both described by Rayleigh in his Theory of Sound); the Quartz Wind phenomenon first described by Eckart¹¹, and utilization of the latter effect in a sound absorption coefficient measuring device by Piercy¹²; and finally, the breeze one feels when near a large loudspeaker operating at an appreciable sound level. These phenomena essentially involve entrainment of stagnant fluid particles by a travelling wave, as depicted in Figure 4.

Dauphinee¹³ has described an acoustic pump which is simply a long tube held in front of a loudspeaker. Roleau¹⁴ describes both a modified version of the Dauphinee pump, and a Piercy pump, based on Piercy's original absorption measuring device with a crystal driver. An analysis assuming travelling plane waves is presented for the Piercy pump, with numerical results.

In an amplifier executing low frequency blocked load oscillations, the receiver most likely embraces a standing wave. Thus, instead of considering plane waves in a tube, the analysis must of necessity involve the transverse oscillations of the jet and the appropriate entrainment behavior. Experimental data on what is believed to be a form of acoustic pumping as observed in a fluid amplifier of the author's design¹⁵ are shown in Figures 5 and 6.

The mean pressure (manometer) tap was located at a fixed position in the amplifier output channel. A Kistler piezoelectric pressure pickup was located in the end of a capped adjustable length tube connected to the amplifier output port. Figure 5 shows the variation of the mean output pressure with tube length for constant supply and control settings. The maxima of the mean pressure seemed to roughly correspond to the maximum oscillation amplitudes recorded by the pressure pickup, although the results were inconclusive. The large amplitude oscillation frequency was never greater than the quarter wave length frequency for the tube and receiver combination¹⁶. The latter result precludes the possibility that the pressure tap was situated in a standing wave node at the observed minima and in an antinode at the observed maxima, since only the fundamental (at best) occurred.

It appears likely that the explanation of this amplifier-load sensitivity is a coupling of the mode of the receiver with that of the jet. Since the device utilized boundary layer separation from a curved surface, the intrinsic separation instability, probably of relatively low frequency, could explain the low observed output frequencies (approximately 200-400 cps). Figure 6 shows typical dynamic pressure traces obtained for a given tube length by

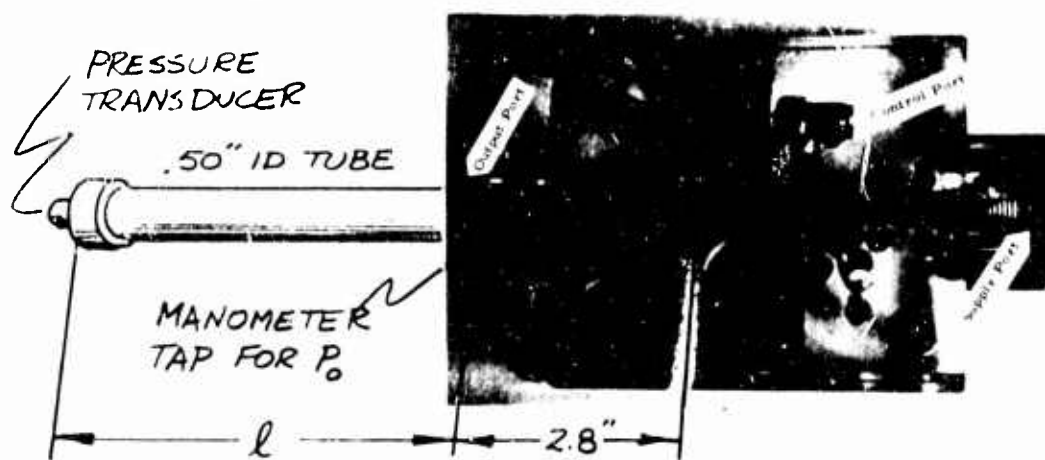
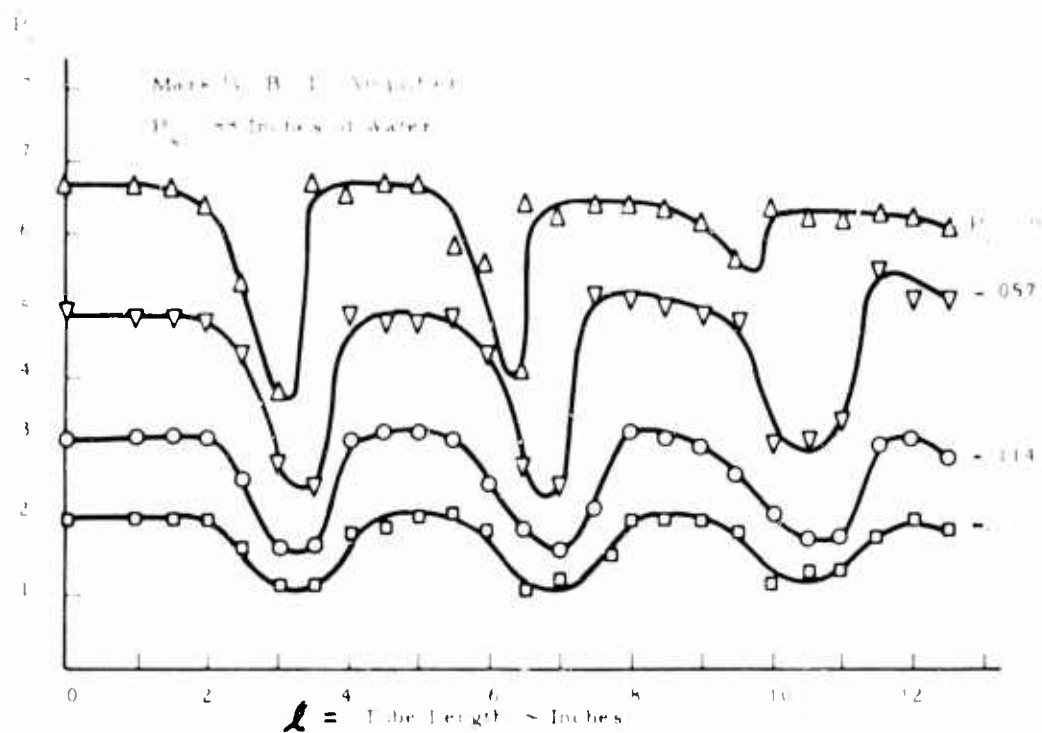


FIGURE 5 BOUNDARY LAYER AMPLIFIER BLOCKED LOAD INSTABILITY¹⁶

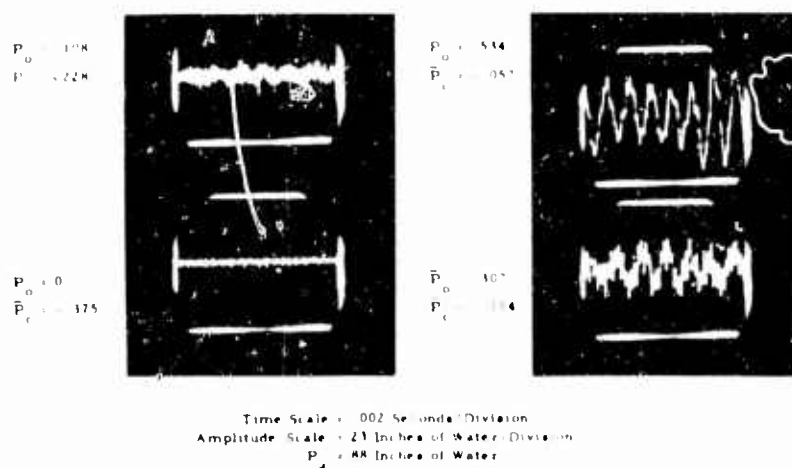


FIGURE 6 EFFECT OF CONTROL PRESSURE ON B.L. AMPLIFIER INSTABILITY (TUBE LENGTH = 5.2")

increasing the control pressure. There are two distinct modes, one at about 350 cps, and the other at about 2000 cps. The origin and significance of the 2000-cps signal is somewhat of a mystery, since it was present (at various levels) over virtually the entire range of control pressures, supply pressures, and tube lengths. It was not a resonance of the transducer or its mount.

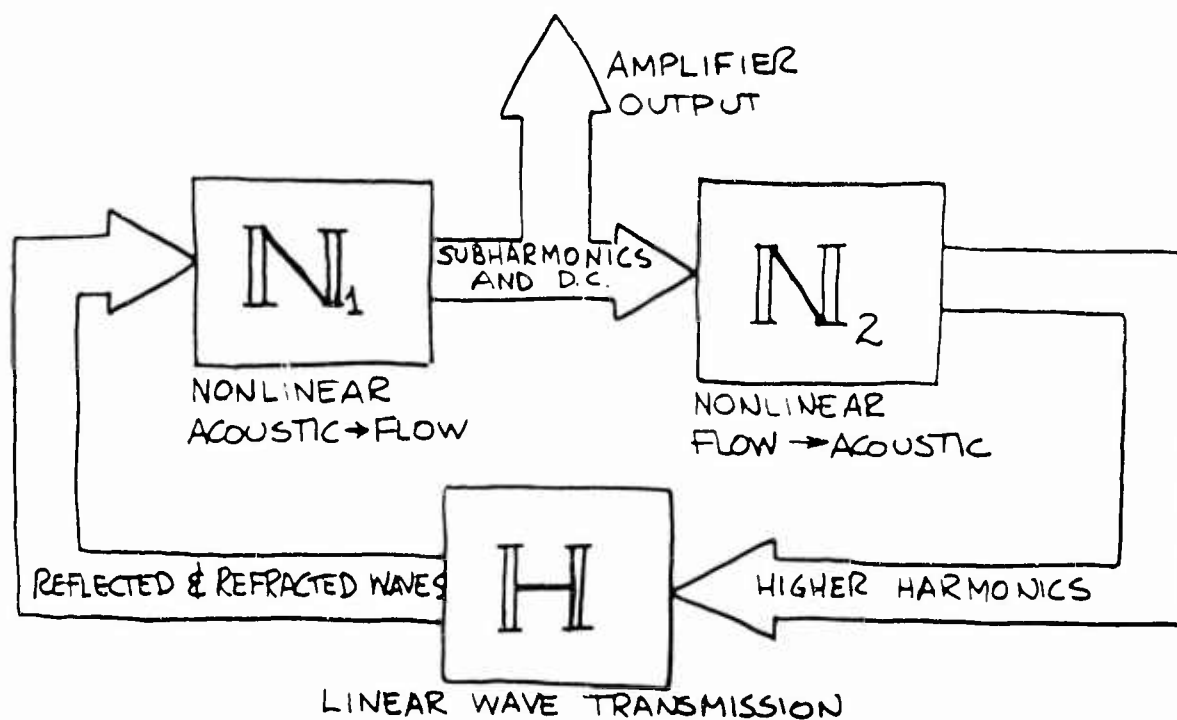
Since it is known that boundary layer separation can be induced by an acoustic field¹⁷, it would appear that the coupling of the load and amplifier described is amenable to the acoustic feedback method of stability analysis. The combination of an acoustic (or hydrodynamic) loop with the nonlinear modal (subharmonic) interaction might be a valid dynamical model for many low frequency blocked load instabilities. A conceptual block diagram of this loop is given in Figure 7.

DYNAMIC TESTING AND STABILITY PREDICTION

If a physical system of partially indeterminate structure is to be studied, experimental techniques can be quite involved. A simple example of this is the linear dynamical description of a push-pull amplifier. Due to the uncertainty as to transferences and couplings between the control and output variables, an experimental approach is necessary. Belsterling¹⁸, Boothe¹⁹, and Brown²⁰ have experimentally investigated similar momentum-interaction beam amplifiers.

It is obviously a nontrivial experimental task to find all the elements in the $n \times n$ dynamic admittance (or impedance) matrix which describes an active n port element. The general technique involves holding flows and/or pressures constant (or related in known fashion) at all ports except one, which is sinusoidally driven. This procedure is then repeated for all n ports. References 18 and 19 assume symmetry and zero control and output cross coupling. They thus involve the determination of only three elements in the 4×4 matrix describing the four port amplifier. The reduction in experimental difficulty is obvious, since all the test data can be obtained by driving just one control port. The method of Reference 20 is somewhat more realistic (and difficult to implement), as an attempt is made to determine all 16 matrix elements. Only static (zero frequency) data is presented, however, and thus the experimental difficulties encountered in actual dynamic testing are not known.

None of these methods is satisfactory for high frequencies, since wave effects in the flow measuring apparatus, signal generator circuit, etc. introduce uncertainties in the data interpretation. It is further evident that the treatment of load induced instabilities (especially of the acoustic feedback variety) is totally outside the scope of these procedures.



N_1 describes the subharmonic generation due to "acoustic pumping", sound sensitive flow phenomena, etc.

N_2 describes aerodynamic sound generation, harmonic distortion due to velocity profile, receiver and vent resonances, etc.

H is a linear acoustic transmission matrix

FIGURE 7 CONCEPTUAL PICTURE OF NONLINEAR ACOUSTIC LOOP FOR LOW FREQUENCY SUSTAINED OSCILLATIONS

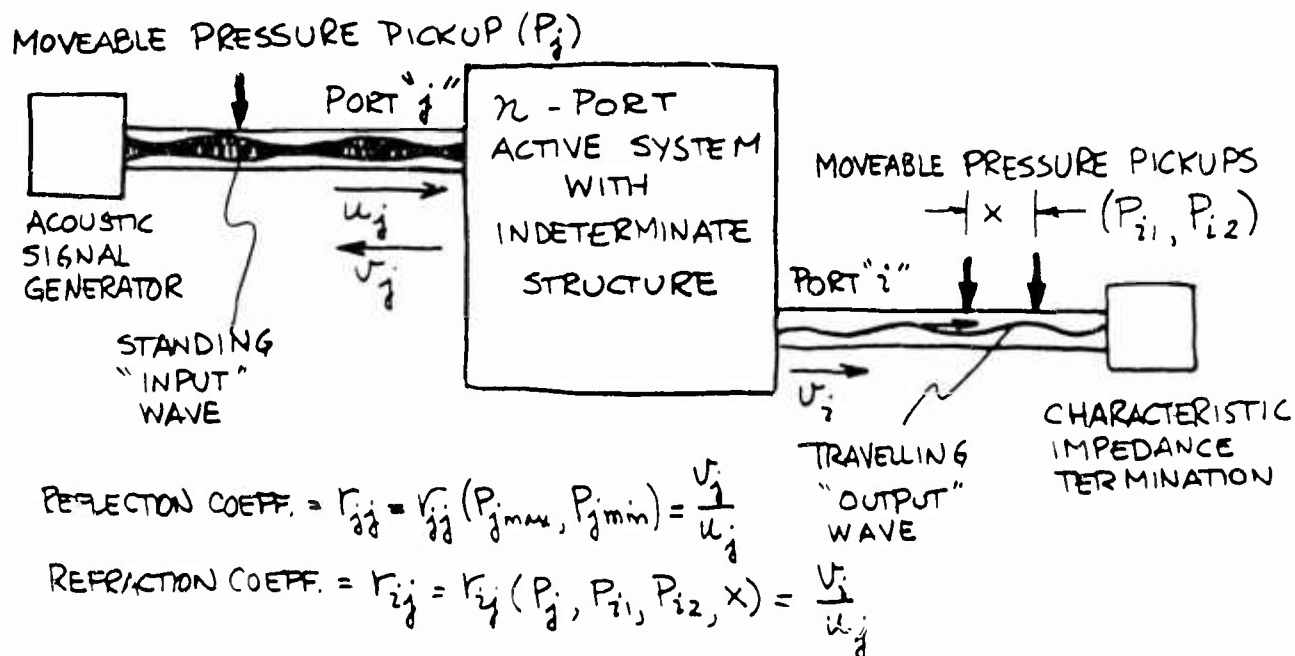


FIGURE 8 HIGH FREQUENCY LINEAR SYSTEM TESTING (AFTER BROWN²⁰)

Brown²⁰ suggests a transformation of the admittance matrix into a form more convenient for high frequency testing. Briefly, the pressure and flow variables at a given port are transformed into incident and reflected pressure waves. The idea, then, is to connect the port j to an acoustic signal generator with a line whose standing wave amplitude envelope is measurable. This yields the complex wave reflection coefficient r_{ij} for that port, as shown in Figure 8. By connecting a travelling wave line (one terminated in its own characteristic impedance) to another port i , and measuring the travelling wave amplitude and phase, the reflection coefficient r_{ij} for the two ports is determined. The general relation between the incoming waves u_j and the outgoing waves v_i is:

$$v_i = \sum_{j=1}^n r_{ij} u_j, \quad i = 1, 2, \dots, n$$

or, $\underline{v} = \underline{R} \underline{u}$

where $\underline{R} \triangleq [r_{ij}]$, $\underline{v} = \begin{bmatrix} v_1 \\ v_2 \\ \vdots \\ v_n \end{bmatrix}$, $\underline{u} = \begin{bmatrix} u_1 \\ u_2 \\ \vdots \\ u_n \end{bmatrix}$
 \underline{R} = wave transmission matrix

This method of testing appears attractive if the necessary large amount of experimental data can be obtained.

From \underline{R} , the scattering matrix and the impedance matrix may be constructed. It should be noted that retrieval of the intrinsic impedance matrix of the n port requires that the admittances of the testing lines themselves be "removed" from the measured admittance matrix. At the relatively high frequencies of interest, however, this should present no problem, since the lines are sufficiently well described by their characteristic admittances.

CONCLUSIONS

It would be of great value to combine the experimental scattering matrix approach (or a simplified version) with the physical theory of the acoustic feedback loop in the case of a simple beam amplifier. The quantitative results could very well represent a breakthrough in the theory of linear stability prediction for circuits composed of such elements. A logical extension of this would be the treatment of the supply nozzle and vents as additional ports for the design of optimal (high signal-to-noise) beam deflection devices.

A similar approach could be used for prediction of low frequency nonlinear oscillations in systems utilizing more complex flow phenomena (e.g. boundary layer separation). Since systems of this sort are usually characterized by strong harmonic distortion, the structuring becomes more difficult (Figure 7), but not impossible.

Wider dissemination of data on observed instabilities is imperative in order that the various dynamical theories may be tested and refined, or rejected. Fluid amplifier instabilities and/or noise problems exist as very real obstacles to the design of optimal systems. These obstacles should be removed by analytical and experimental methods, and not simply ignored.

REFERENCES

1. Nature of the Feedback Mechanism in Some Fluid Flows Producing Sound
A. Powell
Fourth International Congress on Acoustics, August 1962.
2. Experiments Concerning the Hole Tone
R.C. Chanaud
Report No. 63-38, July 1963. UCLA.
3. Edge Tones
E.G. Richardson
Proc. Phys. Soc. 43, pp. 394-404, 1931.
4. The Mechanism of Edge Tone Production
G.B. Brown
Proc. Phys. Soc. 49, pp. 508-521, 1937.
5. An Experimental Study of Low Speed Edgetones
A. Powell and H.H. Unfried
Report No. 64-29, November 1964. M.E. Department, UCLA.
6. Self-Maintained Oscillations of the Jet in a Jet-Edge System
W.L. Nyborg
Jour. Acoust. Soc. Am. 26, pp. 174-182, 1954.
7. On the Edgetone
A. Powell
Jour. Acoust. Soc. Am. 33, pp. 395-409, 1961.
8. The Mechanics of Edge-Tones
N. Curle
Proc. Roy. Soc. (Gt Brit) 216A, pp. 412-424, 1953.

9. Acoustical Characteristics of Jet-Edge and Jet-Edge Resonator Systems
W.L. Nyborg, M.D. Burkhard, and H.K. Schilling
Jour. Acoust. Soc. Am. 24, pp. 293-304, 1952.
10. Noise Reduction by Jet-Edge and Resonator Coupling
R.N. Gottron
Proc. Fluid Amp. Sym. Vol. 1, May 1964
Harry Diamond Laboratories, Washington D.C.
11. Vortices and Streams Caused by Sound Waves
C. Eckart
Phys. Rev. 73, pp. 68-76, 1948.
12. Acoustic Streaming in Liquids
J.E. Piercy and J. Lamb
Proc. Roy. Soc. (Gt Brit) 226A, pp. 43-50, 1954.
13. Acoustical Pump
T.N. Dauphinee
Applied Research in Industry (Gt brit) 13, pp. 300-303, 1960.
14. Unconventional Methods for Influencing Fluid Flow
W.T. Roleau
TDR No. ASD-TDR-63-776 Vol. 1, November 1963.
Carnegie Institute of Technology
15. Development of a Pure Fluid Power Amplifier
P.A. Orner and C.K. Taft
Proc. JACC, pp. 159-168, June 1965.
16. A Fluid Amplifier Controlled Pneumatic Turbine Servomechanism
P.A. Orner
Report EDC 7-64-5, pp. 135-146, Oct. 1964. Case Inst. of Tech.
17. Acoustic Control of Pneumatic Digital Amplifiers
R.N. Gottron
Proc. Fluid Amp. Sym. Vol. 1, May 1964
Harry Diamond Laboratories, Washington D.C.
18. Analysis of the Dynamics of Proportional Pure Fluid Amplifiers
C.A. Belsterling and K.C. Tsui
Report I-B2148-01, August 1964. The Franklin Institute.
19. A Lumped Parameter Technique for Predicting Analog Fluid Amplifier Dynamics
W.A. Boothe
Proc. JACC, June 1964.
20. Investigation of Stability Predictions of Fluid Jet Amplifier Systems
F.T. Brown, S.D. Graber, and R.E. Wallhagen
Semiannual Report NASA CR-54244, October 30, 1964.
Massachusetts Institute of Technology.

IMPEDANCE MATCHING IN BISTABLE AND PROPORTIONAL FLUID AMPLIFIERS THROUGH THE USE OF A VORTEX VENT

by

W.F. Hayes¹ and C. Kwok²
Research and Development Division
Engineering Department
Aviation Electric Limited
Montreal, Quebec, Canada

1. INTRODUCTION

The use of fluid amplifiers in circuits requires a means of matching the fluid flow output to the applied load in order to accommodate the total system input flow. In the closed system of impedance matching, each successive amplifier is made larger in order to accommodate the total flow input to all previous stages. This technique generally involves the matching of the non-linear amplifier characteristics to the load by a graphical solution at each interconnection. This approach is used in multi-stage fluid flow and pressure amplification in which optimum power efficiency is essential.

Incorrect matching results in a portion of the fluid input mass flow being diverted into the inactive outlet channel as a result of the high back pressure in the loaded active outlet channel.

With a low stability fluid amplifier, the power jet may be switched and attach to the opposite adjacent wall under large active outlet load impedance conditions.

¹Supervisor, Fluid State Technology, Aviation Electric Ltd., Montreal, Quebec, Canada.

²Research Engineer, Fluid State Technology, Aviation Electric Ltd., Montreal, Quebec, Canada.

In the vented system of impedance matching, the excess fluid flow is vented or bled off to a suitable sink, so that over an appreciable operating range, each fluid amplifier is automatically matched to its applied load. This approach, although somewhat inefficient from input fluid power considerations, is quite adequate in many circuit applications in which the total fluid power input per amplifier is very low.

The isolation of fluid amplifiers from output load effects has been previously achieved with a vent channel positioned perpendicularly to the amplifier outlet passage, immediately downstream of the attachment bubble region.

The conversion of power jet dynamic pressure to static pressure at the vent passage input with increasing output loading (i.e. decreasing the element output mass flow) decreases the fluid stream momentum and reduces the effective vent "resistance", thus inducing increased mass flow venting. This type of vent may be made effective over a load range up to infinite impedance, if the stability level in the amplifier is capable of withstanding the static pressure realized under high load conditions.

The second phenomenon associated with impedance matching relates to the disturbance effects of acoustic or finite pressure wave disturbances, and involves the complex interaction between fluid flow and acoustic perturbations.

The acoustic disturbances are propagated out through the circuit lines, portions of the acoustic energy being reflected at circuit discontinuities in accordance with the laws for wave reflections. If not suppressed or by-passed, such disturbances, in the form of reflected compression waves, can cause fluid circuit instability.

There is evidence that in the perpendicular channel type of vent configuration, such acoustic disturbances are not effectively attenuated, the vents themselves frequently being sources of acoustic energies in the form of organ pipe oscillation under transient operational conditions.

This paper discusses a different vent configuration, called the Latched Vortex Vent, which can be applied to both proportional and digital fluid amplifiers. This unique configuration attains impedance matching over a wide range of load conditions, from zero load up to and including large negative loads (i.e. reverse flow into the amplifier).

Appreciable pressure recovery capabilities can be maintained while compression pulses propagated back into the amplifier interaction region are largely attenuated.

2. PRINCIPLE OF LATCHED VORTEX VENT

The latched vortex vent is a pure fluid device (no moving parts) consisting of a circular vent orifice positioned adjacent to a fluid stream, with the orifice axis perpendicular to the fluid stream velocity vector. An associated fluid channel configuration used in conjunction with the vent induces and maintains a vortex swirl flow, the core of which is coincident with the orifice axis (Figure 1).

Consideration of vortex vent flow patterns associated with increasing downstream impedance loading conditions indicates the principle of operation of the vent, as illustrated in Figure 2.

Case 1: Low load impedance (unrestricted output flow).
Substantially, no flow occurs within the swirl chamber or through the vent orifice.

Case 2: Moderate load impedance (restricted output flow).
A substantial portion of the input fluid flow is diverted or vented out through the vent orifice via a swirl motion within the vortex inducing chamber.

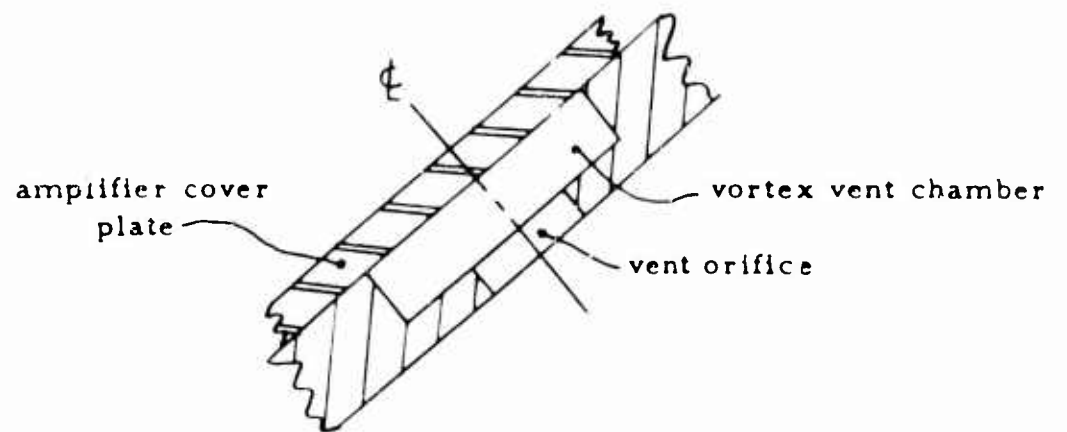
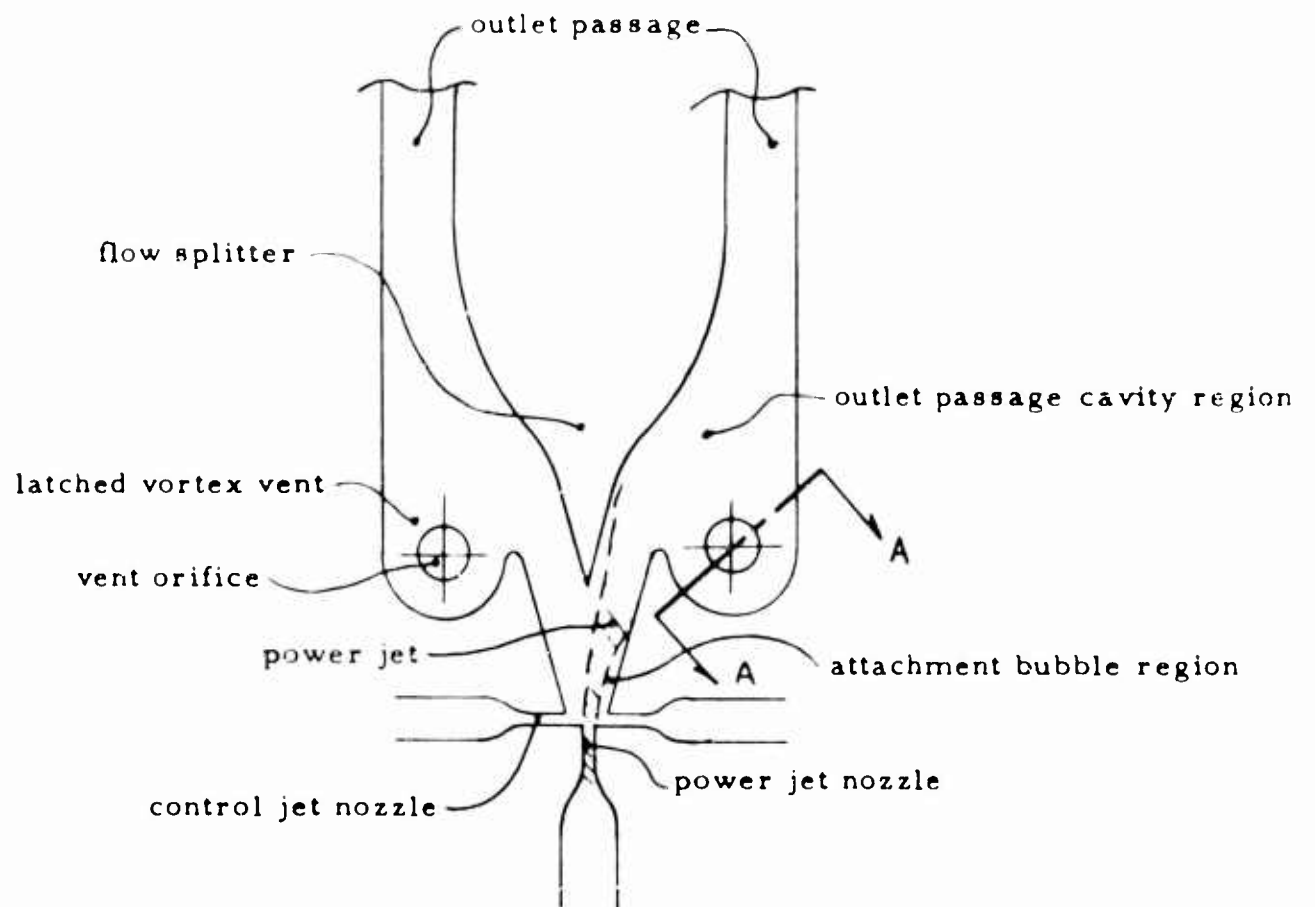
Case 3: Infinite impedance load (completely blocked output).
All the input flows out through the vent orifice via a swirl motion within the vortex inducing chamber.

As is evident from the diagram for both Cases 2 and 3, a segment of the outer periphery of the fluid swirl flow which is exposed to the fluid flow in the main stream forms, in effect, a moving wall for the diffusion process as applied to the portion of the fluid flowing into the load. By this means, the vortex vent flow is used to provide increased diffusion efficiency or pressure recovery of the output flow.

Case 4: Negative impedance load (reversed flow into active outlet).
All the input flow plus all the load reverse flow exits out through the vent orifice, the load reverse flow fluid being induced into the vortex vent swirl flow, through viscous entrainment.

Figure 1

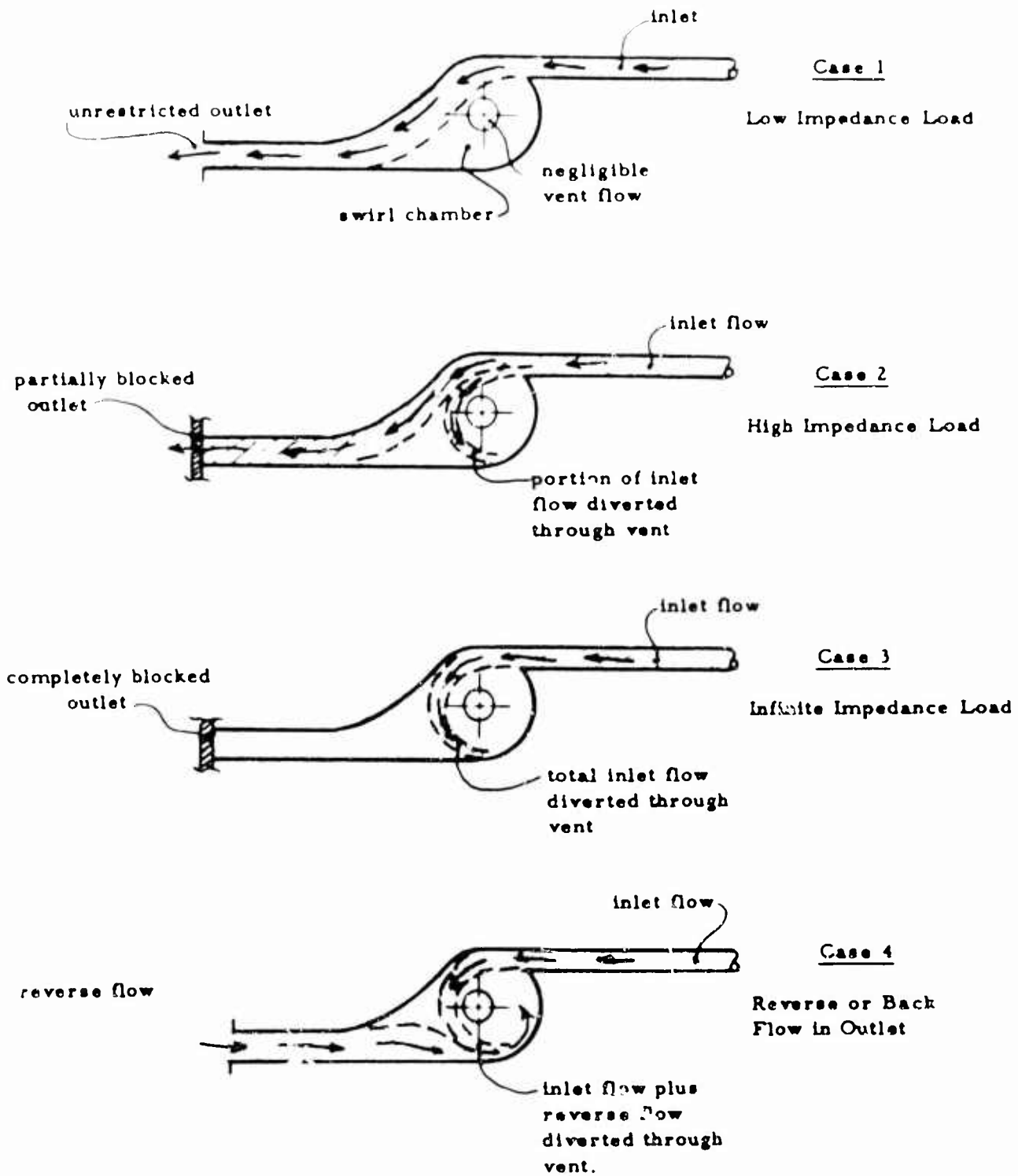
Latched Vortex Vent Configuration as Applied to
Fluid Amplifier



Section A-A

Figure 2

Matched Vortex Vent Operating Principle



3. THEORETICAL CONSIDERATIONS

High pressure recovery characteristics may be attained in fluid amplifiers which incorporate latched vortex vents by adaptation of the vortex "moving wall" diffusion process, and by optimization of the variable vent impedance inherent in the vent viscous swirl flow. The vent variable impedance or vent flow resistance results from the pressure drop across the swirl flow within the vortex inducing chamber, this pressure drop resulting in turn from two flow phenomena:

- (a) Pressure drop due to viscous drag and turbulent flow energy dissipation (both effects are included in an "apparent" viscosity number).
- (b) Pressure drop associated with increasing fluid flow tangential velocity towards the vent orifice, resulting from flow angular momentum conservation considerations.

Accordingly, the greater the degree of swirl of the fluid flow within the vortex vent, the greater the effective vent flow "resistance". The degree of swirl flow is dependent primarily upon the ratio between vent vortex chamber effective radius and orifice radius (r_i/r_o) and upon the vent mass flow (Q_r).

The mathematical model of the latched vortex vent flow is based on a flow model which consists of a thin cylindrical chamber with the tangential injection of fluid at the outer edge and subsequent discharge through a central orifice, as illustrated in Figure 3.

The following mathematical analysis is unique in that it is based on the flow within very low aspect ratio chambers. Furthermore, the analysis takes into consideration the viscous effects of the real fluid, being a particular solution of the Navier-Stokes equations.

3.1 Flow Conditions Initially Assumed

Four basic assumptions regarding the flow conditions are initially established in order to facilitate simplification of the Navier-Stokes differential equations to a soluble form:

3.1.1 It is assumed that the fluid flow within the vortex chamber is incompressible.

3.1.2 It is assumed that the flow is symmetrical with respect to the Z axis (i. e. $\frac{\gamma}{r\phi} = 0$ and $\frac{\gamma}{rz} = 0$).

This assumption implies the symmetrical injection of fluid about the Z-axis into the vortex chamber as well as constant axial velocity (V_z) at any given radius in the core flow region bounded by $r_0 > r > 0$.

Discrepancies between the assumed symmetrical flow ($\frac{\gamma}{r\phi} = 0$) and the actual non-symmetrical flow at the outer periphery, due to the tangential injection of fluid into the chamber over a limited sector, are rapidly eliminated as a result of the viscous effects of the real fluid.

3.1.3 It is assumed that the flow is continuous (i. e. steady state) rather than transient (i. e. $\frac{\gamma}{rt} = 0$).

3.1.4 It is assumed that fully established channel flow exists in a plane defined by the flow velocity vector throughout the annular region bounded by $r_i > r > r_0$ as a result of the build up of the wall boundary layer within the low aspect ratio vortex chamber. It is further assumed that the non-dimensional velocity profile (i. e. local velocity 'u' divided by maximum velocity 'V') for the assumed fully established two-dimensional channel flow is identical at all points in the specified bounded flow region (i. e. non-dimensional velocity profile is independent of Reynold's No.), an assumption which closely approximates the experimental data.

Accordingly, for purposes of the analysis it is justified, on the basis of the fully developed channel flow assumption, to consider the fluid tangential and radial velocities (V_ϕ and V_r) as average velocities, constant with respect to Z at any given location in the $r - \phi$ plane.

3.2 Mathematical Flow Analysis

3.2.1 Basic Flow Equations: On the basis of the assumed axially symmetrical incompressible flow within the vortex chamber (reference assumptions 3.1.1 and 3.1.2), it is convenient from analysis considerations to utilize the Navier-Stokes equations for three-dimensional incompressible flow expressed in terms of cylindrical co-ordinates, as indicated below:

$$\begin{aligned} \rho \left[\frac{\partial V_r}{\partial t} + V_r \frac{\partial V_r}{\partial r} + \frac{V_\phi}{r} \frac{\partial V_r}{\partial \phi} - \frac{V_\phi^2}{r} + V_z \frac{\partial V_r}{\partial z} \right] \\ = - \frac{\partial p}{\partial r} + \mu \left[\frac{\partial^2 V_r}{\partial r^2} + \frac{1}{r} \frac{\partial V_r}{\partial r} - \frac{V_r}{r^2} + \frac{1}{r^2} \frac{\partial^2 V_r}{\partial \phi^2} - \frac{2}{r} \frac{\partial V_\phi}{\partial \phi} + \frac{\partial^2 V_r}{\partial z^2} \right] \end{aligned} \quad (1)$$

$$\begin{aligned} \rho \left[\frac{\partial V_\phi}{\partial t} + V_r \frac{\partial V_\phi}{\partial r} + \frac{V_\phi}{r} \frac{\partial V_\phi}{\partial \phi} + \frac{V_r V_\phi}{r} + V_z \frac{\partial V_\phi}{\partial z} \right] \\ = - \frac{1}{r} \frac{\partial p}{\partial \phi} + \mu \left[\frac{\partial^2 V_\phi}{\partial r^2} + \frac{1}{r} \frac{\partial V_\phi}{\partial r} - \frac{V_\phi}{r^2} + \frac{1}{r^2} \frac{\partial^2 V_\phi}{\partial \phi^2} + \frac{2}{r^2} \frac{\partial V_r}{\partial \phi} + \frac{\partial^2 V_\phi}{\partial z^2} \right] \end{aligned} \quad (2)$$

where the Z, r and ϕ co-ordinates and the associated sign are defined as in Figure 3, (i.e. V_r , V_ϕ and V_z denote radial, tangential and axial velocity respectively).

3.2.1 (continued)

It is required to solve the tangential velocity variation (V_ϕ) and the static pressure variation (p) with respect to the chamber radius ' r '.

3.2.2 Pressure and Tangential Velocity Equations for Outer Annulus Flow Region

Consider the steady state swirl flow within the vortex chamber in the annular region bounded by r_o and r_i .

But $\frac{\gamma}{\gamma\phi} = 0$, $\frac{\gamma}{\gamma z} = 0$ and $\frac{\gamma}{\gamma t} = 0$ as a result of the axial flow symmetry assumption (3.1.1) and the steady state flow assumption (3.1.3) respectively.

Accordingly, differential equation (1) may be simplified to the readily soluble one-dimensional flow case as follows:

$$V_r \frac{dV_r}{dr} - \frac{V_\phi^2}{r} = - \frac{1}{\rho} \frac{dp}{dr} + \gamma \left[\frac{d}{dr} \left(\frac{V_r}{r} + \frac{dV_r}{dr} \right) \right] \quad (3)$$

From mass continuity considerations in the steady state incompressible flow, the volume flow rate and radial velocities may be expressed in differential form as:

$$\frac{dV_r}{dr} = \frac{Q_i}{2\pi r^2 h} = \frac{-V_r}{h} \quad (4)$$

(NOTE: The sign of V_r is negative in accordance with the defined sign convention in Figure 3). Substituting equation (4) into equation (3) gives, for steady state flow conditions:

$$V_r \frac{dV_r}{dr} - \frac{V_\phi^2}{r} = - \frac{1}{\rho} \frac{dp}{dr} \quad (5)$$

3.2.2 (continued)

Similarly equation (2) may be simplified to the form

$$r^2 \frac{d^2 V_\phi}{dr^2} + r(1+\alpha) \frac{dV_\phi}{dr} - (1-\alpha)V_\phi = 0 \quad (6)$$

where the parameter α is defined as

$$\alpha = \frac{Q_i}{2\pi h \gamma}$$

With the application of boundary conditions (at $r = r_i$; $V_\phi = V_{\phi i}$ and at $r = r_o$; $V_\phi = V_{\phi o}$), the required expression for the tangential velocity distribution in the annular flow region bounded by $r_i > r > r_o$ may be obtained:

$$V_{\phi r} = V_{\phi i} \frac{r_i}{r} \left[1 - \frac{r_i^{(2-\alpha)} - r^{(2-\alpha)}}{r_i^{(2-\alpha)} - r_o^{(2-\alpha)}} \left(1 - \frac{V_{\phi o} r_o}{V_{\phi i} r_i} \right) \right] \quad (7)$$

The required static pressure drop may be readily evaluated by integrating equation (5).

$$\left(\frac{V_r^2}{2} - \frac{V_n^2}{2} \right) + \frac{1}{A} \left\{ \frac{B^2}{2} \left(\frac{1}{r^2} - \frac{1}{r_i^2} \right) + \frac{2BC}{\alpha} \left(\frac{1}{r^\alpha} - \frac{1}{r_i^\alpha} \right) - \frac{C^2}{2(1-\alpha)} \left[r^{2(1-\alpha)} - r_i^{2(1-\alpha)} \right] \right\} = \frac{1}{\rho} (p_n - p_r) \quad (8)$$

3.2.2 (continued)

$$\text{where the constants } A = \left[r_i^{(2-\alpha)} - r_o^{(2-\alpha)} \right]^2$$

$$B = \left[V_{\phi o} r_o r_i^{(2-\alpha)} - V_{\phi i} r_i r_o^{(2-\alpha)} \right]$$

$$C = (V_{\phi i} r_i - V_{\phi o} r_o)$$

Equation (7) may be evaluated for limiting values of the apparent viscosity (i. e. $\nu = 0$ and $\nu = \infty$). For the case of $\nu \rightarrow \infty$, the value of the parameter α approaches 0 and by applying L'Hospital Rule for this limiting case, Equation (7) reduces to $\frac{V_{\phi i}}{r_i} = \frac{V_{\phi o}}{r_o}$ which is the equation for a forced vortex.

For the case of $\nu \rightarrow 0$, the value of the parameter α approaches ∞ and equation (10) reduces to $V_{\phi o} r = V_{\phi o} r_o$ which is the equation for a free vortex.

3.2.3 Pressure and Tangential Velocity Equations for Inner Core Flow Region: Consider the steady state swirl flow within the vortex chamber in the circular core region where $r_o > r > 0$.

Based on the mass conservation equation for steady state three-dimensional incompressible flow, the instantaneous radial velocity within the vortex core ($r_o > r > 0$) may be expressed in differential form as:

$$\frac{dV_r}{dr} = \frac{-Q_o}{2\pi h r_o^2} \quad (9)$$

3.2.3 (continued)

Similarly, by substituting Equation (9) into equation (2), it may be simplified to the form

$$r^2 \frac{d^2 V_\phi}{dr^2} + r \left(1 + \frac{\alpha r^2}{r_o^2} \right) \frac{dV_\phi}{dr} - \left(1 - \frac{\alpha r^2}{r_o^2} \right) V_\phi = 0. \quad (10)$$

Equation (10) is a non-homogeneous second-order linear differential equation, and can be solved for the required tangential velocity distribution $V_{\phi r}$ by the substitution method in the circular core flow region bounded by $r_o > r > 0$. Applying the boundary conditions at $r = r_o$ where $V_\phi = V_{\phi o}$ and $r = 0$ where $V_{\phi o} = 0$, the general solution of Equation (10) becomes:

$$V_\phi = V_{\phi o} \frac{r_o}{r} \left\{ 1 + \frac{e^{-\frac{\alpha}{2}} \left[1 - e^{\frac{\alpha}{2} \left[1 - \left(\frac{r}{r_o} \right)^2} \right]} \right]}{1 - e^{-\frac{\alpha}{2}}} \right\} \quad (11)$$

where the parameter α is defined as previously.

The required static pressure drop may be readily evaluated, as in the annular flow case, by integrating equation (5):

$$\frac{1}{2} \left\{ V_{r_o}^2 \left[\left(\frac{r}{r_o} \right)^2 - 1 \right] + V_{\phi o}^2 \left[1 - \left(\frac{r}{r_o} \right)^2 \right] \right\} = \frac{1}{\rho} (p_o - p_r) \quad (12)$$

3.2.4 Boundary Conditions Between the Outer Annulus and the Core Flow Regions: It is necessary, in order to solve equation (11) for the tangential velocity distribution within the core flow region, to evaluate the boundary velocity $V_{\phi 0}$ at $r = r_0$ in terms of the known input tangential velocity $V_{\phi i}$.

The necessary equivalence at the boundary $r = r_0$ is that the fluid shear stress is equal for both the outer annulus and the core flow regions. The tangential shear, as derived from the Navier-Stokes equations for incompressible flow, is:

$$\tau_{r\phi} = \mu \left[r \frac{\partial}{\partial r} \left(\frac{V_{\phi}}{r} \right) + \frac{1}{r} \frac{\partial V_r}{\partial \phi} \right] \quad (13)$$

Equation (13) may be simplified as a result of the flow symmetry assumption ($\frac{\partial}{\partial \phi} = 0$) to:

$$\tau_{r\phi} = \mu r \frac{d}{dr} \left(\frac{V_{\phi}}{r} \right) \quad (14)$$

Substituting the expression of equation (14) for $V_{\phi r}$ in the outer annulus flow region, (reference equation (7)) and rearranging:

$$\begin{aligned} [\tau_{r\phi}]_{r=r_0} &= \mu r_0 \frac{V_{\phi 0}}{r_0^2} \left(\frac{\alpha r_0^{(2-\alpha)} - 2r_i^{(2-\alpha)}}{r_i^{(2-\alpha)} - r_0^{(2-\alpha)}} \right) \\ &\quad - \frac{(\alpha-2) V_{\phi i} r_i r_0^{-(\alpha+1)}}{r_i^{(2-\alpha)} - r_0^{(2-\alpha)}} \end{aligned} \quad (15)$$

Substituting the expression of equation (14) for $V_{\phi r}$ in the core flow region (reference equation (11)) and rearranging:

$$[\tau_{r\phi}]_{r=r_0} = \mu r_0 \frac{V_{\phi 0}}{r_0^2} \left(\frac{\alpha e^{-\frac{\alpha}{2}}}{1 - e^{-\frac{\alpha}{2}}} - 2 \right) \quad (16)$$

3.2.4 (continued)

Equating equations (15) and (16) results in the required expression for the boundary tangential velocity $V_{\phi o}$ in terms of the input tangential velocity $V_{\phi i}$:

$$V_{\phi o} = \frac{(\alpha-2) V_{\phi i} r_i r_o^{(1-\alpha)} (1 - e^{-\frac{\alpha}{2}})}{r_o^{(2-\alpha)} [\alpha - 2 + 2e^{-\frac{\alpha}{2}}] - \alpha e^{-\frac{\alpha}{2}} r_i^{(2-\alpha)}} \quad (17)$$

Accordingly, $V_{\phi o}$ may be readily evaluated for given geometric and operating conditions and consequently be used in the evaluation of the tangential velocity equation (11) in the core flow region.

3.2.5 Non-Dimensionalized Flow Equations: It is advantageous, for computational considerations, to non-dimensionalize the tangential velocity and static pressure equations. Accordingly, by rearranging equation (17) for the tangential velocity at the flow region interface into non-dimensionalized form gives:

$$\frac{V_{\phi o}}{V_{\phi i}} = \frac{(\alpha-2) (1 - e^{-\frac{\alpha}{2}})}{\left(\frac{r_o}{r_i}\right) (\alpha - 2 + 2e^{-\frac{\alpha}{2}}) - \alpha e^{-\frac{\alpha}{2}} \left(\frac{r_o}{r_i}\right)^{\alpha-1}} \quad (18)$$

The equation for the tangential velocity and pressure distribution in the outer annulus flow region may be non-dimensionalized as follows:

$$\frac{V_{\phi r}}{V_{\phi i}} = \frac{r_i}{r} \left\{ 1 - \frac{1 - \left(\frac{r}{r_i}\right)^{2-\alpha}}{1 - \left(\frac{r_o}{r_i}\right)^{2-\alpha}} \left[1 - \frac{V_{\phi o} r_o}{V_{\phi i} r_i} \right] \right\} \quad (19)$$

$$\begin{aligned} \frac{p_{r_i} - p_r}{\rho V_{\phi i}^2} = & \frac{1}{2} \left[\frac{V_r^2}{V_{\phi i}^2} - \frac{V_{r_i}^2}{V_{\phi i}^2} \right] + \frac{1}{A'} \left\{ \frac{B'^2}{2} \left[\frac{1}{\left(\frac{r}{r_i}\right)^2} - 1 \right] \right. \\ & \left. + \frac{2B'C'}{\alpha} \left[\frac{1}{\left(\frac{r}{r_i}\right)^{\alpha}} - 1 \right] - \frac{C'^2}{2(1-\alpha)} \left[\left(\frac{r}{r_i}\right)^{2(1-\alpha)} - 1 \right] \right\} \end{aligned} \quad (20)$$

3.2.5 (continued)

$$\begin{aligned} \text{where } A' &= \left[1 - \left(\frac{r_o}{r_i} \right)^{2-d} \right] \\ B' &= \left[\frac{V_o}{V_{\phi i}} \frac{r_o}{r_i} - \left(\frac{r_o}{r_i} \right)^{2-d} \right] \\ C' &= \left[1 - \frac{V_o}{V_{\phi i}} \frac{r_o}{r_i} \right] \end{aligned}$$

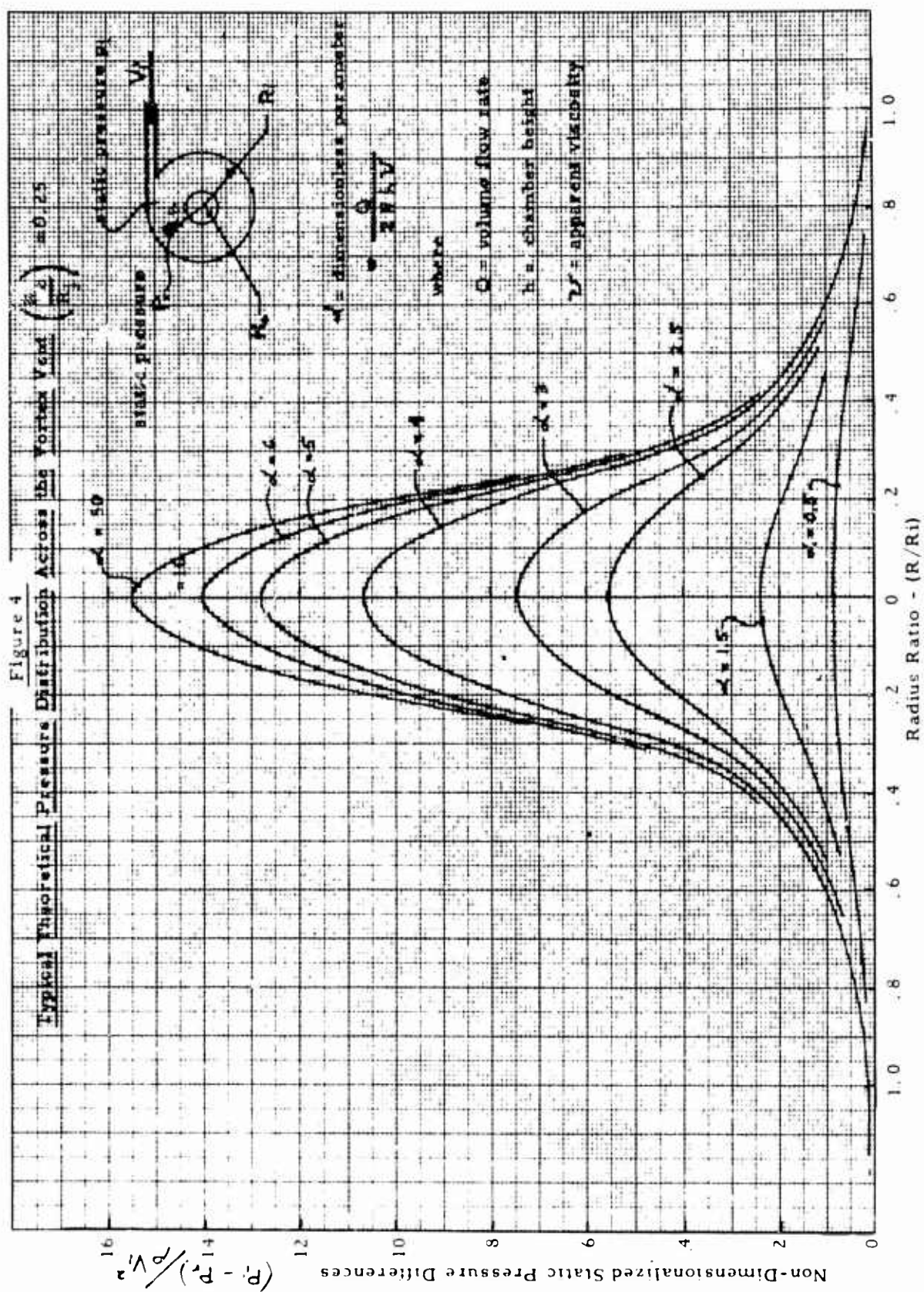
The equation for the tangential velocity and pressure distribution in the core flow region may be non-dimensionalized as follows:

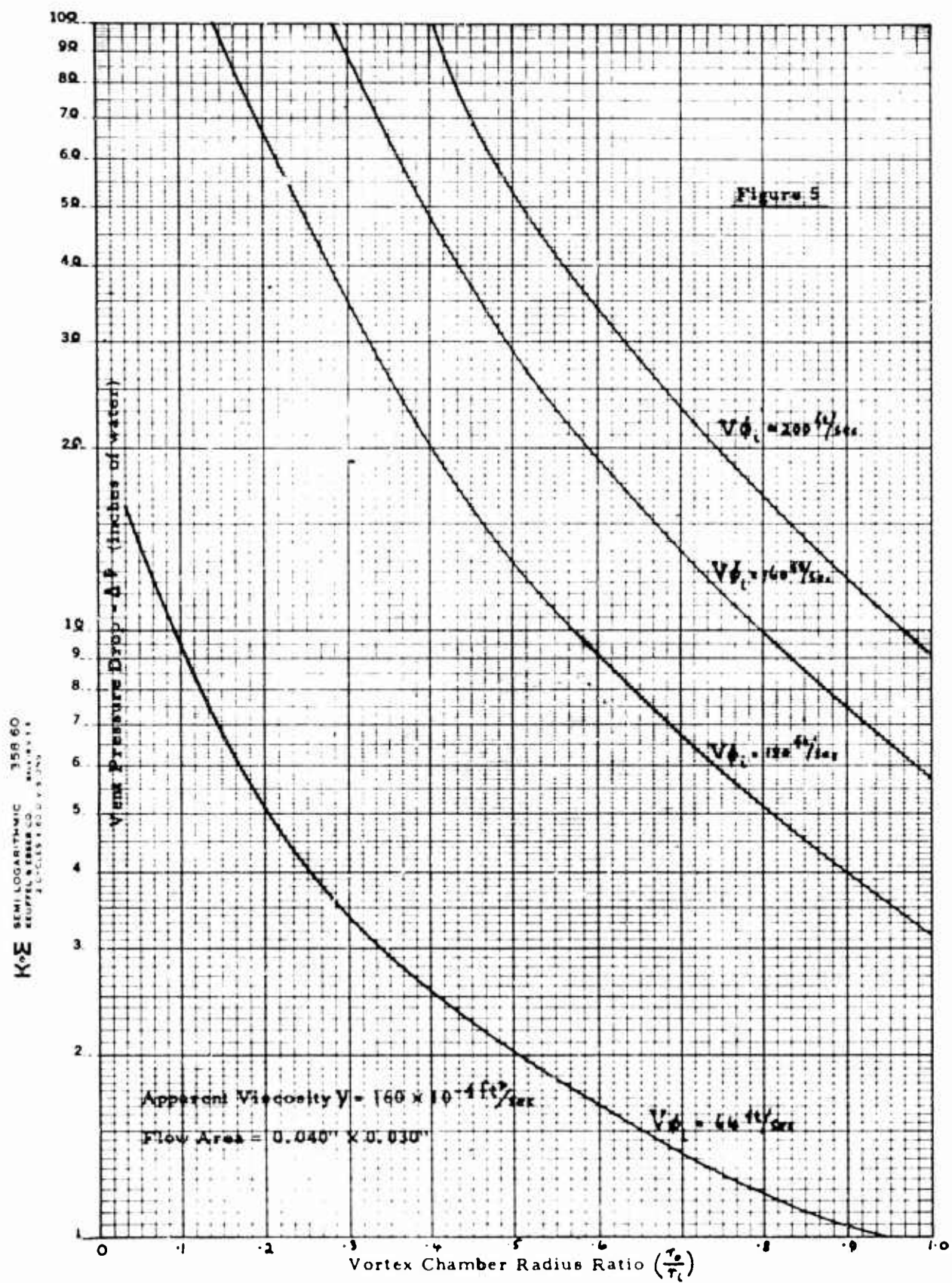
$$\frac{V_{\phi r}}{V_{\phi i}} = \frac{V_o}{V_{\phi i}} \frac{r_o}{r} \left\{ 1 + \frac{e^{-\frac{r}{r_o}} \left[1 - e^{\frac{r}{r_o} (1 - (\frac{r_o}{r_i})^2)} \right]}{1 - e^{-\frac{r_o}{r_i}}} \right\} \quad (21)$$

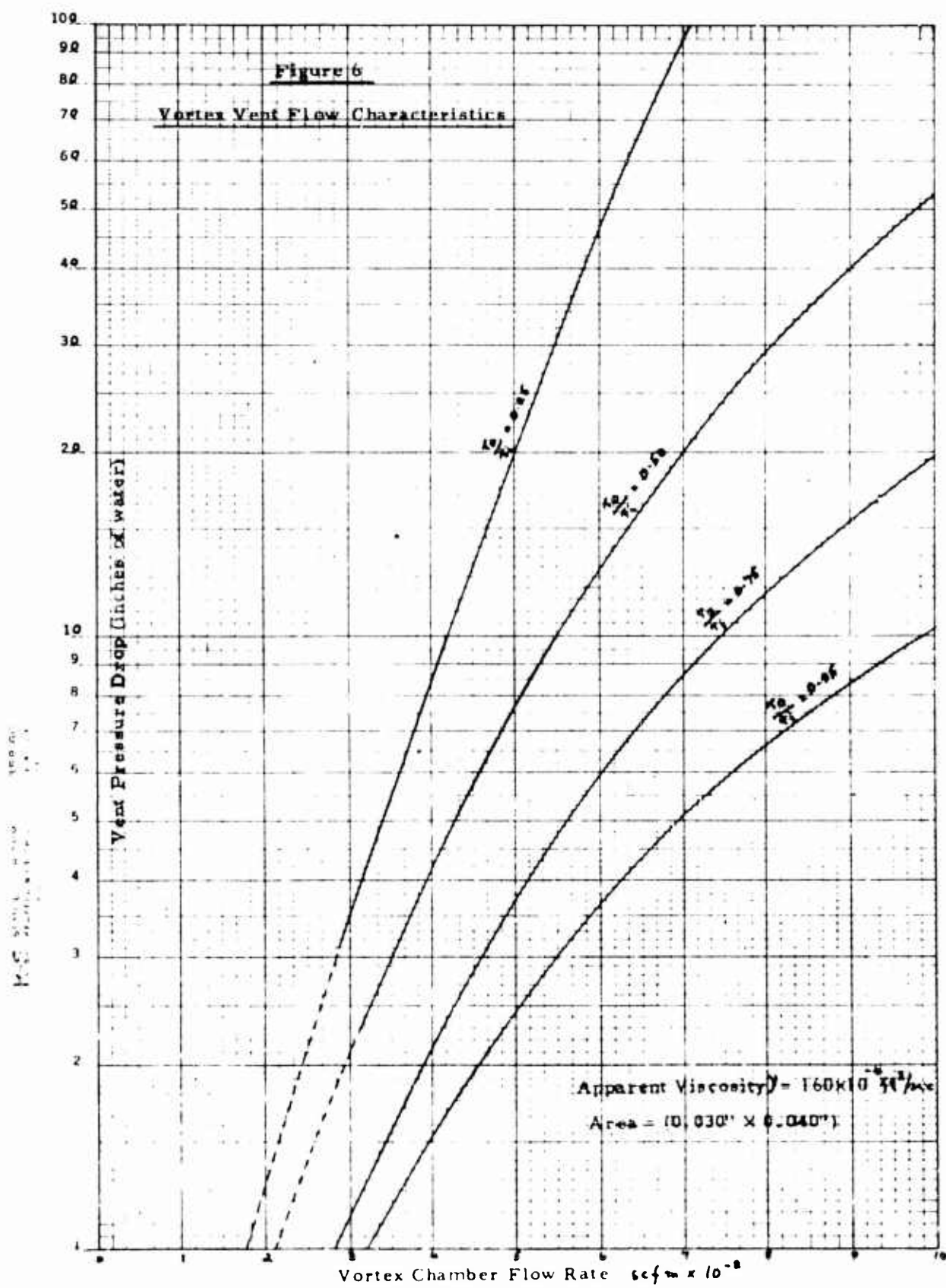
$$\frac{p_o - p_r}{\rho V_{\phi i}^2} = \frac{1}{2} \left\{ \left[1 - \left(\frac{r}{r_o} \right)^2 \right] \left[\left(\frac{V_o}{V_{\phi i}} \right)^2 - \left(\frac{V_{\phi r}}{V_{\phi i}} \right)^2 \right] \right\} \quad (22)$$

The flow characteristics of the vortex vent may be determined through the numerical evaluation of the derived vent flow equations, using a digital computer. Typical results for the mathematically predicted vortex non-dimensional pressure drop for a given vent configuration and various apparent viscosity values are plotted in Figure 4.

The dependency of the computed pressure drop across the vent upon the vent chamber radius ratio $\left(\frac{r_o}{r_i} \right)$ and upon the vent mass flow may be graphically illustrated as in Figures 5 and 6 respectively for typical values of air apparent viscosity (ν) which is assumed to be 100 times the laminar kinematic viscosity and vent input tangential velocity ($V_{\phi i}$).





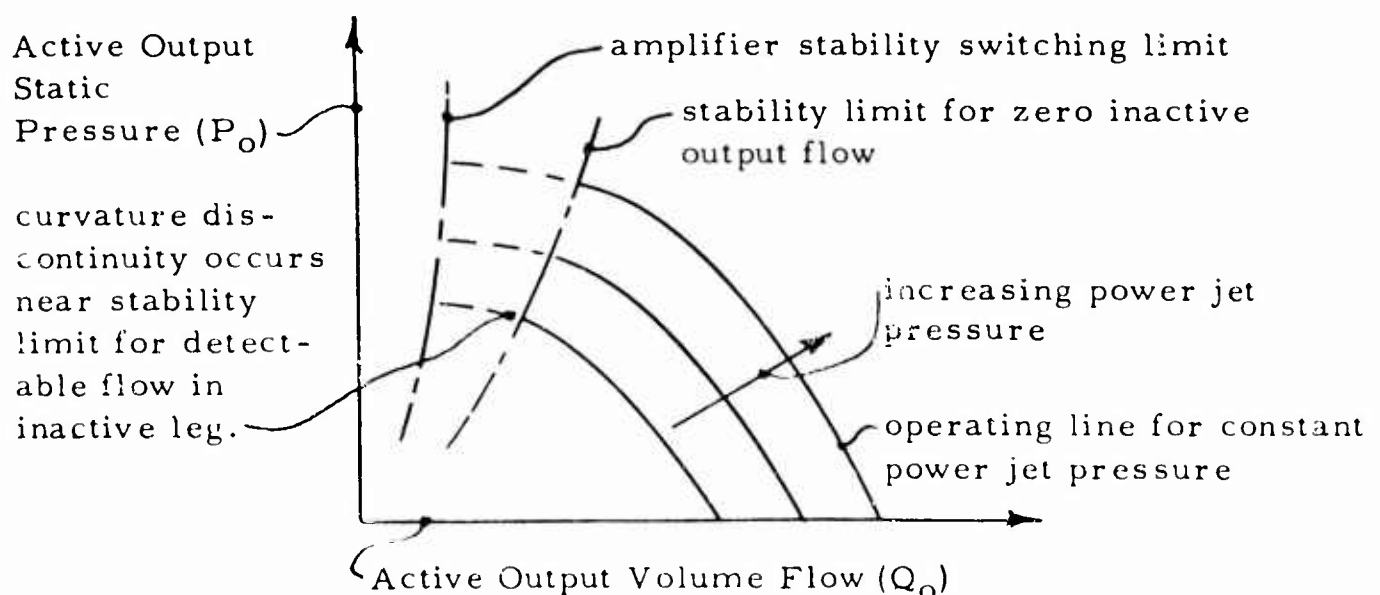


3.2.5 (continued)

It is necessary to "match" the resultant non-linear vent characteristics with the fluid amplifier stability characteristics to obtain the desired amplifier stability limit for a particular application. It is convenient to "match" the vent to the amplifier by experimental stability performance evaluation of the complete amplifier-vent combination rather than by analytical prediction, in that accurate evaluation of the vent flow apparent viscosity (ν) and input tangential velocity ($V_{\phi i}$) involves extensive experimentation.

Experimental optimization of the vortex vent configuration on the basis of the maximum amplifier impedance matching capability as defined by the amplifier stability limit results in a vent/amplifier combination which exhibits substantial reverse flow capability.

The stability limit is defined as the amplifier operating point at which flow out of the inactive output channel is initially detected. This stability limit does not necessarily coincide with the switching limit of a digital amplifier where the power jet attaches to the alternate wall. In particular, a very appreciable flow out of the inactive leg may occur prior to actual switching in a high stability amplifier, the resulting amplifier flow/pressure performance curves having the general characteristic as illustrated below:



4. VORTEX VENT INTEGRATION WITH FLUID AMPLIFIER

It is essential to locate the vortex vent in the optimum position relative to the fluid amplifier power jet in order to ensure that the vent inflow conditions required to induce swirl flow are attained. Additionally, it is advantageous to minimize the flow energy dissipation in the channels adjacent to the vent in order to maintain appreciable amplifier pressure recovery under high load conditions.

The detailed design of the vent/amplifier geometric configuration was established on the basis of qualitative flow visualization studies, using scaled-up models in a closed water tunnel. The incompressible air flow within the actual fluid amplifier is simulated in the water tunnel model by maintaining Reynold's No. equivalence. The flow within the transparent model is visualized by observing the monochromatic light reflected from aluminum particles suspended in the water. The light source is a narrow beam from a mercury arc lamp, projected through the transparent model in the plane of the amplifier profile. The flow pattern is viewed perpendicular to the plane of the light beam. Steady state flow patterns are readily recorded by time exposure photographs, approximate quantitative water velocities being determined from the photographs by measurement of individual particle light streak lengths, as related to the film exposure time.

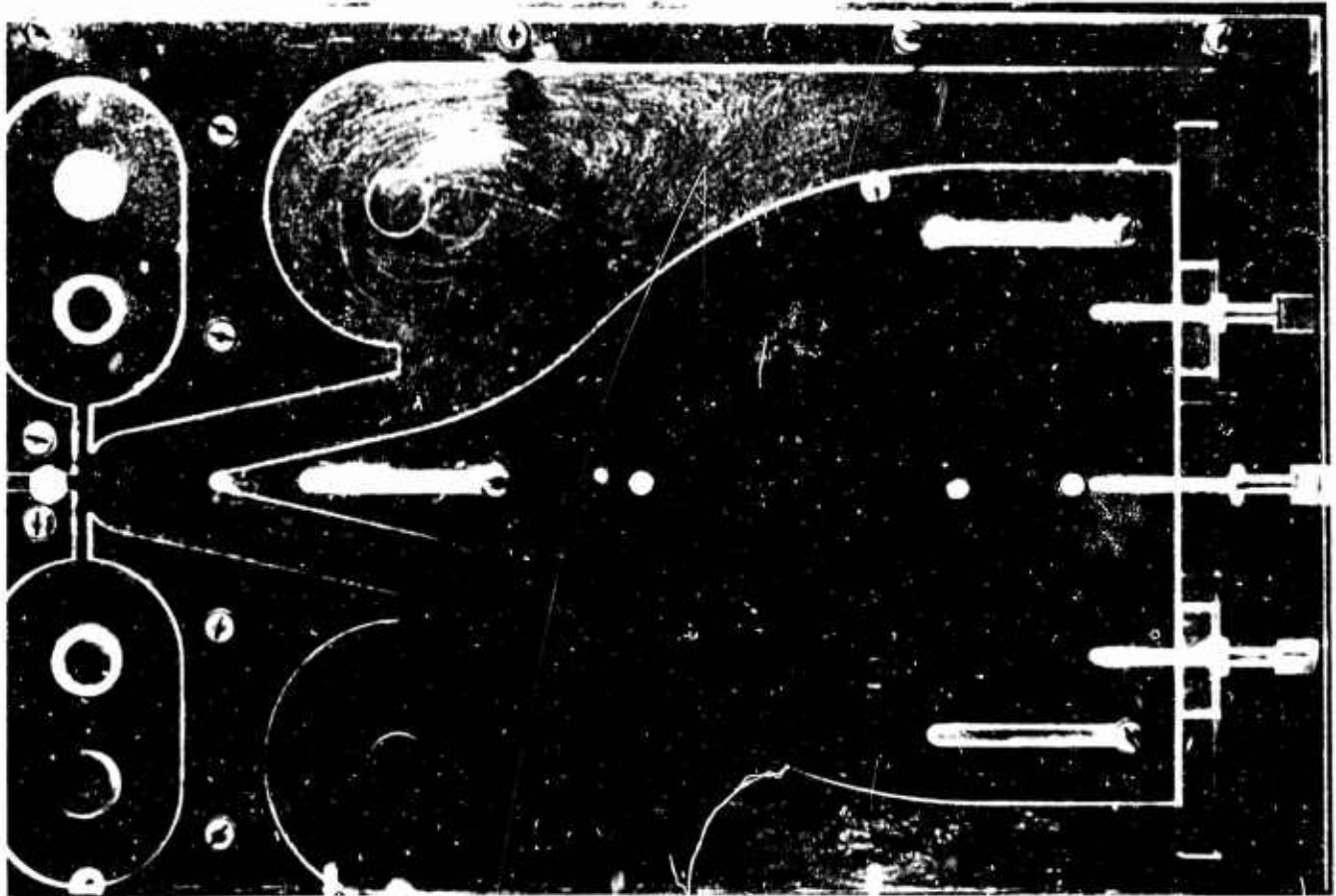
A typical example of Aluminum particle light reflection flow visualization within a vortex vented bistable fluid amplifier model is shown in Figure 7.

Correlation between the flow qualitatively assessed in the scaled-up models and the performance of actual fluid amplifiers operating with air has been consistently attained when Reynold's No. equivalence has been maintained.

Optimization of the vented fluid amplifier design by use of the flow visualization technique was carried out on the basis of maximum amplifier fan-out capability, wherein fan-out to one similar amplifier was assumed to constitute the maximum applied load.

Figure 7

Bistable Fluid Amplifier Flow Visualization with Aluminium
Light Reflection



Reynold's No. approximately 1800 based on nozzle width.

Moderate impedance at outlet channel causes swirl flow
in vortex vent.

4. (continued)

The overall performance characteristics of the resultant amplifier design, with a vortex vent "matched" to the amplifier to attain substantial reverse flow capabilities, are plotted in Figures 8 and 9. Figure 8 indicates the portion of the operational range from active leg maximum output flow to complete output flow blockage. The operating lines correspond to fluid amplifier operation with the control jets inactive and open to the atmosphere, resulting in the minimal stability condition likely to be encountered in system applications. Figure 9 indicates the magnitude of the reverse flow back into the active leg, up to the stability limit of the fluid amplifier. Two amplifier stability limits are plotted. The lower stability limit, at approximately 200% reverse flow, is the point at which the element switches out of the load when the test element control jet input ports are open to the atmosphere; the onset of detectable flow in the inactive output and the switching of the amplifier occurring simultaneously. The upper stability limit, at approximately 400% reverse flow, is the point at which the onset flow in the inactive leg is detected when both the control jet input ports are blocked; the actual amplifier switching limit being at appreciably higher reverse flow magnitudes.

5. REFLECTED WAVE ATTENUATION CHARACTERISTICS OF THE LATCHED VORTEX VENT

It is essential to isolate fluid amplifiers from the detrimental effects of reflected compression waves, to the extent of obviating fluid circuit instability, as indicated in Para. 1.

The wave disturbance transmission characteristics of the latched vortex vent configuration are effective to a large degree in attaining the desired characteristics of reflected compression wave blockage.

The pulse transmission characteristics of the vortex vent were experimentally obtained by passing externally generated short duration pressure pulses through an isolated plastic vortex vent model while monitoring the pressure variation with high response pressure transducers, as illustrated in Figure 10.

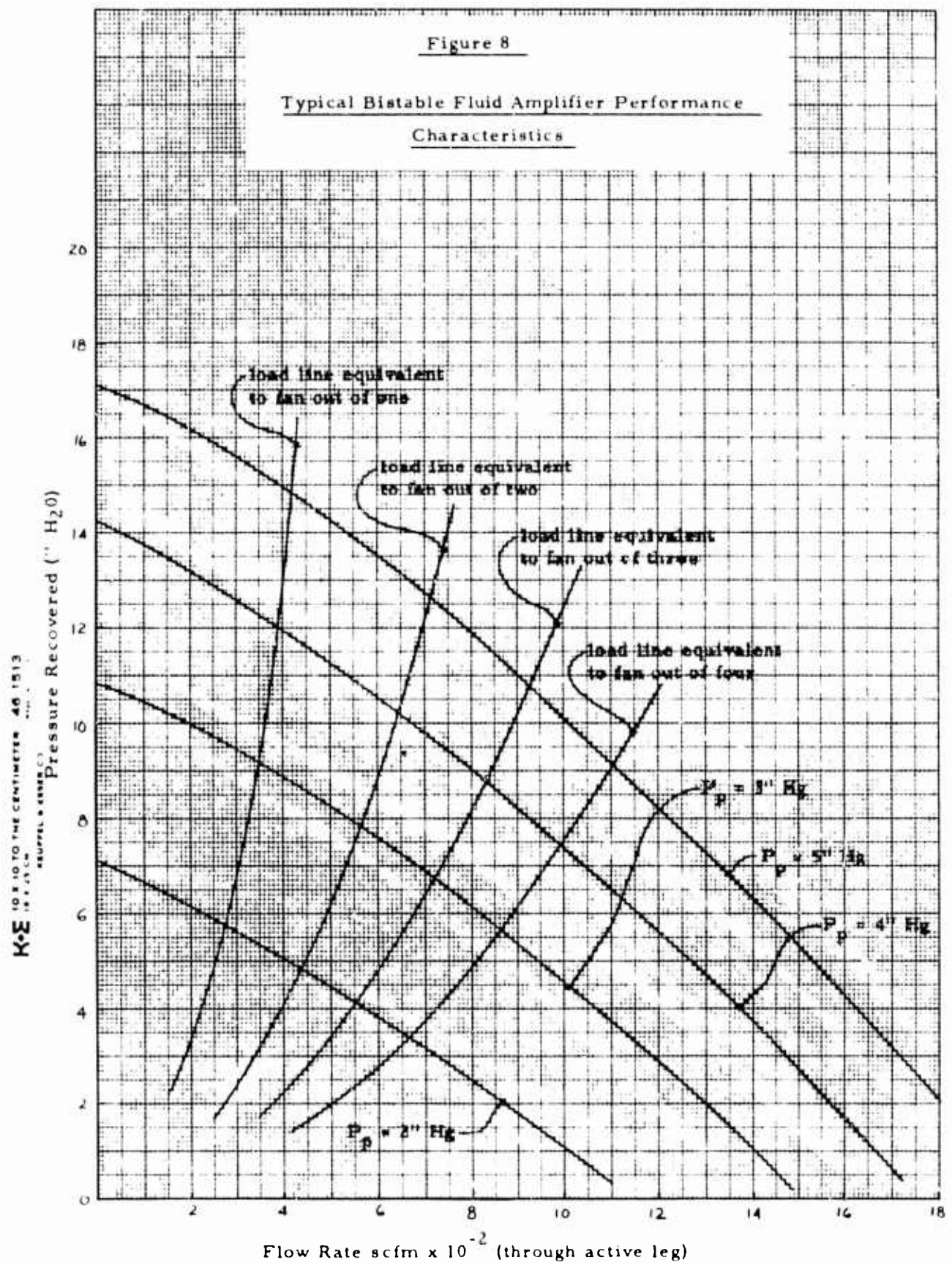


Figure 9

Bistable Fluid Amplifier Back Flow Characteristics

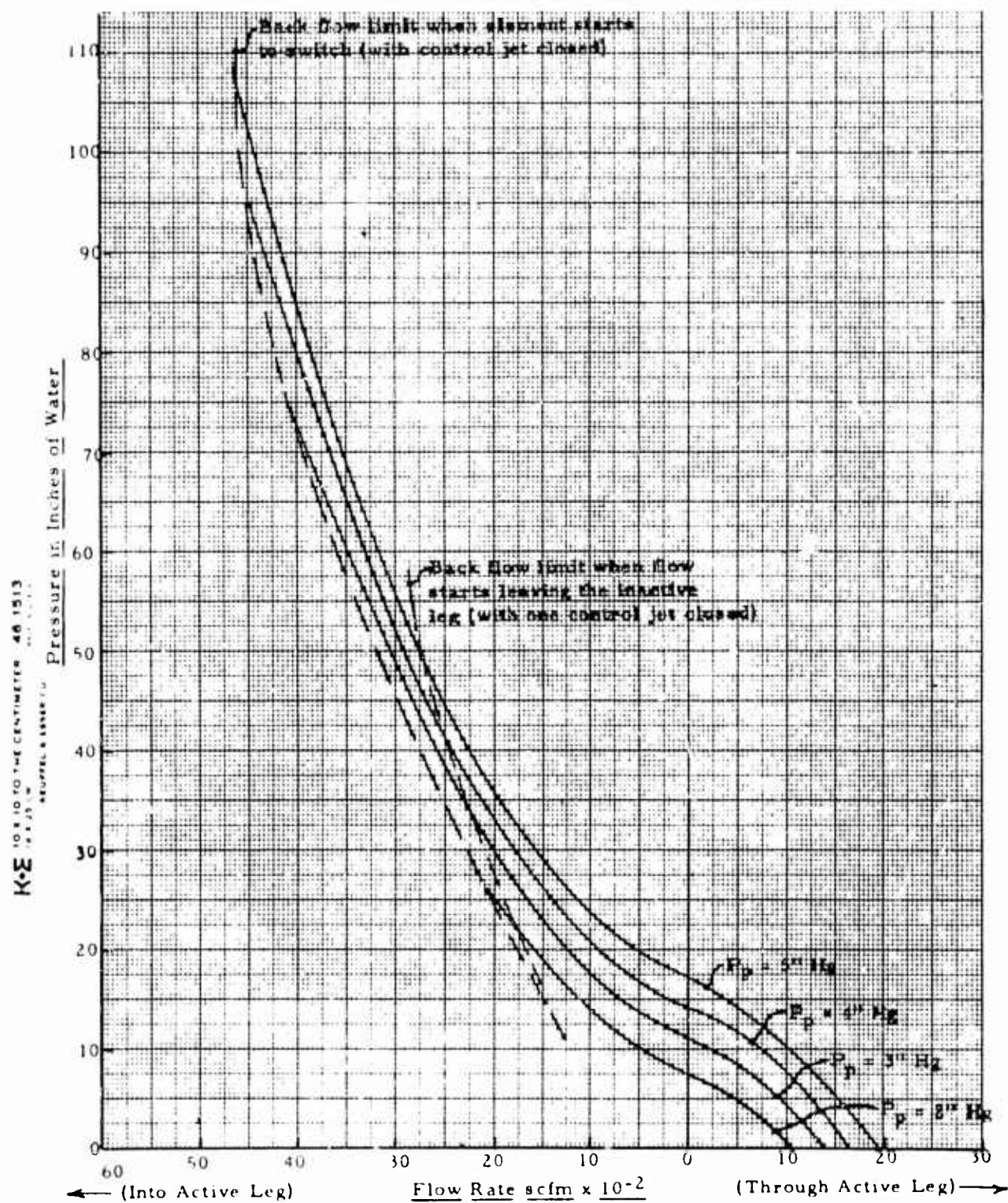
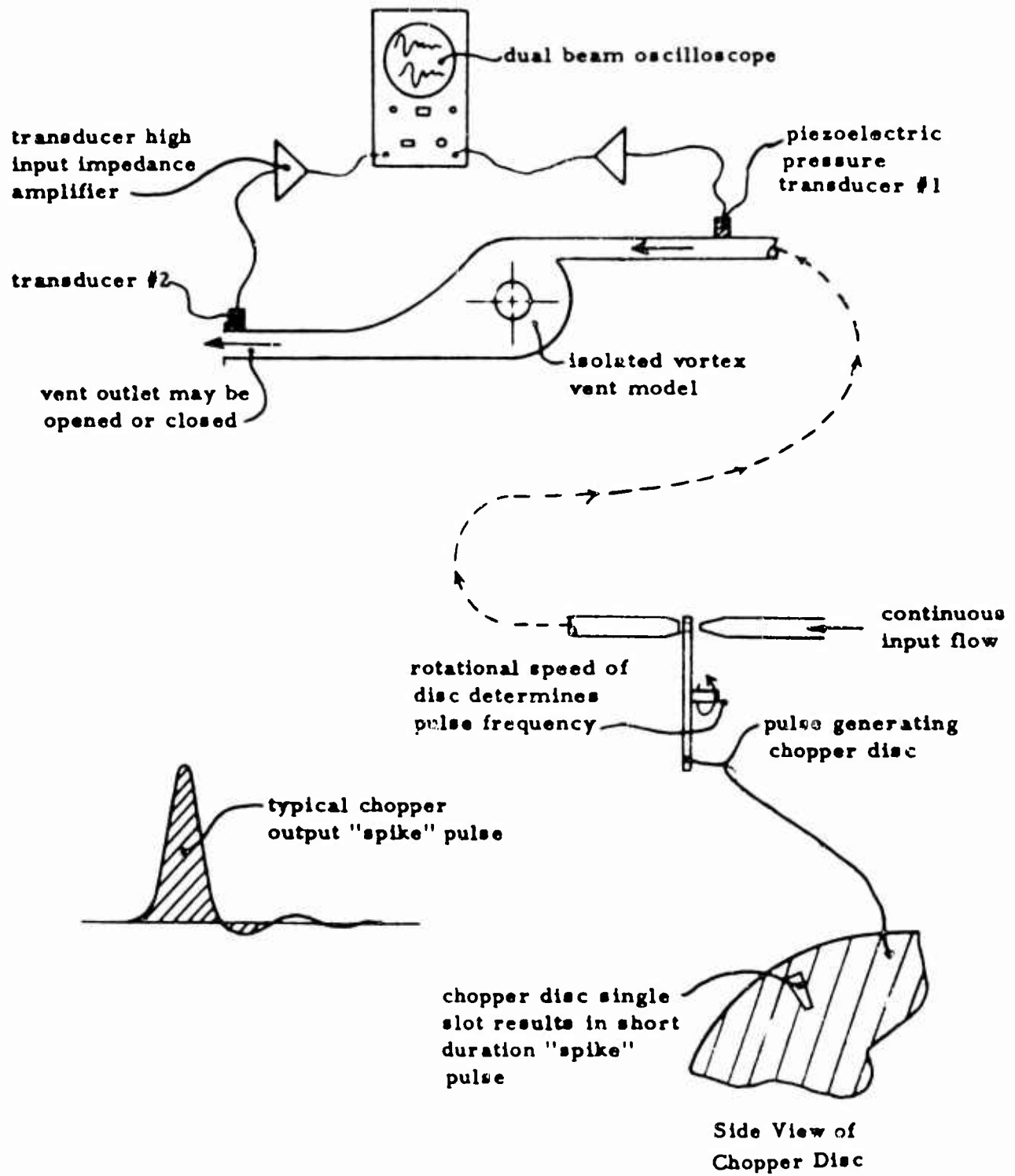


Figure 10

Vortex Vent Reflected Pulse Attenuation Experiment



5. (continued)

Fluid amplifier infinite impedance load was simulated by a completely blocked or "closed" vent outlet passage. Fluid amplifier low impedance load was simulated by a completely unrestricted or "open" vent outlet passage. Following the input of the chopper-generated square wave pressure pulse, experimental transient pressure variations are sensed by the two transducers and are recorded as oscilloscope trace photographs.

Variations in transmission line lengths between the transducers and the vortex vent allow for the identification of each experimentally observed pressure pulse by relating the experimentally observed time delays to the calculated distance travelled by the pulse at theoretical sonic velocity.

Extensive experimentation, including the time delay pulse identification process, indicates that the vortex vent orifice functions as a minor transmission line discontinuity for input compression pulses and as an open-ended pipe for reflected pulses.

Accordingly, in a vortex vented fluid amplifier the major portion of the incoming compression pulse generated by switching is transmitted through the vent region, while the remaining small portion is reflected as a rarefaction wave back from the vent into the interaction region. This vent reflected rarefaction wave increases, rather than decreases, the amplifier stability in that it has the effect of reducing the load impedance (see Case 1 of Figure 2). Subsequent rarefaction and compression waves reflected from downstream circuit line discontinuities are largely reflected by the vortex vent as compression and rarefaction waves, respectively (see Cases 2 and 3 of Figure 2), the experimental data suggesting a vent reflected compression wave blockage capability in the order of 80% to 90% effective.

Hence, circuit line discontinuity generated pressure waves are largely contained between the discontinuity and the vent, the wave amplitude being attenuated exponentially with repeated reflections.

6. CONCLUSIONS

It has been shown that pure fluid amplifiers, both digital and proportional, designed to incorporate the latched vortex vent, can be made to perform independently of the downstream loading conditions. Some reasonably high stability elements with matched vortex vents can even be made to withstand a substantial amount of reverse flow through the active leg without false switching. The outstanding capability of the vortex vent in attenuating reflected compression pulses minimizes malfunctions likely to occur in integrated fluid logic circuits. Fluid elements, especially digital elements, are automatically matched to their particular downstream loading conditions.

The mathematical analysis of the viscous vortex flow provides an indication of the vortex vent performance dependency upon the vent geometric configuration.

This analysis also gives an insight into the mechanism of viscous swirl flow within thin cylindrical chambers, thereby providing a basis for the analysis of the flow phenomena associated with other types of fluid devices.

LIST OF SYMBOLS

Symbol

ν	Apparent Kinematic viscosity
μ	Absolute viscosity
ρ	Density
τ	Fluid Shear stress
α	$\frac{Q}{2\pi h \nu}$ Dimensionless parameter
h	Height of the vortex chamber
p	Static Pressure
Q	Volume flow
r	Radius of the vortex chamber
t	Time
V	Velocity
u	Local velocity

Subscripts

r	Radial component
ϕ	Tangential component
z	Axial component
i	Initial
o	Interface between free and forced vortex

UNCLASSIFIED

Security Classification

DOCUMENT CONTROL DATA - R&D		
(Security classification of title, body of abstract and indexing annotation must be entered when the overall report is classified)		
1 ORIGINATING ACTIVITY (Corporate author) Harry Diamond Laboratories, Washington, D. C. 20436		2a REPORT SECURITY CLASSIFICATION UNCLASSIFIED
		2b GROUP
3 REPORT TITLE PROCEEDINGS OF THE FLUID AMPLIFICATION SYMPOSIUM—Volume I, October 1965		
4 DESCRIPTIVE NOTES (Type of report and inclusive dates) Compilation of 17 papers on fluid amplification and devices.		
5 AUTHOR(S) (Last name, first name, initial)		
6 REPORT DATE October 1965	7a TOTAL NO OF PAGES 309	7b NO OF REFS
8a. CONTRACT OR GRANT NO. A. PROJECT NO. DA-11PC10:01A001 oAMCMS Code 5011.11.71100 oADL Proj No. 31100	9a ORIGINATOR'S REPORT NUMBER(S)	
	9b OTHER REPORT NO(S) (Any other numbers that may be assigned this report)	
10 AVAILABILITY/LIMITATION NOTICES Qualified requesters may obtain copies of this report from DDC. DDC release to Clearinghouse for Federal Scientific and Technical Information is authorized.		
11 SUPPLEMENTARY NOTES	12 SPONSORING MILITARY ACTIVITY Hq. AMC	
13 ABSTRACT This document is the first of five volumes, covering the October 1965 symposium on fluid amplification at the Harry Diamond Laboratories. These volumes include 17 papers, prepared by personnel from various Government agencies, universities, and industrial firms.		

DD FORM 1473
1 JAN 64UNCLASSIFIED
Security Classification

389

UNCLASSIFIED
Security Classification

1a KEY WORDS	LINK A		LINK B		LINK C	
	ROLE	WT	ROLE	WT	ROLE	WT
Pneumatic control systems						
Fluid circuit theory						
Flow isolation of fluid amplifiers						
Fluid amplifiers—theoretical analysis						

INSTRUCTIONS

1. **ORIGINATING ACTIVITY:** Enter the name and address of the contractor, subcontractor, grantee, Department of Defense activity or other organization (corporate author) issuing the report.

2a. **REPORT SECURITY CLASSIFICATION:** Enter the overall security classification of the report. Indicate whether "Restricted Data" is included. Marking is to be in accordance with appropriate security regulations.

2b. **GROUP:** Automatic downgrading is specified in DoD Directive 5200.10 and Armed Forces Industrial Manual. Enter the group number. Also, when applicable, show that optional markings have been used for Group 3 and Group 4 as authorized.

3. **REPORT TITLE:** Enter the complete report title in all capital letters. Titles in all cases should be unclassified. If a meaningful title cannot be selected without classification, show title classification in all capitals in parentheses immediately following the title.

4. **DESCRIPTIVE NOTES:** If appropriate, enter the type of report, e.g., interim, progress, summary, annual, or final. Give the inclusive dates when a specific reporting period is covered.

5. **AUTHOR(S):** Enter the name(s) of author(s) as shown on or in the report. Enter last name, first name, middle initial. If military, show rank and branch of service. The name of the principal author is an absolute minimum requirement.

6. **REPORT DATE:** Enter the date of the report as day, month, year, or month, year. If more than one date appears on the report, use date of publication.

7a. **TOTAL NUMBER OF PAGES:** The total page count should follow normal pagination procedures, i.e., enter the number of pages containing information.

7b. **NUMBER OF REFERENCES:** Enter the total number of references cited in the report.

8a. **CONTRACT OR GRANT NUMBER:** If appropriate, enter the applicable number of the contract or grant under which the report was written.

8b, 8c, & 8d. **PROJECT NUMBER:** Enter the appropriate military department identification, such as project number, subproject number, system numbers, task number, etc.

9a. **ORIGINATOR'S REPORT NUMBER(S):** Enter the official report number by which the document will be identified and controlled by the originating activity. This number must be unique to this report.

9b. **OTHER REPORT NUMBER(S):** If the report has been assigned any other report numbers (either by the originator or by the sponsor), also enter this number(s).

10. **AVAILABILITY/LIMITATION NOTICES:** Enter any limitations on further dissemination of the report, other than those

imposed by security classification, using standard statements such as:

- (1) "Qualified requesters may obtain copies of this report from DDC."
- (2) "Foreign announcement and dissemination of this report by DDC is not authorized."
- (3) "U. S. Government agencies may obtain copies of this report directly from DDC. Other qualified DDC users shall request through _____."
- (4) "U. S. military agencies may obtain copies of this report directly from DDC. Other qualified users shall request through _____."
- (5) "All distribution of this report is controlled. Qualified DDC users shall request through _____."

If the report has been furnished to the Office of Technical Services, Department of Commerce, for sale to the public, indicate this fact and enter the price, if known.

11. **SUPPLEMENTARY NOTES:** Use for additional explanatory notes.

12. **SPONSORING MILITARY ACTIVITY:** Enter the name of the departmental project office or laboratory sponsoring (paying for) the research and development. Include address.

13. **ABSTRACT:** Enter an abstract giving a brief and factual summary of the document indicative of the report, even though it may also appear elsewhere in the body of the technical report. If additional space is required, a continuation sheet shall be attached.

It is highly desirable that the abstract of classified reports be unclassified. Each paragraph of the abstract shall end with an indication of the military security classification of the information in the paragraph, represented as (TS), (S), (C), or (U).

There is no limitation on the length of the abstract. However, the suggested length is from 150 to 225 words.

14. **KEY WORDS:** Key words are technically meaningful terms or short phrases that characterize a report and may be used as index entries for cataloging the report. Key words must be selected so that no security classification is required. Identifiers, such as equipment model designation, trade name, military project code name, geographic location, may be used as key words but will be followed by an indication of technical context. The assignment of links, rules, and weights is optional.

UNCLASSIFIED
Security Classification



DEPARTMENT OF THE ARMY

HARRY DIAMOND LABORATORIES

WASHINGTON, D.C. 20438 Mr. Kirshner/cg/7556

IN REPLY REFER TO:
AMXDO-RCA

1 NOV 1965

TO : Recipients of Fluid Amplification Symposium Proceedings
Volume I, October 1965

FROM : Chief, Fluid Systems Branch, HDL

SUBJECT: Errata in "A Definition of the Mechanical Potential Necessary
to a Fluid Circuit Theory," by Joseph M. Kirshner, HDL,
(page 248)

Page 248, lines following equation (6) should read:

"...where ds_r and ds_i are the reversible and irreversible portions of the entropy change associated with heat and viscous effects, respectively; since the reversible portion of the entropy is due to the heat flux,

$$\frac{d}{dz} \int_{A_1} (T ds_r) \rho v \cdot n dA = \alpha$$

and therefore equation 5 becomes

$$\frac{d}{dz} \int_{A_1} \left[T ds_i + \frac{v^2}{2} + \int \frac{dp}{\rho} \right] \rho v \cdot n dA = 0 \quad (7) \dots "$$

AD 623455

X